



# Supported Cobalt Oxide Catalysts for the Preferential Oxidation of Carbon Monoxide: *An in situ* Investigation

by

**Thulani Mvelo Nyathi**

MSc(Eng) in Chemical Engineering, University of Cape Town (2015)

BSc(Hons) in Chemistry, University of Cape Town (2013)

BSc in Chemistry and Biochemistry, University of Cape Town (2012)

Thesis presented to the University of Cape Town in fulfilment of the requirements  
for the degree of

**Doctor of Philosophy in Chemical Engineering**

Catalysis Institute – Department of Chemical Engineering

Faculty of Engineering and the Built Environment

University of Cape Town

South Africa

April 2021

The copyright of this thesis vests in the author. No quotation from it or information derived from it is to be published without full acknowledgement of the source. The thesis is to be used for private study or non-commercial research purposes only.

Published by the University of Cape Town (UCT) in terms of the non-exclusive license granted to UCT by the author.



*“Only those who will risk going too far, can possibly find out how far they can go.”*

*—Thomas Stearns Eliot*



# Declaration

I, **Mr. Thulani Mvelo Nyathi**, hereby declare that the work on which this thesis is based, is my original work (except where acknowledgements indicate otherwise) and that neither the whole work nor any part of it has been, is being, or is to be submitted for another degree in this or any other university. I authorise the University to reproduce for the purpose of research either the whole or any portion of the contents in any manner whatsoever.

Signature:

Signed by candidate

Date: **13 April 2021**

**Mr. T. M. Nyathi**



# Acknowledgements

I would firstly like to thank God for the strength and drive which enabled me to complete my Ph.D. project. All of this would not have been possible without His will and grace.

A very special thanks goes to my UCT supervisors, Prof. Michael Claeys and A/Prof. Nico Fischer, for giving me the opportunity to complete my Ph.D. degree under their supervision. I am particularly grateful to Prof. Claeys for his trust and confidence in me, his constant support, the knowledge and time he has dedicated towards my entire postgraduate research training. I would like to also thank Dr. Andrew York, from the Johnson Matthey Technology Centre (Reading, UK), for continuing to work with Prof. Claeys and I after the MSc(Eng) project and for his advice throughout the duration of this work.

To the current and past members of Prof. Claeys's and A/Prof. Fischer's research group (*i.e.*, 2016 – 2020), their assistance in the lab, motivation and friendship is greatly appreciated. I wish each of them the very best of luck for the future.

Special thanks are also relayed to the National Research Foundation (NRF) for awarding me the Innovation Doctoral Scholarship (2017 – 2019) and to Johnson Matthey p.l.c. for providing funding for the operational costs of the project (2016 – 2019). Additional funding from the DSI-NRF Centre of Excellence in Catalysis (*c\*change*), *via* UCT's Chemical Engineering department (2016 – 2020), is also greatly appreciated.

My gratitude also extends to the team in the Analytical Laboratory of the Chemical Engineering department for their assistance with ICP-OES, N<sub>2</sub> physisorption and H<sub>2</sub>-TPR. I would also like to thank Dr. Jaco Olivier and Prof. Jan Neethling for the use of the advanced HRTEM instrument at the Nelson Mandela University. Dr. Olivier is particularly thanked for the extensive analyses he performed and his involvement in discussing the obtained data. Dr. Peter Wells (University of Southampton), Dr. Emma Gibson (Glasgow University), Dr. Nitya Ramanan (UK Catalysis Hub) and Mr. Monik Panchal (UK Catalysis Hub) are gratefully acknowledged for carrying out the *ex situ* XAS analysis and for their assistance with the data interpretation. With regards to the XAS analysis, the funding from the GCRF (*via* the START project) is also gratefully acknowledged.

Finally, I would like to thank my family back in Durban, and my fiancée in Cape Town for their constant love, patience and support throughout this Ph.D. journey. Without them, I would not be where I am today.

*This thesis is dedicated to my late paternal grandmother, who passed away in July 2020.  
She will always be missed in our family.*

## Synopsis

The study presented in this thesis has placed great focus on  $\text{Co}_3\text{O}_4$ -based catalysts for producing CO-free  $\text{H}_2$ -rich gas streams for power generation using proton-exchange or polymer electrolyte membrane fuel cells (PEMFCs). The removal of CO (0.5 – 2%) is essential as it negatively affects the performance of the Pt-based anode catalyst of PEMFCs. Among the various CO removal processes reported, the preferential oxidation of CO (CO-PrOx) to  $\text{CO}_2$  is a very attractive catalytic process for decreasing the CO content to acceptable levels (*i.e.*, <10 ppm) for operating the PEMFC.  $\text{Co}_3\text{O}_4$ -based catalysts have shown very good catalytic activity for the total oxidation of CO in the absence of  $\text{H}_2$ ,  $\text{H}_2\text{O}$  and  $\text{CO}_2$ . More specifically, the performance of  $\text{Co}_3\text{O}_4$  is known to be influenced by numerous factors such as particle size, particle shape, and the preparation method. As a result, there has also been growing interest in  $\text{Co}_3\text{O}_4$  as a cheaper alternative to noble metals for the CO-PrOx reaction.

However, the  $\text{H}_2$  (40 – 75%) in the CO-PrOx feed can also react with  $\text{O}_2$  (0.5 – 4%) to produce  $\text{H}_2\text{O}$ , which consequently decreases the selectivity towards  $\text{CO}_2$  (based on the total  $\text{O}_2$  conversion). Aside from  $\text{H}_2$ , the CO-PrOx feed also contains  $\text{H}_2\text{O}$  and  $\text{CO}_2$  which may affect the CO oxidation process as well. The use of  $\text{Co}_3\text{O}_4$  as the active catalyst for CO-PrOx can have shortcomings – the main one being its relatively high susceptibility to reduction by  $\text{H}_2$ , forming less active and selective Co-based phases (*viz.*, CoO and metallic Co). Particularly over metallic Co, the conversion pathway of CO can change from oxidation to hydrogenation, forming  $\text{CH}_4$  instead of  $\text{CO}_2$ . Therefore, the first objective of the work carried out was to investigate the effect of the gas feed components (*viz.*,  $\text{H}_2$ ,  $\text{H}_2\text{O}$  and  $\text{CO}_2$ ; co-fed individually and simultaneously) on the progress of the CO oxidation reaction and the phase stability of  $\text{Co}_3\text{O}_4$  over a wide temperature range (50 – 450 °C). It should be noted that the presence of these three gases can also introduce more side reactions, *viz.*, the forward and reverse water-gas shift, respectively, as well as CO and  $\text{CO}_2$  methanation, respectively.

In the supported state, the choice of support, as well as the nature and/or strength of the interaction between the  $\text{Co}_3\text{O}_4$  nanoparticles and the support can influence catalytic performance and phase stability. CO oxidation over metal oxides such as  $\text{Co}_3\text{O}_4$ , is believed to proceed *via* the Mars-van Krevelen mechanism, which depends on the surface of the catalyst being reducible in order to release lattice oxygen species. Generally, strong metal-support interactions (MSIs) or nanoparticle-support interactions (NPSIs) can hinder the removal of surface (and bulk) oxygen species, which

can negatively affect the catalytic performance. Strong interactions can also promote the solid-state reaction between the species from the nanoparticle with those from the support, leading to the formation of metal-support compounds (MSCs). The supports  $\text{SiO}_2$ ,  $\text{TiO}_2$  and  $\text{Al}_2\text{O}_3$  are well known for this phenomenon, and consequently, allow for the formation of silicates, titanates and aluminates, respectively. Support materials such as  $\text{CeO}_2$ ,  $\text{ZrO}_2$  and  $\text{SiC}$ , are not known for interacting strongly with nanoparticles and often do not react to form MSCs. Therefore, the second objective of this Ph.D. study was to investigate the effect of different support materials (*viz.*,  $\text{CeO}_2$ ,  $\text{ZrO}_2$ ,  $\text{SiC}$ ,  $\text{SiO}_2$ ,  $\text{TiO}_2$  and  $\text{Al}_2\text{O}_3$ ) on the catalytic performance and phase stability of  $\text{Co}_3\text{O}_4$  under different CO-PrOx reaction gas environments.

Before carrying out the lab-based experiments, theoretical evaluations were performed by means of thermodynamic calculations based on the Gibbs-Helmholtz Equation. The calculations helped determine the equilibrium conversions of each gas-phase reaction, revealing the extent to which a certain reaction can be expected to take place between 0 and 500 °C. Thermodynamic calculations were also performed to predict the stability of  $\text{Co}_3\text{O}_4$ ,  $\text{CoO}$  and metallic  $\text{Co}$  at different temperatures and partial pressure ratios of  $\text{H}_2$ -to- $\text{H}_2\text{O}$ . In the case of supported nanoparticles, the formation of the Co-support compounds -  $\text{Co}_2\text{SiO}_4$ ,  $\text{CoTiO}_3$  and  $\text{CoAl}_2\text{O}_4$  from  $\text{SiO}_2$ ,  $\text{TiO}_2$  and  $\text{Al}_2\text{O}_3$ , respectively - was shown to be thermodynamically feasible in  $\text{H}_2$ - $\text{H}_2\text{O}$  mixtures.

Unsupported  $\text{Co}_3\text{O}_4$  nanoparticles were synthesised using the reverse microemulsion technique, while supported  $\text{Co}_3\text{O}_4$  nanoparticles were prepared using incipient wetness impregnation. *In situ* PXRD- and magnetometry-based CO-PrOx catalytic testing was performed in different gas environments as depicted in Figure S.1. The different conditions chosen allowed for the effect of  $\text{H}_2$ ,  $\text{H}_2\text{O}$  and  $\text{CO}_2$  on the progress of the CO oxidation reaction and on the reducibility of  $\text{Co}_3\text{O}_4$  to be studied.

For the first time, this work has identified all the possible gas-phase side reactions (in addition to CO oxidation) that can take place under CO-PrOx conditions. Each reaction could be linked to a specific Co-based phase which is responsible for its occurrence. Furthermore, the temperatures and the extent to which these reactions take place were in-line with the predictions from the thermodynamic calculations. The presence of a support does stabilise the  $\text{Co}_3\text{O}_4$  (and  $\text{CoO}$ ) phase over a wide temperature range. Over the weakly-interacting supports (*i.e.*,  $\text{ZrO}_2$  and  $\text{SiC}$ ), high CO conversions (91.5% and 80.8%, respectively) and  $\text{O}_2$  selectivities (55.2% and 55.9%, respectively) to  $\text{CO}_2$  could be obtained, in addition to the improved phase stability of  $\text{Co}_3\text{O}_4$ . In agreement with the thermodynamic predictions, the presence of  $\text{Co}_2\text{SiO}_4$  (7.7%),  $\text{CoTiO}_3$  (13.8% (from  $\text{TiO}_2$ -

anatase) and 8.9% (from  $\text{TiO}_2$ -rutile), and  $\text{CoAl}_2\text{O}_4$  (26.6%) was confirmed using *ex situ* X-Ray Absorption Spectroscopy in the spent samples of  $\text{Co}_3\text{O}_4/\text{SiO}_2$ ,  $\text{Co}_3\text{O}_4/\text{TiO}_2$ -anatase,  $\text{Co}_3\text{O}_4/\text{TiO}_2$ -rutile and  $\text{Co}_3\text{O}_4/\text{Al}_2\text{O}_3$ , respectively, after CO-PrOx. These three samples also exhibited relatively low CO oxidation activities and selectivities, as well as low  $\text{Co}_3\text{O}_4$  reducibility.

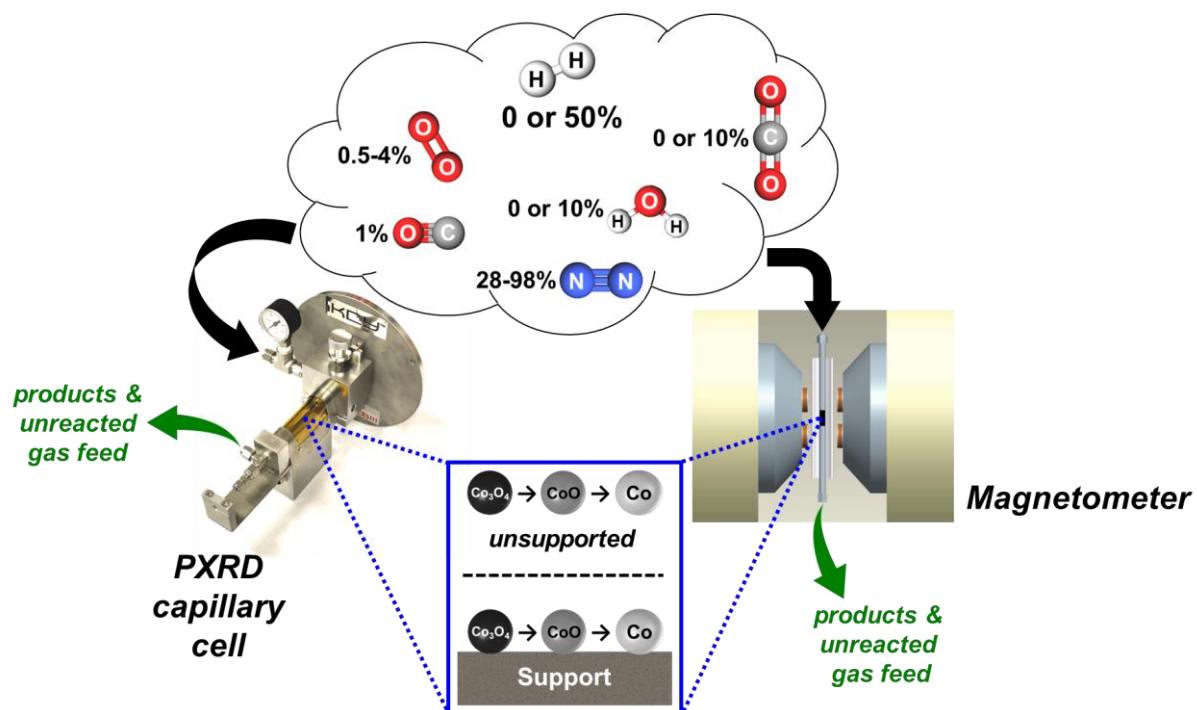


**Figure S.1:** Graphical representation of CO-PrOx performed over un-/supported  $\text{Co}_3\text{O}_4$  catalysts in different gas environments, coupled with the use of *in situ* catalyst characterisation techniques.



# Contents

<b>List of Figures</b>	<b>vii</b>
<b>List of Tables</b>	<b>xix</b>
<b>Nomenclature</b>	<b>xxi</b>
<b>Chapter 1: Introduction</b>	<b>1</b>
1.1. Electrical Energy from Fuel Cells	1
1.2. Hydrogen Production for PEM Fuel Cells	3
References	8
<b>Chapter 2: Literature Review</b>	<b>11</b>
2.1. Catalysts for the Preferential Oxidation of Carbon Monoxide	11
2.1.1. Noble metals	11
2.1.2. Base metal oxides	12
2.2. Effect of the Support on CO-PrOx Catalysts	14
2.2.1. Weakly interacting supports	15
2.2.2. Strongly interacting supports	16
2.2.3. Inert supports	18
2.3. Effect of the Gas Feed Components on CO-PrOx Catalysts	19
2.3.1. Effect of hydrogen	19
2.3.2. Effect of water and carbon dioxide	26
2.3.3. Effect of varying oxygen feed levels	28
2.4. Catalyst Deactivation	30
2.4.1. Gas-solid and solid-solid reactions	31
2.4.2. Sintering	32
2.4.3. Poisoning	34
2.4.4. Other deactivation mechanisms	34
2.5. Catalyst Preparation	35
2.5.1. Conventional methods	35
2.5.2. Model catalyst synthesis: Reverse microemulsion technique	37
2.6. <i>In situ</i> Catalyst Characterisation: Magnetism and Magnetometry	40
References	47

<b>Chapter 3: Scope of Study</b>	<b>57</b>
3.1. Context and Objectives	57
3.2. Research Approach	58
References	60
<b>Chapter 4: Methodology</b>	<b>63</b>
4.1. Thermodynamic Calculations	63
4.2. Catalyst Preparation	65
4.2.1. Chemicals	65
4.2.2. Preparation of unsupported Co <sub>3</sub> O <sub>4</sub> nanoparticles using the Reverse Microemulsion technique	65
4.2.3. Preparation of supported Co <sub>3</sub> O <sub>4</sub> nanoparticles using Incipient Wetness Impregnation	67
4.3. <i>Ex situ</i> Catalyst Characterisation	69
4.3.1. Powder X-Ray Diffraction	69
4.3.2. Scanning Transmission Electron Microscopy-Electron Energy Loss Spectroscopy	71
4.3.3. Nitrogen Physisorption	72
4.3.4. Inductively Coupled Plasma-Optical Emission Spectrometry	72
4.3.5. X-Ray Absorption Spectroscopy	72
4.4. <i>In situ</i> Catalyst Characterisation and Testing	73
4.4.1. Conventional Hydrogen-Temperature Programmed Reduction	73
4.4.2. Powder X-Ray Diffraction	75
4.4.3. Magnetometry	81
4.4.4. Product Analysis	87
References	91
<b>Chapter 5: <i>Ex situ</i> Catalyst Characterisation</b>	<b>95</b>
5.1. Thermodynamic Calculations on the Bulk Phase Transformation of Cobalt Precursors during Calcination	95
5.1.1. Oxidation/Decomposition of Co(OH) <sub>2</sub>	95
5.1.2. Decomposition of Co(NO <sub>3</sub> ) <sub>2</sub> on support materials	97
5.2. Powder X-Ray Diffraction and X-Ray Absorption Spectroscopy	100
5.2.1. Unsupported Co(OH) <sub>2</sub> and Co <sub>3</sub> O <sub>4</sub>	100
5.2.2. Support materials	102
5.2.3. Supported Co <sub>3</sub> O <sub>4</sub>	105
5.3. Scanning Transmission Electron Microscopy-Electron Energy Loss Spectroscopy	109

---

5.4. Nitrogen Physisorption and Inductively Coupled Plasma-Optical Emission Spectrometry	118
5.5. Summary: <i>Catalyst Synthesis and ex situ Characterisation</i>	119
References	121
<b>Chapter 6: Thermodynamic Calculations and Experimental Evaluation of the Stability of Cobalt-based Compounds</b>	<b>125</b>
6.1. Thermodynamic Calculations on the Stability of Cobalt-based Compounds in Hydrogen-Water Mixtures	125
6.1.1. Unsupported Co-based compounds	125
6.1.2. Supported Co-based compounds	128
6.2. Reduction of Unsupported and Supported Co <sub>3</sub> O <sub>4</sub> in Hydrogen	132
6.2.1. Unsupported Co <sub>3</sub> O <sub>4</sub>	132
6.2.2. Supported Co <sub>3</sub> O <sub>4</sub>	136
6.3. Summary: <i>Stability of Un-/Supported Co<sub>3</sub>O<sub>4</sub> in Hydrogen-Water Mixtures</i>	145
References	146
<b>Chapter 7: Thermodynamic Calculations and Experimental Evaluation of CO-PrOx and Side Reactions</b>	<b>151</b>
7.1. Thermodynamic Calculations on Gas-Phase Reaction Equilibria	151
7.2. Reduction of Unsupported Co <sub>3</sub> O <sub>4</sub> under Different Gas Environments	158
7.2.1. Reduction under co-fed H <sub>2</sub> and CO	158
7.2.2. Reduction under co-fed H <sub>2</sub> and O <sub>2</sub>	162
7.2.3. Reduction under co-fed H <sub>2</sub> and H <sub>2</sub> O or co-fed H <sub>2</sub> and CO <sub>2</sub>	164
7.2.4. Reduction under co-fed CO and H <sub>2</sub> O	168
7.3. Summary: <i>Evaluation of CO-PrOx and Side Reactions</i>	169
References	173
<b>Chapter 8: Support Material Effects on the Preferential Oxidation of Carbon Monoxide</b>	<b>177</b>
8.1. Dry CO-PrOx over Unsupported Co <sub>3</sub> O <sub>4</sub>	178
8.2. Dry CO-PrOx over Supported Co <sub>3</sub> O <sub>4</sub>	184
8.3. Evaluation of the Reduction Mechanism of Un-/Supported Co <sub>3</sub> O <sub>4</sub>	200
8.4. Characterisation of Spent Catalysts after Dry CO-PrOx using <i>ex situ</i> (HR)STEM-EELS	204
8.5. Characterisation of Spent Catalysts after Dry CO-PrOx using <i>ex situ</i> XAS	215
8.6. Summary: <i>Support Effects on CO-PrOx</i>	221
References	225

<b>Chapter 9: Gas Environment Effects on the Preferential Oxidation of Carbon Monoxide</b>	<b>231</b>
9.1. Further Thermodynamic Calculations on Gas-Phase Reaction Equilibria	231
9.2. Effect of CO-PrOx Gas Feed Components on CO Oxidation	235
9.2.1. Total oxidation of CO in the absence of H <sub>2</sub> , H <sub>2</sub> O and CO <sub>2</sub>	235
9.2.2. Effect of co-fed H <sub>2</sub> O during CO-PrOx (wet CO-PrOx)	237
9.2.3. Effect of co-fed CO <sub>2</sub> during CO-PrOx (dry CO-PrOx with co-fed CO <sub>2</sub> )	243
9.2.4. Effect of co-fed H <sub>2</sub> O and CO <sub>2</sub> during CO-PrOx (wet CO-PrOx with co-fed CO <sub>2</sub> )	249
9.2.5. Characterisation of spent catalysts after wet CO-PrOx with co-fed CO <sub>2</sub> using <i>ex situ</i> (HR)STEM-EELS	262
9.2.6. Characterisation of spent catalysts after wet CO-PrOx with co-fed CO <sub>2</sub> using <i>ex situ</i> XAS	267
9.2.7. Effect of varying the O <sub>2</sub> concentration during dry CO-PrOx	269
9.3. Summary: <i>Gas Environment-dependent CO-PrOx</i>	272
References	277
<b>Chapter 10: Summary and Conclusions</b>	<b>281</b>
10.1. Thermodynamic Calculations	282
10.2. Catalyst Synthesis and <i>ex situ</i> Characterisation	283
10.3. Effect of the Support on Catalytic Performance and Phase Stability	284
10.4. Effect of the CO-PrOx Gas Feed Components on Catalytic Performance and Phase Stability	286
References	288
<b>Chapter 11: Recommendations for Future Work</b>	<b>293</b>
11.1. Catalyst Synthesis	293
11.2. <i>In situ</i> Catalyst Characterisation during CO-PrOx	294
11.3. Catalyst Testing during CO-PrOx	294
References	296
<b>Appendices</b>	<b>297</b>
A.1. Equations and Coefficients for Thermodynamic Calculations	297
A.2. PXRD Reference Patterns Accessed from the ICDD PDF-2 Database	300
A.3. Magnetometer Calibration	301
A.4. Example of Results from the Rietveld Refinement of an <i>ex situ</i> Pattern	302
A.5. <i>In situ</i> PXRD Patterns Recorded during Reduction and Results from Rietveld Refinement	303

A.6. Example of <i>in situ</i> PXRD-based GC-TCD Data	307
A.7. <i>In situ</i> PXRD Patterns Recorded under Different CO-PrOx Conditions and Results from Rietveld Refinement	310
A.8. STEM Micrographs and EELS Maps	315
A.9. Example of Results from the Linear Combination Fitting of <i>ex situ</i> XAS Data	318
A.10. Curriculum Vitae	319
A.11. List of Publications	322
A.12. List of Conference Contributions	323



# List of Figures

- Figure 1.1:** Schematic of a typical PEMFC. (From [10,11]). 3
- Figure 1.2:** The processes involved in the production of H<sub>2</sub>-rich reformat gas including a CO-PrOx unit between a low temperature WGS unit and a PEMFC unit. 6
- Figure 2.1:** Langmuir-Hinshelwood mechanism for CO oxidation over a monometallic catalyst. The mechanism is also applicable to bimetallic catalysts. 12
- Figure 2.2:** Mars-van Krevelen mechanism for CO oxidation over a metal oxide catalyst. 13
- Figure 2.3:** (a) Calculated CO conversion, (b) O<sub>2</sub> selectivity to CO<sub>2</sub>, as well as (c) CH<sub>4</sub> detected using mass spectrometry as a function of temperature over Co<sub>3</sub>O<sub>4</sub> anchored on various metal oxide support materials during dry CO-PrOx. Conditions: GHSV: 30000 ml/g<sub>cat</sub>-hr, Pressure: 1.013 bar, Gas composition: 1% CO, 1% O<sub>2</sub>, 60% H<sub>2</sub>, bal. He. (Adapted from [32]). 18
- Figure 2.4:** (a) On-top view of the *in situ* PXRD patterns recorded during dry CO-PrOx over 10 wt.-% Co<sub>3</sub>O<sub>4</sub>/Al<sub>2</sub>O<sub>3</sub>. (b) Changes in the outlet flow rates of CO, O<sub>2</sub>, CO<sub>2</sub> and CH<sub>4</sub> calculated from GC-TCD data. (c) Magnetometry-derived degree of reduction of Co<sub>3</sub>O<sub>4</sub> to metallic fcc Co. Conditions: GHSV: 6000 ml/g<sub>cat</sub>/hr, Pressure: 1.013 bar, Gas composition: 0.9% CO, 0.9% O<sub>2</sub>, 50% H<sub>2</sub>, bal. N<sub>2</sub>. (Adapted from [35]). 22
- Figure 2.5:** (a) Changes in the CO conversion to CO<sub>2</sub> during CO oxidation (in the absence of H<sub>2</sub>) over mesoscopic CoO during heating and cooling of the reactor. (b) XP spectra, and (c) NEXAFS spectra recorded at 100, 150 and 200 °C, respectively, during the same reaction. Conditions: GHSV: 150000 ml/g<sub>cat</sub>/hr, Pressure: 1.013 bar, Gas composition: 5% CO, 10% O<sub>2</sub>, bal. He. (Adapted from [23]). 23
- Figure 2.6:** (a) Illustration of the stages involved during nanoparticle reduction *via* the nucleation mechanism. Plots of the (b) degree of reduction ( $\alpha$ ) as a function of time, as well as the (c) derivative of the degree of reduction ( $da/dt$ ) as a function of  $\alpha$  at a constant arbitrary temperature. (Adapted from [49,98–102]). 24
- Figure 2.7:** (a) Illustration of the stages involved during nanoparticle reduction *via* the shrinking core mechanism. Plots of the (b) degree of reduction ( $\alpha$ ) as a function of time, as well as the (c) derivative of the degree of reduction ( $da/dt$ ) as a function of  $\alpha$  at a constant arbitrary temperature. (Adapted from [49,98–102]). 25
- Figure 2.8:** Changes in the (a) CO conversion, and (b) O<sub>2</sub> selectivity to CO<sub>2</sub> as a function of temperature under different CO-PrOx conditions over a 10 wt.-% Co<sub>3</sub>O<sub>4</sub>/meso-CeO<sub>2</sub> catalyst. Conditions: GHSV: 40000 ml/g<sub>cat</sub>.hr, Pressure: 1.013 bar, Gas composition: 1% CO, 1% O<sub>2</sub>, 10% H<sub>2</sub>O (when co-fed), 20% CO<sub>2</sub> (when co-fed), 50% H<sub>2</sub>, bal. N<sub>2</sub>. (Replotted from [105]). 27

**Figure 2.9:** Temperature-programmed reduction profile of a CuO-CeO<sub>2</sub> catalyst in (a) 10% H<sub>2</sub> in N<sub>2</sub>, (b) 1% H<sub>2</sub>O/10% H<sub>2</sub> in N<sub>2</sub>, and (c) 1% CO<sub>2</sub>/1% H<sub>2</sub>O/10% H<sub>2</sub> in N<sub>2</sub>. Other conditions: GHSV: 200000 ml/g<sub>cat</sub>.hr, Pressure: 1.013 bar. (From [64]). 28

**Figure 2.10:** (a) CO conversion, and (b) O<sub>2</sub> selectivity to CO<sub>2</sub> as a function of temperature at various CO:O<sub>2</sub> ratios (indicated in red) during CO-PrOx over a 3 wt.-% Co/1 wt.-% Pt/Al<sub>2</sub>O<sub>3</sub> catalyst. Conditions: GHSV: 40000 ml/g<sub>cat</sub>.hr, Pressure: 1.013 bar, Gas composition: 1.1% CO, 0.55-1.98% O<sub>2</sub>, 9% H<sub>2</sub>O (when co-fed), 20% CO<sub>2</sub> (when co-fed), 67% H<sub>2</sub>, bal. N<sub>2</sub>. (Adapted from [15]). 29

**Figure 2.11:** Changes in the degree of reduction (%DOR) of a fully reduced cobalt catalyst upon exposure to (top) 1% O<sub>2</sub> in N<sub>2</sub>, (far-right) 21% O<sub>2</sub> in N<sub>2</sub> and (bottom) 90% CO<sub>2</sub> in Ar. The changes in the %DOR were monitored using the UCT-SASOL developed *in situ* magnetometer [92–94]. The blue shading is for metallic Co, the grey is for CoO and the black is for Co<sub>3</sub>O<sub>4</sub>. (From [110]). 30

**Figure 2.12:** Illustration of nanoparticle encapsulation by oxide support species. (Adapted from [76–78]). 31

**Figure 2.13:** Depiction of nanoparticle sintering *via* (a) coalescence, and (b) Ostwald ripening. (Adapted from [111–113]). 32

**Figure 2.14:** Depiction of a typical (incipient) wetness impregnation procedure. (Adapted from [124]). 36

**Figure 2.15:** Illustration of a normal and reverse micelle, respectively. (Adapted from [134,135]). 38

**Figure 2.16:** Stages involved in the synthesis of nanoparticles using the reverse microemulsion technique involving the preparation of (a) two microemulsions, or (b) one microemulsion, respectively. (Adapted from [134,135,138]). 40

**Figure 2.17:** (a) Top-view of the UCT-SASOL developed *in situ* magnetometer instrument used for the detection of ferromagnetic and superparamagnetic materials. (b) Front-view showing the stainless steel *in situ* magnetometer reactor placed between two electro-magnetic pole caps. Note that the front infra-red heater is not shown in the figure (b). (Adapted from [92–94]). 43

**Figure 2.18:** Measured magnetisation of a purely superparamagnetic sample as a function of the applied magnetic field. (Adapted from [109,148]). 44

**Figure 2.19:** M-H plot obtained when the magnetisation of a ferromagnetic sample is measured as function of the applied magnetic field. (Adapted from [109,148]). 45

**Figure 4.1:** Stages involved in the synthesis of unsupported Co<sub>3</sub>O<sub>4</sub> using the reverse microemulsion technique followed by drying and calcination. (Adapted from [14,15]). 67

**Figure 4.2:** Stages involved in the synthesis of supported Co<sub>3</sub>O<sub>4</sub> using incipient wetness impregnation followed by drying and calcination. (Adapted from [17]). 68

- Figure 4.3:** In-house developed in situ PXRD capillary reaction cell. (Adapted from [37–40]). 76
- Figure 4.4:** (a) Photograph showing the overall set-up for the water co-feeding experiments. Also included are close-up photographs showing the (b) side view, and (c) top view of the modified PXRD cell. 79
- Figure 4.5:** Set-up of the catalyst testing unit used for the *in situ* CO-PrOx experiments in the magnetometer. 84
- Figure 4.6:** Front view of a loaded *in situ* magnetometer reactor placed between two electromagnetic pole caps. (Adapted from [14,42]). 85
- Figure 4.7:** *In situ* magnetometer reactor set-up. (a) Top view, and (b) side view. (Adapted from [14,42]). 86
- Figure 5.1:** Changes in the Gibbs free energy as a function of temperature at 1.013 bar for the oxidation and decomposition of Co-based compounds. The light blue shaded area indicates the temperature region where bulk hcp Co transforms into bulk fcc Co. 97
- Figure 5.2:** Changes in the Gibbs free energy as a function of temperature at 1.013 bar for the thermal decomposition of  $\text{Co}(\text{NO}_3)_2$  to various Co-based compounds. The green y-axis on the right is for the change in the Gibbs free energy for the decomposition of  $\text{Co}(\text{NO}_3)_2$  to metallic Co. 99
- Figure 5.3:** PXRD pattern (radiation source:  $\text{Co K}\alpha_1 = 1.78897 \text{ \AA}$ ) of the *as prepared*  $\text{Co}(\text{OH})_x$  precipitate from the reverse microemulsion technique. Also included are the reference reflection lines of  $\alpha$ - and  $\beta$ - $\text{Co}(\text{OH})_2$ , respectively. See Table A.2.1 of Appendix A.2. for the ICDD PDF-2 entries of  $\alpha$ - and  $\beta$ - $\text{Co}(\text{OH})_x$ , respectively. 101
- Figure 5.4:** PXRD pattern of the fresh calcined unsupported  $\text{Co}_3\text{O}_4$  catalyst from the reverse microemulsion technique. Also included are the reference reflection lines of  $\text{Co}_3\text{O}_4$ . See Table A.2.1 for the ICDD PDF-2 entry of  $\text{Co}_3\text{O}_4$ . 102
- Figure 5.5:** PXRD patterns of the bare support materials (*i.e.*, before incipient wetness impregnation) and the corresponding relevant reference reflection lines. See Table A.2.1 for the ICDD PDF-2 entries of all reference phases. 104
- Figure 5.6:** PXRD patterns of the fresh supported catalysts (*i.e.*, after incipient wetness impregnation and calcination) and the reference reflection lines of the relevant Co-based oxides. The black triangles indicate reflections from  $\text{Co}_3\text{O}_4$ . See Table A.2.1 for the ICDD PDF-2 entries of all reference phases. 107
- Figure 5.7:** Normalised XANES spectrum of the fresh  $\text{Co}_3\text{O}_4/\text{CeO}_2$  catalyst. Also included are the XANES spectra of the reference compounds;  $\text{Co}_3\text{O}_4$  [6,7],  $\text{CoO}$  [52] and metallic Co (*i.e.*, Co foil) [53]. 108
- Figure 5.8:** (a) Bright-field STEM micrograph of unsupported  $\text{Co}_3\text{O}_4$ , and (b) the corresponding derived number-based size distribution. 110

**Figure 5.9:** EELS spectra of pure TiO<sub>2</sub>-anatase and TiO<sub>2</sub>-rutile, respectively. The orange rectangular box shows the features that are dissimilar between the spectra of the two titania phases. (Adapted from [59]). 111

**Figure 5.10:** (a) Bright-field, and (b) dark-field STEM micrographs of the fresh Co<sub>3</sub>O<sub>4</sub>/TiO<sub>2</sub>-P25 catalyst. (c) Phase composition maps derived using EELS showing anatase and rutile regions in the fresh catalyst. 112

**Figure 5.11:** (a) Bright-field STEM micrograph of the fresh Co<sub>3</sub>O<sub>4</sub>/TiO<sub>2</sub>-P25 catalyst. (b) Composite STEM-EELS elemental map showing the regions with Ti, O and Co. (c) Corresponding STEM-EELS maps of the individual elements. The solid white circles indicate the “single” Co-bearing particles and the dashed circles indicate “clusters” of particles (or Co-bearing material). 113

**Figure 5.12:** (a) Bright-field STEM micrograph of the fresh Co<sub>3</sub>O<sub>4</sub>/SiC catalyst. (b) Magnified STEM-EELS elemental maps showing the regions with Si, O, as well as (c) carbon. 114

**Figure 5.13:** (a) Bright-field STEM micrographs of some of the fresh supported Co<sub>3</sub>O<sub>4</sub> catalysts, and (b) the corresponding magnified STEM-EELS Co maps. The solid white circles indicate the “single” Co-bearing particles and the dashed circles indicate “clusters” of particles (or Co-bearing material). 115

**Figure 5.14:** (a) Bright-field STEM micrographs of the remaining fresh supported Co<sub>3</sub>O<sub>4</sub> catalysts, and (b) the corresponding EFSTEM Co maps. The solid white circles indicate the “single” Co-bearing particles and the dashed circles indicate “clusters” of particles (or Co-bearing material). 116

**Figure 5.15:** STEM-derived number-based size distributions for all prepared supported Co<sub>3</sub>O<sub>4</sub> catalysts. 117

**Figure 6.1:** (a) Changes in the Gibbs free energy, and (b) partial pressure ratio of H<sub>2</sub> and H<sub>2</sub>O (*i.e.*,  $p_{\text{H}_2}/p_{\text{H}_2\text{O}}$ ) as a function of temperature at 1.013 bar during the reduction of Co<sub>3</sub>O<sub>4</sub> and CoO. Note that “>” means “more stable than”. This is used to depict the stability trend between the Co-based phases at different temperatures and  $p_{\text{H}_2}/p_{\text{H}_2\text{O}}$ . 127

**Figure 6.2:** (a) Changes in the Gibbs free energy, and (b)  $p_{\text{H}_2}/p_{\text{H}_2\text{O}}$  as a function of temperature at 1.013 bar during the reduction of Co<sub>3</sub>O<sub>4</sub> forming CoO, metallic Co or Co-support compounds. 129

**Figure 6.3:** Changes in the Gibbs free energy as a function of temperature at 1.013 bar during the reduction of CoO forming metallic Co as well as during the solid state-reaction between CoO and some supports forming Co-support compounds. 130

**Figure 6.4:** (a) Changes in the Gibbs free energy, and (b) partial pressure ratio of H<sub>2</sub>O and H<sub>2</sub> (*i.e.*,  $p_{\text{H}_2\text{O}}/p_{\text{H}_2}$ ) as a function of temperature at 1.013 bar during the oxidation of metallic Co forming CoO, Co<sub>3</sub>O<sub>4</sub> or Co-support compounds. 132

**Figure 6.5:** (a) On-top view of the PXRD patterns (radiation source: Mo  $K\alpha_1 = 0.7093 \text{ \AA}$ ) recorded as a function of temperature during the reduction of unsupported  $\text{Co}_3\text{O}_4$  at atmospheric pressure in a 50:50  $\text{H}_2:\text{N}_2$  mixture. The reflections in each pattern were assigned using the ICDD PDF-2 entries of  $\text{Co}_3\text{O}_4$ , CoO, hcp Co and fcc Co - see Table A.2.1. (b) Changes in the relative fraction, and (c) average crystallite size of the different cobalt phases formed during the reduction. Refer to the red y-axis on the right of (c) for the crystallite size of fcc Co. However, note that these crystallite sizes may not bear significant physical meaning due to granularity effects and/or intergrowth of hcp and fcc Co. 135

**Figure 6.6:** On-top view of the *in situ* PXRD patterns recorded during the reduction of (a)  $\text{Co}_3\text{O}_4/\text{CeO}_2$ , (b)  $\text{Co}_3\text{O}_4/\text{ZrO}_2$ , (c)  $\text{Co}_3\text{O}_4/\text{SiC}$ , (d)  $\text{Co}_3\text{O}_4/\text{SiO}_2$ , (e)  $\text{Co}_3\text{O}_4/\text{TiO}_2$ -anatase, (f)  $\text{Co}_3\text{O}_4/\text{TiO}_2$ -rutile, (g)  $\text{Co}_3\text{O}_4/\text{TiO}_2$ -P25, and (h)  $\text{Co}_3\text{O}_4/\text{Al}_2\text{O}_3$  at atmospheric pressure in a 50:50  $\text{H}_2:\text{N}_2$  mixture. Note that the patterns recorded for the  $\text{Co}_3\text{O}_4/\text{CeO}_2$  catalyst had no detectable reflections from any Co-based phase. 140

**Figure 6.7:** *In situ* PXRD patterns of (a)  $\text{Co}_3\text{O}_4/\text{TiO}_2$ -anatase, (b)  $\text{Co}_3\text{O}_4/\text{TiO}_2$ -Rutile, and (c)  $\text{Co}_3\text{O}_4/\text{TiO}_2$ -P25 recorded at  $450 \text{ }^\circ\text{C}$  during reduction in a 50:50  $\text{H}_2:\text{N}_2$  mixture at atmospheric pressure. The reference reflection lines of hcp and fcc Co, as well as  $\text{TiO}_2$ -anatase and -rutile are also included (see Table A.2.1 for the ICDD PDF-2 entries of the reference phases). See the black arrows in (a) and (c) indicating hcp Co reflections. 141

**Figure 6.8:** (a) Temperatures at which the Co-based phases are detected using *in situ* PXRD during the reduction of all un/-supported catalysts at atmospheric pressure in a 50:50  $\text{H}_2:\text{N}_2$  mixture. (b) Relative fraction, and (c) crystallite size of CoO, hcp and fcc Co after reduction at  $450 \text{ }^\circ\text{C}$ . The white and black error bars in (b) are for hcp and fcc Co, respectively. The presence of metallic Co in the  $\text{Al}_2\text{O}_3$ -supported catalyst, depicted in (a), is inferred from the decreasing intensity of the CoO reflections above  $365 \text{ }^\circ\text{C}$  in Figure 6.6(h). The size of fcc Co in the unsupported catalyst is not reported in (c) due to possible granularity effects and/or intergrowth of hcp and fcc Co. 142

**Figure 6.9:** Reduction profiles of the bare and  $\text{Co}_3\text{O}_4$ -loaded  $\text{CeO}_2$  support material measured during conventional  $\text{H}_2$ -TPR at atmospheric pressure in a 5:95  $\text{H}_2:\text{Ar}$  mixture. 144

**Figure 7.1:** Changes in the Gibbs free energy as a function of temperature at 1.013 bar during the various individual reactions possible under CO-PrOx conditions. 152

**Figure 7.2:** Changes in the equilibrium conversions of (a) CO, and (b)  $\text{O}_2$  as a function of temperature at 1.013 bar during CO oxidation and  $\text{H}_2$  oxidation, respectively. Note that these were calculated assuming different  $\text{CO}:\text{O}_2$  and  $\text{O}_2:\text{H}_2$  feed ratios, respectively, as indicated on the plots. 154

**Figure 7.3:** Changes in the equilibrium conversions of CO and  $\text{CO}_2$  as a function of temperature at 1.013 bar during the forward and reverse WGS reaction, respectively. Note that these were calculated assuming different  $\text{CO}:\text{H}_2\text{O}$  and  $\text{CO}_2:\text{H}_2$  feed ratios, respectively, as indicated on the plots. 155

**Figure 7.4:** Changes in the equilibrium conversions of CO and  $\text{CO}_2$ , respectively, as a function of temperature at 1.013 bar during methanation. Note that these were calculated assuming different  $\text{CO}:\text{H}_2$  and  $\text{CO}_2:\text{H}_2$  feed ratios, respectively, as indicated on the plots. 157

**Figure 7.5:** (a) On-top view of the recorded *in situ* PXRD patterns, and (b) changes in the relative fraction of the different cobalt phases formed during the reduction of unsupported  $\text{Co}_3\text{O}_4$  at atmospheric pressure in a 1:50:49  $\text{CO}:\text{H}_2:\text{N}_2$  mixture. (c) Changes in the normalised outlet flow rates of  $\text{CO}$  and  $\text{CH}_4$  calculated from GC-TCD data. 161

**Figure 7.6:** (a) On-top view of the *in situ* PXRD patterns recorded during the reduction of unsupported  $\text{Co}_3\text{O}_4$  at atmospheric pressure in a 1:50:49  $\text{O}_2:\text{H}_2:\text{N}_2$  mixture. (b) Changes in the normalised outlet flow rate of  $\text{O}_2$  calculated from GC-TCD data. 163

**Figure 7.7:** On-top view of the *in situ* PXRD patterns recorded during the reduction of unsupported  $\text{Co}_3\text{O}_4$  at atmospheric pressure in a (a) 1:50:49  $\text{H}_2\text{O}:\text{H}_2:\text{N}_2$ , and a (b) 1:50:49  $\text{CO}_2:\text{H}_2:\text{N}_2$  gas mixture, respectively. 165

**Figure 7.8:** On-top view of the *in situ* PXRD patterns recorded during the reduction of unsupported  $\text{Co}_3\text{O}_4$  at atmospheric pressure in a (a) 10:50:40  $\text{H}_2\text{O}:\text{H}_2:\text{N}_2$ , and a (b) 10:50:40  $\text{CO}_2:\text{H}_2:\text{N}_2$  mixture, respectively. (c) Changes in the normalised outlet flow rates of  $\text{CO}_2$ ,  $\text{CH}_4$  and  $\text{CO}$  calculated from GC-TCD data during the reduction in 10:50:40  $\text{CO}_2:\text{H}_2:\text{N}_2$ . 167

**Figure 7.9:** (a) On-top view of the *in situ* PXRD patterns recorded during the reduction of unsupported  $\text{Co}_3\text{O}_4$  at atmospheric pressure in a 1:10:89  $\text{CO}:\text{H}_2\text{O}:\text{N}_2$  mixture. (b) Changes in the normalised outlet flow rates of  $\text{CO}$ ,  $\text{CO}_2$  and  $\text{H}_2$  calculated from GC-TCD data. 169

**Figure 7.10:** (a) Temperatures at which the Co-based phases were detected using *in situ* PXRD under the different reduction conditions. (b) Relative fraction of hcp and fcc Co, as well as the (c) crystallite size of hcp Co after full reduction of unsupported  $\text{Co}_3\text{O}_4$  at 450 °C and at atmospheric pressure. The white and black error bars in (b) are for hcp and fcc Co, respectively. The size of fcc Co is not reported in (c) due to possible granularity effects and/or intergrowth of hcp and fcc Co. 172

**Figure 8.1:** (a) On-top view of the recorded *in situ* PXRD patterns, (b) changes in the relative fraction, and (c) average crystallite size of the different cobalt phases formed during dry CO-PrOx over unsupported  $\text{Co}_3\text{O}_4$ . (d) Changes in the normalised outlet flow rates of  $\text{CO}$ ,  $\text{O}_2$ ,  $\text{CO}_2$ ,  $\text{CH}_4$ , and (e)  $\text{H}_2$  calculated from GC-TCD data. (f) Magnetometry-derived degree of reduction of  $\text{Co}_3\text{O}_4$  to metallic Co. Refer to the red y-axis on the right of (c) for the crystallite size of fcc Co. However, note that these crystallite sizes may not bear significant physical meaning due to granularity effects and/or intergrowth of hcp and fcc Co. (Feed composition: 1%  $\text{CO}$ , 1%  $\text{O}_2$ , 50%  $\text{H}_2$  and 48%  $\text{N}_2$ ; pressure: atmospheric, GHSV: 60000 mL(NTP)/g $\text{Co}_3\text{O}_4$ /hr). 181

**Figure 8.2:** (a) Magnetometry-derived M-H curves recorded at 450 and 50 °C (post-reaction) under dry CO-PrOx over unsupported  $\text{Co}_3\text{O}_4$ . (b) Magnified view of the M-H curves indicating the existence of hysteresis behaviour. (Feed composition: 1%  $\text{CO}$ , 1%  $\text{O}_2$ , 50%  $\text{H}_2$  and 48%  $\text{N}_2$ ; pressure: atmospheric, GHSV: 60000 mL(NTP)/g $\text{Co}_3\text{O}_4$ /hr). 183

**Figure 8.3:** (a) On-top view of the *in situ* PXRD patterns recorded during dry CO-PrOx over  $\text{Co}_3\text{O}_4/\text{ZrO}_2$ . ((b) and (c)) Changes in the normalised outlet flow rates of  $\text{CO}$ ,  $\text{O}_2$ ,  $\text{CO}_2$  and  $\text{CH}_4$  calculated from GC-TCD data. ((d) and (e)) Magnetometry-derived degree of reduction of  $\text{Co}_3\text{O}_4$  to metallic Co. Note that PXRD analysis for the  $\text{Co}_3\text{O}_4/\text{CeO}_2$  catalyst was not performed as reflections from Co-based phases are not visible (see Figures 5.6 and 6.6(a)). (Feed composition:

1% CO, 1% O<sub>2</sub>, 50% H<sub>2</sub> and 48% N<sub>2</sub>; pressure: atmospheric, GHSV: 60000 mL(NTP)/g<sub>Co<sub>3</sub>O<sub>4</sub></sub>/hr).  
190

**Figure 8.4:** (a) On-top view of the *in situ* PXRD patterns recorded during dry CO-PrOx over (left) Co<sub>3</sub>O<sub>4</sub>/SiC, and (right) Co<sub>3</sub>O<sub>4</sub>/SiO<sub>2</sub>. (b) Changes in the normalised outlet flow rates of CO, O<sub>2</sub>, CO<sub>2</sub> and CH<sub>4</sub> calculated from GC-TCD data. (c) Magnetometry-derived degree of reduction of Co<sub>3</sub>O<sub>4</sub> to metallic Co. (Feed composition: 1% CO, 1% O<sub>2</sub>, 50% H<sub>2</sub> and 48% N<sub>2</sub>; pressure: atmospheric, GHSV: 60000 mL(NTP)/g<sub>Co<sub>3</sub>O<sub>4</sub></sub>/hr).  
191

**Figure 8.5:** (a) On-top view of the *in situ* PXRD patterns recorded during dry CO-PrOx over (left) Co<sub>3</sub>O<sub>4</sub>/TiO<sub>2</sub>-anatase, and (right) Co<sub>3</sub>O<sub>4</sub>/TiO<sub>2</sub>-rutile. (b) Changes in the normalised outlet flow rates of CO, O<sub>2</sub>, CO<sub>2</sub> and CH<sub>4</sub> calculated from GC-TCD data. (c) Magnetometry-derived degree of reduction of Co<sub>3</sub>O<sub>4</sub> to metallic Co. (Feed composition: 1% CO, 1% O<sub>2</sub>, 50% H<sub>2</sub> and 48% N<sub>2</sub>; pressure: atmospheric, GHSV: 60000 mL(NTP)/g<sub>Co<sub>3</sub>O<sub>4</sub></sub>/hr).  
192

**Figure 8.6:** (a) On-top view of the *in situ* PXRD patterns recorded during dry CO-PrOx over (left) Co<sub>3</sub>O<sub>4</sub>/TiO<sub>2</sub>-P25, and (right) Co<sub>3</sub>O<sub>4</sub>/Al<sub>2</sub>O<sub>3</sub>. (b) Changes in the normalised outlet flow rates of CO, O<sub>2</sub>, CO<sub>2</sub> and CH<sub>4</sub> calculated from GC-TCD data. (c) Magnetometry-derived degree of reduction of Co<sub>3</sub>O<sub>4</sub> to metallic Co. (Feed composition: 1% CO, 1% O<sub>2</sub>, 50% H<sub>2</sub> and 48% N<sub>2</sub>; pressure: atmospheric, GHSV: 60000 mL(NTP)/g<sub>Co<sub>3</sub>O<sub>4</sub></sub>/hr).  
193

**Figure 8.7:** (a) Temperatures at which the Co-based phases were detected using *in situ* PXRD during dry CO-PrOx over the prepared catalysts. (b) Relative fraction, and (c) crystallite size of CoO, hcp and fcc Co at 450 °C. The white error bars in (b) are for CoO and hcp Co, while the black error bars are for fcc Co. The presence of metallic Co in the Al<sub>2</sub>O<sub>3</sub>-supported catalyst, depicted in (a), is inferred from the slightly decreasing intensity of the CoO reflections at 450 °C in Figure 8.6((a), right). The size of fcc Co in the unsupported and TiO<sub>2</sub>-P25-supported catalyst is not reported in (c) due to possible granularity effects and/or intergrowth of hcp and fcc Co. (Feed composition: 1% CO, 1% O<sub>2</sub>, 50% H<sub>2</sub> and 48% N<sub>2</sub>; pressure: atmospheric, GHSV: 60000 mL(NTP)/g<sub>Co<sub>3</sub>O<sub>4</sub></sub>/hr).  
194

**Figure 8.8:** Changes in the (a) CO conversion, and (b) O<sub>2</sub> selectivity to CO<sub>2</sub> via oxidation, (c) CO conversion to CH<sub>4</sub> via hydrogenation, and the (d) magnetometry-derived degree of reduction of Co<sub>3</sub>O<sub>4</sub> to metallic Co during dry CO-PrOx over all prepared catalysts. Note that the O<sub>2</sub> selectivity to CO<sub>2</sub> was calculated at temperatures where both CO and O<sub>2</sub> were converted (see Figures 8.3 – 8.6). Also see Figure A.6.2 showing the changes in the CO conversion and O<sub>2</sub> selectivity to CO<sub>2</sub> between 50 and 200 °C, where the Co<sub>3</sub>O<sub>4</sub> phase is believed to be intact in all evaluated catalysts. (Feed composition: 1% CO, 1% O<sub>2</sub>, 50% H<sub>2</sub> and 48% N<sub>2</sub>; pressure: atmospheric, GHSV: 60000 mL(NTP)/g<sub>Co<sub>3</sub>O<sub>4</sub></sub>/hr).  
195

**Figure 8.9:** (a) Magnetometry-derived M-H curves recorded at 450 °C under dry CO-PrOx over CeO<sub>2</sub>-, ZrO<sub>2</sub>-, SiC- and SiO<sub>2</sub>-supported Co<sub>3</sub>O<sub>4</sub> catalysts. (b) Magnified view of the M-H curves indicating the existence of hysteresis behaviour. (Feed composition: 1% CO, 1% O<sub>2</sub>, 50% H<sub>2</sub> and 48% N<sub>2</sub>; pressure: atmospheric, GHSV: 60000 mL(NTP)/g<sub>Co<sub>3</sub>O<sub>4</sub></sub>/hr).  
198

**Figure 8.10:** (a) Magnetometry-derived M-H curves recorded at 450 °C under dry CO-PrOx gas over TiO<sub>2</sub>- and Al<sub>2</sub>O<sub>3</sub>-supported Co<sub>3</sub>O<sub>4</sub> catalysts. (b) Magnified view of the M-H curves indicating

the existence of hysteresis behaviour. (Feed composition: 1% CO, 1% O<sub>2</sub>, 50% H<sub>2</sub> and 48% N<sub>2</sub>; pressure: atmospheric, GHSV: 60000 mL(NTP)/g<sub>Co<sub>3</sub>O<sub>4</sub></sub>/hr). 199

**Figure 8.11:** On-top view of the *in situ* PXRD patterns of (a) unsupported Co<sub>3</sub>O<sub>4</sub>, and (b) Co<sub>3</sub>O<sub>4</sub>/ZrO<sub>2</sub>. Changes in the (c) degree of reduction with time, and the (d) derivative of the DoR at 225 °C during dry CO-PrOx. (Feed composition: 1% CO, 1% O<sub>2</sub>, 50% H<sub>2</sub> and 48% N<sub>2</sub>; pressure: atmospheric, GHSV: 60000 mL(NTP)/g<sub>Co<sub>3</sub>O<sub>4</sub></sub>/hr). 203

**Figure 8.12:** Changes in the magnetometry-derived (a) degree of reduction, and the (b) derivative of the DoR with time at 275 °C for the unsupported sample and 325 °C for the Co<sub>3</sub>O<sub>4</sub>/ZrO<sub>2</sub> sample during dry CO-PrOx. Effect of temperature on the (c) degree of reduction with time, and the (d) derivative of the DoR for the unsupported Co<sub>3</sub>O<sub>4</sub> sample only. (Feed composition: 1% CO, 1% O<sub>2</sub>, 50% H<sub>2</sub> and 48% N<sub>2</sub>; pressure: atmospheric, GHSV: 60000 mL(NTP)/g<sub>Co<sub>3</sub>O<sub>4</sub></sub>/hr). 204

**Figure 8.13:** (a) TEM micrograph of the spent sample after dry CO-PrOx, and (b) a magnified STEM micrograph showing the very small particles that make up the agglomerates. The black arrows indicate the small (possibly) hcp Co particles and the red arrow indicates the large (possibly) fcc Co-containing particles. 206

**Figure 8.14:** (a) Bright-field STEM micrograph of the spent Co<sub>3</sub>O<sub>4</sub>/TiO<sub>2</sub>-anatase catalyst obtained after dry CO-PrOx. (b) Magnified STEM-EELS elemental map showing the regions with Ti, O and Co. (c) Corresponding magnified STEM-EELS maps of the individual elements. 209

**Figure 8.15:** (a) Bright-field STEM micrographs of the spent Co<sub>3</sub>O<sub>4</sub>/TiO<sub>2</sub>-rutile and Co<sub>3</sub>O<sub>4</sub>/TiO<sub>2</sub>-P25 catalysts, respectively, obtained after dry CO-PrOx. (b) Magnified STEM-EELS elemental maps showing the regions with Ti, O and Co. 210

**Figure 8.16:** (a) Bright-field STEM micrograph of the spent Co<sub>3</sub>O<sub>4</sub>/Al<sub>2</sub>O<sub>3</sub> catalyst obtained after dry CO-PrOx. (b) Magnified STEM-EELS elemental map showing the regions with Al, O and Co. (c) Corresponding magnified STEM-EELS maps of the individual elements. The white arrows on the Al map show the bright regions which are believed to be the Al species that are chemically mixed with Co. 212

**Figure 8.17:** (a) Bright-field STEM micrograph of the spent Co<sub>3</sub>O<sub>4</sub>/CeO<sub>2</sub> catalyst obtained after dry CO-PrOx. (b) Magnified STEM-EELS elemental map showing the regions with Ce, O and Co. (c) Corresponding magnified STEM-EELS maps of the individual elements. 213

**Figure 8.18:** STEM-derived number-based size distributions for the ZrO<sub>2</sub>- and TiO<sub>2</sub>-supported Co<sub>3</sub>O<sub>4</sub> catalysts. 214

**Figure 8.19:** Normalised XANES spectra of the reference compounds; Co<sub>3</sub>O<sub>4</sub> [66,101], CoO [102], Co<sub>2</sub>SiO<sub>4</sub> [103], CoTiO<sub>3</sub> [100], CoAl<sub>2</sub>O<sub>4</sub> [100,104] and metallic Co [105] (*i.e.*, Co foil) where applicable. 217

**Figure 8.20:** Normalised XANES spectra of the (a) CeO<sub>2</sub>-, (b) ZrO<sub>2</sub>-, (c) SiC- and (d) SiO<sub>2</sub>-supported spent samples obtained after dry CO-PrOx, together with the resulting linear combination fit of the spectral components in each sample. 218

**Figure 8.21:** Normalised XANES spectra of the (a) TiO<sub>2</sub>-anatase-, (b) TiO<sub>2</sub>-rutile-, (c) TiO<sub>2</sub>-P25-, and (d) Al<sub>2</sub>O<sub>3</sub>-supported spent samples obtained after dry CO-PrOx, together with the resulting linear combination fit of the spectral components in each sample. 220

**Figure 9.1:** Changes in the equilibrium conversions of (a) CO, and (b) CO<sub>2</sub> as a function of temperature at 1.013 bar during the forward and reverse WGS reaction, respectively. Note the different feed compositions indicated on the plots. 233

**Figure 9.2:** Changes in the equilibrium conversions of (a) CO, and (b) CO<sub>2</sub>, respectively, as a function of temperature at 1.013 bar during methanation. Note the different feed compositions indicated on the plots. 234

**Figure 9.3:** (a) On-top view of the *in situ* PXRD patterns of (left) unsupported Co<sub>3</sub>O<sub>4</sub>, and (right) Co<sub>3</sub>O<sub>4</sub>/ZrO<sub>2</sub> recorded during dry CO-TOx. (b) Changes in the normalised outlet flow rates of CO, O<sub>2</sub> and CO<sub>2</sub> calculated from GC-TCD data. (Feed composition: 1% CO, 1% O<sub>2</sub> and 98% N<sub>2</sub>; pressure: atmospheric, GHSV: 60000 mL(NTP)/gCo<sub>3</sub>O<sub>4</sub>/hr). 236

**Figure 9.4:** (a) On-top view of the *in situ* PXRD patterns of (left) unsupported Co<sub>3</sub>O<sub>4</sub>, and (right) Co<sub>3</sub>O<sub>4</sub>/ZrO<sub>2</sub> recorded during wet CO-PrOx. (b) Changes in the normalised outlet flow rates of CO, O<sub>2</sub>, CO<sub>2</sub> and CH<sub>4</sub> calculated from GC-TCD data. (c) Magnetometry-derived degree of reduction of Co<sub>3</sub>O<sub>4</sub> to metallic Co. (Feed composition: 1% CO, 1% O<sub>2</sub>, 45% H<sub>2</sub>, 10% H<sub>2</sub>O and 43% N<sub>2</sub>; pressure: atmospheric, GHSV: 60000 mL(NTP)/gCo<sub>3</sub>O<sub>4</sub>/hr). 241

**Figure 9.5:** (a) Magnetometry-derived M-H curves recorded at 450 °C during wet CO-PrOx over unsupported and ZrO<sub>2</sub>-supported Co<sub>3</sub>O<sub>4</sub>. (b) Magnified view of the M-H curves indicating the existence of hysteresis behaviour. (Feed composition: 1% CO, 1% O<sub>2</sub>, 45% H<sub>2</sub>, 10% H<sub>2</sub>O and 43% N<sub>2</sub>; pressure: atmospheric, GHSV: 60000 mL(NTP)/gCo<sub>3</sub>O<sub>4</sub>/hr). 243

**Figure 9.6:** (a) On-top view of the *in situ* PXRD patterns of (left) unsupported Co<sub>3</sub>O<sub>4</sub>, and (right) Co<sub>3</sub>O<sub>4</sub>/ZrO<sub>2</sub> recorded during dry CO-PrOx with co-fed CO<sub>2</sub>. (b) Changes in the net outlet flow rates of CO, O<sub>2</sub>, CO<sub>2</sub> and CH<sub>4</sub> calculated from GC-TCD data. (c) Magnetometry-derived degree of reduction of Co<sub>3</sub>O<sub>4</sub> to metallic Co. (Feed composition: 1% CO, 1% O<sub>2</sub>, 50% H<sub>2</sub>, 10% CO<sub>2</sub> and 38% N<sub>2</sub>; pressure: atmospheric, GHSV: 60000 mL(NTP)/gCo<sub>3</sub>O<sub>4</sub>/hr). 247

**Figure 9.7:** (a) Magnetometry-derived M-H curves recorded at 450 °C during dry CO-PrOx with co-fed CO<sub>2</sub> over unsupported and ZrO<sub>2</sub>-supported Co<sub>3</sub>O<sub>4</sub>. (b) Magnified view of the M-H curves indicating the existence of hysteresis behaviour. (Feed composition: 1% CO, 1% O<sub>2</sub>, 50% H<sub>2</sub>, 10% CO<sub>2</sub> and 38% N<sub>2</sub>; pressure: atmospheric, GHSV: 60000 mL(NTP)/gCo<sub>3</sub>O<sub>4</sub>/hr). 249

**Figure 9.8:** (a) On-top view of the *in situ* PXRD patterns of (left) unsupported Co<sub>3</sub>O<sub>4</sub>, and (right) Co<sub>3</sub>O<sub>4</sub>/ZrO<sub>2</sub> recorded during dry CO-PrOx with co-fed CO<sub>2</sub>. (b) Changes in the net outlet flow rates of CO, O<sub>2</sub>, CO<sub>2</sub> and CH<sub>4</sub> calculated from GC-TCD data. (c) Magnetometry-derived degree of reduction of Co<sub>3</sub>O<sub>4</sub> to metallic Co. (Feed composition: 1% CO, 1% O<sub>2</sub>, 46% H<sub>2</sub>, 10% H<sub>2</sub>O, 9% CO<sub>2</sub> and 33% N<sub>2</sub>; pressure: atmospheric, GHSV: 60000 mL(NTP)/gCo<sub>3</sub>O<sub>4</sub>/hr). 254

**Figure 9.9:** (a) On-top view of the *in situ* PXRD patterns of (left) Co<sub>3</sub>O<sub>4</sub>/SiC, and (right) Co<sub>3</sub>O<sub>4</sub>/TiO<sub>2</sub>-P25 recorded during dry CO-PrOx with co-fed CO<sub>2</sub>. (b) Changes in the net outlet flow rates of CO, O<sub>2</sub>, CO<sub>2</sub> and CH<sub>4</sub> calculated from GC-TCD data. (c) Magnetometry-derived degree

of reduction of  $\text{Co}_3\text{O}_4$  to metallic Co. (Feed composition: 1%  $\text{CO}$ , 1%  $\text{O}_2$ , 46%  $\text{H}_2$ , 10%  $\text{H}_2\text{O}$ , 9%  $\text{CO}_2$  and 33%  $\text{N}_2$ ; pressure: atmospheric, GHSV: 60000 mL(NTP)/g $\text{Co}_3\text{O}_4$ /hr). 255

**Figure 9.10:** (a) Magnetometry-derived M-H curves recorded at 450 °C during wet CO-PrOx with co-fed  $\text{CO}_2$  over unsupported,  $\text{ZrO}_2$ -, SiC- and  $\text{TiO}_2$ -P25-supported  $\text{Co}_3\text{O}_4$ , respectively. (b) Magnified view of the M-H curves indicating the existence of hysteresis behaviour. (Feed composition: 1%  $\text{CO}$ , 1%  $\text{O}_2$ , 46%  $\text{H}_2$ , 10%  $\text{H}_2\text{O}$ , 9%  $\text{CO}_2$  and 33%  $\text{N}_2$ ; pressure: atmospheric, GHSV: 60000 mL(NTP)/g $\text{Co}_3\text{O}_4$ /hr). 257

**Figure 9.11:** (a) Temperatures at which the Co-based phases are detected using *in situ* PXRD under different CO-PrOx conditions at atmospheric pressure over unsupported and  $\text{ZrO}_2$ -supported  $\text{Co}_3\text{O}_4$ . (b) Relative fraction, and (c) crystallite size of CoO, hcp and fcc Co at 450 °C. The white and black error bars in (b) are for hcp and fcc Co, respectively. In some cases, the size of fcc Co in the unsupported catalyst is not reported in (c) due to possible granularity effects and/or intergrowth of hcp and fcc Co. 258

**Figure 9.12:** (a) Temperatures at which the Co-based phases are detected using *in situ* PXRD under different CO-PrOx conditions at atmospheric pressure over  $\text{Co}_3\text{O}_4$ /SiC and  $\text{Co}_3\text{O}_4$ / $\text{TiO}_2$ -P25. (b) Relative fraction, and (c) crystallite size of CoO and fcc Co at 450 °C. The white error bars in (b) are for CoO and hcp Co, while the black error bars are for fcc Co. The size of fcc Co in the  $\text{TiO}_2$ -P25-supported catalyst is not reported in (c) due to possible granularity effects and/or intergrowth of hcp and fcc Co. 259

**Figure 9.13:** (a) Changes in the CO conversion to  $\text{CO}_2$  ( $X_{\text{CO} \rightarrow \text{CO}_2}$ ) via oxidation, (b) CO conversion to  $\text{CH}_4$  ( $X_{\text{CO} \rightarrow \text{CH}_4}$ ) via hydrogenation, (c)  $\text{CO}_2$  conversion to  $\text{CH}_4$  ( $X_{\text{CO}_2 \rightarrow \text{CH}_4}$ ) via hydrogenation and to CO ( $X_{\text{CO}_2 \rightarrow \text{CO}}$ ) via reverse WGS, respectively, and the (d) magnetometry-derived degree of reduction of  $\text{Co}_3\text{O}_4$  to metallic Co under different CO-PrOx conditions at atmospheric pressure performed over (left) unsupported  $\text{Co}_3\text{O}_4$ , and (right)  $\text{Co}_3\text{O}_4$ / $\text{ZrO}_2$ . 260

**Figure 9.14:** (a) Changes in the CO conversion to  $\text{CO}_2$  ( $X_{\text{CO} \rightarrow \text{CO}_2}$ ) via oxidation, (b) CO conversion to  $\text{CH}_4$  ( $X_{\text{CO} \rightarrow \text{CH}_4}$ ) via hydrogenation, (c)  $\text{CO}_2$  conversion to  $\text{CH}_4$  ( $X_{\text{CO}_2 \rightarrow \text{CH}_4}$ ) via hydrogenation and to CO ( $X_{\text{CO}_2 \rightarrow \text{CO}}$ ) via reverse WGS, respectively, and the (d) magnetometry-derived degree of reduction of  $\text{Co}_3\text{O}_4$  to metallic Co under different CO-PrOx conditions at atmospheric pressure performed over (left)  $\text{Co}_3\text{O}_4$ /SiC, and (right)  $\text{Co}_3\text{O}_4$ / $\text{TiO}_2$ -P25. 261

**Figure 9.15:** (a) TEM micrograph of the spent sample after wet CO-PrOx with co-fed  $\text{CO}_2$ . 263

**Figure 9.16:** (a) Bright-field STEM micrographs of the spent  $\text{Co}_3\text{O}_4$ / $\text{ZrO}_2$ ,  $\text{Co}_3\text{O}_4$ /SiC and  $\text{Co}_3\text{O}_4$ / $\text{TiO}_2$ -P25 catalysts, respectively, obtained after wet CO-PrOx (with co-fed  $\text{CO}_2$ ). (b) Magnified STEM-EELS elemental maps showing the regions with the elements Zr, Si, Ti, O, C and Co where applicable. 265

**Figure 9.17:** STEM-derived number-based size distributions for the  $\text{ZrO}_2$ - and  $\text{TiO}_2$ -P25-supported  $\text{Co}_3\text{O}_4$  catalysts. 266

**Figure 9.18:** Normalised XANES spectra of the (a) reference compounds  $\text{Co}_3\text{O}_4$  [63,64], CoO [65],  $\text{Co}_2\text{SiO}_4$  [66],  $\text{CoTiO}_3$  [67] and Co foil [68]; as well as normalised XANES spectra of the (b)

ZrO<sub>2</sub>-, (c) SiC- and (d) TiO<sub>2</sub>-P25-supported spent samples obtained after dry CO-PrOx, together with the resulting linear combination fit of the spectral components in each sample. 268

**Figure 9.19:** (a) On-top view of the *in situ* PXRD patterns recorded during dry CO-PrOx at varying CO:O<sub>2</sub> ratios over unsupported Co<sub>3</sub>O<sub>4</sub>. (b) Changes in the normalised outlet flow rates of CO, O<sub>2</sub>, CO<sub>2</sub> and CH<sub>4</sub> calculated from GC-TCD data. (Feed composition: 1 – 0.9% CO, 0.5 – 4% O<sub>2</sub>, 51 – 43% H<sub>2</sub> and 47.5 – 52.1% N<sub>2</sub>; pressure: atmospheric, GHSV: 60000 mL(NTP)/g<sub>Co<sub>3</sub>O<sub>4</sub></sub>/hr). 271

**Figure 9.20:** (a) On-top view of the *in situ* PXRD patterns recorded during dry CO-PrOx at varying CO:O<sub>2</sub> ratios over Co<sub>3</sub>O<sub>4</sub>/ZrO<sub>2</sub>. (b) Changes in the normalised outlet flow rates of CO, O<sub>2</sub>, CO<sub>2</sub> and CH<sub>4</sub> calculated from GC-TCD data. (Feed composition: 1 – 0.9% CO, 0.5 – 4% O<sub>2</sub>, 51 – 43% H<sub>2</sub> and 47.5 – 52.1% N<sub>2</sub>; pressure: atmospheric, GHSV: 60000 mL(NTP)/g<sub>Co<sub>3</sub>O<sub>4</sub></sub>/hr). 272

**Figure A.3.1:** Magnetisation (recorded under argon flow) of a 0.1 g pre-reduced unsupported metallic cobalt sample measured as a function of temperature. The sample had been pre-reduced between room temperature and 700 °C under H<sub>2</sub> flow starting from the Co<sub>3</sub>O<sub>4</sub> phase. 301

**Figure A.4.1:** Results from after performing Rietveld refinement on the *ex situ* PXRD pattern of the fresh Co<sub>3</sub>O<sub>4</sub>/TiO<sub>2</sub>-P25 sample. 302

**Figure A.5.1:** Results obtained after performing Rietveld refinement on the last *in situ* PXRD pattern recorded at 450 °C during the reduction of unsupported Co<sub>3</sub>O<sub>4</sub> at atmospheric pressure in a 50:50 H<sub>2</sub>:N<sub>2</sub> gas mixture. 303

**Figure A.5.2:** Changes in the average crystallite size of the different cobalt phases formed during the reduction of unsupported Co<sub>3</sub>O<sub>4</sub> at atmospheric pressure in a 1:50:49 CO:H<sub>2</sub>:N<sub>2</sub> gas mixture. Note that the crystallite sizes for fcc Co (see transparent red plot and y-axis) may not bear significant physical meaning due to granularity effects and/or intergrowth of hcp and fcc Co. 303

**Figure A.5.3:** On-top view of the *in situ* PXRD patterns recorded during the reduction of unsupported Co<sub>3</sub>O<sub>4</sub> at atmospheric pressure in a 1:99 CO:N<sub>2</sub> gas mixture. 304

**Figure A.6.1:** Normalised outlet flow rates of CO, O<sub>2</sub>, CO<sub>2</sub> and CH<sub>4</sub> calculated from the GC-TCD data obtained during dry CO-PrOx over unsupported Co<sub>3</sub>O<sub>4</sub> in the *in situ* PXRD cell. (Feed composition: 1% CO, 1% O<sub>2</sub>, 50% H<sub>2</sub> and 48% N<sub>2</sub>; pressure: atmospheric, GHSV: 60000 mL(NTP)/g<sub>Co<sub>3</sub>O<sub>4</sub></sub>/hr). 307

**Figure A.6.2:** Changes in the (a) CO conversion, and (b) O<sub>2</sub> selectivity to CO<sub>2</sub> *via* oxidation during dry CO-PrOx over all prepared catalysts. Note that the O<sub>2</sub> selectivity to CO<sub>2</sub> was calculated at temperatures where both CO and O<sub>2</sub> were converted (see Figures 8.3 – 8.6). (Feed composition: 1% CO, 1% O<sub>2</sub>, 50% H<sub>2</sub> and 48% N<sub>2</sub>; pressure: atmospheric, GHSV: 60000 mL(NTP)/g<sub>Co<sub>3</sub>O<sub>4</sub></sub>/hr). 308

**Figure A.6.3:** Changes in the O<sub>2</sub> selectivity to CO<sub>2</sub> under different CO-PrOx conditions at atmospheric pressure and as a function of temperature over (a) unsupported Co<sub>3</sub>O<sub>4</sub>, (b) Co<sub>3</sub>O<sub>4</sub>/ZrO<sub>2</sub>, (c) Co<sub>3</sub>O<sub>4</sub>/SiC, and (d) Co<sub>3</sub>O<sub>4</sub>/TiO<sub>2</sub>-P25. 309

**Figure A.7.1:** *In situ* PXRD patterns of (a)  $\text{Co}_3\text{O}_4/\text{TiO}_2$ -anatase, (b)  $\text{Co}_3\text{O}_4/\text{TiO}_2$ -Rutile, and (c)  $\text{Co}_3\text{O}_4/\text{TiO}_2$ -P25 recorded at 450 °C during dry CO-PrOx. The reference reflection lines of hcp and fcc Co, as well as  $\text{TiO}_2$ -anatase and -rutile are also included. See the black arrows in (b) and (c) indicating hcp Co reflections. (Feed composition: 1% CO, 1%  $\text{O}_2$ , 50%  $\text{H}_2$  and 48%  $\text{N}_2$ ; pressure: atmospheric, GHSV: 60000 mL(NTP)/g $\text{Co}_3\text{O}_4$ /hr). 310

**Figure A.7.2:** ((a) and (d)) On-top view of the PXRD patterns recorded as a function of temperature during (left) wet CO-PrOx, and (right) dry CO-PrOx with co-fed  $\text{CO}_2$  at atmospheric pressure. ((b) and (e)) Changes in the relative fraction, and ((c) and (f)) average crystallite size of the different cobalt phases formed during the respective reactions. 311

**Figure A.7.3:** (a) On-top view of the PXRD patterns recorded as a function of temperature during wet CO-PrOx with co-fed  $\text{CO}_2$ . (b) Changes in the relative fraction, and (c) average crystallite size of the different cobalt phases formed during the reaction. Note that the crystallite sizes for fcc Co (see transparent red plot and y-axis in (c)) may not bear significant physical meaning due to granularity effects and/or intergrowth of hcp and fcc Co. (Feed composition: 1% CO, 1%  $\text{O}_2$ , 46%  $\text{H}_2$ , 10%  $\text{H}_2\text{O}$ , 9%  $\text{CO}_2$  and 33%  $\text{N}_2$ ; pressure: atmospheric, GHSV: 60000 mL(NTP)/g $\text{Co}_3\text{O}_4$ /hr). 312

**Figure A.7.4:** *In situ* PXRD pattern of  $\text{Co}_3\text{O}_4/\text{TiO}_2$ -P25 recorded at 450 °C during wet CO-PrOx with co-fed  $\text{CO}_2$ . The reference reflection lines of hcp and fcc Co, as well as  $\text{TiO}_2$ -anatase and -rutile are also included. See the black arrows indicating hcp Co reflections. (Feed composition: 1% CO, 1%  $\text{O}_2$ , 46%  $\text{H}_2$ , 10%  $\text{H}_2\text{O}$ , 9%  $\text{CO}_2$  and 33%  $\text{N}_2$ ; pressure: atmospheric, GHSV: 60000 mL(NTP)/g $\text{Co}_3\text{O}_4$ /hr). 313

**Figure A.8.1:** (a) Bright-field STEM image of the spent  $\text{Co}_3\text{O}_4/\text{TiO}_2$ -anatase catalyst obtained after dry CO-PrOx. (b) Magnified STEM-EELS elemental map showing the regions with Ti, O and Co. (c) Corresponding magnified STEM-EELS maps of the individual elements. 315

**Figure A.8.2:** (a) Bright-field STEM image of the spent  $\text{Co}_3\text{O}_4/\text{SiC}$  catalyst after dry CO-PrOx. (b) Magnified STEM-EELS elemental map showing the regions with Si, O, Co as well as (c) carbon. 316

**Figure A.8.3:** (a) Bright-field STEM image of the spent  $\text{Co}_3\text{O}_4/\text{SiO}_2$  and  $\text{Co}_3\text{O}_4/\text{SiO}_2$  catalysts, respectively, obtained after dry CO-PrOx. (b) Magnified STEM-EELS elemental maps showing the regions with the elements Si, Zr, O and Co where applicable. 317

**Figure A.9.1:** Results from after performing a linear combination fitting of the first derivative XANES spectrum of  $\text{Co}_3\text{O}_4/\text{CeO}_2$  obtained after dry CO-PrOx. 318

## List of Tables

<b>Table 2.1:</b> Chemical phases present before and after dry CO-PrOx (1.00% CO, 1.86% O <sub>2</sub> , 90.20% H <sub>2</sub> , bal. N <sub>2</sub> ), and the onset temperature for methane formation reported by Teng <i>et al.</i> [26] for different metal oxide catalysts.	14
<b>Table 2.2:</b> Onset reduction temperatures of Co <sub>3</sub> O <sub>4</sub> on different metal oxide support materials during H <sub>2</sub> -TPR. (From [32]).	17
<b>Table 2.3:</b> Melting temperatures of common metal and metal oxide CO-PrOx catalysts as well as their corresponding calculated Hüttig and Tamman temperatures.	33
<b>Table 2.4:</b> Magnetic properties of common cobalt-based materials relevant to this study.	42
<b>Table 4.1:</b> Chemicals used for the synthesis of un-/supported Co <sub>3</sub> O <sub>4</sub> using the reverse microemulsion technique or incipient wetness impregnation, respectively.	65
<b>Table 4.2:</b> Composition of the reverse microemulsion prepared for the synthesis of the unsupported Co(OH) <sub>x</sub> precipitate.	67
<b>Table 4.3:</b> Appearance of the bare and Co <sub>3</sub> O <sub>4</sub> -loaded before and after impregnation and calcination, respectively.	69
<b>Table 4.4:</b> Gas compositions for the reduction experiments.	78
<b>Table 4.5:</b> Gas compositions for the total and preferential oxidation of CO.	81
<b>Table 4.6:</b> Parameters set for achieving gas separation in the respective modules of the micro-GC.	88
<b>Table 5.1:</b> Results from after performing Rietveld refinement (using TOPAS 5.0) on the <i>ex situ</i> PXRD patterns of the fresh supported catalysts.	109
<b>Table 5.2:</b> STEM-derived average number- and volume-based particle sizes.	117
<b>Table 5.3:</b> Summary of the results from nitrogen physisorption and ICP-OES.	119
<b>Table 6.1:</b> Hydrogen consumption and degree of reduction calculated for the bare CeO <sub>2</sub> support and Co <sub>3</sub> O <sub>4</sub> /CeO <sub>2</sub> catalyst during conventional H <sub>2</sub> -TPR.	144
<b>Table 7.1:</b> Summary of the calculated equilibrium conversions at 450 °C of the limiting reactants of each gas-phase reaction considered in the thermodynamic evaluation.	158
<b>Table 8.1:</b> Summary of the $\gamma$ values calculated from magnetometry data recorded at 450 °C during dry CO-PrOx at atmospheric pressure.	199

<b>Table 8.2:</b> STEM-derived average number- and volume-based particle sizes for a selected number of spent catalysts.	214
<b>Table 8.3:</b> Summary of the results obtained after performing a linear combination fit of the normalised XANES spectra.	221
<b>Table 9.1:</b> Summary of the $\gamma$ values calculated from magnetometry data recorded at 450 °C under different CO-PrOx conditions at atmospheric pressure.	262
<b>Table 9.2:</b> STEM-derived average number- and volume-based particle sizes for a selected number of spent catalysts.	266
<b>Table 9.3:</b> Summary of the results obtained after performing a linear combination fit of the normalised XANES spectra.	269
<b>Table A.1.1:</b> Heat capacity coefficients as well as standard formation enthalpy and Gibbs free energy values of each substance considered in the thermodynamic evaluations.	299
<b>Table A.2.1:</b> ICDD PDF-2 entries of all chemical/crystal phases relevant to the current study.	300
<b>Table A.5.1:</b> Summary of the Rietveld refinement results performed on the last <i>in situ</i> PXRD pattern ( <i>i.e.</i> , at 450 °C) recorded during reduction at atmospheric pressure in a 50:50 H <sub>2</sub> :N <sub>2</sub> mixture.	305
<b>Table A.5.2:</b> Summary of the Rietveld refinement results performed on the last <i>in situ</i> PXRD pattern ( <i>i.e.</i> , at 450 °C) recorded under different reduction conditions at atmospheric pressure over unsupported Co <sub>3</sub> O <sub>4</sub> .	306
<b>Table A.7.1:</b> Summary of the Rietveld refinement results performed on the last <i>in situ</i> PXRD pattern ( <i>i.e.</i> , at 450 °C) recorded under different CO-PrOx conditions at atmospheric pressure over selected catalysts.	314

# Nomenclature

## Abbreviations

3WV	Three-Way Valve
BET	Brunauer–Emmett–Teller
BJH	Barrett, Joyner and Halenda
BPR	Back Pressure Regulator
CO-PrOx	Preferential Oxidation of CO (carbon monoxide)
CO-TOx	Total Oxidation of CO
DFT	Density Functional Theory
DoR	Degree of Reduction
EDX	Energy-Dispersive X-ray spectroscopy
EELS	Electron Energy Loss Spectroscopy
EXAFS	Extended X-ray Absorption Fine Structure
fcc	Face-Centred Cubic
FIC	Flow Indicator and Control
GC	Gas Chromatography
GHSV	Gas Hourly Space Velocity
hcp	Hexagonal Closed-Packed
HRTEM	High-Resolution Transmission Electron Microscopy
ICDD	International Centre for Diffraction Data
ICP-OES	Inductively Coupled Plasma-Optical Emission Spectroscopy
LCF	Linear Combination Fitting
MFC	Mass Flow Controller
MSC	Metal-Support Compound
MSI	Metal-Support Interaction
MSSA	Mass-Specific Surface Area
MvK	Mars-van Krevelen
NPSI	NanoParticle-Support Interaction
NTP	Normal Temperature and Pressure (298.15 K and 1.013 bar)
NV	Needle Valve

PDF-2	Powder Diffraction File-2
PEGDE	Penta-Ethylene Glycol Dodecyl-Ether
PIC	Pressure Indicator and Control
PONKCS	Partial or No Known Crystal Structures
PR	Pressure Regulator
PXRD	Powder X-Ray Diffraction
rWGS	Reverse Water-Gas Shift
STEM	Scanning Transmission Electron Microscopy
TCD	Thermal Conductivity Detector
TEM	Transmission Electron Microscopy
TIC	Temperature Indicator and Control
TOPAS	Total Pattern Analysis Solutions
TPR	Temperature Programmed Reduction
WGS	Water-Gas Shift
XANES	X-ray Absorption Near Edge Structure
XAS	X-ray Absorption Spectroscopy
XRD	X-Ray Diffraction

### **Chemical formulas**

$\text{Al}_2\text{O}_3$	Aluminium oxide or Alumina
$\text{CeO}_2$	Cerium(IV) oxide or Ceria
$\text{CH}_4$	Methane
Co	Cobalt
CO	Carbon monoxide
$\text{Co}(\text{NO}_3)_2 \cdot 6\text{H}_2\text{O}$	Cobalt(II) nitrate hexahydrate
$\text{Co}(\text{OH})_2$	Cobalt(II) hydroxide
$\text{CO}_2$	Carbon dioxide
$\text{Co}_2\text{SiO}_4$	Cobalt(II) silicon oxide or Cobalt(II) silicate
$\text{Co}_3\text{O}_4$	Cobalt(II, III) oxide
$\text{CoAl}_2\text{O}_4$	Cobalt(II) aluminium oxide or Cobalt(II) aluminate
CoO	Cobalt(II) oxide
$\text{CoTiO}_3$	Cobalt(II) titanium(IV) oxide or Cobalt(II) titanate

---

H <sub>2</sub>	Molecular hydrogen
H <sub>2</sub> O	Water
N <sub>2</sub>	Molecular nitrogen
NH <sub>3</sub>	Ammonia
O <sub>2</sub>	Molecular oxygen
SiC	Silicon carbide
SiO <sub>2</sub>	Silicon dioxide or Silica
TiO <sub>2</sub>	Titanium(IV) oxide or Titania
ZrO <sub>2</sub>	Zirconium(IV) oxide or Zirconia

## Notations

A	Area in gas chromatogram
d	Particle diameter, in nm or interplanar distance (or d-spacing), in Å
F	Response factor
H	Enthalpy, in kJ/mol or external magnetic field, in kOe or Tesla
k <sub>B</sub>	Boltzmann constant, $1.380649 \times 10^{-23}$ J/K
M	Sample magnetisation, in emu or mass loading, in g
M <sub>rem</sub>	Remnant magnetisation, in emu
M <sub>s</sub>	Saturation magnetisation, in emu
N <sub>A</sub>	Avogadro's number, $6.02214076 \times 10^{23}$ mol <sup>-1</sup>
S	Selectivity, in %
T	Temperature, in °C or K
T <sub>C</sub>	Curie temperature, in K
T <sub>Hüttig</sub>	Hüttig temperature, in K
T <sub>melting</sub>	Melting temperature, in K
T <sub>N</sub>	Néel temperature, in K
T <sub>Tamman</sub>	Tamman temperature, in K
v	Volumetric flow rate, in ml/min
X	Conversion, in %

## **Greek notations**

$\gamma$	Amount of magnetic material displaying remnant magnetisation, in wt.-%
$\theta$	Powder X-Ray Diffraction angle, in $^{\circ}$
$\lambda$	Wavelength, in $\text{\AA}$
$\rho$	Density, in $\text{g/cm}^3$
$\sigma$	Mass-specific magnetisation, in emu/g or standard deviation, in nm
$\omega$	Water-to-surfactant molar ratio

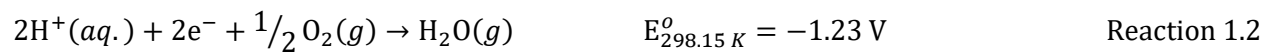
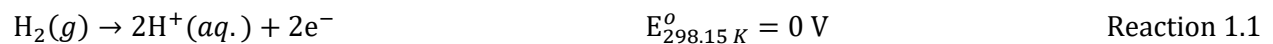
# Chapter 1: Introduction

## 1.1. Electrical Energy from Fuel Cells

The development of the fuel cell technology offers a unique opportunity for producing electrical energy from hydrogen ( $H_2$ ) for mobile and stationary applications in an environmentally friendly manner [2–4], especially if the  $H_2$  is produced from carbon-free sources, for example, *via* the electrolysis of  $H_2O$  [5] or  $NH_3$  [6]. The use of fuel cells can also be environmentally viable if the  $H_2$  is produced from carbon-based sources that were originally manufactured from sequestered carbon dioxide ( $CO_2$ ), which would aid in the attempt of reducing  $CO_2$  emissions in line with the Paris Agreement [7].

A fuel cell is an electrochemical battery that is divided into three compartments, *viz.*, the anode, cathode and electrolyte, with the latter separating the former two compartments. There are different kinds of fuel cells and each is named according to the kind of electrolyte used [3,8]. These include proton-exchange or polymer electrolyte membrane fuel cells (PEMFCs), alkaline fuel cells (AFCs), phosphoric acid fuel cells (PAFCs), molten carbonate fuel cells (MCFCs) and solid oxide fuel cells (SOFCs). They are all operated at different temperatures ranging from 40 – 80 °C for PEMFCs, and going up to as high as 600 – 1000 °C for SOFCs. Each type of fuel cell is suited for different applications, for example, PEMFCs are mostly efficient for automotive and small stationary platforms, whereas SOFCs are more suitable for residential and commercial purposes [3,8]. Out of the total number of fuel cells being produced, 80% of these are the PEMFCs due to their lightweight, efficiency for both mobile and stationary applications, low start-up and operating temperatures, and high-power density. It is for these reasons that great attention has been focused on PEMFCs, particularly finding ways to improve their overall performance.

PEMFCs consist of two gas diffusion layers (GDLs) and two catalyst layers (CL's) – with one GDL and CL on the anode side, and one GDL and CL on the cathode side as shown in Figure 1.1 [4,9]. Ideally at the anode side, pure H<sub>2</sub> fuel is fed and diffuses through the GDL to a platinum-based CL where it is oxidised by being split into two protons and two electrons (Reaction 1.1). The electrons are transported *via* an external circuit (creating an external current), while the protons are transported along the membrane to the cathode compartment. At the cathode side, O<sub>2</sub> is fed and diffuses through the GDL to a platinum-based CL where it is reduced to H<sub>2</sub>O (Reaction 1.2) as also shown in Figure 1.1. The maximum theoretical potential that can be achieved by a single PEMFC at 298 K and 1.013 bar is 1.23 V (see the sum of Reactions 1.1 and 1.2 giving Reaction 1.3) [2,4,9]. However, at 353 K and 1.013 bar, this theoretical value decreases to about 1.169 V. Under realistic conditions, the operating potential of a single cell can be far below these mentioned theoretical potentials due to reaction activation, proton-electron transport and gas transport losses of the cell. Therefore, at normal current densities, the cell potential can be expected to be between 0.6 and 0.95 V [2,4,9].



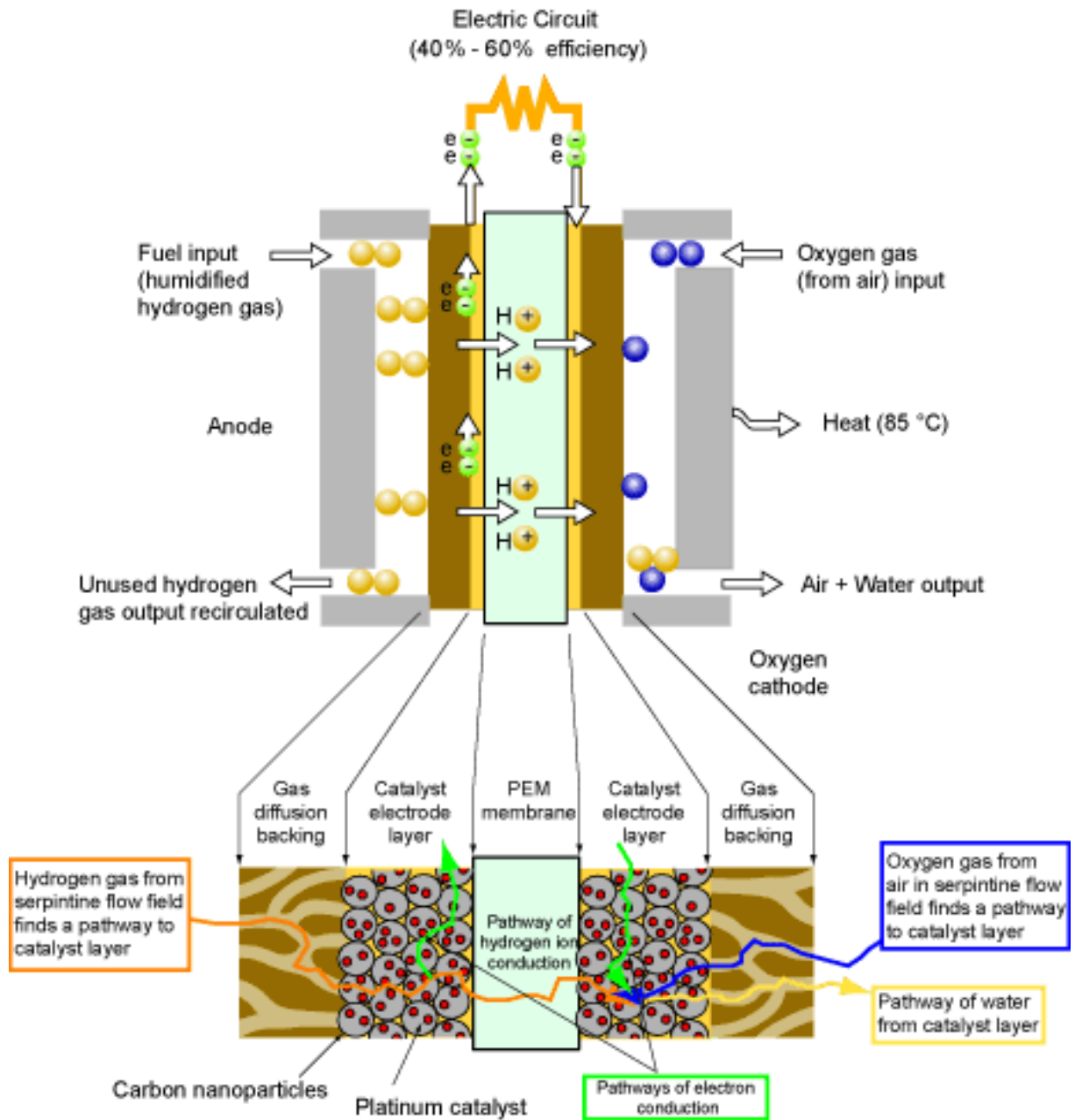


**Figure 1.1:** Schematic of a typical PEMFC. (From [10,11]).

## 1.2. Hydrogen Production for PEM Fuel Cells

Hydrogen is the main component of the universe, more specifically, it represents 74 wt.-% of the sun. However, the sun's  $H_2$  disappears every second by fusion to form helium and energy, and only part of this energy reaches the Earth [12]. To date, the main processes for producing  $H_2$  on Earth are coal gasification [13] and steam reforming of hydrocarbons and alcohols [14,15]. Steam

reforming for instance also yields carbon monoxide (CO), carbon dioxide (CO<sub>2</sub>) and H<sub>2</sub>O. Particularly, CO is in the 0.5 – 2% range in the H<sub>2</sub>-rich reformat gas after applying the high- and low-temperature water-gas shift (WGS) processes [15–22]. This concentration of CO has been reported to be poisonous to the platinum-based anode catalyst of the PEMFC. More specifically, CO competitively adsorbs on the anode catalyst and as a result, interferes with the dissociative adsorption of H<sub>2</sub> and the subsequent charge transfer processes required to take place in the PEMFC. Therefore, great effort is currently going towards decreasing this amount of CO to below 10 ppm (which is equivalent to a minimum conversion/removal of 99.999% of the CO) in the reformat before entering the PEMFC [15–22].

Processes including, i) pressure swing adsorption, ii) membrane separation, iii) selective methanation of CO and the iv) preferential oxidation of CO have been considered for this purpose [21,22]. Briefly, **pressure swing adsorption (PSA)** is based on a changing pressure gradient during which gases are adsorbed on either a single adsorber (batch process) or on multiple adsorbers (continuous process). PSA is unfortunately not suited for the small-scale production of H<sub>2</sub> for PEMFCs as it cannot be incorporated into the on-board H<sub>2</sub> production chain. This is the case for devices with integrated fuel processing units, including steam reforming and water-gas shift [23–25] (see Figure 1.2). In addition to this, high pressures are required for high efficiency which means, strong and highly expensive adsorbers would be needed [15,22,26].

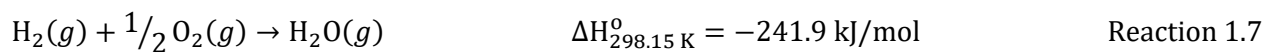
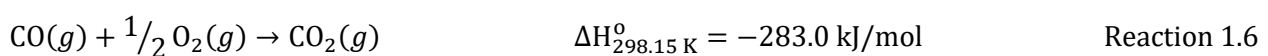
**Membrane separation** involves the use of a semi-permeable membrane which should ideally allow H<sub>2</sub> to permeate and not the other gases in the reformat. Unlike PSA, this process can be incorporated into the on-board H<sub>2</sub> production for PEMFCs but to date, highly expensive palladium-based membranes have shown higher efficiencies for this process [27,28]. Also, some of the membranes used tend to undergo embrittlement and can also form hydrides, which results in the loss of selectivity [29].

**Selective methanation of CO** can be used for the large- and small-scale production of CO-free H<sub>2</sub>. The process involves converting one unit of CO to one unit of methane (CH<sub>4</sub>) using three units of the H<sub>2</sub> present in the reformat (Reaction 1.4) over a heterogeneous catalyst (*e.g.*, nickel (Ni) or ruthenium (Ru)) [30,31]. However, this process decreases the amount of H<sub>2</sub> that gets fed into the PEMFC as a result of CO hydrogenation. Since CO<sub>2</sub> is also present in the reformat, this can affect the selectivity of the process at high temperatures where CO<sub>2</sub> can also be hydrogenated to CH<sub>4</sub>. The conversion of one unit of CO<sub>2</sub> to one unit of CH<sub>4</sub> requires four units of H<sub>2</sub> present in the reformat (Reaction 1.5), which further decreases the amount of H<sub>2</sub> [23,24].



The **preferential oxidation of CO (CO-PrOx)** is also suitable for the large- and small-scale on-board production of H<sub>2</sub> and involves the oxidation of CO to CO<sub>2</sub> by co-feeding a relatively low amount O<sub>2</sub> in the form of air over a heterogeneous catalyst (Reaction 1.6) [15–22]. This process aims to also minimise the consumption of H<sub>2</sub> which could potentially take place *via* oxidation to H<sub>2</sub>O as shown in Reaction 1.7. However, finding a cheap, stable, active and (a 100%) selective catalyst is still a challenge as far as the development of this process is concerned [15–22]. CO-PrOx lies between a low-temperature WGS unit and a PEMFC unit, respectively, as shown in Figure 1.2. The low temperature WGS process is normally operated between 250 and 300 °C, whereas a PEMFC is normally operated between 40 and 80 °C. Therefore, this implies that CO-PrOx should ideally be effective between 80 and 250 °C [15,17–22].

The commercialisation of CO-PrOx was first attempted by Engelhard Industries (which later merged into BASF) in the early 1960's for the purification of H<sub>2</sub> to be used in the synthesis of ammonia [30,32,33]. The H<sub>2</sub> was obtained from reforming natural gas, and then applying water-gas shift and CO-PrOx to decrease the CO content below 20 ppm. Johnson Matthey also proposed an integrated fuel processing device in the late 1990's, which firstly involved methanol steam reforming and then CO-PrOx, before feeding the CO-free H<sub>2</sub> into the PEMFC [23–25]. Note that this integrated fuel processing device did not include a water-gas shift unit/reactor as the CO content after applying methanol steam reforming was low enough (below 4%) to begin the CO-PrOx process. It is worth mentioning that the common challenge faced in industry is the high exothermicity of the CO oxidation reaction (see Reaction 1.6) [22–25,30]. This complicates the design and/or integration of a CO-PrOx unit into the fuel processing chain as measures for effective cooling will need to be in place. Despite these challenges, CO-PrOx is still regarded as the most effective process for decreasing the amount of CO in the reformat gas for ultimate use in PEMFCs.



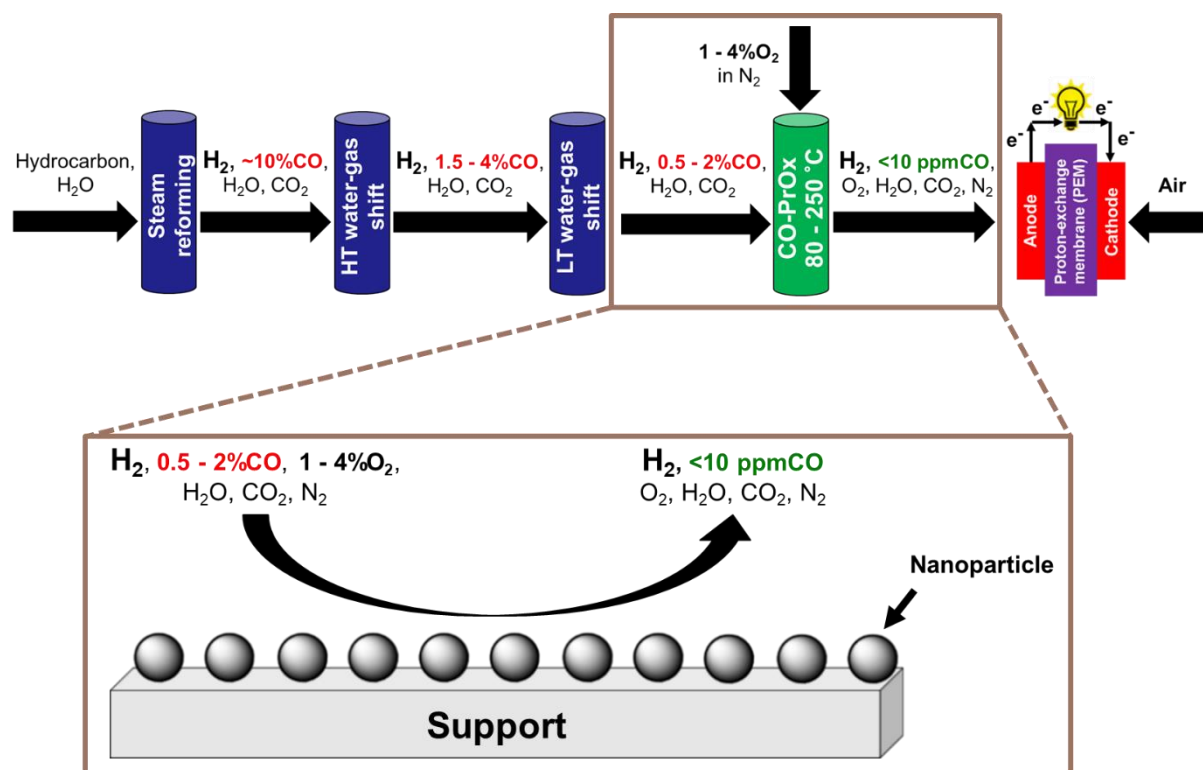
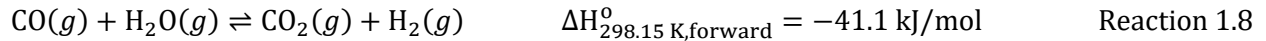


**Figure 1.2:** The processes involved in the production of H<sub>2</sub>-rich reformat gas including a CO-PrOx unit between a low temperature WGS unit and a PEMFC unit.

The work presented herein investigated cobalt(II, III) oxide (Co<sub>3</sub>O<sub>4</sub>) nanoparticles, supported on a variety of common support materials, as potential cheaper alternative catalysts to the widely used noble metal-based ones for CO-PrOx. Co<sub>3</sub>O<sub>4</sub> has been extensively studied and reported to possess good CO oxidation activity in the absence of H<sub>2</sub>, H<sub>2</sub>O and CO<sub>2</sub> [34–38]. It has also shown great promise for the CO-PrOx process, mostly when only H<sub>2</sub> is co-fed with the CO and O<sub>2</sub>. However, recent *in situ* work (and some *ex situ* work) shows Co<sub>3</sub>O<sub>4</sub> reducing at elevated reaction temperatures to CoO and metallic Co [39–44]. The formation of metallic Co changes the conversion pathway of CO from oxidation to hydrogenation, forming CH<sub>4</sub> instead of CO<sub>2</sub>.

Very little is known about the effect of H<sub>2</sub>O and CO<sub>2</sub> particularly on the performance (*i.e.*, activity and selectivity) and phase stability of Co<sub>3</sub>O<sub>4</sub>. Also, there are additional side reactions that have been speculated when H<sub>2</sub>O and CO<sub>2</sub> are co-fed, *viz.*, the forward and reverse water-gas shift reactions (Reaction 1.7), as well as CO<sub>2</sub> hydrogenation to CH<sub>4</sub> (Reaction 1.5) [30,41,45]. However, evidence for their occurrence has not been shown yet. Therefore, this study aimed to investigate the individual and combined effect of these two gases on Co<sub>3</sub>O<sub>4</sub> during CO-PrOx. The study also

investigated the occurrence of the mentioned side reactions and attempted to identify the cobalt-based phase(s) responsible for each side/undesired reaction.



In general, the phase stability of oxide nanoparticles can be improved by support materials through the introduction of nanoparticle-support interactions. The type of support and supported catalyst preparation method are some of the factors that influence the phase stability of the oxide nanoparticles [40,46,47]. In the context of CO-PrOx, the effect of the support in stabilising the catalyst (*i.e.*, Co<sub>3</sub>O<sub>4</sub>) has not been studied in detail yet. In addition to phase stability, the effect of the support on the catalytic performance is not well understood [40]. Therefore, the presented work also considered a wide range of support materials which have been grouped according to their known interacting nature with most nanoparticles: i) “**weakly interacting**” supports (*viz.*, CeO<sub>2</sub> and ZrO<sub>2</sub>), ii) “**strongly interacting**” supports (*viz.*, SiO<sub>2</sub>, TiO<sub>2</sub> and Al<sub>2</sub>O<sub>3</sub>) and, iii) “**inert**” supports (*viz.*, SiC). The aim was to study the effect of these supports on both phase stability and catalytic performance.

The evaluation of the catalysts was conducted in two complementary *in situ* instruments – a Powder X-Ray Diffraction (PXRD) capillary reaction cell [48–51] and a low-frequency vibrating sample magnetometer [49,51,52] – which allowed for studying the phase changes of the Co<sub>3</sub>O<sub>4</sub> under different reaction conditions and on different supports. Note that the experiments were carried out between 50 and 450 °C (or 100 and 450 °C, if H<sub>2</sub>O was co-fed), which is a wider temperature range than that reported for ideal CO-PrOx (*i.e.*, 80 – 250 °C) [15,17–22]. A wider range was chosen for this study so that the phase stability of Co<sub>3</sub>O<sub>4</sub> can be well-assessed over the various supports, and for the selectivity changes (caused by the reduction of Co<sub>3</sub>O<sub>4</sub> to CoO and metallic Co) to be adequately detected and quantified. This information would be valuable for future studies involving the development of Co<sub>3</sub>O<sub>4</sub>-based catalysts and in the optimisation of the reaction conditions (including temperature).

## References

- [1] G. Kolb, in: G. Kolb (Ed.), *Fuel Process. Fuel Cells*, Wiley-VCH Verlag GmbH & Co. KGaA, Weinheim, Germany, 2008, pp. 1–2.
- [2] F. Barbir, S. Yazici, *Int. J. Energy Res.* 32 (2008) 369–378.
- [3] G. Kolb, in: G. Kolb (Ed.), *Fuel Process. Fuel Cells*, Wiley-VCH Verlag GmbH & Co. KGaA, Weinheim, Germany, 2008, pp. 3–16.
- [4] Y.-J. Wang, J. Qiao, R. Baker, J. Zhang, *Chem. Soc. Rev.* 42 (2013) 5768–5787.
- [5] S. Shiva Kumar, V. Himabindu, *Mater. Sci. Energy Technol.* 2 (2019) 442–454.
- [6] N. Hanada, S. Hino, T. Ichikawa, H. Suzuki, K. Takai, Y. Kojima, *Chem. Commun.* 46 (2010) 7775.
- [7] Paris Agreement: Sustainable Development Knowledge Platform.  
<https://sustainabledevelopment.un.org/frameworks/parisagreement> (accessed April 2021).
- [8] B. Kalmula, V.R. Kondapuram, *Renew. Sustain. Energy Rev.* 45 (2015) 409–418.
- [9] F. Barbir, in: N. Sammes (Ed.), *Fuel Cell Technol.*, Springer London, London, 2006, pp. 27–51.
- [10] NIST. PEM Fuel Cells. 2006.  
<https://physics.nist.gov/MajResFac/NIF/pemFuelCells.html> (accessed February 2020).
- [11] Y. Wang, K.S. Chen, J. Mishler, S.C. Cho, X.C. Adroher, *Appl. Energy* 88 (2011) 981–1007.
- [12] N.N. Greenwood, A. Earnshaw, in: N.N. Greenwood, A. Earnshaw (Eds.), *Chem. Elem.*, 2nd ed., Elsevier, 1997, pp. 32–67.
- [13] T. Kaneko, F. Derbyshire, E. Makino, D. Gray, M. Tamura, in: *Ullmann’s Encycl. Ind. Chem.*, Wiley-VCH Verlag GmbH & Co. KGaA, Weinheim, Germany, 2001, pp. 311–389.
- [14] J.N. Armor, *Appl. Catal. A* 176 (1999) 159–176.
- [15] N. Bion, F. Epron, M. Moreno, F. Mariño, D. Duprez, *Top. Catal.* 51 (2008) 76–88.
- [16] S.H. Oh, R.M. Sinkevitch, *J. Catal.* 142 (1993) 254–262.
- [17] T.V. Choudhary, D.W. Goodman, *Catal. Today* 77 (2002) 65–78.
- [18] A. Faur Ghenciu, *Curr. Opin. Solid State Mater. Sci.* 6 (2002) 389–399.
- [19] G. Zhou, Y. Jiang, H. Xie, F. Qiu, *Chem. Eng. J.* 109 (2005) 141–145.

- [20] S. Huang, K. Hara, A. Fukuoka, *Energy Environ. Sci.* 2 (2009) 1060–1068.
- [21] E.D. Park, D. Lee, H.C. Lee, *Catal. Today* 139 (2009) 280–290.
- [22] A. Mishra, R. Prasad, *Bull. Chem. React. Eng. Catal.* 6 (2011) 1–14.
- [23] N. Edwards, S.R. Ellis, J.C. Frost, S.E. Golunski, A.N.J. van Keulen, N.G. Lindewald, J.G. Reinkingh, *J. Power Sources* 71 (1998) 123–128.
- [24] S. Golunski, *Platin. Met. Rev.* 42 (1998) 2–7.
- [25] P.G. Gray, M.I. Petch, *Platin. Met. Rev.* 44 (2000) 108–111.
- [26] S. Sircar, T.C. Golden, *Sep. Sci. Technol.* 35 (2000) 667–687.
- [27] Y. Sakamoto, F.L. Chen, Y. Kinari, F. Sakamoto, *Int. J. Hydrog. Energy* 21 (1996) 1017–1024.
- [28] S. Adhikari, S. Fernando, *Ind. Eng. Chem. Res.* 45 (2006) 875–881.
- [29] T.M. Adams, J. Mickalonis, *Mater. Lett.* 61 (2007) 817–820.
- [30] M.L. Brown Jr., A.W. Green, G. Cohn, H.C. Andersen, *Ind. Eng. Chem.* 52 (1960) 841–844.
- [31] A. Rehmat, S.S. Randhava, *Ind. Eng. Chem. Prod. Res. Dev.* 9 (1970) 512–515.
- [32] M.L. Brown Jr., A.W. Green, *Treatment of Gases*, US Patent 3,088,919 A, 1963.
- [33] J.G.E. Cohn, *Process for Selectively Removing Carbon Monoxide from Hydrogen-Containing Gases*, US Patent 3,216,783 A, 1965.
- [34] J. Jansson, *J. Catal.* 194 (2000) 55–60.
- [35] M.M. Yung, E.M. Holmgren, U.S. Ozkan, *Catal. Lett.* 118 (2007) 180–186.
- [36] Y.-Z. Wang, Y.-X. Zhao, C.-G. Gao, D.-S. Liu, *Catal. Lett.* 125 (2008) 134–138.
- [37] L. Lukashuk, N. Yigit, R. Rameshan, E. Kolar, D. Teschner, M. Hävecker, A. Knop-Gericke, R. Schlögl, K. Föttinger, G. Rupprechter, *ACS Catal.* 8 (2018) 8630–8641.
- [38] L. Lukashuk, N. Yigit, H. Li, J. Bernardi, K. Föttinger, G. Rupprechter, *Catal. Today* 336 (2019) 139–147.
- [39] Y. Teng, H. Sakurai, A. Ueda, T. Kobayashi, *Int. J. Hydrog. Energy* 24 (1999) 355–358.
- [40] Z. Zhao, M.M. Yung, U.S. Ozkan, *Catal. Commun.* 9 (2008) 1465–1471.
- [41] L. Lukashuk, K. Föttinger, E. Kolar, C. Rameshan, D. Teschner, M. Hävecker, A. Knop-Gericke, N. Yigit, H. Li, E. McDermott, M. Stöger-Pollach, G. Rupprechter, *J. Catal.* 344 (2016) 1–15.

- [42] T.M. Nyathi, N. Fischer, A.P.E. York, M. Claeys, *Faraday Discuss.* 197 (2017) 269–285.
- [43] M. Khasu, T. Nyathi, D.J. Morgan, G.J. Hutchings, M. Claeys, N. Fischer, *Catal. Sci. Technol.* 7 (2017) 4806–4817.
- [44] T.M. Nyathi, N. Fischer, A.P.E. York, D.J. Morgan, G.J. Hutchings, E.K. Gibson, P.P. Wells, C.R.A. Catlow, M. Claeys, *ACS Catal.* 9 (2019) 7166–7178.
- [45] M.P. Woods, P. Gawade, B. Tan, U.S. Ozkan, *Appl. Catal. B* 97 (2010) 28–35.
- [46] S.J. Tauster, S.C. Fung, R.L. Garten, *J. Am. Chem. Soc.* 100 (1978) 170–175.
- [47] L.J. Garces, B. Hincapie, R. Zerger, S.L. Suib, *J. Phys. Chem. C* 119 (2015) 5484–5490.
- [48] M.C.M. Claeys, N.F. Fischer, Sample Presentation Device for Radiation-Based Analytical Equipment, US Patent 8,597,598 B2, 2013.
- [49] N. Fischer, B. Clapham, T. Feltes, E. van Steen, M. Claeys, *Angew. Chemie - Int. Ed.* 53 (2014) 1342–1345.
- [50] N. Fischer, M. Claeys, *Catal. Today* 275 (2016) 149–154.
- [51] N. Fischer, M. Claeys, *J. Phys. D. Appl. Phys.* 53 (2020) 293001.
- [52] M.C.M. Claeys, E.W.J. van Steen, J.L. Visagie, J. van de Loosdrecht, Magnetometer, US Patent 8,773,118 B2, 2014.

## Chapter 2: Literature Review

### 2.1. Catalysts for the Preferential Oxidation of Carbon Monoxide

#### 2.1.1. Noble metals

The preferential oxidation of carbon monoxide (CO-PrOx) is a heterogeneously catalysed gas-phase reaction between CO and O<sub>2</sub> to form CO<sub>2</sub> (see Reaction 1.6) in a H<sub>2</sub>-rich environment [1–10]. The catalysts mostly used for this process are noble metal-based ones as these have shown very good catalytic performance, owing to their strong binding of CO. Recently, significant research interest has shifted towards base metal oxides which have shown great promise as cheaper alternatives to the noble metals for the CO-PrOx reaction [6–10].

Other than the mentioned cost differences, CO oxidation over noble metals is based on a different reaction mechanism to that observed over base metal oxides. Over noble metals, a Langmuir-Hinshelwood (L-H)-type mechanism is observed [11,12]. This mechanism is based on the surface adsorption of CO and dissociative adsorption of O<sub>2</sub>, followed by the formation of adsorbed CO<sub>2</sub> which ultimately desorbs from the surface of the noble metal (Figure 2.1). Since the CO-PrOx feed also contains H<sub>2</sub> which can also be oxidised to H<sub>2</sub>O, it is believed that this oxidation process also goes *via* a similar mechanism. The reaction temperature, adsorption strength of CO and H<sub>2</sub> by the catalyst and the concentration of O<sub>2</sub> in the feed, all determine which reaction will be kinetically favoured. It should also be noted that H<sub>2</sub> is often present in very high amounts relative to CO, which also increases its likelihood to react with the available O<sub>2</sub> [11,12].

Some reported work has involved bimetallic catalysts, either including two noble metals [13,14] or one noble metal and one base metal [15,16]. In the noble-base bimetallic case, the cost of the

catalyst is also decreased. Bimetallic systems can also carry bifunctionality in that, one metal can have better ability of adsorbing CO, and the other can have the ability to dissociatively adsorb O<sub>2</sub>. An added advantage would be using a metal that can preferentially adsorb CO over H<sub>2</sub>. However, just as in the case of monometallic systems, CO oxidation over bimetallic systems is also believed to take place *via* the L-H mechanism.

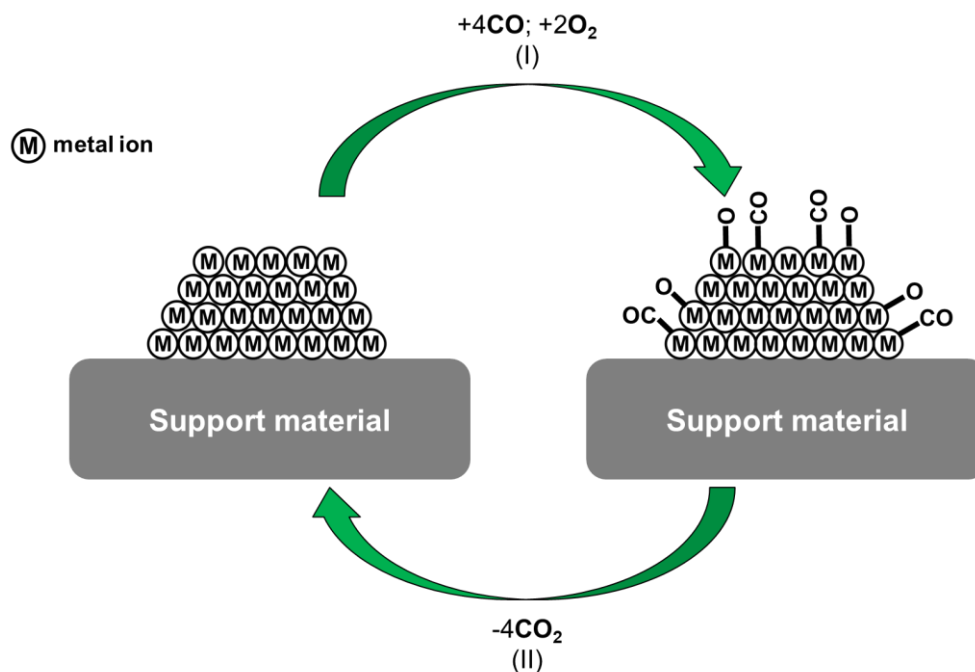


**Figure 2.1:** Langmuir-Hinshelwood mechanism for CO oxidation over a monometallic catalyst. The mechanism is also applicable to bimetallic catalysts.

### 2.1.2. Base metal oxides

Over base metal oxides, a Mars-van Krevelen (MvK)-type mechanism is reported [17–21]. In this mechanism, the CO adsorbs and instead of being oxidised by gas-phase O<sub>2</sub>, the responsible oxygen species come from the lattice of the metal oxide. Upon removal of lattice oxygen species from the surface of the base metal oxide, the surface is left partially reduced, *i.e.*, with oxygen vacancies. The gas-phase O<sub>2</sub> co-fed with the CO then replenishes the removed oxygen atoms to regenerate the metal oxide, creating an overall RedOx (Reduction-Oxidation) cycle (see Figure 2.2.). The regeneration of the catalyst during CO oxidation is highly dependent on the amount of O<sub>2</sub> in the

feed. According to Reaction 1.6, there should at least be a 1:2  $O_2:CO$  ratio in the feed for the mechanism to be sustainable. Higher  $O_2$  concentrations increase the rate of O replenishment in the vacancies, thus increasing the overall rate of CO oxidation [15,21,22]. On the other hand, lower  $O_2$  concentrations and increased reaction temperature, would increase the chances of the surface and bulk phase of the catalyst to be reduced [21,23]. The MvK mechanism can also be observed over noble metals, especially when the  $O_2:CO$  ratio is above 0.5. The excess  $O_2$  is reported to oxidise the surface of the metal oxide, forming a thin oxide layer which allows for the conversion of CO via the MvK mechanism [24,25].

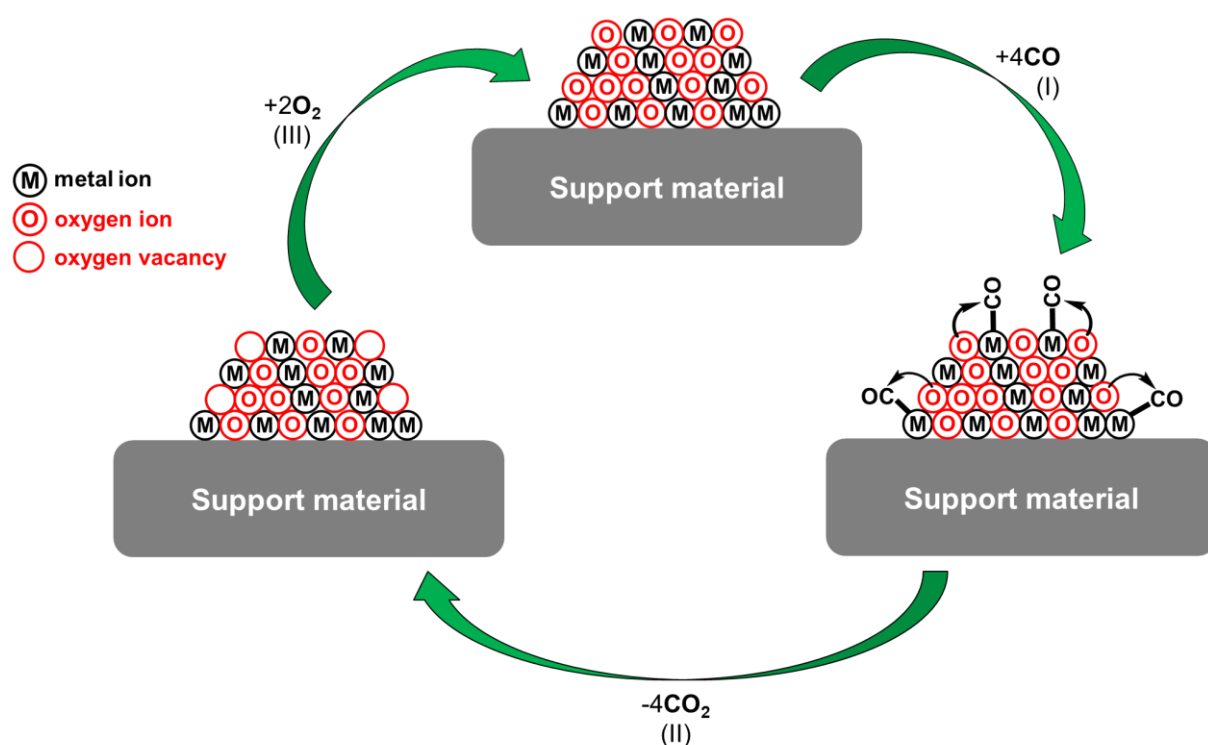


**Figure 2.2:** Mars-van Krevelen mechanism for CO oxidation over a metal oxide catalyst.

Metal oxides such as CuO [26–29] and  $Co_3O_4$  [22,26,30–37], have been extensively investigated for the CO-PrOx reaction, as well as NiO [26,38,39] and CoO [26,40] in a few cases. All these metal oxides have shown great promise as CO-PrOx catalysts and can potentially serve as alternatives to noble metals. The problem with metal oxides is that they are susceptible to phase change *via* reduction which forms less active and/or selective forms of the catalyst. The reduction is caused by the high amounts of  $H_2$  and high reaction temperatures that the catalyst gets exposed to. Teng *et al.* [26], provided the first *ex situ* evidence for the reduction of these oxides (see Table

2.1) and reported reduction as one of the deactivation mechanisms of metal oxide-based CO-PrOx catalysts. They further showed that upon reduction, the formed metallic catalysts (except for metallic Cu) catalysed the methanation of CO instead of oxidation. Others have recently provided *in situ* evidence for the reduction of some of these metal oxides, which will be discussed in detail in sub-section 2.3.1.

**Table 2.1:** Chemical phases present before and after dry CO-PrOx (1.00% CO, 1.86% O<sub>2</sub>, 90.20% H<sub>2</sub>, bal. N<sub>2</sub>), and the onset temperature for methane formation reported by Teng *et al.* [26] for different metal oxide catalysts.

Catalyst (before reaction)	Mass-specific surface area (m <sup>2</sup> /g)	Temperature for CH <sub>4</sub> production (°C)	Catalyst (after reaction)
CoO	13.5	> 250	Co, CoO
Co <sub>3</sub> O <sub>4</sub>	16.7	> 200	Co
CuO	9.2	-	Cu
NiO	53.1	> 200	Ni, NiO

## 2.2. Effect of the Support on CO-PrOx Catalysts

Heterogeneous catalysts (*e.g.*, noble metals and base metal oxides) are often made up of nano-sized particles which are deposited on a mechanically- and thermo-stable material referred to as a “support” [41]. Support materials are either base metal oxides (*e.g.*, SiO<sub>2</sub> and Al<sub>2</sub>O<sub>3</sub>), metal carbides (*e.g.*, SiC) or just mostly made up of carbon (*e.g.*, graphene or graphite) with high mass-specific surface areas (MSSA). The high MSSA is generally preferred as it ideally allows for uniform distribution of the nanoparticles and for the deposition of relatively high amounts (in mass) of the nanoparticles on the support [41].

The support material often does not participate in the reaction but in several oxidation reactions, some metal oxide supports have been reported to play a significant role in the conversion of substrates. This is believed to be related to the nature and/or strength of the metal-support

interaction (MSI) or nanoparticle-support interaction (NPSI) [37,42–44]. The reducibility of supported oxide nanoparticles in H<sub>2</sub> or CO can also be affected by these interactions. The nature and/or strength of the interactions can limit access to the available surface area of the nanoparticles because of their location (*e.g.*, those located inside the pores of the support) [41,45–47], alter the gas adsorption/dissociation capabilities of the nanoparticle or alter the strength of the metal-oxygen bonds in the oxide through electronic [48–52] and/or ligand-type effects [49,53–55]. The reactivity of the support and the strength of the interactions may also result in the formation of metal-support compounds (MSCs), for example, metal aluminates, -titanates or -silicates, arising from Al<sub>2</sub>O<sub>3</sub>, TiO<sub>2</sub> or SiO<sub>2</sub>, respectively. Note that these effects are also dependent on the catalyst preparation technique [37,56] and the size of the supported nanoparticles (with small ones (< 5 nm) being more likely to be affected) [25,57,58].

In this section (*i.e.*, section 2.2.) and in other parts of the thesis, the support materials used have been categorised as either being “**weakly interacting**”, “**strongly interacting**” or “**inert**”; based on their reported likelihood to form MSCs. However, it should be noted that this classification of the support materials is only used in the context of the current Ph.D. study and may not necessarily apply to other catalytic systems where different catalysts and/or reactions (or reaction conditions) are being studied. Furthermore, the exact classification does not originate from any published work, but it is based on the numerous publications that report the different behaviours of Co<sub>3</sub>O<sub>4</sub> nanoparticles when anchored on the supports used in the current study. This implies that the behaviours of the other Co-based phases (*viz.*, CoO and metallic Co) and of other metals and metal oxides, when anchored on the same supports, may not be the same as those of Co<sub>3</sub>O<sub>4</sub>.

### 2.2.1. Weakly interacting supports

The description “**weakly interacting**” refers to those metal oxide supports that seldom react with the nanoparticles to form MSCs. Such supports include ceria (CeO<sub>2</sub>) [22,25,32,33] and zirconia (ZrO<sub>2</sub>) [31,32,59,60]. In fact, after an exhaustive search of the literature, there are no known or well characterised Co-Ce or Co-Zr oxides. Nonetheless, CeO<sub>2</sub> is known to have good oxygen-storage and -release capabilities which are thought to be useful for reactions such as CO oxidation [25,29,61] and the water-gas shift [62,63]. It is mentioned that CeO<sub>2</sub> can alternate between the storage and release functions depending on the availability of oxygen species originating from the

reaction gas environment (*e.g.*, O<sub>2</sub> or H<sub>2</sub>O). In Co<sub>3</sub>O<sub>4</sub>/CeO<sub>2</sub> or CuO/CeO<sub>2</sub> catalysts, the interface between the CeO<sub>2</sub> and the Co or Cu oxide, respectively, is thought to have weakly bound lattice oxygen species that promote CO oxidation [25,64,65]. The Co or Cu oxide is also reducible on CeO<sub>2</sub>, and this also includes possible reduction of (near-)surface species of CeO<sub>2</sub> at very high temperatures (above 600 °C) [66–68].

The ZrO<sub>2</sub> support is not known for oxygen-storage and -release capabilities as it is a less reducible support. However, Co<sub>3</sub>O<sub>4</sub> nanoparticles supported on ZrO<sub>2</sub> have exhibited very good CO oxidation activity, sometimes comparable or higher than the nanoparticles supported on CeO<sub>2</sub> [28,32] (also see Figure 2.3). ZrO<sub>2</sub> also encourages H<sub>2</sub> dissociation over cobalt oxides and metallic Co which has been shown using Density Functional Theory (DFT) studies [69] and laboratory-based experiments [70]. This ensures high reducibility of the cobalt oxide and enhances the catalytic activity of metallic Co during hydrogenation reactions, for example. To prevent the formation of Co aluminates, -titanates and -silicates; the corresponding support materials have been impregnated with Zr prior to the impregnation with Co for reactions such as the Fischer-Tropsch synthesis (FTS) [59,60,71]. This sequential impregnation minimises or prevents the (strong) interaction of Co with the support.

### 2.2.2. Strongly interacting supports

Alumina (Al<sub>2</sub>O<sub>3</sub>), titania (TiO<sub>2</sub>) and silica (SiO<sub>2</sub>) are very well known for strongly interacting with supported metal oxide nanoparticles, sometimes leading to the formation of MSCs under certain reaction conditions [42,43,57,58,72,73]. In some literature, TiO<sub>2</sub> is regarded as a partially reducible support (especially the anatase crystal phase) [74–78] but, on the other hand, it is not known for having oxygen-storage and -release capabilities (as observed with CeO<sub>2</sub>) that could help enhance CO oxidation. In contrast, Al<sub>2</sub>O<sub>3</sub> and SiO<sub>2</sub> are known to be irreducible oxide materials. The reduction of supported metal oxides nanoparticles on these three support materials is often low, especially in the case of Al<sub>2</sub>O<sub>3</sub>. The behaviour of TiO<sub>2</sub> and SiO<sub>2</sub> sometimes varies in terms of the extent they affect metal oxide reduction, and with TiO<sub>2</sub>, the effect can also depend on its crystal phase (anatase or rutile) [72,73].

Assuming the MvK mechanism for CO oxidation over supported oxide nanoparticles, the low reducibility on Al<sub>2</sub>O<sub>3</sub>, TiO<sub>2</sub> and SiO<sub>2</sub> could also imply low CO oxidation activity since the MvK

mechanism relies on the metal oxide catalyst being reducible (ideally on the surface) [32,79,80]. An example of a study by Zhao *et al.* [32], showed that  $\text{Co}_3\text{O}_4$  on  $\text{CeO}_2$  and  $\text{ZrO}_2$  had a low onset temperature for reduction, while on  $\text{TiO}_2$  and  $\text{Al}_2\text{O}_3$ , the reduction was first observed at very high temperature (see summarised  $\text{H}_2$ -TPR results in Table 2.2). These catalysts were then tested under dry CO-PrOx conditions (*i.e.*, with no  $\text{H}_2\text{O}$  and  $\text{CO}_2$  in the feed) and high CO oxidation activity was exhibited by the easily reduced catalysts (see Figure 2.3(a)). During CO-PrOx,  $\text{Co}_3\text{O}_4$  can reduce to metallic Co, which favours methane formation from CO and  $\text{H}_2$ . Methane formation was first observed for the  $\text{CeO}_2$ - and  $\text{ZrO}_2$ -supported catalysts and only observed for the  $\text{TiO}_2$ - and  $\text{Al}_2\text{O}_3$ -supported catalysts at higher temperatures (Figure 2.3(c)).

**Table 2.2:** Onset reduction temperatures of  $\text{Co}_3\text{O}_4$  on different metal oxide support materials during  $\text{H}_2$ -TPR. (From [32]).

$\text{Co}_3\text{O}_4/\text{CeO}_2$	$\text{Co}_3\text{O}_4/\text{ZrO}_2$	$\text{Co}_3\text{O}_4/\text{SiO}_2$	$\text{Co}_3\text{O}_4/\text{TiO}_2$	$\text{Co}_3\text{O}_4/\text{Al}_2\text{O}_3$
320 °C	330 °C	330 °C	390 °C	470 °C

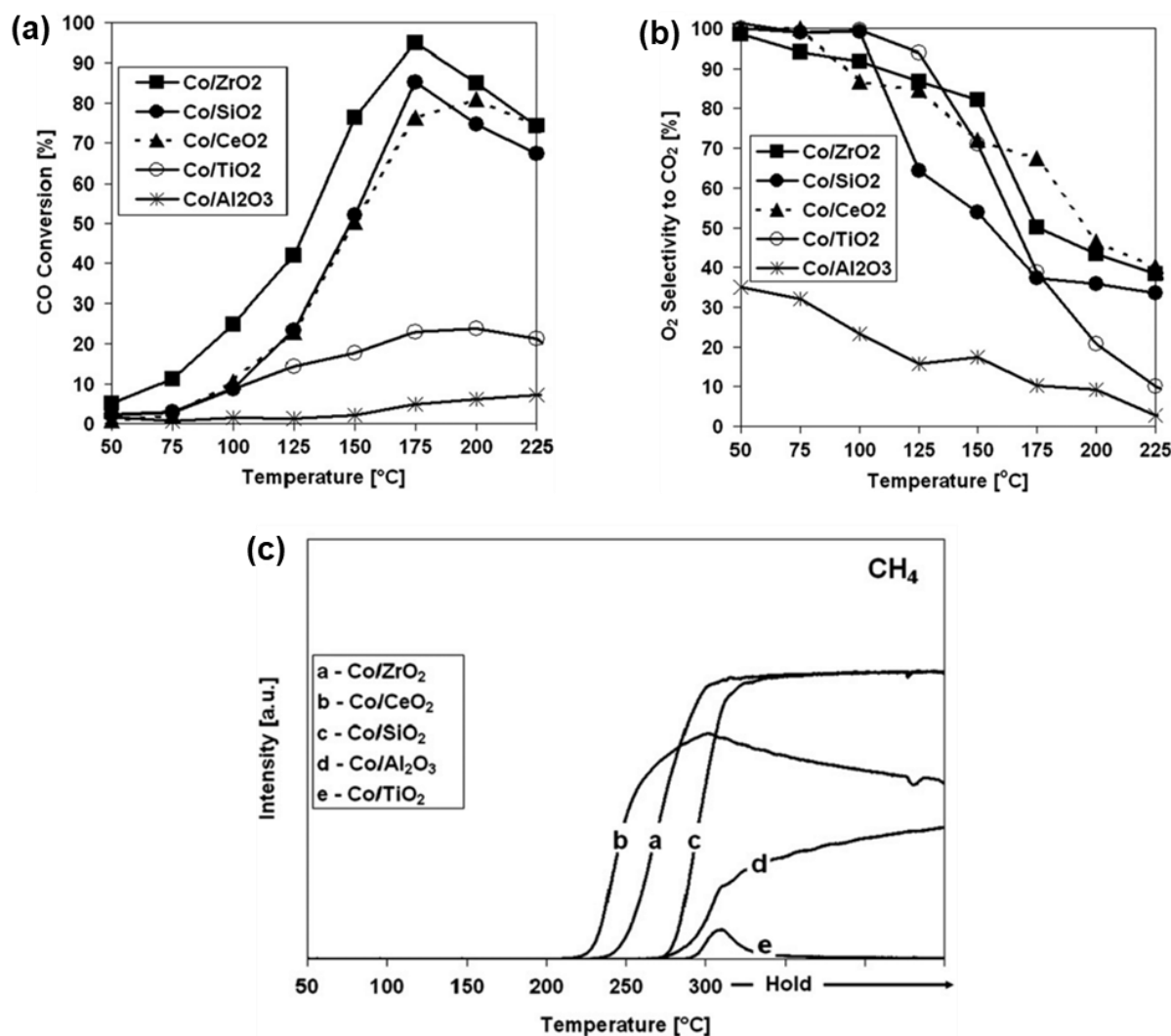


**Figure 2.3:** (a) Calculated CO conversion, (b) O<sub>2</sub> selectivity to CO<sub>2</sub>, as well as (c) CH<sub>4</sub> detected using mass spectrometry as a function of temperature over Co<sub>3</sub>O<sub>4</sub> anchored on various metal oxide support materials during dry CO-PrOx. Conditions: GHSV: 30000 ml/g<sub>cat</sub>.hr, Pressure: 1.013 bar, Gas composition: 1% CO, 1% O<sub>2</sub>, 60% H<sub>2</sub>, bal. He. (Adapted from [32]).

### 2.2.3. Inert supports

Inert support materials are those supports that are not expected to react with the nanoparticles deposited on them to form MSCs. These are generally carbon or carbon-containing support materials, such as graphene/graphite or silicon carbide (SiC). Carbon supports rarely come in the form of pure carbon as they often contain trace amounts of oxygen-containing functional groups (*e.g.*, alcohols, carboxylic acids *etc.*) on the surface. However, the amount of the oxygen-

containing functional groups can be increased by treating the support in acidic media or in air [81–83]. There has also been the introduction of nitrogen-containing functional groups (amines, pyridines *etc.*) in few layered graphene [84,85], solid carbon spheres [86], and carbon nanotubes [87] *via* chemical vapour deposition using nitrogen-containing sources such as ammonia or acetonitrile. The introduced functional groups can act as nucleation and/or anchor points for nanoparticles, thus affording them with enhanced stability and increased dispersion. The other benefit of carbon supports is that the metal or metal oxide nanoparticles can be easily recovered by burning off the carbon [81–83].

The support SiC can be prepared in several ways - either involving solid Si<sup>0</sup>, gaseous SiO (silicon monoxide) or gaseous SiCl<sub>4</sub> reacting with CO, C or CH<sub>4</sub>, respectively, at very high temperatures (> 1000 °C). In most cases, the residual carbon species are removed by combustion (~ 800 °C) but this step tends to also oxidise the surface of the SiC, creating a thin overlayer (1 – 2 nm) of Si<sub>x</sub>O<sub>y</sub> or Si<sub>x</sub>O<sub>y</sub>C<sub>z</sub> [88–90]. This layer is advantageous in that it protects the core/bulk SiC from further oxidising. The layer is also hydrophilic, which means it can allow for aqueous solutions containing a metal precursor(s) to easily wet the surface of the support (during wetness impregnation, for example) to distribute the metal precursor [88–90].

It is worth mentioning that carbon and SiC supports are seldom used in CO-PrOx but have found extensive application in other reactions [88–90]. Also, note that the formation of MSCs has not yet been reported through the use of these support materials. Therefore, in the present work, SiC was chosen as the only non-oxidic support for anchoring Co<sub>3</sub>O<sub>4</sub> nanoparticles and to compare its influence in CO-PrOx with the previously discussed oxidic support materials.

## 2.3. Effect of the Gas Feed Components on CO-PrOx Catalysts

### 2.3.1. Effect of hydrogen

The reformat gas obtained after the low-temperature WGS process is made up of 40 – 75% H<sub>2</sub> [6–10]. During CO-PrOx, the H<sub>2</sub> can potentially react with O<sub>2</sub> to form H<sub>2</sub>O (Reaction 1.7). At high enough temperatures and over a suitable catalyst, it can also react with CO to form CH<sub>4</sub> and more H<sub>2</sub>O (Reaction 1.4). The oxidation of H<sub>2</sub> results in a decrease in the CO<sub>2</sub> selectivity, based on the

overall conversion of O<sub>2</sub>. Although CO adsorption over most metals and metal oxides is more favoured than that of H<sub>2</sub> at low temperatures [8–10], upon increasing the reaction temperature, H<sub>2</sub> adsorption and oxidation becomes kinetically favoured. This can take place even before the CO conversion levels can reach 100%, depending on the catalyst used and the amount of O<sub>2</sub> co-fed. The formation of CH<sub>4</sub> can also take place over a few metal-based catalysts including ruthenium (Ru) [1,91], nickel (Ni) [26,38] and cobalt (Co) [26,32,34–37]. The corresponding metal oxides of the above-mentioned metals have not been reported as active for methanation. The formation of CH<sub>4</sub> also decreases the CO<sub>2</sub> selectivity as less CO is converted to CO<sub>2</sub> *via* oxidation. Further, more H<sub>2</sub> is converted (in addition to that converted *via* oxidation) which depletes the overall amount of H<sub>2</sub> that would be available for power generation in the PEM fuel cell.

In a study by Nyathi *et al.* [35], Co<sub>3</sub>O<sub>4</sub> catalysts of different crystallite sizes (ranging from 3 – 16 nm) supported on Al<sub>2</sub>O<sub>3</sub> were investigated in the CO-PrOx reaction. The experiments were performed in a gas feed with 1:1:52:46 ratio of CO:O<sub>2</sub>:H<sub>2</sub>:N<sub>2</sub>, which served as a model CO-PrOx feed since CO<sub>2</sub> and H<sub>2</sub>O were not co-fed. The changes in the amount of CO, CO<sub>2</sub>, O<sub>2</sub> and CH<sub>4</sub> exiting the reactor, as well as the changes in the phase composition of a 15.3 nm Co<sub>3</sub>O<sub>4</sub>/Al<sub>2</sub>O<sub>3</sub> catalyst as a function of temperature and time under the mentioned model conditions are shown in Figure 2.4. The changes in the phase composition were captured using two complementary *in situ* instruments developed at the University of Cape Town (UCT) - a low-frequency vibrating sample magnetometer [92–94], and a capillary reaction cell mounted on a Powder X-Ray Diffractometer (PXRD) [93–96].

It can be seen in Figure 2.4 that the Co<sub>3</sub>O<sub>4</sub> phase remained intact between the temperatures 50 and 225 °C and that within this temperature range, CO was exclusively converted to CO<sub>2</sub>. Above 225 °C, the bulk transformation of Co<sub>3</sub>O<sub>4</sub> into cobalt(II) oxide (CoO) was captured using *in situ* PXRD (Figure 2.4(a)). The onset of CoO formation coincided with the depletion of O<sub>2</sub>, even when CO was not completely consumed. This was because of the competing H<sub>2</sub> oxidation reaction, which decreases the O<sub>2</sub> available for CO oxidation and leaves the Co<sub>3</sub>O<sub>4</sub> phase susceptible to reduction by the H<sub>2</sub> [34–37]. The decrease in CO<sub>2</sub> formation in the presence of CoO may also imply that CoO is less active when compared with Co<sub>3</sub>O<sub>4</sub> [23,26,34–37]. A further increase in the temperature from 250 to 350 °C resulted in the partial reduction of CoO to metallic cobalt (Co) as confirmed by both *in situ* magnetometry and PXRD (Figure 2.4(a) and (c)). The formation of metallic Co consequently resulted in the formation of CH<sub>4</sub> and the suppression of the CO oxidation pathway.

Note that 100% CH<sub>4</sub> and 0% CO<sub>2</sub> yields (both based on the conversion of CO), respectively, were reached at 300 °C when the degree of reduction to metallic Co was still at 20%. This may have been a kinetic effect where the methanation was favoured over CO oxidation on the metallic phase. The other possibility could be that core-shell structured nanoparticles were formed, *i.e.*, with a CoO core and a metallic Co, as the starting average crystallite size of the Co<sub>3</sub>O<sub>4</sub> nanoparticles was 15.3 nm. If such structured nanoparticles were formed, then this also gives an idea of the kind of reduction mechanism that was followed during the CO-PrOx experiment. There are two commonly reported mechanisms for the reduction of metal oxides, and these will be discussed in sub-sections 2.3.1.1. (nucleation model) and 2.3.1.2. (shrinking core model).

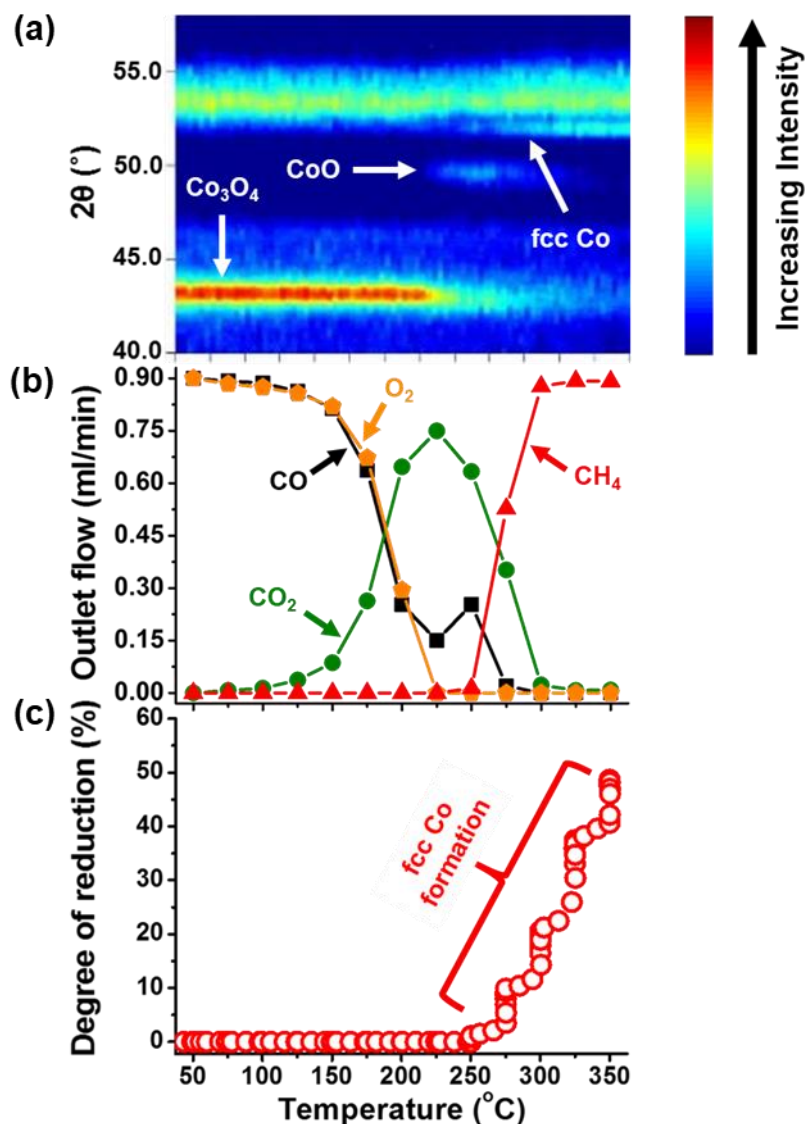


**Figure 2.4:** (a) On-top view of the *in situ* PXR D patterns recorded during dry CO-PrOx over 10 wt.-%  $\text{Co}_3\text{O}_4/\text{Al}_2\text{O}_3$ . (b) Changes in the outlet flow rates of CO,  $\text{O}_2$ ,  $\text{CO}_2$  and  $\text{CH}_4$  calculated from GC-TCD data. (c) Magnetometry-derived degree of reduction of  $\text{Co}_3\text{O}_4$  to metallic fcc Co. Conditions: GHSV: 6000 ml/g<sub>cat</sub>/hr, Pressure: 1.013 bar, Gas composition: 0.9% CO, 0.9%  $\text{O}_2$ , 50%  $\text{H}_2$ , bal.  $\text{N}_2$ . (Adapted from [35]).

The recent *operando* studies by Lukashuk *et al.* [23] supported the claim that  $\text{Co}_3\text{O}_4$  was the more active phase of cobalt when compared with CoO. In their work, mesoscopic (or mesoscale) CoO was tested for CO oxidation (in the absence of  $\text{H}_2$ ) using a feed with 5:10:85 CO: $\text{O}_2$ :He and the surface of the CoO was monitored using X-ray Photoelectron Spectroscopy (XPS) and Near Edge X-ray Absorption Fine Structure (NEXAFS) as shown in Figure 2.5. Upon heating between 130 and 310 °C, the CoO surface is seen oxidising to  $\text{Co}_3\text{O}_4$  at 200 °C and cooling the sample back to 130 from 310 °C, higher CO conversions to  $\text{CO}_2$  are obtained. This observation implied that the

catalyst had gained activity as a result of a change in the surface composition. Various DFT studies [19,97] have also reported the importance of the  $\text{Co}^{3+}$  species that exists in  $\text{Co}_3\text{O}_4$  (but not in  $\text{CoO}$ ) for the adsorption of  $\text{CO}$ . Furthermore, the O ions bonded to  $\text{Co}^{3+}$  have also been reported to be more accessible than those bound to  $\text{Co}^{2+}$ .

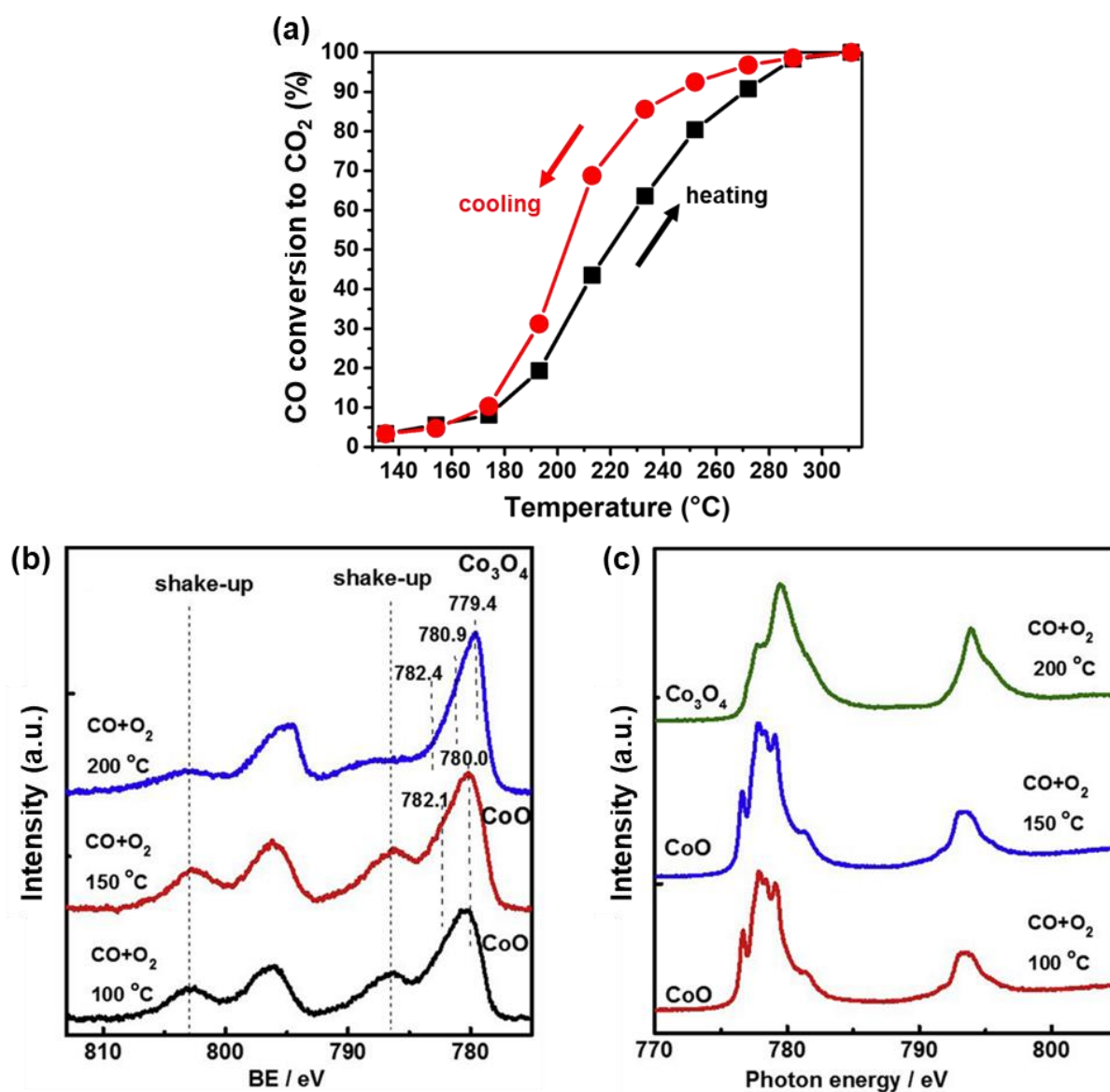


**Figure 2.5:** (a) Changes in the CO conversion to  $\text{CO}_2$  during CO oxidation (in the absence of  $\text{H}_2$ ) over mesoscopic  $\text{CoO}$  during heating and cooling of the reactor. (b) XP spectra, and (c) NEXAFS spectra recorded at 100, 150 and 200  $^{\circ}\text{C}$ , respectively, during the same reaction. Conditions: GHSV: 150000  $\text{ml/g}_{\text{cat}}/\text{hr}$ , Pressure: 1.013 bar, Gas composition: 5%  $\text{CO}$ , 10%  $\text{O}_2$ , bal. He. (Adapted from [23]).

### 2.3.1.1. Reduction mechanism (I): Nucleation model

The nucleation reduction model is depicted in Figure 2.6(a), as well as the expected plot for the change in the degree of reduction ( $\alpha$ ) as a function of time Figure 2.6(b), and the plot expected for the derivative of the degree of reduction ( $d\alpha/dt$ ) as a function of the degree of reduction Figure 2.6(c), at a constant arbitrary temperature. In the early stage of the reduction process, small metallic nuclei form at different areas of the nanoparticle. The nuclei grow until there are enough metallic surface-active sites available for efficient  $H_2$  activation/dissociation. This initial nucleation stage is called the induction period, as reduction of the catalyst is still slow [49,98–101]. Upon forming enough active sites for  $H_2$  dissociation, the reduction proceeds faster and becomes autocatalytic as the continued reduction of the oxide nanoparticle is being enhanced by the presence of metallic active sites. The interface between the oxidic and the metallic areas (represented by thin red lines in Figure 2.6(a)) continues to grow until the nuclei begin to merge. At this point, the reduction rate decreases as the interfacial area becomes smaller [49,98–101]. The reduction of any oxide species at the core of the nanoparticle proceeds *via* diffusion of the dissociated reducing molecules through the metallic region. This type of mechanism is often reported for non-noble metal oxides that are large in crystallite/nanoparticle size [100].

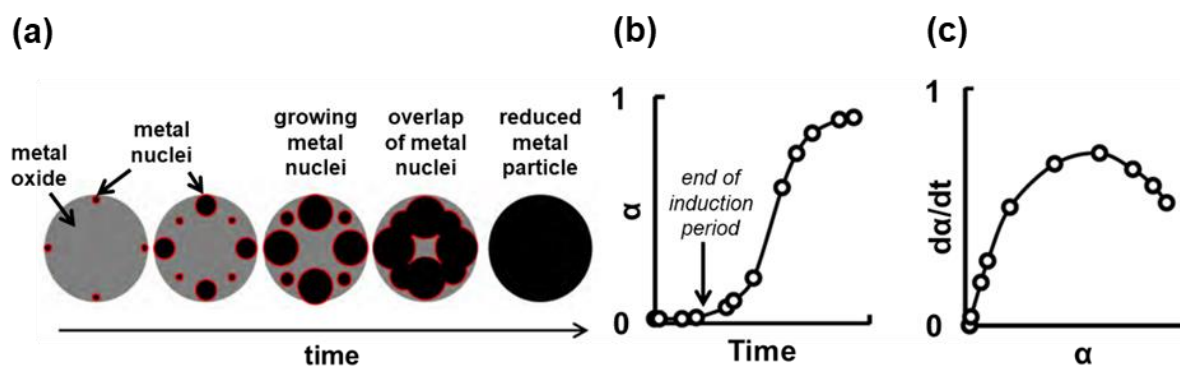


**Figure 2.6:** (a) Illustration of the stages involved during nanoparticle reduction *via* the nucleation mechanism. Plots of the (b) degree of reduction ( $\alpha$ ) as a function of time, as well as the (c) derivative of the degree of reduction ( $d\alpha/dt$ ) as a function of  $\alpha$  at a constant arbitrary temperature. (Adapted from [49,98–102]).

### 2.3.1.2. Reduction mechanism (II): Shrinking core or contracting volume model

The shrinking core or contracting volume model is not based on autocatalysis as the reduction of the (near-)surface atoms takes place rather fast and simultaneously, which creates a metallic shell around the core oxide (Figure 2.7(a)) [49,98–101]. Therefore, the reduction rate at the beginning is at its highest since the interfacial area (illustrated with a thin red line in Figure 2.7(a)) is largest at this point (also see Figure 2.7(c)) [49,98–101]. As the metallic shell grows, the interfacial area decreases, which results in a decrease in the reduction rate. The continued reduction of the core oxide depends on the diffusion of the dissociated reducing molecules through the metallic region and/or the outward diffusion of lattice oxygen [49,98–101]. Since noble metal-based catalysts are often synthesised as small nanoparticles (mostly a result of low loading) on support materials, the shrinking core model is generally observed for such particles [100]. Small-sized non-noble metal nanoparticles may also reduce *via* this reduction mechanism.

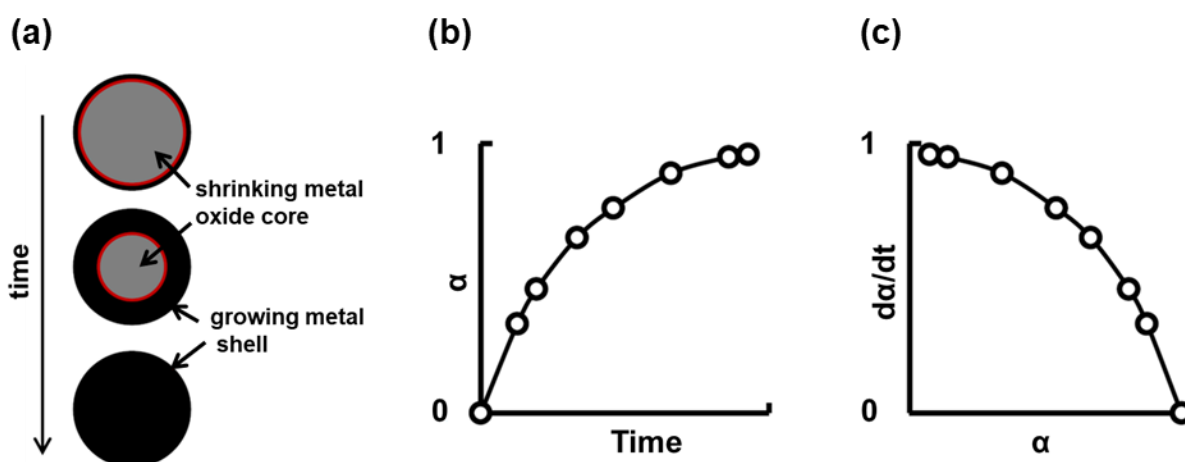


**Figure 2.7:** (a) Illustration of the stages involved during nanoparticle reduction *via* the shrinking core mechanism. Plots of the (b) degree of reduction ( $\alpha$ ) as a function of time, as well as the (c) derivative of the degree of reduction ( $d\alpha/dt$ ) as a function of  $\alpha$  at a constant arbitrary temperature. (Adapted from [49,98–102]).

However, it should always be noted that the degree of reduction as a function of time is highly dependent on temperature, and therefore, the shape of the  $\alpha$  vs. time curve (and consequently the  $d\alpha/dt$  vs.  $\alpha$  curve) can vary with temperature [49,98–101,103,104]. Relatively low temperatures

may favour the nucleation model, while elevated temperatures may favour the shrinking core model, with a low dependency on nanoparticle size. The rate of reduction and/or the mechanism can also determine what kind of metallic or oxidic species (and their concentration) are exposed on the nanoparticle surface, during CO-PrOx (for example), which would determine the likely reactions to be observed at a particular temperature. The reduction mechanism has been studied in this work for unsupported and ZrO<sub>2</sub>-supported Co<sub>3</sub>O<sub>4</sub> nanoparticles, under dry CO-PrOx conditions, using *in situ* PXRD and magnetometry, respectively (see section 8.3).

### 2.3.2. Effect of water and carbon dioxide

A realistic CO-PrOx feed also contains H<sub>2</sub>O (~10%) and CO<sub>2</sub> (10 – 25%), and very few studies have investigated their effect on the CO oxidation activity/selectivity, as well as on the reducibility of CO-PrOx catalysts (in this case, base metal oxides). The presence of H<sub>2</sub>O and CO<sub>2</sub> in the CO-PrOx feed can also have a negative effect on the catalyst's performance especially at low temperatures (*i.e.*, below 200 °C) [33,105,106]. This effect is normally attributed to the co-adsorption of these gases at the low temperatures, thus blocking several active sites for CO on the catalyst's surface. However, as the reaction temperature is increased, an increase in the CO conversion to CO<sub>2</sub> is normally observed as shown in Figure 2.8. Noted that the extent to which the H<sub>2</sub>O and the CO<sub>2</sub> individually affect the CO conversion to CO<sub>2</sub>, strongly depends on their concentrations and on the catalyst. From the literature, there is no clear indication of which of the two has a greater effect mainly because these gases are not fed at similar concentrations. The presence of H<sub>2</sub>O in the feed can also result in the water gas shift reaction (Reaction 1.8), which produces CO<sub>2</sub> and H<sub>2</sub> from CO and H<sub>2</sub>O [62,63,68,107]. On the other hand, co-feeding CO<sub>2</sub> can result in methane formation (Reaction 1.5) or in the reverse water-gas shift (the reverse of Reaction 1.8) [1,22,34]. Both these reactions are undesirable as they consume valuable H<sub>2</sub>. It should be noted that these reactions have been mentioned in the literature as being possible under realistic CO-PrOx conditions but evidence for their occurrence has not been shown.

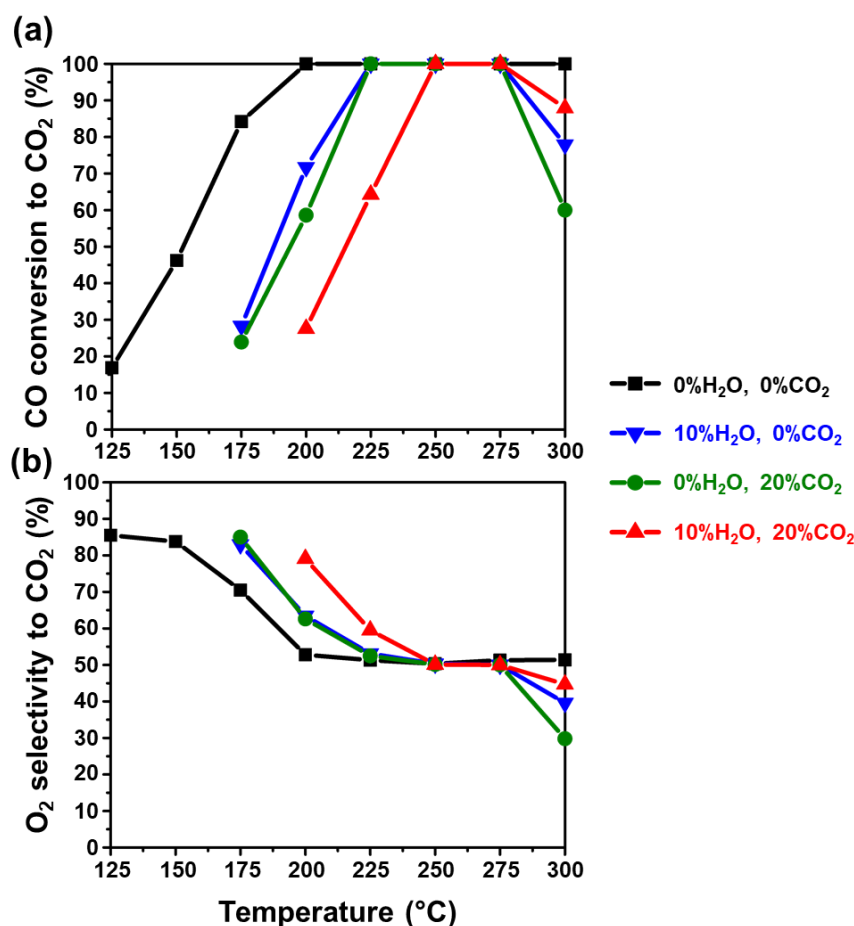


**Figure 2.8:** Changes in the (a) CO conversion, and (b) O<sub>2</sub> selectivity to CO<sub>2</sub> as a function of temperature under different CO-PrOx conditions over a 10 wt.-% Co<sub>3</sub>O<sub>4</sub>/meso-CeO<sub>2</sub> catalyst. Conditions: GHSV: 40000 ml/g<sub>cat</sub>.hr, Pressure: 1.013 bar, Gas composition: 1% CO, 1% O<sub>2</sub>, 10% H<sub>2</sub>O (when co-fed), 20% CO<sub>2</sub> (when co-fed), 50% H<sub>2</sub>, bal. N<sub>2</sub>. (Replotted from [105]).

When focusing on the phase stability of the catalyst, Kim and Cha [64] revealed that CO<sub>2</sub> and H<sub>2</sub>O can affect the bulk reducibility of metal oxide catalysts after having performed hydrogen-temperature programmed reduction (H<sub>2</sub>-TPR) experiments. The H<sub>2</sub>-TPR profiles obtained after passing a gas mixture of 10% H<sub>2</sub> in N<sub>2</sub>, 1% H<sub>2</sub>O/10% H<sub>2</sub> in N<sub>2</sub> and 1% CO<sub>2</sub>/1% H<sub>2</sub>O/10% H<sub>2</sub> in N<sub>2</sub>, respectively, through a CuO-CeO<sub>2</sub> catalyst are shown in Figure 2.9. It can be seen that in a reducing gas containing H<sub>2</sub>O or both H<sub>2</sub>O and CO<sub>2</sub>, the reduction peaks for copper(II) oxide (CuO) shift to higher temperatures, *i.e.*, CuO became harder to reduce to metallic copper (Cu). This was attributed to the oxidising nature of both H<sub>2</sub>O and CO<sub>2</sub> which offered stability to the CuO phase. Although the bulk reduction studies showed that H<sub>2</sub>O and CO<sub>2</sub> stabilise the active CuO phase, the CO oxidation activity was still diminished by the presence of H<sub>2</sub>O and CO<sub>2</sub> under CO-PrOx

conditions. Note that, to date, there has not been a study that has shown *in situ* evidence for the effect of CO<sub>2</sub> and H<sub>2</sub>O on the phase stability of a CO-PrOx metal oxide catalyst.

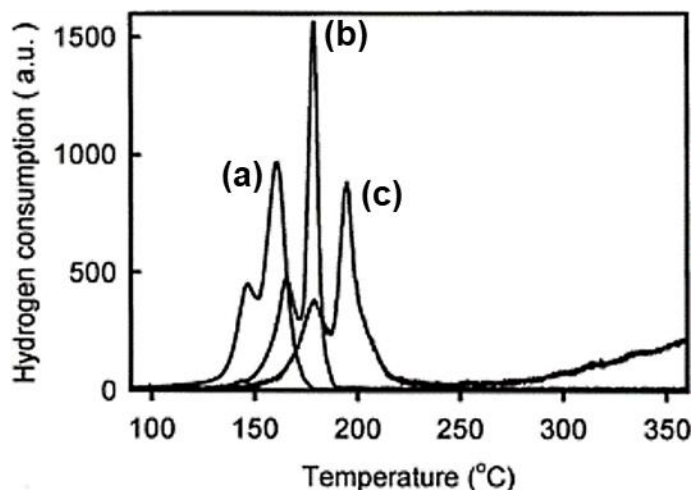


**Figure 2.9:** Temperature-programmed reduction profile of a CuO-CeO<sub>2</sub> catalyst in (a) 10% H<sub>2</sub> in N<sub>2</sub>, (b) 1% H<sub>2</sub>O/10% H<sub>2</sub> in N<sub>2</sub>, and (c) 1% CO<sub>2</sub>/1% H<sub>2</sub>O/10% H<sub>2</sub> in N<sub>2</sub>. Other conditions: GHSV: 200000 ml/g<sub>cat</sub>.hr, Pressure: 1.013 bar. (From [64]).

### 2.3.3. Effect of varying oxygen feed levels

During a typical CO-PrOx reaction, more often than not, amounts higher than the stoichiometric amount of O<sub>2</sub> needed (which is half the amount of CO – see Reaction 1.6) are co-fed in order to obtain high CO conversions to CO<sub>2</sub> in the presence of H<sub>2</sub> [1–5]. However, some studies have shown that if the catalyst is also active for H<sub>2</sub> oxidation, O<sub>2</sub>:CO ratios above 0.5 can result in an overall decrease in the CO<sub>2</sub> selectivity (based on the amount of O<sub>2</sub> converted) since there is always O<sub>2</sub> remaining for H<sub>2</sub> oxidation even after achieving 100% CO conversion levels [15,22] (also see Figure 2.10).

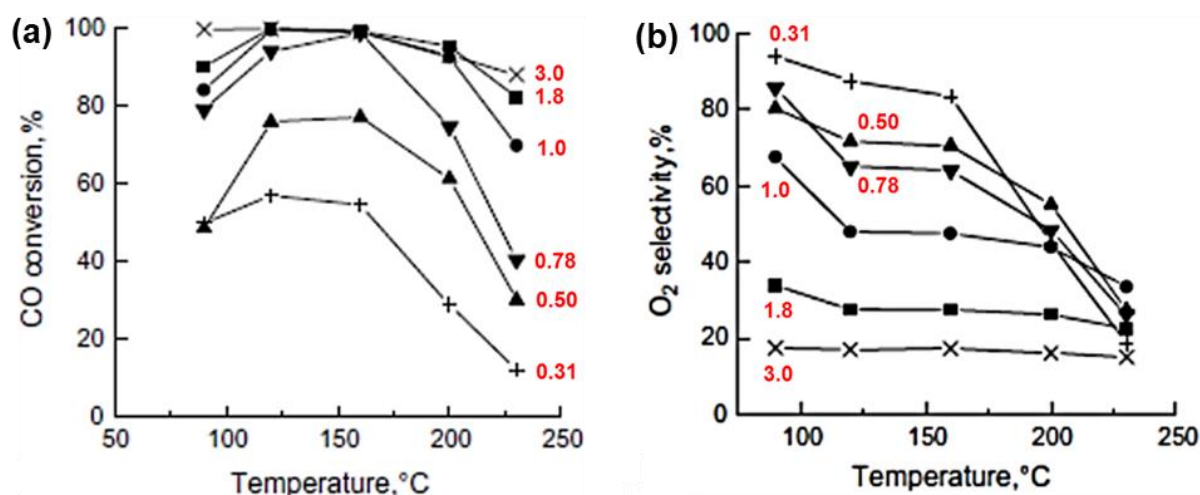


**Figure 2.10:** (a) CO conversion, and (b) O<sub>2</sub> selectivity to CO<sub>2</sub> as a function of temperature at various CO:O<sub>2</sub> ratios (indicated in red) during CO-PrOx over a 3 wt.-% Co/1 wt.-% Pt/Al<sub>2</sub>O<sub>3</sub> catalyst. Conditions: GHSV: 40000 ml/g<sub>cat</sub>.hr, Pressure: 1.013 bar, Gas composition: 1.1% CO, 0.55-1.98% O<sub>2</sub>, 9% H<sub>2</sub>O (when co-fed), 20% CO<sub>2</sub> (when co-fed), 67% H<sub>2</sub>, bal. N<sub>2</sub>. (Adapted from [15]).

Oxygen is also well known for its oxidising capabilities which may also stabilise the metal oxide phase against bulk reduction during CO-PrOx. Pure (base) metals exposed to an O<sub>2</sub>-containing environment can partially or completely oxidise to their corresponding oxide phases [108–110]. An *in situ* magnetometry study by Wolf *et al.* [110] investigated the effect of a 1% O<sub>2</sub> in N<sub>2</sub> mix and a 90% CO<sub>2</sub> in argon (Ar) mix on the passivation (*i.e.*, formation of an oxidic protective layer) of a reduced metallic Co catalyst. The results from the study, summarised in Figure 2.11, show that the high concentration of CO<sub>2</sub> at 30 and at 150 °C was not able to passivate the reduced cobalt catalyst, *i.e.*, there was no decrease in the measured magnetic signal observed. It was only upon exposure to air (21% O<sub>2</sub> in N<sub>2</sub>) that the nanoparticles almost completely oxidised to Co<sub>3</sub>O<sub>4</sub> which was firstly observed by a drastic decrease in the measured magnetic signal (since CoO and Co<sub>3</sub>O<sub>4</sub> are antiferromagnetic) and then later confirmed by *ex situ* PXRD analysis.

On the other hand, first exposing the freshly reduced catalyst to 1% O<sub>2</sub> in N<sub>2</sub> at 30 °C, a thin CoO layer (~1.3 nm in thickness) was formed around the core of the metallic Co nanoparticles (~11.8 nm before passivation and 9.8 nm after passivation). The thickness of this CoO layer did not increase even upon exposing the passivated catalyst to air. It should be noted that in the context of CO-PrOx, the stability offered by the O<sub>2</sub> depends on its partial pressure during the reaction. The combined presence of CO and H<sub>2</sub> can eventually deplete the feed O<sub>2</sub> at elevated temperatures and leave the catalyst susceptible to reduction (as shown with the example from Nyathi *et al.* [35]).

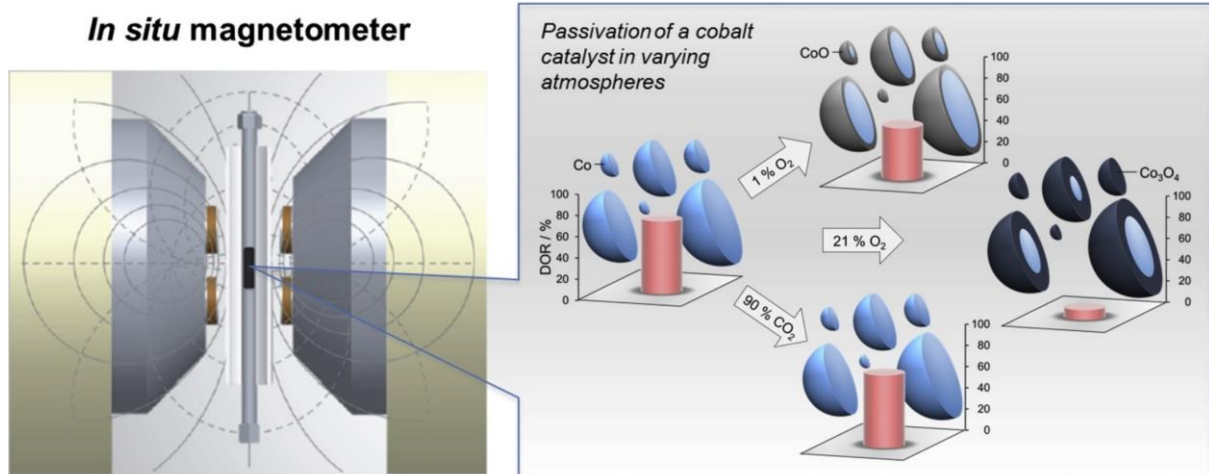


**Figure 2.11:** Changes in the degree of reduction (%DOR) of a fully reduced cobalt catalyst upon exposure to (top) 1% O<sub>2</sub> in N<sub>2</sub>, (far-right) 21% O<sub>2</sub> in N<sub>2</sub> and (bottom) 90% CO<sub>2</sub> in Ar. The changes in the %DOR were monitored using the UCT-SASOL developed *in situ* magnetometer [92–94]. The blue shading is for metallic Co, the grey is for CoO and the black is for Co<sub>3</sub>O<sub>4</sub>. (From [110]).

## 2.4. Catalyst Deactivation

A chemical reaction over a heterogeneous catalyst will take place for a finite amount of time as there are either physical or chemical changes (expected or unexpected) that the catalyst may undergo. Some catalysts can last 5 - 10 years without needing replacement or re-activation, for example, iron-based catalysts for ammonia synthesis, and timescales as short as a fraction of seconds have been reported for zeolite-based catalysts for fluid catalytic cracking [111–113]. There are two classes of deactivation mechanisms [114]: i) Inherent and, ii) Operational. Inherent deactivation includes mechanisms that would take place as a result of the normal working conditions of the catalyst. Such mechanisms include transformation of the catalytically active phase, particle growth/sintering and coking. For such mechanisms, measures of dealing with them may already be in place if the same catalyst has been used before under the same conditions. Operational deactivation more appropriately applies to chemical processes performed in industry where, for example, an impure feed is introduced, or the catalyst loses mechanical strength because of exposure to harsh start-up/operating conditions. Some mechanisms include fouling, poisoning and attrition.

### 2.4.1. Gas-solid and solid-solid reactions

This deactivation mechanism is one of the most well-known inherent deactivation mechanisms. If we consider a heterogeneous catalyst intended to convert gaseous reactants to gaseous products, some of the gas reactants/products may change the chemical phase of the catalyst. However, the reaction between the gases and the catalyst may only be possible under specific conditions of temperature and/or gas partial pressure. As previously mentioned, the hydrogen gas in the CO-PrOx feed varies between 40 and 75% [6–10] and these concentrations are high enough to cause chemical changes to CO-PrOx metal oxide catalysts *via* reduction [26,29,34–37]. This reduction process is often not desired as the low oxidation state species formed may not be as active for or selective to CO<sub>2</sub> formation from CO.

The loss of active material may also take place *via* solid-solid reactions - some species of the active nanoparticles reacting with the species of the support. This is a phenomenon often associated with the existence of strong metal-support interactions or nanoparticle-support interactions introduced during catalyst synthesis [37,42,43]. The species resulting from such solid-solid reactions are called metal-support compounds, which are often in the form of mixed-metal oxides. Species of the support material can also decorate or encapsulate active nanoparticles (see Figure 2.12) due to significant differences in surface energy between the support and the nanoparticle. This has been commonly reported for TiO<sub>2</sub>(anatase)-supported metal nanoparticles (Ru, Co, Ni *etc.*) [76–78]. It should again be noted that such chemical transformations may only be possible at certain temperatures and even assisted by the presence of some gases. In the CO-PrOx process, such chemical transformations (as a result of solid-solid reactions) have not been reported as a major concern but may be a possibility. In other reaction processes, such as the FTS, the formation of MSCs has been reported both during catalyst activation (mostly in H<sub>2</sub>) and during the FTS where the by-product water is formed at high CO conversion levels [58,73].

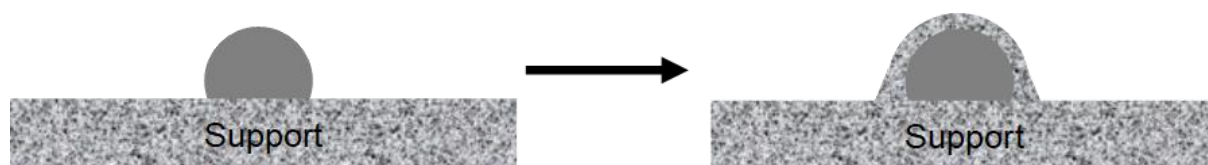


**Figure 2.12:** Illustration of nanoparticle encapsulation by oxide support species. (Adapted from [76–78]).

## 2.4.2. Sintering

Sintering involves the loss of surface area through particle growth. Since very small nanoparticles have high surface energies, it is the need to minimise this surface energy that drives the sintering process [111–113]. The process can occur through the migration of whole particles which coalesce or through atom migration (known as Ostwald ripening) as shown in Figure 2.13. The process is also driven by temperature, and the exact temperature where it can be expected is related to the melting point ( $T_{\text{melting}}$ ) of the solid material. Atom migration generally takes place at a low temperature than that observed for particle migration, and the temperatures for both processes are known as the Hüttig temperature ( $T_{\text{Hüttig}}$ ) and Tamman temperature ( $T_{\text{Tamman}}$ ), respectively, calculated using Equations 2.1 and 2.2.

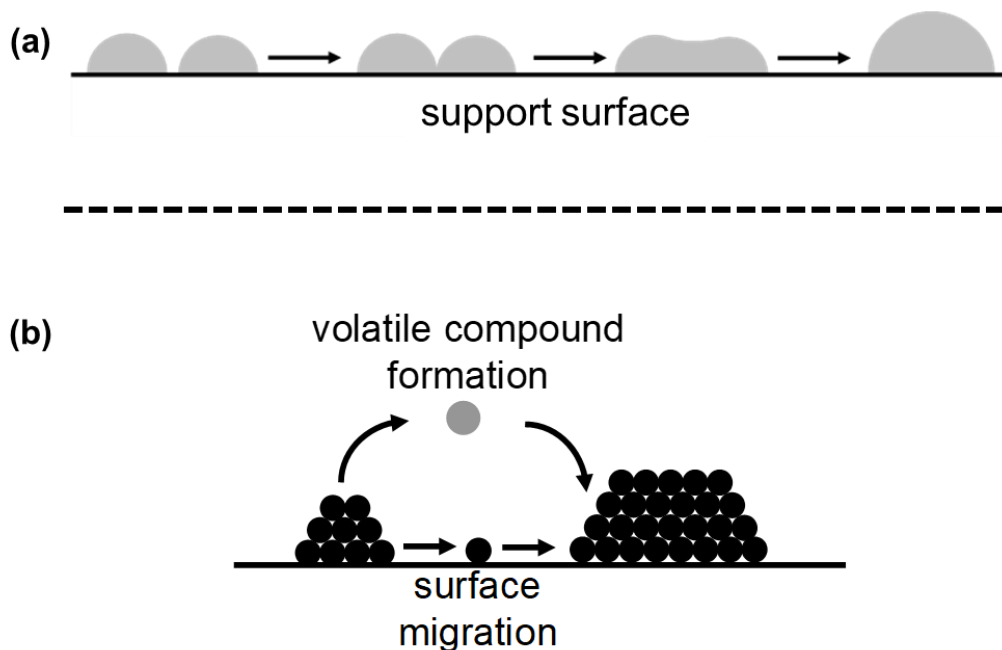


**Figure 2.13:** Depiction of nanoparticle sintering *via* (a) coalescence, and (b) Ostwald ripening. (Adapted from [111–113]).

$$T_{\text{Hüttig}} = 0.3 \cdot T_{\text{melting}} \quad \text{Equation 2.1}$$

$$T_{\text{Tamman}} = 0.5 \cdot T_{\text{melting}} \quad \text{Equation 2.2}$$

Table 2.3 summarises the melting points and the calculated Hüttig and Tamman temperatures of common metals and metal oxides often used as CO-PrOx catalysts. Since these melting temperatures are for the bulk form of the material, the temperatures at which nanoparticles can be expected to sinter can be even lower than those found in Table 2.3 [115]. The reason for this is the inverse relationship between surface energy and particle size. This also explains the common practice of anchoring active nanoparticles on thermostable support materials to minimise the extent of sintering under reaction conditions. The gas environment can also play a role in sintering, in addition to temperature. Gases such as H<sub>2</sub>O can enhance the growth of metal particles [73,116,117], while H<sub>2</sub> can facilitate the growth of metal oxide particles and a loss of surface area of support materials [118,119].

**Table 2.3:** Melting temperatures of common metal and metal oxide CO-PrOx catalysts as well as their corresponding calculated Hüttig and Tamman temperatures.

Chemical Species	T <sub>melting</sub> (in °C)	T <sub>Hüttig</sub> (in °C)	T <sub>Tamman</sub> (in °C)
Co*	1495	444	740
CoO*	1795	540	900
Co <sub>3</sub> O <sub>4</sub> *	900 - 950 <sup>#</sup>	270 - 285	450 - 475
CuO <sup>§</sup>	1326	398	663
Ni <sup>§</sup>	1452	436	726
NiO <sup>§</sup>	1955	587	978
Pd <sup>§</sup>	1555	467	778
Pt <sup>§</sup>	1755	527	878
Rh <sup>§</sup>	1985	596	993
Ru <sup>§</sup>	2450	735	1225

\* obtained from [120].

§ obtained from [112].

# decomposes to CoO within temperature range.

### 2.4.3. Poisoning

Poisoning is the chemical adsorption of one or more feed impurities onto the surface of nanoparticles which leads to the blockage of active sites. The “poison” is often not directly involved in the chemical reaction of interest [111–113]. In terms of CO oxidation (which is the reaction of interest), in the context of CO-PrOx, the chemical poisons that can be identified are H<sub>2</sub>, H<sub>2</sub>O and CO<sub>2</sub>, all of which are formed in the upstream fuel processing steps [6,9,10]. These gases do not only adsorb on the surface, but they can also react with the catalyst and form undesired forms of the catalyst (*e.g.*, H<sub>2</sub> reducing metal oxides [34,37], or H<sub>2</sub>O oxidising metal catalysts [73,93,121]). The strong adsorption of CO<sub>2</sub> can also lead to the formation of surface carbonates, which can also block access to active sites. This is common at low reaction temperatures or low feed oxygen partial pressures [21,118].

### 2.4.4. Other deactivation mechanisms

A less commonly reported deactivation mechanism in the context of CO-PrOx is fouling. This involves the physical adsorption of feed or product species which also results in the blockage of active sites [111–113]. For example, this type of deactivation is observed in reactions which can cause coke/carbon formation either from CO or organic compounds. This is especially possible at low H<sub>2</sub> or O<sub>2</sub> partial pressures, or high reaction temperatures (in the case of organic compounds). Coke formation is less likely during CO-PrOx as relatively high amounts of H<sub>2</sub> and O<sub>2</sub> are present in the feed which would most likely react with the CO to form CH<sub>4</sub> or CO<sub>2</sub>, respectively. The other uncommon deactivation mechanism in CO-PrOx is mechanical failure or attrition. This is when the catalyst (in the form of pellets, extrudates *etc.*) breaks up into fines, for example, in fluidised or slurry bed reactors where the reaction fluid causes vigorous collisions between the catalyst and walls of the reactor [111–113]. The formation of fines can block the transport of fluid through the reactor or can cause a loss of active material where the fines end up as part of the product (especially in slurry beds). It should also be noted that CO-PrOx has not yet been widely commercialised and so it may be possible that some of these deactivation mechanisms will only be observed in industrial/commercial applications, and not necessarily in laboratory-scale experiments.

## 2.5. Catalyst Preparation

### 2.5.1. Conventional methods

#### 2.5.1.1. Impregnation

Slurry wetness impregnation and incipient wetness impregnation are two widely used techniques for anchoring catalytically active material on a support [41,45–47]. Slurry wetness impregnation involves firstly dissolving a metal precursor in a solvent (*e.g.*, water, ethanol *etc.*) and then contacting the support material with this solution (*i.e.*, impregnating the support). The amount of liquid used for the impregnation is normally higher than the pore volume of the support, which implies that the precursor will be distributed inside and outside of the support pore structure. The advantage of this method is that relatively high metal loadings and well-distributed nanoparticles can be formed on the support in a single impregnation step. However, relatively wide size distributions for the nanoparticles are obtained using this method [45].

In incipient wetness impregnation (IWI), the precursor is dissolved in a volume of solvent equal to (or slightly less than) the pore volume of the support being used [41,45–47]. Therefore, the term “incipient wetness” refers to the point at which the pores of the support are just completely filled with the solution. At this point, the support appears “dry” and a few more drops of the impregnating solution would turn the mixture into a slurry. In principle, catalysts prepared using IWI have a high concentration of nanoparticles within the support pore structure. Therefore, the size of the formed nanoparticles can be expected to be within the size of the pores of the support. The interaction between the nanoparticles and support can also be expected to be stronger within the pores than outside of the pores. A disadvantage of this method is that, for supports with low pore volumes or for metal precursors with low solubilities in the chosen solvent, at least two impregnation steps may be required [41,45–47].

After impregnating the support, the drying and calcination processes usually follow [41,46]. Drying refers to the removal of the solvent from the support and calcination refers to the high-temperature immobilisation of the metal precursor in the form of nanoparticles. The immobilisation is accompanied by a chemical transformation of the metal precursor into a more

durable phase for storage or for use as a catalyst precursor or active catalyst. This process is normally carried out in an air atmosphere and therefore, yields nanoparticles in the metal oxide form [41,46]. Sometimes this high-temperature treatment can be performed in an inert environment to also form metal oxide nanoparticles, making it a thermal decomposition (of metal nitrates, for example) instead of a traditional oxidation procedure [122,123]. However, care must be taken to prevent sintering and the formation of metal-support compounds (if this is undesired) as both are facile at very high temperatures. See Figure 2.14 for a simple depiction of the impregnation process followed by drying and calcination.

Supporting nanoparticles in this way induces some interactions (electronic [48–52] and/or ligand-type effects [49,53–55]) between the nanoparticle and the support, so much that the reduction, adsorption and catalytic properties of the nanoparticle become different from those of the unsupported phase. The extent to which these properties are altered lies in the choice of the support material.

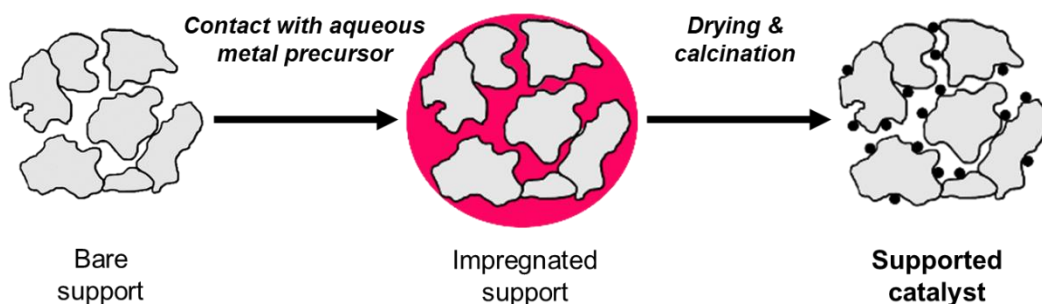


**Figure 2.14:** Depiction of a typical (incipient) wetness impregnation procedure. (Adapted from [124]).

### 2.5.1.2. (Co-)Precipitation and deposition

Precipitation involves forming an insoluble solid (*i.e.*, the precipitate) from a homogeneous solution, by adding a precipitating agent (or precipitant) to this solution. The success of the process is dependent on numerous factors like pH, precipitating agent (nature and strength), temperature and solvent just to mention a few [125]. The chemical nature of the precipitate formed depends on the chemical nature of the precipitating agent and the solvent. For example, the use of precipitating agents that are hydroxides or carbonates results in the formation of precipitates that are hydroxides or carbonates, respectively.

Co-precipitation is when two different metal ions in a mixed solution are precipitated to form a hydroxide or carbonate of two different metal ions [47,126]. This is a common route for the formation of mixed-metal oxides and alloys [47,126,127]. (Note: Impregnation methods can also be employed for forming mixed-metal oxides and alloys, and this is called co-impregnation [47,128]). After the precipitation/co-precipitation, the normal drying and calcination processes are followed to obtain the target catalyst.

Both kinds of precipitation processes can also be carried out in the presence of a support material, making the method (co-)precipitation-deposition [41,47,125,126]. The method also allows for high metal loadings to be achieved and well-distributed nanoparticles to be formed on the support. It is, however, uncertain as to how strong the interaction between the nanoparticles and support is as nanoparticles are formed/deposited on various regions of the support material. Co-precipitation-deposition can also be used to synthesise an insoluble solid form of the support precursor *in situ* from a viable soluble metal precursor. The precipitate, that would later be transformed into the active material, is deposited onto the formed solid support precursor within the same reaction environment [125]. Both precipitates can then be subjected to further heat treatments (calcination and/or reduction) to form the targeted supported catalyst. It should be noted that the formation of the support material *via* this route can lead to the formation of unintended, irreducible metal-support compounds [125].

### 2.5.2. Model catalyst synthesis: Reverse microemulsion technique

The major disadvantage with the discussed conventional methods is that there is very little control of the nanoparticle size and shape [129,130]. Therefore, finding or developing a method which would enable the formation of nanoparticles with a consistent and tuneable size is also important. One such method is the reverse microemulsion (or micelle) technique, which has been widely reported to produce nanoparticles with a narrow size distribution.

A microemulsion is a thermodynamically stable and optically clear system of three liquids, *viz.*, a non-polar (or oil) phase, amphiphilic (or surfactant) phase and a polar (or water) phase [131]. The optical clarity of this system is largely controlled by the surfactant phase, which has properties enabling it to partly dissolve in both the oil and water phases [131,132]. Temperature also plays a

role in the stability of the microemulsion [131,133–135] as it allows for the correct proportions of the surfactant to be dissolved in both the oil and water phases, respectively.

There are two types of microemulsions - normal micelles and reverse micelles. A normal micelle system has the water in amounts much higher than those of the surfactant and the oil phase. On the other hand, a reverse micelle is formed when the oil is present in large amounts relative to the surfactant and the water. In both systems, the phase present in the least amount forms small droplets in the microemulsion [134–138] and these droplets are stabilised by the surfactant as shown in Figure 2.15. The molar ratio of the oil to the surfactant ( $o/s$ ) and the molar ratio of the water to the surfactant ( $w/s$  or  $\omega$ ) determine the size of the droplets. Therefore, the droplets can be used as “nano-reactors” or “nano-vessels” for forming particles (or their solid precursors) of a desired average size [35,134–140]. This makes reverse micelle systems more attractive than normal micelles as most inorganic metal precursors would be highly soluble in water droplets than in oil droplets. The concentration of the metal precursor can also determine the size of the final nanoparticles [35,134–140].

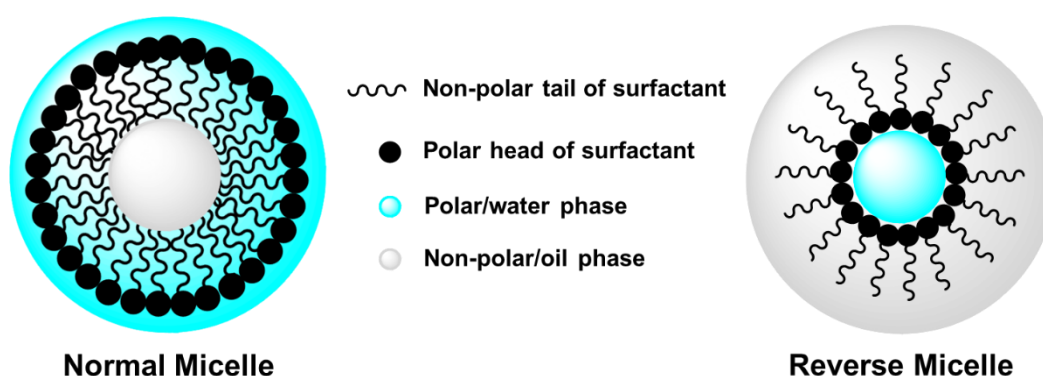


**Figure 2.15:** Illustration of a normal and reverse micelle, respectively. (Adapted from [134,135]).

There are two ways of synthesising nanoparticles using the reverse micelle technique as shown in Figure 2.16 [134,135,138]. The first one involves preparing two similar stable reverse micelle systems - one having the water phase containing the metal precursor and the other having the precipitating agent dissolved in the water phase. After preparing the reverse micelle systems, they are then be mixed causing the reverse micelle droplets to collide, thus initiating precipitation of the metal precursor.

The other way of synthesising nanoparticles is to prepare a single stable reverse micelle system with the water phase containing the metal precursor. The precipitating agent is then introduced as an aqueous solution dropwise into the reverse micelle system and makes its way to the water droplets containing the metal precursor in order to initiate precipitation [134,135,138]. The strength and concentration of the precipitating agent influences the rate of nucleation for particle formation/growth.

The formed precipitate from using either of the two routes discussed remains confined in the droplets of the reverse micelle. Therefore, the next step involves flocculation, whereby substances like acetone or tetrahydrofuran (THF) are added to the reverse micelle system to destabilise it and liberate the precipitate [35,37,135,139,141,142]. The flocculating agent would need to be added a couple more times as a washing procedure to remove the surfactant around the precipitate. After extensively washing the nanoparticles, they could then be adhered to a support material and that itself can be done in various ways [37,135,139,142]. There is also some work that has reported the preparation of supported catalysts where the support is added in the reverse microemulsion, mostly before the flocculation step. In this procedure, the support is “impregnated” with the metal precursor while confined within the reverse micelle. It has also been shown that supported nanoparticles prepared in this manner are hard to reduce and are formed in very small sizes (almost undetectable using PXRD) [37,135,142,143].

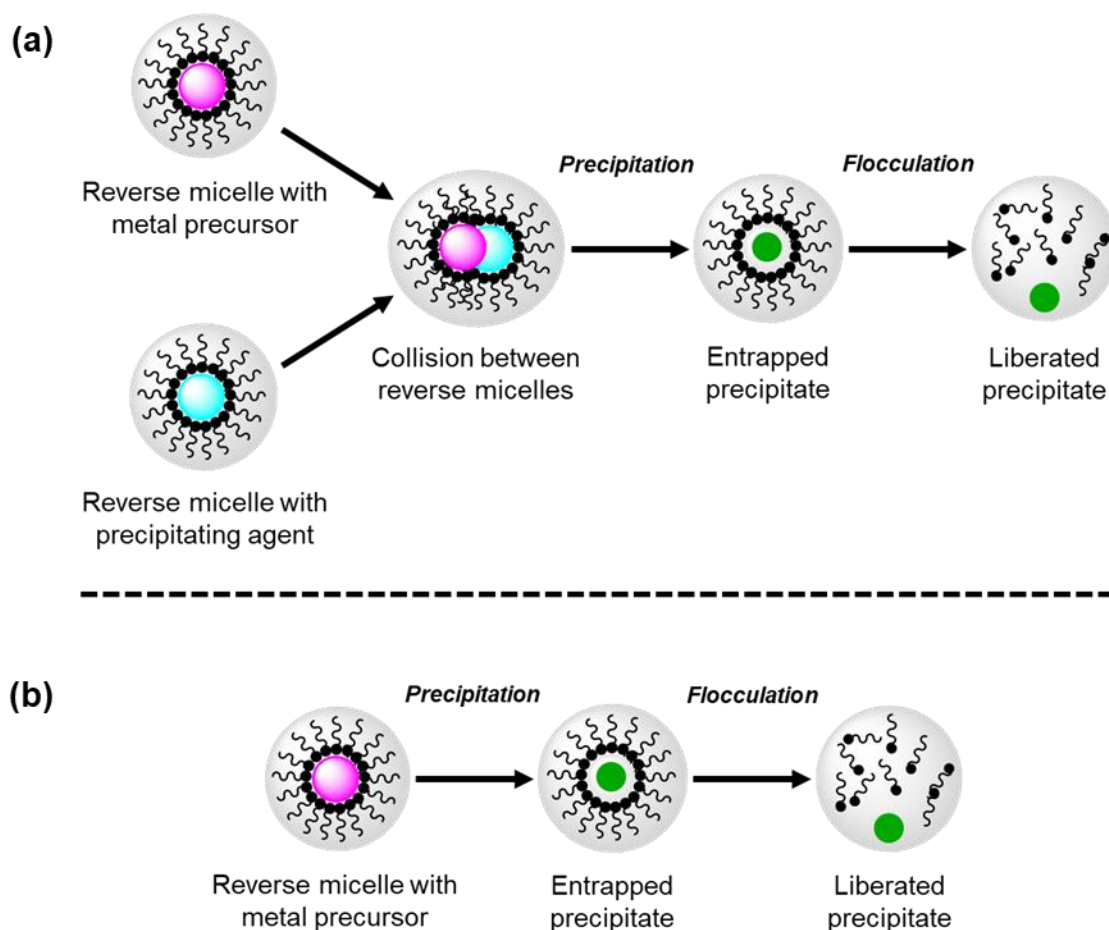


**Figure 2.16:** Stages involved in the synthesis of nanoparticles using the reverse microemulsion technique involving the preparation of (a) two microemulsions, or (b) one microemulsion, respectively. (Adapted from [134,135,138]).

## 2.6. *In situ* Catalyst Characterisation: Magnetism and Magnetometry

Characterisation techniques used in heterogeneous catalysis exploit one or more of the known chemical/physical properties of materials to identify them. For instance, molecular vibrations/rotations (Raman and Infra-Red spectroscopy), crystallinity (XRD) or electronic transitions (X-Ray based spectroscopic techniques, XAS or XPS). The magnetic properties of nanoparticles are less exploited in comparison, but few studies have shown that targeting this property can prove very useful in determining the chemical nature of materials [35–37,73,93,144–146]. The most common magnetic elements are Fe, Ni and Co, and their magnetic properties can change depending on their chemical phase (oxidic, metallic, or part of a mixed-metal oxide or an alloy) and particle size. There are three classes of magnetic materials that will be discussed which

are relevant to the current study: i) Ferromagnetic, ii) Antiferromagnetic, and iii) Superparamagnetic materials.

Ferromagnetic materials are attracted by an applied magnetic field (symbol:  $H$ , units: T (Tesla) or kOe (kilo-Oersted)) *via* the parallel alignment of neighbouring electron spins forming microscopic regions called magnetic domains [147–149]. Upon removal of this external field, the material, or a fraction of it, can remain magnetised and the observed magnetisation is called remnant magnetisation ( $M_{\text{rem}}$ ). This behaviour is a result of the strong coupling between the neighbouring electron spins. Ferromagnetism is temperature-dependent and material-specific, therefore, there exists a critical temperature above which ferromagnetic materials lose their ferromagnetic character and become paramagnetic. This critical temperature is called the Curie temperature ( $T_C$ ). The loss in ferromagnetic behaviour above the  $T_C$  is a result of an increase in the thermal energy which mitigates the strong interaction between neighbouring spins [148].

Antiferromagnetic materials are almost like ferromagnetic materials except that the neighbouring spins align themselves in opposite directions in the presence of an applied field [148,149]. Antiferromagnetic behaviour is also temperature-dependent and the critical temperature below which antiferromagnetic behaviour can be observed is called the Néel temperature ( $T_N$ ). Above this critical temperature, antiferromagnetic materials also become paramagnetic.

Superparamagnetic behaviour is a special case of ferromagnetism whereby small crystallites (normally in the nanometre range) lose their magnetisation upon removal of an external field. Superparamagnetism is particle size-dependent and material-specific, therefore, there exists a critical particle size below which a ferromagnetic sample will display superparamagnetic behaviour [148,150,151]. It should also be noted that most reported Curie temperatures are for bulk materials, but these temperatures could slightly be lower for nanoparticles as a result of their small sizes relative to the corresponding bulk material (*e.g.*, Fe-based [152,153] and Ni-based nanoparticles [154,155]).

Recent *in situ* studies have shown that  $\text{Co}_3\text{O}_4$  can reduce to  $\text{CoO}$  and metallic  $\text{Co}$  at elevated temperatures due to the abundant  $\text{H}_2$  present in the  $\text{CO-PrOx}$  feed [26,32,34–37].  $\text{Co}_3\text{O}_4$  and  $\text{CoO}$  are antiferromagnetic oxides, with a Néel temperature of  $-241\text{ }^\circ\text{C}$  [156,157] and  $18\text{ }^\circ\text{C}$  [158], respectively. Metallic  $\text{Co}$  is ferromagnetic, with a Curie temperature of  $1130\text{ }^\circ\text{C}$  [149]. Table 2.4 summarises the magnetic properties of other cobalt-based species relevant to the current study).

The UCT-SASOL developed *in situ* magnetometer set-up [92–94], shown in Figure 2.17, was designed for the detection of ferromagnetic and superparamagnetic materials of mass fractions significantly lower than 1 wt.-%, making it far more sensitive than conventional methods such as PXRD. The magnetic susceptibility of antiferromagnetic and paramagnetic material is orders of magnitude weaker than that of ferromagnetic and superparamagnetic materials and, as a result, cannot be adequately detected in this *in situ* magnetometer. Therefore, the magnetometer was used in this study to detect the presence of ferromagnetic and superparamagnetic metallic Co only. The critical size below which metallic Co nanoparticles is believed to be superparamagnetic is still under debate. Bean and Livingston [150] reported a theoretical size of 8 nm for hcp cobalt and 28 nm for fcc Co at room temperature. Barbier *et al.* [159], based on their experimental work, reported that this critical size for cobalt was in the 16 – 20 nm range, without making a distinction between the two allotropes of Co – hcp and fcc Co.

**Table 2.4:** Magnetic properties of common cobalt-based materials relevant to this study.

Chemical formula	Chemical name	Magnetism	T <sub>C</sub> or T <sub>N</sub> (in °C)
Co	Cobalt	Ferromagnetic	1130 [149]
CoAl <sub>2</sub> O <sub>4</sub>	Cobalt(II) aluminium oxide	Antiferromagnetic	-269 [156]
CoO	Cobalt(II) oxide	Antiferromagnetic	18 [158]
Co <sub>3</sub> O <sub>4</sub>	Cobalt(II,III) oxide	Antiferromagnetic	-241 [156,157]
Co <sub>2</sub> SiO <sub>4</sub>	Co(II) silicon oxide	Antiferromagnetic	-224 [160–162]
CoTiO <sub>3</sub>	Cobalt(II) titanium(IV) oxide	Antiferromagnetic	-235 [163]

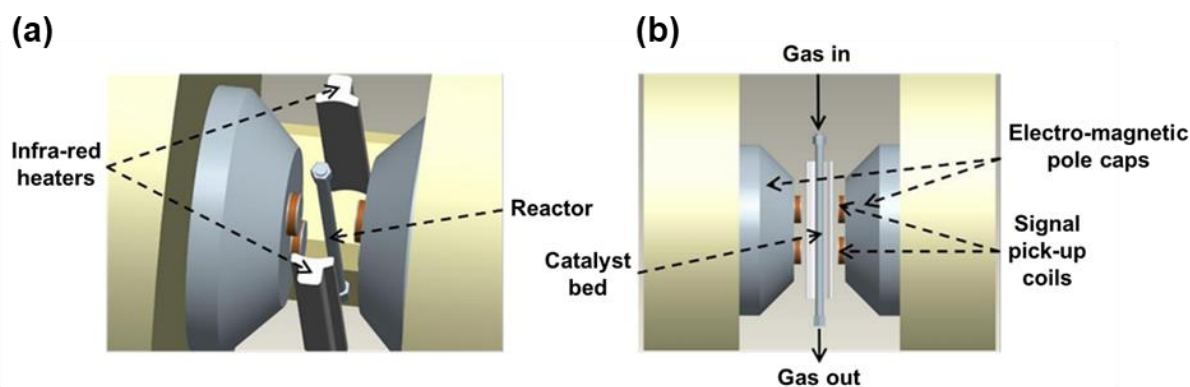


**Figure 2.17:** (a) Top-view of the UCT-SASOL developed *in situ* magnetometer instrument used for the detection of ferromagnetic and superparamagnetic materials. (b) Front-view showing the stainless steel *in situ* magnetometer reactor placed between two electro-magnetic pole caps. Note that the front infra-red heater is not shown in the figure (b). (Adapted from [92–94]).

The strength of the external field required to align neighbouring electron spins in superparamagnetic particles is strongly dependent on particle size, *i.e.*, a much stronger external field is required to magnetise very small particles than that required for the magnetisation of larger particles due to thermal effects. Therefore, when varying the strength of the applied field, the magnetisation measured at low fields is a result of the relatively larger particles, and the magnetisation at higher fields being a cumulative result of both small and large particles. This maximum magnetisation measured at high field strengths is called the saturation magnetisation ( $M_{\text{sat}}$ ). Upon removal of the external field (*i.e.*, at 0 T), the particles lose their magnetisation as shown in Figure 2.18 [109,148].

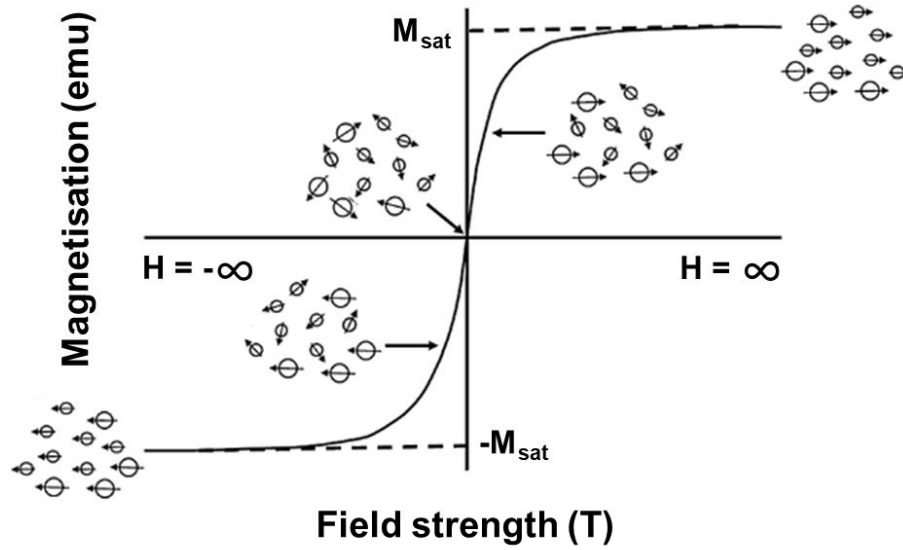


**Figure 2.18:** Measured magnetisation of a purely superparamagnetic sample as a function of the applied magnetic field. (Adapted from [109,148]).

For a sample which exhibits superparamagnetic behaviour, a particle size distribution and average particle size can be obtained from the plot shown in Figure 2.18. The Langevin equation, shown as Equation 2.3, can be used to obtain a particle size distribution by superimposing a number of these equations according to the contribution of the various particle sizes [109,148].

$$\frac{M}{M_{sat}} = \coth\left(\frac{\rho \cdot \sigma_{sat} \cdot \pi \cdot d^3 \cdot H}{6 \cdot k_B \cdot T}\right) - \left(\frac{6 \cdot k_B \cdot T}{\rho \cdot \sigma_{sat} \cdot \pi \cdot d^3 \cdot H}\right) \quad \text{Equation 2.3}$$

$\frac{M}{M_{sat}}$  is the ratio of the measured sample magnetisation to the extrapolated saturation magnetisation at an infinite applied field,  $\rho$  is the density of the magnetic material and  $\sigma_{sat}$  is the specific saturation magnetisation of the magnetic material (for Co: 168 emu/g at 27 °C [164]) which is independent of crystallite size [165]. The variable  $d$  is the particle diameter (assuming a spherical shape),  $H$  is the applied magnetic field,  $k_B$  is the Boltzmann constant and  $T$  is the temperature.

As mentioned above, ferromagnetic materials are those that remain magnetised (*i.e.*, having a remnant magnetisation,  $M_{rem}$ ) upon removal of an applied external field. So, when varying the

external field and measuring the magnetisation, a magnetisation *versus* applied field plot (or M-H plot) is obtained showing hysteresis behaviour as shown in Figure 2.19.

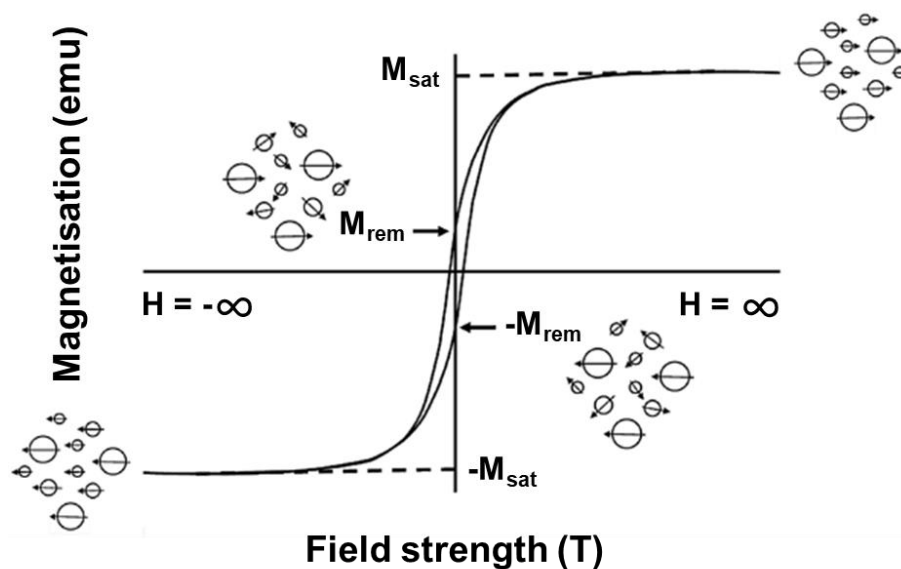


**Figure 2.19:** M-H plot obtained when the magnetisation of a ferromagnetic sample is measured as function of the applied magnetic field. (Adapted from [109,148]).

In general, a particle size distribution is not easily attainable from the M-H plot in Figure 2.19 using the Langevin equation (Equation 2.3), but the relative amount of material with remnant magnetisation at 0 T ( $\gamma$ ) in a catalyst sample can be obtained using Equation 2.4 [109,148]. However, as a special precaution, samples with a  $\gamma$  value below 10 wt.-% can be regarded as being mostly “superparamagnetic” which then allows for the use of the Langevin equation. Therefore,  $\gamma$  can give qualitative information about the particle size, and any changes thereof, especially if a sample started off with a  $\gamma$  that is less than 10 wt.-% which then increases above 10 wt.-% as a result of some high-temperature treatment and/or reaction condition [73,145].

$$\gamma \text{ (wt.-%)} = \frac{2 \cdot M_{rem}}{M_{sat}} \times 100$$

Equation 2.4

$\gamma$  is the amount of material displaying remnant magnetisation relative to the total amount of ferromagnetic material present in a sample. This material comprises of crystallites having a size which is greater than the critical size for superparamagnetism.  $M_{rem}$  is the sample's remnant magnetisation and  $M_{sat}$  is the sample's saturation magnetisation.

As mentioned previously, increasing temperature tends to decrease the strong interaction between neighbouring spins in ferromagnetic and superparamagnetic samples [148]. This effect is more pronounced for relatively small particles, and therefore, the remnant magnetisation (and consequently the  $\gamma$  value) of samples can be expected to decrease with increasing temperature. On the other hand, the critical diameter for superparamagnetism can be expected to increase as a function of temperature as an increased fraction of the sample gradually loses ferromagnetic behaviour due to the inverse relationship between temperature and particle size [148,151].

## References

- [1] M.L. Brown Jr., A.W. Green, G. Cohn, H.C. Andersen, *Ind. Eng. Chem.* 52 (1960) 841–844.
- [2] S.H. Oh, R.M. Sinkevitch, *J. Catal.* 142 (1993) 254–262.
- [3] N. Edwards, S.R. Ellis, J.C. Frost, S.E. Golunski, A.N.J. van Keulen, N.G. Lindewald, J.G. Reinkingh, *J. Power Sources* 71 (1998) 123–128.
- [4] S. Golunski, *Platin. Met. Rev.* 42 (1998) 2–7.
- [5] P.G. Gray, M.I. Petch, *Platin. Met. Rev.* 44 (2000) 108–111.
- [6] T.V. Choudhary, D.W. Goodman, *Catal. Today* 77 (2002) 65–78.
- [7] A. Faur Ghenciu, *Curr. Opin. Solid State Mater. Sci.* 6 (2002) 389–399.
- [8] G. Zhou, Y. Jiang, H. Xie, F. Qiu, *Chem. Eng. J.* 109 (2005) 141–145.
- [9] E.D. Park, D. Lee, H.C. Lee, *Catal. Today* 139 (2009) 280–290.
- [10] A. Mishra, R. Prasad, *Bull. Chem. React. Eng. Catal.* 6 (2011) 1–14.
- [11] D.H. Kim, M.S. Lim, *Appl. Catal. A* 224 (2002) 27–38.
- [12] A. Wootsch, C. Descorme, D. Duprez, *J. Catal.* 225 (2004) 259–266.
- [13] A. Parinyaswan, S. Pongstabodee, A. Luengnaruemitchai, *Int. J. Hydrog. Energy* 31 (2006) 1942–1949.
- [14] P. Naknam, A. Luengnaruemitchai, S. Wongkasemjit, S. Osuwan, *J. Power Sources* 165 (2007) 353–358.
- [15] J. Yan, J. Ma, P. Cao, P. Li, *Catal. Lett.* 93 (2004) 55–60.
- [16] M. Kotobuki, A. Watanabe, H. Uchida, H. Yamashita, M. Watanabe, *J. Catal.* 236 (2005) 262–269.
- [17] P. Mars, D.W. van Krevelen, *Chem. Eng. Sci.* 3 (1954) 41–59.
- [18] D. Perti, R.L. Kabel, G.J. McCarthy, *AIChE J.* 31 (1985) 1435–1440.
- [19] P. Broqvist, I. Panas, H. Persson, *J. Catal.* 210 (2002) 198–206.
- [20] J. Jansson, A.E.C. Palmqvist, E. Fridell, M. Skoglundh, L. Österlund, P. Thormählen, V. Langer, *J. Catal.* 211 (2002) 387–397.
- [21] L. Lukashuk, N. Yigit, R. Rameshan, E. Kolar, D. Teschner, M. Hävecker, A. Knop-

- Gericke, R. Schlögl, K. Föttinger, G. Rupprechter, *ACS Catal.* 8 (2018) 8630–8641.
- [22] M.P. Woods, P. Gawade, B. Tan, U.S. Ozkan, *Appl. Catal. B* 97 (2010) 28–35.
- [23] L. Lukashuk, N. Yigit, H. Li, J. Bernardi, K. Föttinger, G. Rupprechter, *Catal. Today* 336 (2019) 139–147.
- [24] B. Roldan Cuenya, *Thin Solid Films* 518 (2010) 3127–3150.
- [25] B. Roldan Cuenya, F. Behafarid, *Surf. Sci. Rep.* 70 (2015) 135–187.
- [26] Y. Teng, H. Sakurai, A. Ueda, T. Kobayashi, *Int. J. Hydrog. Energy* 24 (1999) 355–358.
- [27] J.-W. Park, J.-H. Jeong, W.-L. Yoon, H. Jung, H.-T. Lee, D.-K. Lee, Y.-K. Park, Y.-W. Rhee, *Appl. Catal. A* 274 (2004) 25–32.
- [28] P. Ratnasamy, D. Srinivas, C.V.V. Satyanarayana, P. Manikandan, R.S. Senthil Kumaran, M. Sachin, V.N. Shetti, *J. Catal.* 221 (2004) 455–465.
- [29] D. Gamarra, C. Belver, M. Fernández-García, A. Martínez-Arias, *J. Am. Chem. Soc.* 129 (2007) 12064–12065.
- [30] K. Omata, T. Takada, S. Kasahara, M. Yamada, *Appl. Catal. A* 146 (1996) 255–267.
- [31] M.M. Yung, Z. Zhao, M.P. Woods, U.S. Ozkan, *J. Mol. Catal. A Chem.* 279 (2008) 1–9.
- [32] Z. Zhao, M.M. Yung, U.S. Ozkan, *Catal. Commun.* 9 (2008) 1465–1471.
- [33] P. Gawade, B. Bayram, A.-M.C. Alexander, U.S. Ozkan, *Appl. Catal. B* 128 (2012) 21–30.
- [34] L. Lukashuk, K. Föttinger, E. Kolar, C. Rameshan, D. Teschner, M. Hävecker, A. Knop-Gericke, N. Yigit, H. Li, E. McDermott, M. Stöger-Pollach, G. Rupprechter, *J. Catal.* 344 (2016) 1–15.
- [35] T.M. Nyathi, N. Fischer, A.P.E. York, M. Claeys, *Faraday Discuss.* 197 (2017) 269–285.
- [36] M. Khasu, T. Nyathi, D.J. Morgan, G.J. Hutchings, M. Claeys, N. Fischer, *Catal. Sci. Technol.* 7 (2017) 4806–4817.
- [37] T.M. Nyathi, N. Fischer, A.P.E. York, D.J. Morgan, G.J. Hutchings, E.K. Gibson, P.P. Wells, C.R.A. Catlow, M. Claeys, *ACS Catal.* 9 (2019) 7166–7178.
- [38] S. Malwadkar, P. Bera, M.S. Hegde, C.V.V. Satyanarayana, *React. Kinet. Mech. Catal.* 107 (2012) 405–419.
- [39] Z. Mohamed, V.D.B.C. Dasireddy, S. Singh, H.B. Friedrich, *Appl. Catal. B* 180 (2016) 687–697.
- [40] L. Zhong, T. Kropp, W. Baaziz, O. Ersen, D. Teschner, R. Schlögl, M. Mavrikakis, S. Zafeiratos, *ACS Catal.* 9 (2019) 8325–8336.

- [41] C. Perego, P. Villa, *Catal. Today* 34 (1997) 281–305.
- [42] G. Jacobs, T.K. Das, Y. Zhang, J. Li, G. Racoillet, B.H. Davis, *Appl. Catal. A* 233 (2002) 263–281.
- [43] S. Storsæter, Ø. Borg, E.A. Blekkan, A. Holmen, *J. Catal.* 231 (2005) 405–419.
- [44] C.-B. Wang, C.-W. Tang, H.-C. Tsai, S.-H. Chien, *Catal. Lett.* 107 (2006) 223–230.
- [45] A.A. Adesina, *Appl. Catal. A* 138 (1996) 345–367.
- [46] E. Marceau, X. Carrier, M. Che, O. Clause, C. Marcilly, in: G. Ertl, H. Knözinger, F. Schüth, J. Weitkamp (Eds.), *Handb. Heterog. Catal.*, Wiley-VCH Verlag GmbH & Co. KGaA, Weinheim, Germany, 2008, pp. 467–484.
- [47] P. Munnik, P.E. de Jongh, K.P. de Jong, *Chem. Rev.* 115 (2015) 6687–6718.
- [48] J.M. Herrmann, *J. Catal.* 89 (1984) 404–412.
- [49] B. Delmon, in: G. Ertl, H. Knözinger, J. Weitkamp (Eds.), *Prep. Solid Catal.*, Wiley-VCH Verlag GmbH, Weinheim, Germany, 1999, pp. 541–579.
- [50] W.E. Kaden, T. Wu, W.A. Kunkel, S.L. Anderson, *Science* 326 (2009) 826–829.
- [51] A. Bruix, J.A. Rodriguez, P.J. Ramírez, S.D. Senanayake, J. Evans, J.B. Park, D. Stacchiola, P. Liu, J. Hrbek, F. Illas, *J. Am. Chem. Soc.* 134 (2012) 8968–8974.
- [52] T.W. van Deelen, C. Hernández Mejía, K.P. de Jong, *Nat. Catal.* 2 (2019) 955–970.
- [53] S.J. Tauster, S.C. Fung, *J. Catal.* 55 (1978) 29–35.
- [54] M.A. Vannice, C. Sudhakar, *J. Phys. Chem.* 88 (1984) 2429–2432.
- [55] F.P. da Silva, J.L. Fiorio, L.M. Rossi, *ACS Omega* 2 (2017) 6014–6022.
- [56] C.-B. Wang, C.-W. Tang, S.-J. Gau, S.-H. Chien, *Catal. Lett.* 101 (2005) 59–63.
- [57] N.E. Tsakoumis, R.E. Johnsen, W. van Beek, M. Rønning, E. Rytter, A. Holmen, *Chem. Commun.* 52 (2016) 3239–3242.
- [58] N.E. Tsakoumis, J.C. Walmsley, M. Rønning, W. van Beek, E. Rytter, A. Holmen, *J. Am. Chem. Soc.* 139 (2017) 3706–3715.
- [59] B. Jongsomjit, J. Panpranot, J.G. Goodwin Jr., *J. Catal.* 215 (2003) 66–77.
- [60] G.R. Johnson, A.T. Bell, *ACS Catal.* 6 (2016) 100–114.
- [61] J. Fonseca, S. Royer, N. Bion, L. Pirault-Roy, M. do C. Rangel, D. Duprez, F. Epron, *Appl. Catal. B* 128 (2012) 10–20.
- [62] A. Jha, Y.-L. Lee, W.-J. Jang, J.-O. Shim, K.-W. Jeon, H.-S. Na, H.-M. Kim, H.-S. Roh, D.-W. Jeong, S.G. Jeon, J.-G. Na, W.L. Yoon, *Mol. Catal.* 433 (2017) 145–152.

- [63] D. Vovchok, C.J. Guild, S. Dissanayake, J. Llorca, E. Stavitski, Z. Liu, R.M. Palomino, I. Waluyo, Y. Li, A.I. Frenkel, J.A. Rodriguez, S.L. Suib, S.D. Senanayake, *J. Phys. Chem. C* 122 (2018) 8998–9008.
- [64] D.H. Kim, J.E. Cha, *Catal. Lett.* 86 (2003) 107–112.
- [65] T. Caputo, L. Lisi, R. Pirone, G. Russo, *Ind. Eng. Chem. Res.* 46 (2007) 6793–6800.
- [66] L. Wang, H. Liu, Y. Chen, S. Yang, *Int. J. Hydrog. Energy* 42 (2017) 3682–3689.
- [67] L. Wang, H. Liu, *Catal. Today* 316 (2018) 155–161.
- [68] Y. Cao, X. Peng, Z. Tan, Y. Liu, X. Wang, W. Zhao, L. Jiang, *Ind. Eng. Chem. Res.* 58 (2019) 17692–17698.
- [69] X. Nie, H. Wang, W. Li, Y. Chen, X. Guo, C. Song, *J. CO<sub>2</sub> Util.* 24 (2018) 99–111.
- [70] W. Li, X. Nie, X. Jiang, A. Zhang, F. Ding, M. Liu, Z. Liu, X. Guo, C. Song, *Appl. Catal. B* 220 (2018) 397–408.
- [71] G. Moradi, M. Basir, A. Taeb, A. Kiennemann, *Catal. Commun.* 4 (2003) 27–32.
- [72] B. Jongsomjit, C. Sakdamnusun, P. Praserttham, *Mater. Chem. Phys.* 89 (2005) 395–401.
- [73] M. Wolf, E.K. Gibson, E.J. Olivier, J.H. Neethling, C.R.A. Catlow, N. Fischer, M. Claeys, *ACS Catal.* 9 (2019) 4902–4918.
- [74] T. Komaya, A.T. Bell, Z. Weng-Sieh, R. Gronsky, F. Engelke, T.S. King, M. Pruski, *J. Catal.* 149 (1994) 142–148.
- [75] T. Komaya, A.T. Bell, Z. Weng-Sieh, R. Gronsky, F. Engelke, T.S. King, M. Pruski, *J. Catal.* 150 (1994) 400–406.
- [76] A.T. Bell, *Science* 299 (2003) 1688–1691.
- [77] V.A. de la Peña O’Shea, M. Consuelo Álvarez Galván, A.E. Platero Prats, J.M. Campos-Martin, J.L.G. Fierro, *Chem. Commun.* 47 (2011) 7131–7133.
- [78] J. Li, Y. Lin, X. Pan, D. Miao, D. Ding, Y. Cui, J. Dong, X. Bao, *ACS Catal.* 9 (2019) 6342–6348.
- [79] M. Voß, D. Borgmann, G. Wedler, *J. Catal.* 212 (2002) 10–21.
- [80] C.-B. Wang, C.-W. Tang, H.-C. Tsai, M.-C. Kuo, S.-H. Chien, *Catal. Lett.* 107 (2006) 31–37.
- [81] A.E. Aksoylu, M.M.A. Freitas, J.L. Figueiredo, *Appl. Catal. A* 192 (2000) 29–42.
- [82] A.E. Aksoylu, M. Madalena, A. Freitas, M.F.R. Pereira, J.L. Figueiredo, *Carbon N. Y.* 39 (2001) 175–185.

- [83] G.C. Torres, E.L. Jablonski, G.T. Baronetti, A.A. Castro, S.R. de Miguel, O.A. Scelza, M.D. Blanco, M.A. Peña Jiménez, J.L.G. Fierro, *Appl. Catal. A* 161 (1997) 213–226.
- [84] B.J. Matsoso, K. Ranganathan, B.K. Mutuma, T. Lerotholi, G. Jones, N.J. Coville, *RSC Adv.* 6 (2016) 106914–106920.
- [85] B.J. Matsoso, T. Lerotholi, N.J. Coville, G. Jones, *Johnson Matthey Technol. Rev.* 63 (2019) 76–88.
- [86] B.K. Mutuma, B.J. Matsoso, K. Ranganathan, J.M. Keartland, D. Wamwangi, N.J. Coville, *RSC Adv.* 7 (2017) 21187–21195.
- [87] I.B. Usman, B. Matsoso, K. Ranganathan, D. Naidoo, N.J. Coville, D. Wamwangi, *Mater. Chem. Phys.* 209 (2018) 280–290.
- [88] P. Nguyen, C. Pham, *Appl. Catal. A* 391 (2011) 443–454.
- [89] A.R. de la Osa, A. De Lucas, J. Díaz-Maroto, A. Romero, J.L. Valverde, P. Sánchez., *Catal. Today* 187 (2012) 173–182.
- [90] J. Labuschagne, R. Meyer, Z.H. Chonco, J.M. Botha, D.J. Moodley, *Catal. Today* 275 (2016) 2–10.
- [91] Y.H. Kim, E.D. Park, H.C. Lee, D. Lee, K.H. Lee, *Catal. Today* 146 (2009) 253–259.
- [92] M.C.M. Claeys, E.W.J. van Steen, J.L. Visagie, J. van de Loosdrecht, *Magnetometer*, US Patent 8,773,118 B2, 2014.
- [93] N. Fischer, B. Clapham, T. Feltes, E. van Steen, M. Claeys, *Angew. Chemie - Int. Ed.* 53 (2014) 1342–1345.
- [94] N. Fischer, M. Claeys, *J. Phys. D. Appl. Phys.* 53 (2020) 293001.
- [95] M.C.M. Claeys, N.F. Fischer, *Sample Presentation Device for Radiation-Based Analytical Equipment*, US Patent 8,597,598 B2, 2013.
- [96] N. Fischer, M. Claeys, *Catal. Today* 275 (2016) 149–154.
- [97] F. Zasada, W. Piskorz, J. Janas, J. Gryboš, P. Indyka, Z. Sojka, *ACS Catal.* 5 (2015) 6879–6892.
- [98] N.W. Hurst, S.J. Gentry, A. Jones, B.D. McNicol, *Catal. Rev.* 24 (1982) 233–309.
- [99] A. Khawam, D.R. Flanagan, *J. Phys. Chem. B* 110 (2006) 17315–17328.
- [100] J.W. Niemantsverdriet, in: J.W. Niemantsverdriet (Ed.), *Spectrosc. Catal.*, 3rd ed., Wiley-VCH Verlag GmbH & Co. KGaA, Weinheim, Germany, 2007, pp. 11–38.
- [101] A. Gervasini, in: A. Auroux (Ed.), *Calorim. Therm. Methods Catal.*, Springer-Verlag, Berlin, Heidelberg, 2013, pp. 175–195.

- [102] D. Nabaho, Hydrogen Spillover in the Fischer-Tropsch Synthesis: The Role of Platinum and Gold as Promoters in Cobalt-Based Catalysts, Ph.D. thesis, University of Cape Town, 2015.
- [103] J.Y. Kim, J.A. Rodriguez, J.C. Hanson, A.I. Frenkel, P.L. Lee, *J. Am. Chem. Soc.* 125 (2003) 10684–10692.
- [104] J.A. Rodriguez, J.Y. Kim, J.C. Hanson, M. Pérez, A.I. Frenkel, *Catal. Lett.* 85 (2003) 247–254.
- [105] Q. Guo, Y. Liu, *React. Kinet. Catal. Lett.* 92 (2007) 19–25.
- [106] S. Monyanon, S. Pongstabodee, A. Luengnaruemitchai, *J. Chinese Inst. Chem. Eng.* 38 (2007) 435–441.
- [107] M.E. Dry, in: A.P. Steynberg, M.E. Dry (Eds.), *Fischer-Tropsch Technol.*, Elsevier B.V., Amsterdam, 2004, pp. 533–600.
- [108] F. Pinna, *Catal. Today* 41 (1998) 129–137.
- [109] P.A. Chernavskii, J.-A. Dalmon, N.S. Perov, A.Y. Khodakov, *Oil Gas Sci. Technol. - Rev. l'IFP* 64 (2009) 25–48.
- [110] M. Wolf, N. Fischer, M. Claeys, *Catal. Today* 275 (2016) 135–140.
- [111] C.H. Bartholomew, *Appl. Catal. A* 212 (2001) 17–60.
- [112] J.A. Moulijn, A.E. van Diepen, F. Kapteijn, *Appl. Catal. A* 212 (2001) 3–16.
- [113] M. Argyle, C. Bartholomew, *Catalysts* 5 (2015) 145–269.
- [114] E. van Steen, M. Claeys, *Chem. Eng. Technol.* 31 (2008) 655–666.
- [115] W. Thomson, London, Edinburgh, Dublin *Philos. Mag. J. Sci.* 42 (1871) 448–452.
- [116] G.L. Bezemer, T.J. Remans, A.P. van Bavel, A.I. Dugulan, *J. Am. Chem. Soc.* 132 (2010) 8540–8541.
- [117] N. Fischer, B. Clapham, T. Feltes, M. Claeys, *ACS Catal.* 5 (2015) 113–121.
- [118] G. Marbán, I. López, T. Valdés-Solís, *Appl. Catal. A* 361 (2009) 160–169.
- [119] S. Zeng, K. Liu, L. Zhang, B. Qin, T. Chen, Y. Yin, H. Su, *J. Power Sources* 261 (2014) 46–54.
- [120] International Agency for Research on Cancer (IARC), in: *IARC Monogr. Eval. Carcinog. Risks to Humans - Chlorinated Drink. Chlorination By-Products; Some Other Halogenated Compd. Cobalt Cobalt Compd.*, Geneva, 1991, pp. 363–472.
- [121] P.J. van Berge, J. van de Loosdrecht, S. Barradas, A.M. van der Kraan, *Catal. Today* 58 (2000) 321–334.

- [122] T. Cseri, S. Békássy, G. Kenessey, G. Liptay, F. Figueras, *Thermochim. Acta* 288 (1996) 137–154.
- [123] J.-S. Girardon, A.S. Lermontov, L. Gengembre, P.A. Chernavskii, A. Griboval-Constant, A.Y. Khodakov, *J. Catal.* 230 (2005) 339–352.
- [124] T.M. Eggenhuisen, P. Munnik, H. Talsma, P.E. de Jongh, K.P. de Jong, *J. Catal.* 297 (2013) 306–313.
- [125] F. Schüth, M. Hesse, K.K. Unger, in: G. Ertl, H. Knözinger, F. Schüth, J. Weitkamp (Eds.), *Handb. Heterog. Catal.*, Wiley-VCH Verlag GmbH & Co. KGaA, Weinheim, Germany, 2008, pp. 100–119.
- [126] J.W. Geus, A.J. van Dillen, in: G. Ertl, H. Knözinger, F. Schüth, J. Weitkamp (Eds.), *Handb. Heterog. Catal.*, Wiley-VCH Verlag GmbH & Co. KGaA, Weinheim, Germany, 2008, pp. 428–467.
- [127] Z. Ma, T. Zhang, C. Jiang, *Chem. Eng. J.* 264 (2015) 610–616.
- [128] P. van Helden, F. Prinsloo, J.-A. van den Berg, B. Xaba, W. Erasmus, M. Claeys, J. van de Loosdrecht, *Catal. Today* 342 (2020) 88–98.
- [129] R.C. Reuel, C.H. Bartholomew, *J. Catal.* 85 (1984) 78–88.
- [130] L. Fu, C.H. Bartholomew, *J. Catal.* 92 (1985) 376–387.
- [131] I. Danielsson, B. Lindman, *Colloids Surf.* 3 (1981) 391–392.
- [132] J. Klier, C.J. Tucker, T.H. Kalantar, D.P. Green, *Adv. Mater.* 12 (2000) 1751–1757.
- [133] M.-J. Schwuger, K. Stickdorn, R. Schomäcker, *Chem. Rev.* 95 (1995) 849–864.
- [134] S. Eriksson, S. Rojas, M. Boutonnet, *Appl. Catal. A* 265 (2004) 207–219.
- [135] N. Fischer, T. Feltes, M. Claeys, in: B.I. Kharisov, O.V. Kharissova, U. Ortiz-Mendez (Eds.), *CRC Concise Encycl. Nanotechnol.*, 1st ed., CRC Press, Boca Raton, 2015, pp. 547–560.
- [136] M. Boutonnet, J. Kizling, P. Stenius, G. Maire, *Colloids Surf.* 5 (1982) 209–225.
- [137] M. Boutonnet, S. Lögdberg, E. Elm Svensson, *Curr. Opin. Colloid Interface Sci.* 13 (2008) 270–286.
- [138] M. Boutonnet, M. Sanchez-Dominguez, *Catal. Today* 285 (2017) 89–103.
- [139] D. Barkhuizen, I. Mabaso, E. Viljoen, C. Welker, M. Claeys, E. van Steen, J.C.Q. Fletcher, *Pure Appl. Chem.* 78 (2006) 1759–1769.
- [140] N. Fischer, E. van Steen, M. Claeys, *Catal. Today* 171 (2011) 174–179.
- [141] N. Fischer, Preparation of Nano- and Ångström-Sized Cobalt Ensembles and Their

- Performance in the Fischer-Tropsch Synthesis, Ph.D. thesis, University of Cape Town, 2011.
- [142] N. Fischer, M. Minnermann, M. Baeumer, E. van Steen, M. Claeys, *Catal. Lett.* 142 (2012) 830–837.
- [143] C.A. Welker, Ruthenium-Based Fischer-Tropsch Synthesis on Crystallites and Clusters of Different Sizes: From “Nano” to “Ångström”, Ph.D. thesis, University of Cape Town, 2007.
- [144] M. Claeys, M.E. Dry, E. van Steen, E. du Plessis, P.J. van Berge, A.M. Saib, D.J. Moodley, *J. Catal.* 318 (2014) 193–202.
- [145] M. Claeys, M.E. Dry, E. van Steen, P.J. van Berge, S. Booyens, R. Crous, P. van Helden, J. Labuschagne, D.J. Moodley, A.M. Saib, *ACS Catal.* 5 (2015) 841–852.
- [146] M. Wolf, H. Kotzé, N. Fischer, M. Claeys, *Faraday Discuss.* 197 (2017) 243–268.
- [147] C. Kittel, *Rev. Mod. Phys.* 21 (1949) 541–583.
- [148] J.-A. Dalmon, in: B. Imelik, J.C. Vedrine (Eds.), *Catal. Charact. - Phys. Tech. Solid Mater.*, Springer US, Boston, MA, 1994, pp. 585–609.
- [149] V. Sechovský, in: K.H.J. Buschow, R.W. Cahn, M.C. Flemings, B. Ilschner, E.J. Kramer, S. Mahajan, P. Veysière (Eds.), *Encycl. Mater. Sci. Technol.*, 2nd ed., Elsevier Science Ltd, 2001, pp. 5018–5032.
- [150] C.P. Bean, J.D. Livingston, *J. Appl. Phys.* 30 (1959) S120–S129.
- [151] P.W. Selwood, in: P.W. Selwood (Ed.), *Chemisorpt. Magn.*, Elsevier, 1975, pp. 17–29.
- [152] J.P. Chen, C.M. Sorensen, K.J. Klabunde, G.C. Hadjipanayis, E. Devlin, A. Kostikas, *Phys. Rev. B Condens. Matter Mater. Phys.* 54 (1996) 9288–9296.
- [153] A. Demortière, P. Panissod, B.P. Pichon, G. Pourroy, D. Guillon, B. Donnio, S. Bégin-Colin, *Nanoscale* 3 (2011) 225–232.
- [154] H. Amekura, Y. Fudamoto, Y. Takeda, N. Kishimoto, *Phys. Rev. B Condens. Matter Mater. Phys.* 71 (2005) 172404.
- [155] X. He, W. Zhong, C.-T. Au, Y. Du, *Nanoscale Res. Lett.* 8 (2013) 446.
- [156] W.L. Roth, *J. Phys.* 25 (1964) 507–515.
- [157] T. Mousavand, T. Naka, K. Sato, S. Ohara, M. Umetsu, S. Takami, T. Nakane, A. Matsushita, T. Adschiri, *Phys. Rev. B Condens. Matter Mater. Phys.* 79 (2009) 144411.
- [158] C.G. Shull, W.A. Strauser, E.O. Wollan, *Phys. Rev.* 83 (1951) 333–345.
- [159] A. Barbier, A. Hanif, J.-A. Dalmon, G.A. Martin, *Appl. Catal. A* 168 (1998) 333–343.
- [160] S. Nomura, R. Santoro, J. Fang, R. Newnham, *J. Phys. Chem. Solids* 25 (1964) 901–905.

- [161] W. Schmidt, C. Brotzeller, P. Schweiss, H. Tietze-Jaensch, R. Geick, W. Treutmann, J. Magn. Mater. 140–144 (1995) 1989–1990.
- [162] I.S. Hagemann, P.G. Khalifah, A.P. Ramirez, R.J. Cava, Phys. Rev. B Condens. Matter Mater. Phys. 62 (2000) R771–R774.
- [163] R.E. Newnham, J.H. Fang, R.P. Santoro, Acta Crystallogr. 17 (1964) 240–242.
- [164] H. Niu, Q. Chen, H. Zhu, Y. Lin, X. Zhang, J. Mater. Chem. 13 (2003) 1803–1805.
- [165] P.W. Selwood, Chemisorption and Magnetization, Elsevier, 1975.



## Chapter 3: Scope of Study

### 3.1. Context and Objectives

Cobalt(II, III) oxide ( $\text{Co}_3\text{O}_4$ ) is an extensively studied material that has shown very good catalytic activity for the total oxidation of CO in the absence of  $\text{H}_2$ ,  $\text{H}_2\text{O}$  and  $\text{CO}_2$  [1–7]. The performance of  $\text{Co}_3\text{O}_4$  as a CO oxidation catalyst can be influenced by numerous parameters including; particle size [6], particle shape [5], and preparation method [4]. As a result, there has been growing interest in  $\text{Co}_3\text{O}_4$  as a cheaper alternative to noble metals for the preferential oxidation of CO (CO-PrOx). However, in the presence of the reducing gas  $\text{H}_2$ , not only does the conversion of CO to  $\text{CO}_2$  get negatively affected, but a few recent studies have shown *in situ* evidence that  $\text{Co}_3\text{O}_4$  reduces to low oxidation state cobalt species, *i.e.*, CoO and metallic Co. The phase change affects the  $\text{CO}_2$  yield (based on the CO conversion) and selectivity (based on the  $\text{O}_2$  conversion) during CO-PrOx, with the possibility of  $\text{CH}_4$  formation in the presence of metallic Co at high enough reaction temperatures [8–13].

The reformat gas also contains other components, including  $\text{H}_2\text{O}$  and  $\text{CO}_2$ , which can potentially affect the progress of the targeted CO oxidation reaction [14–16]. However, very little is known about their exact effect on catalytic activity and selectivity. The possibility of the forward and reverse water-gas shift, as well as  $\text{CO}_2$  methanation taking place has been suggested in the literature but evidence of their occurrence has not been shown, under realistic CO-PrOx conditions. There is also no information on the temperature and cobalt phase dependency of these side reactions. Therefore, this study investigates the effects of  $\text{H}_2$ ,  $\text{H}_2\text{O}$  and  $\text{CO}_2$  on the performance and phase transformation of un-/supported  $\text{Co}_3\text{O}_4$ . The work also aims to identify the occurrence of the above-mentioned side reactions and identify the cobalt phase(s) responsible for each side reaction.

The phase change of  $\text{Co}_3\text{O}_4$  can be slowed down (or prevented) with the help of certain support materials. More specifically, the nature of the support, the kind of interaction the support has with the  $\text{Co}_3\text{O}_4$  nanoparticles and the supported catalyst preparation method; are some of the most common factors that determine the degree of reduction of  $\text{Co}_3\text{O}_4$  [9,17–19]. While the use of certain support materials may help stabilise the  $\text{Co}_3\text{O}_4$  phase, these materials (through their interaction with the  $\text{Co}_3\text{O}_4$ ) could also affect the CO oxidation activity of  $\text{Co}_3\text{O}_4$  [9,19]. It is also worth mentioning that this has not been extensively studied by other researchers, at least, not in the context of CO-PrOx. Therefore, the study presented herein also investigates a wide range of common support materials which have been grouped according to their known interactions with most active nanoparticles: i) “**weakly interacting**” supports (*viz.*,  $\text{CeO}_2$  and  $\text{ZrO}_2$ ), ii) “**strongly interacting**” supports (*viz.*,  $\text{SiO}_2$ ,  $\text{TiO}_2$  and  $\text{Al}_2\text{O}_3$ ) as well as, iii) “**inert**” supports (*viz.*,  $\text{SiC}$ ).

## 3.2. Research Approach

The overall approach for the current study involves firstly making theoretical predictions based on the outcomes of thermodynamic calculations and appropriately relating these with the planned experimental work. The chemical reactions involved during the synthesis of un-/supported  $\text{Co}_3\text{O}_4$  nanoparticles (also including metal-support compound (MSC) formation), during the reduction of the nanoparticles (including MSC formation), as well as the gas-phase reactions that are likely to occur during CO-PrOx (other than CO oxidation); were theoretically evaluated. As for the individual gas-phase reactions, equilibrium conversions were also determined as a function of temperature, taking into consideration the change in the Gibbs free energy with temperature.

To experimentally investigate the effect of each support, the interaction between the support and the  $\text{Co}_3\text{O}_4$  nanoparticles needs to be strong enough for the support to provide sufficient phase stability to the nanoparticles. The strength of the  $\text{Co}_3\text{O}_4$ -support interaction should also be such that each support can influence the catalytic performance of  $\text{Co}_3\text{O}_4$ . The chosen catalyst preparation method for achieving the above is incipient wetness impregnation of a dry powder support material with an aqueous solution containing cobalt(II) nitrate hexahydrate ( $\text{Co}(\text{NO}_3)_2 \cdot 6\text{H}_2\text{O}$ ) as the metal precursor. After the impregnation, the water is removed by drying and the remaining powder is calcined to convert the precursor to  $\text{Co}_3\text{O}_4$  [20–22]. For comparison, an unsupported  $\text{Co}_3\text{O}_4$  catalyst was also prepared using the reverse microemulsion technique.

The physicochemical properties of the un-/supported oxide catalysts were studied *ex situ* using various conventional techniques; *viz.*, Powder X-Ray Diffraction (PXRD), Scanning Transmission Electron Microscopy coupled with Electron Energy Loss Spectroscopy (STEM-EELS), N<sub>2</sub> physisorption, Inductively Coupled Plasma-Optical Emission Spectroscopy (ICP-OES), X-Ray Absorption Spectroscopy (XAS).

Before catalytic testing, a series of *in situ* reduction experiments were performed in the presence of H<sub>2</sub> for all prepared catalysts. This involved the extensive use of the in-house developed PXRD capillary reaction cell [23–26] for detecting all the three cobalt-based phases (*viz.*, Co<sub>3</sub>O<sub>4</sub>, CoO and metallic Co) formed during the reduction process. *In situ* reduction experiments in a gas mixture of H<sub>2</sub> with each of the other CO-PrOx feed gases (for example, in a H<sub>2</sub>O/H<sub>2</sub> mixture or a CO<sub>2</sub>/H<sub>2</sub> mixture *etc.*) were also performed, but using unsupported Co<sub>3</sub>O<sub>4</sub> only. Where it was deemed appropriate, the reduction was coupled with on-line Gas Chromatography (GC) analysis of the reactor outlet. The experiments carried out at this stage provided very useful insights into the reduction profiles of the un-/supported catalysts in the different reducing environments and informed on the kind of reduction profile that can be expected during CO-PrOx when all gases are present in the feed.

For the catalytic testing and *in situ* characterisation under various CO-PrOx conditions, the fixed-bed reactors of the in-house *in situ* PXRD reaction cell [23–26] and the low-frequency vibrating sample magnetometer [24,26,27], respectively, were used. While by PXRD one can in principle detect Co<sub>3</sub>O<sub>4</sub>, CoO and metallic Co; the magnetometer in comparison is highly sensitive to low amounts (< 1.0 wt.-%) of metallic Co (which can be ferromagnetic or superparamagnetic) and can therefore, accurately detect and quantify the amount of metallic Co formed during CO-PrOx. The gas feed composition was varied to study the effect of certain gas components. Testing experiments were first performed in the presence of 1% CO, 1% O<sub>2</sub>, 50% H<sub>2</sub> and a balance of N<sub>2</sub> for all prepared catalysts. Thereafter, over a selected number of catalysts (unsupported, as well as ZrO<sub>2</sub>-, SiC- and TiO<sub>2</sub>-supported Co<sub>3</sub>O<sub>4</sub>), the gases H<sub>2</sub>O and/or CO<sub>2</sub> were also co-fed at a concentration of 10% each. Finally, the effect of varying the O<sub>2</sub> concentration between 0.5 and 4% was also studied using unsupported and ZrO<sub>2</sub>-supported Co<sub>3</sub>O<sub>4</sub>. The real-time monitoring of the phase changes in each catalyst using the above-mentioned *in situ* techniques was also coupled with GC analysis of the reactor outlet which helped link each product formed (or each reaction taking place) with a certain cobalt (oxide) phase detected.

## References

- [1] D. Perti, R.L. Kabel, *AIChE J.* 31 (1985) 1420–1426.
- [2] D. Perti, R.L. Kabel, G.J. McCarthy, *AIChE J.* 31 (1985) 1435–1440.
- [3] J. Jansson, A.E.C. Palmqvist, E. Fridell, M. Skoglundh, L. Österlund, P. Thormählen, V. Langer, *J. Catal.* 211 (2002) 387–397.
- [4] C.-B. Wang, C.-W. Tang, S.-J. Gau, S.-H. Chien, *Catal. Lett.* 101 (2005) 59–63.
- [5] Y. Teng, Y. Kusano, M. Azuma, M. Haruta, Y. Shimakawa, *Catal. Sci. Technol.* 1 (2011) 920–922.
- [6] V. Iablokov, R. Barbosa, G. Pollefeyt, I. van Driessche, S. Chenakin, N. Kruse, *ACS Catal.* 5 (2015) 5714–5718.
- [7] L. Lukashuk, N. Yigit, R. Rameshan, E. Kolar, D. Teschner, M. Hävecker, A. Knop-Gericke, R. Schlögl, K. Föttinger, G. Rupprechter, *ACS Catal.* 8 (2018) 8630–8641.
- [8] Y. Teng, H. Sakurai, A. Ueda, T. Kobayashi, *Int. J. Hydrog. Energy* 24 (1999) 355–358.
- [9] Z. Zhao, M.M. Yung, U.S. Ozkan, *Catal. Commun.* 9 (2008) 1465–1471.
- [10] L. Lukashuk, K. Föttinger, E. Kolar, C. Rameshan, D. Teschner, M. Hävecker, A. Knop-Gericke, N. Yigit, H. Li, E. McDermott, M. Stöger-Pollach, G. Rupprechter, *J. Catal.* 344 (2016) 1–15.
- [11] T.M. Nyathi, N. Fischer, A.P.E. York, M. Claeys, *Faraday Discuss.* 197 (2017) 269–285.
- [12] M. Khasu, T. Nyathi, D.J. Morgan, G.J. Hutchings, M. Claeys, N. Fischer, *Catal. Sci. Technol.* 7 (2017) 4806–4817.
- [13] T.M. Nyathi, N. Fischer, A.P.E. York, D.J. Morgan, G.J. Hutchings, E.K. Gibson, P.P. Wells, C.R.A. Catlow, M. Claeys, *ACS Catal.* 9 (2019) 7166–7178.
- [14] S. Monyanon, S. Pongstabodee, A. Luengnaruemitchai, *J. Chinese Inst. Chem. Eng.* 38 (2007) 435–441.
- [15] Q. Guo, Y. Liu, *React. Kinet. Catal. Lett.* 92 (2007) 19–25.
- [16] P. Gawade, B. Bayram, A.M.C. Alexander, U.S. Ozkan, *Appl. Catal. B* 128 (2012) 21–30.
- [17] G. Jacobs, T.K. Das, Y. Zhang, J. Li, G. Racoillet, B.H. Davis, *Appl. Catal. A* 233 (2002) 263–281.
- [18] S. Storsæter, Ø. Borg, E.A. Blekkan, A. Holmen, *J. Catal.* 231 (2005) 405–419.
- [19] C.-B. Wang, C.-W. Tang, H.-C. Tsai, S.-H. Chien, *Catal. Lett.* 107 (2006) 223–230.

- [20] A.A. Adesina, *Appl. Catal. A* 138 (1996) 345–367.
- [21] E. Marceau, X. Carrier, M. Che, O. Clause, C. Marcilly, in: G. Ertl, H. Knözinger, F. Schüth, J. Weitkamp (Eds.), *Handb. Heterog. Catal.*, Wiley-VCH Verlag GmbH & Co. KGaA, Weinheim, Germany, 2008, pp. 467–484.
- [22] P. Munnik, P.E. de Jongh, K.P. de Jong, *Chem. Rev.* 115 (2015) 6687–6718.
- [23] M.C.M. Claeys, N.F. Fischer, Sample Presentation Device for Radiation-Based Analytical Equipment, US Patent 8,597,598 B2, 2013.
- [24] N. Fischer, B. Clapham, T. Feltes, E. van Steen, M. Claeys, *Angew. Chemie - Int. Ed.* 53 (2014) 1342–1345.
- [25] N. Fischer, M. Claeys, *Catal. Today* 275 (2016) 149–154.
- [26] N. Fischer, M. Claeys, *J. Phys. D. Appl. Phys.* 53 (2020) 293001.
- [27] M.C.M. Claeys, E.W.J. van Steen, J.L. Visagie, J. van de Loosdrecht, Magnetometer, US Patent 8,773,118 B2, 2014.



## Chapter 4: Methodology

### 4.1. Thermodynamic Calculations

To complement the experimental work done in this project, theoretical predictions were made on the outcome of selected chemical reactions of interest by carrying out thermodynamic calculations. The calculations were based on the Gibbs-Helmholtz equation (Equation 4.1 or 4.2) [1] which describes the change in the Gibbs free energy of a chemical reaction ( $\Delta G_{rxn}$ ) as a function of temperature ( $T$ ) and the change in the reaction enthalpy ( $\Delta H_{rxn}$ , calculated using Equation 4.3). The Gibbs-Helmholtz equation also depends on the standard Gibbs free energy ( $\Delta G_{rxn}^o$ , at 298.15 K and 1.013 bar), the standard enthalpy of a reaction ( $\Delta H_{rxn}^o$ , at 298.15 K and 1.013 bar), as well as the change in the heat capacity ( $\Delta C_{p,rxn}$ , calculated using Equation 4.4). The coefficients  $\Delta a_{rxn}$ ,  $\Delta b_{rxn}$ ,  $\Delta c_{rxn}$  and  $\Delta d_{rxn}$  in Equation 4.4 result from the difference of the sum of all chemical product coefficients and the sum of all chemical reactant coefficients. The  $a$ ,  $b$ ,  $c$  and  $d$  values of each chemical product and reactant species were obtained from Knacke *et al.* [2] and have been summarised in Table A.1.1 of Appendix A.1. A graphical plot of  $\Delta G_{rxn}$  versus  $T$  helps visualise the conditions of temperature where a reaction can be expected to be spontaneous or non-spontaneous, *i.e.*, thermodynamically favourable or unfavourable, respectively. Values of  $T$  were varied between 273.15 and 773.15 K (*i.e.*, 0 and 500 °C) in 5 K increments.

$$\frac{\partial \left( \frac{\Delta G_{rxn}(T)}{T} \right)}{\partial T} = - \frac{\Delta H_{rxn}(T)}{T^2} \quad \text{Equation 4.1}$$

$$\frac{\Delta G_{rxn}(T)}{T} - \frac{\Delta G_{rxn}^o(T)}{T^o} = - \int_{T^o}^T \frac{\Delta H_{rxn}(T)}{T^2} dT \quad \text{Equation 4.2}$$

$$\Delta H_{rxn}(T) = \Delta H_{rxn}^{\circ} + \int_{T^{\circ}}^T C_{p,rxn}(T) dT \quad \text{Equation 4.3}$$

$$\Delta C_{p,rxn}(T) = \Delta a_{rxn} + \Delta b_{rxn} \cdot \frac{T}{1000} + \Delta c_{rxn} \cdot \left(\frac{1000}{T}\right)^2 + \Delta d_{rxn} \cdot \left(\frac{T}{1000}\right)^2 \quad \text{Equation 4.4}$$

For a chemical reaction at equilibrium in the form,  $vV + wW \rightleftharpoons yY + zZ$ , the term  $\Delta G_{rxn}$  can also be calculated using Equation 4.5 if the reaction involves gaseous products and/or reactants. The term  $R$  is the ideal gas constant and  $K_{eq.}$  is the equilibrium constant calculated using Equation 4.6. Modulation and substitution of the terms in Equations 4.3 - 4.6 into Equation 4.2, results in Equation 4.7 which calculates the partial pressure ratio of gaseous products to gaseous reactants as a function of temperature. Therefore, a graphical plot of product-reactant partial pressure ratio *versus*  $T$  will show the conditions of both partial pressure and temperature that allow for a chemical reaction to be thermodynamically feasible.

Furthermore, Equation 4.7 can be used to calculate the equilibrium conversion ( $X_{eq.}$ ) that can be expected for a limiting gas reactant taking into consideration the stoichiometry of the reaction. It should be noted that the assumed ratio of the feed components will affect  $X_{eq.}$  but not  $K_{eq.}$  (at some value of  $T$ ) according to Le Chatelier's Principle [1]. Since determining  $X_{eq.}$  using Equation 4.7 can require solving 2<sup>nd</sup>- or even up to 5<sup>th</sup>-order polynomials, the freeware Scilab 6.0.2 [3] was accessed to solve the polynomials using the Newton-Raphson method [4].

$$\Delta G_{rxn}(T) = -RT \ln K_{eq.} \quad \text{Equation 4.5}$$

$$K_{eq.} = \frac{(p_Y)^y \cdot (p_Z)^z}{(p_V)^v \cdot (p_W)^w} \quad \text{Equation 4.6}$$

$$\frac{(p_Y)^y \cdot (p_Z)^z}{(p_V)^v \cdot (p_W)^w} = \exp \left\{ -\frac{1}{R} \cdot \left( \frac{\Delta G_{rxn}^{\circ}(T)}{T^{\circ}} - \int_{T^{\circ}}^T \frac{\Delta H_{rxn}^{\circ} + \int_{T^{\circ}}^T \Delta C_{p,rxn}(T) dT}{T^2} dT \right) \right\} \quad \text{Equation 4.7}$$

## 4.2. Catalyst Preparation

### 4.2.1. Chemicals

**Table 4.1:** Chemicals used for the synthesis of un-/supported  $\text{Co}_3\text{O}_4$  using the reverse microemulsion technique or incipient wetness impregnation, respectively.

Chemical name	Supplier	Mesh/particle size	Purity
Acetone	Kimix	n/a	$\geq 99.3\%$
$\gamma$ -Aluminium oxide or PURALOX	SASOL Germany	150 – 200 $\mu\text{m}$	$\geq 98.0\%$
25 wt.-% Ammonia aqueous solution	Kimix	n/a	
Cerium(IV) oxide	US Nano	10 – 30 nm	$\geq 99.97\%$
Cobalt(II) nitrate hexahydrate	Sigma-Aldrich	n/a	$\geq 98.0\%$
n-Hexane	Kimix	n/a	$\geq 99.5\%$
Pentaethylene glycol dodecylether	Akzo Nobel	n/a	
Silicon oxide (fumed) or Aerosil 150	Evonik Industries	~ 14 nm (average)	$\geq 99.8\%$
$\beta$ -Silicon carbide (mesoporous)	SiCAT	1 mm extrudates, later crushed $\leq 150 \mu\text{m}$	$\geq 99.9\%$
Titanium(IV) oxide (anatase)	Sigma-Aldrich	< 25 nm	$\geq 99.7\%$
Titanium(IV) oxide (4:1 anatase:rutile) or P25	Evonik Industries	~ 21 nm (average)	> 99.5%
Titanium(IV) oxide (rutile)	Sigma-Aldrich	< 100 nm	$\geq 99.5\%$
Zirconium(IV) oxide	US Nano	~ 40 nm (average)	$\geq 99.0\%$

### 4.2.2. Preparation of unsupported $\text{Co}_3\text{O}_4$ nanoparticles using the Reverse Microemulsion technique

It is worth mentioning that the procedure followed was first developed in-house and described by Fischer *et al.* [5,6]. To prepare a stable reverse microemulsion, n-hexane was mixed with pentaethylene glycol dodecylether (PEGDE) using an over-head stirrer (with a stainless-steel impeller) for 60 min at 600 rpm in a 2000 ml Schott bottle at room temperature and atmospheric pressure. An aqueous solution of  $\text{Co}(\text{NO}_3)_2 \cdot 6\text{H}_2\text{O}$  was added to the stirring n-hexane-PEGDE mixture after 60 min. This new ternary mixture was stirred for a further 2 hr before being allowed

to stabilise overnight. After stabilisation, an optically clear pink reverse microemulsion was obtained (see depiction in Figure 4.1) which indicated that the right proportions of the non-polar (n-hexane), amphiphilic (PEGDE) and polar ( $\text{Co}(\text{NO}_3)_2 \cdot 6\text{H}_2\text{O}$  (*aq.*)) phases had been mixed at room temperature and atmospheric pressure (see Table 4.2).

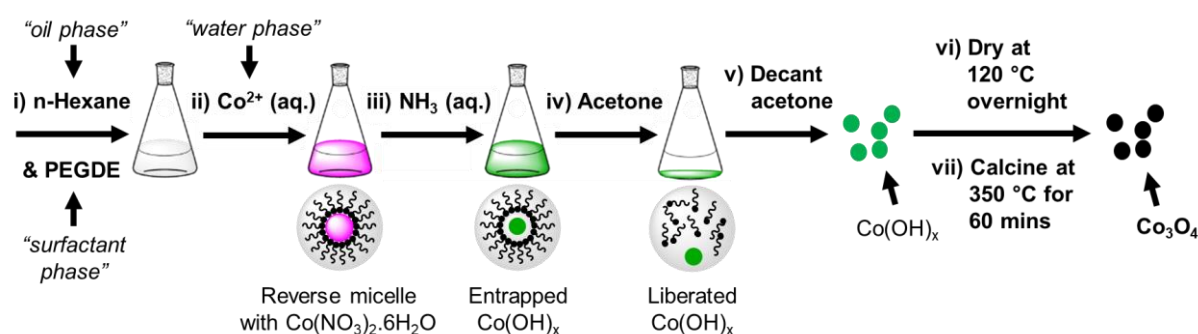
To the stable ternary mixture, a 25 wt.-%  $\text{NH}_3$  aqueous solution was added dropwise under stirring and left to stir for a further 30 min allowing for the precipitation of cobalt nitrate to form a green amorphous material (believed to be some  $\text{Co}(\text{OH})_x$  species [7]). A  $\text{Co}^{2+}:\text{NH}_3$  molar ratio of 1:4 was used to ensure the complete precipitation of cobalt nitrate. The produced green  $\text{Co}(\text{OH})_x$  precipitate was still entrapped in the reverse micelle system and needed to be liberated through flocculation, *i.e.*, the destabilisation of the reverse microemulsion [8–12]. This was done by adding acetone dropwise under stirring until a volume of acetone that is approximately double the total volume of the initial reverse microemulsion had been added. After flocculation, the precipitate was allowed to settle to the bottom of the Schott bottle and the resulting supernatant was siphoned out using a long piece of silicon tubing.

The precipitate was washed a couple of times with high amounts of acetone until a colourless supernatant was obtained. This extensive washing procedure also ensured that little (or no) surfactant remained around the  $\text{Co}(\text{OH})_x$  precipitate. After the washing procedure, the precipitate was transferred into a dry 250 ml beaker and allowed to settle to the bottom of the beaker before siphoning the excess acetone. The remaining acetone after siphoning was evaporated at room temperature and atmospheric pressure and thereafter, the precipitate was ground into a fine powder. This powder was further dried in a Memmert oven (Lasec SA) overnight at 120 °C and subsequently calcined in a Labofurn furnace (Kiln Contracts) in stagnant air at 350 °C for 60 min and a black powder (most likely  $\text{Co}_3\text{O}_4$  [7,13]) was obtained. The physicochemical properties of this black powder were confirmed using various *ex situ* techniques before being tested in the CO-PrOx reaction as prepared.

**Table 4.2:** Composition of the reverse microemulsion prepared for the synthesis of the unsupported  $\text{Co(OH)}_x$  precipitate.

n-Hexane (g)	PEGDE (g)	Water (g)	o/s (mol/mol)*	w/s ( $\omega$ , mol/mol) <sup>§</sup>	$\text{Co(NO}_3)_2 \cdot 6\text{H}_2\text{O}$ (g)
500.0	50.0	30.0	47.2	13.7	4.4

\* oil-to-surfactant molar ratio.

<sup>§</sup> water-to-surfactant molar ratio ( $\omega$ ).**Figure 4.1:** Stages involved in the synthesis of unsupported  $\text{Co}_3\text{O}_4$  using the reverse microemulsion technique followed by drying and calcination. (Adapted from [14,15]).

### 4.2.3. Preparation of supported $\text{Co}_3\text{O}_4$ nanoparticles using Incipient Wetness Impregnation

Before the impregnation, each bare powder support was placed in a crucible and dried/calcined at 300 °C in a Labofurn furnace in stagnant air for 2 hr to remove any surface moisture. After cooling down to room temperature, the support was removed from the furnace and either used immediately for catalyst synthesis or stored in a closed crucible at 120 °C in a Memmert oven. Since the SiC support was received from SiCAT as 1 mm extrudates, these were ground using a mortar and pestle to a fine powder. The powder was sieved to recover fractions of the powder with particles/agglomerates of 150  $\mu\text{m}$  and below.

An aqueous solution of  $\text{Co(NO}_3)_2 \cdot 6\text{H}_2\text{O}$  was prepared with approximately 1.3 g of the cobalt precursor for every 1 ml of water, which is close to the solubility of the precursor in water [7]. A volume of this solution, which was equivalent to the pore volume of each support (determined

using nitrogen physisorption), was used for the impregnation at room temperature and atmospheric pressure, aiming for a final  $\text{Co}_3\text{O}_4$  loading of 10 wt.-%. Generally, supports with a calculated pore volume that is below  $0.2 \text{ cm}^3/\text{g}$  were impregnated twice to obtain the targeted loading. The impregnated samples were dried at  $60 \text{ }^\circ\text{C}$  for 16 hr under nitrogen flow [16] (typically  $50 \text{ ml(NTP)/min}$  for every 2 g sample) in a glass calcination tube reactor (I.D.: 15 mm, length: 240 mm; Lasec SA) which allows for fluidised-bed flow through the sample. After 16 hr, the sample was heated from  $60$  to  $350 \text{ }^\circ\text{C}$  at a rate of  $2 \text{ }^\circ\text{C}/\text{min}$  and the temperature at  $350 \text{ }^\circ\text{C}$  was held for 60 min [16] before cooling down to room temperature at a rate of  $4 \text{ }^\circ\text{C}/\text{min}$ . In cases where a second impregnation step was required, this was done using the calcined material obtained after the first impregnation.

Figure 4.2 depicts the main steps of the catalyst synthesis including drying and calcination. Summarised in Table 4.3 are the appearances of all bare supports before incipient wetness impregnation and of the impregnated supports after calcination. The dark appearance of the impregnated and calcined supports indicates the presence of oxidic cobalt, most likely in the form of  $\text{Co}_3\text{O}_4$  [7,13].

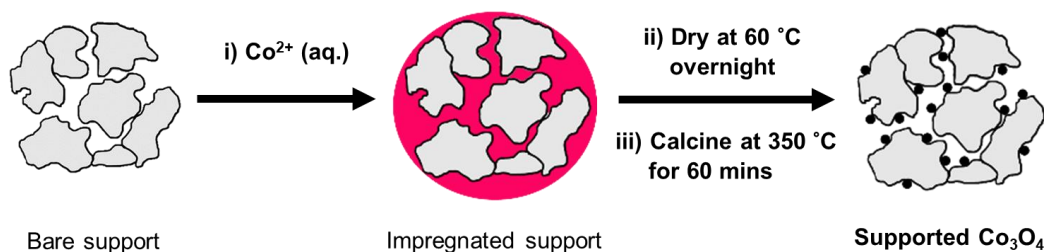


**Figure 4.2:** Stages involved in the synthesis of supported  $\text{Co}_3\text{O}_4$  using incipient wetness impregnation followed by drying and calcination. (Adapted from [17]).

**Table 4.3:** Appearance of the bare and Co<sub>3</sub>O<sub>4</sub>-loaded before and after impregnation and calcination, respectively.

Sample name	Bare support appearance before IWI	Impregnated support appearance after calcination
Co <sub>3</sub> O <sub>4</sub> /CeO <sub>2</sub>	yellow	black
Co <sub>3</sub> O <sub>4</sub> /ZrO <sub>2</sub>	white	black
Co <sub>3</sub> O <sub>4</sub> /SiC	grey	dark grey
Co <sub>3</sub> O <sub>4</sub> /SiO <sub>2</sub>	white	black
Co <sub>3</sub> O <sub>4</sub> /TiO <sub>2</sub> -anatase	white	dark brown
Co <sub>3</sub> O <sub>4</sub> /TiO <sub>2</sub> -rutile	white	dark grey
Co <sub>3</sub> O <sub>4</sub> /TiO <sub>2</sub> -P25	white	black
Co <sub>3</sub> O <sub>4</sub> /Al <sub>2</sub> O <sub>3</sub>	white	black

### 4.3. *Ex situ* Catalyst Characterisation

#### 4.3.1. Powder X-Ray Diffraction

Powder X-ray diffraction (PXRD) was performed in a Bruker D8 Advance Laboratory X-ray diffractometer operated at 40 kV and 35 mA, equipped with a cobalt source ( $\lambda_{\text{Co}} = 1.78897 \text{ \AA}$ ) and a position-sensitive detector (LYNXEYE XE, Bruker AXS). The optics were set to Bragg-Brentano geometry. A  $2\theta$  range of  $20 - 120^\circ$ , corresponding to  $0.19 \text{ \AA}^{-1} \leq 1/d \leq 0.97 \text{ \AA}^{-1}$  (where  $d$  is the d-spacing), was chosen as the measurement window. A step size of  $0.043^\circ$  ( $4.2 \times 10^{-4} \text{ \AA}^{-1}$ ) and a time per step of 0.75 sec was used, giving a total scan time of 29 min and 50 sec for the *ex situ* analysis. The interconversion between  $2\theta$  and  $1/d$  is possible using the Bragg Law (Equation 4.8) [18]. Note that two different X-ray sources were used in this work, *i.e.*, cobalt for *ex situ* analysis and molybdenum ( $\lambda_{\text{Mo}} = 0.7093 \text{ \AA}$ ) for *in situ* analysis (see sub-section 4.4.2.). Therefore, using  $1/d$  instead of  $2\theta$  for plotting PXRD patterns eliminates the effect of the X-ray sources on the position of the detected reflections on the  $2\theta$  scale.

$$\frac{1}{d} (\text{\AA}^{-1}) = \frac{2\sin\theta_{\text{Co}}}{\lambda_{\text{Co}}} = \frac{2\sin\theta_{\text{Mo}}}{\lambda_{\text{Mo}}} \quad \text{Equation 4.8}$$

Where  $d$  is the interplanar distance or d-spacing,  $\theta_{Co}$  and  $\theta_{Mo}$  are the measured diffraction angles (normally reported as  $2\theta$ ) from a PXRD instrument equipped either with a cobalt source of X-Ray wavelength  $\lambda_{Co}$  or a molybdenum source of X-Ray wavelength  $\lambda_{Mo}$ , respectively.

All recorded *ex situ* diffraction patterns were compared with known diffraction patterns found in the International Centre for Diffraction Data (ICDD) Powder Diffraction File-2 (PDF-2) database [19] to determine the species present. The ICDD PDF-2 entries of the reference diffraction patterns accessed are summarised in Table A.2.1 of Appendix A.2. To quantify the identified Co-based phases and obtain average volume-based crystallite sizes, Rietveld refinement [20] was carried out utilising the software package Bruker AXS TOPAS 5.0 [21]. For the refinement of the PXRD pattern of  $Co_3O_4/Al_2O_3$ , a method developed by Scarlett and Madsen [22], called PONKCS (Partial or No Known Crystal Structures), was used. This is because the  $Al_2O_3$  support used composes of a mixture of  $Al_2O_3$  crystal phases [23] and one of these phases ( $\delta$ - $Al_2O_3$ ) does not have a known crystal structure (or crystallographic information) [19].

The PONKCS method involves firstly creating a so-called “peaks” phase from the pattern of the pure material with partially or no known crystallographic information ( $Al_2O_3$  in this case). Thereafter, a known amount of the  $Al_2O_3$  is physically mixed with relatively small amounts of some other material (*e.g.*,  $Y_2O_3$ ) that has known crystallographic information, which should ideally be thermally treated at very high temperatures ( $\geq 1000$  °C) to remove all strain in the material. A PXRD pattern of this physical mixture is recorded and fitted using the previously generated peaks phase of  $Al_2O_3$  and the structure file of  $Y_2O_3$  (from the Crystallography Open Database [24]) in TOPAS 5.0. The parameters ZMV ( $Z$  = number of atoms in a unit cell,  $M$  = molecular mass,  $V$  = unite cell volume) for both materials are manually adjusted until the  $Al_2O_3:Y_2O_3$  mass ratio is as close as possible to the ratio in the physical mixture. When the correct ZMV parameters have been obtained, these should be kept constant. This well-defined  $Al_2O_3$  peaks phase can then be used with other known crystal phases to quantify species in  $Al_2O_3$ -bearing samples.

### 4.3.2. Scanning Transmission Electron Microscopy-Electron Energy Loss Spectroscopy

Scanning Transmission Electron Microscopy (STEM) analysis of all un-/supported fresh and spent samples was performed at the Centre for High-Resolution TEM which is based at the Nelson Mandela University (NMU), in South Africa. The images were taken at atomic resolution in a JEM-ARM200F microscope (JEOL) equipped with a field emission cathode and an integrated correction of the spherical aberrations of the objective and condenser lenses. The instrument is fitted with an advanced GIF (Gatan Image Filter) electron spectrometer with dual Electron Energy Loss Spectrometry (EELS) capabilities, as well as with an XMax 100 TLE high collection angle, ultra-sensitive detector (Oxford Instruments) for analysis by means of Energy-Dispersive Spectrometry (EDS). Lacey carbon sample grids (Agar Scientific) were utilised for HRTEM purposes.

Elemental EELS mapping was performed to identify cobalt-containing areas in each supported sample as normal bright-field and high angle annular dark-field imaging could not be adequately used for the identification. The measurement of particle sizes was done using the freeware ImageJ [25]. Both number- and volume-based average particle sizes together with the corresponding standard deviations could be calculated using Equations 4.9 to 4.12 [26]. The volume-based STEM average particle sizes calculated can be compared with the PXRD average crystallite sizes obtained using Rietveld refinement, since they are also volume-based.

$$\text{number – based average } (\bar{d}_{c,n}) = \frac{\sum_{i=1}^N n_i d_i}{N} \quad \text{Equation 4.9}$$

$$\text{volume – based average } (\bar{d}_{c,v}) = \frac{\sum_{i=1}^N n_i d_i^4}{\sum_{i=1}^N n_i d_i^3} \quad \text{Equation 4.10}$$

$$\text{number – based standard deviation } (sd_n) = \sqrt{\frac{\sum_{i=1}^N n_i (d_i - \bar{d}_{c,n})^2}{N - 1}} \quad \text{Equation 4.11}$$

$$\text{volume – based standard deviation } (sd_v) = \sqrt{\frac{\sum_{i=1}^N n_i d_i^3 (d_i - \bar{d}_{c,v})^2}{\frac{N - 1}{N} \sum_{i=1}^N n_i d_i^3}} \quad \text{Equation 4.12}$$

The variable  $d_i$  is the diameter of particle  $i$ ,  $n_i$  is the number of particles of size  $d_i$  and  $N$  is the total number of particles counted.

### 4.3.3. Nitrogen Physisorption

The N<sub>2</sub> physisorption analysis of the materials was conducted on a Micromeritics TriStar II 3020 after degassing the samples (~ 300 mg each) at 200 °C overnight. The mass-specific surface area of each bare support and the fresh supported Co<sub>3</sub>O<sub>4</sub> samples was determined using the Brunauer–Emmett–Teller (BET) method, based on physical adsorption [27]. The pore volume and pore size were obtained by applying the Barrett-Joyner-Halenda (BJH) method [28].

### 4.3.4. Inductively Coupled Plasma-Optical Emission Spectrometry

Powder samples (~ 50 mg each) for elemental analysis *via* inductively coupled plasma-optical emission spectrometry (ICP-OES) were pre-treated overnight in a 4:1 molar ratio of aqua regia:HF, corresponding to a 3:1:1 mixture of HCl:HNO<sub>3</sub>:HF. Subsequently, the mixture was heated at a rate of 6.4 °C/min to 180 °C for 40 min for digestion in a MARS-5 microwave digester, in order to obtain the cobalt loadings/concentrations in a Varian ICP-OES 730 (Agilent).

### 4.3.5. X-Ray Absorption Spectroscopy

X-ray Absorption Spectroscopy (XAS) measurements were performed at the Co K-edge (7709 eV) on beamline B18 at Diamond Light Source (United Kingdom), operating with a ring energy 3 GeV and at a ring current of 300 mA [29]. A Si (111) double crystal monochromator was used for energy selection. A Pt-coated mirror was used to reject higher harmonics from the beam. A Co foil was used for energy calibration.

Calculated amounts of samples were mixed with appropriate amounts of cellulose and homogenized using a mortar and pestle. They were then compressed into pellets of 13 mm diameter using a pellet press. The pellets were mounted on a pellet rack for XAS measurements. Depending on the concentration of Co in the samples, XAS data were measured in transmission/fluorescence mode. The scans were performed in Quick Extended X-ray Absorption Fine Structure (QEXAFS) mode, from 7509 to 8559 eV, with a resolution of 0.3 eV/point, and each scan was roughly 3 min. A few scans were recorded on each sample to check reproducibility and to have a reasonable signal-to-noise ratio.

For the measurements performed in transmission mode, the photon flux of the incoming and outgoing X-ray beam was detected with two ionization chambers  $I_0$  and  $I_t$ , respectively, filled with appropriate mixtures of  $N_2/Ar$ . A 36 element Ge detector, placed at  $90^\circ$  with respect to the incident beam, was used for data collection in fluorescence mode. A third ionization chamber ( $I_{ref}$ ) was used in series to simultaneously measure a Co reference metal foil for alignment. The data processing was performed in Athena, which is part of the open-source software package Demeter [30]. Demeter is based on the IFEFFIT [31] library. The linear combination fitting (LCF) was performed in Athena using the normalised XANES spectra between 7700 and 7800 eV. The reference spectra considered for the LCF were  $Co_3O_4$  [5,6], CoO [32], Co foil [29],  $CoAl_2O_4$  [33,34],  $CoTiO_3$  [34] and  $Co_2SiO_4$  [35]. The reference/standard compounds were synthesised using the procedures outlined in the cited literature.

## 4.4. *In situ* Catalyst Characterisation and Testing

### 4.4.1. Conventional Hydrogen-Temperature Programmed Reduction

Hydrogen-Temperature Programmed Reduction ( $H_2$ -TPR) was conducted to study the reduction behaviour of bare  $CeO_2$  and  $Co_3O_4/CeO_2$  only. This was due to the poor visibility of the PXRD reflections from Co-based phases in the presence of the  $CeO_2$  support (see details in sub-sections 5.2.3. and 6.2.2.). The reduction behaviour of all the other catalysts was studied using *in situ* PXRD (described in sub-section 4.4.2.1.). A sample of 100 mg was placed between two pieces of quartz wool in a U-shape quartz reactor. The reduction was conducted in a Micromeritics AutoChem 2920

instrument, equipped with a thermal conductivity detector (TCD) for measuring hydrogen consumption. The sample was firstly dried by flowing argon (flow rate: 10 ml(NTP)/min) through the system while heating to 120 °C at a rate of 10 °C/min and then holding the temperature at 120 °C for 60 min. Thereafter, the system was cooled to 60 °C and after reaching this temperature, 5% hydrogen in argon (flow rate: 50 ml(NTP)/min) was flowed through the sample. The system was then heated to 920 °C at a rate of 10 °C/min and remained at 920 °C for 60 min before cooling it back to room temperature. The hydrogen consumption was measured every 0.15 min (9 sec) between 60 and 920 °C after introducing the reducing gas mixture. The H<sub>2</sub> consumption and degree of reduction was calculated using Equations 4.13 and 4.14 [36], respectively, considering the stoichiometric reactions, Reactions 4.1 and 4.2. Equation 4.13 is a calibration equation based on the reduction of known amounts of silver(I) oxide (Ag<sub>2</sub>O) previously analysed in the H<sub>2</sub>-TPR instrument.



$$\text{H}_2 \text{ consumption (mmol)} = 2.8 \cdot 10^{-2} + A_{peak} \cdot 2.3 \cdot 10^{-1} \quad \text{Equation 4.13}$$

$$\text{Degree of reduction (\%)} = \frac{\text{H}_2 \text{ consumption}}{x \cdot n_{\text{metal oxide loaded}}} \times 100 \quad \text{Equation 4.14}$$

$A_{peak}$  is the area of the peak in the chromatogram.  $x = 0.5$  or  $4$ , depending on the stoichiometric H<sub>2</sub>:metal oxide molar ratio as shown in Reactions 4.1 and 4.2.  $n_{\text{metal oxide loaded}}$  is the amount (in mmol) of CeO<sub>2</sub> (bare support) or Co<sub>3</sub>O<sub>4</sub> (in Co<sub>3</sub>O<sub>4</sub>/CeO<sub>2</sub>) loaded in the H<sub>2</sub>-TPR quartz reactor.

## 4.4.2. Powder X-Ray Diffraction

### 4.4.2.1. PXRD instrument and capillary reaction cell set-up

Reduction and CO-PrOx experiments were also coupled with *in situ* PXRD to monitor the phase changes of  $\text{Co}_3\text{O}_4$  in the prepared catalysts. An in-house developed capillary reaction cell [37–40] - mounted on a Bruker D8 Advance Laboratory X-Ray diffractometer operated at 50 kV and 35 mA, equipped with a molybdenum source ( $\lambda_{\text{K}\alpha 1} = 0.7093 \text{ \AA}$ ) and a position sensitive detector (VANTEC, Bruker AXS) - was used for these experiments. The optics of the diffractometer were set to parallel beam geometry to minimize possible peak shifts due to sample height differences. A  $2\theta$  range of  $15 - 30^\circ$  (corresponding to  $0.37 \text{ \AA}^{-1} \leq 1/d \leq 0.73 \text{ \AA}^{-1}$ ), a step size of  $0.019^\circ$  ( $4.7 \times 10^{-4} \text{ \AA}^{-1}$ ), and a time per step of 0.2 sec (giving a total scan time of 4 min 2 sec, and an added delay of 58 sec between scans) was chosen for the *in situ* analysis. All recorded *in situ* diffraction patterns were again compared with known diffraction patterns from the ICDD PDF-2 database [19]. Rietveld refinement [20] was also carried out on the obtained *in situ* diffraction patterns utilising the software package TOPAS 5.0 (Bruker AXS) [21]. For the  $\text{Al}_2\text{O}_3$ -supported sample, the method PONKCS [22] was again employed during refinement.

The capillaries used were made up of borosilicate (Capillary Tube Supplies LTD, UK) and had a length of 75 mm, a wall thickness of 0.02 mm and a tube opening of 1.0 mm. The catalyst bed length in the capillary reactor was limited to 15 mm along the centre as this length serves as the isothermal region of the reactor [37,41]. The catalyst bed was supported by two pieces of glass wool (Supelco) which filled up the empty volume on either side of the bed. An internal K-type thermocouple (Temperature Controls, RSA), with a diameter of 0.5 mm and a maximum-rated operating temperature of  $1000 \text{ }^\circ\text{C}$ , was placed inside the capillary reactor as shown Figure 4.3, with its tip in contact with the catalyst bed but still outside the path of the X-Rays.

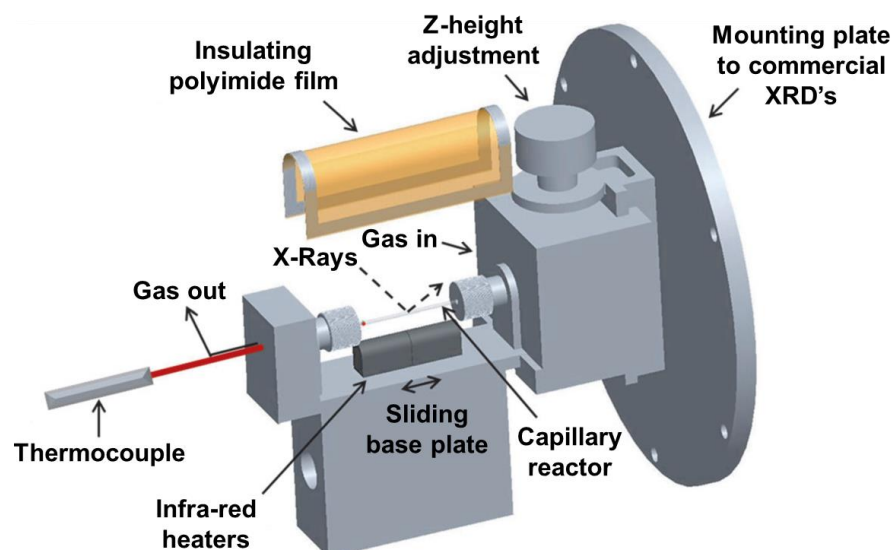


**Figure 4.3:** In-house developed *in situ* PXRD capillary reaction cell. (Adapted from [37–40]).

The capillary reactor was placed between the X-Ray source and detector, and then covered with a polyimide film casing (DuPont, Kapton, RS components) which has screwed-on stainless steel heat shields on the inside (not shown in Figure 4.3). Note that the polyimide film does not interfere with the incident or diffracted X-Rays. However, the heat shields can interfere with the X-Rays and therefore, were attached to the polyimide film such that they are not in the path of the X-Rays. The cell was heated using a Gefran 800P programmable temperature controller (Unitemp, RSA). The maximum operating temperature and pressure of the borosilicate capillaries is 500 °C and 25 bar, respectively, which made them suitable for use under the chosen experimental conditions for reduction and CO-PrOx.

#### 4.4.2.2. *In situ* reduction studies

Shown in Table 4.4. are the different environments considered for the reduction experiments. As already discussed in detail in sub-section 2.3.1., the H<sub>2</sub> in the CO-PrOx feed is known for reducing metal oxide catalysts resulting in the formation of less active/selective chemical phases. In addition to reduction, H<sub>2</sub> can also react with the other CO-PrOx feed gases, *viz.*, O<sub>2</sub>, CO and CO<sub>2</sub>, respectively. However, these reactions may only be possible at certain temperatures and/or over certain cobalt-based phases. This was crucial to determine before carrying out the CO-PrOx

experiments where there would be three or more gases being co-fed (excluding the inert N<sub>2</sub>), and two or more reactions taking place simultaneously. Therefore, the individual gas-phase reactions involving H<sub>2</sub> were also considered (see Table 4.4.). A few other reduction conditions involved co-feeding H<sub>2</sub> with H<sub>2</sub>O, and reacting CO with H<sub>2</sub>O (*i.e.*, water-gas shift) in the absence of H<sub>2</sub>. It is worth noting that the reduction experiments in Table 4.4. (columns 2 – 5) were all performed using unsupported Co<sub>3</sub>O<sub>4</sub> only, while the experiment mentioned in column 1 of Table 4.4. was performed using all prepared catalysts. The concentration of each gas in each experiment was chosen to lie within the range found in a typical CO-PrOx feed.

The temperature was varied between 50 °C (or 100 °C, if H<sub>2</sub>O is co-fed) and 450 °C at atmospheric pressure using a heating rate of 1 °C/min and was held once at 450 °C for 120 min. PXRD patterns were recorded every 5 min throughout each experiment. The total gas flow was fixed at 10 ml(NTP)/min using mass flow controllers (Brooks Instruments) and the individual gases were flowed from pure gas cylinders (H<sub>2</sub>, N<sub>2</sub>, and CO<sub>2</sub> (as separate pure gas cylinders) from Air Products, and CO from Linde), except for O<sub>2</sub> which was flowed from a synthetic air cylinder containing 21% O<sub>2</sub> in N<sub>2</sub> (Air Products). The reactor effluent of each temperature programmed reduction/reaction was analysed with an on-line gas chromatography system, of which the details can be found in sub-section 4.4.4.

For the reduction experiments requiring the co-feeding of water vapour, pre-boiled deionised liquid water was fed using a Sykam S1125 High-Performance Liquid Chromatography (HPLC) pump (Sykam GmbH). The pump can realise liquid flow rates as low as 0.001 ml/min. The liquid water was pumped into an in-house developed vapouriser oven (Figure 4.4). The design allows for quick water evaporation in a SiC-filled 25 ml vessel up to 180 °C. Through a combination of 6-port valves, bypasses of the vapouriser and the PXRD capillary reaction cell can be achieved. As the required steam flow rates for the capillary reactor in the studied reactions are still significantly lower than the achievable water pump flow rates, the steam/gas mixture is split into 10 equal streams using equal lengths of untreated fused silica capillaries (I.D.: 0.1 mm, length: ~60 cm, from Supelco). The effluent of one such capillary represents the feed for the capillary reactor, while the balance is combined and vented before condensing the vapour at room temperature. This design allows accurate control of the feed gases by increasing the amount of gas flowing into the vapouriser oven by a factor of 10, relative to the amount of gas flowing into the capillary reactor. Water from the reactor outlet gas stream is condensed at room temperature before analysis using an on-line gas chromatography system. The 1/8-inch gas lines connecting the vaporiser oven to the inlet and outlet of the cell, as well as the terminal members of the capillary reaction cell were

heated to 150 °C (Gefran 600 temperature controller, from Unitemp RSA) to avoid condensation (Figure 4.4).

**Table 4.4:** Gas compositions for the reduction experiments.

Gases	<b>H<sub>2</sub>-containing environments</b>					<b>Water-gas shift</b>
	<b>no co-feeding</b>	<b>w/ CO co-feeding</b>	<b>w/ O<sub>2</sub> co-feeding</b>	<b>w/ H<sub>2</sub>O co-feeding</b>	<b>w/ CO<sub>2</sub> co-feeding</b>	
CO	-	1%	-	-	-	1%
O <sub>2</sub>	-	-	1%	-	-	-
H <sub>2</sub>	50%	50%	50%	50%	50%	-
H <sub>2</sub> O	-	-	-	1 or 10%	-	10%
CO <sub>2</sub>	-	-	-	-	1 or 10%	-
N <sub>2</sub>	50%	49%	49%	49 or 40%	49 or 40%	89%

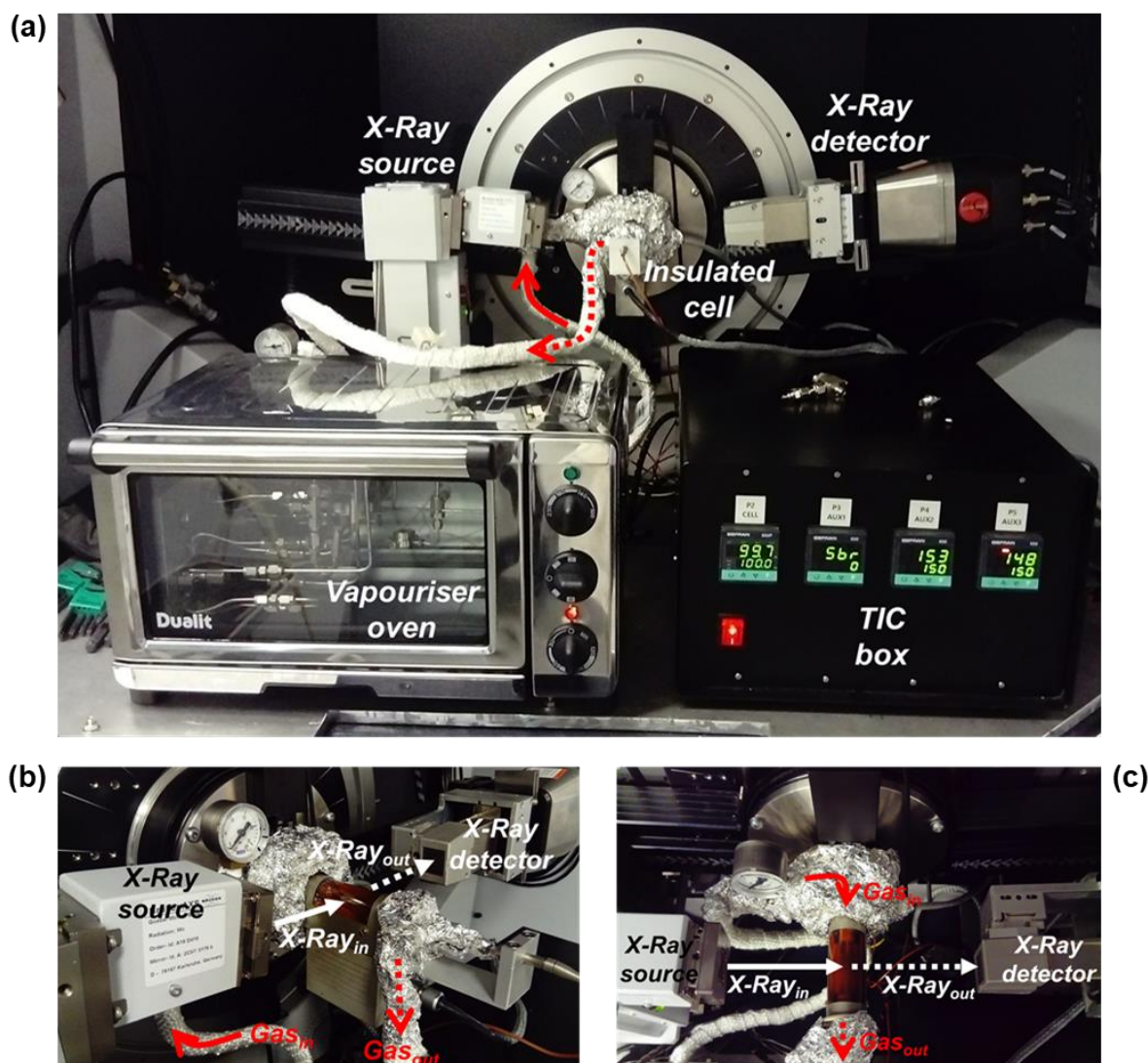


**Figure 4.4:** (a) Photograph showing the overall set-up for the water co-feeding experiments. Also included are close-up photographs showing the (b) side view, and (c) top view of the modified PXRD cell.

#### 4.4.2.3. Total and preferential oxidation of CO

A set of CO oxidation experiments were performed in different gas environments with the intention of understanding the effect each gas being co-fed has on the oxidation of CO and the phase changes of  $\text{Co}_3\text{O}_4$ . Firstly, all prepared catalysts were tested under dry CO-PrOx conditions (*i.e.*, in 1% CO, 1%  $\text{O}_2$ , 50%  $\text{H}_2$  and a balance of  $\text{N}_2$ ) as this was the standard condition for comparing the catalysts. Based on their performance under dry CO-PrOx, the best performing supported catalyst (based on the  $\text{CO}_2$  yields achieved as a function of temperature) and the unsupported catalyst were then tested

in “Dry CO-PrOx with co-fed CO<sub>2</sub>”, in “Wet CO-PrOx” (which includes H<sub>2</sub>O but not CO<sub>2</sub>), and in “Wet CO-PrOx with co-fed CO<sub>2</sub>” (see Table 4.5 for details). The same two catalysts were also tested in the dry Total Oxidation of CO (“Dry CO-TOx”) and then used for studying the effect of varying the O<sub>2</sub> concentration between 0.5 and 4%. Under the “Wet CO-PrOx with CO<sub>2</sub>” condition only, two more supported catalysts were also included.

The temperature was varied between 50 °C (or 100 °C, when H<sub>2</sub>O was fed) and 450 °C at atmospheric pressure in a stepwise manner, *i.e.*, holding the temperature at every 25 °C for 60 min and heating at 1 °C/min. *In situ* PXRD patterns were recorded every 5 min at each holding temperature, giving a total of 12 patterns per holding temperature. The total gas flow was carefully adjusted depending on the maximum mass of un-/supported Co<sub>3</sub>O<sub>4</sub> that could be loaded along the 15 mm isothermal zone of the capillary reactor. The target GHSV was 60000 ml(NTP)/g<sub>Co<sub>3</sub>O<sub>4</sub></sub>/hr in all CO-TOx and CO-PrOx experiments. For the CO-TOx work, pure CO (Linde) and pure N<sub>2</sub> (Air Products) were flowed from individual cylinders, and O<sub>2</sub> was fed from a synthetic air gas cylinder (Air Products). In the dry and wet CO-PrOx experiments, O<sub>2</sub> was also fed from synthetic air and the other gases were fed from either of two special gas mix cylinders: “Gas Mix 1” containing 1.07% CO, 52.36% H<sub>2</sub> and 46.57% N<sub>2</sub> (AFROX) for performing experiments not involving CO<sub>2</sub> co-feeding; and “Gas Mix 2” containing 1.05% CO, 53.15% H<sub>2</sub>, 10.60% CO<sub>2</sub> and 35.20% N<sub>2</sub> (AFROX) which was for experiments involving CO<sub>2</sub> co-feeding. Water vapour was fed using the set-up already described in sub-section 4.4.2.2. and shown in Figure 4.4. Also see sub-section 4.4.4. for the details on gas product analysis.

After the dry CO-PrOx experiments, a study on the reduction mechanism of unsupported Co<sub>3</sub>O<sub>4</sub> and one supported Co<sub>3</sub>O<sub>4</sub> catalyst was performed. This was done at 225 °C to monitor the formation of CoO only (see sub-section 4.4.3.1. for the reduction leading to metallic Co). The catalyst was loaded in the capillary reactor within the 15 mm isothermal zone, and thereafter N<sub>2</sub> was flowed through the catalyst at a space velocity of 60000 ml(NTP)/g<sub>Co<sub>3</sub>O<sub>4</sub></sub>/hr. The reactor was heated at 2 °C/min from 50 to 225 °C and upon reaching 225 °C, the N<sub>2</sub> gas was replaced with a 1:1:50:48 CO:O<sub>2</sub>:H<sub>2</sub>:N<sub>2</sub> gas mixture. This temperature was held for 4 hr while PXRD patterns were being recorded every 5 min.

Lastly, for studying the effect of the O<sub>2</sub> concentration, the temperature was increased from 50 to 225 °C at 1 °C/min, with 1-hr temperature holding steps every 25 °C. The temperature at 225 °C was held for 21 hr before cooling the capillary reactor to room temperature. The starting feed was a 1:0.5:51:47.5 CO:O<sub>2</sub>:H<sub>2</sub>:N<sub>2</sub> gas mixture (GHSV: 60000 ml(NTP)/g<sub>Co<sub>3</sub>O<sub>4</sub></sub>/hr), which represented

a stoichiometric ratio of CO and O<sub>2</sub>. “Gas Mix 1” and the synthetic air cylinder were used for this experiment. The starting feed composition was maintained from 50 to 225 °C, and for a further 3 hr at 225 °C. After this first 3 hr, the O<sub>2</sub> concentration was increased to give a 1:1 CO:O<sub>2</sub>, which slightly changed the feed H<sub>2</sub> and N<sub>2</sub> concentrations as well to maintain the GHSV of 60000 ml(NTP)/g<sub>Co<sub>3</sub>O<sub>4</sub></sub>/hr. This feed ratio was maintained for a further 3 hr and then followed by a switch back to the initial 1:0.5 CO:O<sub>2</sub> ratio for another 3 hr. Thereafter, the oxygen concentration was increased again to obtain a 1:2 CO:O<sub>2</sub> ratio and then switched back to 1:0.5. A final increase in the O<sub>2</sub> concentration was made to attain a 1:4 CO:O<sub>2</sub> ratio, which was again followed by a switch back to a ratio of 1:0.5. *In situ* PXRD patterns were continuously recorded every 5 min at every holding temperature between 50 and 225 °C, as well as throughout the 21-hr holding time at 225 °C.

**Table 4.5:** Gas compositions for the total and preferential oxidation of CO.

Gases	CO-TOx	Dry	Wet	Dry CO-PrOx	Wet CO-PrOx
		CO-PrOx*	CO-PrOx	w/ CO <sub>2</sub>	w/ CO <sub>2</sub>
CO	1%	1 – 0.9%	1%	1%	1%
O <sub>2</sub>	1%	0.5 – 4%	1%	1%	1%
H <sub>2</sub>	-	51 – 43%	45%	50%	46%
H <sub>2</sub> O	-	-	10%	-	10%
CO <sub>2</sub>	-	-	-	10%	9%
N <sub>2</sub>	98%	47.5 – 52.1%	43%	38%	33%

\* also includes conditions used for studying the effect of the O<sub>2</sub> concentration in the *in situ* PXRD set-up at 225 °C.

### 4.4.3. Magnetometry

#### 4.4.3.1. Catalyst test unit

Depicted in Figure 4.5 is the set-up of the catalyst testing unit used for the *in situ* magnetometry [38,40,42] studies performed under both dry and wet CO-PrOx conditions. Among other things, it shows the two gas flow channels and the reactor used for the magnetic measurements. The same two special gas mix cylinders (*i.e.*, “Gas Mix 1” and “Gas Mix 2”) and the synthetic air cylinder

used for the *in situ* PXRD-based CO-PrOx studies were also used in the magnetometer [38,40,42]. Therefore, only mass flow controllers MFC1 and MFC2 (Brooks Instruments) were used for feeding synthetic air (“Syn Air”) and either of the special gas mixtures, respectively, to the testing unit (see Figure 4.5). The 3-way valves 3WV-2 and 3WV-3 were used for controlling the gas flow in and out of the SiC-filled 150 ml vapouriser during the H<sub>2</sub>O co-feeding experiments. Also flowed into the vapouriser was pre-boiled deionised water kept in a 1000 ml Schott bottle and pumped using a Sykam HPLC pump. The vapouriser and the gas lines downstream of it were all heated to a minimum of 150 °C to avoid any condensation until the water could be caught in the cold trap. The valves 3WV-4 and 3WV-5 were used for controlling the total gas flow in and out of the reactor during both dry and wet CO-PrOx.

The experiments were all performed at atmospheric pressure, the total gas flow was 25 ml (NTP)/min and the amount of catalyst loaded in the reactor was varied between 0.25 and 0.27 g in order to achieve the same Co<sub>3</sub>O<sub>4</sub> loading in the reactor and to compensate for the differences in the Co<sub>3</sub>O<sub>4</sub> loadings as determined by ICP-OES. The gas volumetric flow ratios used for both dry and wet CO-PrOx experiments in the magnetometer were similar to those used for the PXRD studies (see also Table 4.5) and each time, the GHSV was kept constant at 60000 ml(NTP)/g<sub>Co<sub>3</sub>O<sub>4</sub></sub>/hr. The reaction temperature was also varied similarly from 50 °C (or 100 °C, if H<sub>2</sub>O was co-fed) to 450 °C using a 1 °C/min heating rate. The temperature was held for 1 hr at 50 °C (or 100 °C), and at every 25 °C up to 450 °C. After the 1 hr at 450 °C had lapsed, the reactor was cooled back down to 50 °C (or 100 °C) at a rate of 5 °C/min and then held for 1 hr. Details on the analysis of products and unreacted gases can be found in sub-section 4.4.4.

Magnetisation measurements were taken every 5 min at 2 T (*i.e.*, 20 kOe) throughout every experiment. This allowed for determining an approximate saturation magnetisation which can be used to calculate the degree of reduction (see sub-section 4.4.3.2.). At 450 °C, a single M-H measurement was taken by varying the magnetic field strength in 65 steps from +2 to -2 T and back to +2 T, which took approximately 40 min. This allowed for  $\gamma$  to be calculated using Equation 4.15. As mentioned in section 2.6., metallic Co (both hcp and fcc crystal phases) is the only species (in this study) that can be detected using the magnetometer as it is ferromagnetic [43]. Catalysts with a  $\gamma$  that is below 10 wt.-% are regarded as being mostly superparamagnetic, implying that a volume-based size distribution can be obtained using the Langevin equation (Equation 4.16) [44–47]. Values of  $\gamma$  that are above 10 wt.-% indicate that the sample has a significant amount of particles/crystallites that are above the critical size for the superparamagnetism of metallic hcp Co

(8 nm at 50 °C, 11 nm at 450 °C [40]) and/or fcc Co (12 – 15(20) nm at 50 °C, and 16 – 20(26) nm at 450 °C [40]).

$$\gamma \text{ (wt. -\%)} = \frac{2 \cdot M_{rem}}{M_{sat}} \times 100 \quad \text{Equation 4.15}$$

$\gamma$  is the amount of material displaying remnant magnetisation relative to the total amount of ferromagnetic material present in a sample (also see section 2.6.). This material comprises of crystallites having a size which is greater than the critical size for superparamagnetism.  $M_{rem}$  is the sample's remnant magnetisation (in emu) and  $M_{sat}$  is the sample's saturation magnetisation (in emu).

$$\frac{M}{M_{sat}} = \coth\left(\frac{\rho \cdot \sigma_{sat} \cdot \pi \cdot d^3 \cdot H}{6 \cdot k_B \cdot T}\right) - \left(\frac{6 \cdot k_B \cdot T}{\rho \cdot \sigma_{sat} \cdot \pi \cdot d^3 \cdot H}\right) \quad \text{Equation 4.16}$$

$\frac{M}{M_{sat}}$  is the ratio of the measured sample magnetisation to the extrapolated saturation magnetisation at an infinite applied field,  $\rho$  is the density of the magnetic material and  $\sigma_{sat}$  is the specific saturation magnetisation of the magnetic material (for Co: 168 emu/g at 27 °C [48]) which is independent of crystallite size [49]. The variable  $d$  is the particle diameter (assuming a spherical shape),  $H$  is the applied magnetic field,  $k_B$  is the Boltzmann constant and  $T$  is the temperature.

Another study on the reduction mechanism of unsupported  $\text{Co}_3\text{O}_4$  and one supported  $\text{Co}_3\text{O}_4$  catalyst was performed. This was done at 275 and 325 °C to monitor the formation of metallic Co, starting from  $\text{Co}_3\text{O}_4$ . The catalyst was loaded in the reactor and thereafter,  $\text{N}_2$  was flowed through the catalyst at a space velocity of 60000 ml(NTP)/g $\text{Co}_3\text{O}_4$ /hr. The reactor was heated at 2 °C/min from 50 to 275 or 325 °C, respectively. Upon reaching the target temperature, the  $\text{N}_2$  gas was replaced with a 1:1:50:48  $\text{CO}:\text{O}_2:\text{H}_2:\text{N}_2$  gas mixture. Each time, the temperature was held for 4 hr while magnetisation measurements were recorded every 5 min at 2 T. respectively.

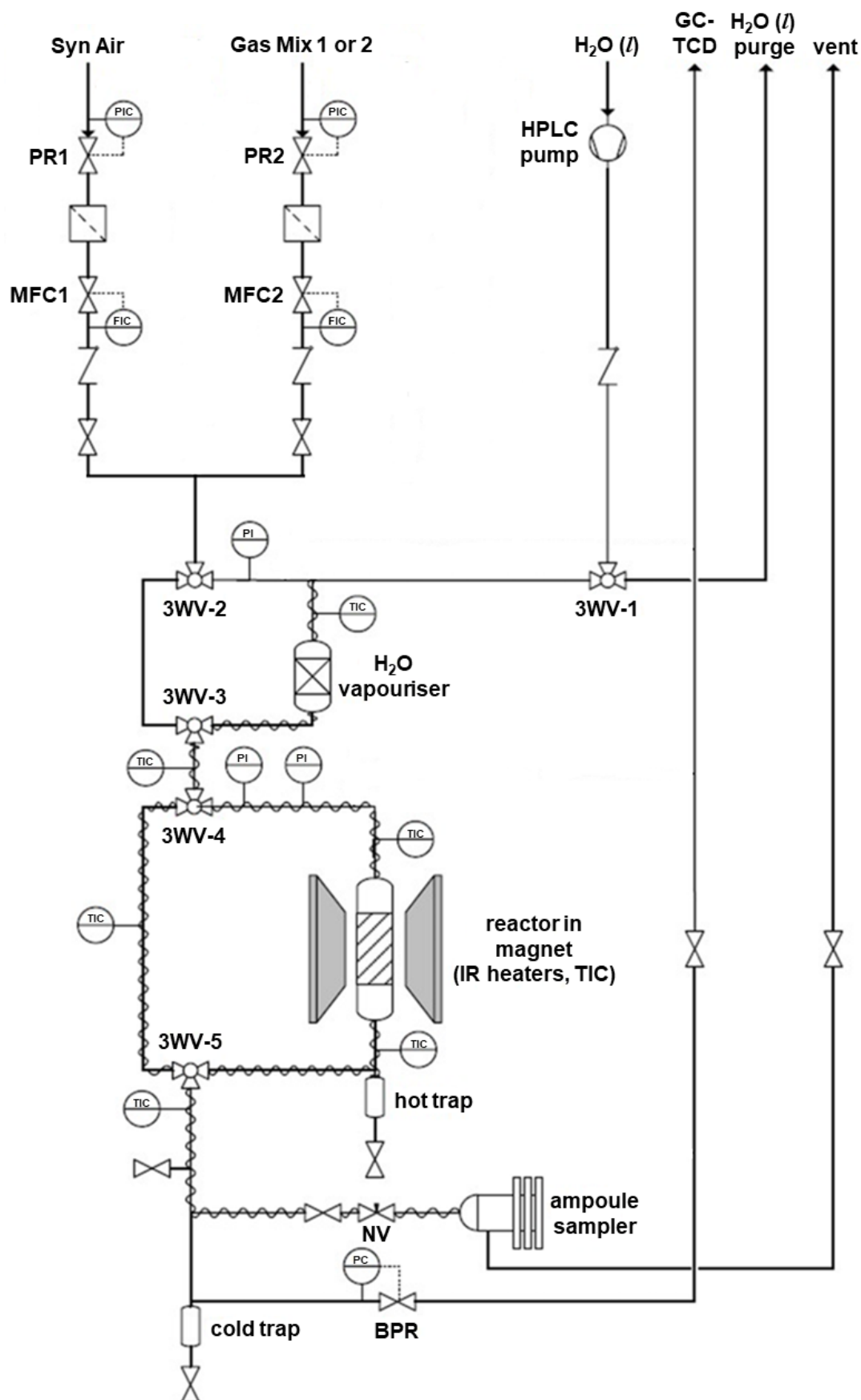


**Figure 4.5:** Set-up of the catalyst testing unit used for the *in situ* CO-PrOx experiments in the magnetometer.

#### 4.4.3.2. Reactor set-up

The set-up of the reactor used for the magnetic measurements is depicted in Figure 4.6. A 1/2-inch stainless steel tube reactor (I.D.: 9.7 mm) was placed between two pole caps of the electro-magnet (maximum field strength of 2 T, Bruker Analytik GmbH), at a 48 mm air gap, and contained a brass frit which supported the catalyst bed and prevented the loss of catalyst through the reactor. The reactor tube was spray-painted with high-temperature black paint to increase the reactor's heat absorption from the two infra-red heaters (Elstein) on either side. Above this brass frit was a layer of glass wool (Supelco) onto which the measured amount of catalyst was placed. Above the catalyst bed was another layer of glass wool. Then a non-magnetic N-type thermocouple was placed inside the catalyst bed, and to ensure the thermocouple's radially central positioning in the reactor, a star-shaped guide was used. Silicon carbide (600  $\mu\text{m}$ , Chemgrit SA) was used to fill up the reactor and to also help in pre-heating the gases before reaching the catalyst bed.

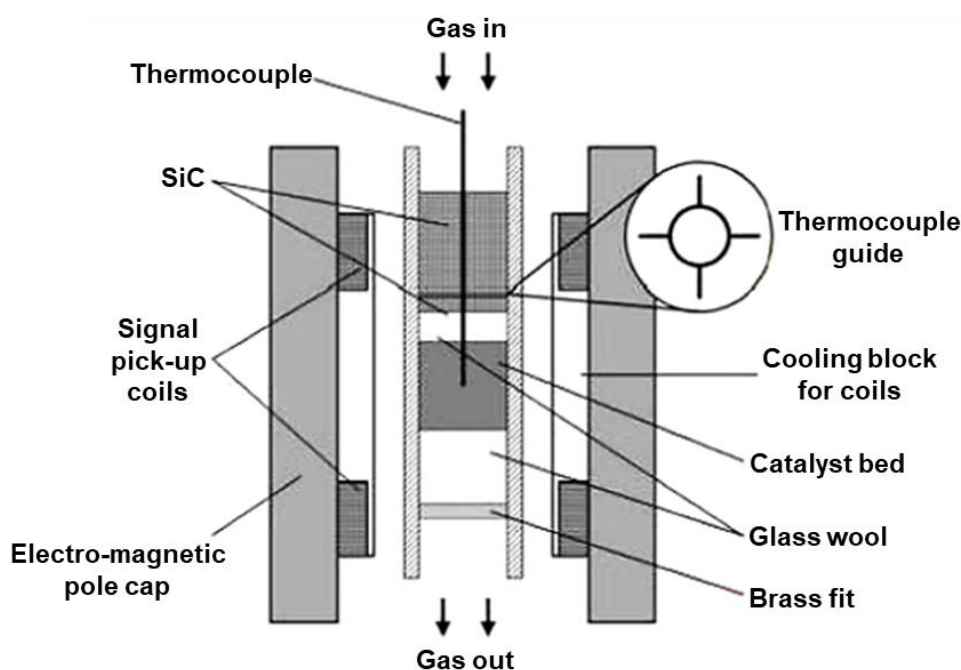


**Figure 4.6:** Front view of a loaded *in situ* magnetometer reactor placed between two electro-magnetic pole caps. (Adapted from [14,42]).

The loaded reactor was placed on the aluminium holding bracket equidistant from the two infra-red heaters which were used to heat the reactor (Figure 4.7). The electro-magnet supplied a

homogenous field which could be accurately controlled (in current-control mode) and measured *via* a field probe (FM 3002 Teslameter, Projekt Elektronik GmbH) - not shown in Figure 4.7). Varying the field strength from +2 to -2 T and back to +2 T allowed for recording of a magnetisation *versus* applied field plot (or M-H plot). For ideal signal strength, it was important that the catalyst bed be placed exactly in the centre of the detection coils on the pole caps of the electro-magnet as shown in Figure 4.6. This was done by adjusting the vertical position of the reactor using the aluminium holding bracket (Figure 4.7). This bracket also facilitated the movement of the reactor (*via* an electromotor (not shown); amplitude: 37.5 mm, frequency: 2 Hz) to induce a signal/voltage from the magnetised catalyst in the pick-up coils. To allow the movement of the reactor and gas flow to and from the reactor, flexible 1/16-inch tubing was used. The magnetisation of the sample is proportional to the induced signal measured by the four pick-up coils. The set-up was calibrated with a known amount of pure metallic cobalt powder (~ 0.1 g) and the procedure involved varying the temperature at a constant external field of 2 T and measuring the sample magnetisation. As a result, a calibration curve was obtained (see Appendix A.3., Figure A.3.1) and this later enabled the calculation of the degree of reduction (DoR) of  $\text{Co}_3\text{O}_4$  to metallic Co using the general equation, Equation 4.17.

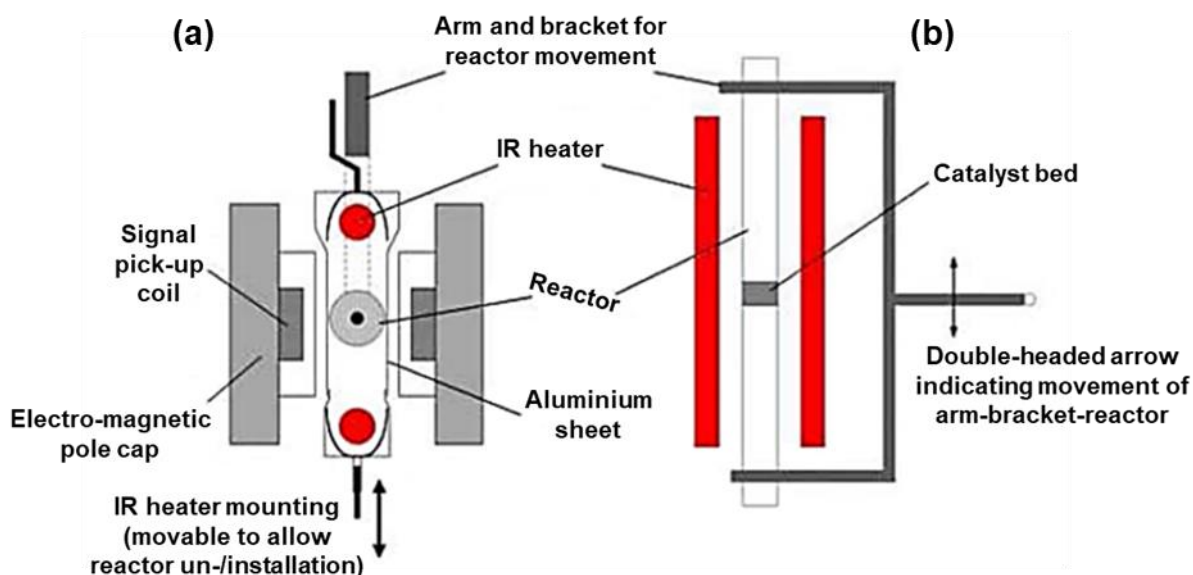


**Figure 4.7:** *In situ* magnetometer reactor set-up. (a) Top view, and (b) side view. (Adapted from [14,42]).

$$DoR(\%) = \frac{M_{sample} \cdot 0.1 \text{ g}}{M_{calibration} \cdot X_{loading} \cdot m_{unreduced \text{ sample}}} \times 100 \quad \text{Equation 4.17}$$

$M_{sample}$  is the measured magnetisation of the sample (in emu) at a particular temperature and  $M_{calibration}$  is the corresponding magnetisation of Co calculated from the calibration curve (in emu) at the same temperature.  $X_{loading}$  is the metal loading as calculated from ICP-OES and  $m_{unreduced\ sample}$  is the mass of unreduced sample loaded into the reactor (in g).

#### 4.4.4. Product Analysis

Online gas chromatography (GC) was conducted using an Agilent Technologies 490 micro-GC fitted with thermal conductivity detectors (TCDs) for detecting CO, O<sub>2</sub>, H<sub>2</sub>, CO<sub>2</sub>, CH<sub>4</sub> and N<sub>2</sub>. The TCDs have a detection limit/threshold of 2 ppm and a linear dynamic range of 2 – 10<sup>6</sup> ppm [50], which makes them particularly suitable for detecting CO concentrations below 10 ppm as this is the target for CO-PrOx (see section 1.2.). The reactor effluent was sampled every 5 min during all experiments performed. The micro-GC has three modules which have different columns – two of these columns were a 20 m and a 10 m Molecular Sieve 5Å PLOT columns. The 20 m column uses H<sub>2</sub> as the carrier gas for the separation and detection of O<sub>2</sub>, N<sub>2</sub> and CO. The 10 m column uses Ar as the carrier gas for mainly detecting H<sub>2</sub>. The last column was a 10 m PoraPLOT Q column, which also uses H<sub>2</sub> as the carrier gas, and was used for the separation and detection of CH<sub>4</sub> and CO<sub>2</sub>. See Table 4.6 for the full parameters chosen for achieving gas separation in the micro-GC. The software program Varian Galaxie Chromatography Data System 1.9.3.2 was used to operate the gas chromatographic analysis and to calculate the peak areas of each eluent. The water produced from the reactions performed was not analysed as it is condensed before the other reactor outlet components enter the micro-GC, as a safety precaution for the Molecular Sieve 5Å PLOT columns.

**Table 4.6:** Parameters set for achieving gas separation in the respective modules of the micro-GC.

Channel	1	2	3
Detector type	TCD	TCD	TCD
Column type and length	Molecular Sieve 5Å PLOT, 20 m	PoraPLOT Q, 10 m	Molecular Sieve 5Å PLOT, 10 m
Injection temperature (°C)	100	100	100
Injection time (msec)	40	40	40
Carrier gas	H <sub>2</sub>	H <sub>2</sub>	Ar
Column temperature (°C)	80	60	80
Column pressure (kPa)	150	80	150
Duration (sec)	270	270	270
Gas(es) analysed	O <sub>2</sub> , N <sub>2</sub> and CO	CH <sub>4</sub> and CO <sub>2</sub>	H <sub>2</sub>

The micro-GC was calibrated using two calibration gas cylinders - one having a mixture of 39.8% H<sub>2</sub>, 18.5% CO, 15.9% CH<sub>4</sub>, 10.1% CO<sub>2</sub>, 9.9% Ar and 5.8% N<sub>2</sub> (AFROX), and the other gas cylinder had synthetic air (21% O<sub>2</sub> in N<sub>2</sub>, Air Products). From the chromatograms, response factors for each gas (except for N<sub>2</sub> and Ar) were calculated (see Equation 4.18) using N<sub>2</sub> as the reference, since it was present in both gas cylinders and was the only gas that would not get consumed under reaction conditions. To calculate the volumetric flow rate for each gas, Equation 4.19 was used.

$$F_i = \frac{A_{N_2} \cdot v_{i,in}}{A_i \cdot v_{N_2,in}} \quad \text{Equation 4.18}$$

$$v_{i,out}(\text{ml/min}) = F_i \cdot \frac{A_i \cdot v_{N_2,in}}{A_{N_2}} \quad \text{Equation 4.19}$$

$F_i$  is the response factor of gas component  $i$  with reference to N<sub>2</sub>.  $A_{N_2}$  is the calculated peak area of nitrogen, and  $A_i$  is the calculated peak area of gas component  $i$ .  $v_{N_2,in}$  is the volumetric gas flow rate of nitrogen, and  $v_{i,in}$  is the volumetric gas flow rate of gas component  $i$  entering the system during the GC-TCD calibrations, the reduction or CO-PrOx experiments. Finally,  $v_{i,out}$  is the volumetric gas flow rate of gas component  $i$  exiting the reactor during the reduction experiments (*in situ* PXRD) and CO-PrOx experiments (*in situ* PXRD and magnetometry).

The performance of each catalyst, either during the different reduction experiments (see sub-section 4.4.2.2.) or during the different CO-PrOx experiments (see sub-section 4.4.2.3.), was assessed by calculating normalised gas outlet flow rates (Equation 4.20), conversions (Equations 4.21, 4.23 – 4.25) and selectivities (Equation 4.22). Through these equations and the knowledge of the occurred reactions, water consumption or formation could be adequately inferred.

$$\overline{v}_{j,out} = \frac{v_{j,out}}{v_{i,in}} \quad \text{Equation 4.20}$$

$$X_{CO \rightarrow CO_2}(\%) = \frac{v_{CO,in} - v_{CO,out} - v_{CH_4,out}}{v_{CO,in}} \times 100 = \frac{v_{CO_2,out} - v_{CO_2,in}}{v_{CO,in}} \times 100 \quad \text{Equation 4.21}$$

$$S_{O_2 \rightarrow CO_2}(\%) = \frac{v_{CO,in} - v_{CO,out} - v_{CH_4,out}}{2 \cdot (v_{O_2,in} - v_{O_2,out})} \times 100 = \frac{v_{CO_2,out} - v_{CO_2,in}}{2 \cdot (v_{O_2,in} - v_{O_2,out})} \times 100 \quad \text{Equation 4.22}$$

$$X_{CO \rightarrow CH_4}(\%) = \frac{v_{CO,in} - v_{CO,out} - (v_{CO_2,out} - v_{CO_2,in})}{v_{CO,in}} \times 100 \quad \text{Equation 4.23}$$

$$X_{CO_2 \rightarrow CH_4}(\%) = \frac{v_{CO_2,in} - v_{CO_2,out} - (v_{CO,out} - v_{CO,in})}{v_{CO_2,in}} \times 100 \quad \text{Equation 4.24}$$

$$X_{CO_2 \rightarrow CO}(\%) = \frac{v_{CO_2,in} - v_{CO_2,out} - v_{CH_4,out}}{v_{CO_2,in}} \times 100 = \frac{v_{CO,out} - v_{CO,in}}{v_{CO_2,in}} \times 100 \quad \text{Equation 4.25}$$

Under the different CO-PrOx conditions mentioned in sub-section 4.4.2.3., there are multiple reactions that can take place (*viz.*, CO and H<sub>2</sub> oxidation, CO and CO<sub>2</sub> methanation, as well the forward and reverse WGS – also see sections 1.2. and 2.3.), which makes the analysis of the product stream complicated since a particular gas can be involved in two or more reactions, either

as a reactant or as a product. Therefore, the use of the above equations is only valid under the following specific conditions:

- 1) **for CO oxidation:** Equations 4.21 and 4.22 are only valid when the difference “ $v_{CO_2,out} - v_{CO_2,in}$ ”  $\geq 0$ , and when  $0 \leq v_{CO,out}, v_{CH_4,out} \leq v_{CO,in}$ .
- 2) **for CO methanation:** Equation 4.23 is only valid when the difference “ $v_{CO_2,out} - v_{CO_2,in}$ ”  $\geq 0$ , and when  $0 \leq v_{CO,out} \leq v_{CO,in}$ .
- 3) **for CO<sub>2</sub> methanation:** Equation 4.24 is only valid when the difference “ $v_{CO,out} - v_{CO,in}$ ”  $\geq 0$ , and when  $0 \leq v_{CO_2,out} \leq v_{CO_2,in}$ .
- 4) **for the reverse WGS:** Equation 4.25 is only valid when the difference “ $v_{CO,out} - v_{CO,in}$ ”  $\geq 0$ , and when  $0 \leq v_{CO_2,out}, v_{CH_4,out} \leq v_{CO_2,in}$ .

Note that  $\overline{v_{j,out}}$  is the normalised gas outlet flow rate of the gas  $j$ . Also note that the forward WGS under wet CO-PrOx conditions (with or without co-fed CO<sub>2</sub>) could not be quantitatively analysed as this would require co-feeding isotope-labelled water vapour (*i.e.*, D<sub>2</sub>O<sup>16</sup>, H<sub>2</sub>O<sup>18</sup> or D<sub>2</sub>O<sup>18</sup> - depending on availability), which would need to be analysed using mass spectrometry.

## References

- [1] P. Atkins, J. de Paula, *Atkins' Physical Chemistry 8th Edition*, 8th ed., Oxford University Press, 2009.
- [2] O. Knacke, O. Kubaschewski, K. Hesselmann, eds., *Thermochemical Properties of Inorganic Substances*, 2nd ed., Springer-Verlag, Berlin, 1991.
- [3] Scilab Enterprises, *Scilab: Free and Open Source Software for Numerical Computation*. <https://www.scilab.org/download/6.0.2> (accessed February 2020).
- [4] T. Dence, *Math. Gaz.* 81 (1997) 403–408.
- [5] N. Fischer, E. van Steen, M. Claeys, *Catal. Today* 171 (2011) 174–179.
- [6] N. Fischer, M. Minnermann, M. Baeumer, E. van Steen, M. Claeys, *Catal. Lett.* 142 (2012) 830–837.
- [7] International Agency for Research on Cancer (IARC), in: *IARC Monogr. Eval. Carcinog. Risks to Humans - Chlorinated Drink. Chlorination By-Products; Some Other Halogenated Compd. Cobalt Cobalt Compd.*, Geneva, 1991, pp. 363–472.
- [8] M. Boutonnet, J. Kizling, P. Stenius, G. Maire, *Colloids Surf.* 5 (1982) 209–225.
- [9] S. Eriksson, U. Nylén, S. Rojas, M. Boutonnet, *Appl. Catal. A* 265 (2004) 207–219.
- [10] D. Barkhuizen, I. Mabaso, E. Viljoen, C. Welker, M. Claeys, E. van Steen, J.C.Q. Fletcher, *Pure Appl. Chem.* 78 (2006) 1759–1769.
- [11] M. Boutonnet, S. Lögdberg, E. Elm Svensson, *Curr. Opin. Colloid Interface Sci.* 13 (2008) 270–286.
- [12] N. Fischer, T. Feltes, M. Claeys, in: B.I. Kharisov, O.V. Kharissova, U. Ortiz-Mendez (Eds.), *CRC Concise Encycl. Nanotechnol.*, 1st ed., CRC Press, Boca Raton, 2015, pp. 547–560.
- [13] J.D. Donaldson, D. Beyersmann, in: *Ullmann's Encycl. Ind. Chem.*, Wiley-VCH Verlag GmbH & Co. KGaA, Weinheim, Germany, 2005, pp. 429–465.
- [14] N. Fischer, *Preparation of Nano- and Ångström-Sized Cobalt Ensembles and their Performance in the Fischer-Tropsch Synthesis*, Ph.D. thesis, University of Cape Town, 2011.
- [15] T.M. Nyathi, *Preferential Oxidation of Carbon Monoxide in Hydrogen-Rich Gases over Supported Cobalt Oxide Catalysts*, MSc(Eng) dissertation, University of Cape Town, 2016.
- [16] P. Munnik, N.A. Krans, P.E. de Jongh, K.P. de Jong, *ACS Catal.* 4 (2014) 3219–3226.

- [17] T.M. Eggenhuisen, P. Munnik, H. Talsma, P.E. de Jongh, K.P. de Jong, *J. Catal.* 297 (2013) 306–313.
- [18] W.H. Bragg, W.L. Bragg, *Proc. R. Soc. London. Ser. A, Contain. Pap. a Math. Phys. Character* 88 (1913) 428–438.
- [19] ICDD PDF-2 Release 2008 (Database), International Centre for Diffraction Data, Newtown Square, PA, USA, 2008.
- [20] H.M. Rietveld, *J. Appl. Crystallogr.* 2 (1969) 65–71.
- [21] A.A. Coelho, *J. Appl. Crystallogr.* 36 (2003) 86–95.
- [22] N.V.Y. Scarlett, I.C. Madsen, *Powder Diffr.* 21 (2006) 278–284.
- [23] SASOL PURALOX and CATALOX.  
<https://products.sasol.com/pic/products/home/grades/AS/5puralox-and-catalox/index.html>  
(accessed February 2020).
- [24] S. Gražulis, D. Chateigner, R.T. Downs, A.F.T. Yokochi, M. Quirós, L. Lutterotti, E. Manakova, J. Butkus, P. Moeck, A. Le Bail, *J. Appl. Crystallogr.* 42 (2009) 726–729.
- [25] C.A. Schneider, W.S. Rasband, K.W. Eliceiri, *Nat. Methods* 9 (2012) 671–675.
- [26] G. Bergeret, P. Gallezot, in: G. Ertl, H. Knözinger, F. Schüth, J. Weitkamp (Eds.), *Handb. Heterog. Catal.*, Wiley-VCH Verlag GmbH & Co. KGaA, Weinheim, Germany, 2008, pp. 738–765.
- [27] S. Brunauer, P.H. Emmett, E. Teller, *J. Am. Chem. Soc.* 60 (1938) 309–319.
- [28] E.P. Barrett, L.G. Joyner, P.P. Halenda, *J. Am. Chem. Soc.* 73 (1951) 373–380.
- [29] A.J. Dent, G. Cibir, S. Ramos, A.D. Smith, S.M. Scott, L. Varandas, M.R. Pearson, N.A. Krumpa, C.P. Jones, P.E. Robbins, *J. Phys. Conf. Ser.* 190 (2009) 012039.
- [30] B. Ravel, M. Newville, *J. Synchrotron Radiat.* 12 (2005) 537–541.
- [31] M. Newville, *J. Synchrotron Radiat.* 8 (2001) 322–324.
- [32] M. Wolf, N. Fischer, M. Claeys, *Mater. Chem. Phys.* 213 (2018) 305–312.
- [33] M. Karmaoui, N.J.O. Silva, V.S. Amaral, A. Ibarra, Á. Millán, F. Palacio, *Nanoscale* 5 (2013) 4277–4283.
- [34] M. Wolf, S.J. Roberts, W. Marquart, E.J. Olivier, N.T.J. Luchters, E.K. Gibson, C.R.A. Catlow, J.H. Neethling, N. Fischer, M. Claeys, *Dalt. Trans.* 48 (2019) 13858–13868.
- [35] L.A. Bruce, J.V. Sanders, T.W. Turney, *Clays Clay Miner.* 34 (1986) 25–36.
- [36] A.P. Petersen, *Alumina-Modified Cobalt Catalysts for the Fischer-Tropsch Synthesis*, Ph.D. thesis, University of Cape Town, 2018.

- [37] M.C.M. Claeys, N.F. Fischer, Sample Presentation Device for Radiation-Based Analytical Equipment, US Patent 8,597,598 B2, 2013.
- [38] N. Fischer, B. Clapham, T. Feltes, E. van Steen, M. Claeys, *Angew. Chemie - Int. Ed.* 53 (2014) 1342–1345.
- [39] N. Fischer, M. Claeys, *Catal. Today* 275 (2016) 149–154.
- [40] N. Fischer, M. Claeys, *J. Phys. D. Appl. Phys.* 53 (2020) 293001.
- [41] B. Clapham, The Development of an *in situ* X-Ray Diffraction Cell for Fischer-Tropsch Catalyst Characterisation, MSc(Eng) dissertation, University of Cape Town, 2012.
- [42] M.C.M. Claeys, E.W.J. van Steen, J.L. Visagie, J. van de Loosdrecht, Magnetometer, US Patent 8,773,118 B2, 2014.
- [43] V. Sechovský, in: K.H.J. Buschow, R.W. Cahn, M.C. Flemings, B. Ilschner, E.J. Kramer, S. Mahajan, P. Veyssi re (Eds.), *Encycl. Mater. Sci. Technol.*, 2nd ed., Elsevier Science Ltd, 2001, pp. 5018–5032.
- [44] J.-A. Dalmon, in: B. Imelik, J.C. Vedrine (Eds.), *Catal. Charact. - Phys. Tech. Solid Mater.*, Springer US, Boston, MA, 1994, pp. 585–609.
- [45] P.A. Chernavskii, J.-A. Dalmon, N.S. Perov, A.Y. Khodakov, *Oil Gas Sci. Technol.* 64 (2009) 25–48.
- [46] M. Claeys, M.E. Dry, E. van Steen, P.J. van Berge, S. Booyens, R. Crous, P. van Helden, J. Labuschagne, D.J. Moodley, A.M. Saib, *ACS Catal.* 5 (2015) 841–852.
- [47] M. Wolf, E.K. Gibson, E.J. Olivier, J.H. Neethling, C.R.A. Catlow, N. Fischer, M. Claeys, *ACS Catal.* 9 (2019) 4902–4918.
- [48] H. Niu, Q. Chen, H. Zhu, Y. Lin, X. Zhang, *J. Mater. Chem.* 13 (2003) 1803–1805.
- [49] P.W. Selwood, *Chemisorption and Magnetization*, Elsevier, 1975.
- [50] Agilent 490-PRO Micro GC for Process Monitoring.  
<https://www.agilent.com/cs/library/datasheets/public/5991-6056EN.pdf> (accessed April 2021).

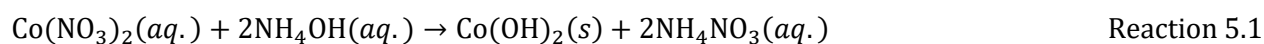


## Chapter 5: *Ex situ* Catalyst Characterisation

### 5.1. Thermodynamic Calculations on the Bulk Phase Transformation of Cobalt Precursors during Calcination

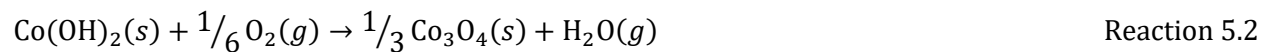
#### 5.1.1. Oxidation/Decomposition of Co(OH)<sub>2</sub>

In this study, unsupported Co<sub>3</sub>O<sub>4</sub> was to be synthesised using the reverse microemulsion technique - a precipitation-based method that converts a water-soluble metal precursor into an insoluble solid/precipitate [1–5]. The metal precursor chosen was cobalt(II) nitrate hexahydrate (Co(NO<sub>3</sub>)<sub>2</sub>·6H<sub>2</sub>O), while ammonium hydroxide (in the form of 25 wt.-% NH<sub>3</sub> (aq.)) was used as the precipitating agent [6,7]. Reaction 5.1 shows the expected reaction between Co(NO<sub>3</sub>)<sub>2</sub> and NH<sub>4</sub>OH yielding solid cobalt(II) hydroxide (Co(OH)<sub>2</sub>) and dissolved ammonium nitrate (NH<sub>4</sub>NO<sub>3</sub>).



After forming the Co(OH)<sub>2</sub> precipitate, the sample was dried at 120 °C overnight in an oven and calcined at 350 °C in a furnace. In both heat treatments, the sample was exposed to stagnant air at atmospheric pressure (see sub-section 4.2.2.). Thermodynamic calculations were done to predict the phase that the cobalt hydroxide would likely be converted to in the presence of oxygen (in the form of air). Note that these calculations were performed assuming bulk Co-based phases, and that

the predictions reported may not necessarily apply to nanoparticles, where crystallite/particle size effects could play a role. Reaction 5.2 shows the oxidation of  $\text{Co}(\text{OH})_2$  to  $\text{Co}_3\text{O}_4$ , while Reactions 5.3 and 5.4 are for the decomposition of  $\text{Co}(\text{OH})_2$  to  $\text{CoO}$  and metallic  $\text{Co}$ , respectively. Figure 5.1 shows the plot of the change in the reaction Gibbs free energy as a function of temperature for these reactions calculated using Equation 5.1. It can be clearly observed that between 0 and 500 °C,  $\text{Co}(\text{OH})_2$  is likely to be oxidised to  $\text{Co}_3\text{O}_4$  than to decompose to  $\text{CoO}$  or to metallic  $\text{Co}$  in the presence of oxygen. In fact, the decomposition to metallic  $\text{Co}$  remains highly unfeasible within this temperature range, while the decomposition to  $\text{CoO}$  only becomes feasible above 150 °C. The sudden decrease in the  $\Delta G$  between 400 and 430 °C for the decomposition of  $\text{Co}(\text{OH})_2$  to metallic  $\text{Co}$  (Figure 5.1 - green plotted line) is a result of the predicted bulk crystal structure change of the metal from the hexagonal closed-pack (hcp) structure to the face-centred cubic (fcc) structure [8–11].



$$\Delta G_{\text{rxn}}(T) = T \cdot \left( \frac{\Delta G_{\text{rxn}}^{\circ}(T)}{T^{\circ}} - \int_{T^{\circ}}^T \frac{\Delta H_{\text{rxn}}^{\circ} + \int_{T^{\circ}}^T \Delta C_{p,\text{rxn}}(T) dT}{T^2} dT \right) \quad \text{Equation 5.1}$$

A further condition was considered where the decomposition of  $\text{Co}(\text{OH})_2$  to either  $\text{CoO}$  or  $\text{Co}^0$  was to take place first instead of the direct oxidation to  $\text{Co}_3\text{O}_4$ . In this case, obtaining  $\text{Co}_3\text{O}_4$  would require the  $\text{CoO}$  or the  $\text{Co}^0$  to be oxidised in the subsequent step. Reactions 5.5 and 5.6 show these oxidation processes and Reaction 5.7 considers the oxidation of  $\text{Co}^0$  to  $\text{CoO}$  for comparison. In the experimental procedure followed (sub-section 4.2.2.), the  $\text{Co}(\text{OH})_2$  was dried at 120 °C and calcined at 350 °C in stagnant air, which would make the oxidation of  $\text{CoO}$  or  $\text{Co}^0$  to  $\text{Co}_3\text{O}_4$  highly possible if  $\text{Co}(\text{OH})_2$  decomposed first to either of the two former  $\text{Co}$ -based phases. As shown in Figure 5.1, all three oxidation processes are thermodynamically favourable, even more so for the oxidation of metallic  $\text{Co}$ . Therefore, medium-to-high temperature treatment of  $\text{Co}(\text{OH})_2$  in air is

more likely to yield  $\text{Co}_3\text{O}_4$ , which has also been supported by numerous experimental studies [6,7,12–14].

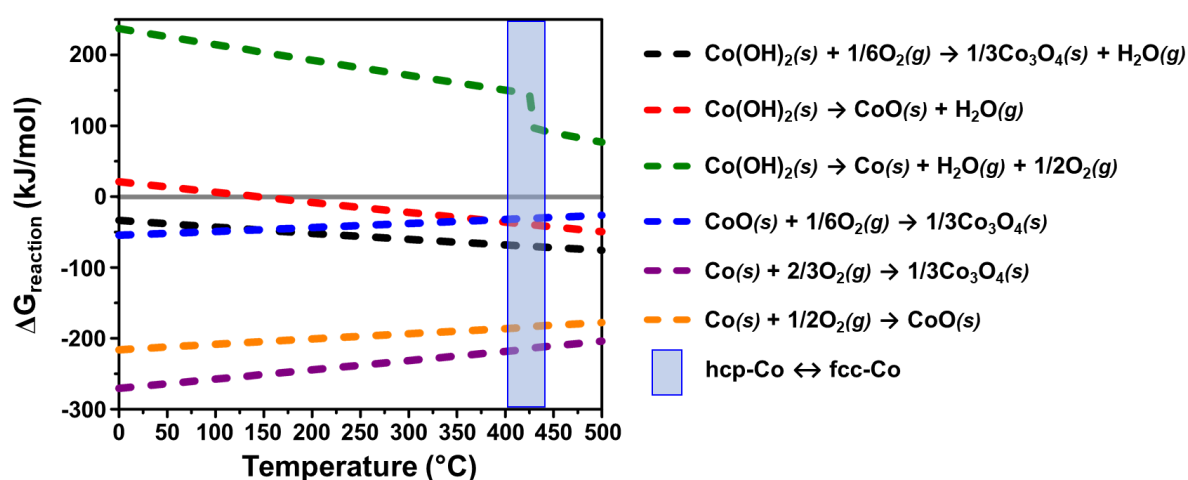


**Figure 5.1:** Changes in the Gibbs free energy as a function of temperature at 1.013 bar for the oxidation and decomposition of Co-based compounds. The light blue shaded area indicates the temperature region where bulk hcp Co transforms into bulk fcc Co.

### 5.1.2. Decomposition of $\text{Co}(\text{NO}_3)_2$ on support materials

Supported  $\text{Co}_3\text{O}_4$  nanoparticles were to be prepared using conventional incipient wetness impregnation. Again, the metal precursor chosen was  $\text{Co}(\text{NO}_3)_2 \cdot 6\text{H}_2\text{O}$ . Different support materials (*viz.*,  $\text{Al}_2\text{O}_3$ ,  $\text{TiO}_2$  (both anatase and rutile),  $\text{SiO}_2$ ,  $\text{SiC}$ ,  $\text{ZrO}_2$  and  $\text{CeO}_2$ ) were used in this study. The impregnated supports were dried at 60 °C under  $\text{N}_2$  flow overnight and calcined at 350 °C under  $\text{N}_2$  flow as well [15,16] (also see sub-section 4.2.3.). For the CO-PrOx reaction,  $\text{Co}_3\text{O}_4$  is regarded as the most active cobalt-based phase for oxidising CO. Therefore, it was important that

this phase was obtained over the various support materials after calcination. The impregnation method is generally known for introducing strong metal-support interactions (MSIs) or nanoparticle-support interactions (NPSIs) [17–19]. This can lead to the formation of bulk-like metal-support compounds (MSCs) or small amounts of amorphous MSCs at the nanoparticle-support interface. Supports well-known for this phenomenon are  $\text{Al}_2\text{O}_3$  [20–23],  $\text{TiO}_2$  [20,21] and  $\text{SiO}_2$  [20,21,24,25], with their most common Co-bearing bulk MSCs being  $\text{CoAl}_2\text{O}_4$ ,  $\text{CoTiO}_3$  and  $\text{Co}_2\text{SiO}_4$ , respectively. In contrast, the supports  $\text{SiC}$ ,  $\text{ZrO}_2$  and  $\text{CeO}_2$  are not known for this phenomenon. Based on an extensive literature search, there are no known or well characterised bulk Co-Zr or Co-Ce oxides reported in previous publications.

Nonetheless, thermodynamic calculations were also performed to predict the likely product of the thermal decomposition of cobalt nitrate. Reactions 5.8 and 5.10 show the decomposition reaction of  $\text{Co}(\text{NO}_3)_2$  to  $\text{Co}_3\text{O}_4$  and  $\text{Co}^0$ , respectively. Reaction 5.9 shows the general solid-state reaction of  $\text{Co}(\text{NO}_3)_2$  with the support forming MSCs. Note that the only supports considered were  $\text{Al}_2\text{O}_3$ ,  $\text{TiO}_2$  (anatase and rutile, respectively) and  $\text{SiO}_2$ , as well as their corresponding MSCs; *viz.*,  $\text{CoAl}_2\text{O}_4$ ,  $\text{CoTiO}_3$  and  $\text{Co}_2\text{SiO}_4$ , for the thermodynamic calculations. “Me” in Reaction 5.9 represents any of the metal ions Al, Ti or Si. Reaction 5.8 can also be used to describe the decomposition of  $\text{Co}(\text{NO}_3)_2$  to  $\text{CoO}$ , when the subscripts  $x$  and  $y = 0$ , and  $a = 1$ . It should again be noted that these calculations were performed assuming bulk Co-based phases only.

Figure 5.2 shows the change in the reaction Gibbs free energy as a function of temperature for these processes. It can be seen that  $\text{Co}(\text{NO}_3)_2$  is far less likely to decompose to metallic Co as indicated by the positive  $\Delta G$  values between 0 and 500 °C (follow green y-axis in Figure 5.2). As for the other cobalt-based compounds, their formation seems to be unfavourable below 175 °C. Above 175 °C,  $\text{Co}_3\text{O}_4$  formation is the most thermodynamically favoured route up to approximately 400 °C. Increasing the temperature beyond 400 °C begins to favour the formation of  $\text{CoAl}_2\text{O}_4$  over that of  $\text{Co}_3\text{O}_4$ . Experimentally, researchers have observed the decomposition of  $\text{Co}(\text{NO}_3)_2$  at or below 150 °C to mainly  $\text{Co}_3\text{O}_4$  [26,27]. The thermal decomposition of  $\text{Co}(\text{NO}_3)_2$  involves the autocatalytic oxidation of the  $\text{Co}^{2+}$  (even in an inert environment), which favours the formation of  $\text{Co}_3\text{O}_4$  over  $\text{CoO}$  and  $\text{Co}^0$ . According to Reaction 5.8, the decomposition of  $\text{Co}(\text{NO}_3)_2$  to  $\text{Co}_3\text{O}_4$  also produces  $\text{O}_2$ , which shows that the thermal treatment of  $\text{Co}(\text{NO}_3)_2$  to form  $\text{Co}_3\text{O}_4$  does not require  $\text{O}_2$ , despite this being widely practiced.

There are studies that have investigated the effect of the gas environment (air, pure  $\text{N}_2$ , or 1%  $\text{NO}$  in  $\text{N}_2$ ) in which the thermal treatment of  $\text{Co}(\text{NO}_3)_2$  pre-loaded onto support materials (such as

$\text{Al}_2\text{O}_3$  and  $\text{SiO}_2$ ) is performed [15,16,28–30]. These studies reported that in all gas environments,  $\text{Co}_3\text{O}_4$  was always the product formed but the size of the nanoparticles produced depended on the environment in which the thermal treatment was performed. Interestingly, the environment with 1% NO in  $\text{N}_2$  consistently produced relatively small particles (< 6 nm) than those formed under air or pure  $\text{N}_2$  flow. The NO (nitrogen monoxide) is reported to immobilise the cobalt nitrate by converting it into a cobalt hydroxy nitrate ( $\text{Co}_3(\text{NO}_3)_2(\text{OH})_4$ ) intermediate. The decomposition of this intermediate results in the formation of the very small  $\text{Co}_3\text{O}_4$  nanoparticles. The formation of MSCs is also possible experimentally, but is often observed at very high calcination temperatures (above 550 °C) [24,27,31]. Therefore, the calculations performed predict  $\text{Co}_3\text{O}_4$  as the likely decomposition product from  $\text{Co}(\text{NO}_3)_2$ , especially at low-to-medium calcination temperatures under an inert environment.

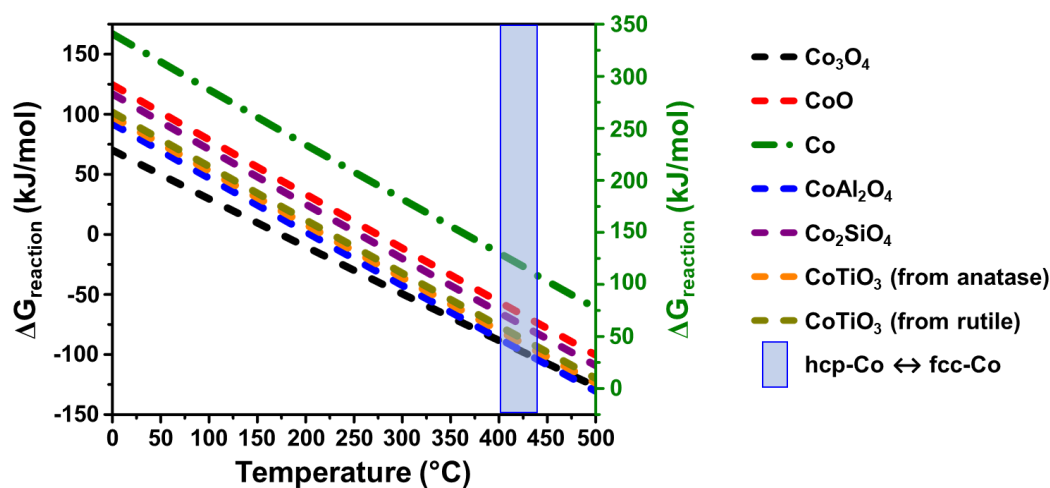
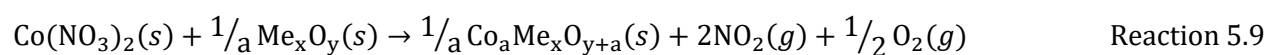
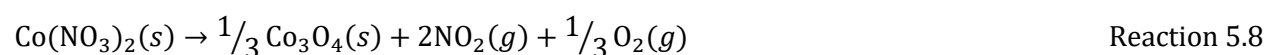


**Figure 5.2:** Changes in the Gibbs free energy as a function of temperature at 1.013 bar for the thermal decomposition of  $\text{Co}(\text{NO}_3)_2$  to various Co-based compounds. The green y-axis on the right is for the change in the Gibbs free energy for the decomposition of  $\text{Co}(\text{NO}_3)_2$  to metallic Co.

## 5.2. Powder X-Ray Diffraction and X-Ray Absorption Spectroscopy

### 5.2.1. Unsupported $\text{Co}(\text{OH})_2$ and $\text{Co}_3\text{O}_4$

There are two forms of solid  $\text{Co}(\text{OH})_2$  - an  $\alpha$ - and a  $\beta$ -phase. The  $\alpha$ -phase has a blue-ish green appearance and has layers of hydroxide-cobalt-hydroxide with a net positive charge. These layers alternate with layers of anions such as nitrates, acetates, chlorides, sulphates *etc.*, which originate from the cobalt precursor [32–35]. The  $\beta$ -phase is a reddish-pink solid with a hexagonal packing of hydroxyl ions and has  $\text{Co}^{2+}$  ions occupying alternate rows of octahedral sites. This phase, in contrast, has a perfect layer stacking without any intercalated anions [32,35–38].

Figure 5.3 shows the PXRD pattern of the *as prepared* green  $\text{Co}(\text{OH})_x$  precipitate prepared using the reverse microemulsion technique, which was compared with the reference reflection lines of  $\alpha$ - and  $\beta$ - $\text{Co}(\text{OH})_2$  from the ICDD PDF-2 database. It is worth noting that the reflection lines for the  $\alpha$ -phase are not indexed (*i.e.*, have no assigned Miller indices) in the said database and the crystal lattice system is still unknown. Therefore, the quality of the reference pattern shown in Figure 5.3 is rather low. It should also be noted that this is the only reference pattern for the  $\alpha$ -phase available in the database. Nonetheless, it can be observed that the reference reflection lines of both phases do not match the diffraction pattern of the *as prepared* sample.

However, the work by Hu *et al.* [35], which focused on synthesising  $\text{Co}(\text{OH})_2$  from different cobalt salts (nitrate, chloride, acetate and sulphate), showed PXRD patterns very similar to that of the *as prepared* precipitate sample of this work, especially their nitrate-derived hydroxide. Note the reflections at  $1/d = 0.37 \text{ \AA}^{-1}$  and  $1/d = 0.63 \text{ \AA}^{-1}$  of the *as prepared* sample are asymmetric. This is an indication of the loose and defective layer stacking of the atoms/molecules along these planes. This loose packing indicates the formation of the  $\alpha$ -phase of  $\text{Co}(\text{OH})_2$  since it is known to have the previously mentioned layers of positively-charged hydroxide-cobalt-hydroxide with intercalated anions of the cobalt precursor [33–35]. The intercalated anions in the *as prepared* sample would then be the nitrates of the precursor used. Furthermore, Hu *et al.* [35] estimated that the intercalation spacing brought about by the nitrate anions is  $7.852 \text{ \AA}$ , and assigned the Miller indices (0 0 6), (0 1 2) and (1 1 0) to the reflections at  $1/d = 0.21$ ,  $0.37$  and  $0.63 \text{ \AA}^{-1}$ , respectively.

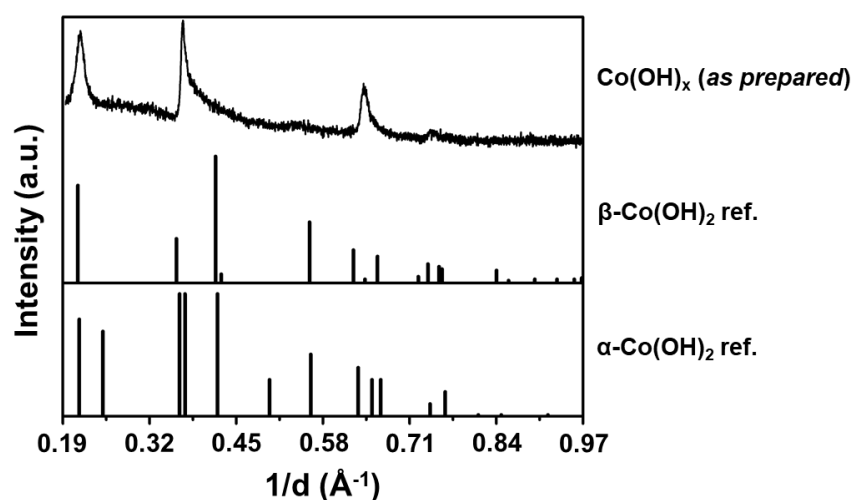


**Figure 5.3:** PXRD pattern (radiation source: Co  $K\alpha_1 = 1.78897 \text{ \AA}$ ) of the *as prepared*  $\text{Co(OH)}_x$  precipitate from the reverse microemulsion technique. Also included are the reference reflection lines of  $\alpha$ - and  $\beta$ - $\text{Co(OH)}_2$ , respectively. See Table A.2.1 of Appendix A.2. for the ICDD PDF-2 entries of  $\alpha$ - and  $\beta$ - $\text{Co(OH)}_x$ , respectively.

After having successfully prepared and confirmed the green precipitate as  $\alpha$ - $\text{Co(OH)}_2$ , the sample was dried at  $120 \text{ }^\circ\text{C}$  and calcined at  $350 \text{ }^\circ\text{C}$  in stagnant air to produce the targeted  $\text{Co}_3\text{O}_4$  catalyst (see sub-section 4.2.2.). Figure 5.4 shows the PXRD pattern of the powder sample obtained after calcination which was compared with the reference pattern of  $\text{Co}_3\text{O}_4$  (see Table A.2.1 of Appendix A.2. for the ICDD PDF-2 entry of the reference pattern). The analysis using PXRD confirmed that the chemical species formed was  $\text{Co}_3\text{O}_4$  having a cubic crystal lattice. This is also in line with the theoretical predictions discussed in sub-section 5.1.1., which showed that  $\text{Co}_3\text{O}_4$  would be the likely product of the transformation of  $\text{Co(OH)}_2$  under oxygen (or air). Further physical evidence was the black appearance of the recovered sample after calcination, which is a result of all the  $\text{Co}^{3+}$  ions (making up 67% of the cobalt in  $\text{Co}_3\text{O}_4$ ) occupying the octahedral sites, leaving the  $\text{Co}^{2+}$  ions to occupy the tetrahedral sites [32]. The mentioned ion site occupancies and the 3:4 Co:O ratio, is what makes  $\text{Co}_3\text{O}_4$  a normal spinel compound. The volume-based crystallite size was calculated using Rietveld refinement in TOPAS 5.0 and was found to be  $12.3 \text{ nm}$  (with an error of  $\pm 0.3 \text{ nm}$ ).

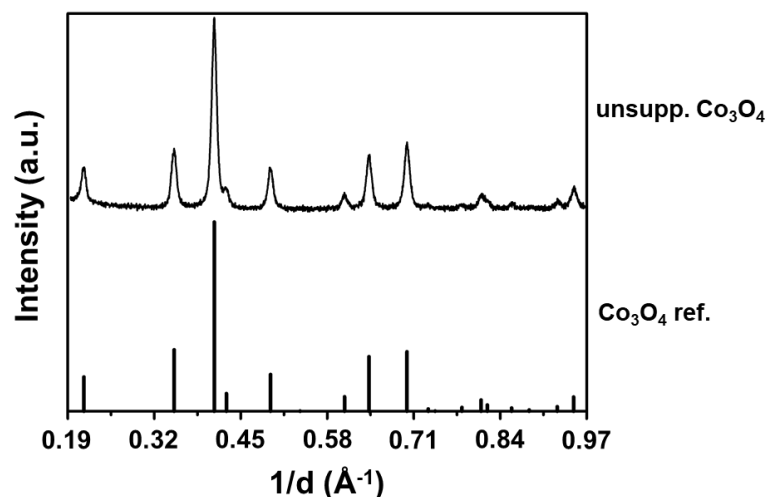


**Figure 5.4:** PXRD pattern of the fresh calcined unsupported  $\text{Co}_3\text{O}_4$  catalyst from the reverse microemulsion technique. Also included are the reference reflection lines of  $\text{Co}_3\text{O}_4$ . See Table A.2.1 for the ICDD PDF-2 entry of  $\text{Co}_3\text{O}_4$ .

### 5.2.2. Support materials

Supported  $\text{Co}_3\text{O}_4$  catalysts were prepared from commercially available powder support materials (see Table 4.1) that were impregnated with an aqueous solution of  $\text{Co}(\text{NO}_3)_2 \cdot 6\text{H}_2\text{O}$  (see sub-section 4.2.3.). In total, eight support materials were used and of these, seven were metal oxides, *viz.*,  $\text{Al}_2\text{O}_3$ ,  $\text{TiO}_2(\text{P25})$ ,  $\text{TiO}_2(\text{rutile})$ ,  $\text{TiO}_2(\text{anatase})$ , fumed  $\text{SiO}_2$ ,  $\text{ZrO}_2$  and  $\text{CeO}_2$ . The eighth support considered was mesoporous  $\text{SiC}$ . Shown in Figure 5.5 are the PXRD patterns of the bare/unloaded support materials used in this study.

The  $\text{Al}_2\text{O}_3$  support is commonly known as  $\gamma\text{-Al}_2\text{O}_3$ , as it contains mostly this crystal phase. However, there are other crystal phases reported by the manufacturer (SASOL Germany) to be present in small amounts in the  $\text{Al}_2\text{O}_3$  support, *viz.*,  $\delta\text{-Al}_2\text{O}_3$  and  $\theta\text{-Al}_2\text{O}_3$ , as well as  $\gamma\text{-AlO}(\text{OH})$  (also known as Boehmite) [39]. Both  $\delta\text{-Al}_2\text{O}_3$  and  $\theta\text{-Al}_2\text{O}_3$  are formed/stable between 600 and 1000 °C, while  $\gamma\text{-AlO}(\text{OH})$  is stable below 400 °C. Depending on the physical properties targeted for the  $\gamma\text{-Al}_2\text{O}_3$  (*e.g.*, surface area, pore volume, pore diameter *etc.*), the conditions for producing it can be such that the product formed is impure, *i.e.*, having the other above-mentioned Al-based phases. Note that the crystallographic information for the  $\delta\text{-Al}_2\text{O}_3$  reference pattern shown in Figure 5.5 is no longer available in the ICDD PDF-2 database as the previously stored information was deemed

incorrect [40]. Currently, there is no known reliable crystallographic information for  $\delta$ - $\text{Al}_2\text{O}_3$ . As a result, performing quantitative analysis (using Rietveld refinement) on the PXRD patterns of samples containing the above-mentioned  $\text{Al}_2\text{O}_3$  support, would involve implementing a special method developed by Scarlett and Madsen [41] called PONKCS (Partial or No Known Crystal Structures – see description in sub-section 4.3.1.).

Three  $\text{TiO}_2$  supports were used - one being the widely applied P25 sample (from Evonik Industries) having a 4:1 anatase:rutile ratio, and the other two being pure anatase and rutile, respectively, from Sigma-Aldrich. PXRD analysis of these bare supports successfully confirmed the presence of the expected phase(s) of  $\text{TiO}_2$  in each sample by comparing them to the reference patterns (Figure 5.5). The  $\text{SiO}_2$  sample obtained was the white fumed, “fluffy-looking” type also supplied by Evonik Industries. The recorded PXRD pattern of this sample shows that the  $\text{SiO}_2$  is amorphous, *i.e.*, with no long-range order and consequently, no detectable reflections within the  $1/d$  (or  $2\theta$ ) measuring range chosen. SiC was obtained as extrudates (from SiCAT) which were crushed using a mortar and pestle, and then sieved to a fraction below  $150\ \mu\text{m}$ . According to the manufacturer [42–44], the SiC is predominantly in the  $\beta$ -phase (with a cubic lattice) but there are also small amounts of the  $\alpha$ -phase (with a hexagonal lattice) present in this sample. PXRD analysis does indeed confirm the presence of both crystal phases and from Rietveld refinement, there seems to be a 1:9  $\alpha$ : $\beta$  ratio. Finally, the  $\text{ZrO}_2$  and the  $\text{CeO}_2$  supports were both supplied by US Nano and their phase purity was also confirmed using PXRD.  $\text{ZrO}_2$  has a monoclinic crystal lattice while the  $\text{CeO}_2$  has a cubic lattice.

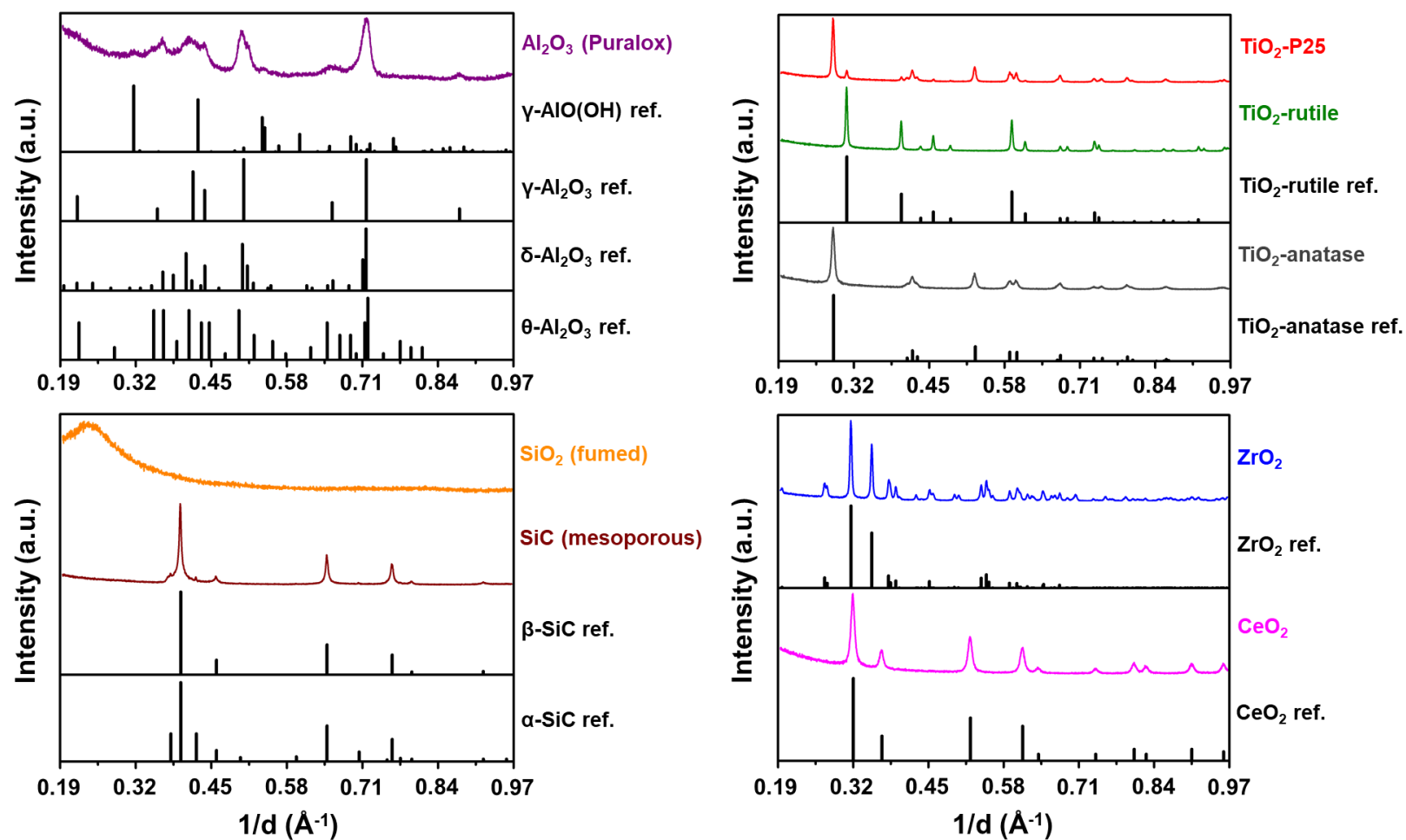


**Figure 5.5:** PXRD patterns of the bare support materials (*i.e.*, before incipient wetness impregnation) and the corresponding relevant reference reflection lines. See Table A.2.1 for the ICDD PDF-2 entries of all reference phases.

### 5.2.3. Supported Co<sub>3</sub>O<sub>4</sub>

Following the impregnation process, the cobalt nitrate-support mixture was dried at 60 °C overnight and calcined at 350 °C for 60 min under N<sub>2</sub> flow in a fluidised-bed glass tube reactor [16]. Co<sub>3</sub>O<sub>4</sub> is formed from Co(NO<sub>3</sub>)<sub>2</sub> via autocatalytic oxidative decomposition, which does not require oxygen flow [26,27]. In fact, according to Reaction 5.8, a third of oxygen (in moles) is produced for every mole of cobalt nitrate decomposed. The results of the calculations reported in sub-section 5.1.2. also indicate that Co<sub>3</sub>O<sub>4</sub> is the thermodynamically favoured product of the decomposition process below 400 °C. PXRD analysis (Figure 5.6) of all Co-bearing support samples was performed to confirm the chemical phase of the cobalt species present. The possibility of forming MSCs from Al<sub>2</sub>O<sub>3</sub>, TiO<sub>2</sub> and SiO<sub>2</sub> was also considered. Unlike for the PXRD patterns in Figures 5.3, 5.4 and 5.5, the 1/d range used to plot the patterns in Figure 5.6 was made shorter to enhance the visibility of the reflections from the Co species.

The mixed metal oxides CoAl<sub>2</sub>O<sub>4</sub> and Co<sub>2</sub>SiO<sub>4</sub> (both with cubic lattices) have very similar diffraction patterns as Co<sub>3</sub>O<sub>4</sub>, which makes it challenging to distinguish between all three metal oxides, especially from a single PXRD pattern. It will be shown in sub-section 6.2.2., using the *in situ* PXRD-derived reduction results, that Co<sub>3</sub>O<sub>4</sub> is present in the starting Al<sub>2</sub>O<sub>3</sub>- and SiO<sub>2</sub>-supported samples since the Co<sub>3</sub>O<sub>4</sub> reflections disappear at elevated temperatures, while reflections from CoO and later from fcc Co appear. From the *in situ* PXRD patterns recorded, the expected reflections from CoAl<sub>2</sub>O<sub>4</sub> and Co<sub>2</sub>SiO<sub>4</sub> were not observed. According to the literature and the thermodynamic predictions in sub-section 5.1.2., cobalt silicates are less likely to form during calcination owing to the high phase stability of SiO<sub>2</sub>. Furthermore, the formation of both cobalt silicates and aluminates is reported at calcination temperatures beyond 550 °C and is said to be less likely below 400 °C [24,27,31]. However, the formation of very small amounts (undetectable using PXRD) of these MSCs, either during calcination or reduction, cannot be completely ruled out.

On the other hand, cobalt titanates can be distinguished from Co<sub>3</sub>O<sub>4</sub> using PXRD as can be seen from the reference patterns in Figure 5.6. The acquired diffraction patterns of the P25-, rutile- and anatase-supported samples show no reflections corresponding to any cobalt titanate compound. It should also be noted that cobalt titanates are not likely to form under the chosen calcination conditions. The reflections from Co<sub>3</sub>O<sub>4</sub> can be observed in all three acquired diffraction patterns; despite the high crystallinity of the TiO<sub>2</sub> supports (also see Figure 5.5), the relatively low targeted

Co<sub>3</sub>O<sub>4</sub> loading of 10 wt.-%, and some overlapping reflections from the supports and Co<sub>3</sub>O<sub>4</sub> in the recorded PXRD patterns. Figure A.4.1 (in Appendix A.4.) shows an example of results from a Rietveld refinement performed for Co<sub>3</sub>O<sub>4</sub>/TiO<sub>2</sub>.

As previously mentioned, the formation of MSCs when either SiC, ZrO<sub>2</sub> and CeO<sub>2</sub> are used as support materials, has not been reported thus far. In fact, the use of SiC generally serves as a reason for avoiding MSC formation since SiC is chemically inert [42–44]. For the Fischer-Tropsch synthesis (FTS), supports like Al<sub>2</sub>O<sub>3</sub> and SiO<sub>2</sub> have been co-impregnated with Co and Zr precursors or impregnated with a Zr precursor prior to impregnating with a Co precursor. The Zr minimises/replaces the Co-support interaction to allow for improved accessibility of the Co species during reduction/activation and FTS [45–47]. It is also worth mentioning that there are no known and/or well characterised Co-Zr or Co-Ce bulk metal oxides reported in the literature. The PXRD patterns for the SiC- and ZrO<sub>2</sub>-supported samples show some of the reflections from Co<sub>3</sub>O<sub>4</sub>; despite the high crystallinity of these supports, low Co<sub>3</sub>O<sub>4</sub> loading, and some overlapping reflections. The PXRD pattern of the CeO<sub>2</sub>-supported fresh sample barely shows the expected major Co<sub>3</sub>O<sub>4</sub>(3 1 1) reflection at a  $1/d$  of 0.41 Å<sup>-1</sup>. However, this is very common for Co<sub>3</sub>O<sub>4</sub>/CeO<sub>2</sub> catalysts with a loading of 10 wt.-% and below [48–51]. In the work by Guo and Liu [48], loadings above 10 wt.-% were needed to adequately detect the Co<sub>3</sub>O<sub>4</sub> phase due to the high crystallinity of CeO<sub>2</sub>.

*Ex situ* X-ray Absorption Spectroscopy (XAS) was used to analyse the fresh Co<sub>3</sub>O<sub>4</sub>/CeO<sub>2</sub> sample following the inconclusive PXRD measurements. The normalised XANES spectrum of this fresh sample is shown in Figure 5.7 together with the spectra for the reference compounds; Co<sub>3</sub>O<sub>4</sub>, CoO and metallic Co. It can be observed that the spectrum of Co<sub>3</sub>O<sub>4</sub>/CeO<sub>2</sub> and that of the Co<sub>3</sub>O<sub>4</sub> reference have a common main edge at 7721 eV, and that their XANES features after the edge are similar, unlike those in the spectra of the CoO and metallic Co references. This observation confirms the presence of Co<sub>3</sub>O<sub>4</sub> as the bulk average Co-based phase in the fresh CeO<sub>2</sub>-supported catalyst. In conclusion, the use of both PXRD and XAS helped in confirming the chemical phase of the cobalt present in each supported catalyst as being Co<sub>3</sub>O<sub>4</sub>.

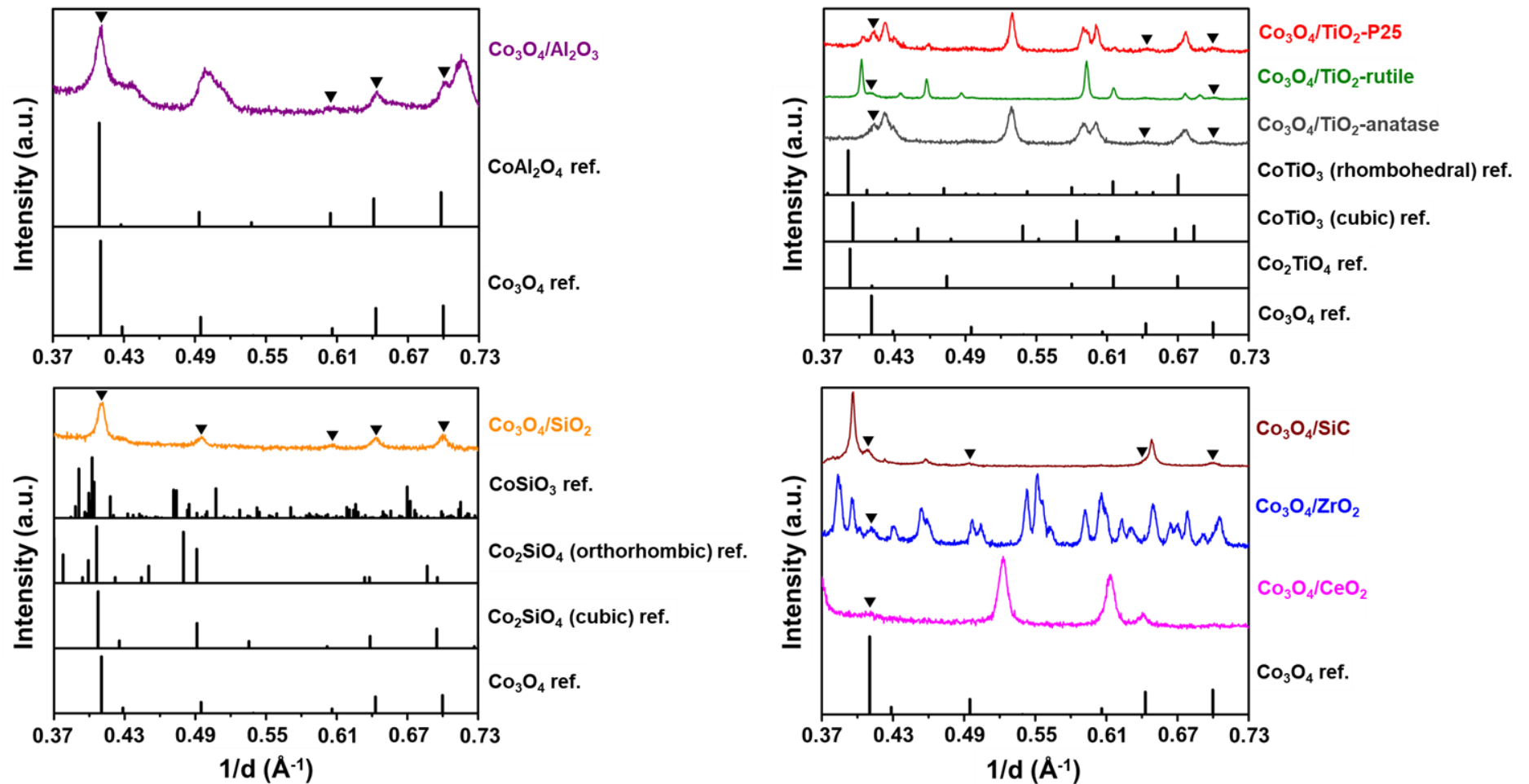


**Figure 5.6:** PXRD patterns of the fresh supported catalysts (*i.e.*, after incipient wetness impregnation and calcination) and the reference reflection lines of the relevant Co-based oxides. The black triangles indicate reflections from  $\text{Co}_3\text{O}_4$ . See Table A.2.1 for the ICDD PDFD-2 entries of all reference phases.

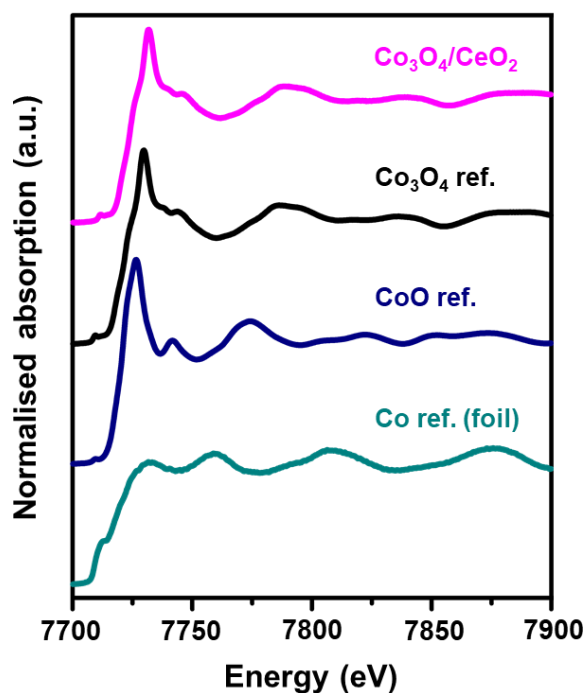


**Figure 5.7:** Normalised XANES spectrum of the fresh  $\text{Co}_3\text{O}_4/\text{CeO}_2$  catalyst. Also included are the XANES spectra of the reference compounds;  $\text{Co}_3\text{O}_4$  [6,7],  $\text{CoO}$  [52] and metallic  $\text{Co}$  (*i.e.*,  $\text{Co}$  foil) [53].

Rietveld refinement was performed on all acquired PXRD patterns to obtain the volume-based average crystallite size and relative fraction of  $\text{Co}_3\text{O}_4$  in each sample, and the results can be found in Table 5.1. The parameter  $R_{\text{wp}}$  in Table 5.1 is a measure of the quality of the fit in percentage value.  $R_{\text{wp}}$  values below 10% indicate a good fit between the reference pattern(s) and the experimental pattern [54,55]. The crystallite size of  $\text{Co}_3\text{O}_4$  in all samples varies in a very narrow range of 11 and 16 nm, which is reasonably good given the difficulty in controlling nanoparticle size using incipient wetness impregnation [56,57]. The low detectability of  $\text{Co}_3\text{O}_4$  in the  $\text{Co}_3\text{O}_4/\text{CeO}_2$  sample may have caused the small crystallite size of  $7.1 \pm 1.6$  nm to be estimated using Rietveld refinement. In the case of the  $\text{Co}_3\text{O}_4/\text{TiO}_2$ -anatase sample, due to the overlap of the (1 0 3) reflection from anatase with the main (3 1 1) reflection from  $\text{Co}_3\text{O}_4$  at  $1/d = 0.41 \text{ \AA}^{-1}$ , this may have also resulted in the slightly small crystallite size of  $9.8 \pm 0.4$  nm. It is worth noting that the estimated relative fraction of  $\text{Co}_3\text{O}_4$  in each sample is very close to the 10 wt.-% loading of  $\text{Co}_3\text{O}_4$  that was targeted during catalyst synthesis (see sub-section 4.2.3.). This confirms the success of employing incipient wetness impregnation for preparing the supported catalysts.

**Table 5.1:** Results from after performing Rietveld refinement (using TOPAS 5.0) on the *ex situ* PXRD patterns of the fresh supported catalysts.

Sample name	Crystallite size (nm)*	Relative fraction of Co <sub>3</sub> O <sub>4</sub> (wt.-%)*	R <sub>wp</sub> (%) <sup>§</sup>
unsupported Co <sub>3</sub> O <sub>4</sub>	12.3 ± 0.3	n/a	5.7
Co <sub>3</sub> O <sub>4</sub> /CeO <sub>2</sub>	7.1 ± 1.6	11.6 ± 1.9	9.0
Co <sub>3</sub> O <sub>4</sub> /ZrO <sub>2</sub>	15.2 ± 1.4	9.8 ± 0.6	5.8
Co <sub>3</sub> O <sub>4</sub> /SiC	13.3 ± 0.5	11.3 ± 0.4	6.8
Co <sub>3</sub> O <sub>4</sub> /SiO <sub>2</sub>	13.2 ± 0.3	n/a <sup>#</sup>	5.2
Co <sub>3</sub> O <sub>4</sub> /TiO <sub>2</sub> -anatase	9.8 ± 0.4	11.5 ± 1.0	8.4
Co <sub>3</sub> O <sub>4</sub> /TiO <sub>2</sub> -rutile	11.8 ± 0.8	10.3 ± 0.5	6.6
Co <sub>3</sub> O <sub>4</sub> /TiO <sub>2</sub> -P25	11.1 ± 1.3	11.0 ± 0.9	7.5
Co <sub>3</sub> O <sub>4</sub> /Al <sub>2</sub> O <sub>3</sub>	13.0 ± 0.4	10.3 ± 0.3	4.6

\* crystallite size and relative fraction of Co<sub>3</sub>O<sub>4</sub> in each catalyst reported with the associated errors.

§ informs on the quality of the fit with values between 2 and 10% indicating a good fit [54,55].

# could not be determined as SiO<sub>2</sub> is amorphous.

### 5.3. Scanning Transmission Electron Microscopy-Electron Energy Loss Spectroscopy

STEM-EELS was primarily used for the identification of cobalt-bearing nanoparticles (or clusters) on each support after the calcination. Specifically, EELS elemental maps were recorded which showed regions with Co, O and the metal ion of the support (*i.e.*, Ce, Zr, Si, Ti or Al), respectively. For consistency, bright-field STEM micrographs for the fresh unsupported sample were taken as well but without any elemental mapping. Figure 5.8 shows the selected micrograph for the unsupported sample as well as the derived number-based particle size distribution. The micrograph and the size distribution show that there are nanoparticles of varying sizes within the sample, even though the reverse microemulsion technique is well-known for producing particles with sizes varying within a small range. However, it should be noted that the targeted average size was relatively large (10 – 15 nm), and previous studies have shown that obtaining small variations in samples where large average sizes are targeted, is rather challenging [3,5,6,12]. Nonetheless, a

number-based average size of  $10.0 \pm 3.1$  nm and a volume-based average of  $13.0 \pm 3.8$  nm was achieved, both of which are within the target size range.

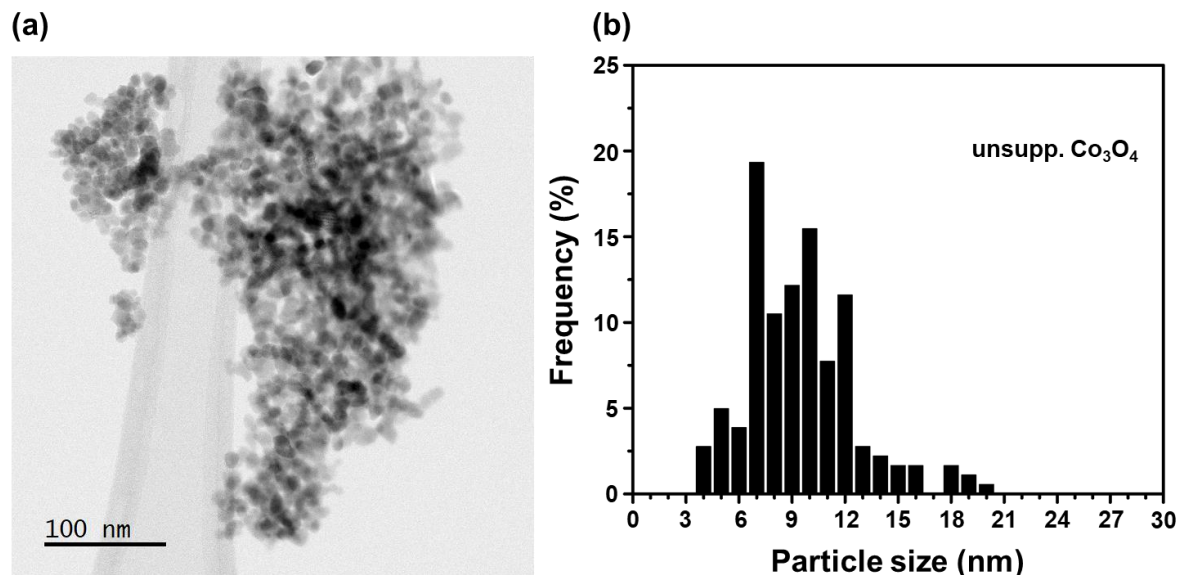


**Figure 5.8:** (a) Bright-field STEM micrograph of unsupported  $\text{Co}_3\text{O}_4$ , and (b) the corresponding derived number-based size distribution.

As previously mentioned in sub-sections 4.2.1. and 5.2.2., the support  $\text{TiO}_2$ -P25 has the crystal forms anatase and rutile, in a 4:1 ratio. The distribution of the two crystal forms can be distinguished using STEM-EELS by employing a method called energy-loss near-edge structure (ELNES) [58,59]. The energy loss spectra of pure anatase and pure rutile have similar features except between 458 and 462 eV (see Figure 5.9). This dissimilarity can be exploited using ELNES to produce a map showing the distribution of anatase and rutile in the sample. Figure 5.10 shows the bright- and dark-field STEM micrographs of fresh  $\text{Co}_3\text{O}_4/\text{TiO}_2$ . Also included are the resulting maps which show the distribution of anatase and rutile on the selected area of the STEM micrographs. The EELS maps qualitatively show the abundance of the anatase phase relative to rutile in the  $\text{TiO}_2$ -P25 support, which is in good agreement with the information reported in the literature and by the supplier (Evonik Industries). Thereafter, composite and individual Ti, O and Co maps were recorded for the same area to follow the distribution of cobalt-bearing particles and clusters over the  $\text{TiO}_2$  crystal phases (Figure 5.11). It can clearly be seen that the distribution of

Co is independent of the TiO<sub>2</sub> crystal phase as the Co is well distributed over the entire shown area.

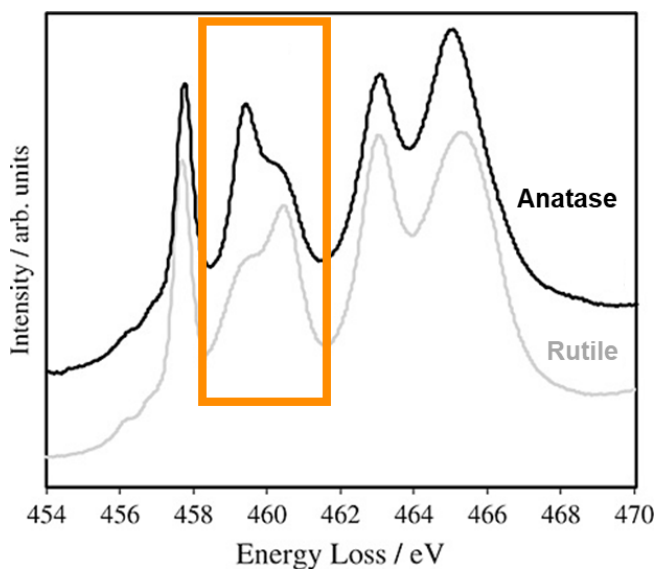


**Figure 5.9:** EELS spectra of pure TiO<sub>2</sub>-anatase and TiO<sub>2</sub>-rutile, respectively. The orange rectangular box shows the features that are dissimilar between the spectra of the two titania phases. (Adapted from [59]).

The SiC support has been reported to have a 1 – 2 nm oxide layer (Si<sub>x</sub>O<sub>y</sub> and/or Si<sub>x</sub>O<sub>y</sub>C<sub>z</sub>) around the main SiC particles which is formed during the final stages of the synthesis process [42–44] (also see sub-section 2.2.3.). This layer is regarded as advantageous since it makes the SiC slightly hydrophilic and allows for easy wetting of the SiC surface during impregnation. Again, EELS mapping was used to characterise the support by confirming the presence of this thin oxide layer. Figure 5.12 shows the bright-field micrograph and the elemental maps (excluding Co) generated from the same area for the fresh Co<sub>3</sub>O<sub>4</sub>/SiC sample. The edges of the main SiC particles indeed show the existence of a thin layer of oxygen species, which is in line with the literature.

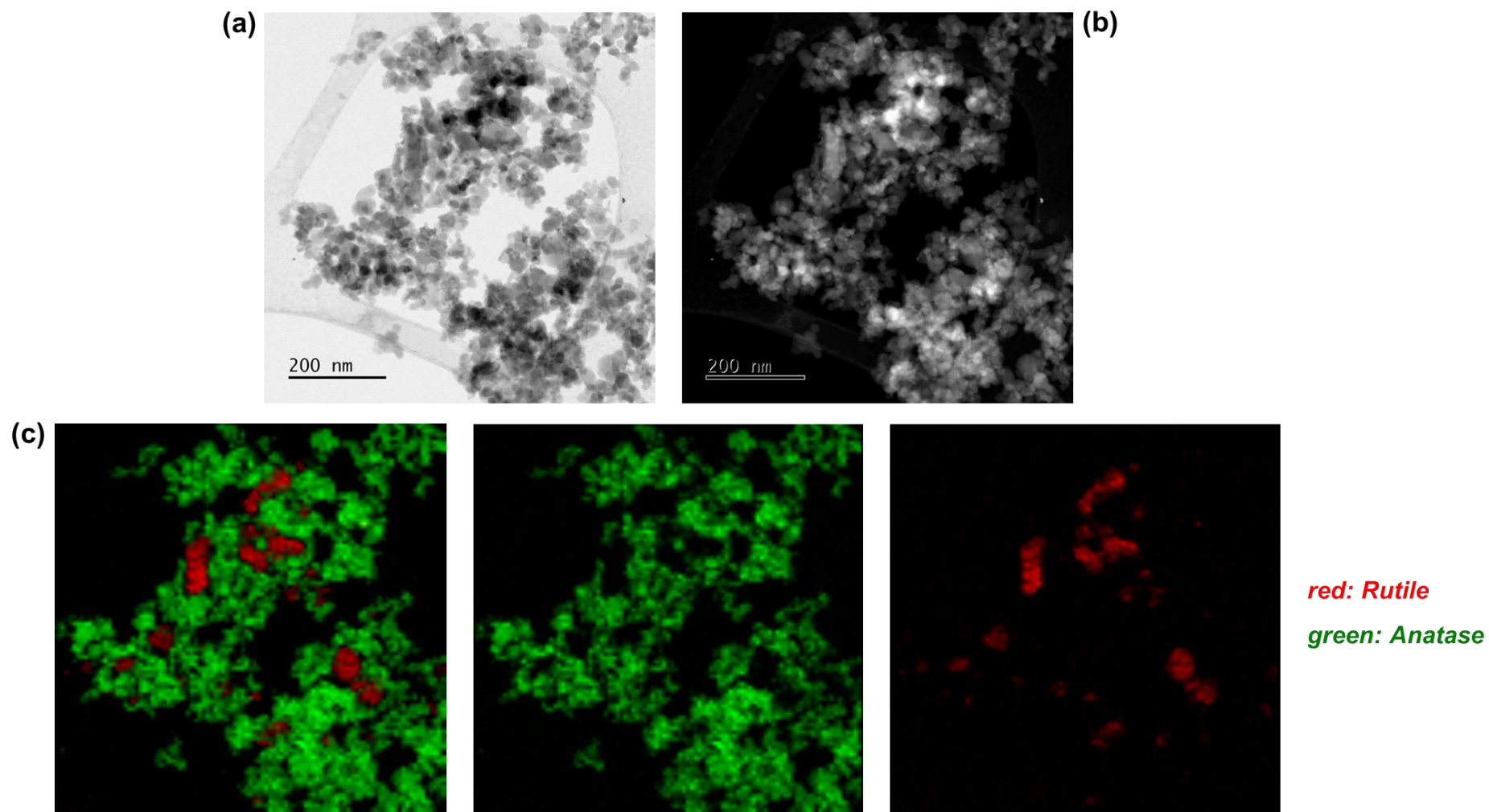


**Figure 5.10:** (a) Bright-field, and (b) dark-field STEM micrographs of the fresh  $\text{Co}_3\text{O}_4/\text{TiO}_2\text{-P25}$  catalyst. (c) Phase composition maps derived using EELS showing anatase and rutile regions in the fresh catalyst.

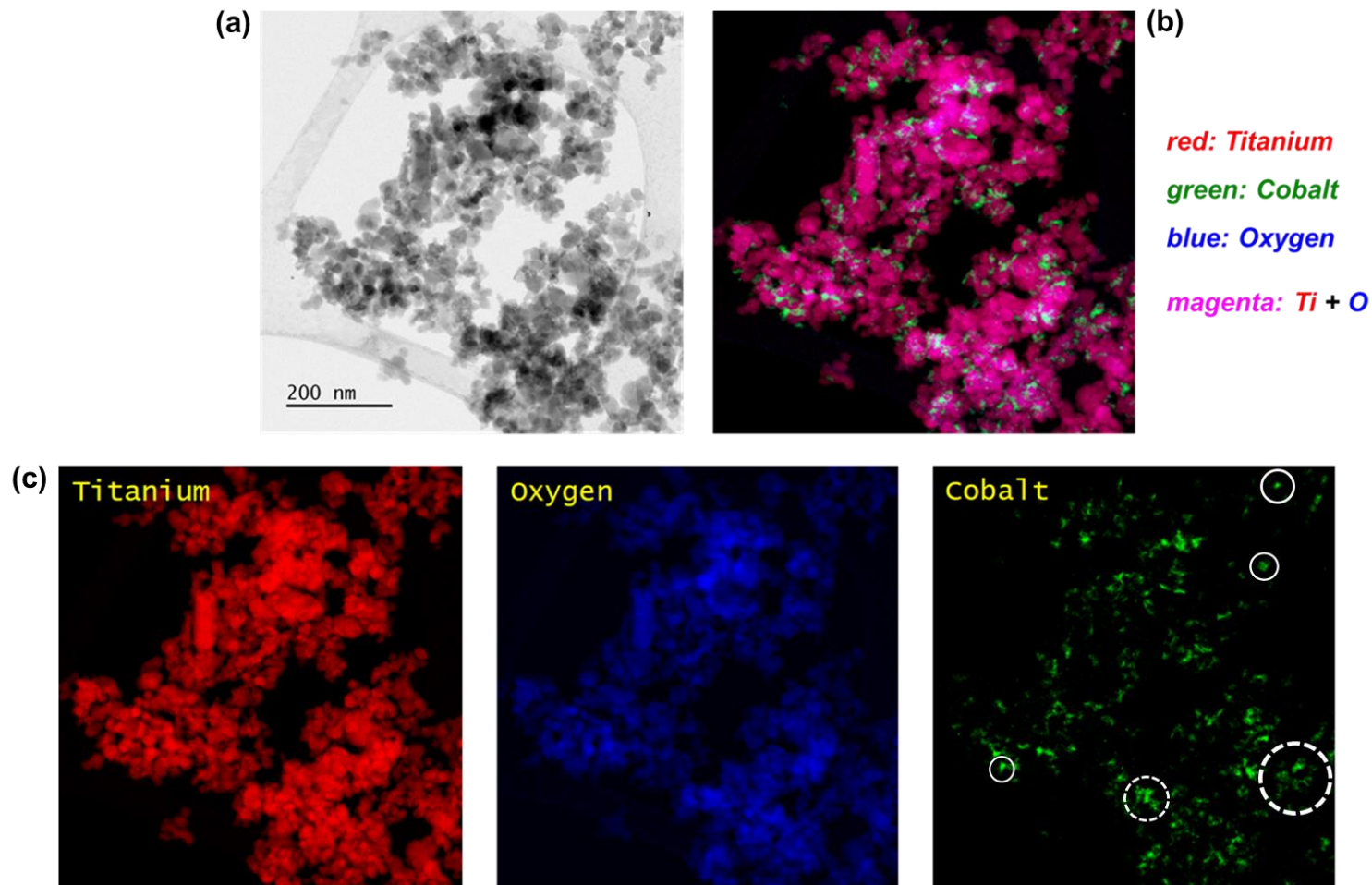


**Figure 5.11:** (a) Bright-field STEM micrograph of the fresh  $\text{Co}_3\text{O}_4/\text{TiO}_2\text{-P25}$  catalyst. (b) Composite STEM-EELS elemental map showing the regions with Ti, O and Co. (c) Corresponding STEM-EELS maps of the individual elements. The solid white circles indicate the “single” Co-bearing particles and the dashed circles indicate “clusters” of particles (or Co-bearing material).

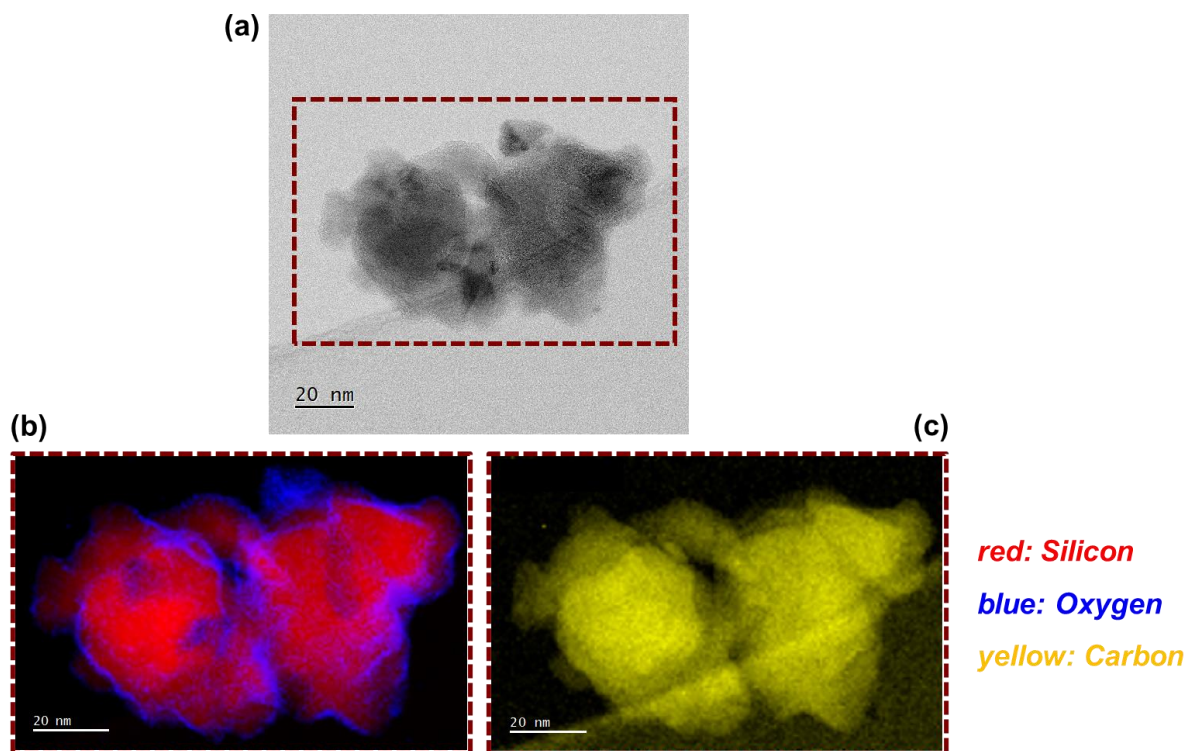


**Figure 5.12:** (a) Bright-field STEM micrograph of the fresh  $\text{Co}_3\text{O}_4/\text{SiC}$  catalyst. (b) Magnified STEM-EELS elemental maps showing the regions with Si, O, as well as (c) carbon.

The distribution and size of the cobalt-bearing particles and clusters in the remaining catalysts was studied, and the bright-field micrographs as well as the Co maps are shown in Figures 5.13 and 5.14. Note that the Co maps in Figure 5.13 were generated using EELS, while those in Figure 5.14 were generated using EFTEM (energy-filtered transmission electron microscopy) using the entire Co L-edge in both cases. Nonetheless, cobalt-bearing regions were adequately identified. As a result of employing incipient wetness impregnation for preparing supported catalysts, there are a number of clustered Co regions as well as single particles that could be identified [15–19,28–30,60]. The single particles were measured (*i.e.*, between 80 and 100 particles) to obtain a number-based size distribution for each fresh sample (Figure 5.15). Table 5.2 shows the number- and volume-based average sizes of  $\text{Co}_3\text{O}_4$  derived from the size distributions, and it can be seen that most samples have particles within the targeted 10 – 15 nm range. Furthermore, the volume-based STEM average sizes are mostly higher than the volume-based PXRD average sizes, which may suggest the presence of slightly smaller crystallites that make up the  $\text{Co}_3\text{O}_4$  particles [61].

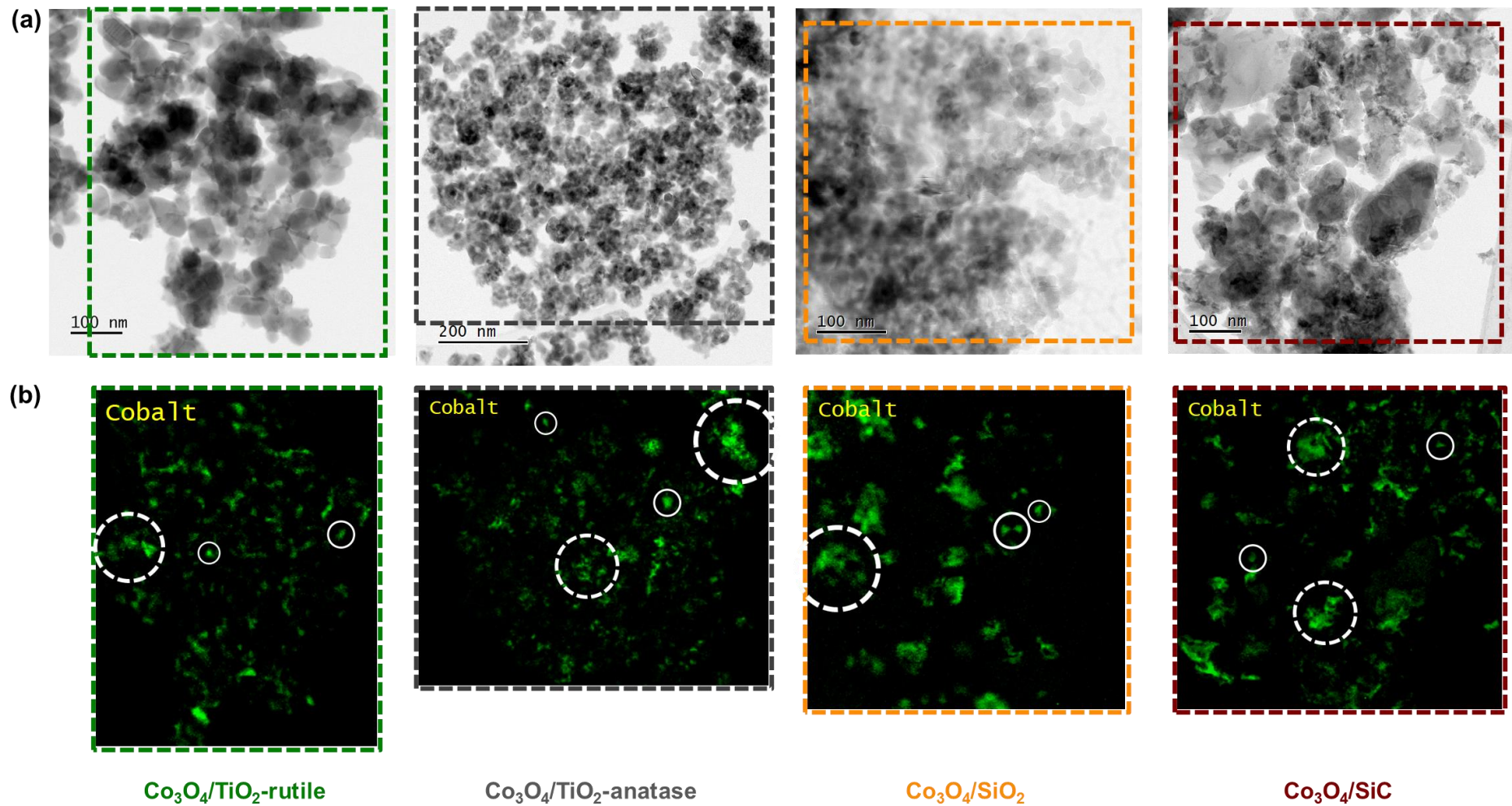


**Figure 5.13:** (a) Bright-field STEM micrographs of some of the fresh supported  $\text{Co}_3\text{O}_4$  catalysts, and (b) the corresponding magnified STEM-EELS Co maps. The solid white circles indicate the “single” Co-bearing particles and the dashed circles indicate “clusters” of particles (or Co-bearing material).

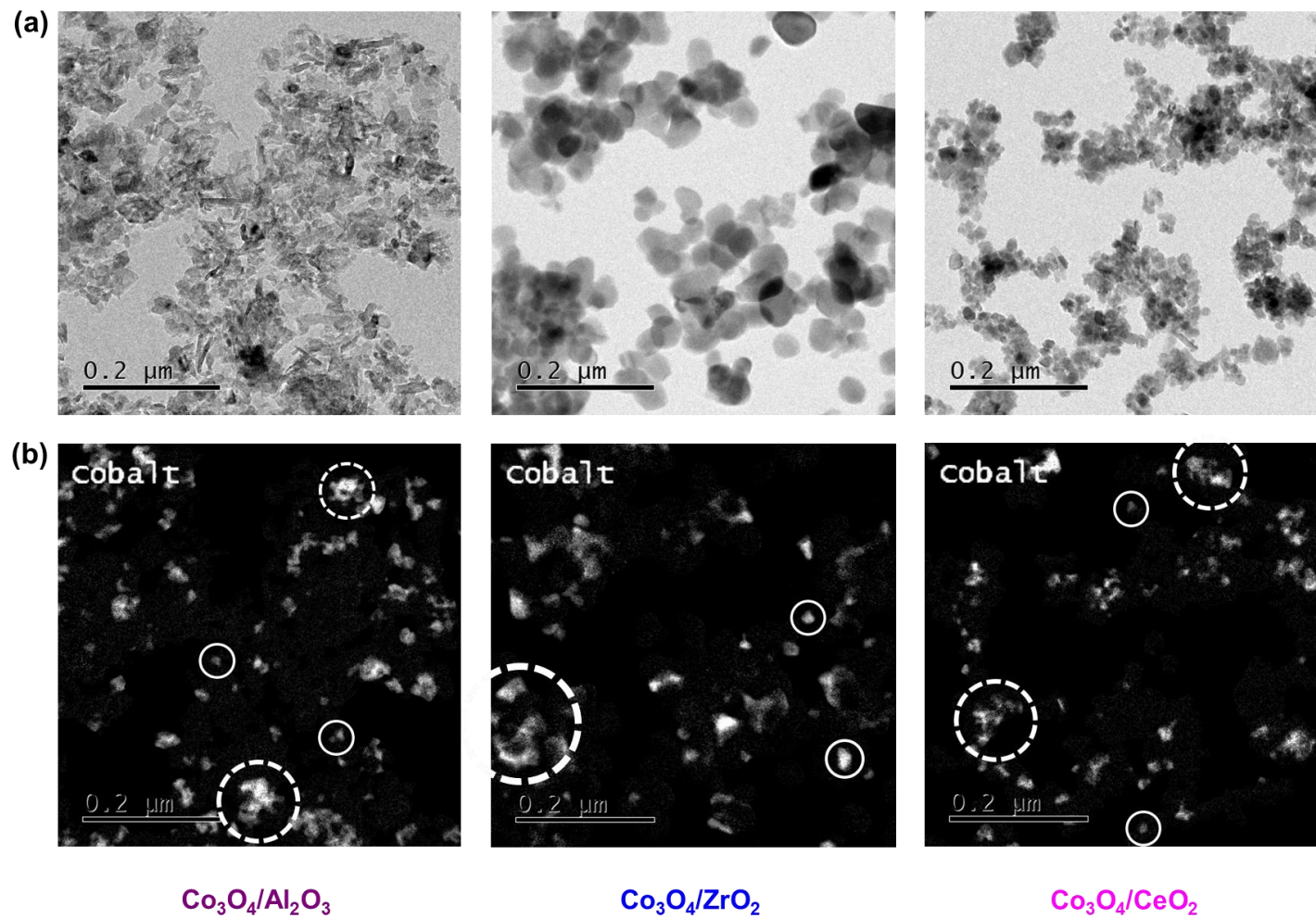


**Figure 5.14:** (a) Bright-field STEM micrographs of the remaining fresh supported  $\text{Co}_3\text{O}_4$  catalysts, and (b) the corresponding EFSTEM Co maps. The solid white circles indicate the “single” Co-bearing particles and the dashed circles indicate “clusters” of particles (or Co-bearing material).

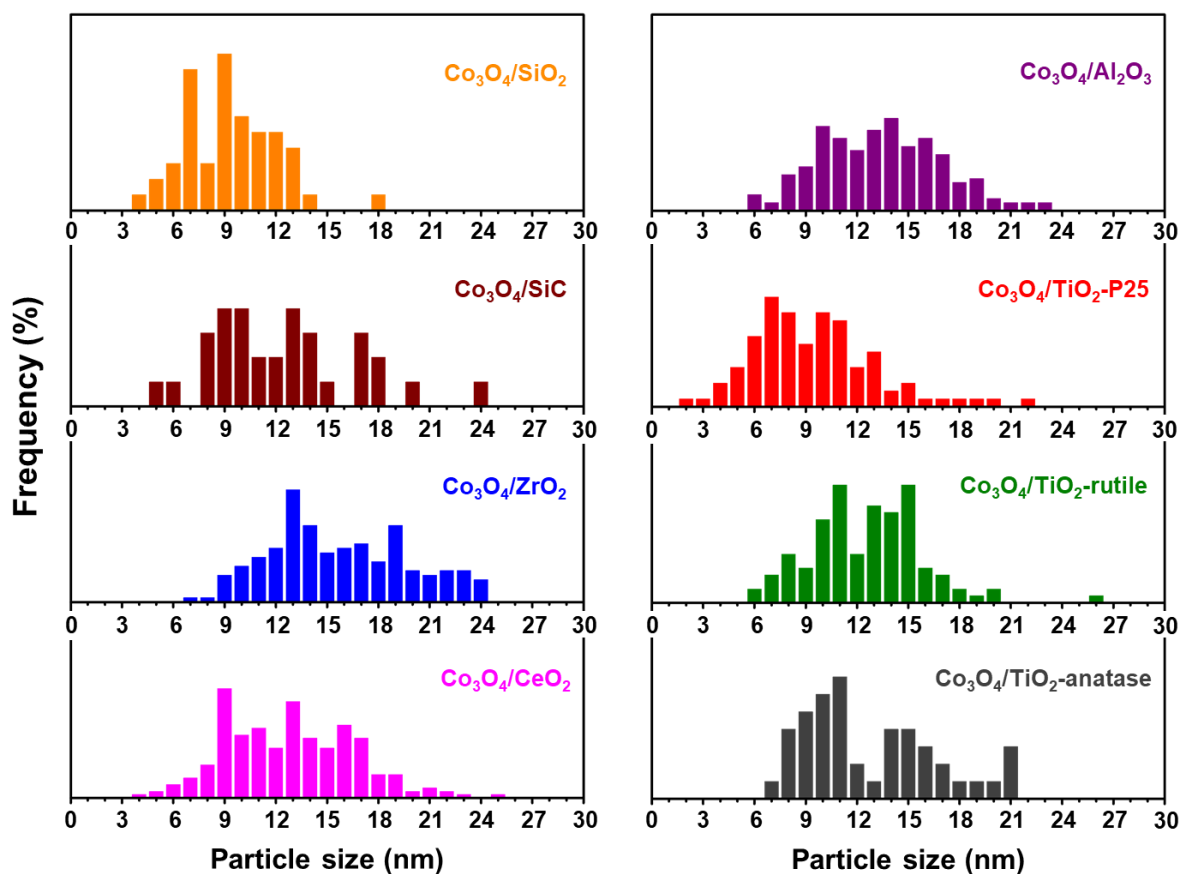


**Figure 5.15:** STEM-derived number-based size distributions for all prepared supported  $\text{Co}_3\text{O}_4$  catalysts.

**Table 5.2:** STEM-derived average number- and volume-based particle sizes.

Sample name	Number-based average size (nm)*	Volume-based average size (nm) <sup>§</sup>
unsupported $\text{Co}_3\text{O}_4$	$10.0 \pm 3.1$	$13.0 \pm 3.8$
$\text{Co}_3\text{O}_4/\text{CeO}_2$	$13.3 \pm 3.8$	$16.3 \pm 3.7$
$\text{Co}_3\text{O}_4/\text{ZrO}_2$	$16.3 \pm 4.1$	$19.1 \pm 3.8$
$\text{Co}_3\text{O}_4/\text{SiC}$	$12.9 \pm 4.3$	$16.9 \pm 4.5$
$\text{Co}_3\text{O}_4/\text{SiO}_2$	$9.9 \pm 2.7$	$12.0 \pm 2.8$
$\text{Co}_3\text{O}_4/\text{TiO}_2\text{-anatase}$	$13.3 \pm 3.9$	$16.6 \pm 3.9$
$\text{Co}_3\text{O}_4/\text{TiO}_2\text{-rutile}$	$13.0 \pm 3.3$	$15.5 \pm 3.8$
$\text{Co}_3\text{O}_4/\text{TiO}_2\text{-P25}$	$9.9 \pm 3.7$	$14.2 \pm 4.6$
$\text{Co}_3\text{O}_4/\text{Al}_2\text{O}_3$	$13.9 \pm 3.5$	$16.5 \pm 3.5$

\* number-based average particle size and standard deviation calculated using Equations 4.9 and 4.11, respectively.

<sup>§</sup> volume-based average particle size and standard deviation calculated using Equations 4.10 and 4.12, respectively.

## 5.4. Nitrogen Physisorption and Inductively Coupled Plasma-Optical Emission Spectrometry

Nitrogen physisorption was performed on all catalysts (*i.e.*, unsupported and supported) to determine their physical characteristics in terms of surface area, pore volume and pore diameter. These parameters give an indication on the success of the incipient wetness impregnation method as most of the  $\text{Co}_3\text{O}_4$  nanoparticles were intended to be present in the pores of each support after calcination. The physisorption experiments were also performed on the bare supports for comparison with the  $\text{Co}_3\text{O}_4$ -loaded samples. Table 5.3 summarises the BET surface areas and the BJH pore volumes and diameters of each bare and  $\text{Co}_3\text{O}_4$ -loaded support, as well as that of the unsupported catalyst. For most supported samples, the mass-specific surface area (MSSA), as well as the pore volume and diameter of each supported catalyst after synthesis is slightly lower than that of the corresponding bare support. This indicates the presence of  $\text{Co}_3\text{O}_4$  nanoparticles mostly in the pores of each support.

The concentration of the Co present as  $\text{Co}_3\text{O}_4$  in the fresh supported catalysts was determined using ICP-OES. The targeted loading of  $\text{Co}_3\text{O}_4$  was 10 wt.-%, which corresponds to ~7.3 wt.-% of Co. The ICP-OES results are also summarised in Table 5.3. The loading in each catalyst is very close to the targeted 10 wt.-%, which further indicates the success of the catalyst synthesis method chosen. The ICP-OES loadings are also in good agreement with the relative fraction of  $\text{Co}_3\text{O}_4$  in each supported catalyst calculated using Rietveld refinement (Table 5.1). Also note that the decrease in the surface area, pore volume and pore diameter after catalyst synthesis is almost proportional to the  $\text{Co}_3\text{O}_4$  loading estimated using ICP-OES.

**Table 5.3:** Summary of the results from nitrogen physisorption and ICP-OES.

Sample name	BET MSSA (m <sup>2</sup> /g)*	BJH pore volume (cm <sup>3</sup> /g)*	BJH pore diameter (nm)*	Co <sub>3</sub> O <sub>4</sub> loading (wt.-%) <sup>§</sup>
unsupported Co <sub>3</sub> O <sub>4</sub>	41.5	0.21	12.3	n/a
Co <sub>3</sub> O <sub>4</sub> /CeO <sub>2</sub>	47.5 (53.2)	0.13 (0.18)	9.7 (11.1)	9.0
Co <sub>3</sub> O <sub>4</sub> /ZrO <sub>2</sub>	29.3 (23.1)	0.11 (0.20)	15.2 (28.2)	9.4
Co <sub>3</sub> O <sub>4</sub> /SiC	25.0 (27.9)	0.13 (0.16)	19.9 (21.0)	9.8
Co <sub>3</sub> O <sub>4</sub> /SiO <sub>2</sub>	135.8 (149.0)	0.45 (0.41)	12.9 (11.1)	9.5
Co <sub>3</sub> O <sub>4</sub> /TiO <sub>2</sub> -anatase	73.5 (97.6)	0.23 (0.28)	9.4 (8.5)	9.9
Co <sub>3</sub> O <sub>4</sub> /TiO <sub>2</sub> -rutile	23.7 (26.6)	0.08 (0.12)	12.3 (16.0)	9.8
Co <sub>3</sub> O <sub>4</sub> /TiO <sub>2</sub> -P25	46.0 (48.7)	0.13 (0.19)	9.7 (14.7)	9.4
Co <sub>3</sub> O <sub>4</sub> /Al <sub>2</sub> O <sub>3</sub>	136.4 (151.0)	0.40 (0.49)	9.7 (9.6)	9.5

\* from N<sub>2</sub> physisorption. In parentheses are the values for the physical properties of the corresponding bare/unloaded support.

<sup>§</sup> calculated from the Co concentration determined using ICP-OES.

## 5.5. Summary: Catalyst Synthesis and ex situ Characterisation

One of the objectives of this Ph.D. study is to investigate the effect of the support material on the catalytic performance and phase stability of Co<sub>3</sub>O<sub>4</sub> under realistic CO-PrOx conditions. This requires the support and the nanoparticles to be in close contact, which should ideally be achieved during catalyst synthesis. A suitable and well-known technique for achieving such an interaction is incipient wetness impregnation [17–19]. The technique is simple and is widely applied for the synthesis of most industrial catalysts. For comparison, unsupported Co<sub>3</sub>O<sub>4</sub> nanoparticles were also prepared using the reverse microemulsion technique, which offers size control through adjusting certain synthesis parameters (see sub-section 2.5.2.) [1–5].

The average sizes of the un-/supported Co<sub>3</sub>O<sub>4</sub> nanoparticles, as confirmed by PXRD and STEM-EELS, were between 11 and 19 nm (with the exception of Co<sub>3</sub>O<sub>4</sub>/CeO<sub>2</sub> and Co<sub>3</sub>O<sub>4</sub>/TiO<sub>2</sub>-anatase regarding PXRD – see sub-section 5.2.3., as well as Tables 5.2 and 5.3), which is a reasonably narrow range considering the difficulty in controlling the nanoparticle size using incipient wetness impregnation. Except for the CeO<sub>2</sub>-supported fresh catalyst, the sole presence of Co<sub>3</sub>O<sub>4</sub> in the other prepared catalysts was confirmed with PXRD. XAS analysis confirmed the presence of Co<sub>3</sub>O<sub>4</sub> as

the only Co-based phase in the fresh CeO<sub>2</sub>-supported catalyst. It should be noted that the recorded PXRD patterns showed no evidence for the presence of Co<sub>2</sub>SiO<sub>4</sub>, CoTiO<sub>3</sub> and CoAl<sub>2</sub>O<sub>4</sub>. This will be further supported with *in situ* PXRD-derived results, which are discussed in sub-section 6.2.2. The thermodynamic calculations in sub-section 5.1.2. suggest that these MSCs would be less likely to form during the decomposition of cobalt nitrate in an inert environment (*e.g.*, N<sub>2</sub> flow) at 350 °C. In other work, the presence of MSCs after synthesis has only been reported at calcination temperatures above 550 °C [24,27,31]. The general decrease in the BET surface area, as well as the BJH pore volume and diameter after synthesis (Table 5.3), possibly suggests that most of the Co<sub>3</sub>O<sub>4</sub> nanoparticles are located in the pores of each support, as intended with the chosen synthesis technique. This further encourages the close contact between the Co<sub>3</sub>O<sub>4</sub> nanoparticles with each support. Lastly, all supported samples had Co<sub>3</sub>O<sub>4</sub> loadings varying between 9.0 and 9.9 wt.-%, which is close to the targeted 10 wt.-% (Table 5.3). These loadings were also in agreement with the relative fraction of Co<sub>3</sub>O<sub>4</sub> in each supported catalyst estimated using Rietveld refinement (Table 5.1).

## References

- [1] M. Boutonnet, J. Kizling, P. Stenius, G. Maire, *Colloids Surf.* 5 (1982) 209–225.
- [2] S. Eriksson, U. Nylén, S. Rojas, M. Boutonnet, *Appl. Catal. A* 265 (2004) 207–219.
- [3] D. Barkhuizen, I. Mabaso, E. Viljoen, C. Welker, M. Claeys, E. van Steen, J.C.Q. Fletcher, *Pure Appl. Chem.* 78 (2006) 1759–1769.
- [4] M. Boutonnet, S. Lögdberg, E. Elm Svensson, *Curr. Opin. Colloid Interface Sci.* 13 (2008) 270–286.
- [5] N. Fischer, T. Feltes, M. Claeys, in: B.I. Kharisov, O.V. Kharissova, U. Ortiz-Mendez (Eds.), *CRC Concise Encycl. Nanotechnol.*, 1st ed., CRC Press, Boca Raton, 2015, pp. 547–560.
- [6] N. Fischer, E. van Steen, M. Claeys, *Catal. Today* 171 (2011) 174–179.
- [7] N. Fischer, M. Minnermann, M. Baeumer, E. van Steen, M. Claeys, *Catal. Lett.* 142 (2012) 830–837.
- [8] O. Knacke, O. Kubaschewski, K. Hesselmann, eds., *Thermochemical Properties of Inorganic Substances*, 2nd ed., Springer-Verlag, Berlin, 1991.
- [9] E. Klugmann, H.J. Blythe, F. Walz, *Phys. Status Solidi* 146 (1994) 803–813.
- [10] S. Ram, *Mater. Sci. Eng. A* 304–306 (2001) 923–927.
- [11] L.J. Garces, B. Hincapie, R. Zerger, S.L. Suib, *J. Phys. Chem. C* 119 (2015) 5484–5490.
- [12] T.M. Nyathi, N. Fischer, A.P.E. York, M. Claeys, *Faraday Discuss.* 197 (2017) 269–285.
- [13] M. Khasu, T. Nyathi, D.J. Morgan, G.J. Hutchings, M. Claeys, N. Fischer, *Catal. Sci. Technol.* 7 (2017) 4806–4817.
- [14] T.M. Nyathi, N. Fischer, A.P.E. York, D.J. Morgan, G.J. Hutchings, E.K. Gibson, P.P. Wells, C.R.A. Catlow, M. Claeys, *ACS Catal.* 9 (2019) 7166–7178.
- [15] M. Wolters, L.J.W. van Grotel, T.M. Eggenhuisen, J.R.A. Sietsma, K.P. de Jong, P.E. de Jongh, *Catal. Today* 163 (2011) 27–32.
- [16] P. Munnik, N.A. Krans, P.E. de Jongh, K.P. de Jong, *ACS Catal.* 4 (2014) 3219–3226.
- [17] A.A. Adesina, *Appl. Catal. A* 138 (1996) 345–367.
- [18] E. Marceau, X. Carrier, M. Che, O. Clause, C. Marcilly, in: G. Ertl, H. Knözinger, F. Schüth, J. Weitkamp (Eds.), *Handb. Heterog. Catal.*, Wiley-VCH Verlag GmbH & Co. KGaA, Weinheim, Germany, 2008, pp. 467–484.

- [19] P. Munnik, P.E. de Jongh, K.P. de Jong, *Chem. Rev.* 115 (2015) 6687–6718.
- [20] M. Voß, D. Borgmann, G. Wedler, *J. Catal.* 212 (2002) 10–21.
- [21] C.-B. Wang, C.-W. Tang, H.-C. Tsai, S.-H. Chien, *Catal. Lett.* 107 (2006) 223–230.
- [22] N.E. Tsakoumis, R.E. Johnsen, W. van Beek, M. Rønning, E. Rytter, A. Holmen, *Chem. Commun.* 52 (2016) 3239–3242.
- [23] N.E. Tsakoumis, J.C. Walmsley, M. Rønning, W. van Beek, E. Rytter, A. Holmen, *J. Am. Chem. Soc.* 139 (2017) 3706–3715.
- [24] E. van Steen, G.S. Sewell, R.A. Makhothe, C. Micklethwaite, H. Manstein, M. de Lange, C.T. O'Connor, *J. Catal.* 162 (1996) 220–229.
- [25] G. Jacobs, T.K. Das, Y. Zhang, J. Li, G. Racoillet, B.H. Davis, *Appl. Catal. A* 233 (2002) 263–281.
- [26] T. Cseri, S. Békássy, G. Kenessey, G. Liptay, F. Figueras, *Thermochim. Acta* 288 (1996) 137–154.
- [27] J.-S. Girardon, A.S. Lermontov, L. Gengembre, P.A. Chernavskii, A. Griboval-Constant, A.Y. Khodakov, *J. Catal.* 230 (2005) 339–352.
- [28] T.M. Eggenhuisen, H. Friedrich, F. Nudelman, J. Zečević, N.A.J.M. Sommerdijk, P.E. de Jongh, K.P. de Jong, *Chem. Mater.* 25 (2013) 890–896.
- [29] T.M. Eggenhuisen, P. Munnik, H. Talsma, P.E. de Jongh, K.P. de Jong, *J. Catal.* 297 (2013) 306–313.
- [30] P. Munnik, P.E. de Jongh, K.P. de Jong, *J. Am. Chem. Soc.* 136 (2014) 7333–7340.
- [31] P.A. Chernavskii, A.Y. Khodakov, G. V. Pankina, J.-S. Girardon, E. Quinet, *Appl. Catal. A* 306 (2006) 108–119.
- [32] International Agency for Research on Cancer (IARC), in: *IARC Monogr. Eval. Carcinog. Risks to Humans - Chlorinated Drink. Chlorination By-Products; Some Other Halogenated Compd. Cobalt Cobalt Compd.*, Geneva, 1991, pp. 363–472.
- [33] J. Ismail, M.F. Ahmed, P.V. Kamath, G.N. Subbanna, S. Uma, J. Gopalakrishnan, *J. Solid State Chem.* 114 (1995) 550–555.
- [34] R. Xu, H.C. Zeng, *J. Phys. Chem. B* 107 (2003) 12643–12649.
- [35] Z.-A. Hu, Y.-L. Xie, Y.-X. Wang, L.-J. Xie, G.-R. Fu, X.-Q. Jin, Z.-Y. Zhang, Y.-Y. Yang, H.-Y. Wu, *J. Phys. Chem. C* 113 (2009) 12502–12508.
- [36] P. Benson, G.W.D. Briggs, W.F.K. Wynne-Jones, *Electrochim. Acta* 9 (1964) 275–280.
- [37] C. Mockenhaupt, T. Zeiske, H.D. Lutz, *J. Mol. Struct.* 443 (1998) 191–196.

- [38] J.D. Donaldson, D. Beyersmann, in: Ullmann's Encycl. Ind. Chem., Wiley-VCH Verlag GmbH & Co. KGaA, Weinheim, Germany, 2005, pp. 429–465.
- [39] SASOL PURALOX and CATALOX.  
<https://products.sasol.com/pic/products/home/grades/AS/5puralox-and-catalox/index.html>  
(accessed February 2020).
- [40] ICDD PDF-2 Release 2008 (Database), International Centre for Diffraction Data, Newtown Square, PA, USA, 2008.
- [41] N.V.Y. Scarlett, I.C. Madsen, Powder Diffr. 21 (2006) 278–284.
- [42] P. Nguyen, C. Pham, Appl. Catal. A 391 (2011) 443–454.
- [43] A.R. de la Osa, A. de Lucas, J. Díaz-Maroto, A. Romero, J.L. Valverde, P. Sánchez., Catal. Today 187 (2012) 173–182.
- [44] J. Labuschagne, R. Meyer, Z.H. Chonco, J.M. Botha, D.J. Moodley, Catal. Today 275 (2016) 2–10.
- [45] B. Jongsomjit, J. Panpranot, J.G. Goodwin Jr., J. Catal. 215 (2003) 66–77.
- [46] G.R. Moradi, M.M. Basir, A. Taeb, A. Kiennemann, Catal. Commun. 4 (2003) 27–32.
- [47] G.R. Johnson, A.T. Bell, ACS Catal. 6 (2016) 100–114.
- [48] Q. Guo, Y. Liu, React. Kinet. Catal. Lett. 92 (2007) 19–25.
- [49] P. Gawade, B. Bayram, A.M.C. Alexander, U.S. Ozkan, Appl. Catal. B 128 (2012) 21–30.
- [50] T. Cwele, N. Mahadevaiah, S. Singh, H.B. Friedrich, Appl. Catal. B 182 (2016) 1–14.
- [51] T. Cwele, N. Mahadevaiah, S. Singh, H.B. Friedrich, A.K. Yadav, S.N. Jha, D. Bhattacharyya, N.K. Sahoo, Catal. Sci. Technol. 6 (2016) 8104–8116.
- [52] M. Wolf, N. Fischer, M. Claeys, Mater. Chem. Phys. 213 (2018) 305–312.
- [53] A.J. Dent, G. Cibin, S. Ramos, A.D. Smith, S.M. Scott, L. Varandas, M.R. Pearson, N.A. Krumpa, C.P. Jones, P.E. Robbins, J. Phys. Conf. Ser. 190 (2009) 012039.
- [54] A.A. Coelho, J. Appl. Crystallogr. 36 (2003) 86–95.
- [55] C.T. Kniess, J.C. de Lima, P.B. Prates, in: V. Shatokha (Ed.), Sinter. - Methods Prod., InTech, London, 2012, pp. 293–316.
- [56] R.C. Reuel, C.H. Bartholomew, J. Catal. 85 (1984) 78–88.
- [57] L. Fu, C.H. Bartholomew, J. Catal. 92 (1985) 376–387.
- [58] R. Brydson, H. Sauer, W. Engel, J.M. Thomass, E. Zeitler, N. Kosugi, H. Kuroda, J. Phys. Condens. Matter 1 (1989) 797–812.

- [59] T. Akita, M. Kohyama, *Surf. Interface Anal.* 46 (2014) 1249–1252.
- [60] D. Moodley, M. Claeys, E. van Steen, P. van Helden, D. Kistamurthy, K.-J. Weststrate, H. Niemantsverdriet, A. Saib, W. Erasmus, J. van de Loosdrecht, *Catal. Today* 342 (2020) 59–70.
- [61] C. Weidenthaler, *Nanoscale* 3 (2011) 792–810.

# **Chapter 6: Thermodynamic Calculations and Experimental Evaluation of the Stability of Cobalt-based Compounds**

## **6.1. Thermodynamic Calculations on the Stability of Cobalt-based Compounds in Hydrogen-Water Mixtures**

### **6.1.1. Unsupported Co-based compounds**

In sub-sections 2.3.1. and 2.5.1., the reducibility of  $\text{Co}_3\text{O}_4$  during CO-PrOx as one of the catalyst deactivation mechanisms was discussed in detail. The cause of the reduction is the abundant  $\text{H}_2$  gas (40 – 75%) in the feed. The reduction transforms  $\text{Co}_3\text{O}_4$  into  $\text{CoO}$  and ultimately to metallic Co as the reaction temperature is increased. The  $\text{CoO}$  phase is less active for CO oxidation, while metallic Co is known to catalyse the undesired hydrogenation of CO (and  $\text{CO}_2$ ) to  $\text{CH}_4$  [1–6]. Reactions 6.1 to 6.3 show the reduction of  $\text{Co}_3\text{O}_4$  to  $\text{CoO}$ ,  $\text{Co}_3\text{O}_4$  to metallic Co, and  $\text{CoO}$  to metallic Co, respectively, which are all caused by the  $\text{H}_2$  and lead to the product  $\text{H}_2\text{O}$ . An evaluation of the stability of these cobalt species was performed by means of thermodynamic calculations, the results of which can be seen in Figure 6.1. Note that these calculations were performed assuming bulk Co-based phases, and that the predictions reported may not necessarily apply to nanoparticles, where crystallite/particle size effects could play a role [4,7–13].



The results show that all three reduction routes are thermodynamically favourable within the temperature range considered. Experimentally, the onset of unsupported  $\text{Co}_3\text{O}_4$  reduction by  $\text{H}_2$  can be expected anywhere from 200 to 300 °C; depending on the partial pressure of  $\text{H}_2$ , space velocity, size of the  $\text{Co}_3\text{O}_4$  particles, heating rate *etc.* [3,14–17]. The  $\text{CoO}$  phase is normally formed before the metallic phase, however, there have been instances where both phases are formed at the same time [3,15]. Although no kinetic information was incorporated into the calculations performed, it can be observed that the direct reduction of  $\text{Co}_3\text{O}_4$  to metallic  $\text{Co}$  is in fact the most favourable route (Figure 6.1(a)).

Figure 6.1(b) shows the conditions of temperature and partial pressure ratio of  $\text{H}_2$  to  $\text{H}_2\text{O}$  ( $p_{\text{H}_2}/p_{\text{H}_2\text{O}}$ ) where the different cobalt phases are stable relative to each other. For this evaluation, each of the three reactions were assumed to be at equilibrium to allow for  $p_{\text{H}_2}/p_{\text{H}_2\text{O}}$  to be calculated using Equation 6.4 (after modulation and substitution of Equations 6.2 and 6.3 in Equation 6.1). At very low  $p_{\text{H}_2}/p_{\text{H}_2\text{O}}$ ,  $\text{Co}_3\text{O}_4$  is the most stable cobalt phase. However, a gradual increase in both  $p_{\text{H}_2}/p_{\text{H}_2\text{O}}$  and temperature makes  $\text{CoO}$  the most stable phase and this remains the case over a wide range of  $p_{\text{H}_2}/p_{\text{H}_2\text{O}}$  (also see the depicted stability trends between all Co-based phases in Figure 6.1(b)). At  $p_{\text{H}_2}/p_{\text{H}_2\text{O}}$  above  $10^{-2}$ , metallic  $\text{Co}$  then becomes the most stable phase. Even though the thermodynamic calculations predict that very low  $p_{\text{H}_2}$  can reduce  $\text{Co}_3\text{O}_4$  or  $\text{CoO}$ , there are still other barriers that may need to be overcome experimentally, for example,  $\text{H}_2$  dissociation rate [18–23], nanoparticle size [4,7–13] and nanoparticle-support interactions (in the case of supported nanoparticles) [2,6,14,24–26].

It should also be noted that during a reduction in a continuous flow-through system (such as a fixed bed or fluidised bed reactor), the reduction products are constantly being removed, which implies that the equilibrium is constantly shifting towards the products [27]. Therefore, the  $p_{\text{H}_2}/p_{\text{H}_2\text{O}}$  and temperatures predicted for the formation and stability of the different Co-based phases, based on the thermodynamic calculations, may not necessarily correspond with those observed during a reactor-based reduction. This applies to the reduction of both unsupported and supported metal oxide catalysts.

$$\Delta G_{rxn}(T) = T \cdot \left( \frac{\Delta G_{rxn}^o(T)}{T^o} - \int_{T^o}^T \frac{\Delta H_{rxn}^o + \int_{T^o}^T \Delta C_{p,rxn}(T) dT}{T^2} dT \right) \quad \text{Equation 6.1}$$

$$\Delta G_{rxn}(T) = -RT \ln K_{eq}. \quad \text{Equation 6.2}$$

$$K_{eq.} = \frac{(p_{H_2O})^v}{(p_{H_2})^w} \quad \text{Equation 6.3}$$

$$\frac{(p_{H_2})^w}{(p_{H_2O})^v} = \exp \left\{ \frac{1}{R} \cdot \left( \frac{\Delta G_{rxn}^o(T)}{T^o} - \int_{T^o}^T \frac{\Delta H_{rxn}^o + \int_{T^o}^T \Delta C_{p,rxn}(T) dT}{T^2} dT \right) \right\} \quad \text{Equation 6.4}$$

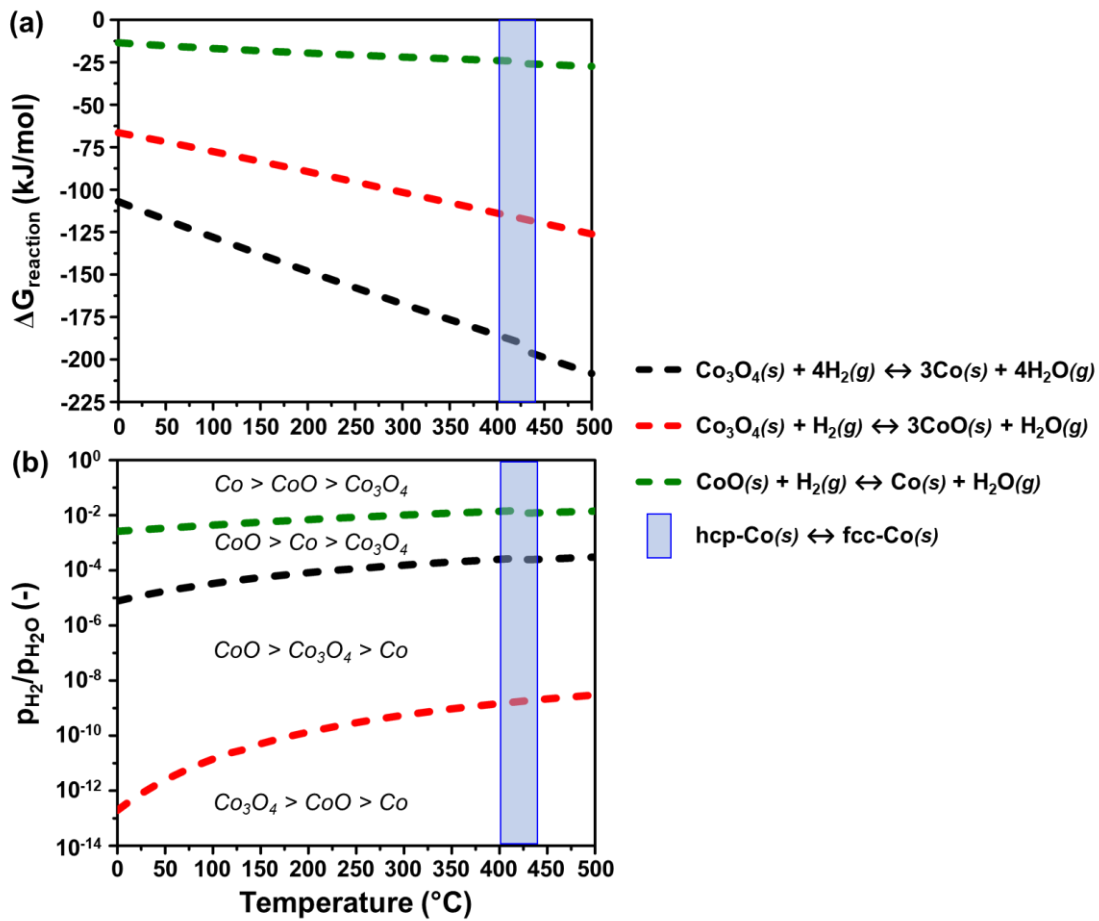


**Figure 6.1:** (a) Changes in the Gibbs free energy, and (b) partial pressure ratio of H<sub>2</sub> and H<sub>2</sub>O (i.e.,  $p_{\text{H}_2}/p_{\text{H}_2\text{O}}$ ) as a function of temperature at 1.013 bar during the reduction of Co<sub>3</sub>O<sub>4</sub> and CoO. Note that “>” means “more stable than”. This is used to depict the stability trend between the Co-based phases at different temperatures and  $p_{\text{H}_2}/p_{\text{H}_2\text{O}}$ .

### 6.1.2. Supported Co-based compounds

As most of the prepared samples in this work include supported  $\text{Co}_3\text{O}_4$  catalysts, it was also appropriate to perform some predictions on the likely Co species that can be formed during the reduction of supported  $\text{Co}_3\text{O}_4$ . Depending on the synthesis method for obtaining the supported  $\text{Co}_3\text{O}_4$ , the reduction can be difficult when compared with that of the unsupported catalyst [14,15,28]. This is because of the MSIs or NPSIs introduced largely through the catalyst synthesis method. In processes such as FTS,  $\text{Co}_3\text{O}_4$  should ideally be reduced fully to metallic Co but in most cases, partial metallic Co formation is achieved owing to the nature and strength of the NPSI [10,14,15,28,29]. Some researchers have reported the possibility of Co species reacting with the support to form MSCs during the reduction process [10,14,29]. Therefore, the formation of the MSCs –  $\text{CoAl}_2\text{O}_4$ ,  $\text{CoTiO}_3$  and  $\text{Co}_2\text{SiO}_4$  – was considered in the thermodynamic calculations as a possibility during CO-PrOx.

The general reaction, Reaction 6.4, shows the direct route to the MSCs mentioned above during reduction and Figure 6.2 shows the results of the thermodynamic calculations. The reduction of  $\text{Co}_3\text{O}_4$  to CoO and metallic Co, respectively, was also considered in these calculations for comparison. Reactions 6.1 and 6.2 shows these respective reduction routes. Interestingly, the formation of MSCs is far more favourable than the formation of CoO from  $\text{Co}_3\text{O}_4$ . The direct formation of metallic Co from  $\text{Co}_3\text{O}_4$  is more favourable than  $\text{Co}_2\text{SiO}_4$  formation but only more favourable than  $\text{CoTiO}_3$  formation at elevated temperatures (Figure 6.2(a)).  $\text{CoAl}_2\text{O}_4$  formation is the most favourable route at all temperatures considered. MSC formation is also more likely at considerably low  $p_{\text{H}_2}/p_{\text{H}_2\text{O}}$  than those required for the formation of CoO or metallic Co (Figure 6.2(b)). In line with these results is the experimental evidence that shows the increased likelihood of MSC formation in  $\text{Al}_2\text{O}_3$ -supported cobalt catalysts than in  $\text{TiO}_2$ - or  $\text{SiO}_2$ -supported cobalt catalysts [10,14,25,29].

Note the dependency of the formation of  $\text{CoTiO}_3$  on the phase of the  $\text{TiO}_2$  support (*i.e.*, anatase or rutile). Rutile shows slightly better resistance to MSC formation owing to its higher stability over anatase (Figure 6.2). Experimentally, the higher likelihood for the formation of MSCs from anatase is thought to be facilitated by its high reducibility in  $\text{H}_2$ . During reduction, surface  $\text{TiO}_{2-x}$  species are reported to migrate over reduced  $\text{CoO}_x$  nanoparticles (or other reduced metal oxide nanoparticles), thus encapsulating them and in some cases, forming Ti-based MSCs [30–34].

A crucial point to highlight is that supporting nanoparticles does not always lead to MSC formation, especially at moderate reduction temperatures (300 – 450 °C). In fact, CoO and metallic Co are still the most observed species after the reduction of supported  $\text{Co}_3\text{O}_4$  catalysts, which may indicate a kinetic hindrance regarding the formation of MSCs [35–37]. Furthermore, in the studies which have investigated supported  $\text{Co}_3\text{O}_4$  catalysts for CO-PrO<sub>x</sub>, the formation of MSCs has not been reported. However, higher reduction/reaction temperatures do increase the probability of MSC formation [35–37]. The nanoparticle size of  $\text{Co}_3\text{O}_4$  [8,10,11,29,38] and the physical properties of the support (surface area, pore diameter *etc.*) [39] can also play a role in determining the Co species formed after reduction.

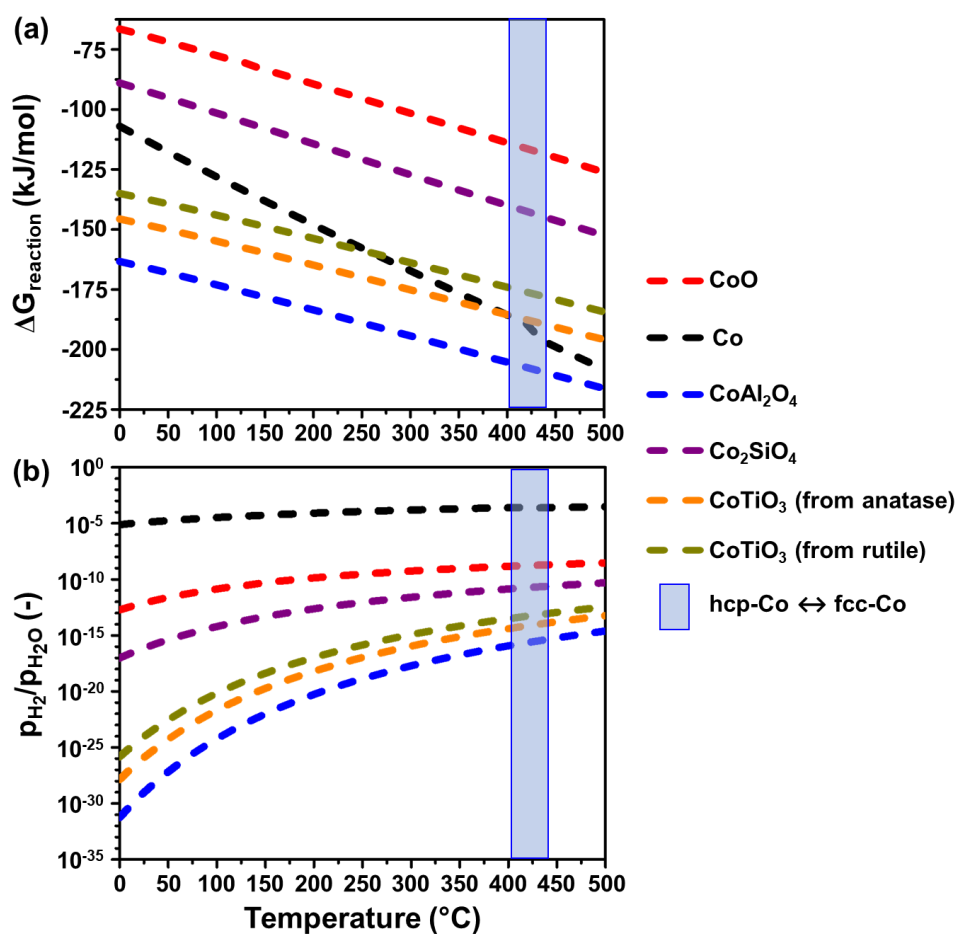
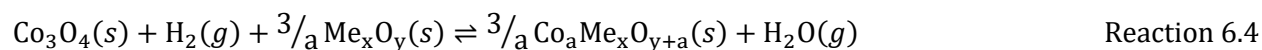


**Figure 6.2:** (a) Changes in the Gibbs free energy, and (b)  $p_{\text{H}_2}/p_{\text{H}_2\text{O}}$  as a function of temperature at 1.013 bar during the reduction of  $\text{Co}_3\text{O}_4$  forming CoO, metallic Co or Co-support compounds.

The formation of MSCs from CoO was also considered and is represented by the general reaction, Reaction 6.5. For comparison, the reduction of CoO to metallic Co was also included (Reaction 6.3). According to Reaction 6.5, the formation of MSCs from CoO and the support does not require the involvement of H<sub>2</sub>. Therefore, thermodynamically, MSC formation is only determined by the temperature. Just as in the case of Co<sub>3</sub>O<sub>4</sub>, the formation of MSCs from CoO is also thermodynamically favourable as shown in Figure 6.3. Metallic Co formation is more favourable than Co<sub>2</sub>SiO<sub>4</sub> formation at all temperatures and more favourable than CoTiO<sub>3</sub> formation at elevated temperatures.

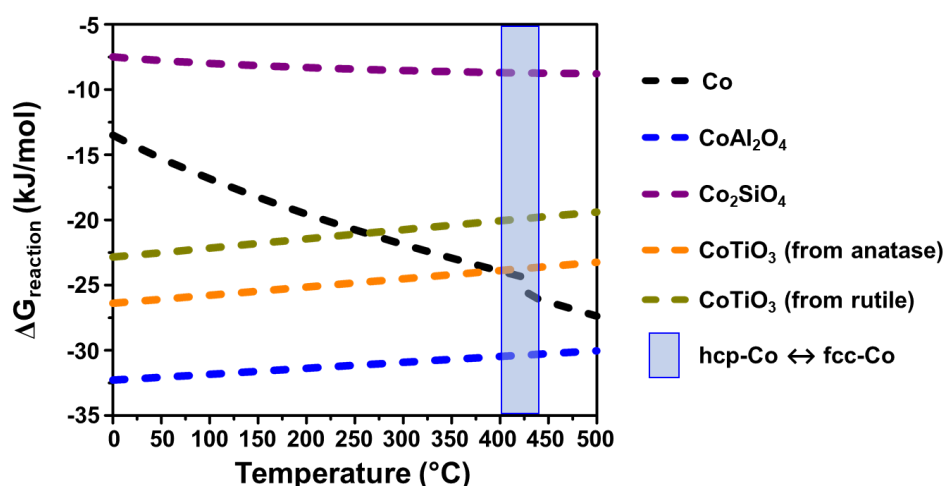
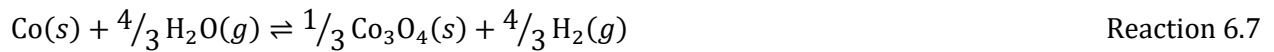
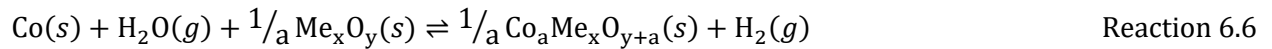


**Figure 6.3:** Changes in the Gibbs free energy as a function of temperature at 1.013 bar during the reduction of CoO forming metallic Co as well as during the solid state-reaction between CoO and some supports forming Co-support compounds.

Finally, MSC formation from metallic Co was evaluated. This pathway has been reported experimentally for reduced supported cobalt catalysts for FTS, for example [8,11,29,38,40,41]. Unlike CoO and Co<sub>3</sub>O<sub>4</sub>, the formation of MSCs from metallic Co involves H<sub>2</sub>O as the reactant and results in H<sub>2</sub> formation. Reaction 6.6 is the general reaction showing the formation of the MSCs from metallic Co. When the subscripts x and y = 0, and a = 1, this reaction becomes the reverse of Reaction 6.3, leading to the formation of CoO. Reaction 6.7 represents the formation of Co<sub>3</sub>O<sub>4</sub>

from metallic Co. From Figure 6.4, the formation of CoO, Co<sub>3</sub>O<sub>4</sub> and Co<sub>2</sub>SiO<sub>4</sub> is not thermodynamically favoured at all considered temperatures. The formation of CoTiO<sub>3</sub> and CoAl<sub>2</sub>O<sub>4</sub> becomes less favourable as the temperature is increased. In terms of the partial pressure ratios of H<sub>2</sub>O to H<sub>2</sub> ( $p_{\text{H}_2\text{O}}/p_{\text{H}_2}$ ) calculated using Equation 6.5, these range from 10<sup>-4</sup> to 1 for the formation of CoTiO<sub>3</sub> and CoAl<sub>2</sub>O<sub>4</sub>, while ratios above 10 are required for the formation of Co<sub>2</sub>SiO<sub>4</sub>. The formation of CoO and Co<sub>3</sub>O<sub>4</sub> require ratios above 100 and 10000, respectively.

A typical CO-PrOx feed having 1% CO, 1% O<sub>2</sub>, 10% CO<sub>2</sub>, 10% H<sub>2</sub>O, 50% H<sub>2</sub> and a balance of N<sub>2</sub>, has a starting  $p_{\text{H}_2\text{O}}/p_{\text{H}_2} = 0.2$  (i.e., 10:50). This ratio could increase in the presence of metallic Co to about 6.6 assuming all the O<sub>2</sub> in the feed forms H<sub>2</sub>O and, all the CO and CO<sub>2</sub> forms CH<sub>4</sub> over the metallic Co. A  $p_{\text{H}_2\text{O}}/p_{\text{H}_2}$  of 6.6 increases the chances of CoAl<sub>2</sub>O<sub>4</sub> and CoTiO<sub>3</sub> formation from metallic Co according to the thermodynamic predictions. However, as previously mentioned, this process could be kinetically hindered [8,11,29,35–38,41] and may also be dependent on the size of the metallic nanoparticles [10,11,29,38,42], as well as the physical properties of the support (surface area, pore volume and diameter) [39].



$$\frac{(p_{\text{H}_2\text{O}})^v}{(p_{\text{H}_2})^w} = \exp \left\{ \frac{1}{R} \cdot \left( \frac{\Delta G_{rxn}^o(T)}{T^o} - \int_{T^o}^T \frac{\Delta H_{rxn}^o + \int_{T^o}^T \Delta C_{p,rxn}(T) dT}{T^2} dT \right) \right\} \quad \text{Equation 6.5}$$

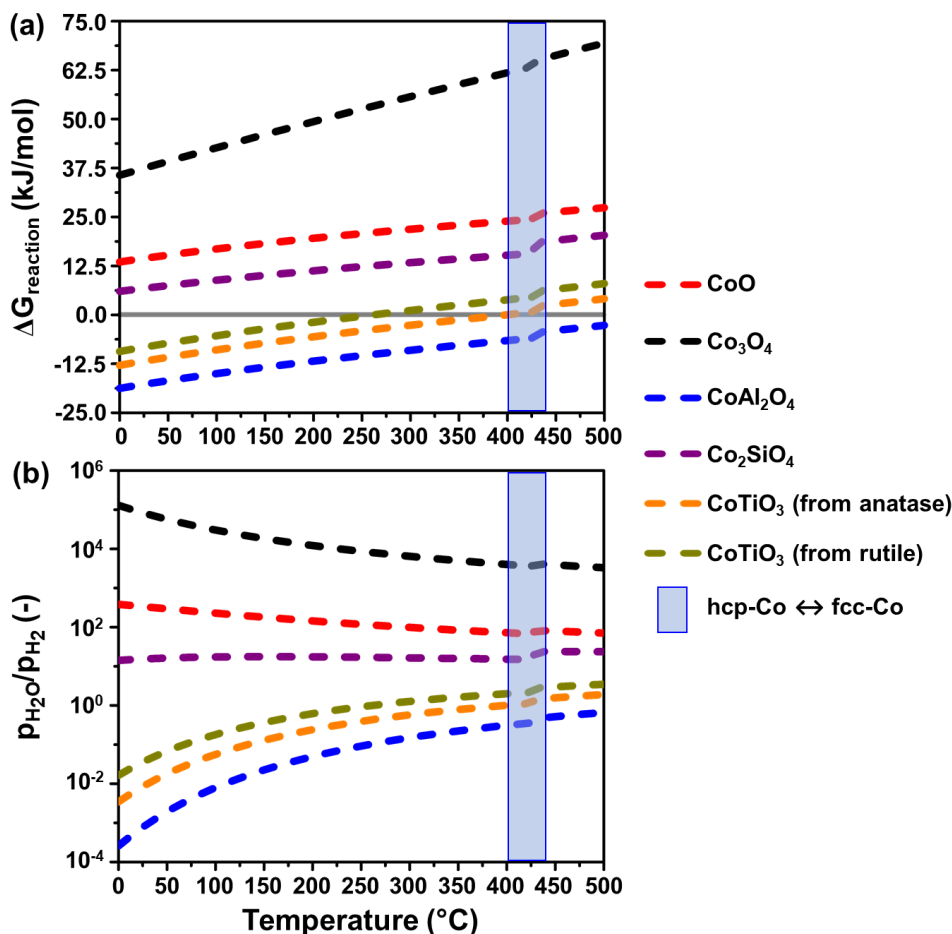


**Figure 6.4:** (a) Changes in the Gibbs free energy, and (b) partial pressure ratio of H<sub>2</sub>O and H<sub>2</sub> (*i.e.*,  $p_{\text{H}_2\text{O}}/p_{\text{H}_2}$ ) as a function of temperature at 1.013 bar during the oxidation of metallic Co forming CoO, Co<sub>3</sub>O<sub>4</sub> or Co-support compounds.

## 6.2. Reduction of Unsupported and Supported Co<sub>3</sub>O<sub>4</sub> in Hydrogen

### 6.2.1. Unsupported Co<sub>3</sub>O<sub>4</sub>

The first reduction experiment was performed in 50% H<sub>2</sub> (with a balance of N<sub>2</sub>) as this is the relative concentration of H<sub>2</sub> in a typical CO-PrOx feed [43–47]. It was also important to first study the reduction of the unsupported material in the absence of any other reducing (*e.g.*, CO) or oxidising gases (*e.g.*, O<sub>2</sub>, H<sub>2</sub>O and CO<sub>2</sub>) as these would mask the sole effect of H<sub>2</sub> on the phase

stability of  $\text{Co}_3\text{O}_4$ . Figure 6.5(a) – (c) shows the PXRD patterns recorded as a function of temperature, as well as the calculated relative concentrations and crystallite sizes of each detected cobalt-based phase, respectively.

$\text{Co}_3\text{O}_4$  reduces at 175 °C mostly into hcp Co but the existence of fcc Co is also observed (Figure 6.5(a) and (b)). Note that the CoO phase is only detected between 195 and 235 °C, which is after forming the initial metallic phase. It is generally reported that the reduction of  $\text{Co}_3\text{O}_4$  proceeds *via* CoO before forming metallic Co. Based on the TEM analysis of this sample (Figure 5.8), a rather wide size distribution of the  $\text{Co}_3\text{O}_4$  particles is present. Therefore, it is possible that the larger particles reduce rapidly and surpass the CoO phase, while the smaller particles reduce *via* CoO, in accordance with previous experimental [4,8,9,11,38] and theoretical evaluations [7]. The size thresholds for the fast and slow reduction processes are not known at this stage. Nonetheless, it can be seen in Figure 6.5(c) that the calculated average crystallite size for fcc Co increases very rapidly between 175 and 215 °C, and end up being larger than the starting  $\text{Co}_3\text{O}_4$  average size.

A closer analysis of the PXRD pattern recorded at 450 °C over a wider  $1/d$  range (0.32 – 1.30  $\text{\AA}^{-1}$ ), displaying more fcc reflections (despite also overlapping with those from hcp Co - see Figure A.5.1), clearly shows evidence of granularity [48,49]. This effect is caused by a very low number of large crystallites of a specific phase in the beam path not allowing for a full refinement. Normally this can be overcome through milling or re-packing of the sample [48,49], but since it is a phase evolving under reaction conditions, this is not a possibility. In the present case, the granularity results in significant uncertainty in the crystallite size of the fcc Co phase. The final size of 150 nm only represents the maximum size allowed in the refinement and does not carry significant physical meaning. However, the presence of granularity in the reduced sample may indicate some level of sintering.

In the experiments involving unsupported  $\text{Co}_3\text{O}_4$  - either discussed in Chapters 7, 8 and 9, or shown in the Appendices section - the presence of granularity in the reduced sample is generally indicated by the large final size of fcc Co (150 nm). On the other hand, the size for hcp Co is between 4 and 8 nm, between 175 and 215 °C, as shown in Figure 6.5(c). Above 215 °C, the amount of hcp Co significantly increases as the amount of CoO decreases, but the size of the hcp crystallites only grows slightly to  $10.1 \pm 0.4$  nm at 450 °C (also see Table A.5.1).

The formation of both hcp and fcc Co when reducing  $\text{Co}_3\text{O}_4$  is common - unsupported or supported [15,50–59]. In a high number of these cases, the two phases are believed to be (partially) intergrown, *i.e.*, both phases existing within the same nanoparticle. A typical hcp atomic layer

stacking is in the form ABABAB along the [001] direction, while a fcc stacking is in the form ABCABCABC along the [111] direction. When the two crystal forms are (partially) intergrown, the stacking can be randomised, resulting in smaller crystallites of hcp Co than those of fcc Co. The resulting PXRD pattern of such a reduced sample typically has a broader hcp Co(1 0 1) reflection at  $0.52 \text{ \AA}^{-1}$  when compared with the hcp Co(1 0 0) and (0 0 2) reflections at  $1/d = 0.46$  and  $0.49 \text{ \AA}^{-1}$  (the latter reflection also coincides with the fcc Co(1 1 1) reflection), respectively [15,51,53–59]. Others have simulated PXRD patterns with different stacking fault probabilities to quantify the degree of intergrowth in experimental patterns [53,55,58,59]. Note that in the refinements performed in this work, no peak broadening of the hcp Co(1 0 1) reflection was observed or corrected for, which may indicate the absence of intergrowth.

Metallic hcp Co crystallites are thermodynamically stable above 20 nm [15,60,61]. However, below 20 nm, the presence of hcp Co is mostly believed to be possible when it is intergrown with fcc Co [15,51,53–59]. The calculated crystallite size of hcp Co during the reduction in a 50:50 H<sub>2</sub>:N<sub>2</sub> mixture is much smaller than 20 nm at all temperatures (Figure 6.5(c)). Therefore, it is also possible that (partially) intergrown particles as well as those with pure hcp or fcc Co, respectively, are present in the reduced sample.

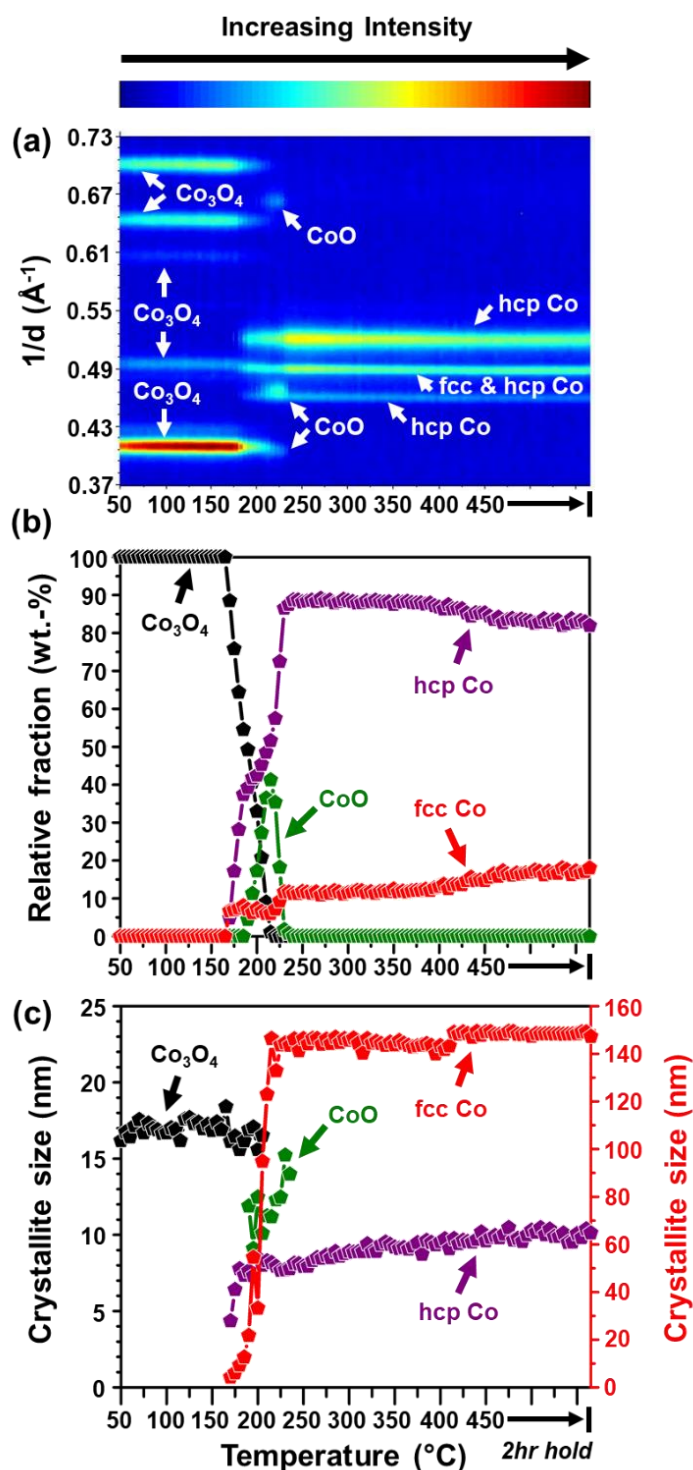


**Figure 6.5:** (a) On-top view of the PXRD patterns (radiation source: Mo  $\text{K}\alpha_1 = 0.7093 \text{ \AA}$ ) recorded as a function of temperature during the reduction of unsupported  $\text{Co}_3\text{O}_4$  at atmospheric pressure in a 50:50  $\text{H}_2:\text{N}_2$  mixture. The reflections in each pattern were assigned using the ICDD PDF-2 entries of  $\text{Co}_3\text{O}_4$ ,  $\text{CoO}$ , hcp Co and fcc Co - see Table A.2.1. (b) Changes in the relative fraction, and (c) average crystallite size of the different cobalt phases formed during the reduction. Refer to the red y-axis on the right of (c) for the crystallite size of fcc Co. However, note that these crystallite sizes may not bear significant physical meaning due to granularity effects and/or intergrowth of hcp and fcc Co.

### 6.2.2. Supported Co<sub>3</sub>O<sub>4</sub>

All prepared supported Co<sub>3</sub>O<sub>4</sub> catalysts were also reduced under the same conditions as the unsupported sample to study the effect each support has on the reducibility of Co<sub>3</sub>O<sub>4</sub>. In the *ex situ* PXRD pattern of Co<sub>3</sub>O<sub>4</sub>/CeO<sub>2</sub> (Figure 5.6), the reflections of Co<sub>3</sub>O<sub>4</sub> were hardly visible. Similarly, the *in situ* PXRD patterns recorded during the reduction of this sample (Figure 6.6(a)) showed no reflections from any Co-based phase. Therefore, for Co<sub>3</sub>O<sub>4</sub>/CeO<sub>2</sub> and bare CeO<sub>2</sub>, conventional H<sub>2</sub>-TPR was performed, and the results are shown in Figure 6.9. The *in situ* PXRD patterns recorded during the reduction of the other supported samples are shown in Figure 6.6. Figure 6.8(a) summarises the range of temperatures in which each cobalt-based phase is observed during the reduction of all un-/supported catalysts. Figures 6.8(b) and (c) show the calculated relative fraction and crystallite size of CoO, hcp and fcc Co, respectively, at the maximum temperature of 450 °C.

In contrast with the unsupported catalyst, the Co<sub>3</sub>O<sub>4</sub> nanoparticles over most of the support materials are ultimately reduced to fcc Co only (see plots in Figure 6.6). Interestingly, metallic Co over TiO<sub>2</sub>-anatase and TiO<sub>2</sub>-P25 is formed in both the hcp and fcc crystal forms, which can be clearly observed in Figures 6.7(a) and (c), despite some overlapping reflections from hcp Co with those from either anatase or rutile. Similar to the unsupported sample, hcp Co is formed in higher amounts than fcc Co in the above-mentioned TiO<sub>2</sub>-supported catalysts (Figure 6.8(b)). The Al<sub>2</sub>O<sub>3</sub>-supported catalyst mostly exhibits CoO reflections between 235 and 450 °C, but the intensity of these reflections decreases above 365 °C. Furthermore, there is a slight broadening of the Al<sub>2</sub>O<sub>3</sub> reflection at  $1/d = 0.51 \text{ \AA}^{-1}$  at these high temperatures, which may be caused by the appearance of the main fcc Co reflection at  $1/d = 0.49 \text{ \AA}^{-1}$  (see Figure 6.6(h)). However, it should be noted that this formed metallic Co could not be reliably quantified using Rietveld refinement possibly due to the extent of the overlap between the fcc Co and Al<sub>2</sub>O<sub>3</sub> reflections, or due to the very low concentration and/or small crystallite size of the metallic phase.

The formation of both hcp and fcc Co in some of the catalysts (*i.e.*, unsupported catalyst, as well as in the TiO<sub>2</sub>-anatase- and TiO<sub>2</sub>-P25-supported catalysts), and the sole formation of fcc Co in the other supported samples is not clearly understood at this stage. Some reports in the literature have also shown the formation of the supported metallic phase as either both hcp and fcc Co formed simultaneously, or only as fcc Co. However, this seems to be independent of supporting and independent of the support material chosen [15,51,53,54,56–58]. It is known that metallic Co is thermodynamically more stable in the fcc form below 20 nm, and more stable in the hcp form

above 20 nm [15,60,61]. However, some researchers have reported the possibility of forming metallic nanoparticles with intergrown domains of hcp and fcc Co. In such cases, fcc Co could be stabilised above 20 nm and hcp Co below 20 nm [53,55,58,59]. Therefore, it is possible that the starting particle/crystallite size distribution of Co<sub>3</sub>O<sub>4</sub> in the present study causes the effect on the final crystallographic structure and average size of the metallic crystallites.

According to Equation 6.6, the final size of metallic Co (assuming either pure hcp or fcc Co) is expected to be approximately 80% of the initial size of Co<sub>3</sub>O<sub>4</sub>. It can be observed that in the SiO<sub>2</sub>-, TiO<sub>2</sub>-anatase- and TiO<sub>2</sub>-P25-supported catalysts, the average size of the fcc Co crystallites is larger than the size of the starting Co<sub>3</sub>O<sub>4</sub> crystallites (compare results in Table 5.1 with those in Figure 6.8(c) and Table A.5.1), which indicates sintering. The hcp Co in the TiO<sub>2</sub>-anatase- and TiO<sub>2</sub>-P25-supported catalysts is present in sizes below 9 nm, which could suggest possible intergrowth of this crystal phase with the large fcc Co crystallites – in accordance with the reported literature [53,55,58,59]. The expected fcc Co sizes from the SiC- and TiO<sub>2</sub>-rutile-supported samples are within the statistical error associated with the average sizes calculated for these catalysts (SiC: expected = 10.6 nm and observed = 12.1 ± 1.3 nm; TiO<sub>2</sub>-rutile: expected = 9.4 nm and observed = 10.6 ± 1.8 nm), suggesting no significant sintering. The fcc Co in the ZrO<sub>2</sub>-supported sample is 7.8 ± 1.0 nm, which is smaller than the expected 12.2 nm (based on the starting Co<sub>3</sub>O<sub>4</sub> size of 15.2 nm). Similarly, the crystallite size of CoO in the Al<sub>2</sub>O<sub>3</sub>-supported catalyst (7.4 ± 0.8 nm) is smaller than the expected size of 12.5 nm (calculated using Equation 6.7 based on the starting Co<sub>3</sub>O<sub>4</sub> size of 13.0 ± 0.4 nm). These lower estimated sizes for the respective supported catalysts may imply the formation of very small crystallites (or crystalline domains) that make up larger fcc Co and CoO particles, respectively [62]. In other words, the crystallite size and particle size (if the latter could be measured using (*quasi*-)in situ TEM) of fcc Co and CoO in the respective catalysts, would possibly not be similar. Further note that the main fcc Co reflection overlaps with the ZrO<sub>2</sub> reflection at 1/d = 0.49 Å<sup>-1</sup>, and this may have also caused the underestimation of the metallic crystallite size.

$$d_{Co} = \sqrt[3]{\frac{3 \cdot \rho_{Co_3O_4} \cdot M_{Co}}{\rho_{Co} \cdot M_{Co_3O_4}}} \cdot d_{Co_3O_4} \approx 0.80 \cdot d_{Co_3O_4} \quad \text{Equation 6.6}$$

$$d_{CoO} = \sqrt[3]{\frac{3 \cdot \rho_{Co_3O_4} \cdot M_{CoO}}{\rho_{CoO} \cdot M_{Co_3O_4}}} \cdot d_{Co_3O_4} \approx 0.96 \cdot d_{Co_3O_4} \quad \text{Equation 6.7}$$

$d_{\text{Co}_3\text{O}_4}$ ,  $d_{\text{CoO}}$  and  $d_{\text{Co}}$  are the crystallite/nanoparticle diameters of  $\text{Co}_3\text{O}_4$ ,  $\text{CoO}$  and metallic  $\text{Co}$ , respectively, assuming spherical shapes.  $\rho_{\text{Co}_3\text{O}_4}$ ,  $\rho_{\text{CoO}}$  and  $\rho_{\text{Co}}$  are the densities and  $M_{\text{Co}_3\text{O}_4}$ ,  $M_{\text{CoO}}$  and  $M_{\text{Co}}$  are the molecular/atomic masses of  $\text{Co}_3\text{O}_4$ ,  $\text{CoO}$  and metallic  $\text{Co}$ , respectively.

The onset formation temperatures of  $\text{CoO}$ , hcp and fcc  $\text{Co}$ , respectively, in the supported catalysts are observed at higher temperatures than in the case of unsupported catalyst (see Figure 6.8(a)). This possibly suggests that supporting  $\text{Co}_3\text{O}_4$  nanoparticles (achieved *via* incipient wetness impregnation) introduces interactions that help stabilise the oxide phase [2,10,14,15,24,25,41,63]. More specifically, this stabilisation could be induced through electronic interactions, which may be slightly strengthening the  $\text{Co-O}$  bonds cobalt oxide and/or slowing down  $\text{H}_2$  adsorption/dissociation, especially at or near the nanoparticle-support interface [20,28,64–66]. The location of (most of) the nanoparticles inside the pores of each support could also delay the onset and/or decrease the extent of reduction as access to the surface of the nanoparticles (to initiate reduction) would be limited [67–70]. It is also possible that the final crystal phase of metallic  $\text{Co}$  (either as intergrown hcp and fcc  $\text{Co}$ , or as pure fcc  $\text{Co}$ ) may also be a result of the nature of the NPSI in the individual supported catalysts.

It can be seen that over  $\text{ZrO}_2$ ,  $\text{SiC}$  and  $\text{SiO}_2$ ; the  $\text{CoO}$  and fcc  $\text{Co}$  are formed at relatively low temperatures (Figure 6.6 and 6.8(a)), which may suggest the presence of weakly bound oxide particles in these samples as also generally reported in the literature [2,25,71–74]. Although the formation of  $\text{CoO}$  and fcc  $\text{Co}$  in the  $\text{TiO}_2$ -supported catalysts is observed at higher temperatures, the  $\text{CoO}$  phase is still completely transformed into metallic  $\text{Co}$  below  $375^\circ\text{C}$ . As mentioned earlier, the reduction of  $\text{Co}_3\text{O}_4/\text{Al}_2\text{O}_3$  possibly forms fcc  $\text{Co}$  above  $365^\circ\text{C}$ , which is inferred from the decreasing intensity of the  $\text{CoO}$  reflections and the broadening of the  $\text{Al}_2\text{O}_3$  reflection at  $1/d = 0.51 \text{ \AA}^{-1}$ . However, there remains a significant amount of  $\text{CoO}$  at  $450^\circ\text{C}$ . This low reducibility of  $\text{CoO}$  over  $\text{Al}_2\text{O}_3$  is generally reported for samples prepared from (incipient) wetness impregnation [2,10,14,15,25,28,63]. The presence of strongly bound oxide nanoparticles is possible, but also some of the  $\text{Co}^{2+}$  species of  $\text{CoO}$  could have migrated into the  $\text{Al}_2\text{O}_3$  lattice, forming  $\text{Co}_x\text{Al}_y\text{O}_z$  species instead. The formation of (bulk)  $\text{CoAl}_2\text{O}_4$  directly from  $\text{Co}_3\text{O}_4$ ,  $\text{CoO}$  and metallic  $\text{Co}$ , respectively, has been predicted in this work to be the most thermodynamically favourable when compared with the formation of  $\text{Co}_2\text{SiO}_4$  and  $\text{CoTiO}_3$  (see Figures 6.2 – 6.4). However, the *in situ* PXRD patterns in Figure 6.6(h) do not show any evidence of a mixed  $\text{Co-Al}$  oxide phase.

It should be noted that the known  $\text{Co-Al}$  oxide phase (*i.e.*,  $\text{CoAl}_2\text{O}_4$ ) has reflections that would overlap with the reflections from the  $\text{Al}_2\text{O}_3$  support and  $\text{Co}_3\text{O}_4$  (Figure 5.6). The overlap would

make it difficult to confirm the presence of this mixed metal oxide using PXRD. It is also possible that this phase formed in amounts and/or crystallite sizes that are below the intrinsic detection limit of the PXRD instrument used, or may have formed as amorphous material. The other possibility may be that these species did not form entirely as some researchers have reported temperatures higher than 450 °C for the formation of cobalt aluminate-like species during H<sub>2</sub> reduction [35–37]. It should be further noted that there exists differences in the starting Co<sub>3</sub>O<sub>4</sub> sizes between the supported catalysts (as confirmed with PXRD and STEM-EELS) which can also influence the onset and degree of reduction, with bigger crystallites (as those in Co<sub>3</sub>O<sub>4</sub>/ZrO<sub>2</sub> – see Tables 5.1 and 5.2, as well as Figure 5.15) being easier to reduce [4,7–9,11,38].

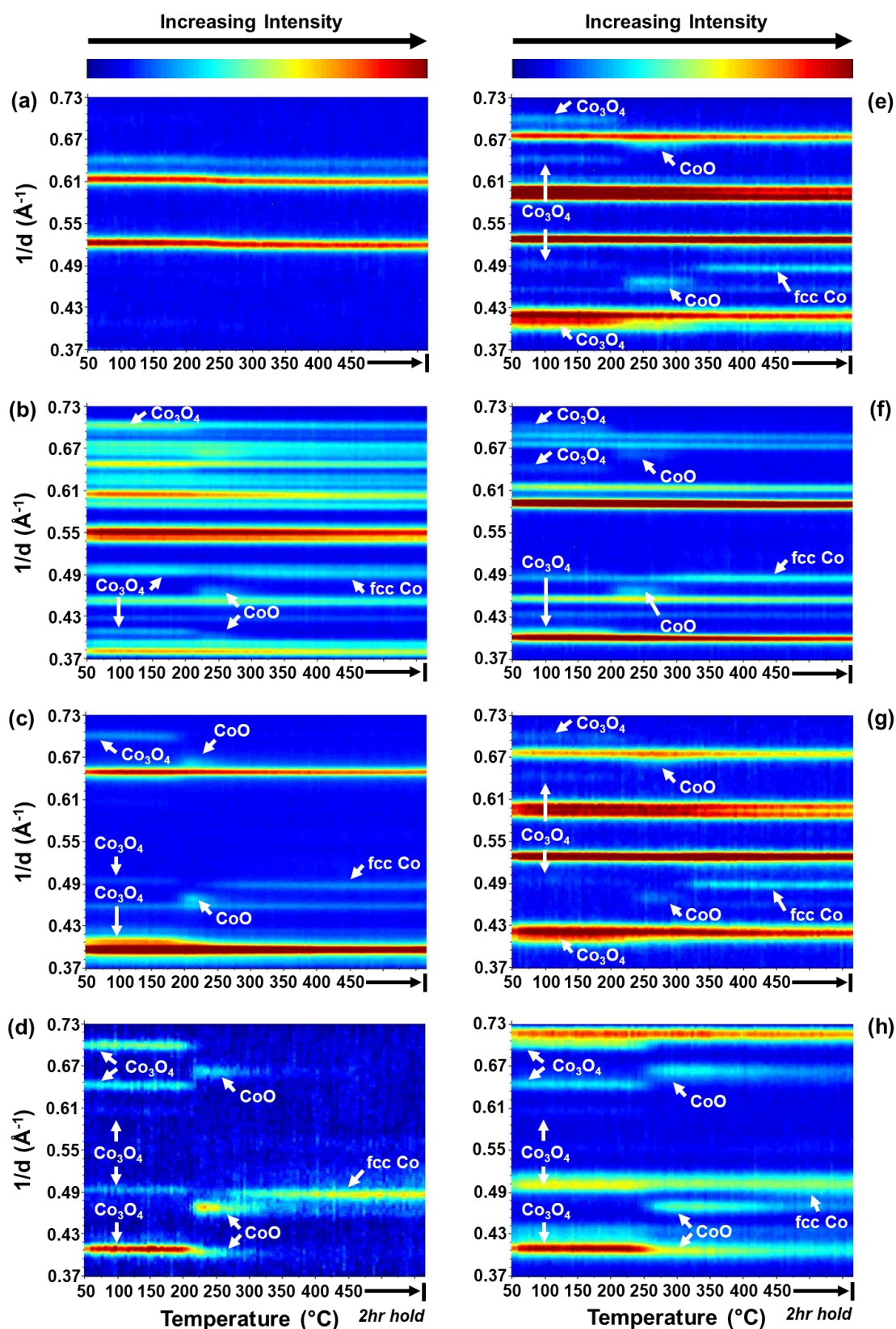


**Figure 6.6:** On-top view of the *in situ* PXRD patterns recorded during the reduction of (a)  $\text{Co}_3\text{O}_4/\text{CeO}_2$ , (b)  $\text{Co}_3\text{O}_4/\text{ZrO}_2$ , (c)  $\text{Co}_3\text{O}_4/\text{SiC}$ , (d)  $\text{Co}_3\text{O}_4/\text{SiO}_2$ , (e)  $\text{Co}_3\text{O}_4/\text{TiO}_2$ -anatase, (f)  $\text{Co}_3\text{O}_4/\text{TiO}_2$ -rutile, (g)  $\text{Co}_3\text{O}_4/\text{TiO}_2$ -P25, and (h)  $\text{Co}_3\text{O}_4/\text{Al}_2\text{O}_3$  at atmospheric pressure in a 50:50  $\text{H}_2/\text{N}_2$  mixture. Note that the patterns recorded for the  $\text{Co}_3\text{O}_4/\text{CeO}_2$  catalyst had no detectable reflections from any Co-based phase.

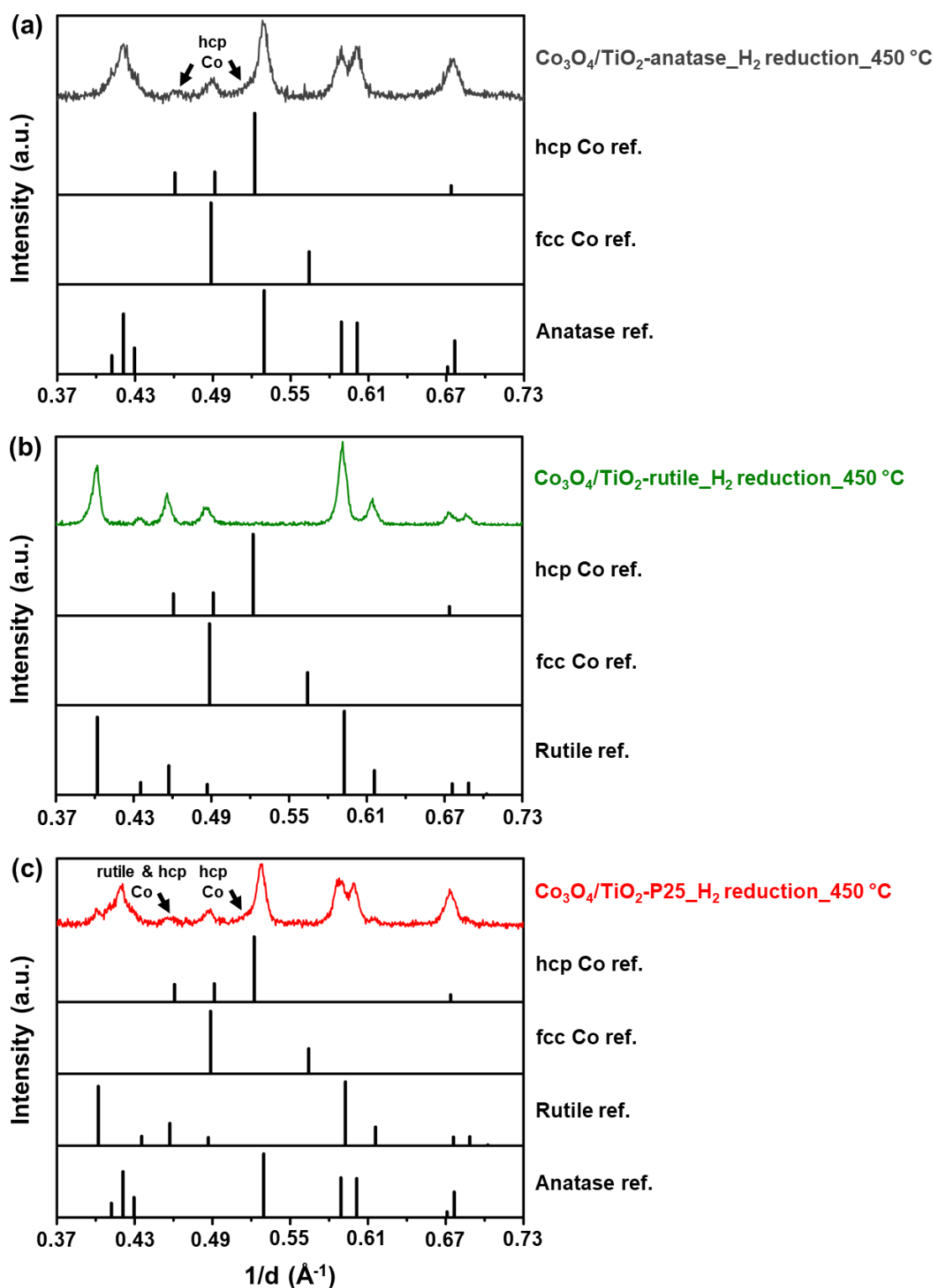


**Figure 6.7:** *In situ* PXRD patterns of (a)  $\text{Co}_3\text{O}_4/\text{TiO}_2$ -anatase, (b)  $\text{Co}_3\text{O}_4/\text{TiO}_2$ -Rutile, and (c)  $\text{Co}_3\text{O}_4/\text{TiO}_2$ -P25 recorded at 450 °C during reduction in a 50:50  $\text{H}_2/\text{N}_2$  mixture at atmospheric pressure. The reference reflection lines of hcp and fcc Co, as well as  $\text{TiO}_2$ -anatase and -rutile are also included (see Table A.2.1 for the ICDD PDF-2 entries of the reference phases). See the black arrows in (a) and (c) indicating hcp Co reflections.

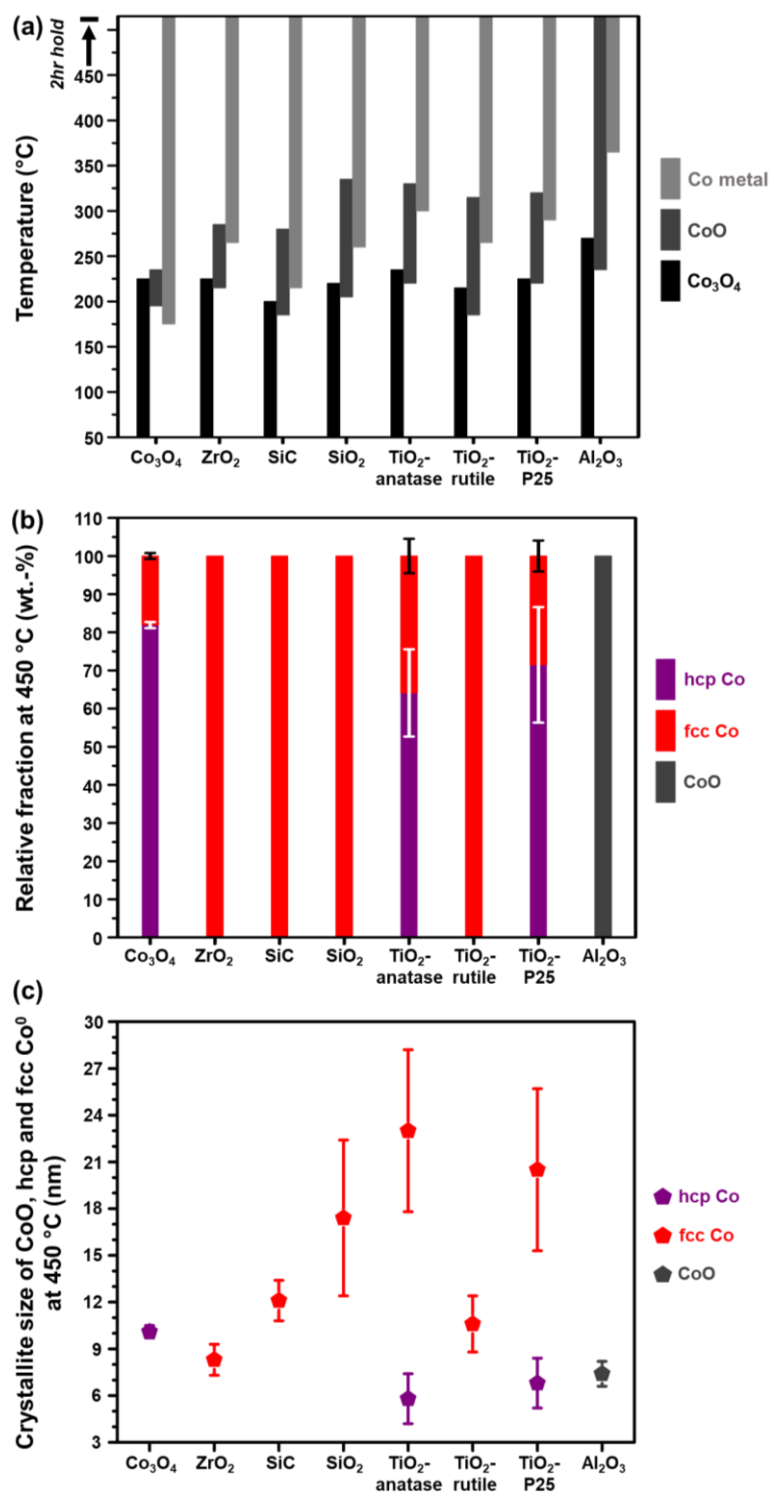


**Figure 6.8:** (a) Temperatures at which the Co-based phases are detected using *in situ* PXRD during the reduction of all un/-supported catalysts at atmospheric pressure in a 50:50 H<sub>2</sub>:N<sub>2</sub> mixture. (b) Relative fraction, and (c) crystallite size of CoO, hcp and fcc Co after reduction at 450 °C. The white and black error bars in (b) are for hcp and fcc Co, respectively. The presence of metallic Co in the Al<sub>2</sub>O<sub>3</sub>-supported catalyst, depicted in (a), is inferred from the decreasing intensity of the CoO reflections above 365 °C in Figure 6.6(h). The size of fcc Co in the unsupported catalyst is not reported in (c) due to possible granularity effects and/or intergrowth of hcp and fcc Co.

As previously mentioned, the reduction of CeO<sub>2</sub>-supported Co<sub>3</sub>O<sub>4</sub> was studied using conventional H<sub>2</sub>-TPR performed under a 5:95 H<sub>2</sub>:Ar gas flow. To better understand the reduction profile obtained for the supported sample, the bare CeO<sub>2</sub> support was also exposed to the aforementioned reduction condition. The TPR profile of the Co<sub>3</sub>O<sub>4</sub>/CeO<sub>2</sub> sample (Figure 6.9) shows three peak maxima below 550 °C and one at 725 °C. The profile for the bare CeO<sub>2</sub> support also has a peak maximum at 725 °C which implies that the reduction taking place in both samples at 725 °C is of bulk CeO<sub>2</sub> to Ce<sub>2</sub>O<sub>3</sub> (cerium(III) oxide) [75–78]. Therefore, the peaks below 550 °C in the TPR profile of Co<sub>3</sub>O<sub>4</sub>/CeO<sub>2</sub> can be attributed to the reduction of Co-bearing species.

The first two low-temperature peaks could be for the formation of CoO and metallic Co, respectively, originating from Co<sub>3</sub>O<sub>4</sub> that is weakly bound to the CeO<sub>2</sub>. The third peak around 400 °C is possibly for the Co species in close contact with the CeO<sub>2</sub> support, probably near the nanoparticle-support interface [76–78]. The peak observed at 475 °C during the reduction of bare CeO<sub>2</sub> can be assigned to the reduction of (sub-)surface CeO<sub>2</sub> species which, in the presence of Co species, reduce at a lower temperature of 400 °C (*i.e.*, the third reduction peak in the TPR profile of Co<sub>3</sub>O<sub>4</sub>/CeO<sub>2</sub>). It has been reported that CoO<sub>1-x</sub> species are capable of H<sub>2</sub> spillover [76–78], which would explain the slight decrease in temperature for the reduction of Co-linked CeO<sub>2</sub> (or possible Co-Ce oxide) species. It is possible that part of the low temperature reduction of (sub-)surface CeO<sub>2</sub> may have also taken place during the PXRD-based reduction (performed between 50 and 450 °C – see Figure 6.6(a)), but was not observed as PXRD is not a surface-sensitive technique and has relatively high detection limits as mentioned earlier.

Table 6.1 summarises the hydrogen consumption and degree of reduction (DoR) calculated for the CeO<sub>2</sub> support and the Co<sub>3</sub>O<sub>4</sub>/CeO<sub>2</sub> catalyst using Equations 6.8 and 6.9 [16], respectively (considering Reactions 6.2 and 6.8). Note when determining the DoR for Co<sub>3</sub>O<sub>4</sub>/CeO<sub>2</sub>, the hydrogen consumption measured between 100 and 550 °C was used as this is the temperature range where the Co-bearing species are assumed to have reduced. It can be seen that increasing the temperature to 920 °C reduces 55.6% of the bare CeO<sub>2</sub> support to Ce<sub>2</sub>O<sub>3</sub>, whereas increasing the temperature to 550 °C reduces approximately 94.3% of the Co<sub>3</sub>O<sub>4</sub> (initially loaded on CeO<sub>2</sub>) to metallic Co. It is possible that the DoR of 94.3% is an over-estimation as some Co-linked CeO<sub>2</sub> species may have also reduced below 550 °C as mentioned earlier. Despite the use of a different technique for studying the reduction of CeO<sub>2</sub>-supported Co<sub>3</sub>O<sub>4</sub>, it is still clear that Co<sub>3</sub>O<sub>4</sub> is more stabilised on CeO<sub>2</sub>, than in the unsupported state, as significantly high temperatures are required for the reduction.

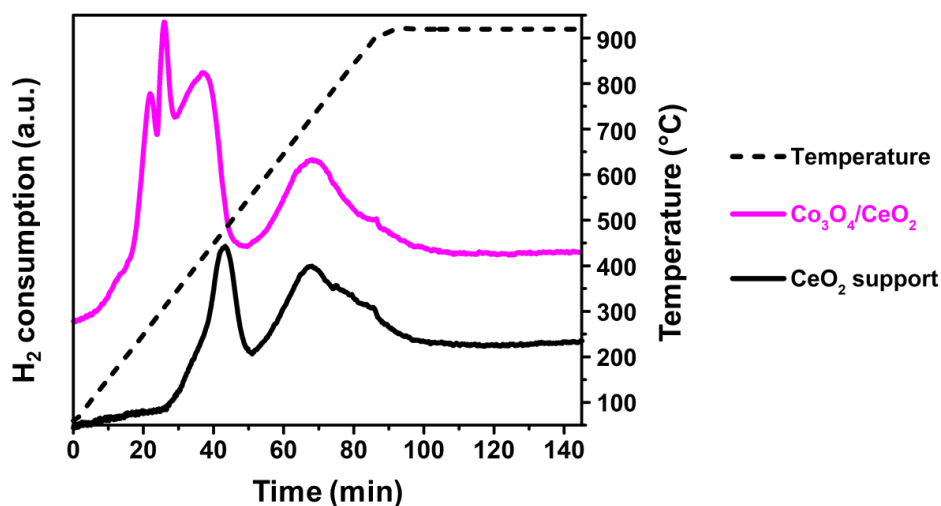


**Figure 6.9:** Reduction profiles of the bare and  $\text{Co}_3\text{O}_4$ -loaded  $\text{CeO}_2$  support material measured during conventional  $\text{H}_2$ -TPR at atmospheric pressure in a 5:95  $\text{H}_2$ :Ar mixture.



$$\text{H}_2 \text{ consumption (mmol)} = 2.8 \cdot 10^{-2} + A_{\text{peak}} \cdot 2.3 \cdot 10^{-1} \quad \text{Equation 6.8}$$

$$\text{Degree of reduction (\%)} = \frac{\text{H}_2 \text{ consumption}}{x \cdot n_{\text{metal oxide loaded}}} \times 100 \quad \text{Equation 6.9}$$

**Table 6.1:** Hydrogen consumption and degree of reduction calculated for the bare  $\text{CeO}_2$  support and  $\text{Co}_3\text{O}_4/\text{CeO}_2$  catalyst during conventional  $\text{H}_2$ -TPR.

Sample name	Hydrogen consumption (mmol)	Degree of reduction (%)
$\text{CeO}_2$ support*	$1.2 \times 10^{-1}$	55.6
$\text{Co}_3\text{O}_4/\text{CeO}_2$ §	$1.6 \times 10^{-1}$	94.3

\*  $\text{H}_2$  consumption and degree of reduction calculated between 325 and 920 °C.

§  $\text{H}_2$  consumption and degree of reduction is for the Co-bearing species assumed to have reduced between 100 and 550 °C.

### 6.3. Summary: Stability of Un-/Supported $\text{Co}_3\text{O}_4$ in Hydrogen-Water Mixtures

The data obtained from the *in situ* reduction studies mainly show that  $\text{Co}_3\text{O}_4$  can be stabilised through the presence of NPSIs introduced during incipient wetness impregnation, followed by drying and calcination. This may further suggest that the supported catalysts would reduce much later than the unsupported sample under CO-PrOx conditions, possibly with the  $\text{Al}_2\text{O}_3$ -supported catalyst being the least reduced. The formation of hcp Co crystallites (intergrown or otherwise) may also be possible under CO-PrOx conditions as some catalysts (such as unsupported  $\text{Co}_3\text{O}_4$ ,  $\text{Co}_3\text{O}_4/\text{TiO}_2$ -anatase,  $\text{Co}_3\text{O}_4/\text{TiO}_2$ -P25) reduced to both the hcp and fcc crystal forms of metallic Co in a 50:50  $\text{H}_2:\text{N}_2$  mixture. However, it remains possible that different gas environments could influence the hcp:fcc ratio, as previously suggested by Sławiński *et al.* [59], who saw a change in this ratio for pre-reduced metallic Co exposed to pure He,  $\text{H}_2$  and CO, respectively, as a function temperature. The reduction experiments also highlighted the possibility of sintering in a  $\text{H}_2$  environment and at elevated temperatures (with a maximum of 450 °C). This can also be expected to have an impact on the activity and selectivity of the CO oxidation reaction under CO-PrOx conditions [79,80].

Thermodynamic calculations predict a higher likelihood for MSC formation in  $\text{H}_2$  directly from  $\text{Co}_3\text{O}_4$ , than from CoO and metallic Co (with the latter involving  $\text{H}_2\text{O}$ ). However, PXRD did not show evidence of such compounds between 50 and 450 °C in any of the supported catalysts. It should again be noted that these species may be present in very small amounts, small crystallite sizes or as amorphous material, which are not detectable using the current PXRD instrument. This might have been the case for the  $\text{Al}_2\text{O}_3$ -supported catalyst which also had some CoO present at 450 °C, indicating the existence of strong interactions between the  $\text{Al}_2\text{O}_3$  and CoO. On the other hand, the  $\text{H}_2$ -TPR profile of the  $\text{CeO}_2$ -supported catalyst suggests the possible reduction of Co-linked  $\text{CeO}_2$  or Co-Ce oxide species at 400 °C, which has also been proposed by other researchers after performing conventional  $\text{H}_2$ -TPR of  $\text{Co}_3\text{O}_4/\text{CeO}_2$  prepared using impregnation [76–78]. These species may have only formed during the reduction process since the XAS analysis of the fresh sample (Figure 5.7) showed  $\text{Co}_3\text{O}_4$  as the only Co-based phase present. Although the  $\text{CeO}_2$  support may be strongly interacting with Co-based species during reduction, this does not seem to hinder the reduction of the cobalt oxide phases as a relatively high DoR was obtained for  $\text{Co}_3\text{O}_4/\text{CeO}_2$  (see Table 6.1).

## References

- [1] Y. Teng, H. Sakurai, A. Ueda, T. Kobayashi, *Int. J. Hydrog. Energy* 24 (1999) 355–358.
- [2] Z. Zhao, M.M. Yung, U.S. Ozkan, *Catal. Commun.* 9 (2008) 1465–1471.
- [3] L. Lukashuk, K. Föttinger, E. Kolar, C. Rameshan, D. Teschner, M. Hävecker, A. Knop-Gericke, N. Yigit, H. Li, E. McDermott, M. Stöger-Pollach, G. Rupprechter, *J. Catal.* 344 (2016) 1–15.
- [4] T.M. Nyathi, N. Fischer, A.P.E. York, M. Claeys, *Faraday Discuss.* 197 (2017) 269–285.
- [5] M. Khasu, T. Nyathi, D.J. Morgan, G.J. Hutchings, M. Claeys, N. Fischer, *Catal. Sci. Technol.* 7 (2017) 4806–4817.
- [6] T.M. Nyathi, N. Fischer, A.P.E. York, D.J. Morgan, G.J. Hutchings, E.K. Gibson, P.P. Wells, C.R.A. Catlow, M. Claeys, *ACS Catal.* 9 (2019) 7166–7178.
- [7] E. van Steen, M. Claeys, M.E. Dry, J. van de Loosdrecht, E.L. Viljoen, J.L. Visagie, *J. Phys. Chem. B* 109 (2005) 3575–3577.
- [8] E.L. Viljoen, E. van Steen, *Catal. Lett.* 133 (2009) 8–13.
- [9] N. Fischer, E. van Steen, M. Claeys, *Catal. Today* 171 (2011) 174–179.
- [10] N.E. Tsakoumis, R.E. Johnsen, W. van Beek, M. Rønning, E. Rytter, A. Holmen, *Chem. Commun.* 52 (2016) 3239–3242.
- [11] M. Wolf, H. Kotzé, N. Fischer, M. Claeys, *Faraday Discuss.* 197 (2017) 243–268.
- [12] A.P. Petersen, R.P. Forbes, S. Govender, P.J. Kooyman, E. van Steen, *Catal. Lett.* 148 (2018) 1215–1227.
- [13] M. Wolf, N. Fischer, M. Claeys, *J. Catal.* 374 (2019) 199–207.
- [14] G. Jacobs, T.K. Das, Y. Zhang, J. Li, G. Racoillet, B.H. Davis, *Appl. Catal. A* 233 (2002) 263–281.
- [15] L.J. Garces, B. Hincapie, R. Zerger, S.L. Suib, *J. Phys. Chem. C* 119 (2015) 5484–5490.
- [16] A.P. Petersen, *Alumina-Modified Cobalt Catalysts for the Fischer-Tropsch Synthesis*, Ph.D. thesis, University of Cape Town, 2018.
- [17] L. Zhong, T. Kropp, W. Baaziz, O. Ersen, D. Teschner, R. Schlögl, M. Mavrikakis, S. Zafeiratos, *ACS Catal.* 9 (2019) 8325–8336.
- [18] N.W. Hurst, S.J. Gentry, A. Jones, B.D. McNicol, *Catal. Rev.* 24 (1982) 233–309.
- [19] T. Ishihara, K. Eguchi, H. Arai, *J. Mol. Catal.* 72 (1992) 253–261.

- [20] B. Delmon, in: G. Ertl, H. Knözinger, J. Weitkamp (Eds.), *Prep. Solid Catal.*, Wiley-VCH Verlag GmbH, Weinheim, Germany, 1999, pp. 541–579.
- [21] A. Khawam, D.R. Flanagan, *J. Phys. Chem. B* 110 (2006) 17315–17328.
- [22] J.W. Niemantsverdriet, in: J.W. Niemantsverdriet (Ed.), *Spectrosc. Catal.*, 3rd ed., Wiley-VCH Verlag GmbH & Co. KGaA, Weinheim, Germany, 2007, pp. 11–38.
- [23] A. Gervasini, in: A. Auroux (Ed.), *Calorim. Therm. Methods Catal.*, Springer-Verlag, Berlin, Heidelberg, 2013, pp. 175–195.
- [24] E. van Steen, G.S. Sewell, R.A. Makhothe, C. Micklethwaite, H. Manstein, M. de Lange, C.T. O'Connor, *J. Catal.* 162 (1996) 220–229.
- [25] C.-B. Wang, C.-W. Tang, H.-C. Tsai, S.-H. Chien, *Catal. Lett.* 107 (2006) 223–230.
- [26] N. Fischer, M. Minnermann, M. Baeumer, E. van Steen, M. Claeys, *Catal. Lett.* 142 (2012) 830–837.
- [27] P. Atkins, J. de Paula, *Atkins' Physical Chemistry 8th Edition*, 8th ed., Oxford University Press, 2009.
- [28] T.W. van Deelen, C. Hernández Mejía, K.P. de Jong, *Nat. Catal.* 2 (2019) 955–970.
- [29] M. Wolf, E.K. Gibson, E.J. Olivier, J.H. Neethling, C.R.A. Catlow, N. Fischer, M. Claeys, *ACS Catal.* 9 (2019) 4902–4918.
- [30] T. Komaya, A.T. Bell, Z. Weng-Sieh, R. Gronsky, F. Engelke, T.S. King, M. Pruski, *J. Catal.* 149 (1994) 142–148.
- [31] T. Komaya, A.T. Bell, Z. Weng-Sieh, R. Gronsky, F. Engelke, T.S. King, M. Pruski, *J. Catal.* 150 (1994) 400–406.
- [32] A.T. Bell, *Science* 299 (2003) 1688–1691.
- [33] V.A. de la Peña O'Shea, M. Consuelo Álvarez Galván, A.E. Platero Prats, J.M. Campos-Martin, J.L.G. Fierro, *Chem. Commun.* 47 (2011) 7131–7133.
- [34] J. Li, Y. Lin, X. Pan, D. Miao, D. Ding, Y. Cui, J. Dong, X. Bao, *ACS Catal.* 9 (2019) 6342–6348.
- [35] A. Moen, D.G. Nicholson, B.S. Clausen, P.L. Hansen, A. Molenbroek, G. Steffensen, *Chem. Mater.* 9 (1997) 1241–1247.
- [36] B. Ernst, A. Bensaddik, L. Hilaire, P. Chaumette, A. Kiennemann, *Catal. Today* 39 (1998) 329–341.
- [37] A. Moen, D.G. Nicholson, M. Rønning, H. Emerich, *J. Mater. Chem.* 8 (1998) 2533–2539.
- [38] M. Wolf, E.K. Gibson, E.J. Olivier, J.H. Neethling, C.R.A. Catlow, N. Fischer, M. Claeys,

- Catal. Today 342 (2020) 71–78.
- [39] A.M. Saib, M. Claeys, E. van Steen, Catal. Today 71 (2002) 395–402.
- [40] P.J. van Berge, J. van de Loosdrecht, S. Barradas, A.M. van der Kraan, Catal. Today 58 (2000) 321–334.
- [41] N.E. Tsakoumis, J.C. Walmsley, M. Rønning, W. van Beek, E. Rytter, A. Holmen, J. Am. Chem. Soc. 139 (2017) 3706–3715.
- [42] N. Fischer, B. Clapham, T. Feltes, E. van Steen, M. Claeys, Angew. Chemie - Int. Ed. 53 (2014) 1342–1345.
- [43] T.V. Choudhary, D.W. Goodman, Catal. Today 77 (2002) 65–78.
- [44] A. Faur Ghenciu, Curr. Opin. Solid State Mater. Sci. 6 (2002) 389–399.
- [45] S. Huang, K. Hara, A. Fukuoka, Energy Environ. Sci. 2 (2009) 1060–1068.
- [46] E.D. Park, D. Lee, H.C. Lee, Catal. Today 139 (2009) 280–290.
- [47] A. Mishra, R. Prasad, Bull. Chem. React. Eng. Catal. 6 (2011) 1–14.
- [48] G.W. Brindley, London, Edinburgh, Dublin Philos. Mag. J. Sci. 36 (1945) 347–369.
- [49] C.R. Gonzalez, Acta Crystallogr. Sect. A Found. Crystallogr. 43 (1987) 769–774.
- [50] O.S. Edwards, H. Lipson, Proc. R. Soc. London. Ser. A. Math. Phys. Sci. 180 (1942) 268–277.
- [51] T.W. van Deelen, H. Yoshida, R. Oord, J. Zečević, B.M. Weckhuysen, K.P. de Jong, Appl. Catal. A Gen. 593 (2020) 117441.
- [52] A.J.C. Wilson, Proc. R. Soc. London. Ser. A. Math. Phys. Sci. 180 (1942) 277–285.
- [53] O. Ducreux, B. Rebours, J. Lynch, M. Roy-Auberger, D. Bazin, Oil Gas Sci. Technol. 64 (2009) 49–62.
- [54] M.M. Hauman, A. Saib, D.J. Moodley, E. du Plessis, M. Claeys, E. van Steen, ChemCatChem 4 (2012) 1411–1419.
- [55] A. Longo, L. Sciortino, F. Giannici, A. Martorana, J. Appl. Crystallogr. 47 (2014) 1562–1568.
- [56] K.H. Cats, B.M. Weckhuysen, ChemCatChem 8 (2016) 1531–1542.
- [57] H.E. du Plessis, J.P.R. de Villiers, A. Tuling, E.J. Olivier, Phys. Chem. Chem. Phys. 18 (2016) 30183–30188.
- [58] S.W.T. Price, D.J. Martin, A.D. Parsons, W.A. Sławiński, A. Vamvakeros, S.J. Keylock, A.M. Beale, J.F.W. Mosselmans, Sci. Adv. 3 (2017) e1602838.

- [59] W.A. Sławiński, E. Zacharaki, H. Fjellvåg, A.O. Sjøstad, *Cryst. Growth Des.* 18 (2018) 2316–2325.
- [60] E. Klugmann, H.J. Blythe, F. Walz, *Phys. Status Solidi* 146 (1994) 803–813.
- [61] S. Ram, *Mater. Sci. Eng. A* 304–306 (2001) 923–927.
- [62] C. Weidenthaler, *Nanoscale* 3 (2011) 792–810.
- [63] S. Storsæter, Ø. Borg, E.A. Blekkan, A. Holmen, *J. Catal.* 231 (2005) 405–419.
- [64] J.M. Herrmann, *J. Catal.* 89 (1984) 404–412.
- [65] W.E. Kaden, T. Wu, W.A. Kunkel, S.L. Anderson, *Science* 326 (2009) 826–829.
- [66] A. Bruix, J.A. Rodriguez, P.J. Ramírez, S.D. Senanayake, J. Evans, J.B. Park, D. Stacchiola, P. Liu, J. Hrbek, F. Illas, *J. Am. Chem. Soc.* 134 (2012) 8968–8974.
- [67] A.A. Adesina, *Appl. Catal. A* 138 (1996) 345–367.
- [68] C. Perego, P. Villa, *Catal. Today* 34 (1997) 281–305.
- [69] E. Marceau, X. Carrier, M. Che, O. Clause, C. Marcilly, in: G. Ertl, H. Knözinger, F. Schüth, J. Weitkamp (Eds.), *Handb. Heterog. Catal.*, Wiley-VCH Verlag GmbH & Co. KGaA, Weinheim, Germany, 2008, pp. 467–484.
- [70] P. Munnik, P.E. de Jongh, K.P. de Jong, *Chem. Rev.* 115 (2015) 6687–6718.
- [71] P. Nguyen, C. Pham, *Appl. Catal. A* 391 (2011) 443–454.
- [72] A.R. de la Osa, A. De Lucas, J. Díaz-Maroto, A. Romero, J.L. Valverde, P. Sánchez., *Catal. Today* 187 (2012) 173–182.
- [73] G.R. Johnson, A.T. Bell, *J. Catal.* 338 (2016) 250–264.
- [74] J. Labuschagne, R. Meyer, Z.H. Chonco, J.M. Botha, D.J. Moodley, *Catal. Today* 275 (2016) 2–10.
- [75] H.C. Yao, Y.F. Yu Yao, *J. Catal.* 86 (1984) 254–265.
- [76] L. Wang, H. Liu, Y. Chen, S. Yang, *Int. J. Hydrog. Energy* 42 (2017) 3682–3689.
- [77] L. Wang, H. Liu, *Catal. Today* 316 (2018) 155–161.
- [78] Y. Cao, X. Peng, Z. Tan, Y. Liu, X. Wang, W. Zhao, L. Jiang, *Ind. Eng. Chem. Res.* 58 (2019) 17692–17698.
- [79] A. Martínez-Arias, A.B. Hungría, G. Munuera, D. Gamarra, *Appl. Catal. B* 65 (2006) 207–216.
- [80] G. Marbán, I. López, T. Valdés-Solís, *Appl. Catal. A* 361 (2009) 160–169.



# Chapter 7: Thermodynamic Calculations and Experimental Evaluation of CO-PrOx and Side Reactions

## 7.1. Thermodynamic Calculations on Gas-Phase Reaction Equilibria

The other significant aspect of the current work is to study the individual reactions that have been said to be possible during CO-PrOx, other than just CO oxidation. These have been discussed in detail in section 2.3. By means of thermodynamic calculations, the individual reactions were evaluated to observe the conditions of temperature (at 1.013 bar) where they are feasible (Figure 7.1). As an added step, the equilibrium conversion ( $X_{eq.}$ ) of the limiting reactant of each reaction was also calculated (Figures 7.2, 7.3 and 7.4) using the general equation, Equation 7.1. Note that the  $X_{eq.}$  at a specific temperature (at 1.013 bar) serves as the maximum conversion that can be realised during a reaction when performed experimentally. To complement the outcomes of these calculations, each reaction was carried out to also investigate the temperatures where they take place and to identify the phase of cobalt (*i.e.*,  $\text{Co}_3\text{O}_4$ ,  $\text{CoO}$  or metallic  $\text{Co}$ ) responsible for the occurrence of each reaction. Therefore, the experimental work was coupled with *in situ* PXRD for monitoring the phase of the catalyst, and the results are discussed in section 7.2.

$$\frac{(p_Y)^y \cdot (p_Z)^z}{(p_V)^v \cdot (p_W)^w} = \exp \left\{ -\frac{1}{R} \cdot \left( \frac{\Delta G_{rxn}^o(T)}{T^o} - \int_{T^o}^T \frac{\Delta H_{rxn}^o + \int_{T^o}^T \Delta C_{p,rxn}(T) dT}{T^2} dT \right) \right\} \quad \text{Equation 7.1}$$

The reactions of interest are represented by Reactions 7.1 to 7.5, and these are: 7.1) CO oxidation, 7.2) H<sub>2</sub> oxidation, 7.3) the forward and reverse water-gas shift reaction, 7.4) CO methanation and 7.5) CO<sub>2</sub> methanation. Figure 7.1 shows the change in the Gibbs free energy of each reaction as a function of temperature. All oxidation and methanation reactions, as well as the forward water-gas shift are thermodynamically favourable between 0 and 500 °C. Therefore, in principle, one can expect these reactions to take place in a typical CO-PrOx feed having CO, O<sub>2</sub>, CO<sub>2</sub>, H<sub>2</sub>O and H<sub>2</sub>. The reverse water-gas shift remains unfavourable under these temperature conditions. It should be noted again that kinetic information is not incorporated into these calculations. Furthermore, the presence of a catalyst may still favour one or a few of these reactions at certain temperatures. This can also depend on the chemical phase of the catalyst at the different temperatures.

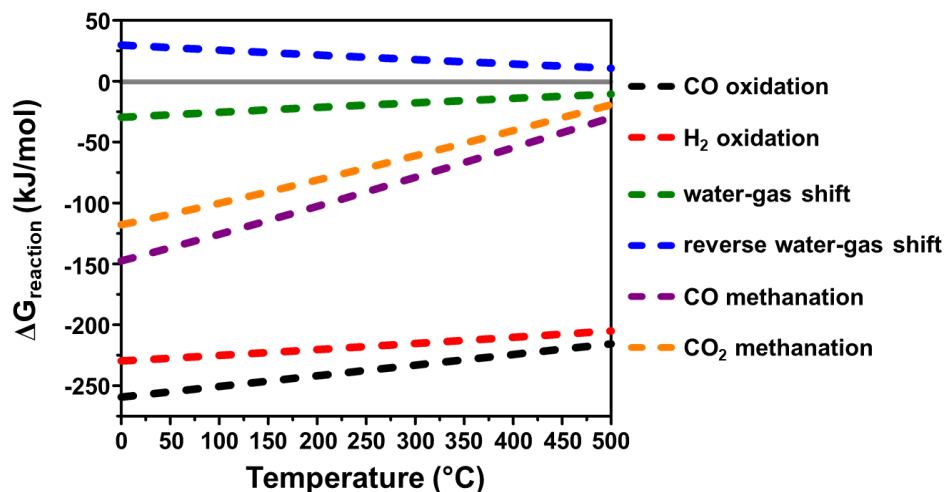
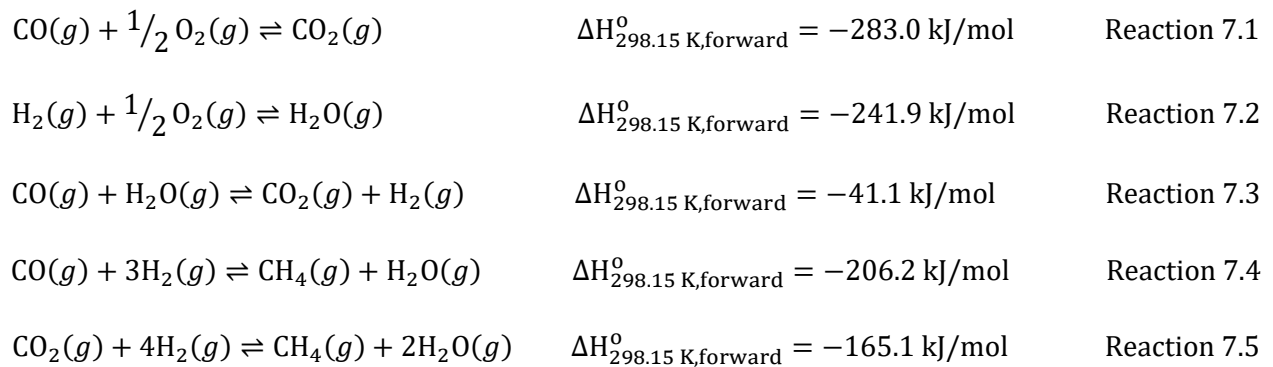


**Figure 7.1:** Changes in the Gibbs free energy as a function of temperature at 1.013 bar during the various individual reactions possible under CO-PrOx conditions.

The forward reactions represented in Reactions 7.1 to 7.5 are all exothermic, which suggests that increasing the reaction temperature would, in principle, negatively affect their equilibrium conversions ( $X_{eq}$ ). It should also be noted that the spontaneity (or  $\Delta G$ ) of a reaction at any given temperature has a significant influence on the  $X_{eq}$ . For these calculations, a CO-PrOx feed containing 1% CO, 1% O<sub>2</sub>, 10% CO<sub>2</sub>, 10% H<sub>2</sub>O, 50% H<sub>2</sub> and a balance of N<sub>2</sub>, was assumed. This is similar to the experimental feed used to study the combined effect of H<sub>2</sub>, H<sub>2</sub>O and CO<sub>2</sub> during CO-PrOx (*i.e.*, “Wet CO-PrOx with co fed CO<sub>2</sub>” - see Table 4.5 and sub-section 9.2.4.). However, Reactions 7.1 to 7.5 were considered individually, and the effect of the other feed gases was ignored as this will be discussed in section 9.1. For example, when calculating the  $X_{eq}$  of CO in CO oxidation, a feed containing 1% CO, 1% O<sub>2</sub> and 98% N<sub>2</sub> was assumed. This way, the effect of CO<sub>2</sub>, H<sub>2</sub>O and H<sub>2</sub> is ignored. Also note that Reactions 7.1 to 7.5 are written in their stoichiometric form, however, the typical CO-PrOx feed assumed has partial pressure ratios of the reactants that do not match the stoichiometric ratios. Therefore, for comparison, values of  $X_{eq}$  assuming stoichiometric ratios were also calculated. Again, using CO oxidation as an example, a stoichiometric feed of 1% CO, 0.5% O<sub>2</sub> and 98.5% N<sub>2</sub> was assumed.

The plots in Figure 7.2 show the equilibrium conversions of the limiting reactants CO (in CO oxidation – Reaction 7.1) and O<sub>2</sub> (in H<sub>2</sub> oxidation – Reaction 7.2), respectively, assuming both a non-stoichiometric and a stoichiometric feed. It can be observed that both non-stoichiometric feeds result in 100% conversion of the respective limiting reactants. This is mostly due to their very low  $\Delta G$  at all temperatures (see Figure 7.1), which results in very high equilibrium constants ( $K_{eq}$ ). Calculating the  $X_{eq}$  assuming a stoichiometric feed in each case results in conversions greater than 99.9%. This means that the ratio of the reactants involved in CO and H<sub>2</sub> oxidation, respectively, has no significant effect on the equilibrium conversion. Furthermore, it can be expected that both CO and H<sub>2</sub> oxidation are reactions highly likely to take place during CO-PrOx. During experimental CO-PrOx conditions, the H<sub>2</sub> is known compete with CO for O<sub>2</sub> which decreases the selectivity towards CO<sub>2</sub> formation [1–5].

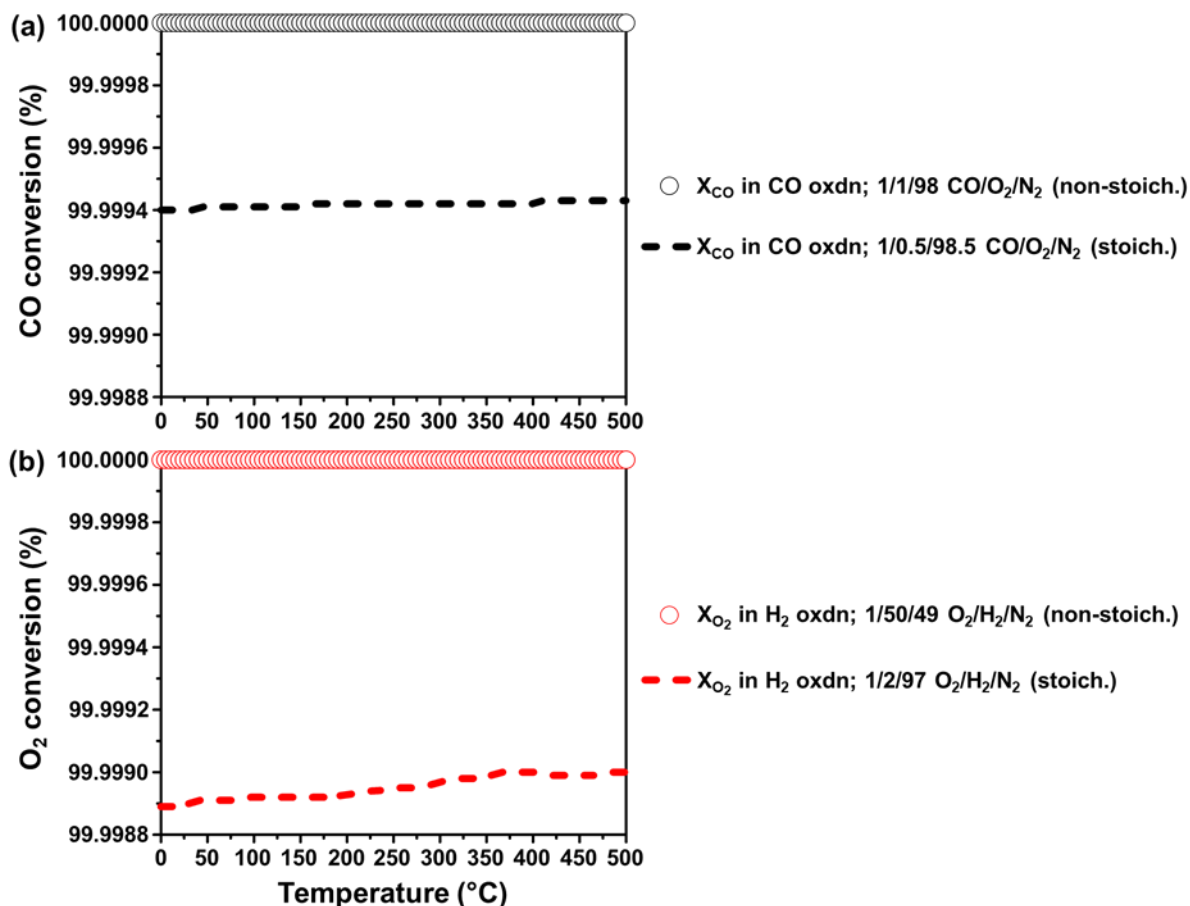


**Figure 7.2:** Changes in the equilibrium conversions of (a) CO, and (b) O<sub>2</sub> as a function of temperature at 1.013 bar during CO oxidation and H<sub>2</sub> oxidation, respectively. Note that these were calculated assuming different CO:O<sub>2</sub> and O<sub>2</sub>:H<sub>2</sub> feed ratios, respectively, as indicated on the plots.

The other reactions that can possibly take place during CO-PrOx are the forward and reverse water-gas shift (WGS) reactions (both represented by Reaction 7.3). For the forward WGS, a feed composing of 1% CO, 10% H<sub>2</sub>O and 89% N<sub>2</sub> was assumed, and for the reverse WGS, a feed with 10% CO<sub>2</sub>, 50% H<sub>2</sub> and 40% N<sub>2</sub> was assumed. Stoichiometric ratios of the reactants were also considered by appropriately decreasing the assumed concentration of the reactant in excess (*i.e.*, H<sub>2</sub>O in the forward WGS, and H<sub>2</sub> in the reverse WGS). The equilibrium conversion of CO in the forward reaction reaches a minimum of 98.0% at 500 °C in a non-stoichiometric feed, and a minimum of 69.6% in a stoichiometric feed at the same temperature, as shown in Figure 7.3. Also, the decrease in the equilibrium conversion with increasing temperature is consistent with the exothermic nature of the reaction. Similarly, the endothermic nature of the reverse reaction leads to an increase in the equilibrium conversion of CO<sub>2</sub> with temperature. The maximum CO<sub>2</sub>

conversion level that can be achieved using a non-stoichiometric feed is 58.9% at 500 °C, while from a stoichiometric feed, a maximum conversion level of 30.4% can be realised at the same temperature.

In agreement with the results in Figure 7.1, the forward WGS reaction is predicted to be more favoured as higher conversions of the CO are possible especially when using a non-stoichiometric feed, which represents a typical CO:H<sub>2</sub>O feed ratio for CO-PrOx. Unlike the other side reactions, the forward WGS converts the unwanted CO to CO<sub>2</sub> and forms the H<sub>2</sub> required for producing electrical energy in a fuel cell. It should be noted that thermodynamically, the presence of CO<sub>2</sub> and H<sub>2</sub> in the CO-PrOx feed can potentially decrease the conversion of CO that can be realised *via* the forward WGS, and this has been considered in section 9.1., as well as experimentally in sub-section 9.2.4.

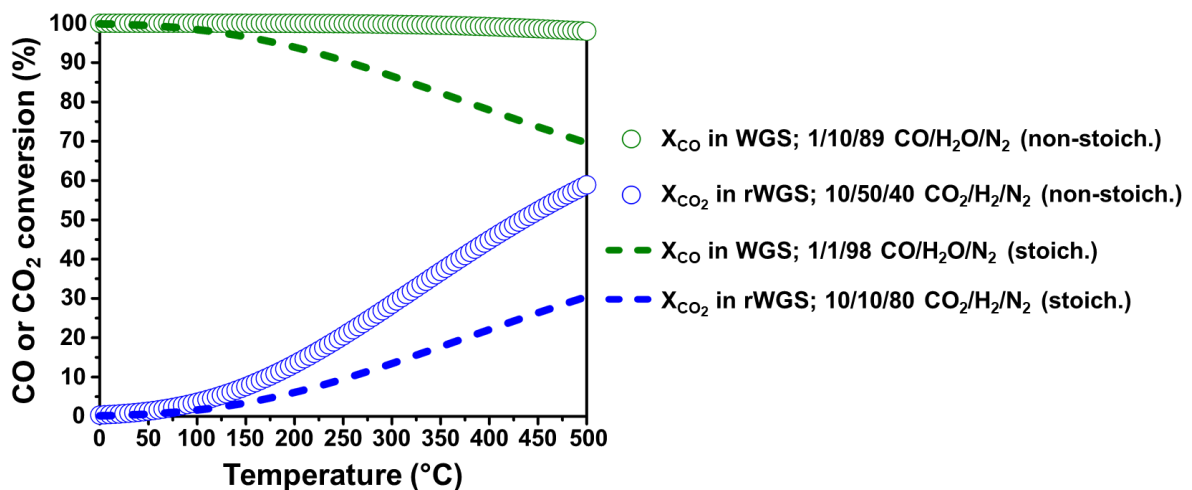


**Figure 7.3:** Changes in the equilibrium conversions of CO and CO<sub>2</sub> as a function of temperature at 1.013 bar during the forward and reverse WGS reaction, respectively. Note that these were calculated assuming different CO:H<sub>2</sub>O and CO<sub>2</sub>:H<sub>2</sub> feed ratios, respectively, as indicated on the plots.

Finally, the other possible reactions are the hydrogenation of CO and CO<sub>2</sub>, respectively, to form CH<sub>4</sub> (Reactions 7.4 and 7.5). In fact, a well reported alternative to CO-PrOx is called Selective Methanation (see section 1.2.) which aims to decrease the CO content in the reformat gas using H<sub>2</sub> [6–9]. However, the presence of CO<sub>2</sub> in the feed can affect the progress of the CO hydrogenation as it can also react with H<sub>2</sub>. (Note that the reaction of CO<sub>2</sub> with H<sub>2</sub> to form CH<sub>4</sub> is in addition to

the reverse WGS reaction considered earlier). Therefore, Selective Methanation is generally less preferred over CO-PrOx as it involves the conversion of relatively high amounts of the valuable H<sub>2</sub> [6,8–10].

Nonetheless, depending on the reaction temperatures reached and the catalyst used, the undesired formation of CH<sub>4</sub> from CO or CO<sub>2</sub> can take place under realistic CO-PrOx conditions. The non-stoichiometric feed of 1% CO, 50% H<sub>2</sub> and 49% N<sub>2</sub> was considered for CO methanation, while a feed with 10% CO<sub>2</sub>, 50% H<sub>2</sub> and 40% N<sub>2</sub> was considered for CO<sub>2</sub> methanation. For comparison, stoichiometric feeds were also considered by appropriately decreasing the assumed concentration of the reactant in excess (*i.e.*, H<sub>2</sub> in both hydrogenation reactions). Figure 7.4 shows the calculated equilibrium conversions of CO and CO<sub>2</sub>, respectively, during methanation as a function of temperature. Owing to the exothermic nature of these two reactions, the conversion of CO and CO<sub>2</sub> decreases as the temperature is increased. The minimum CO conversion at 500 °C in a non-stoichiometric feed is 99.9%, while in a stoichiometric feed the minimum is 27.8% at the same temperature. On the other hand, the minimum CO<sub>2</sub> conversion from a non-stoichiometric feed is 72.2%, while in a stoichiometric feed the conversion decreases slightly to 58.5% at 500 °C. Note that the significant difference in the CO conversion between the non-stoichiometric and stoichiometric feed is a result of the high drop in the H<sub>2</sub> feed concentration from 50 to 3%.

In conclusion, it can be expected that both CO and CO<sub>2</sub> methanation could take place during CO-PrOx, with CO methanation being more thermodynamically favoured (assuming a non-stoichiometric feed – see Figure 7.1). However, as previously mentioned, the choice of catalyst and feed composition can still affect the preference of one reaction over the other at certain temperatures. Furthermore, some literature has reported the possibility of forming CH<sub>4</sub> from a feed with CO<sub>2</sub> and H<sub>2</sub> *via* the reverse WGS reaction to produce CO, which could be subsequently hydrogenated to CH<sub>4</sub> *in situ* [11–13]. Therefore, the reverse WGS could potentially affect the overall formation of CH<sub>4</sub> under realistic CO-PrOx conditions.

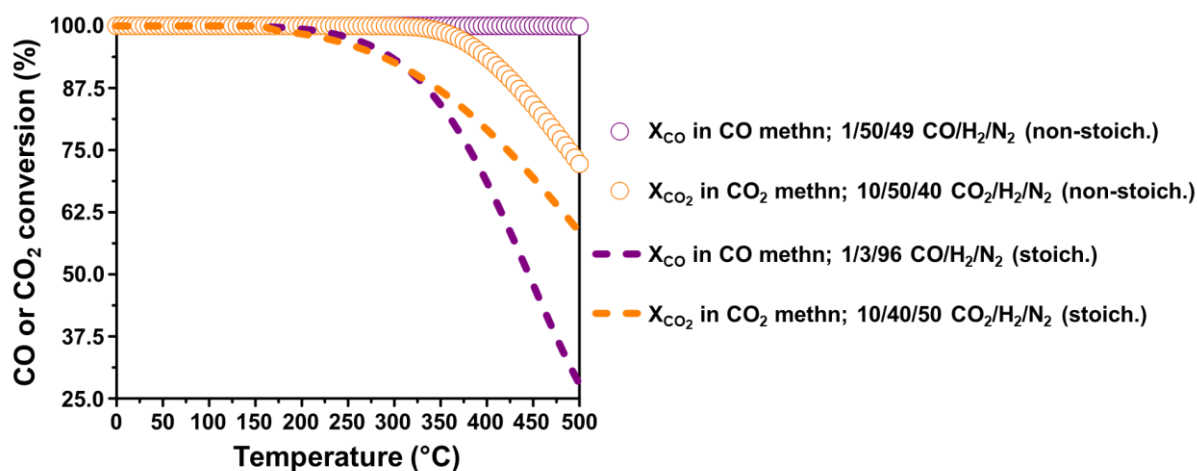


**Figure 7.4:** Changes in the equilibrium conversions of CO and CO<sub>2</sub>, respectively, as a function of temperature at 1.013 bar during methanation. Note that these were calculated assuming different CO:H<sub>2</sub> and CO<sub>2</sub>:H<sub>2</sub> feed ratios, respectively, as indicated on the plots.

Section 7.2. discusses the experimental results from after carrying out the individual side reactions of CO-PrOx (*i.e.*, excluding CO oxidation as this is appropriately discussed in sub-section 9.2.1.). The reaction temperature was varied between 50 to 450 °C in the in-house developed *in situ* PXRD capillary reaction cell, during which, gas products were analysed and PXRD patterns were recorded. Shown in Table 7.1 are the equilibrium conversions of the limiting reactants calculated at 450 °C assuming a non-stoichiometric and stoichiometric feed, respectively. The equilibrium conversions obtained using a non-stoichiometric feed will be compared with those obtained from the experiments discussed in section 7.2. at the same temperature.

**Table 7.1:** Summary of the calculated equilibrium conversions at 450 °C of the limiting reactants of each gas-phase reaction considered in the thermodynamic evaluation.

Chemical Reaction	Equilibrium Conversion (%) at 450 °C	
	Non-stoichiometric	Stoichiometric
	Feed	Feed
X <sub>O<sub>2</sub></sub> in H <sub>2</sub> oxidation	100.0	100.0
X <sub>CO</sub> in water-gas shift	98.6	73.7
X <sub>CO<sub>2</sub></sub> in reverse water-gas shift	52.3	26.4
X <sub>CO</sub> in CO methanation	100.0	47.9
X <sub>CO<sub>2</sub></sub> in CO <sub>2</sub> methanation	84.1	69.4

## 7.2. Reduction of Unsupported Co<sub>3</sub>O<sub>4</sub> under Different Gas Environments

### 7.2.1. Reduction under co-fed H<sub>2</sub> and CO

Following from the experiment discussed in sub-section 6.2.1., the reduction of unsupported Co<sub>3</sub>O<sub>4</sub> was also performed in the presence of co-fed 50% H<sub>2</sub> and 1% CO, since CO is typically present in small amounts in the CO-PrOx feed (*i.e.*, 0.5 – 2%, see section 1.2.) [1–5]. In contrast with the *in situ* experiment discussed in sub-section 6.2.1., the experiments discussed from sub-section 7.2.1. to 7.2.4. were all coupled with GC-TCD analysis of the effluent gas stream of the PXRD capillary reactor. The *in situ* PXRD patterns and the results from the gas product analysis are shown in Figures 7.5(a) and (b), respectively, for the H<sub>2</sub>-CO reduction experiment. However, a summary of the main results from the *in situ* PXRD analysis for all performed reduction experiments (discussed in sub-section 6.2.1., and section 7.2.) can be found in Figure 7.10 and in Table A.5.2. Also note that the gas composition used in each reduction experiment discussed from sub-section 7.2.1. to 7.2.4. is presented in Table 4.4, and that these experiments were also performed at a constant GHSV of 40000 ml(NTP)/g<sub>Co<sub>3</sub>O<sub>4</sub></sub>/hr.

Despite both CO and H<sub>2</sub> being reducing gases, it is only the H<sub>2</sub> that carries out the reduction of the oxide catalyst during CO-PrOx due to its typically high concentration (40 – 75%) in the feed [14–19]. The CO is less likely to reduce the catalyst as there is generally similar or excess amounts of O<sub>2</sub> co-fed during CO-PrOx to ensure complete conversion of the CO to CO<sub>2</sub>. However, in the experiment to be discussed, 1% CO was co-fed with 50% H<sub>2</sub> (and 49% N<sub>2</sub>) in the absence of any oxidising gases. Therefore, CO can be expected to influence the reduction of Co<sub>3</sub>O<sub>4</sub> leading to metallic Co.

From the PXRD analysis, CoO formation is first observed at 200 °C and then followed by the formation of fcc and hcp Co at 225 °C. Similar to the case with no co-fed CO, the amount of hcp Co at 450 °C is significantly higher than that of fcc Co, but at a 3:1 ratio instead of a 4.5:1 ratio (compare the full refinement results in Figures 6.5(b) and 7.5(b), as well as in the summary Figure 7.10(b)). Sławiński *et al.* [20] also showed that different gas environments can alter the hcp:fcc Co ratio and the degree of intergrowth as a function of temperature when they studied a pre-reduced cobalt catalyst under pure He, H<sub>2</sub> and CO, respectively. However, at this stage, the effect of changing the gas environment on the hcp:fcc Co ratio is still not clear. The broadening of the hcp Co(1 0 1) reflection was not corrected for in any way when performing Rietveld refinement, but the formation of nanoparticles with (partial) intergrowth and those with the pure hcp or fcc Co phase, respectively, remains a possibility. The results from the Rietveld refinement (Figure A.5.2 and Table A.5.2) also show that the hcp Co possibly exists as small crystallites (below 6 nm) and the fcc Co as very large crystallites (up to a size of 150 nm). Again, this very large size indicates the existence of granularity and possible sintering, either of pure fcc Co particles and/or particles with intergrown domains of fcc and hcp Co.

In comparison with the case with no co-fed CO (Figure 6.5), the reduction profile in Figure 7.5 follows the commonly reported transitions, *i.e.*, Co<sub>3</sub>O<sub>4</sub> → CoO → Co<sup>0</sup>. It should be noted that CO generally binds more strongly than H<sub>2</sub> on most surfaces at low temperatures [16,21–24] and therefore, it is possible that the conversion of Co<sub>3</sub>O<sub>4</sub> to CoO may have been driven by the CO. The formation of metallic Co from CoO may have then involved the H<sub>2</sub>. The reduction of Co<sub>3</sub>O<sub>4</sub> was also carried out in a 1:99 CO:N<sub>2</sub> mixture (*i.e.*, in the absence of H<sub>2</sub>) and the recorded patterns are shown in Figure A.5.3. These results support the argument being made about the involvement of H<sub>2</sub> in the formation of Co<sup>0</sup> since the onset formation temperature of Co<sup>0</sup> is at 300 °C in the absence of H<sub>2</sub>, which is higher than the 225 °C observed in the case with co-fed H<sub>2</sub> (Figure 7.5). Furthermore, the onset formation temperature for the CoO phase in both experiments is at 200 °C, implying that this transformation was unaffected by the presence of H<sub>2</sub>.

In terms of the gas product analysis, co-feeding CO and H<sub>2</sub> can result in CH<sub>4</sub> formation (Reaction 7.4), which was indeed the case as shown in Figure 7.5(c). The formation of CH<sub>4</sub> is known to be catalysed by metallic Co and it can be observed that high amounts of CH<sub>4</sub> are obtained over the temperature range where metallic Co is present [16–19,25,26]. However, it can also be seen that low amounts of CH<sub>4</sub> already form at 200 °C, which is lower than the temperature at which metallic Co is first observed (*i.e.*, 225 °C). Therefore, it is possible that low amounts of Co<sup>0</sup> (undetectable in PXRD) may have formed at 200 °C, resulting in the activation of CO and H<sub>2</sub>, followed by CH<sub>4</sub> formation. This consumption of dissociated hydrogen hinders the earlier reduction of the oxide, as was observed in the absence of CO (Figure 6.5(a)). Only when the dissociation rates increase with increasing temperature, the reduction of the cobalt phases proceeds. Although the extent of sintering of the fcc Co crystallites cannot be determined due to granularity effects (Figure A.5.2), this may have resulted in the slight decrease in CH<sub>4</sub> formation at 450 °C. Also note that hcp Co is known to be more active for CO activation and hydrogenation than fcc Co [27–29]. Therefore, the continued decrease in the amount of hcp Co from 250 to 450 °C (Figure 7.5(b)) may have also led to the eventual slight decrease in CH<sub>4</sub> formation at 450 °C.

The hydrogenation of CO to CH<sub>4</sub> is a highly exothermic reaction and when assuming a 1:50:49 CO:H<sub>2</sub>:N<sub>2</sub> feed ratio, equilibrium CO conversions above 99.9% are predicted to be possible between 0 and 500 °C (Figure 7.4). However, the experimental results obtained show that the high CO conversions are mostly possible when the cobalt is in the metallic form and when the temperature is above 275 °C, which reveals the importance of the kinetic aspects of the methanation reaction.

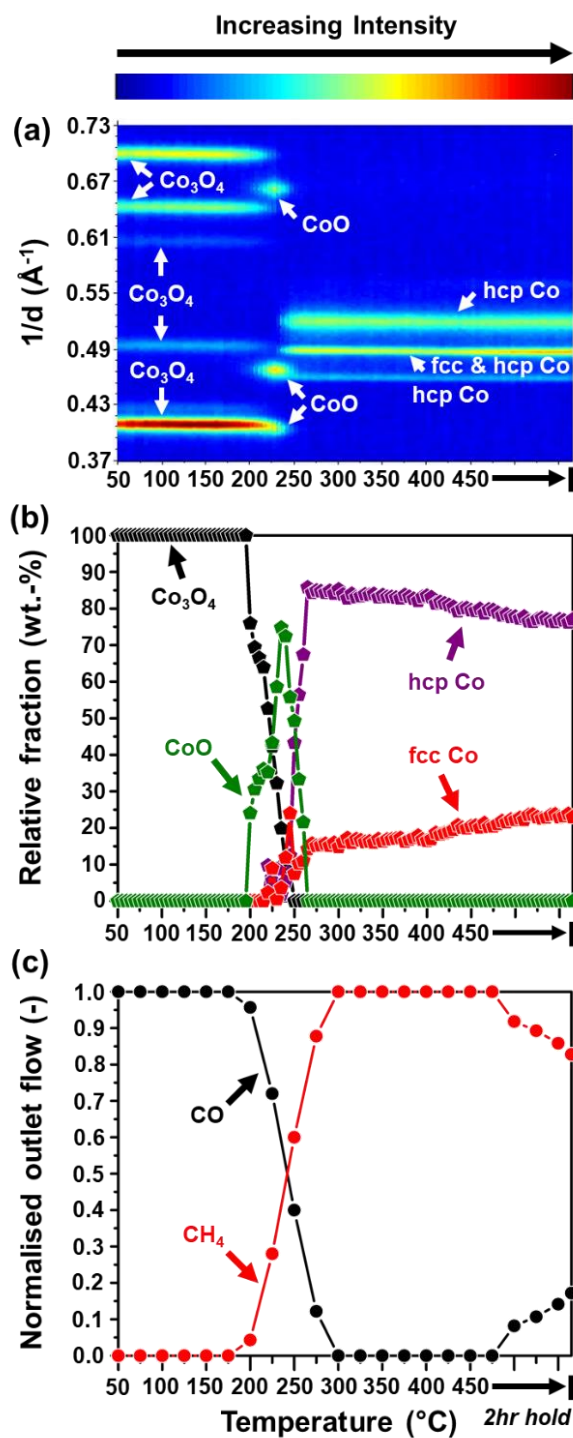


**Figure 7.5:** (a) On-top view of the recorded *in situ* PXRD patterns, and (b) changes in the relative fraction of the different cobalt phases formed during the reduction of unsupported  $\text{Co}_3\text{O}_4$  at atmospheric pressure in a 1:50:49  $\text{CO}:\text{H}_2:\text{N}_2$  mixture. (c) Changes in the normalised outlet flow rates of CO and  $\text{CH}_4$  calculated from GC-TCD data.

## 7.2.2. Reduction under co-fed H<sub>2</sub> and O<sub>2</sub>

The reaction between H<sub>2</sub> and O<sub>2</sub> (Reaction 7.2) is the main competing reaction during CO-PrOx as it can decrease the available O<sub>2</sub> for CO oxidation. Even though excess amounts of O<sub>2</sub> (relative to CO) are often fed during CO-PrOx, the H<sub>2</sub> is always present in much higher concentrations than both CO and O<sub>2</sub> (see section 1.2.) [1–5]. The high concentration of H<sub>2</sub> together with increasing reaction temperature, can kinetically favour H<sub>2</sub> oxidation over CO oxidation. Figure 7.6(a) and (b) show the results from the *in situ* PXRD and gas product analysis, respectively, when 50% H<sub>2</sub> and 1% O<sub>2</sub> were co-fed in the absence of CO.

The reduction of Co<sub>3</sub>O<sub>4</sub> in the 1:50:49 O<sub>2</sub>:H<sub>2</sub>:N<sub>2</sub> mixture results in the simultaneous formation of CoO, hcp and fcc Co crystallites at 200 °C (Figure 7.6(a)). This is similar to the case where only H<sub>2</sub> was fed (see Figure 6.5(a)), which resulted in a fraction of the Co<sub>3</sub>O<sub>4</sub> crystallites forming metallic Co directly, and others going through the CoO phase, possibly due to crystallite/particle size variations within the starting Co<sub>3</sub>O<sub>4</sub> sample [17,30–34]. However, it is worth pointing out that the CoO phase is stabilised between 200 and 275 °C, which is a wider temperature window than that observed for the case with H<sub>2</sub> only (195 and 235 °C, Figure 6.5(a)), and the case with co-fed H<sub>2</sub> and CO (200 and 250 °C, Figure 7.5(a)). This is also depicted in the results summary in Figure 7.10(a). The higher stabilisation of the CoO could be a thermodynamic effect caused by the increasing amounts of the product H<sub>2</sub>O with increasing temperature (Figure 7.6(b)) [35–41].

Also note that the onset temperature for Co<sub>3</sub>O<sub>4</sub> reduction (*i.e.*, 200 °C) coincides with the temperature at which approximately 100% of the O<sub>2</sub> has been converted. This may further indicate that H<sub>2</sub> oxidation, similar to CO oxidation, possibly proceeds *via* the Mars-van Krevelen (MvK) mechanism over the Co<sub>3</sub>O<sub>4</sub> phase [16–19,42] (see details on the MvK mechanism in sub-section 2.1.2.). When there are still significant amounts of unconverted O<sub>2</sub> available, this is enough to keep the catalyst (re-)oxidised. However, when very high O<sub>2</sub> conversions are reached (as from 200 °C), the Co<sub>3</sub>O<sub>4</sub> is left vulnerable to reduction by H<sub>2</sub>. The H<sub>2</sub> oxidation reaction continues after the first onset of reduction, and at temperatures where only metallic Co exists (*i.e.*, above 275 °C). At this stage, it is unclear as to whether both CoO and metallic Co carry out H<sub>2</sub> oxidation between 200 and 275 °C. Further on this, the details of the mechanism by which this reaction takes place over CoO and/or metallic Co are also unclear. Nonetheless, the very high O<sub>2</sub> conversions are in good agreement with the predicted equilibrium conversions (Figure 7.2(b)), especially above 200 °C. Below 200 °C, relatively low O<sub>2</sub> conversions are achieved experimentally due to a kinetic

hindrance caused by the low temperatures and/or the low activity of the catalyst. However, it is important to note that the temperature at which complete oxidation of  $\text{H}_2$  to  $\text{H}_2\text{O}$  achieved by the unsupported catalyst is still much lower than the reported temperature for the non-catalytic combustion of  $\text{H}_2$  in air, which is  $560\text{ }^\circ\text{C}$  [43].

Interestingly, the hcp:fcc Co ratio is 2.6 at  $450\text{ }^\circ\text{C}$  (see Figure 7.10(b) and Table A.5.2), which is slightly below the ratio observed in the reduction with co-fed CO and  $\text{H}_2$  (*i.e.*, a ratio of 3). This may be a consequence of the different gas environment chosen or the changing partial pressures of the gases fed and subsequently formed during the reduction [20].

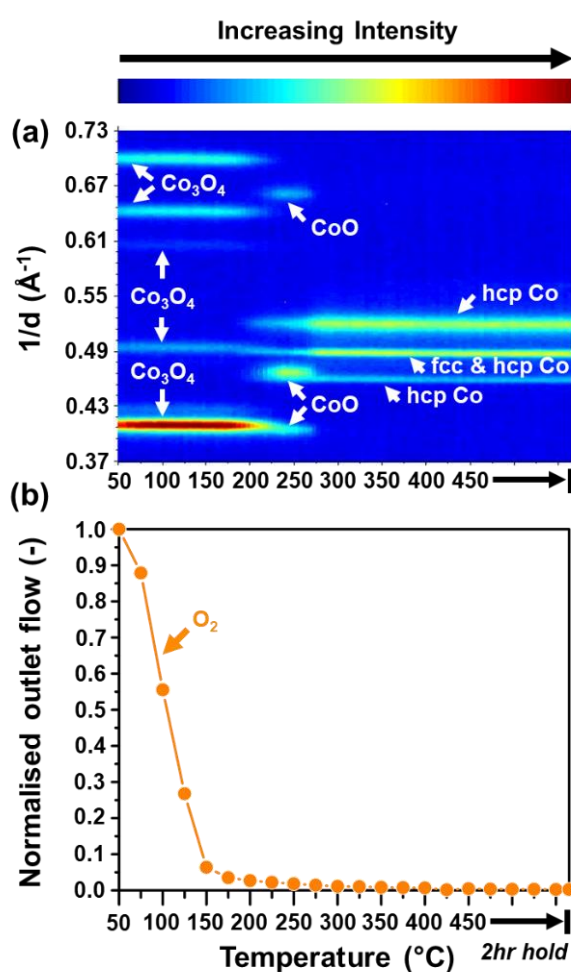


**Figure 7.6:** (a) On-top view of the *in situ* PXRD patterns recorded during the reduction of unsupported  $\text{Co}_3\text{O}_4$  at atmospheric pressure in a 1:50:49  $\text{O}_2$ : $\text{H}_2$ : $\text{N}_2$  mixture. (b) Changes in the normalised outlet flow rate of  $\text{O}_2$  calculated from GC-TCD data.

### 7.2.3. Reduction under co-fed H<sub>2</sub> and H<sub>2</sub>O or co-fed H<sub>2</sub> and CO<sub>2</sub>

The gases O<sub>2</sub>, H<sub>2</sub>O and CO<sub>2</sub> are well known oxidising agents. However, H<sub>2</sub>O (~10%) and CO<sub>2</sub> (10 – 25%) are generally present in higher amounts in the CO-PrOx feed relative to O<sub>2</sub> (0.5 – 4%) [1–5]. Therefore, to compare their oxidising or oxide-stabilising effects, 1% H<sub>2</sub>O and 1% CO<sub>2</sub>, respectively, were first fed with H<sub>2</sub> to reduce Co<sub>3</sub>O<sub>4</sub>, as was done with O<sub>2</sub> (see sub-section 7.2.2.). Note that the experiment involving H<sub>2</sub>O was started at 100 °C to avoid condensation along the catalyst bed (see sub-section 4.4.2.2.).

In a 1:50 H<sub>2</sub>O:H<sub>2</sub> mixture, the Co<sub>3</sub>O<sub>4</sub> nanoparticles reduce *via* CoO at 190 °C before forming metallic Co at 235 °C (Figure 7.7(a), and the summary in Figure 8(a)), while in a 1:50 CO<sub>2</sub>:H<sub>2</sub> mixture, some Co<sub>3</sub>O<sub>4</sub> nanoparticles reduce directly to metallic Co at 185 °C and the others reduce *via* CoO at 200 °C (Figure 7.7(b) and summary in Figure 7.10(a)). The reduction behaviour in the 1:50 CO<sub>2</sub>:H<sub>2</sub> mixture is similar to that observed during reduction in the absence of CO<sub>2</sub> (Figure 6.5(a) and summary in Figure 7.10(a)). These observations confirm that CO<sub>2</sub> is a milder oxidising agent, which hardly provides any stabilisation of the oxidic phase [21,36,44]. At 260 °C, there's complete disappearance of CoO in the 1:50 H<sub>2</sub>O:H<sub>2</sub> mixture (Figure 7.7(a)), while in the 1:50 O<sub>2</sub>:H<sub>2</sub> mixture, full CoO conversion is observed at 275 °C (Figure 7.6(b)). These results show that O<sub>2</sub> stabilises the oxide phase longer and is also a stronger oxidising agent than H<sub>2</sub>O (and CO<sub>2</sub>), in accordance with the literature [22,45,46]. This may further suggest that O<sub>2</sub> is the easiest to activate to allow for the release of oxygen species, while CO<sub>2</sub> is the hardest to activate [21,22,36,44–46]. The hcp:fcc Co ratio, when either 1% CO<sub>2</sub> or 1% H<sub>2</sub>O was co-fed with H<sub>2</sub>, is 2.6 and 2.5, respectively, at 450 °C, which is similar to the case with 1% co-fed O<sub>2</sub> (compare results in Figure 7.10(b) and Table A.5.2).

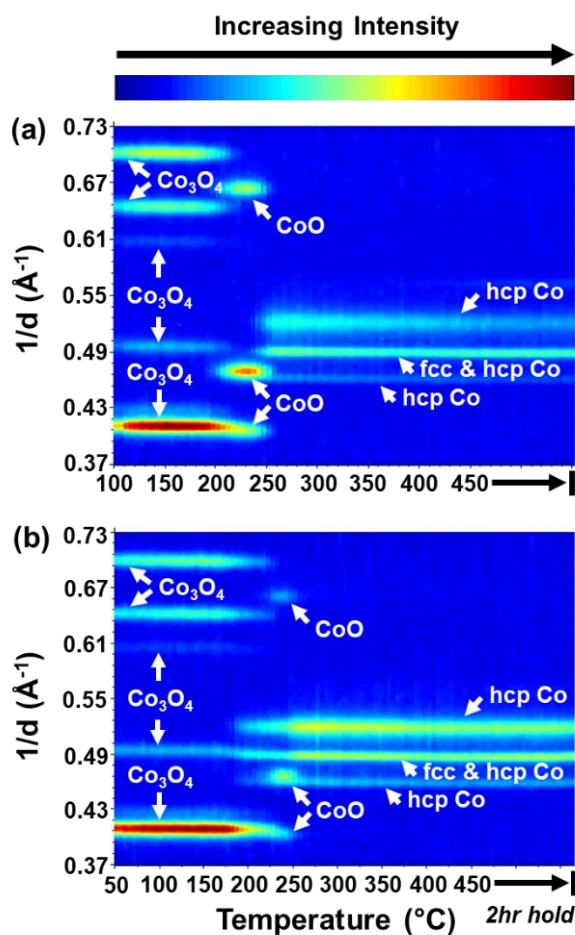


**Figure 7.7:** On-top view of the *in situ* PXRD patterns recorded during the reduction of unsupported  $\text{Co}_3\text{O}_4$  at atmospheric pressure in a (a) 1:50:49  $\text{H}_2\text{O}:\text{H}_2:\text{N}_2$ , and a (b) 1:50:49  $\text{CO}_2:\text{H}_2:\text{N}_2$  gas mixture, respectively.

The following conditions investigated involved feeding 10%  $\text{H}_2\text{O}$  with 50%  $\text{H}_2$ , as well as 10%  $\text{CO}_2$  with 50%  $\text{H}_2$ , respectively, as these concentrations are closer to those found in a typical CO-PrOx feed (see section 1.2.) [1–5]. In the presence of 10%  $\text{H}_2\text{O}$ , the onset formation temperatures for  $\text{CoO}$  and metallic  $\text{Co}$  are at higher temperatures (Figure 7.8(a)) than in the case without  $\text{H}_2\text{O}$  (Figure 6.5(a)) and the case with 1%  $\text{H}_2\text{O}$  (Figure 7.7(a)). This is also depicted in the results summarised in Figure 7.10(a). The delayed reduction may be attributed to the competitive adsorption of the higher amounts of  $\text{H}_2\text{O}$  (*i.e.*, a kinetic effect) and/or the oxidising nature of  $\text{H}_2\text{O}$  (*i.e.*, a thermodynamic effect) [35–41]. Nonetheless, the  $\text{Co}_3\text{O}_4$  appears to be fully reduced to metallic  $\text{Co}$  at 450  $^{\circ}\text{C}$ .

Hydrogen was also co-fed with 10%  $\text{CO}_2$  to investigate its effect on the phase stability of  $\text{Co}_3\text{O}_4$  and the reactions it may be involved in with  $\text{H}_2$ . As shown in Figure 7.8(b),  $\text{Co}_3\text{O}_4$  reduces to  $\text{CoO}$ ,

hcp and fcc Co crystallites at 200 °C and the CoO phase remains stable until 290 °C. Note that even at a concentration of 10%, H<sub>2</sub>O is still a stronger oxidising agent as it stabilises the CoO phase between 190 and 300 °C, while metallic Co is only first observed at 265 °C (see Figure 7.8(a) and the summary in Figure 7.10(a)). The presence of 10% H<sub>2</sub>O or CO<sub>2</sub> during reduction did not cause a significant change to the relative amounts of hcp and fcc Co at 450 °C, as these were similar to the amounts observed when feeding a 1% concentration of each gas (Figure 7.10(b) and Table A.5.2).

The gases CO<sub>2</sub> and H<sub>2</sub> can part-take in two chemical reactions, *viz.*, the reverse water-gas shift (WGS) (the reverse of Reaction 7.3), and CO<sub>2</sub> methanation (Reaction 7.5). Some researchers have reported that the formation of CH<sub>4</sub> from CO<sub>2</sub> and H<sub>2</sub> may proceed *via* the reverse WGS reaction, followed by the *in situ* hydrogenation of CO [11–13]. However, due to the current experimental design, the mechanistic details of the CO<sub>2</sub> methanation reaction cannot be reported. The results from the GC analysis in Figure 7.8(c) show CH<sub>4</sub> formation just above 200 °C, which coincides with the formation of metallic Co. Above 300 °C, the reverse WGS sets in as the amounts of CO increase, while CH<sub>4</sub> formation decreases. At 450 °C, the yield of CO is 40.2% (based on the conversion of CO<sub>2</sub>), while the yield of CH<sub>4</sub> is 46.1% (also based on the conversion of CO<sub>2</sub>). It is worth noting that these experimentally-observed yields are below the predicted equilibrium yields of the individual reactions (reverse WGS: 52.3% and CO<sub>2</sub> methanation: 84.1% (Table 7.1)), when considering a feed with 10:50:40 CO<sub>2</sub>:H<sub>2</sub>:N<sub>2</sub>. Furthermore, it is worth noting that both reactions are catalysed by metallic Co, similar to CO methanation (Figure 7.5).

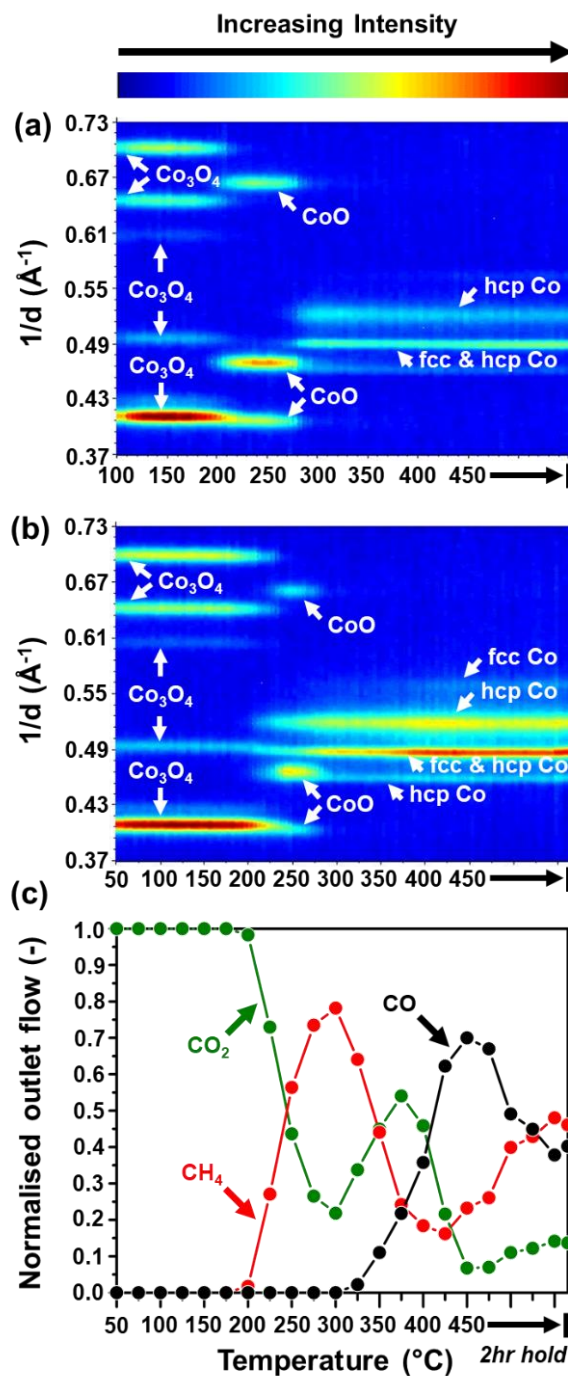


**Figure 7.8:** On-top view of the *in situ* PXRD patterns recorded during the reduction of unsupported Co<sub>3</sub>O<sub>4</sub> at atmospheric pressure in a (a) 10:50:40 H<sub>2</sub>O:H<sub>2</sub>:N<sub>2</sub>, and a (b) 10:50:40 CO<sub>2</sub>:H<sub>2</sub>:N<sub>2</sub> mixture, respectively. (c) Changes in the normalised outlet flow rates of CO<sub>2</sub>, CH<sub>4</sub> and CO calculated from GC-TCD data during the reduction in 10:50:40 CO<sub>2</sub>:H<sub>2</sub>:N<sub>2</sub>.

### 7.2.4. Reduction under co-fed CO and H<sub>2</sub>O

The last phase stability study involved feeding 1% CO and 10% H<sub>2</sub>O in a balance of N<sub>2</sub> to perform the forward WGS reaction (Reaction 7.3), which produces H<sub>2</sub> and CO<sub>2</sub>. Interestingly, the product analysis shows the formation of CO<sub>2</sub> (below 30% yield, based on the CO conversion) from 160 °C but without any H<sub>2</sub> formation (Figure 7.9(b)). H<sub>2</sub> is first observed above 250 °C and increases to a yield of about 80% (also based on the conversion of CO) before decreasing. At 350 °C, the H<sub>2</sub> yield increases again and stabilises close to 100% until 450 °C. This was also in agreement with the calculated equilibrium H<sub>2</sub> yield (equivalent to the CO conversion in this case) of 98.6% at 450 °C, when considering a feed with 1:10:89 CO:H<sub>2</sub>O:N<sub>2</sub> (see Table 7.1). Note that the absence of H<sub>2</sub> between 160 and 260 °C, and the drop in the H<sub>2</sub> yield between 300 and 360 °C, both coincide with the formation of CoO and metallic Co, respectively (Figure 7.9(a) and (b)). In other words, the observed CO<sub>2</sub> within the temperature ranges mentioned, originates from the reduction of Co<sub>3</sub>O<sub>4</sub> and CoO, respectively, and not from the forward WGS reaction.

Note that the amount of unsupported Co<sub>3</sub>O<sub>4</sub> loaded in the capillary reactor was 15 mg and for the reduction of Co<sub>3</sub>O<sub>4</sub> to CoO, the theoretical amount of CO required or CO<sub>2</sub> that would be produced as a consequence is  $6.23 \times 10^{-2}$  mmol. For the reduction of CoO to metallic Co, the theoretical amount is  $1.87 \times 10^{-1}$  mmol of CO<sub>2</sub>. Between 160 and 260 °C (the temperature window for the reduction of Co<sub>3</sub>O<sub>4</sub> to CoO), the amount of CO<sub>2</sub> measured is  $8.13 \times 10^{-2}$  mmol. Even though H<sub>2</sub> is formed between 300 and 360 °C, the outlet CO<sub>2</sub>:H<sub>2</sub> ratio is greater than 1. Therefore, the excess CO<sub>2</sub> can be associated with the observed reduction of CoO to Co (note: measured total amount of CO<sub>2</sub> is  $2.01 \times 10^{-1}$  mmol between 300 and 360 °C). The slight discrepancies between the theoretical and experimental values could be a result of an over-estimation of the amounts of CO<sub>2</sub> detected by the GC within the temperature ranges mentioned, and/or the mathematical analysis of the GC traces. Nonetheless, the results from the calculations do suggest that CO<sub>2</sub> is formed *via* another reaction pathway, *i.e.*, Co<sub>3</sub>O<sub>4</sub> reduction ultimately to metallic Co, in addition to the forward water-gas shift.

In the case of the forward WGS reaction, some of the low-temperature activity can be attributed to the CoO phase but literature has proposed a partially reduced CoO<sub>1-x</sub> surface species (not detectable in PXRD) to be WGS active [47–49]. A continued formation of H<sub>2</sub> and CO<sub>2</sub> over metallic Co *via* the WGS is observed here and has also been reported in the literature [47–50]. The final hcp:fcc Co ratio at 450 °C is 1.1, which is lower than the ratios observed in the other reduction experiments

(see Figure 7.10(b)). As previously mentioned, this may be due to the changing gas partial pressures during catalyst reduction and the forward WGS reaction [20].

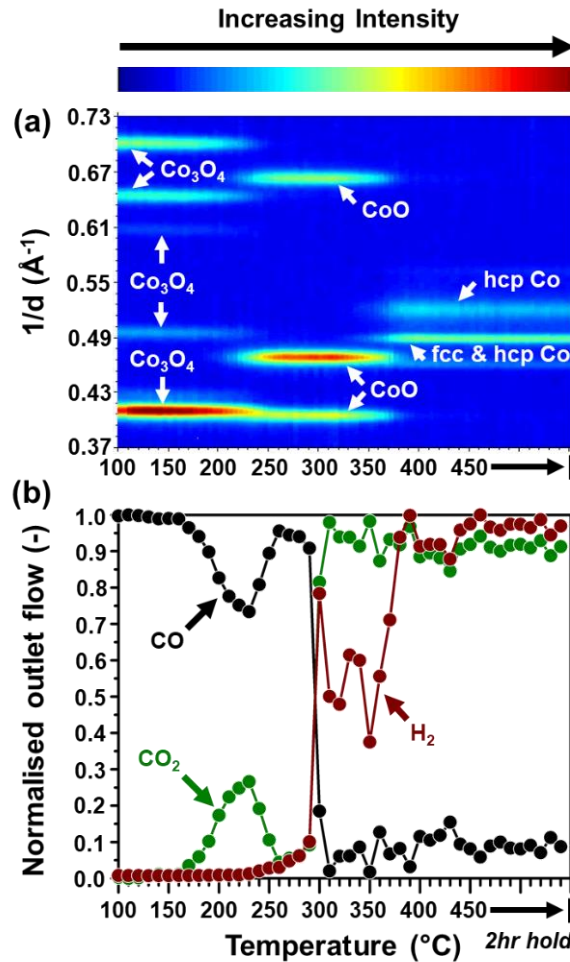


**Figure 7.9:** (a) On-top view of the *in situ* PXRD patterns recorded during the reduction of unsupported  $\text{Co}_3\text{O}_4$  at atmospheric pressure in a 1:10:89  $\text{CO}:\text{H}_2\text{O}:\text{N}_2$  mixture. (b) Changes in the normalised outlet flow rates of  $\text{CO}$ ,  $\text{CO}_2$  and  $\text{H}_2$  calculated from GC-TCD data.

### 7.3. Summary: Evaluation of CO-PrOx and Side Reactions

The CO oxidation reaction as well as the CO-PrOx side reactions –  $\text{H}_2$  oxidation, the forward and reverse water-gas shift, CO and  $\text{CO}_2$  methanation – were individually evaluated by performing thermodynamic calculations. This involved calculating the temperature-dependent equilibrium

conversions of the limiting reactant of each reaction within the temperature range from 0 to 500 °C. The CO and H<sub>2</sub> oxidation reactions were found to be highly favoured and conversions of up to 100% were found possible, assuming typical CO-PrOx feed concentrations of each gas in the separate reactions. This implies that both reactions are also likely to compete during CO-PrOx, especially since H<sub>2</sub> is typically present in very high amounts relative to CO and O<sub>2</sub> in the feed [1–5].

The forward water-gas shift reaction was also found to be thermodynamically favourable, with CO conversions above 98% being possible between 0 and 500 °C, assuming a typical CO-PrOx feed ratio of CO and H<sub>2</sub>O. On the other hand, the reverse WGS reaction was found to be thermodynamically unfavourable (*i.e.*,  $\Delta G > 0$ ) within the same temperature range, with relatively low CO<sub>2</sub> conversions (< 59%) expected when using a 50:10 H<sub>2</sub>:CO<sub>2</sub> ratio. The formation of CH<sub>4</sub> from either CO or CO<sub>2</sub> is thermodynamically favourable, with conversion levels above 72% of each substrate being possible. Experimentally, the forward WGS reaction and CO methanation are potential “competitors” of the CO oxidation reaction during CO-PrOx since all three reactions consume CO. However, the forward WGS is still a suitable reaction as it converts CO and H<sub>2</sub>O to form CO<sub>2</sub> and valuable H<sub>2</sub>, which is required in PEMFCs. On the other hand, CO and CO<sub>2</sub> methanation are not desirable as they consume high amounts of the valuable H<sub>2</sub> [6,8–10].

The above-mentioned CO-PrOx side reactions were also performed experimentally and coupled with *in situ* PXRD characterisation of the catalyst between 50 and 450 °C over unsupported Co<sub>3</sub>O<sub>4</sub>. Note that CO oxidation was also performed but is discussed in sub-section 9.2.1. Figure 7.10(a) shows the range of temperatures in which each cobalt-based phase was observed under the different reducing environments discussed in the preceding sub-sections of this Chapter. Figure 7.10(b) and (c) show the calculated hcp:fcc Co ratios and the crystallite sizes of hcp Co, respectively, at 450 °C after each reduction experiment. The crystallite sizes of fcc Co are not reported due to possible granularity effects as explained in the previous sub-sections. In the absence of CO, O<sub>2</sub>, H<sub>2</sub>O and CO<sub>2</sub>, Co<sub>3</sub>O<sub>4</sub> reduces to Co<sup>0</sup> (*i.e.*, both hcp and fcc) below 200 °C. The presence of H<sub>2</sub>O and O<sub>2</sub>, respectively, helps stabilise Co<sub>3</sub>O<sub>4</sub> and CoO possibly due to their strong oxidising nature [22,36,44–46]. Gaseous CO<sub>2</sub> is mildly oxidising – allowing the formation of metallic Co at relatively low temperatures – which might be related to the difficulty in activating CO<sub>2</sub> molecules to release oxygen [21,22,36,44–46].

Although full reduction of Co<sub>3</sub>O<sub>4</sub> to metallic Co is achieved under all reduction conditions, it was found that the hcp:fcc Co ratio is dependent on the kind of gas environment and/or the changing

partial pressures of the gases fed and subsequently formed during the reduction [20]. In most experiments, hcp Co is formed in high amounts (*i.e.*, > 70 wt.-%) and as small crystallites (< 10 nm). It is possible that the hcp and fcc Co crystalline domains are intergrown in some of the metallic particles formed, but the formation of single-crystal phase particles cannot be ruled out [20,27,51–57]. The variation of the hcp Co size with the different gas environments is not clear at this stage, but this may be closely linked with the effects on the hcp:fcc Co ratio and on the structure of the particles in the sample (whether intergrown or otherwise).

The co-fed gases (except for H<sub>2</sub>O) have also been shown to react with H<sub>2</sub> during the reduction experiments. The gases CO and CO<sub>2</sub> react with H<sub>2</sub> over metallic Co (Figure 7.5 and 7.8), while O<sub>2</sub> reacts with H<sub>2</sub> possibly over all three detected Co-based phases (Figure 7.6). The forward and reverse WGS reaction can also take place over metallic Co, as well as over CoO (in the case of the forward reaction – see Figure 7.9). It is worth noting that the conversion levels achieved in each experiment were below the predicted conversions based on the thermodynamic calculations. For the exothermic reactions especially, kinetic effects were more important at low temperatures since very low conversions are generally achieved when compared with the calculated equilibrium conversions. Furthermore, the occurrence of certain gas-phase reactions may be dependent on the chemical and crystalline phase of cobalt (*i.e.*, oxidic *versus* metallic, hcp Co *versus* fcc Co), which is also a kinetic effect.

Nonetheless, the relationships revealed in this Chapter between each gas-phase reaction, the temperature and each detected Co-based phase are very crucial in adequately understanding the CO-PrOx reaction when a feed with CO, O<sub>2</sub>, H<sub>2</sub>, H<sub>2</sub>O, CO<sub>2</sub> and N<sub>2</sub> is used. This multi-component feed opens the possibility for some of the discussed gas-phase reactions to take place at the same time, within a certain temperature range and/or over a specific Co-based phase(s). Therefore, it was important to perform these reactions individually to establish the now revealed relationships and to ultimately be able to understand CO-PrOx over un-/supported Co<sub>3</sub>O<sub>4</sub> nanoparticles under realistic conditions (see Chapters 8 and 9).

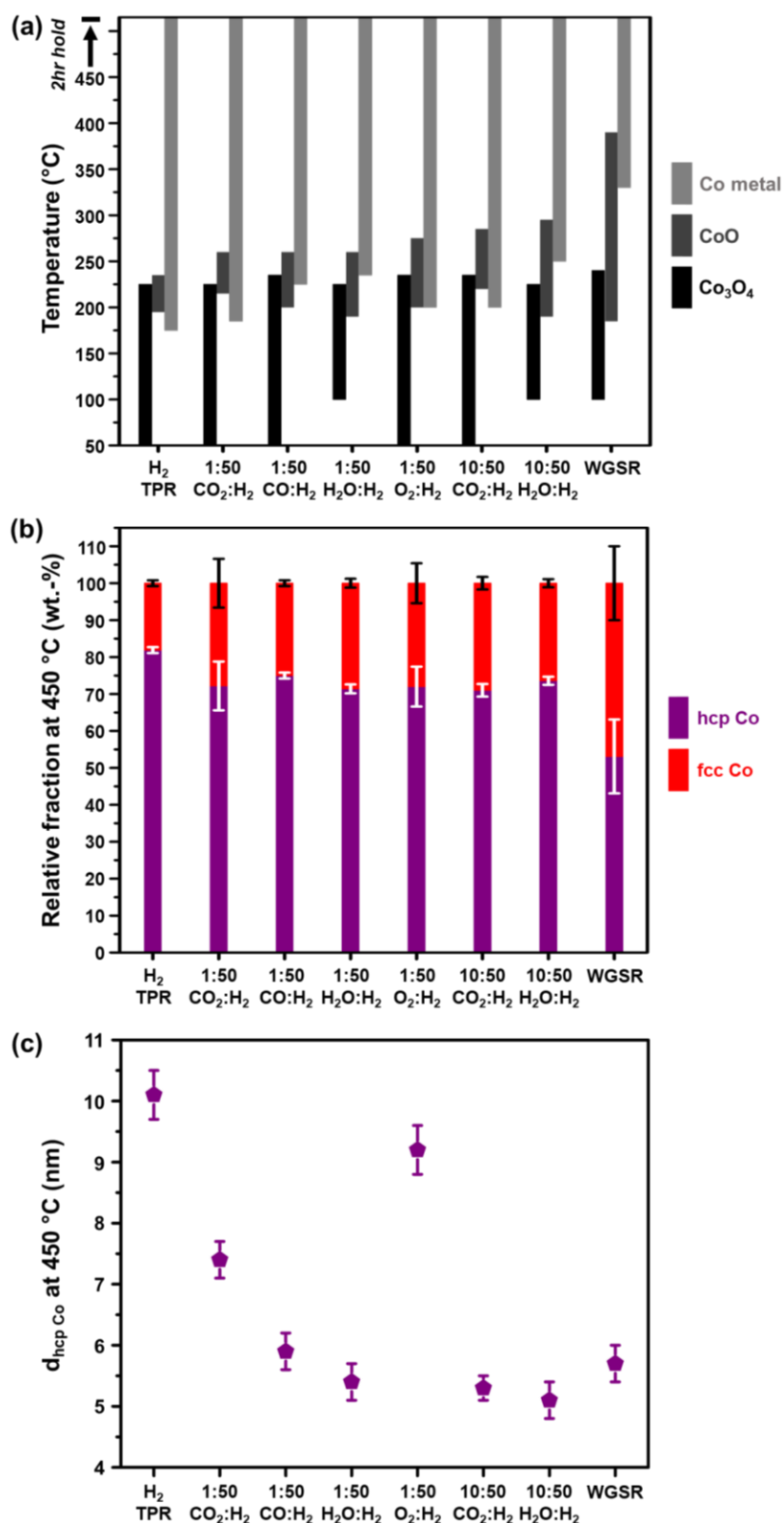


**Figure 7.10:** (a) Temperatures at which the Co-based phases were detected using *in situ* PXRD under the different reduction conditions. (b) Relative fraction of hcp and fcc Co, as well as the (c) crystallite size of hcp Co after full reduction of unsupported  $\text{Co}_3\text{O}_4$  at 450 °C and at atmospheric pressure. The white and black error bars in (b) are for hcp and fcc Co, respectively. The size of fcc Co is not reported in (c) due to possible granularity effects and/or intergrowth of hcp and fcc Co.

## References

- [1] T.V. Choudhary, D.W. Goodman, *Catal. Today* 77 (2002) 65–78.
- [2] A.F. Ghenciu, *Curr. Opin. Solid State Mater. Sci.* 6 (2002) 389–399.
- [3] G. Zhou, Y. Jiang, H. Xie, F. Qiu, *Chem. Eng. J.* 109 (2005) 141–145.
- [4] E.D. Park, D. Lee, H.C. Lee, *Catal. Today* 139 (2009) 280–290.
- [5] A. Mishra, R. Prasad, *Bull. Chem. React. Eng. Catal.* 6 (2011) 1–14.
- [6] M.L. Brown Jr., A.W. Green, G. Cohn, H.C. Andersen, *Ind. Eng. Chem.* 52 (1960) 841–844.
- [7] A. Rehmat, S.S. Randhava, *Ind. Eng. Chem. Prod. Res. Dev.* 9 (1970) 512–515.
- [8] N. Edwards, S.R. Ellis, J.C. Frost, S.E. Golunski, A.N.J. van Keulen, N.G. Lindewald, J.G. Reinkingh, *J. Power Sources* 71 (1998) 123–128.
- [9] S. Golunski, *Platin. Met. Rev.* 42 (1998) 2–7.
- [10] P.G. Gray, M.I. Petch, *Platin. Met. Rev.* 44 (2000) 108–111.
- [11] J. Díez-Ramírez, P. Sánchez, V. Kyriakou, S. Zafeiratos, G.E. Marnellos, M. Konsolakis, F. Dorado, *J. CO<sub>2</sub> Util.* 21 (2017) 562–571.
- [12] X. Nie, H. Wang, W. Li, Y. Chen, X. Guo, C. Song, *J. CO<sub>2</sub> Util.* 24 (2018) 99–111.
- [13] L. Wang, H. Liu, *Catal. Today* 316 (2018) 155–161.
- [14] Y. Teng, H. Sakurai, A. Ueda, T. Kobayashi, *Int. J. Hydrog. Energy* 24 (1999) 355–358.
- [15] Z. Zhao, M.M. Yung, U.S. Ozkan, *Catal. Commun.* 9 (2008) 1465–1471.
- [16] L. Lukashuk, K. Föttinger, E. Kolar, C. Rameshan, D. Teschner, M. Hävecker, A. Knop-Gericke, N. Yigit, H. Li, E. McDermott, M. Stöger-Pollach, G. Rupprechter, *J. Catal.* 344 (2016) 1–15.
- [17] T.M. Nyathi, N. Fischer, A.P.E. York, M. Claeys, *Faraday Discuss.* 197 (2017) 269–285.
- [18] M. Khasu, T. Nyathi, D.J. Morgan, G.J. Hutchings, M. Claeys, N. Fischer, *Catal. Sci. Technol.* 7 (2017) 4806–4817.
- [19] T.M. Nyathi, N. Fischer, A.P.E. York, D.J. Morgan, G.J. Hutchings, E.K. Gibson, P.P. Wells, C.R.A. Catlow, M. Claeys, *ACS Catal.* 9 (2019) 7166–7178.
- [20] W.A. Sławiński, E. Zacharaki, H. Fjellvåg, A.O. Sjøstad, *Cryst. Growth Des.* 18 (2018) 2316–2325.

- [21] A.J. Elliott, M.J. Watson, J. Tabatabaei, F.W. Zemichael, K.C. Waugh, *Catal. Lett.* 79 (2002) 1–6.
- [22] J.M. González-Carballo, S. Sadasivan, P. Landon, R.P. Tooze, *Mater. Charact.* 118 (2016) 519–526.
- [23] E. Patanou, N.E. Tsakoumis, R. Myrstad, E.A. Blekkan, *Appl. Catal. A* 549 (2018) 280–288.
- [24] A. Davó-Quiñonero, I. Such-Basáñez, J. Juan-Juan, D. Lozano-Castelló, P. Stelmachowski, G. Grzybek, A. Kotarba, A. Bueno-López, *Appl. Catal. B* 267 (2020) 118372.
- [25] T. Herranz, X. Deng, A. Cabot, J. Guo, M. Salmeron, *J. Phys. Chem. B* 113 (2009) 10721–10727.
- [26] A. Tuxen, S. Carencó, M. Chintapalli, C.-H. Chuang, C. Escudero, E. Pach, P. Jiang, F. Borondics, B. Beberwyck, A.P. Alivisatos, G. Thornton, W.-F. Pong, J. Guo, R. Perez, F. Besenbacher, M. Salmeron, *J. Am. Chem. Soc.* 135 (2013) 2273–2278.
- [27] O. Ducreux, B. Rebours, J. Lynch, M. Roy-Auberger, D. Bazin, *Oil Gas Sci. Technol.* 64 (2009) 49–62.
- [28] J.-X. Liu, H.-Y. Su, D.-P. Sun, B.-Y. Zhang, W.-X. Li, *J. Am. Chem. Soc.* 135 (2013) 16284–16287.
- [29] S. Lyu, L. Wang, J. Zhang, C. Liu, J. Sun, B. Peng, Y. Wang, K.G. Rappé, Y. Zhang, J. Li, L. Nie, *ACS Catal.* 8 (2018) 7787–7798.
- [30] E. van Steen, M. Claeys, M.E. Dry, J. van de Loosdrecht, E.L. Viljoen, J.L. Visagie, *J. Phys. Chem. B* 109 (2005) 3575–3577.
- [31] E.L. Viljoen, E. van Steen, *Catal. Lett.* 133 (2009) 8–13.
- [32] N. Fischer, E. van Steen, M. Claeys, *Catal. Today* 171 (2011) 174–179.
- [33] M. Wolf, H. Kotzé, N. Fischer, M. Claeys, *Faraday Discuss.* 197 (2017) 243–268.
- [34] M. Wolf, E.K. Gibson, E.J. Olivier, J.H. Neethling, C.R.A. Catlow, N. Fischer, M. Claeys, *Catal. Today* 342 (2020) 71–78.
- [35] Y. Zhang, D. Wei, S. Hammache, J.G. Goodwin, *J. Catal.* 188 (1999) 281–290.
- [36] D.H. Kim, J.E. Cha, *Catal. Lett.* 86 (2003) 107–112.
- [37] S. Storsæter, Ø. Borg, E.A. Blekkan, A. Holmen, *J. Catal.* 231 (2005) 405–419.
- [38] N. Fischer, B. Clapham, T. Feltes, E. van Steen, M. Claeys, *Angew. Chemie - Int. Ed.* 53 (2014) 1342–1345.
- [39] J. Paterson, M. Peacock, E. Ferguson, M. Ojeda, J. Clarkson, *Appl. Catal. A* 546 (2017)

- 103–110.
- [40] N.E. Tsakoumis, J.C. Walmsley, M. Rønning, W. van Beek, E. Rytter, A. Holmen, *J. Am. Chem. Soc.* 139 (2017) 3706–3715.
- [41] M. Wolf, E.K. Gibson, E.J. Olivier, J.H. Neethling, C.R.A. Catlow, N. Fischer, M. Claeys, *ACS Catal.* 9 (2019) 4902–4918.
- [42] P. Mars, D.W. van Krevelen, *Chem. Eng. Sci.* 3 (1954) 41–59.
- [43] ICSC 0001 - HYDROGEN. <http://www.inchem.org/documents/icsc/icsc/eics0001.htm> (accessed July 2020).
- [44] E. Colbourn, R.A. Hadden, H.D. Vandervell, K.C. Waugh, G. Webb, *J. Catal.* 130 (1991) 514–527.
- [45] F. Pinna, *Catal. Today* 41 (1998) 129–137.
- [46] M. Wolf, N. Fischer, M. Claeys, *Catal. Today* 275 (2016) 135–140.
- [47] A. Jha, Y.-L. Lee, W.-J. Jang, J.-O. Shim, K.-W. Jeon, H.-S. Na, H.-M. Kim, H.-S. Roh, D.-W. Jeong, S.G. Jeon, J.-G. Na, W.L. Yoon, *Mol. Catal.* 433 (2017) 145–152.
- [48] D. Vovchok, C.J. Guild, S. Dissanayake, J. Llorca, E. Stavitski, Z. Liu, R.M. Palomino, I. Waluyo, Y. Li, A.I. Frenkel, J.A. Rodriguez, S.L. Suib, S.D. Senanayake, *J. Phys. Chem. C* 122 (2018) 8998–9008.
- [49] Y. Cao, X. Peng, Z. Tan, Y. Liu, X. Wang, W. Zhao, L. Jiang, *Ind. Eng. Chem. Res.* 58 (2019) 17692–17698.
- [50] M.E. Dry, in: A.P. Steynberg, M.E. Dry (Eds.), *Fischer-Tropsch Technol.*, Elsevier B.V., Amsterdam, 2004, pp. 533–600.
- [51] M.M. Hauman, A. Saib, D.J. Moodley, E. du Plessis, M. Claeys, E. van Steen, *ChemCatChem* 4 (2012) 1411–1419.
- [52] A. Longo, L. Sciortino, F. Giannici, A. Martorana, *J. Appl. Crystallogr.* 47 (2014) 1562–1568.
- [53] L.J. Garces, B. Hincapie, R. Zerger, S.L. Suib, *J. Phys. Chem. C* 119 (2015) 5484–5490.
- [54] K.H. Cats, B.M. Weckhuysen, *ChemCatChem* 8 (2016) 1531–1542.
- [55] H.E. du Plessis, J.P.R. de Villiers, A. Tuling, E.J. Olivier, *Phys. Chem. Chem. Phys.* 18 (2016) 30183–30188.
- [56] S.W.T. Price, D.J. Martin, A.D. Parsons, W.A. Sławiński, A. Vamvakeros, S.J. Keylock, A.M. Beale, J.F.W. Mosselmans, *Sci. Adv.* 3 (2017) e1602838.
- [57] T.W. van Deelen, H. Yoshida, R. Oord, J. Zečević, B.M. Weckhuysen, K.P. de Jong, *Appl.*

Catal. A 593 (2020) 117441.

## Chapter 8: Support Material Effects on the Preferential Oxidation of Carbon Monoxide

One of the main objectives of this Ph.D. study was to investigate the effect of support materials on the catalytic performance and phase stability of  $\text{Co}_3\text{O}_4$  nanoparticles for CO-PrOx. In section 6.2., it was shown that the phase of the supported  $\text{Co}_3\text{O}_4$  nanoparticles can be stabilised to varying degrees depending on the nature and strength of the nanoparticle-support interactions (NPSI) when being reduced in a 50:50  $\text{H}_2:\text{N}_2$  mixture. This was important to understand as  $\text{Co}_3\text{O}_4$ -based catalysts have been reported to be susceptible to reduction by  $\text{H}_2$  under CO-PrOx conditions [1–6]. The reduction is one of the reasons for the decrease in activity and selectivity as  $\text{Co}_3\text{O}_4$  is believed to be the most active Co-based phase for CO oxidation [2–8]. Although the experimental results in section 6.2. have shown higher stability of the oxide phase in the supported state (which is desirable), the effect of supporting on the catalytic performance during CO-PrOx still had to be investigated.

In this Chapter, the results obtained after performing dry CO-PrOx (*i.e.*, 1% CO, 1%  $\text{O}_2$ , 50%  $\text{H}_2$  and 48%  $\text{N}_2$  – see Table 4.5) over unsupported and supported  $\text{Co}_3\text{O}_4$  catalysts will be discussed. The catalysts were all characterised *in situ* between 50 and 450 °C using PXRD [9–12] and magnetometry [10,12,13] at atmospheric pressure. As already mentioned in sections 2.6. and 4.4., the two *in situ* set-ups were developed at the University of Cape Town (in collaboration with SASOL for the magnetometer). The PXRD can in principle detect crystalline phases present in a sample above 2 – 3 wt.-% and crystallite sizes above 2 – 3 nm, making it suitable for detecting  $\text{Co}_3\text{O}_4$ , CoO, metallic Co, metal-support compounds ( $\text{CoAl}_2\text{O}_4$ ,  $\text{CoTiO}_3$ ,  $\text{Co}_2\text{SiO}_4$ ), as well as the support materials used. The magnetometer does not detect  $\text{Co}_3\text{O}_4$  [14,15], CoO [16], the MSCs [14,17–20] or any of the support materials used as they are all paramagnetic between 50 and 450 °C. However, the magnetometer can detect amounts of ferromagnetic metallic Co that are significantly lower than 1.0 wt.-% and virtually independent of crystallite size (at the maximum

magnetic field strength of 2 T (20 kOe)), making it far more sensitive than PXRD. Also, the magnetic susceptibility of a supported sample is not influenced by the presence of the support, while in PXRD, the visibility of the reflections from Co-based phases can be negatively affected by the presence of the support, especially at low loadings and small crystallite sizes. Therefore, it was important to employ both techniques to adequately study the catalysts under CO-PrOx conditions.

The PXRD and magnetometer are both equipped with a fixed-bed tube reactor (see section 4.4. for details), allowing for continuous plug flow through the catalyst sample at a constant GHSV of 60000 ml(NTP)/g<sub>Co<sub>3</sub>O<sub>4</sub></sub>/hr. The gases exiting the reactor were analysed every 5 min using a micro-GC, while the temperature along the catalyst bed was held for 60 min every 25 °C between 50 and 450 °C. PXRD patterns and sample magnetisation measurements at 2 T, respectively, were also recorded every 5 min within the same reaction temperature range.

## 8.1. Dry CO-PrOx over Unsupported Co<sub>3</sub>O<sub>4</sub>

Shown in Figures 8.1(a) – (f) are the recorded PXRD patterns and the associated results from Rietveld refinement, the normalised outlet gas flow rates, and the degree of reduction (DoR) to metallic Co calculated from the magnetometry data, respectively. It should be noted that the GC data shown in Figure 8.1(d) and (e) were obtained from the magnetometer, but similar results were also obtained in the PXRD set-up (see Figure A.6.1). The CO conversion to CO<sub>2</sub> (equivalent to CO<sub>2</sub> yield), the O<sub>2</sub> selectivity to CO<sub>2</sub> (based on the O<sub>2</sub> conversion and CO<sub>2</sub> yield), and the CO conversion to CH<sub>4</sub> (equivalent to CH<sub>4</sub> yield) as a function of temperature, can be found in Figures 8.8(a), (b) and (c), respectively. A supplementary figure (Figure A.6.2) showing the changes in the CO conversion and O<sub>2</sub> selectivity to CO<sub>2</sub> between 50 and 200 °C, where the Co<sub>3</sub>O<sub>4</sub> phase is believed to be intact in the unsupported catalyst, can be found in Appendix A.6.

The amounts of CO and O<sub>2</sub> begin to decrease at 75 °C, while the amount of CO<sub>2</sub> increases up to a yield of 84.4% at 175 °C (Figures 8.1(d), 8.8(a) and A.6.2(a)). This CO<sub>2</sub> yield is lower than the 99.999% yield required for fuel cell applications [21–26]. Note that a 1:1 CO:O<sub>2</sub> feed ratio implies an excess of O<sub>2</sub> in the context of CO oxidation (see Reaction 8.1). Therefore, if CO oxidation is the only O<sub>2</sub>-converting reaction taking place, the final total conversion of O<sub>2</sub> at 175 °C is expected

to be 42.2%. However, the measured O<sub>2</sub> conversion at 175 °C is 97.8%, giving a O<sub>2</sub> selectivity to CO<sub>2</sub> of 45.0% (Figures 8.8(b) and A.6.2(b)), and confirming that the undesired H<sub>2</sub> oxidation reaction (Reaction 8.2) is taking place. This is further confirmed by a decrease in H<sub>2</sub> concentration around the same temperature (Figure 8.1(e)). The results in Figures 8.8(b) and A.6.2(b) further show that the H<sub>2</sub> oxidation may have started earlier (at 100 °C) due to the observed drop in the O<sub>2</sub> selectivity to CO<sub>2</sub> from 100 to 80.1%. However, at this low temperature, the H<sub>2</sub> conversion (estimated at 0.1%) is too low to accurately determine using the current GC-TCD instrument. Above 175 °C, the CO conversion to CO<sub>2</sub> decreases until 225 °C due to an increased loss of O<sub>2</sub> to the H<sub>2</sub> oxidation reaction.

Also note that within this narrow temperature range, the Co<sub>3</sub>O<sub>4</sub> phase transforms into CoO (Figures 8.1(a) – (c)), which is believed to be a less active phase for CO oxidation [2–8] and therefore, is also undesired. The full consumption of O<sub>2</sub> from 200 °C due to both CO and H<sub>2</sub> oxidation, leaves the catalyst susceptible to reduction, which explains the onset formation of CoO at the same temperature. Assuming a Mars-van Krevelen (MvK) mechanism for CO oxidation over Co<sub>3</sub>O<sub>4</sub> [7,27–31], this mechanism may no longer be at play after the depletion of O<sub>2</sub> and the formation of CoO, which possibly causes the CO oxidation activity to drop (see details on the MvK mechanism in sub-section 2.1.2.).

At 250 °C, the H<sub>2</sub> and CO conversions increase again forming methane (Reaction 8.3). This coincides with the formation of the metallic Co allotropes (*i.e.*, fcc and hcp Co), evidenced in PXRD (Figures 8.1(a) – (c)) and through the rapid increase in the DoR calculated from the magnetometry data (Figure 8.1(f)). A further increase in temperature up to 450 °C resulted in very low CO<sub>2</sub> yields (*i.e.*, less than 20%), while DoR values above 90% were reached. Note that no CoO reflections were observed in the PXRD patterns above 300 °C even though the magnetometry results suggest the presence of small amounts of unreduced cobalt. This can be explained by the earlier mentioned high sensitivity and low dependence on crystallite size and crystallinity of the magnetometer, underlining the complementarity of the two *in situ* techniques used.

The decrease in the CH<sub>4</sub> yield (based on the CO conversion) above 275 °C was unexpected as previous studies [3–6] have shown a stable CH<sub>4</sub> yield at these high temperatures. The results from the Rietveld refinement of all recorded *in situ* patterns (Figures 8.1(a) and (c)) show that the fcc Co crystallites may have sintered between 250 and 275 °C, which is evidenced by severe granularity above these temperatures. On the other hand, hcp Co is formed in very high amounts but as small crystallites (between 4 and 6 nm). Therefore, the sintering of the fcc Co may have

caused some of the loss in methanation activity. As the temperature is increased from 275 to 450 °C, the fcc Co concentration increases up to  $21.7 \pm 0.8$  wt.-% (Figure 8.1(c) and Table A.7.1) at the expense of hcp Co, which is a thermodynamically favoured process [32–35]. Metallic hcp Co is known to be more active than fcc Co in terms of CO activation and hydrogenation [36–38], therefore, the slight loss in hcp Co may have also negatively affected the progress of the methanation reaction. However, a decrease of about 79.6% in the CH<sub>4</sub> yield may also imply other effects, such as, changes to the surface structure/composition of the metallic Co crystallites/nanoparticles, especially in the event of (partial) intergrowth of hcp and fcc Co [35,36,39–45]. Sławiński *et al.* [44] and du Plessis *et al.* [42] have pointed out the importance of PXRD in determining the probability of intergrowth in reduced cobalt samples (see detailed discussions in sub-section 6.2.1. and section 7.2.). However, the effect of the intergrowth in catalysed reactions (such as CO hydrogenation) is still not clear.

Interestingly, CO<sub>2</sub> formation resumes between 275 and 450 °C, with yields almost reaching 20% at 400 °C (Figure 8.1(d)). Since the *in situ* characterisation shows that the catalyst at these high temperatures is mostly in the metallic phase (which is not active for CO oxidation), it is possible that an *in situ* WGS reaction (Reaction 8.4) may have taken place leading to the formation of CO<sub>2</sub>, as once proposed by Khasu *et al.* [5]. The H<sub>2</sub>O formed during the H<sub>2</sub> oxidation (see O<sub>2</sub> and H<sub>2</sub> consumption in Figures 8.1(d) and (e), respectively) may have re-adsorbed and reacted with CO to form CO<sub>2</sub> and H<sub>2</sub>. The results in sub-section 7.2.4. (Figure 7.9) also support the occurrence of the WGS reaction over metallic Co, and it is possible that this reaction may have also negatively affected the progress of CO methanation.



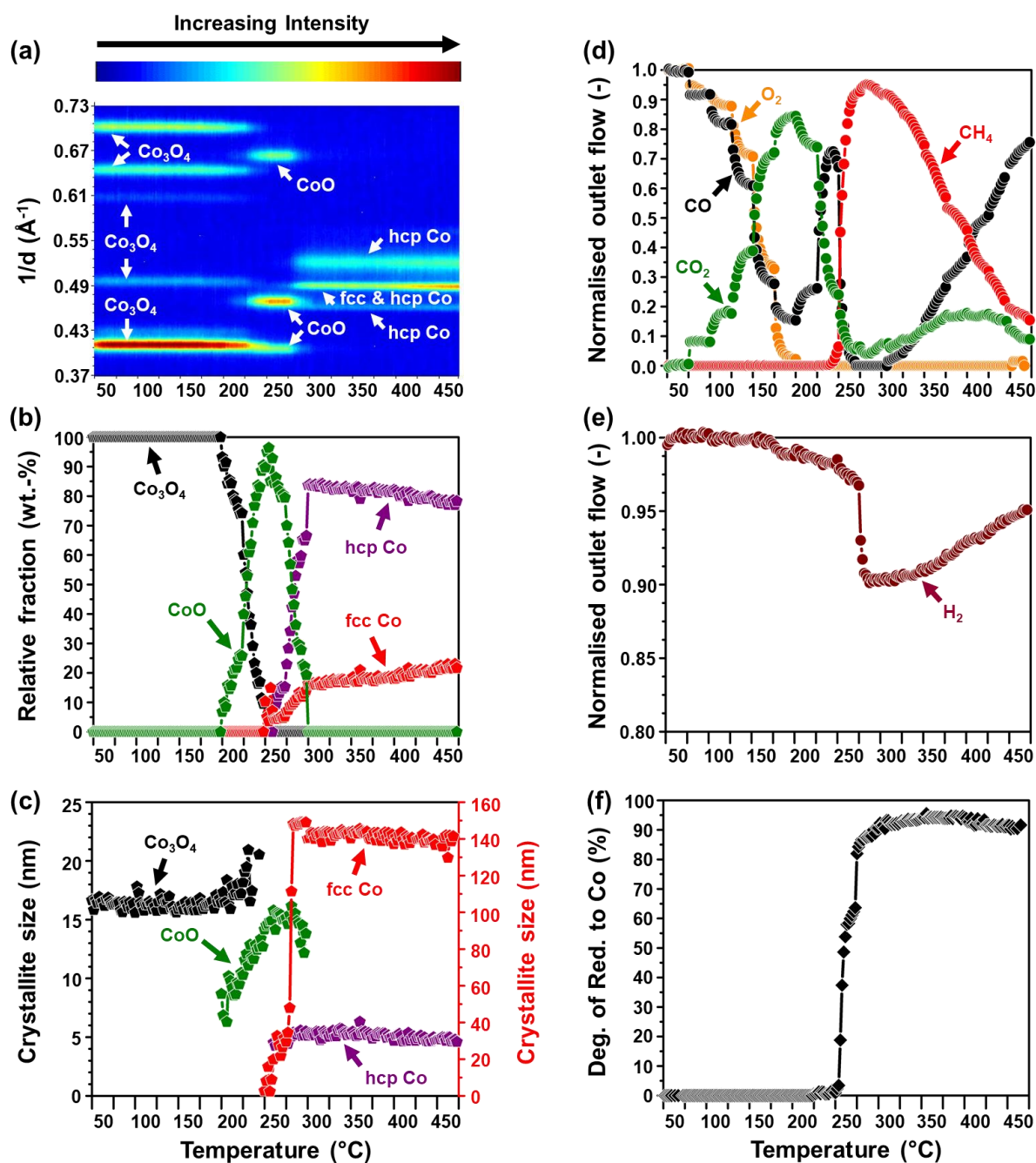


**Figure 8.1:** (a) On-top view of the recorded *in situ* PXRD patterns, (b) changes in the relative fraction, and (c) average crystallite size of the different cobalt phases formed during dry CO-PrOx over unsupported  $\text{Co}_3\text{O}_4$ . (d) Changes in the normalised outlet flow rates of CO,  $\text{O}_2$ ,  $\text{CO}_2$ ,  $\text{CH}_4$ , and (e)  $\text{H}_2$  calculated from GC-TCD data. (f) Magnetometry-derived degree of reduction of  $\text{Co}_3\text{O}_4$  to metallic Co. Refer to the red y-axis on the right of (c) for the crystallite size of fcc Co. However, note that these crystallite sizes may not bear significant physical meaning due to granularity effects and/or intergrowth of hcp and fcc Co. (Feed composition: 1% CO, 1%  $\text{O}_2$ , 50%  $\text{H}_2$  and 48%  $\text{N}_2$ ; pressure: atmospheric, GHSV: 60000 mL(NTP)/g $\text{Co}_3\text{O}_4$ /hr).

Shown in Figure 8.2 are the magnetisation *versus* applied field curves (*i.e.*, M-H curves) measured at 450 °C and 50 °C post-reaction (*i.e.*, after decreasing the temperature from 450 back to 50 °C). As previously mentioned in (sub-)sections 2.6. and 4.4.3., the data for the M-H curves were obtained by varying the applied field from 2 T to -2 T and back to 2 T in 65 steps while measuring the sample magnetisation. The data can be used to calculate the parameter  $\gamma$ , which is the fraction of the sample with crystallites/nanoparticles above the critical size for superparamagnetism (Equation 8.1). Furthermore, plotting a M-H curve for a sample with a  $\gamma < 10$  wt.-% would show no or minor hysteresis behaviour (Figure 2.18), which would then allow for a volume-based size distribution to be calculated using the Langevin equation (Equation 8.2) [46–48].

$$\gamma \text{ (wt.-%)} = \frac{2 \cdot M_{rem}}{M_{sat}} \times 100 \quad \text{Equation 8.1}$$

$$\frac{M}{M_{sat}} = \coth\left(\frac{\rho \cdot \sigma_{sat} \cdot \pi \cdot d^3 \cdot H}{6 \cdot k_B \cdot T}\right) - \left(\frac{6 \cdot k_B \cdot T}{\rho \cdot \sigma_{sat} \cdot \pi \cdot d^3 \cdot H}\right) \quad \text{Equation 8.2}$$

The M-H curves in Figure 8.2 clearly show hysteresis behaviour, which qualitatively indicates the presence of at least 10 wt.-% of the formed metallic crystallites/nanoparticles with a size above the critical size for the superparamagnetism of metallic hcp Co (11 nm at 450 °C, and 8 nm at 50 °C [12]) and/or fcc Co (16 – 20(26) nm at 450 °C, and 12 – 15(20) nm at 50 °C [12]). The calculated  $\gamma$  at 450 and 50 °C post-reaction is 33.0 and 34.8 wt.-%, respectively. In principle, there exists an inverse relationship between  $\gamma$  (or crystallite size) and temperature, which is a result of the inverse relationship between magnetisation and temperature (see details in section 2.6.). Therefore, the very small difference between the two mentioned  $\gamma$  values, despite the large difference in temperature, may suggest the existence of a bimodal size distribution consisting of very large crystallites that contribute to  $\gamma$  at 450 and 50 °C, and smaller crystallites that possibly do not contribute to  $\gamma$  as they are superparamagnetic at both temperatures.

The results from Rietveld refinement (Figure 8.1(b) and (c)) show the presence of approximately  $78.3 \pm 0.8$  wt.-% of hcp Co crystallites with an average size below 6 nm at the end of the experiment, which would be superparamagnetic at 450 and 50 °C (based on the critical sizes mentioned above). The other  $21.7 \pm 0.8$  wt.-% of the reduced material is made up of fcc Co crystallites which may have sintered, although the extent of this could not be confirmed due to

granularity effects. However, it remains possible that the fcc Co crystallites may be the only ones contributing to  $\gamma$  at 450 and 50 °C, making them non-superparamagnetic. This could further imply that  $\gamma$ , specifically in the present case, gives an indication of the amount of fcc Co present in the reduced catalyst after the reaction, especially since the PXRD and magnetometry studies confirmed almost complete reduction of  $\text{Co}_3\text{O}_4$  to metallic Co (Figure 8.1(b) and (f)). Note that there exists a discrepancy in the “amount” of fcc Co crystallites estimated using PXRD ( $21.7 \pm 0.8$  wt.-%) and magnetometry (33.0 wt.-% at 450 °C, and 34.8 wt.-% at 50 °C (post-reaction)). This may be a result of the previously mentioned differences in detection limits and sensitivities between the two *in situ* techniques used, regarding crystallite size, phase concentration and crystallinity.

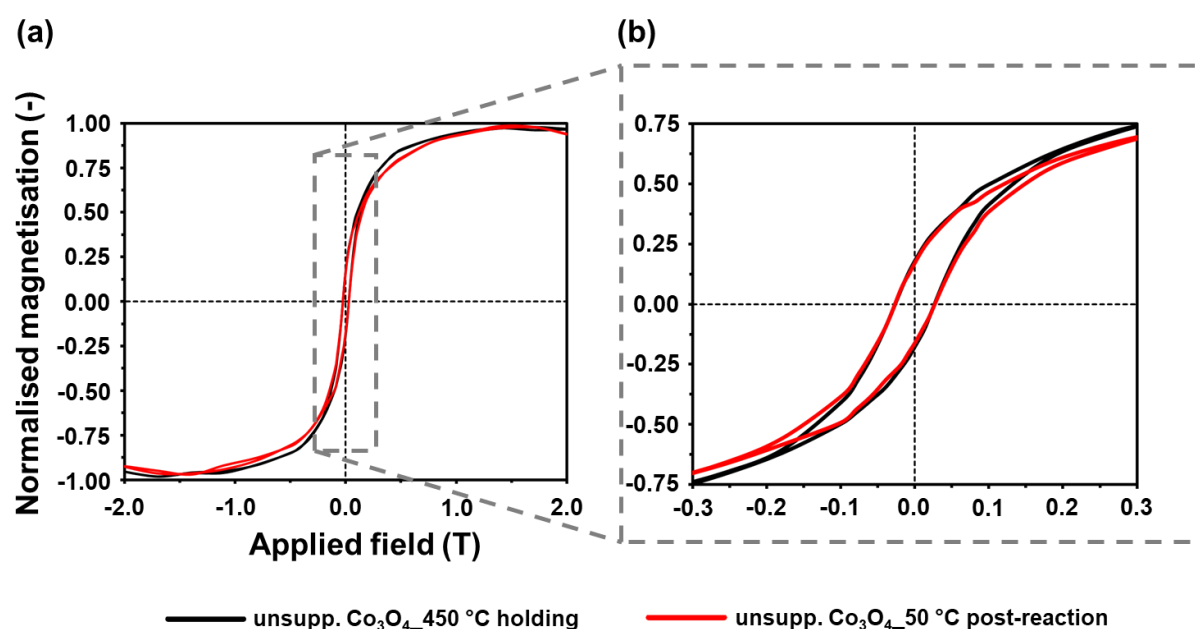


**Figure 8.2:** (a) Magnetometry-derived M-H curves recorded at 450 and 50 °C (post-reaction) under dry CO-PrOx over unsupported  $\text{Co}_3\text{O}_4$ . (b) Magnified view of the M-H curves indicating the existence of hysteresis behaviour. (Feed composition: 1% CO, 1% O<sub>2</sub>, 50% H<sub>2</sub> and 48% N<sub>2</sub>; pressure: atmospheric, GHSV: 60000 mL(NTP)/g<sub>Co<sub>3</sub>O<sub>4</sub></sub>/hr).

## 8.2. Dry CO-PrOx over Supported Co<sub>3</sub>O<sub>4</sub>

All supported catalysts were also tested under dry CO-PrOx conditions and characterised *in situ* using the same PXRD [9–12] and magnetometry [10,12,13] set-ups, respectively. Figures 8.3 - 8.6 show the recorded PXRD patterns, changes in the normalised outlet flow rate of each gas, and the degree of reduction of Co<sub>3</sub>O<sub>4</sub> to metallic Co between 50 and 450 °C, for each supported catalyst. Figure 8.7(a) summarises the range of temperatures in which each cobalt-based phase is observed, while Figures 8.7(b) and (c) show the calculated relative fraction and crystallite size of CoO, hcp and fcc Co, respectively, at 450 °C after each experiment. It is worth noting that PXRD analysis for Co<sub>3</sub>O<sub>4</sub>/CeO<sub>2</sub> was not performed as previously discussed *ex situ* (sub-section 5.2.3.) and *in situ* (sub-section 6.2.2.) analyses have demonstrated the difficulty in detecting Co-based phases in the presence of the CeO<sub>2</sub> support. As mentioned in the previous section, the CO conversion to CO<sub>2</sub>, and O<sub>2</sub> selectivity to CO<sub>2</sub> can be found in Figures 8.8(a) and (b), respectively, while Figure 8.8(c) gives a summary of the CO conversion to CH<sub>4</sub> and Figure 8.8(d) shows the *in situ* magnetometry-derived DoR as a function of temperature. The M-H curves derived from the data recorded at 450 °C for each supported catalyst are presented in Figures 8.9 and 8.10, while Table 8.1 shows the calculated  $\gamma$  values (including that for unsupported Co<sub>3</sub>O<sub>4</sub>). Changes in the CO conversion and O<sub>2</sub> selectivity to CO<sub>2</sub> between 50 and 200 °C, where the Co<sub>3</sub>O<sub>4</sub> phase is believed to be intact in all evaluated catalysts, can be found in Figure A.6.2.

A comparison of all the prepared catalysts shows that the ZrO<sub>2</sub>-supported catalyst exhibits higher CO conversions to CO<sub>2</sub> above 150 °C, while the unsupported catalyst exhibits higher conversions below 150 °C (see Figures 8.8(a) and A.6.2(a)). The highest CO conversion attained with the ZrO<sub>2</sub>-supported catalyst is 91.6% at 200 °C, however, this is still lower than the targeted 99.999% CO conversion in the context of H<sub>2</sub> purification for PEMFCs. Note that the normalised outlet flow rate of O<sub>2</sub> over all catalysts decreases to zero at elevated reaction temperatures, which indicates the concurrent conversion of H<sub>2</sub> to H<sub>2</sub>O as noted in the previous section. Further evidence of this is shown in Figures 8.8(b) and A.6.2(b) where the O<sub>2</sub> selectivity to CO<sub>2</sub> is below 100% at all temperatures, and decreases with temperature above 150 – 175 °C. At low normalised outlet flow rates of O<sub>2</sub> (or high O<sub>2</sub> conversions), the Co<sub>3</sub>O<sub>4</sub> phase in each catalyst reduces to CoO, which is less active and selective, as also evidenced by the decreasing CO conversion and O<sub>2</sub> selectivity to CO<sub>2</sub> with temperature over this phase. The trend in the onset CoO formation temperature is as follows: SiC and SiO<sub>2</sub> (225 °C) < ZrO<sub>2</sub>, TiO<sub>2</sub>-anatase, TiO<sub>2</sub>-rutile and TiO<sub>2</sub>-P25 (250 °C) < Al<sub>2</sub>O<sub>3</sub>

(275 °C) (Figure 8.7(a)). It is also worth noting that the formation of CoO in the supported catalysts takes place at higher temperatures when compared with the unsupported catalyst.

These observations are mostly in line with the reported effects of the individual supports on the reduction of  $\text{Co}_3\text{O}_4$  – where, for example, SiC and  $\text{SiO}_2$  would allow for low-temperature reduction, and  $\text{Al}_2\text{O}_3$  would allow reduction at a higher temperature due to the nature of the nanoparticle-support interactions (NPSIs) [2,35,49–54]. The interactions could be altering the strength of the metal-oxygen bonds of  $\text{Co}_3\text{O}_4$ , or affecting the  $\text{H}_2$  adsorption/dissociation rates, especially at or near the nanoparticle-support interface through electronic effects [55–59]. The location of (most of) the nanoparticles inside the pores of each support could also play a role in slowing down  $\text{Co}_3\text{O}_4$  reduction as access to the surface of the nanoparticles (to initiate reduction) would be limited [60–63]. The differences in the starting  $\text{Co}_3\text{O}_4$  sizes between the supported catalysts (as confirmed with PXRD and STEM-EELS) can also influence the onset of reduction, with bigger particles (as those in  $\text{Co}_3\text{O}_4/\text{ZrO}_2$  – see Tables 5.1 and 5.2, as well as Figure 5.15) being easier to reduce [4,64–68].

Assuming that the  $\text{Co}_3\text{O}_4$  phase is more active than CoO for CO oxidation, and that this reaction takes place *via* the MvK mechanism over  $\text{Co}_3\text{O}_4$ , the observed reduction trends for the  $\text{Co}_3\text{O}_4$ -to-CoO transformation in the unsupported and supported state could be related to the CO oxidation activity. For example,  $\text{Co}_3\text{O}_4$  reduces relatively easier in the unsupported state and over  $\text{ZrO}_2$ , and this could be related to their high CO oxidation activity as the MvK mechanism could be more effective in these samples before  $\text{Co}_3\text{O}_4$  is reduced. The SiC-,  $\text{SiO}_2$ -, and all the  $\text{TiO}_2$ -supported catalysts exhibit  $\text{Co}_3\text{O}_4$  reduction between 225 and 250 °C, but show slightly lower CO oxidation activity than the unsupported and  $\text{ZrO}_2$ -supported catalysts, possibly indicating a less effective MvK mechanism in the aforementioned supported samples. The very low CO oxidation activity of the  $\text{Al}_2\text{O}_3$ -supported catalyst may also be explained by the observed high onset reduction temperature, which possibly points towards an even less effective MvK mechanism.

A further increase in the reaction temperature transforms CoO to metallic Co as confirmed using PXRD and magnetometry. The crystal phase of metallic Co formed in most of the supported catalysts is fcc Co, with the exception of the  $\text{TiO}_2$ -rutile- and  $\text{TiO}_2$ -P25-supported catalysts which form both hcp and fcc Co crystallites (see Figure A.7.1). The formation of hcp and fcc Co over  $\text{TiO}_2$ -rutile was unexpected since only fcc Co was formed during the *in situ* PXRD-based reduction experiments (see sub-section 6.2.2.). The same can be mentioned for the  $\text{TiO}_2$ -anatase-supported catalyst which formed both hcp and fcc Co during the reduction studies, but only forms fcc Co

during dry CO-PrOx (compare results in Figures 8.7(a) and A.7.1(a)). The stabilisation of only fcc Co over most support materials, and the stabilisation of both hcp and fcc Co over the other supports (TiO<sub>2</sub>-rutile and TiO<sub>2</sub>-P25) might also be a result of the nature of the NPSIs - the details of which are not clear at this stage. The change in the gas environment (reduction *versus* dry CO-PrOx) may have also induced a change in the hcp:fcc ratio and/or the growth/size of the Co allotropes [44].

The average crystallite size of fcc Co in the ZrO<sub>2</sub>-, TiO<sub>2</sub>-anatase- and TiO<sub>2</sub>-rutile-supported catalysts is larger than the starting Co<sub>3</sub>O<sub>4</sub> size (compare results in Table 5.1 with those in Figure 8.7(c) and Table A.7.1), which indicates possible sintering. The fcc Co size in the TiO<sub>2</sub>-P25-supported catalyst could not be reliably determined, possibly due to granularity effects which estimate the size to be larger than 150 nm. The hcp Co over TiO<sub>2</sub>-rutile and TiO<sub>2</sub>-P25 is  $6.3 \pm 0.9$  nm and  $11.5 \pm 3.2$  nm, respectively, which may indicate intergrowth with the larger fcc Co crystallites [36,40,43,44]. The CoO and fcc Co in the SiC-supported catalyst has an average size very close to the expected crystallite size for each phase (CoO: expected = 12.8 nm and observed  $12.7 \pm 4.5$  nm; fcc Co: expected = 10.6 nm and observed  $10.3 \pm 3.0$  nm). Similarly, the expected fcc Co size (10.6 nm) in the SiO<sub>2</sub>-supported catalyst is within the statistical error of the calculated size of  $11.7 \pm 5.5$  nm. The high error associated with this average size might be a result of the relatively low concentration of metallic Co formed (see Figure 8.7(b)). On the other hand, the CoO present in the SiO<sub>2</sub>- and Al<sub>2</sub>O<sub>3</sub>-supported samples is much smaller than the expected crystallite size (SiO<sub>2</sub>: expected = 12.7 nm and observed  $7.2 \pm 1.7$  nm; Al<sub>2</sub>O<sub>3</sub>: expected = 12.5 nm and observed  $7.8 \pm 0.8$  nm). These lower estimated CoO sizes for the respective supported catalysts may imply the formation of very small crystallites (or crystalline domains) that make up larger CoO particles, respectively [69]. This is also believed to have been the case during the reduction experiment involving the Co<sub>3</sub>O<sub>4</sub>/Al<sub>2</sub>O<sub>3</sub> catalyst (see sub-section 6.2.2.).

Similar to CoO formation, metallic Co was observed over the different supports at higher temperatures than those observed with the unsupported sample. Interestingly, the trend observed in terms of the onset CoO formation temperature was slightly different from the trend for the formation of metallic Co, which was: CeO<sub>2</sub> and ZrO<sub>2</sub> (250 °C) < SiC and SiO<sub>2</sub> (275 °C) < TiO<sub>2</sub>-rutile (300 °C) < TiO<sub>2</sub>-anatase, TiO<sub>2</sub>-P25 and Al<sub>2</sub>O<sub>3</sub> (325 °C); based on the magnetometry results in Figure 8.8(d). Note that this trend is also different to that observed using PXRD (see Figure 8.7(a)), but this may be explained by the higher intrinsic detection limits of PXRD in terms of crystallite size and phase concentration, as well as crystallinity requirements. Furthermore, there are some overlapping reflections from the metallic Co with those from some of the support

materials (such as  $\text{ZrO}_2$ ,  $\text{TiO}_2$ -rutile and  $\text{Al}_2\text{O}_3$ ), which makes it difficult to accurately note the onset metal formation temperature from the PXRD patterns.

As the reaction temperature is further increased to 450 °C, the catalysts reach different degrees of reduction. The trend in the DoR at 450 °C is as follows:  $\text{ZrO}_2$  (100%) >  $\text{TiO}_2$ -P25 (91.9%) ~ unsupported  $\text{Co}_3\text{O}_4$  (91.7%) >  $\text{TiO}_2$ -rutile (85.9%) >  $\text{TiO}_2$ -anatase (76.4%) >  $\text{CeO}_2$  (72.4%) > SiC (41.5%) >  $\text{SiO}_2$  (22.1%) >  $\text{Al}_2\text{O}_3$  (16.2%) (see magnetometry results in Figure 8.8(d)). The relative amounts of metallic Co (and CoO – see Figure 8.7(b)) detected using PXRD at 450 °C are also different from those calculated from the magnetometry data. Again, this can be ascribed to the previously noted difference in sensitivity between the two *in situ* techniques used. It can also be seen that the magnetometry-derived DoR trend is vastly different from the trend observed for the onset metallic Co formation temperature. The PXRD results depict a stepwise reduction of  $\text{Co}_3\text{O}_4$  to CoO, and then from CoO to metallic Co. Therefore, it is possible that the nature and/or strength of the interaction between the CoO crystallites and each support is different from the interaction between the  $\text{Co}_3\text{O}_4$  crystallites and the respective supports. This could potentially have different effects on the degree of reduction of the CoO phase to metallic Co *versus* that of  $\text{Co}_3\text{O}_4$  to CoO.

It is interesting to note the relatively low DoR of the SiC- and  $\text{SiO}_2$ -supported catalysts, which were unexpected in the current study. In reported literature [70–72], the motivation behind the use of SiC as a support is to limit strong NPSIs that may hinder the reduction of the supported metal oxide and/or cause the metal oxide to react with the support to form metal-support compounds (MSCs). On the other hand,  $\text{SiO}_2$  is generally preferred over supports such as  $\text{TiO}_2$  and  $\text{Al}_2\text{O}_3$ , as it can allow for higher DoRs and is less likely to form MSCs during reduction [50,52,53,73] (also see results from thermodynamic calculations in sub-section 6.1.2.). However, in the present study, all  $\text{TiO}_2$  supports allow for high DoRs of the metal oxide to be reached. Therefore, it is possible that the interaction of the CoO phase with the SiC and  $\text{SiO}_2$ , respectively, is such that the reduction of the oxide becomes limited during dry CO-PrOx. As shown in Figure 5.12 using STEM-EELS, SiC has a 1 - 2 nm  $\text{Si}_x\text{O}_y$  or  $\text{Si}_x\text{O}_y\text{C}_z$  layer around the core SiC particles [70–72], which is in contact with the supported CoO nanoparticles and therefore, possibly limits their reduction under reaction conditions. Furthermore, the reducibility of CoO could also be affected by the varying partial pressure ratio of  $\text{H}_2$ : $\text{H}_2\text{O}$  at high temperatures, which is caused by the occurrence of  $\text{H}_2$  oxidation, CO methanation, as well as the reduction of CoO. The adsorption strengths and/or dissociation rates of the  $\text{H}_2$  and  $\text{H}_2\text{O}$  may also be dependent on the CoO-support interaction.

Although the ultimate formation of metallic Co at elevated temperatures over the different supports decreases the CO oxidation activity and selectivity, most of the catalysts (except  $\text{Co}_3\text{O}_4/\text{ZrO}_2$ ) continue to form relatively small amounts of  $\text{CO}_2$  over the metallic phase (see Figures 8.3(b) – 8.6(b), and 8.8(a)). This may be ascribed to the earlier proposed *in situ* WGS reaction (see section 8.1.) - which firstly requires  $\text{H}_2\text{O}$  to be produced from  $\text{H}_2$  and  $\text{O}_2$ , and then this  $\text{H}_2\text{O}$  subsequently reacts with CO to form  $\text{CO}_2$  and  $\text{H}_2$  [5]. Unlike in previous studies [3–6], the increase in the DoR with increasing temperature in the present study does not necessarily result in high CO conversions to  $\text{CH}_4$ , similarly, low degrees of reduction do not always result in low amounts of  $\text{CH}_4$  being formed (see Figure 8.8(c) and (d)). It should be noted that  $\text{CH}_4$  formation is a “surface-specific process”, while the DoR (based on the characterisation techniques used) is a “bulk property”. Therefore, it is possible that the kind and/or amount of active sites required for CO methanation were not formed or accessible on the surfaces of the catalysts with relatively low methanation activity, even though such catalysts may have reached relatively high DoRs [74,75].

The possible case of this is the methanation activity of the  $\text{CeO}_2$ -supported catalyst, which initially increases between 250 and 325 °C, and then gradually decreases between 325 and 450 °C (Figure 8.3(b)). Taking place concurrently is the continuous increase in the DoR of this catalyst between 250 and 450 °C (Figure 8.3(d)). The  $\text{H}_2$ -TPR profile of the bare  $\text{CeO}_2$  support showed a peak maximum at 475 °C, which was assigned to the possible reduction of some (sub-)surface  $\text{CeO}_2$  species (see Figure 6.9). This reduction peak shifted to 400 °C in the presence of Co-based species (originating from the initial  $\text{Co}_3\text{O}_4/\text{CeO}_2$  catalyst), possibly due to an enhanced  $\text{H}_2$  spillover [76–78]. Note that reduction peak maxima in  $\text{H}_2$ -TPR profiles do not represent reduction onset temperatures, but rather indicate temperatures at which the consumption of  $\text{H}_2$  reaches a maximum during a particular reduction step. Therefore, the reduction of the Co-linked  $\text{CeO}_2$  species during  $\text{H}_2$ -TPR (Figure 6.9) may have been initiated at a temperature below 400 °C. Such reduced ceria species could migrate and adsorb on the surface of metallic Co (and over some  $\text{CoO}_{1-x}$  species), similar to the observations previously made by Bernal *et al.* [79] (*via ex situ* HRTEM) for Rh, Pd and Pt nanoparticles, respectively, supported on  $\text{CeO}_2$ . Correspondingly, the reduction of (sub-)surface ceria species and their subsequent migration, may have also taken place during dry CO-PrOx. This could lead to the blockage of active sites and consequently decrease methanation activity, as observed between 325 and 450 °C (Figure 8.3(b)). Note that the formation of Co-Ce oxides during dry CO-PrOx (as also proposed during  $\text{H}_2$ -TPR [76–78] – see sub-section 6.2.2.) might have taken place, as the  $\text{Co}_3\text{O}_4/\text{CeO}_2$  catalyst reaches a maximum DoR of 72.4% at 450 °C (Figure 8.3(d) and 8.8(d)). However, this DoR is still much higher than that reached by the SiC-

SiO<sub>2</sub>- and Al<sub>2</sub>O<sub>3</sub>-supported catalysts, which possibly suggests that the interactions in Co<sub>3</sub>O<sub>4</sub>/CeO<sub>2</sub> do not significantly hinder the formation of metallic Co.

Another interesting observation is made with the anatase-supported sample which exhibits clear evidence for fcc Co formation during the PXRD and magnetometry studies (Figure 8.5), but does not produce any CH<sub>4</sub> (even in a repeat experiment). The surface of anatase is known to be more reducible when compared with that of rutile. Also, due to differences between the surface energies of anatase (0.44 J/m<sup>2</sup> [80–82]) and fcc Co (2.6 J/m<sup>2</sup> [81,82]), TiO<sub>2-x</sub> species can migrate over the reduced Co nanoparticles and encapsulate them. This encapsulation was first observed over Co nanoparticles by de la Peña O'Shea *et al.* [83] using *ex situ* HRTEM after reducing an anatase-supported Co<sub>3</sub>O<sub>4</sub> catalyst at different temperatures under H<sub>2</sub>. When compared with a Co<sub>3</sub>O<sub>4</sub>/SiO<sub>2</sub> catalyst in the Fischer-Tropsch synthesis, the anatase-supported catalyst achieved much lower CO conversions than the SiO<sub>2</sub>-supported catalyst. Others have also reported the negative effect of TiO<sub>2-x</sub>-encapsulation in anatase-supported Co [73,84,85], Ni [86] and Ru [87–89] catalysts, respectively. Therefore, the encapsulation of the reduced Co nanoparticles by TiO<sub>2-x</sub>-species of anatase is a possible explanation for the absence of CH<sub>4</sub> in the product stream during dry CO-PrOx. The formation of large fcc Co crystallites (20.5 ± 3.4 nm at 450 °C) over the TiO<sub>2</sub>-anatase support may have also had a negative effect on methane formation. It is known that hcp Co has higher CO dissociation and hydrogenation activity than fcc Co [36–38], and since hcp Co is not formed over TiO<sub>2</sub>-anatase (but formed over TiO<sub>2</sub>-rutile and TiO<sub>2</sub>-P25), it is possible that this could have also negatively impacted the methane activity.

Although methane is produced over the TiO<sub>2</sub>-rutile- and TiO<sub>2</sub>-P25-supported catalysts in the presence of metallic Co, it remains possible that smaller amounts of partially reduced TiO<sub>2-x</sub> species may have also formed and migrated to the metallic Co surface. This could explain the relatively low methanation activity of these catalysts when compared with the ZrO<sub>2</sub>-, SiC- and SiO<sub>2</sub>-supported catalysts (Figure 8.8(c)). The Al<sub>2</sub>O<sub>3</sub> supported catalyst may be exhibiting low methanation activity due to the low reducibility and consequently, the low amount of active cobalt. Recent experimental [90] and DFT [91] results have also shown that Al<sub>2</sub>O<sub>3</sub>-supported cobalt oxide catalysts have a lower H<sub>2</sub> adsorption/dissociation activity and stronger Co-O bonds when compared with ZrO<sub>2</sub>-supported cobalt oxide. These electronic effects induced by the Al<sub>2</sub>O<sub>3</sub> may be the cause of the low DoR and methanation activity.

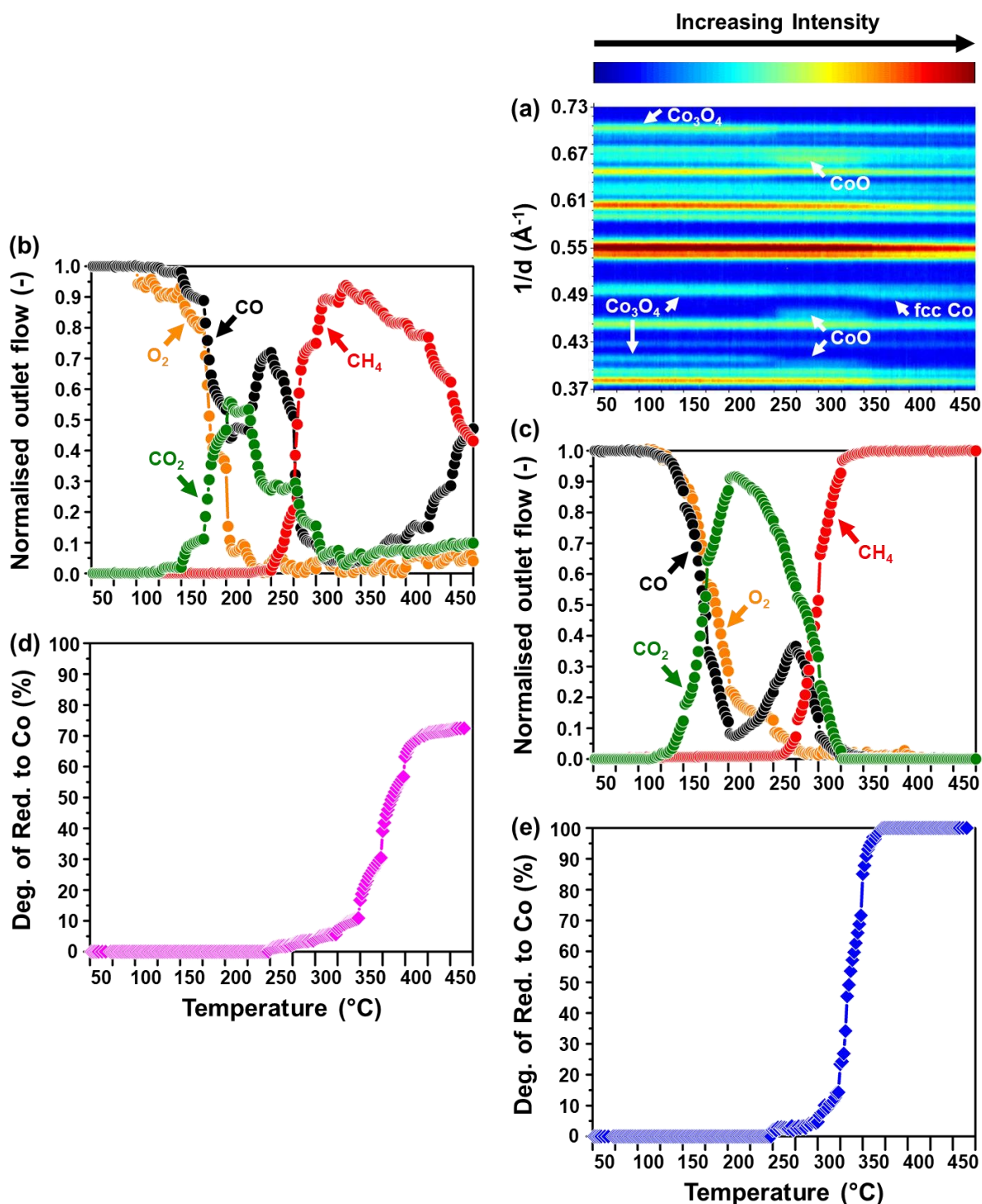


**Figure 8.3:** (a) On-top view of the *in situ* PXRD patterns recorded during dry CO-PrOx over  $\text{Co}_3\text{O}_4/\text{ZrO}_2$ . ((b) and (c)) Changes in the normalised outlet flow rates of  $\text{CO}$ ,  $\text{O}_2$ ,  $\text{CO}_2$  and  $\text{CH}_4$  calculated from GC-TCD data. ((d) and (e)) Magnetometry-derived degree of reduction of  $\text{Co}_3\text{O}_4$  to metallic  $\text{Co}$ . Note that PXRD analysis for the  $\text{Co}_3\text{O}_4/\text{CeO}_2$  catalyst was not performed as reflections from Co-based phases are not visible (see Figures 5.6 and 6.6(a)). (Feed composition: 1%  $\text{CO}$ , 1%  $\text{O}_2$ , 50%  $\text{H}_2$  and 48%  $\text{N}_2$ ; pressure: atmospheric, GHSV: 60000 mL(NTP)/g $\text{Co}_3\text{O}_4$ /hr).

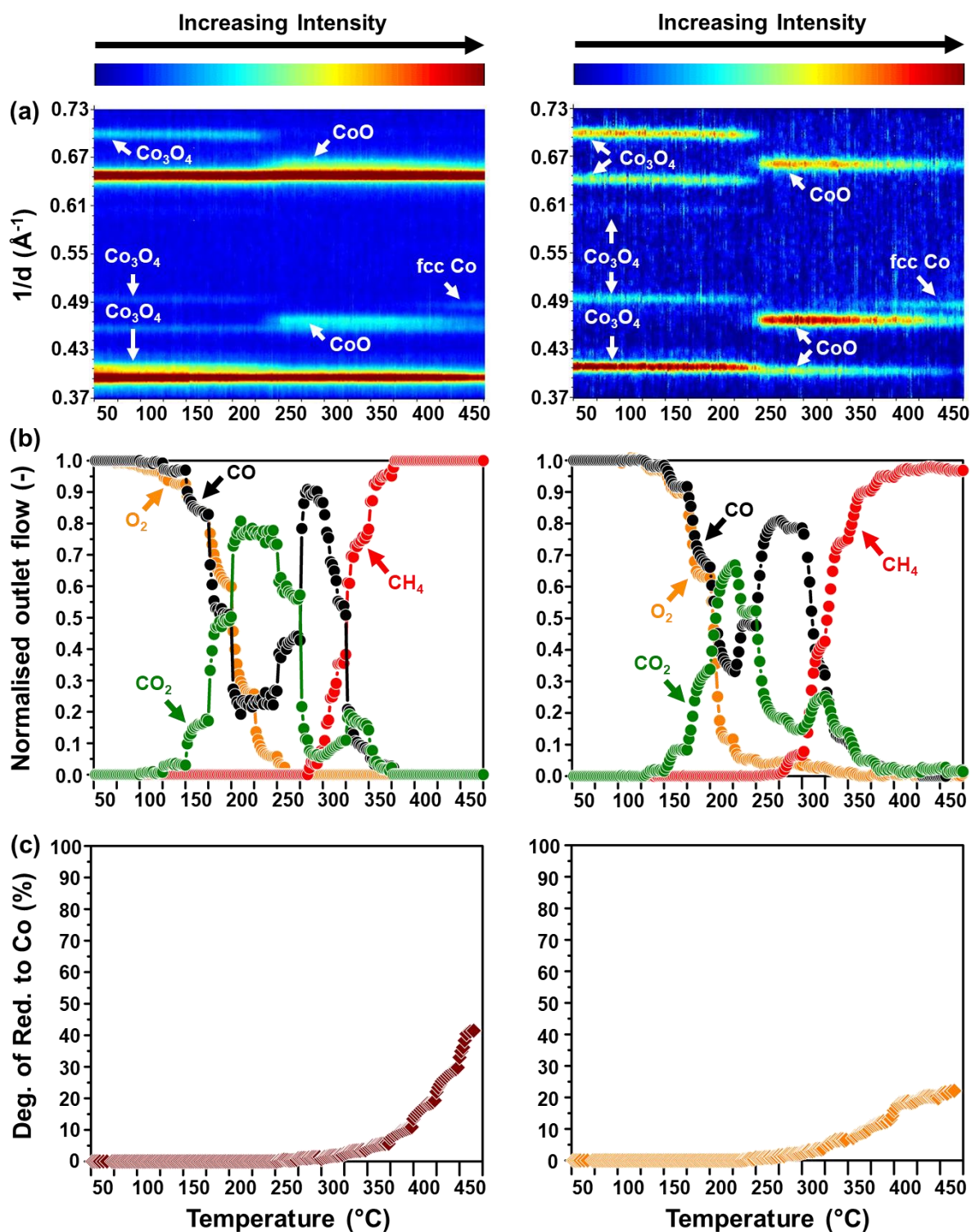


**Figure 8.4:** (a) On-top view of the *in situ* PXR D patterns recorded during dry CO-PrOx over (left)  $\text{Co}_3\text{O}_4/\text{SiC}$ , and (right)  $\text{Co}_3\text{O}_4/\text{SiO}_2$ . (b) Changes in the normalised outlet flow rates of CO,  $\text{O}_2$ ,  $\text{CO}_2$  and  $\text{CH}_4$  calculated from GC-TCD data. (c) Magnetometry-derived degree of reduction of  $\text{Co}_3\text{O}_4$  to metallic Co. (Feed composition: 1% CO, 1%  $\text{O}_2$ , 50%  $\text{H}_2$  and 48%  $\text{N}_2$ ; pressure: atmospheric, GHSV: 60000  $\text{mL(NTP)}/\text{g}_{\text{Co}_3\text{O}_4}/\text{hr}$ ).

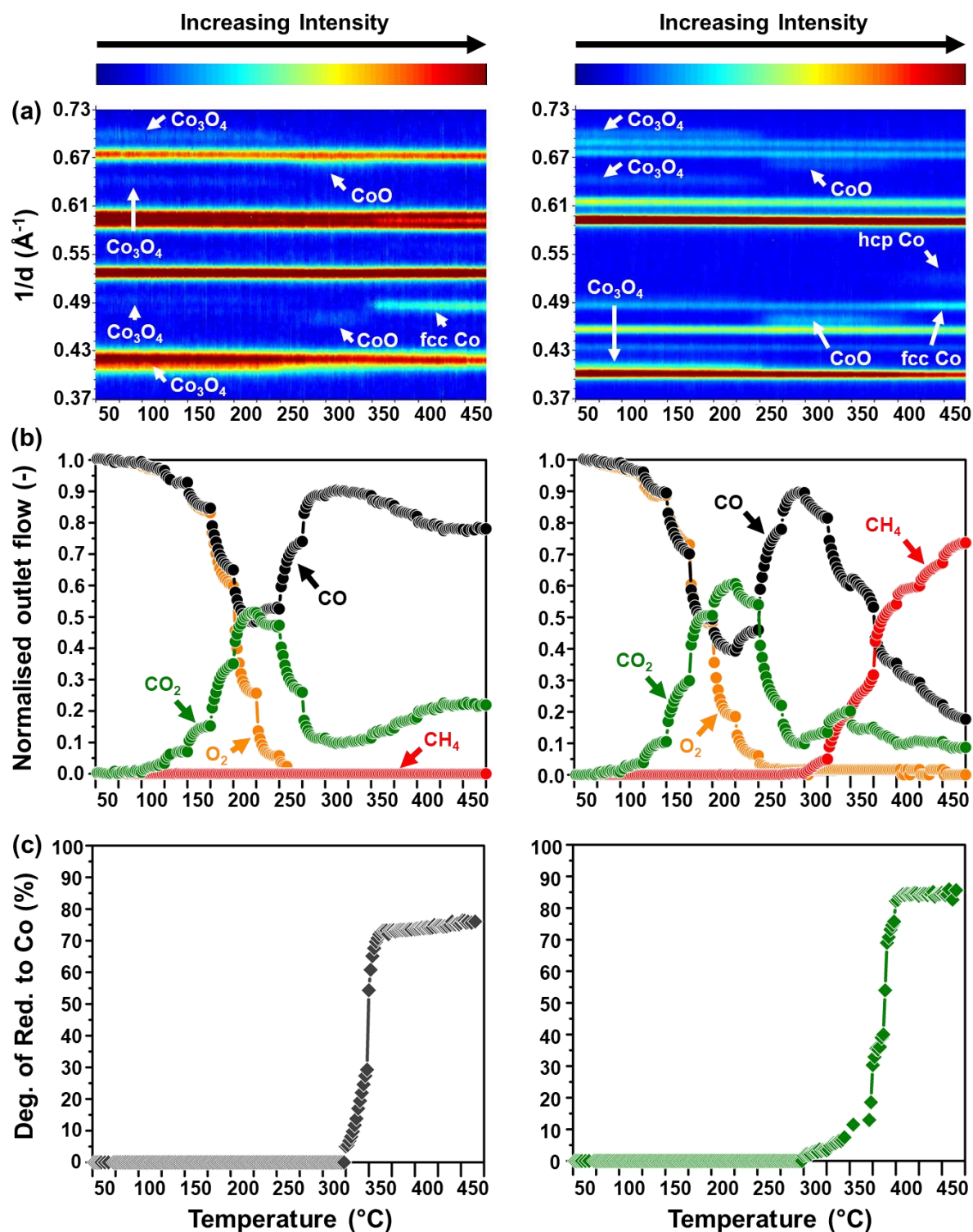


**Figure 8.5:** (a) On-top view of the *in situ* PXRD patterns recorded during dry CO-PrOx over (left)  $\text{Co}_3\text{O}_4/\text{TiO}_2$ -anatase, and (right)  $\text{Co}_3\text{O}_4/\text{TiO}_2$ -rutile. (b) Changes in the normalised outlet flow rates of CO,  $\text{O}_2$ ,  $\text{CO}_2$  and  $\text{CH}_4$  calculated from GC-TCD data. (c) Magnetometry-derived degree of reduction of  $\text{Co}_3\text{O}_4$  to metallic Co. (Feed composition: 1% CO, 1%  $\text{O}_2$ , 50%  $\text{H}_2$  and 48%  $\text{N}_2$ ; pressure: atmospheric, GHSV: 60000 mL(NTP)/g $_{\text{Co}_3\text{O}_4}$ /hr).

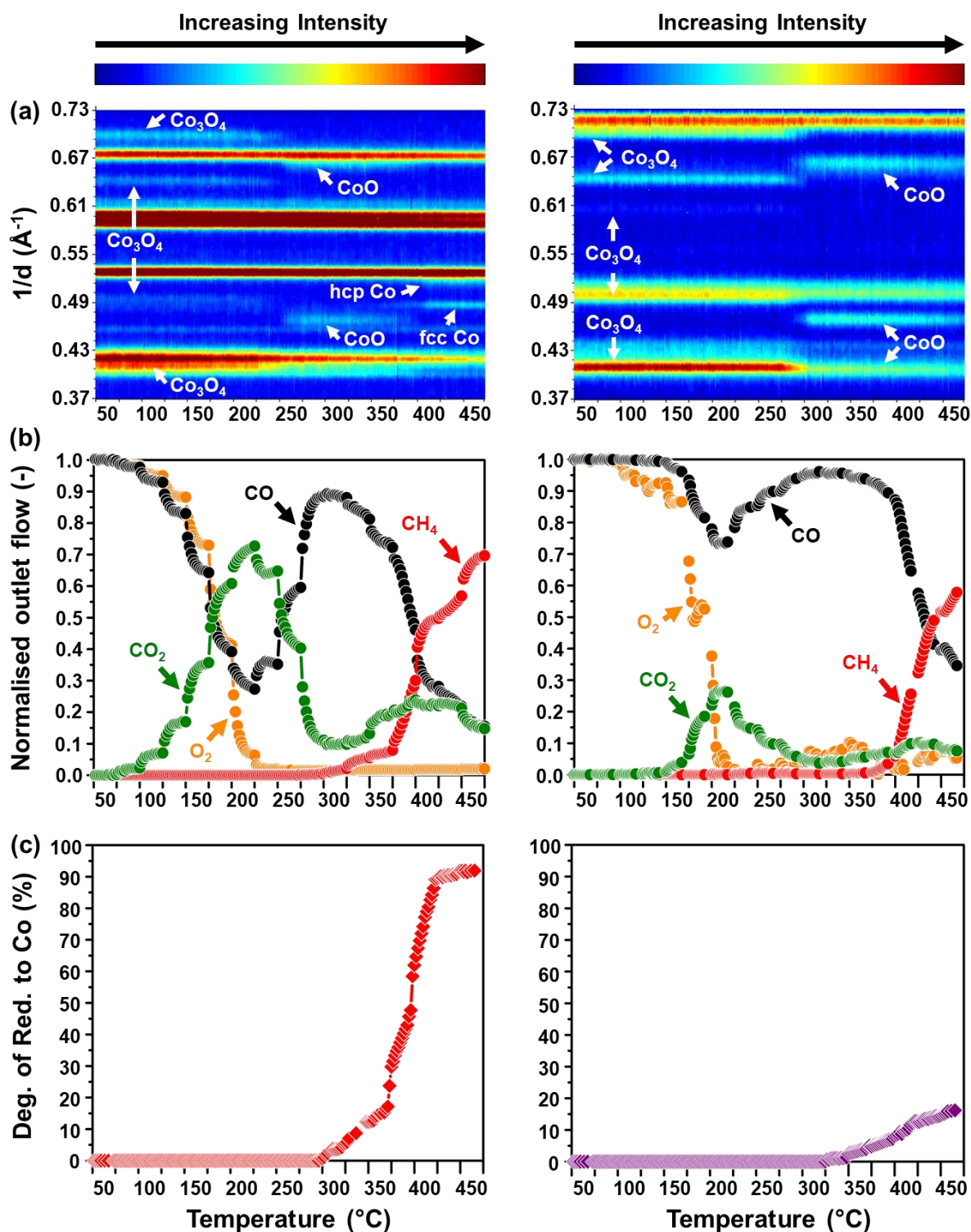


**Figure 8.6:** (a) On-top view of the *in situ* PXR D patterns recorded during dry CO-PrOx over (left)  $\text{Co}_3\text{O}_4/\text{TiO}_2\text{-P25}$ , and (right)  $\text{Co}_3\text{O}_4/\text{Al}_2\text{O}_3$ . (b) Changes in the normalised outlet flow rates of CO,  $\text{O}_2$ ,  $\text{CO}_2$  and  $\text{CH}_4$  calculated from GC-TCD data. (c) Magnetometry-derived degree of reduction of  $\text{Co}_3\text{O}_4$  to metallic Co. (Feed composition: 1% CO, 1%  $\text{O}_2$ , 50%  $\text{H}_2$  and 48%  $\text{N}_2$ ; pressure: atmospheric, GHSV: 60000  $\text{mL(NTP)/g}_{\text{Co}_3\text{O}_4}/\text{hr}$ ).

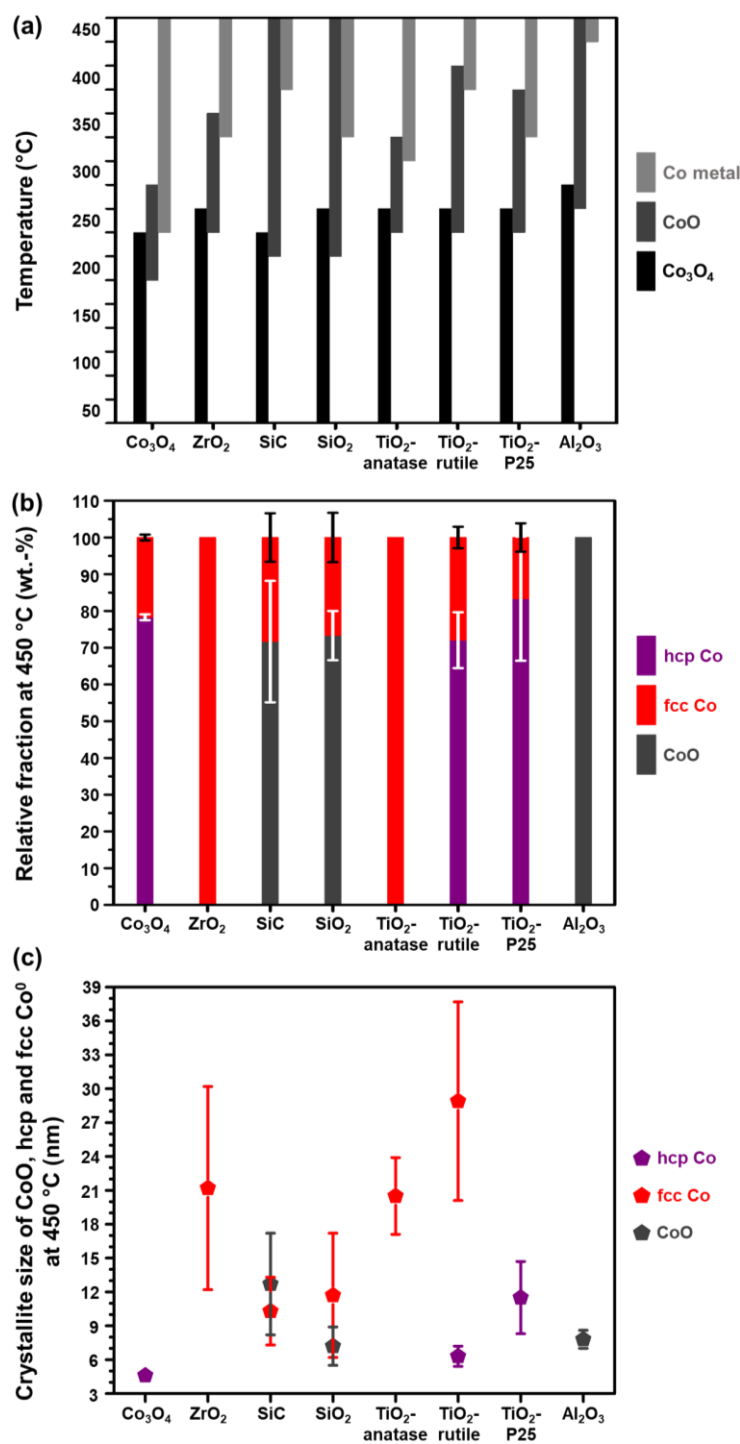


**Figure 8.7:** (a) Temperatures at which the Co-based phases were detected using *in situ* PXRD during dry CO-PrOx over the prepared catalysts. (b) Relative fraction, and (c) crystallite size of CoO, hcp and fcc Co at 450 °C. The white error bars in (b) are for CoO and hcp Co, while the black error bars are for fcc Co. The presence of metallic Co in the Al<sub>2</sub>O<sub>3</sub>-supported catalyst, depicted in (a), is inferred from the slightly decreasing intensity of the CoO reflections at 450 °C in Figure 8.6((a), right). The size of fcc Co in the unsupported and TiO<sub>2</sub>-P25-supported catalyst is not reported in (c) due to possible granularity effects and/or intergrowth of hcp and fcc Co. (Feed composition: 1% CO, 1% O<sub>2</sub>, 50% H<sub>2</sub> and 48% N<sub>2</sub>; pressure: atmospheric, GHSV: 60000 mL(NTP)/gCo<sub>3</sub>O<sub>4</sub>/hr).

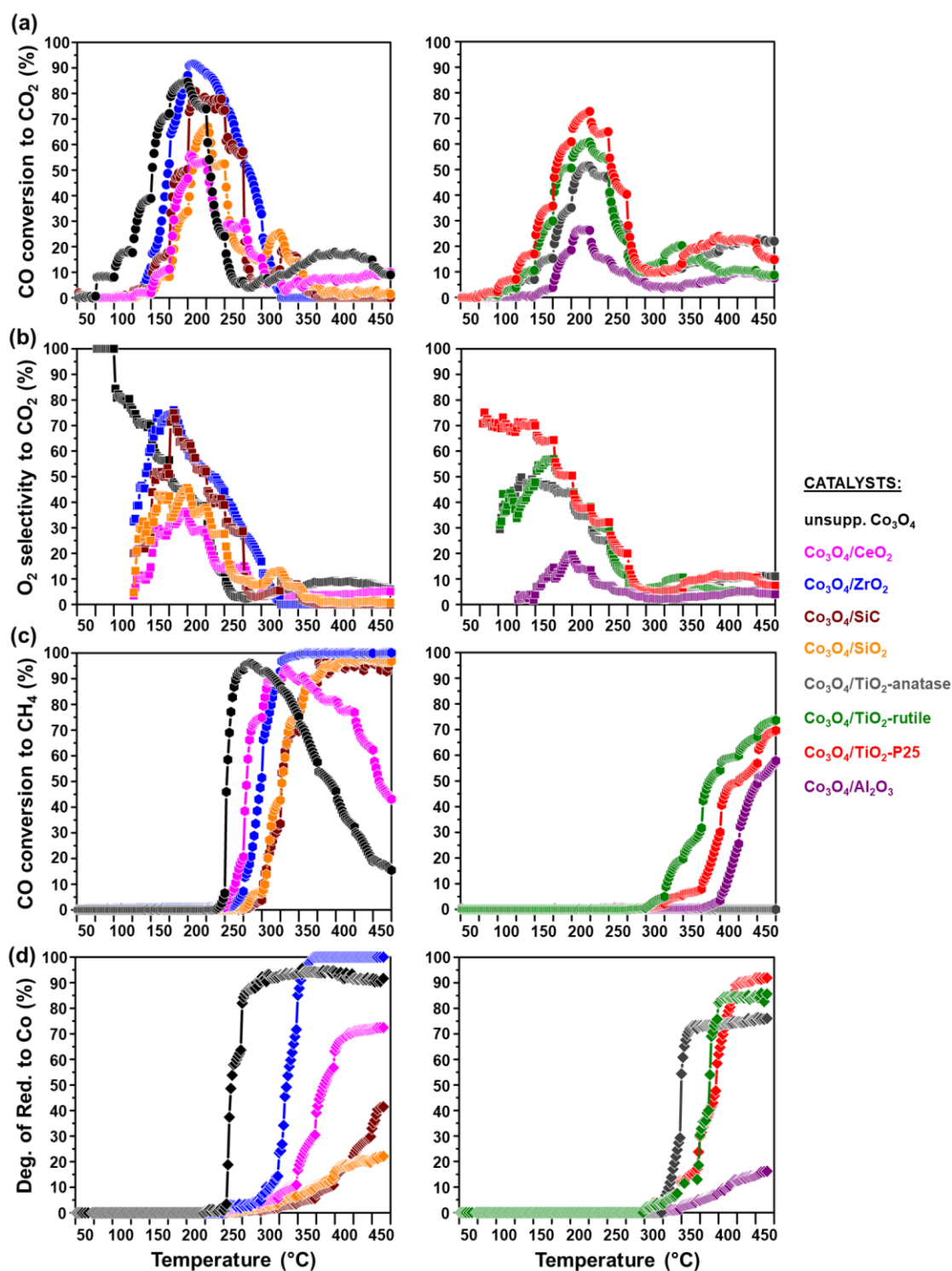


**Figure 8.8:** Changes in the (a) CO conversion, and (b)  $\text{O}_2$  selectivity to  $\text{CO}_2$  via oxidation, (c) CO conversion to  $\text{CH}_4$  via hydrogenation, and the (d) magnetometry-derived degree of reduction of  $\text{Co}_3\text{O}_4$  to metallic Co during dry CO-PrOx over all prepared catalysts. Note that the  $\text{O}_2$  selectivity to  $\text{CO}_2$  was calculated at temperatures where both CO and  $\text{O}_2$  were converted (see Figures 8.3 – 8.6). Also see Figure A.6.2 showing the changes in the CO conversion and  $\text{O}_2$  selectivity to  $\text{CO}_2$  between 50 and 200 °C, where the  $\text{Co}_3\text{O}_4$  phase is believed to be intact in all evaluated catalysts. (Feed composition: 1% CO, 1%  $\text{O}_2$ , 50%  $\text{H}_2$  and 48%  $\text{N}_2$ ; pressure: atmospheric, GHSV: 60000 mL(NTP)/g $\text{Co}_3\text{O}_4$ /hr).

The magnetic behaviour of the reduced supported samples was also assessed by obtaining M-H data at 450 °C, which have been plotted in Figures 8.9 and 8.10. Table 8.1 also shows a summary of the  $\gamma$  values for each catalyst, which are all above 10 wt.-%, indicating that the reduced catalysts are non-superparamagnetic. Note that the M-H curves for  $\text{Co}_3\text{O}_4/\text{SiO}_2$  and  $\text{Co}_3\text{O}_4/\text{Al}_2\text{O}_3$  (Figures 8.9(a) and 8.10(a), respectively) are not completely sigmoidal in shape due to a possible linear contribution from paramagnetic species (such as  $\text{CoO}$  [16],  $\text{Co}_x\text{Si}_y\text{O}_z$  [18–20],  $\text{Co}_x\text{Al}_y\text{O}_z$  [14]). These M-H curves also do not reach magnetic saturation at 2 T, *i.e.*, the electron spins are not all aligned in the direction of the maximum applied field. The linear contribution in the M-H curve of the  $\text{Al}_2\text{O}_3$ -supported catalyst appears to be (qualitatively) greater than that observed in the M-H curve of the  $\text{SiO}_2$ -supported catalyst. This is in line with the very low DoR obtained over  $\text{Al}_2\text{O}_3$  (16.2%) than over  $\text{SiO}_2$  (22.1%), which suggests the existence of stronger interactions between  $\text{CoO}_{1-x}$  species and the  $\text{Al}_2\text{O}_3$ . It is also worth noting the relatively low  $\gamma$  values (Table 8.1) of these two samples, which may have also been affected by the paramagnetic contribution. Nonetheless, the calculated values indicate the presence of particles/crystallites above the critical size for the superparamagnetism of hcp (11 nm at 450 °C [12]) and fcc  $\text{Co}^0$  (16 – 20(26) nm at 450 °C [12]), and further indicate the possibility of some degree of sintering. However, note that these two supported catalysts did not reduce to hcp Co according to PXRD analysis (see Figures 8.4((a), *right*) and 8.6((a), *right*)), implying that the  $\gamma$  values obtained are only based on a fraction of each catalyst with large non-superparamagnetic fcc Co crystallites.

Interestingly,  $\text{Co}_3\text{O}_4/\text{TiO}_2\text{-P25}$  exhibits the lowest  $\gamma$  value of 17.7 wt.-% while achieving a DoR of 91.9% at 450 °C. This high DoR indicates a very low concentration of paramagnetic species (such as  $\text{CoO}$  [16] and  $\text{Co}_x\text{Ti}_y\text{O}_z$  [17]), and therefore, the low  $\gamma$  value most likely suggests the presence of a relatively high amount of superparamagnetic metallic Co. From *in situ* PXRD analysis, it was shown that hcp ( $83.4 \pm 16.9$  wt.-%) and fcc Co ( $16.6 \pm 3.9$  wt.-%) were both formed in this sample, and that the hcp Co size was  $11.5 \pm 3.2$  nm, while the size of fcc Co could not be determined due to possible granularity effects. In reference to the above-mentioned critical sizes of the Co allotropes and the results from Rietveld refinement, it is possible that the fcc Co crystallites are the ones mostly contributing to the  $\gamma$  of 17.7 wt.-% obtained at 450 °C. Furthermore, a fraction of the hcp Co crystallites (especially those with a size above 11 nm) may also be contributing to the  $\gamma$  value. The  $\text{TiO}_2$ -rutile-supported catalyst also reduced to both hcp ( $72.1 \pm 7.6$  wt.-% and  $6.3 \pm 0.9$  nm) and fcc Co ( $27.9 \pm 2.9$  wt.-% and  $28.9 \pm 8.8$  nm) according to PXRD. However, the  $\gamma$  of this sample (51.2 wt.-%) is much higher than the relative concentration of the large fcc Co crystallites determined using Rietveld refinement. Due to the overlap of the hcp Co, fcc Co and  $\text{TiO}_2$ -rutile

reflections at  $1/d = 0.49 \text{ \AA}^{-1}$  in the acquired PXRD patterns (see Figures 8.5((a), *right*) and A.7.1(b)), the fcc Co concentration may have been underestimated. On the other hand, since the magnetometer is more sensitive to ferromagnetic material and that the magnetic signal is not affected by the TiO<sub>2</sub>-rutile support, the estimated relative concentration of fcc Co (through  $\gamma$ ) is much higher. Nonetheless, the small hcp Co crystallites possibly do not contribute to the estimated  $\gamma$  of 51.2 wt.-%, which further indicates a partially sintered catalyst (based on the presence of large fcc Co crystallites).

The ZrO<sub>2</sub>- and TiO<sub>2</sub>-anatase-supported catalysts have a  $\gamma$  value of 33.1 and 62.2 wt.-%, respectively, while the fcc Co size (from Rietveld refinement) for the same samples is  $21.2 \pm 9.0$  and  $20.5 \pm 3.4$  nm, respectively. These results indicate the possibility of sintering under reaction conditions, despite the disagreement between the  $\gamma$  values and the PXRD sizes, which cannot be explained at this stage. The  $\gamma$  value for the reduced SiC-supported catalyst is also high (46.2 wt.-%) – indicative of sintering - but the average fcc Co crystallite size from PXRD is  $10.3 \pm 3.0$  nm at 450 °C. This large discrepancy may be partly caused by the limited detection of fcc Co using PXRD ( $28.3 \pm 6.6$  wt.-% - see Figures 8.4((a), *left*) and 8.7(b)), compared with that of the magnetometer (DoR = 41.5% - see Figure 8.8((d), *left*)). Lastly, the calculated  $\gamma$  for the CeO<sub>2</sub>-supported catalyst is 43.3 wt.-%, also suggesting possible sintering under reaction conditions. However, this cannot be confirmed with PXRD analysis as reflections from Co-based phases are not visible in the presence of CeO<sub>2</sub>, possibly due to the low starting Co<sub>3</sub>O<sub>4</sub> loading and high crystallinity of CeO<sub>2</sub> [92–95]. It is important to note that the CeO<sub>2</sub>-, ZrO<sub>2</sub>-, SiC-, TiO<sub>2</sub>-anatase-supported catalysts did not reduce to hcp Co, and therefore, the  $\gamma$  values obtained are only due to the presence of relatively large fcc Co crystallites.

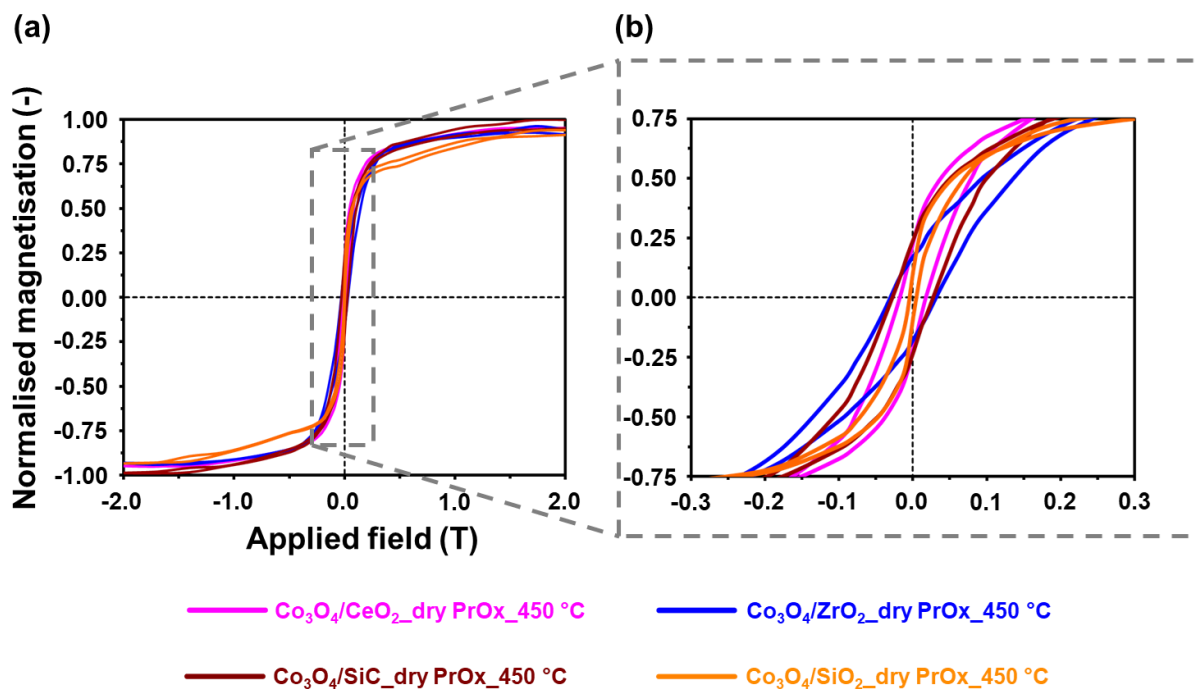


**Figure 8.9:** (a) Magnetometry-derived M-H curves recorded at 450 °C under dry CO-PrOx over  $\text{CeO}_2$ -,  $\text{ZrO}_2$ -, SiC- and  $\text{SiO}_2$ -supported  $\text{Co}_3\text{O}_4$  catalysts. (b) Magnified view of the M-H curves indicating the existence of hysteresis behaviour. (Feed composition: 1% CO, 1%  $\text{O}_2$ , 50%  $\text{H}_2$  and 48%  $\text{N}_2$ ; pressure: atmospheric, GHSV: 60000 mL(NTP)/g $\text{Co}_3\text{O}_4$ /hr).

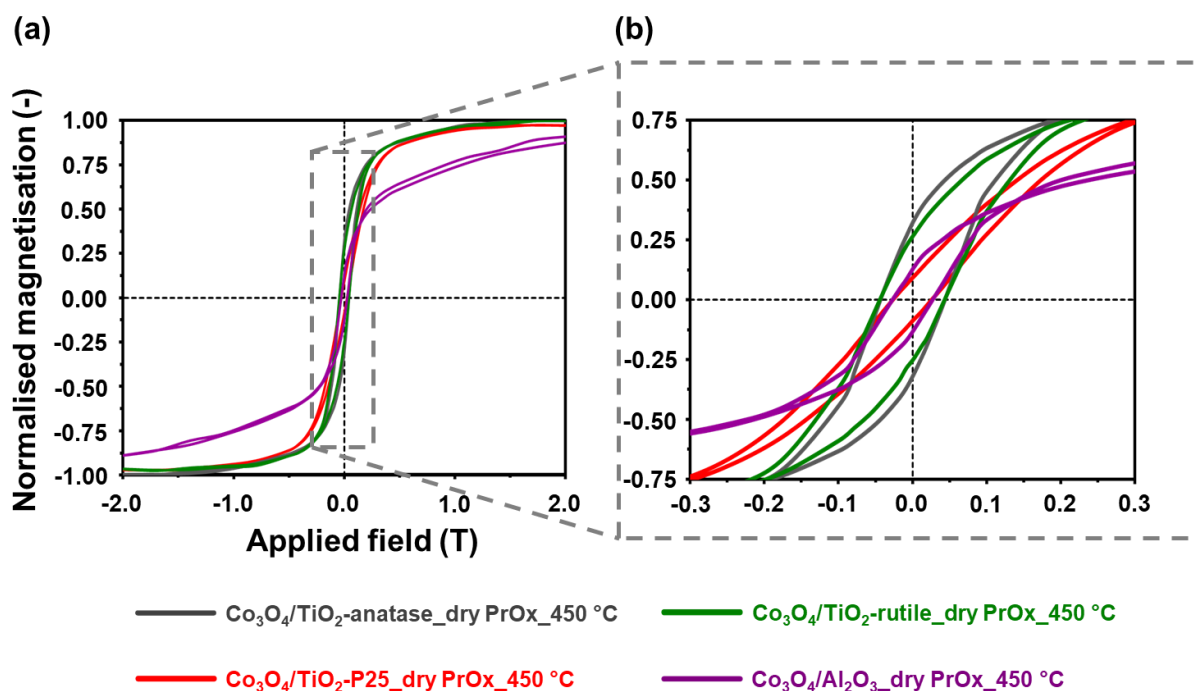


**Figure 8.10:** (a) Magnetometry-derived M-H curves recorded at 450 °C under dry CO-PrOx gas over  $\text{TiO}_2$ - and  $\text{Al}_2\text{O}_3$ -supported  $\text{Co}_3\text{O}_4$  catalysts. (b) Magnified view of the M-H curves indicating the existence of hysteresis behaviour. (Feed composition: 1% CO, 1%  $\text{O}_2$ , 50%  $\text{H}_2$  and 48%  $\text{N}_2$ ; pressure: atmospheric, GHSV: 60000 mL(NTP)/g $\text{Co}_3\text{O}_4$ /hr).

**Table 8.1:** Summary of the  $\gamma$  values calculated from magnetometry data recorded at 450 °C during dry CO-PrOx at atmospheric pressure.

Sample name	$\gamma$ at 450 °C (wt.-%)
unsupported $\text{Co}_3\text{O}_4$	33.0
$\text{Co}_3\text{O}_4/\text{CeO}_2$	43.3
$\text{Co}_3\text{O}_4/\text{ZrO}_2$	33.1
$\text{Co}_3\text{O}_4/\text{SiC}$	46.2
$\text{Co}_3\text{O}_4/\text{SiO}_2$	18.9
$\text{Co}_3\text{O}_4/\text{TiO}_2\text{-anatase}$	62.2
$\text{Co}_3\text{O}_4/\text{TiO}_2\text{-rutile}$	51.2
$\text{Co}_3\text{O}_4/\text{TiO}_2\text{-P25}$	17.7
$\text{Co}_3\text{O}_4/\text{Al}_2\text{O}_3$	21.9

### 8.3. Evaluation of the Reduction Mechanism of Un-/Supported $\text{Co}_3\text{O}_4$

The results in sections 8.1. and 8.2. show that all prepared catalysts are susceptible to (partial) reduction by  $\text{H}_2$  during CO-PrOx. The reduction forms CoO and ultimately metallic Co, which are both less active and selective towards CO oxidation [2–8]. Sub-section 2.3.1. discussed the reduction of metal oxides during CO-PrOx and it is often that the catalysts do not fully reduce. However,  $\text{CH}_4$  is still the only carbon-based product formed over metals such as Ni and Co. Therefore, the question then becomes, is the unreduced oxide not exposed on the surface of the nanoparticles or are the other reactions, *viz.*,  $\text{H}_2$  oxidation and CO methanation, just more kinetically favoured than CO oxidation?

There are two possible reduction mechanisms proposed in the literature (also discussed in sub-section 2.3.1.) - the one is based on a nucleation model and the other is based on a shrinking core model [56,96–99]. Briefly, the nucleation model assumes that initially, small nuclei of the metallic phase (or low oxidation state metal ions) are formed anywhere on the surface or at the core of the nanoparticle. At this point, the degree of reduction is very low. These nuclei continue to grow with time (but at constant temperature) until enough  $\text{H}_2$  activation sites have formed to then induce an autocatalytic reduction process. When the reduction is autocatalytic, the rate of change in the degree of reduction is very high but eventually reaches a maximum. In reality, this means that the nuclei have grown to a point of merging with each other, leaving very little unreduced oxide. Depending on the location of the unreduced oxide, the rate of reduction of this oxide will then be dependent on the rate of  $\text{H}_2$  diffusion through the reduced areas [56,96–99].

The shrinking core model assumes a rapid start to the reduction process, *i.e.*,  $\text{H}_2$  activation/dissociation is not a rate-determining step. In reality, the nanoparticle surface and sub-surface oxidic species are the first to be reduced, creating a thin metallic (or low oxidation state metal ion-containing) shell. The total reduced area at this point is quite large, which explains the high initial reduction rate. As more reduction takes place, the size of the core oxide decreases and therefore, the reduction rate decreases. The rate-determining step of this mechanism is believed to be the diffusion of the reducing molecules and reduction products through the reduced region to and from the oxidic region, respectively [56,96–99].

The reduction of unsupported and  $\text{ZrO}_2$ -supported  $\text{Co}_3\text{O}_4$  catalysts has been studied at three different temperatures (225, 275 and 325 °C), holding the temperature for 4 hr, while flowing a

1:1:50:48 CO:O<sub>2</sub>:H<sub>2</sub>:N<sub>2</sub> gas mixture at a GHSV of 60000 ml(NTP)/g<sub>Co<sub>3</sub>O<sub>4</sub></sub>/hr. The temperature of 225 °C was for monitoring the formation of CoO in both catalysts using *in situ* PXRD, while the 275 °C was for monitoring metallic Co formation in the unsupported sample and 325 °C for monitoring the metallic phase in the ZrO<sub>2</sub>-supported sample using *in situ* magnetometry. However, the unsupported sample was also reduced at 325 °C to study the effect of temperature and for comparing with the ZrO<sub>2</sub>-supported sample (also see sub-sections 4.4.2.3. and 4.4.3.1. for a detailed experimental procedure). These two catalysts were chosen for this part of the study as they exhibited very high degrees of reduction during dry CO-PrOx at relatively low temperatures (see summary in Figure 8.8(d)).

Figure 8.11(a) shows the PXRD patterns recorded during the reduction of the two catalysts (separately) to form CoO at 225 °C. Figure 8.11(b) shows the degree of reduction and the first derivative curves for the degree of reduction of the two samples evaluated. The reduction of Co<sub>3</sub>O<sub>4</sub> to CoO at 225 °C for the unsupported catalyst takes place very rapidly (*i.e.*, within 5 min) but for the ZrO<sub>2</sub>-supported sample, reduction sets in after 25 min, implying that there is an induction period before detectable amounts of CoO are formed. However, for both catalysts, reduction to CoO reaches completion within 1.5 hr. The shape of the degree of reduction curve and the derivative curve for the unsupported sample resembles that observed for nanoparticles reducing *via* the shrinking core mechanism (see Figure 2.7), while the reduction of Co<sub>3</sub>O<sub>4</sub>/ZrO<sub>2</sub> can be described using the nucleation model (Figure 2.6). This means that during the course of the dry CO-PrOx reaction, unsupported Co<sub>3</sub>O<sub>4</sub> possibly forms intermediate core-shell Co<sub>3</sub>O<sub>4</sub>@CoO particles, while the ZrO<sub>2</sub>-supported Co-bearing particles may have an “irregular” composition of reduced and unreduced Co ions. The slow onset of reduction observed for Co<sub>3</sub>O<sub>4</sub>/ZrO<sub>2</sub> at 225 °C may be a result of the relatively strong NPSIs introduced during catalyst synthesis, which may be slightly slowing down the H<sub>2</sub> adsorption/dissociation rate and/or strengthening the Co-O bonds in Co<sub>3</sub>O<sub>4</sub> [55–59].

In Figure 8.12, the degree of reduction and first derivative curves for the reduction of Co<sub>3</sub>O<sub>4</sub> to metallic Co in the magnetometer are shown. Note that during dry CO-PrOx (sections 8.1. and 8.2.), the catalysts formed metallic Co at different reaction temperatures. So, at first, different temperatures were chosen for the reduction mechanism study. These temperatures were made to be as close as possible to the onset formation temperature for the metallic phase but still high enough to enable (almost) complete reduction after 4 hr. The two catalysts have a fast initial reduction (*i.e.*, within 10 min) which continues until completion for the unsupported sample within 2 hr, while the supported sample reaches a DoR of about 95% at the end of the 4 hr. The shape of

the DoR and first derivative curves indicate that the reduction to the metallic phase follows a shrinking core mechanism in both catalysts, with possible formation of intermediate core-shell  $\text{Co}_{3-x}\text{O}_{4-y}@Co^0$  particles.

Lastly, the unsupported sample was reduced at 325 °C to study the effect of temperature and to compare with the  $\text{ZrO}_2$ -supported catalyst, which was also reduced at 325 °C. As expected, the reduction rate of the unsupported sample increases rapidly, and almost complete reduction is achieved within 30 min. The shape of the curves also suggests a shrinking core model.

It is important to note that such an *in situ* study is being performed for the first time under CO-PrOx conditions using  $\text{Co}_3\text{O}_4$ , and this study has provided a useful insight into the possible reduction mechanisms for the oxide phase at selected temperatures. The intermediate formation of core-shell particles, where either CoO or metallic Co is on the outer surface (depending on reaction temperature), seems to explain the sudden drop in the CO oxidation activity and selectivity observed for the unsupported catalyst in Figure 8.1(d). The slow CoO formation in the  $\text{ZrO}_2$ -supported catalyst is in-line with the relatively slow decrease in the CO oxidation activity observed in Figure 8.3(c). However, temperature also plays a significant role in the rate of reduction and determines the kind of mechanism the reduction will follow [56,96–99]. This may have been the case for the  $\text{ZrO}_2$ -supported sample where the reduction to CoO at 225 °C can be described using the nucleation model, while the reduction to metallic Co at 325 °C can be described using the shrinking core model. The possible occurrence of a shrinking core reduction mechanism for both catalysts at 325 °C (and also 275 °C for unsupported  $\text{Co}_3\text{O}_4$ ) could explain the predominant formation of  $\text{H}_2\text{O}$  (*via*  $\text{H}_2$  oxidation and CO hydrogenation, respectively) and  $\text{CH}_4$  (*via* CO hydrogenation) during dry CO-PrOx (see Figure 8.8(c)) as a result of forming intermediate core-shell  $\text{Co}_{3-x}\text{O}_{4-y}@Co^0$  particles.

The magnetometry results summarised in Figure 8.8(d) for all prepared catalysts also highlight the significant differences in the reducibility of the  $\text{Co}_3\text{O}_4$  nanoparticles. These differences are believed to be a result of the nature and strength of the NPSIs which may influence the  $\text{H}_2$  dissociation rates and the rate at which lattice oxygen species are released from the nanoparticles [55–59]. Observing that  $\text{Co}_3\text{O}_4$  (and CoO) are more stabilised in the supported state, it may be possible that at temperatures below 250 °C, the formation of CoO may follow the nucleation model. For some of the supported catalysts, higher temperatures may cause a change in the reduction mechanism leading to the metallic phase.

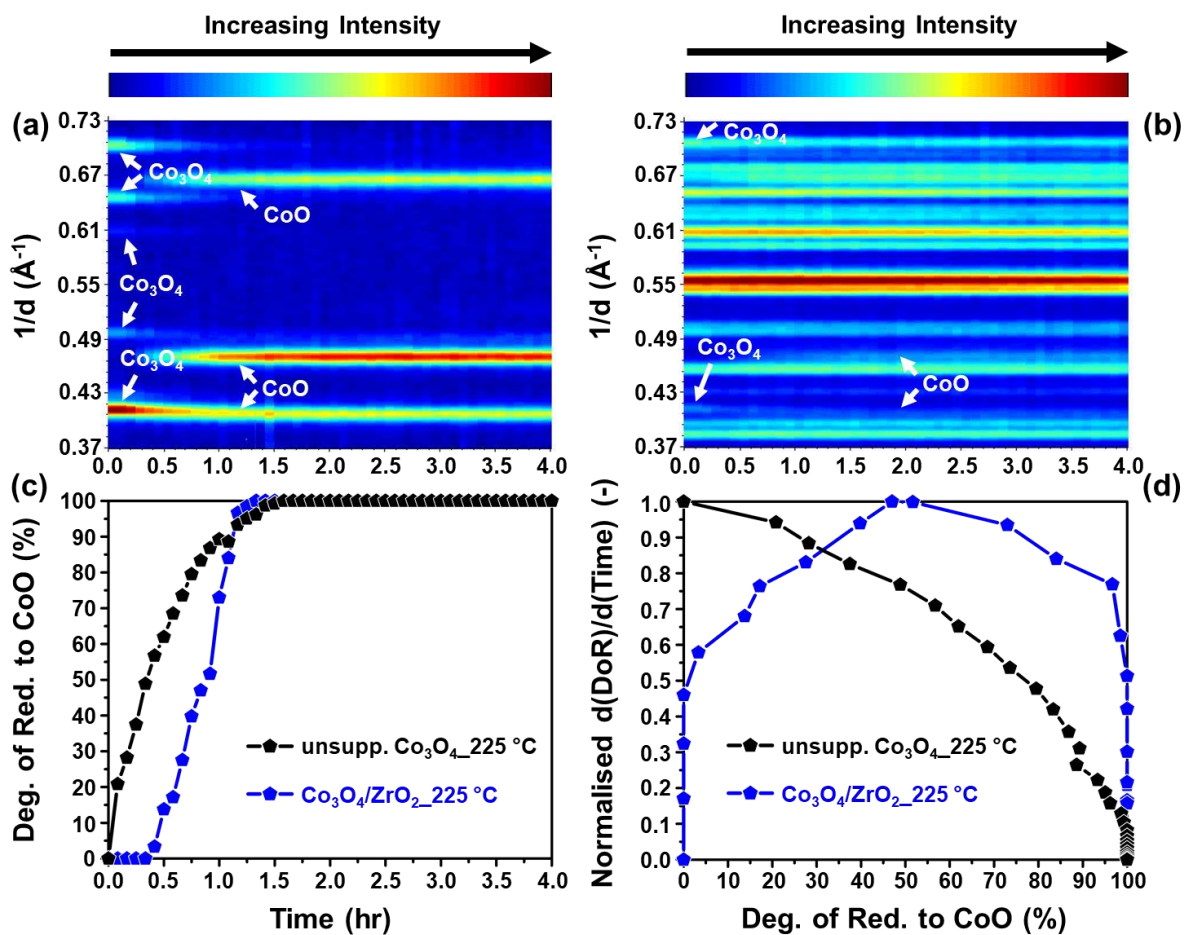


**Figure 8.11:** On-top view of the *in situ* PXRD patterns of (a) unsupported  $\text{Co}_3\text{O}_4$ , and (b)  $\text{Co}_3\text{O}_4/\text{ZrO}_2$ . Changes in the (c) degree of reduction with time, and the (d) derivative of the DoR at 225 °C during dry CO-PrOx. (Feed composition: 1% CO, 1%  $\text{O}_2$ , 50%  $\text{H}_2$  and 48%  $\text{N}_2$ ; pressure: atmospheric, GHSV: 60000  $\text{mL}(\text{NTP})/\text{g}_{\text{Co}_3\text{O}_4}/\text{hr}$ ).

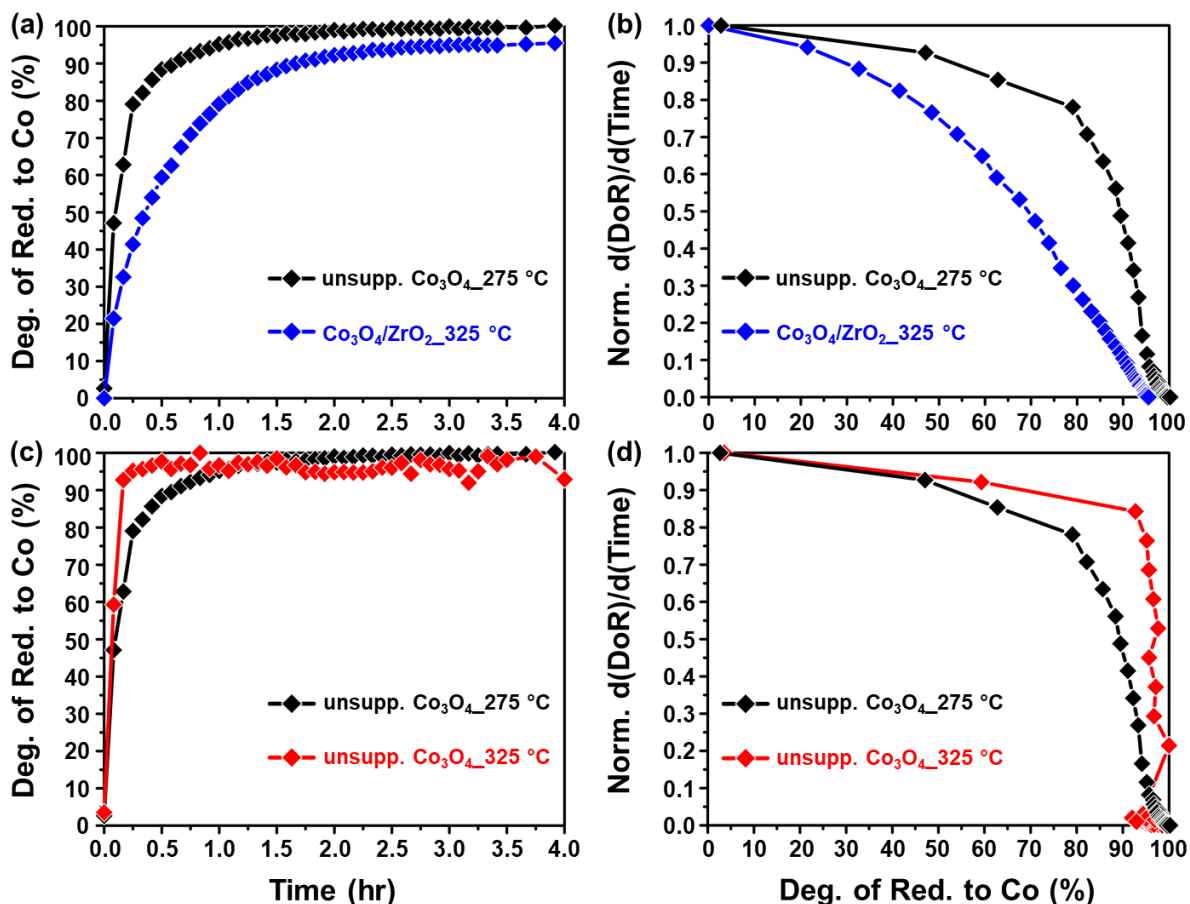


**Figure 8.12:** Changes in the magnetometry-derived (a) degree of reduction, and the (b) derivative of the DoR with time at 275 °C for the unsupported sample and 325 °C for the  $\text{Co}_3\text{O}_4/\text{ZrO}_2$  sample during dry CO-PrOx. Effect of temperature on the (c) degree of reduction with time, and the (d) derivative of the DoR for the unsupported  $\text{Co}_3\text{O}_4$  sample only. (Feed composition: 1% CO, 1%  $\text{O}_2$ , 50%  $\text{H}_2$  and 48%  $\text{N}_2$ ; pressure: atmospheric, GHSV: 60000 mL(NTP)/g $\text{Co}_3\text{O}_4$ /hr).

#### 8.4. Characterisation of Spent Catalysts after Dry CO-PrOx using *ex situ* (HR)STEM-EELS

After performing the dry CO-PrOx experiments, the spent samples were analysed using (HR)STEM-EELS to monitor any significant differences, relative to the fresh samples. However, elemental mapping was not applied when analysing the spent unsupported sample. The spent catalysts analysed were obtained from the magnetometry reactor as high amounts (in mass) of fresh catalyst were initially loaded into it. It is worth noting that due to long sample storage times (6 –

10 months) between obtaining the spent sample and carrying out the STEM-EELS analysis, samples may have partially or fully re-oxidised. However, the re-oxidation is not expected to sinter the particles as these were sealed and kept at room temperature and atmospheric pressure prior to the microscopic analysis.

Figure 8.13(a) and (b), respectively, show the low- and high-magnification micrographs of the spent unsupported catalyst. The sample mostly has large agglomerates which are made up of very small Co-bearing particles (see Figure 8.13(b)). However, in some cases, it is difficult to ascertain whether all the observed large Co-bearing entities are agglomerates or large single particles (*i.e.*, not made up of many small particles) due to possible stacking of these large entities, resulting in the darker regions in Figure 8.13(a)). Nonetheless, based on the results from Rietveld refinement (Figure 8.1(b) and (c)), it is possible that the small particles observed in Figure 8.13(b) are hcp Co, and the larger particles could either be pure fcc Co or a mixture of intergrown hcp and fcc Co domains. It should be noted that the formation of pure hcp Co particles that are smaller than 20 nm, is predicted to be thermodynamically unfavourable [33–35]. Therefore, at this stage, the details on how these very small particles may have formed cannot be provided. On the other hand, the presence of some large particles indicates that sintering took place, as was also suggested by the magnetometry results ( $\gamma = 33.0$  wt.-%). Although the fcc Co crystallite size could not be confirmed using PXRD (due to possible granularity effects), these may have still undergone some degree of sintering.

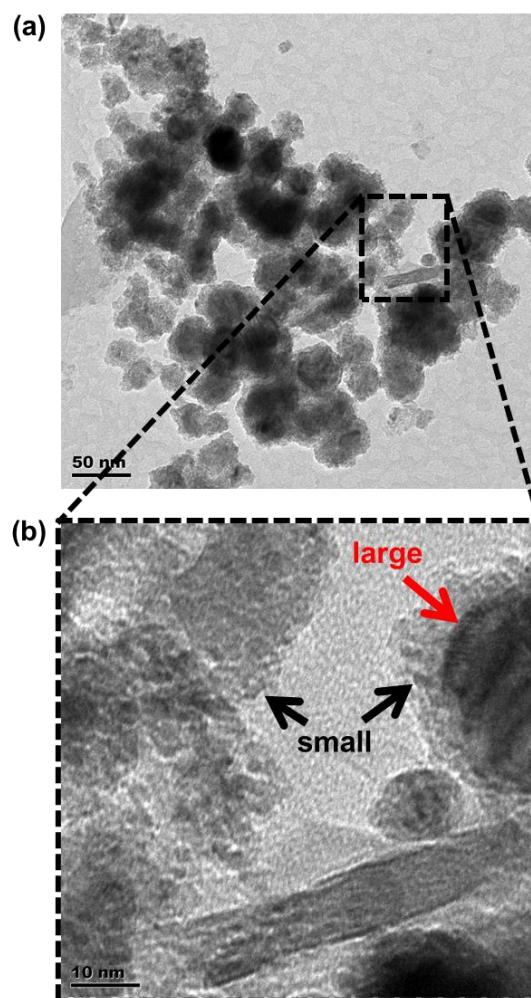


**Figure 8.13:** (a) TEM micrograph of the spent sample after dry CO-PrOx, and (b) a magnified STEM micrograph showing the very small particles that make up the agglomerates. The black arrows indicate the small (possibly) hcp Co particles and the red arrow indicates the large (possibly) fcc Co-containing particles.

Figure 8.14(a) shows a bright-field STEM micrograph for the spent  $\text{Co}_3\text{O}_4/\text{TiO}_2$ -anatase sample, while Figures 8.14(b) and (c) display the composite and individual EELS elemental maps, respectively. During dry CO-PrOx, this sample underwent partial reduction to metallic Co at high reaction temperatures, but this did not result in methane formation as expected (see Figure 8.5(left)). The explanation given in section 8.2. was that the metallic Co may have been encapsulated by  $\text{TiO}_{2-x}$  species formed during the partial reduction of the  $\text{TiO}_2$ -anatase support surface [73,83–86]. The EELS maps generated show an area on the edge of the  $\text{TiO}_2$ -anatase support that has formed  $\text{TiO}_{2-x}$  extensions which interact closely with the small cobalt-bearing particles. Figure A.8.1 in Appendix A.8. also shows a different edge of the anatase support that has similar  $\text{TiO}_{2-x}$  species extending towards a cobalt-bearing nanoparticle. These edge  $\text{TiO}_{2-x}\text{-CoO}_{1-x}$

regions possibly indicate (full or partial) encapsulation of the cobalt, which supports the proposed explanation for the lack of methane formation during dry CO-PrOx.

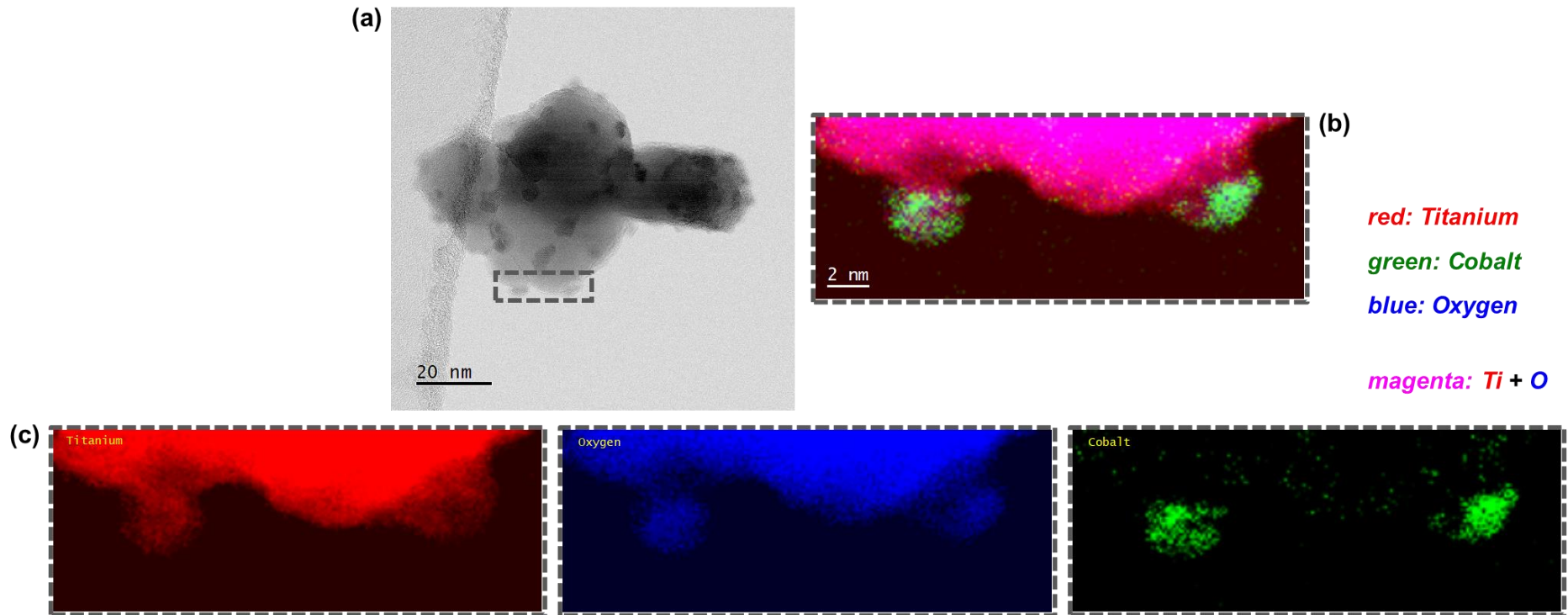
Also note that *in situ* PXRD and magnetometry have indicated the possibility of sintering as a fcc Co size of  $20.5 \pm 3.4$  nm was estimated from the PXRD pattern recorded at 450 °C, and a  $\gamma$  value of 62.2 wt.-% was obtained from the M-H curve recorded at the same temperature. However, an analysis of the spent sample *via* STEM-EELS did not show a high number of large particles (see size distribution in Figure 8.18(*top-left*)). This led to a number-based average size of  $13.9 \pm 4.4$  nm (Table 8.2), which is similar to that of the fresh Co<sub>3</sub>O<sub>4</sub>/TiO<sub>2</sub>-anatase catalyst ( $13.3 \pm 3.9$  nm – see Table 5.2). On the other hand, the volume-base average size of the spent sample is  $17.4 \pm 4.2$  nm (Table 8.2), which is within the statistical error of the fcc Co size from PXRD mentioned above. However, it remains possible that more larger particles may have been present in the spent sample, but were difficult to locate due to their low relative concentration in the spent sample. It is further proposed that these larger fcc Co particles are also encapsulated by the TiO<sub>2-x</sub> species, which prevents methane formation during dry CO-PrOx.

Figure 8.15 shows the STEM micrographs of the TiO<sub>2</sub>-rutile- and TiO<sub>2</sub>-P25-supported spent samples, together with the composite EELS elemental maps generated. The magnified maps show no evidence of encapsulation of the supported cobalt-bearing nanoparticles. This could explain why these two samples formed methane after having partially reduced to metallic Co. However, the possibility of partial encapsulation of some of the Co-bearing particles cannot be ruled out, especially in the TiO<sub>2</sub>-P25-supported catalyst as the support material composes of 80% of anatase (also see PXRD pattern in Figure 5.5 and STEM-EELS mapping in Figure 5.10) [84,85,87–89].

Similar to the spent TiO<sub>2</sub>-anatase-supported catalyst, the STEM analysis of the aforementioned spent samples did not show a high number of large particles (see size distributions in Figure 8.18(*right*)). This resulted in the number-based average sizes of  $14.4 \pm 5.0$  nm (TiO<sub>2</sub>-rutile) and  $13.5 \pm 4.9$  nm (TiO<sub>2</sub>-P25), which are within statistical error with the sizes of the corresponding fresh catalysts ( $13.0 \pm 3.3$  nm (TiO<sub>2</sub>-rutile) and  $9.9 \pm 3.7$  nm (TiO<sub>2</sub>-P25) – see Table 5.2). The STEM-derived volume-based size for the spent TiO<sub>2</sub>-rutile-supported catalyst is  $18.4 \pm 3.7$  nm, which is smaller than the fcc Co size ( $28.9 \pm 8.9$  nm) estimated from PXRD data, but higher than the size of hcp Co ( $6.3 \pm 0.9$  nm). Due to granularity effects, the fcc Co size in the TiO<sub>2</sub>-P25-supported catalyst could not be determined, but the size of hcp Co ( $11.5 \pm 3.2$  nm) is slightly smaller than the STEM-derived volume-based particle size ( $17.7 \pm 3.9$  nm). Although there exist some discrepancies between the STEM- and PXRD-derived sizes, both techniques indicate that

some degree of sintering may have taken place (especially for the fcc Co crystallites) during dry CO-PrOx. This proposed sintering is also in agreement with the relatively high  $\gamma$  values of 51.2 wt.-% (TiO<sub>2</sub>-rutile) and 17.7 wt.-% (TiO<sub>2</sub>-P25) obtained from the M-H curves recorded at 450 °C.

As mentioned in section 8.2., hcp and fcc Co were formed over TiO<sub>2</sub>-rutile and TiO<sub>2</sub>-P25, which is similar to the case of unsupported Co<sub>3</sub>O<sub>4</sub> (see section 8.1). However, STEM analysis of these spent TiO<sub>2</sub>-supported catalysts did not show any large Co-bearing clusters made up of very small particles, as those observed in the unsupported spent sample (compare the micrographs in Figures 8.13 and 8.15). At this stage, it is unclear if the hcp and fcc Co crystallites are (partially) intergrown or if there only exist particles/crystallites with no intergrown domains of the Co allotropes over the TiO<sub>2</sub> supports.



**Figure 8.14:** (a) Bright-field STEM micrograph of the spent  $\text{Co}_3\text{O}_4/\text{TiO}_2$ -anatase catalyst obtained after dry CO-PrOx. (b) Magnified STEM-EELS elemental map showing the regions with Ti, O and Co. (c) Corresponding magnified STEM-EELS maps of the individual elements.

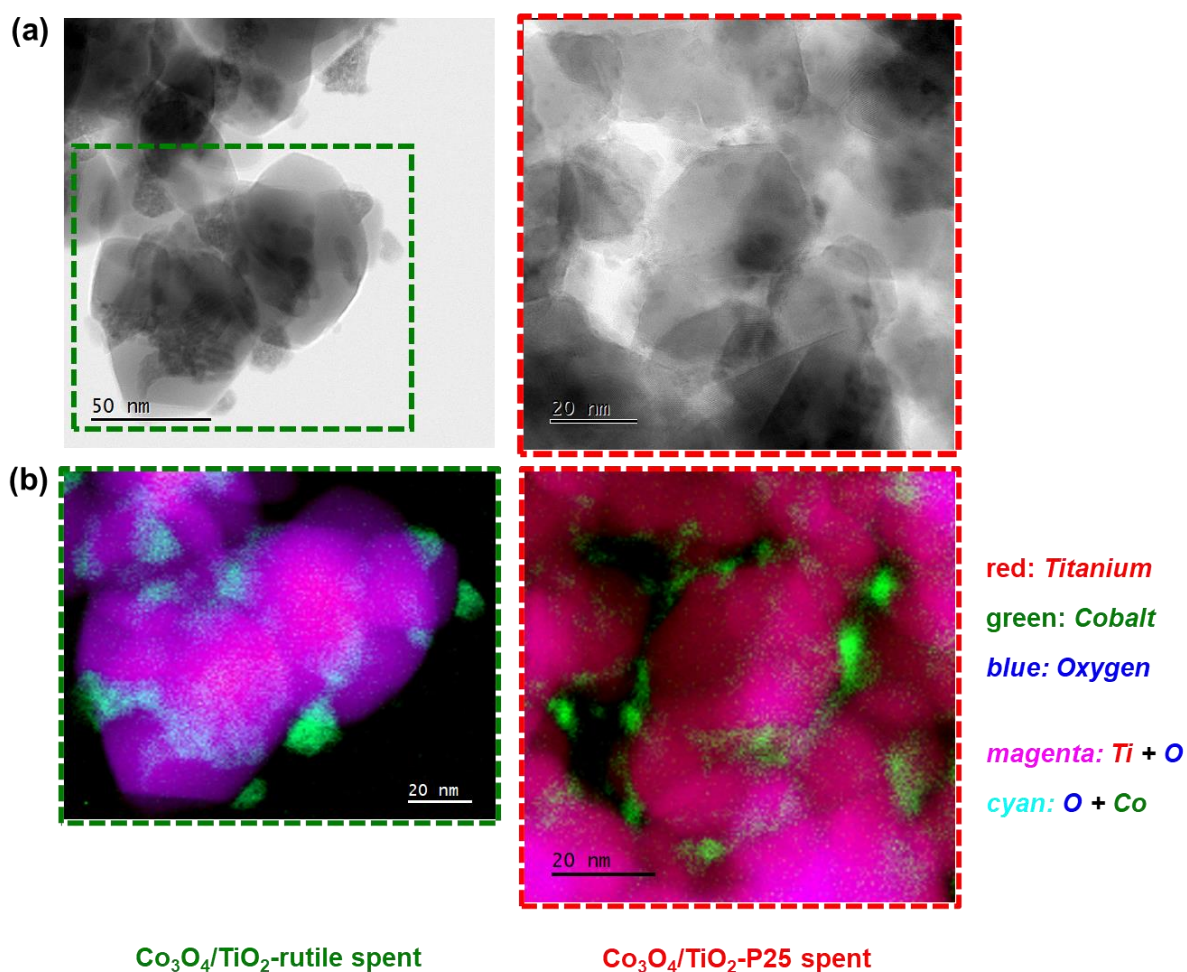


**Figure 8.15:** (a) Bright-field STEM micrographs of the spent  $\text{Co}_3\text{O}_4/\text{TiO}_2$ -rutile and  $\text{Co}_3\text{O}_4/\text{TiO}_2$ -P25 catalysts, respectively, obtained after dry CO-PrOx. (b) Magnified STEM-EELS elemental maps showing the regions with Ti, O and Co.

Shown in Figure 8.16 are the STEM-EELS micrographs for the  $\text{Co}_3\text{O}_4/\text{Al}_2\text{O}_3$  spent sample. Note that the composite map (Figure 8.16(b)) shows a number of yellow regions unlike in the composite maps of the spent  $\text{TiO}_2$ -supported catalysts (Figures 8.14 and 8.15). The aluminium map (Figure 8.16(c), *left*) also shows small regions with a brighter shade of red (see annotations on the map). These bright red regions are also where the cobalt species are located (see composite map in Figure 8.16(b), and the Co map in Figure 8.16(c), *right*). Therefore, these brighter red regions in the aluminium map and the yellow regions in the composite map indicate some possible chemical mixing between the species of Al and Co. This could be a result of the strong interaction between the  $\text{Al}_2\text{O}_3$  support and the starting  $\text{Co}_3\text{O}_4$  nanoparticles, as well as a result of the reaction conditions (*i.e.*, temperature and the presence of  $\text{H}_2/\text{H}_2\text{O}$ ) [50,53,54,73]. The suggested chemical mixing of

Al and Co may have also caused the earlier mentioned paramagnetic contribution observed in the M-H curve of the Al<sub>2</sub>O<sub>3</sub>-supported catalyst (see section 8.2. and Figure 8.10). Due to the extent of the chemical mixing, there were very few distinct Co-bearing nanoparticles that could be identified and considered for obtaining a particle size distribution.

The spent CeO<sub>2</sub>-supported sample (Figure 8.17) has multiple areas with “wetted” or “atomically-distributed” cobalt over the CeO<sub>2</sub> support, and therefore, had very few distinct nanoparticles that could be counted to obtain a size distribution. The same applied for the SiO<sub>2</sub>- and SiC-supported spent samples (see micrographs in Figures A.8.2 and A.8.3 in Appendix A.8.). However, it is worth mentioning that the wetting or atomic distribution of cobalt over these supports may also indicate the existence of strong Co-support interactions. These were also proposed for the CeO<sub>2</sub>-supported catalyst during H<sub>2</sub>-TPR and dry CO-PrOx, where in the latter experiment, the strong interactions may have negatively affected the methanation activity (see section 8.2.). The strong interactions in the SiC- and SiO<sub>2</sub>-supported catalysts and the conditions for dry CO-PrOx possibly caused the low reducibility of the oxide phase to metallic Co (see Figures 8.4(a) and (b), as well as 8.8(d)).

Over the ZrO<sub>2</sub> support, distinct Co-bearing particles were identified and considered for determining a size distribution (see Figures 8.18(*bottom-left*) and A.8.3). The number- and volume-based average sizes for this spent catalyst are  $14.0 \pm 5.3$  nm and  $18.6 \pm 4.0$  nm, respectively. The STEM-derived volume-based average size is within the statistical error of the fcc Co crystallite size ( $21.2 \pm 9.0$  nm) obtained from PXRD. Furthermore, these mentioned sizes for the spent ZrO<sub>2</sub>-supported catalyst are also similar to the STEM-derived volume-based average size for the corresponding fresh catalyst ( $19.1 \pm 3.8$  nm), but slightly larger than the PXRD-derived size for the same fresh catalyst ( $15.2 \pm 1.4$  nm). These observations possibly suggest a very low degree of sintering (if any) in this sample. The  $\gamma$  value (33.1 wt.-%) obtained for this spent catalyst also suggests the presence of a significant amount of particles/crystallites above the critical size for the superparamagnetism of fcc Co<sup>0</sup> (16 – 20(26) nm at 450 °C [12]), which is in agreement with the size analysis from STEM and PXRD.

Despite some discrepancies, PXRD, magnetometry and STEM-EELS were able to confirm increases in the particle/crystallite size in some of the spent catalysts after dry CO-PrOx, possibly caused by temperature and the reaction environment. These techniques were also able to confirm some important chemical changes that took place in some of the catalysts (such as cobalt oxide reduction, possible Al-Co mixing, Co<sub>1-x</sub> encapsulation by TiO<sub>2-x</sub> species, *etc.*). These captured

chemical and physical changes correlate well with observed changes in activity and selectivity as a function of temperature (Figures 8.8).

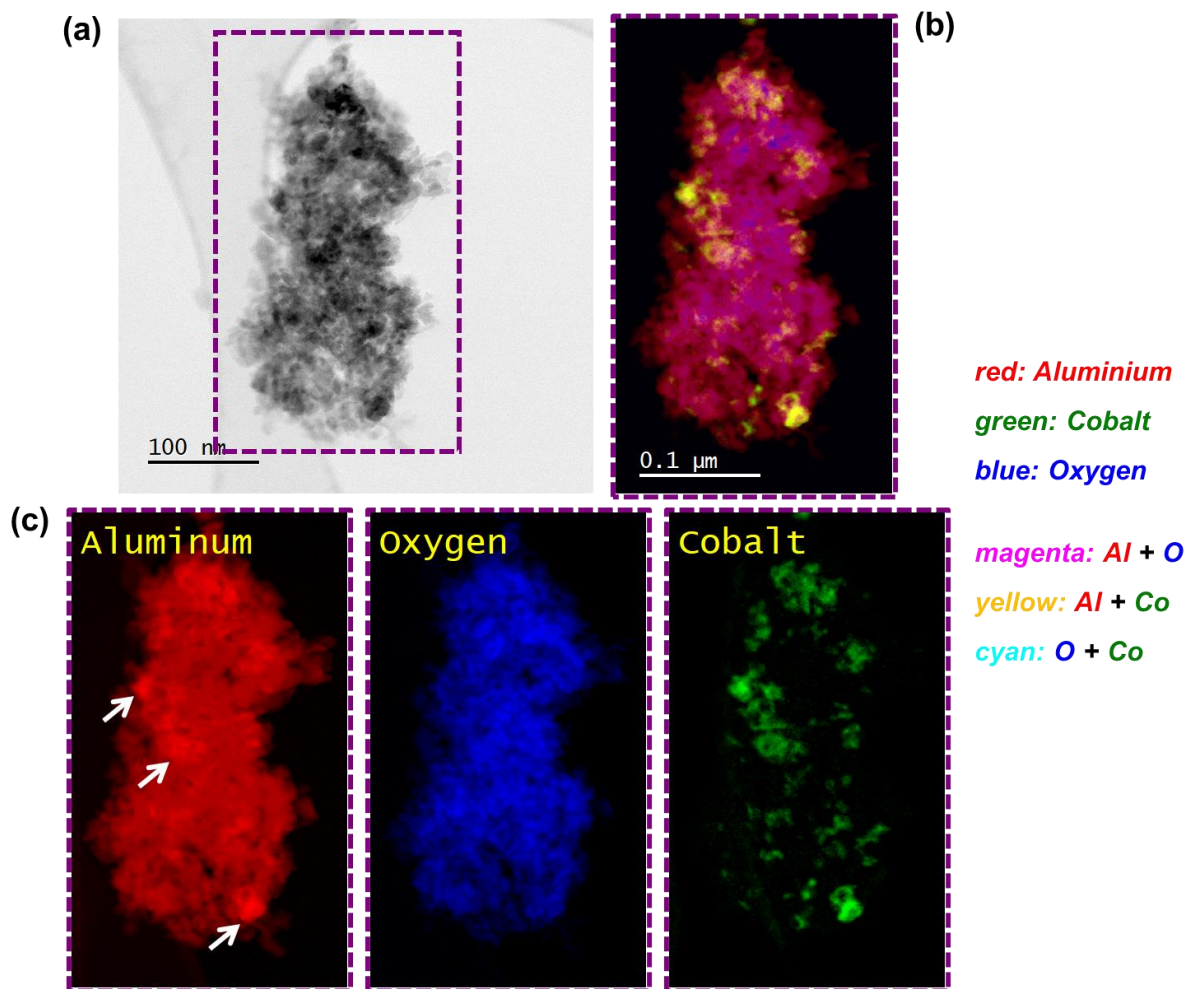


**Figure 8.16:** (a) Bright-field STEM micrograph of the spent  $\text{Co}_3\text{O}_4/\text{Al}_2\text{O}_3$  catalyst obtained after dry CO-PrOx. (b) Magnified STEM-EELS elemental map showing the regions with Al, O and Co. (c) Corresponding magnified STEM-EELS maps of the individual elements. The white arrows on the Al map show the bright regions which are believed to be the Al species that are chemically mixed with Co.

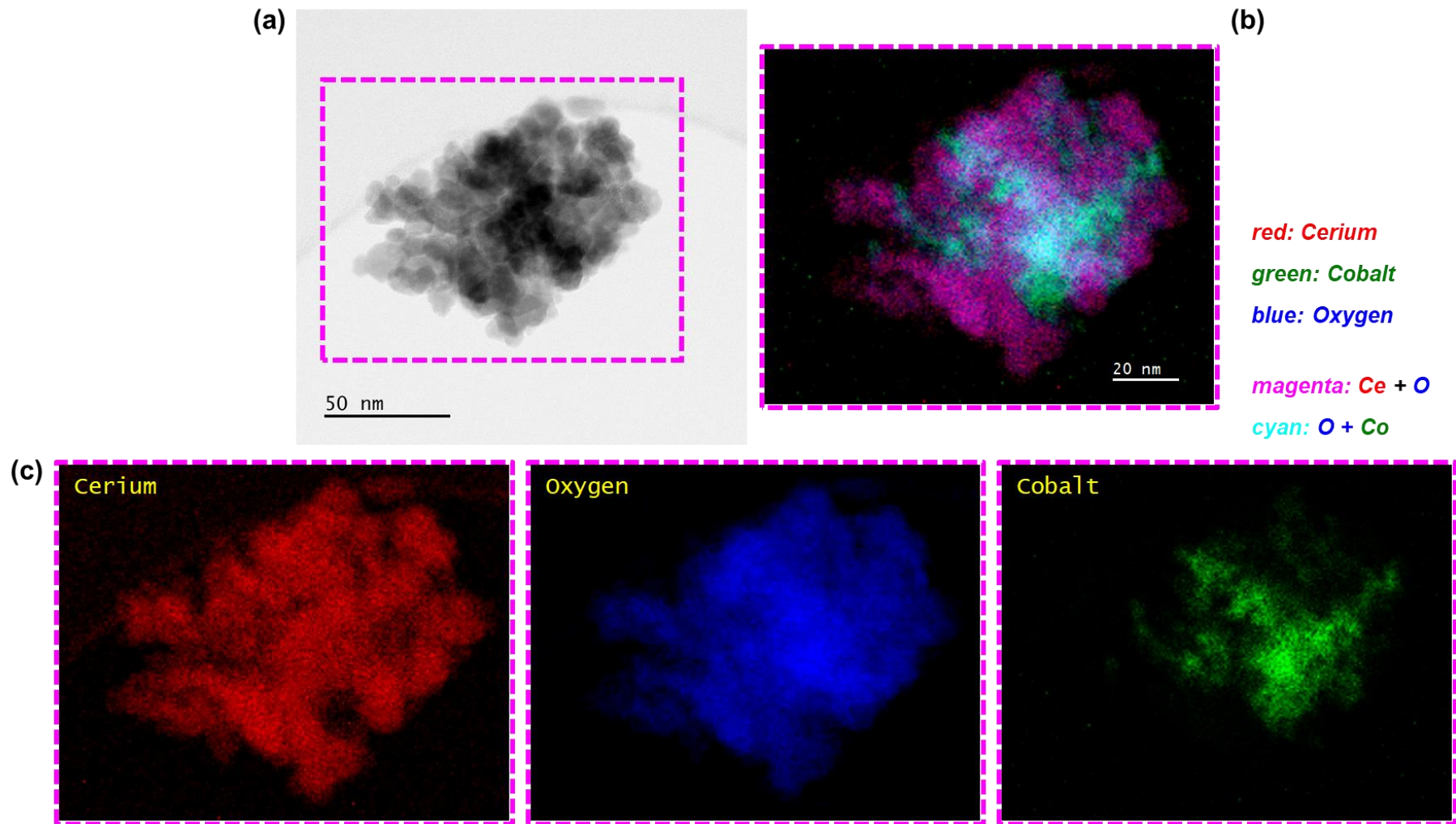


**Figure 8.17:** (a) Bright-field STEM micrograph of the spent  $\text{Co}_3\text{O}_4/\text{CeO}_2$  catalyst obtained after dry CO-PrOx. (b) Magnified STEM-EELS elemental map showing the regions with Ce, O and Co. (c) Corresponding magnified STEM-EELS maps of the individual elements.

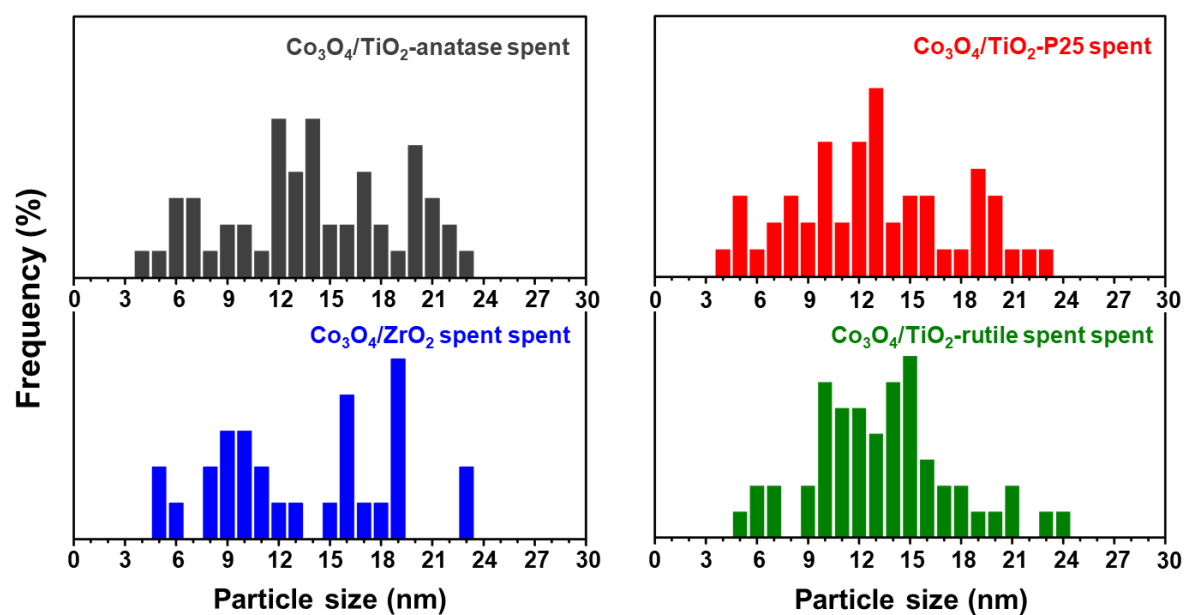


**Figure 8.18:** STEM-derived number-based size distributions for the ZrO<sub>2</sub>- and TiO<sub>2</sub>-supported Co<sub>3</sub>O<sub>4</sub> catalysts.

**Table 8.2:** STEM-derived average number- and volume-based particle sizes for a selected number of spent catalysts.

Sample name	Number-based average size (nm)*	Volume-based average size (nm) <sup>§</sup>
Co <sub>3</sub> O <sub>4</sub> /ZrO <sub>2</sub>	14.0 ± 5.3	18.6 ± 4.0
Co <sub>3</sub> O <sub>4</sub> /TiO <sub>2</sub> -anatase	13.9 ± 4.4	17.4 ± 4.2
Co <sub>3</sub> O <sub>4</sub> /TiO <sub>2</sub> -rutile	14.4 ± 5.0	18.4 ± 3.7
Co <sub>3</sub> O <sub>4</sub> /TiO <sub>2</sub> -P25	13.5 ± 4.9	17.7 ± 3.9

\* number-based average particle size and standard deviation calculated using Equations 4.9 and 4.11, respectively.

<sup>§</sup> volume-based average particle size and standard deviation calculated using Equations 4.10 and 4.12, respectively.

## 8.5. Characterisation of Spent Catalysts after Dry CO-PrOx using *ex situ* XAS

The spent catalysts recovered after the dry CO-PrOx experiments performed in the magnetometer, were analysed using *ex situ* XAS primarily to determine if there were any metal-support compounds present in the spent samples. Due to the long storage times (6 to 10 months) of the samples in a non-inert environment between the time they were recovered from the magnetometer and the time they were analysed using XAS, re-oxidation of the previously formed metallic Co and CoO, forming  $\text{Co}_3\text{O}_4$ , was expected. However, this is not a concern as the metallic phase and CoO have been adequately detected and quantified using PXRD and magnetometry.

The presence of MSCs could not be confirmed using the magnetometer since these are paramagnetic within the chosen reaction temperature range for dry CO-PrOx (see Table 2.4), while PXRD did not show any evidence for the presence of such crystalline bulk compounds. It may still be possible that these species were formed in some of the samples but in amounts that are below the intrinsic detection limit of the current PXRD instrument, and/or formed as amorphous phases. Therefore, should MSCs have formed during dry CO-PrOx, these would remain stable even during the long storage periods leading to their analysis using XAS [68,73,100].

Figure 8.19 shows the normalised XANES spectra of the reference compounds, *viz.*,  $\text{Co}_3\text{O}_4$  [66,101], CoO [102],  $\text{Co}_2\text{SiO}_4$  [103],  $\text{CoTiO}_3$  [100],  $\text{CoAl}_2\text{O}_4$  [100,104] and metallic Co [105]. Figures 8.20 and 8.21 display the normalised spectra of the supported spent samples, and the obtained results from the linear combination fitting (LCF). Table 8.3 summarises the relative fraction of the different Co-based phases detected in each sample and the corresponding R-factor for each LCF performed. The R-factor is a metric for judging misfit in the LCF, with values very close to zero indicating minor or no misfits [106].

The normalised XANES spectrum of the  $\text{CeO}_2$ -supported spent sample mostly exhibits features of CoO, but the LCF results also indicate the presence of small amounts of  $\text{Co}_3\text{O}_4$  and metallic Co (also see Table 8.3). There seems to be an additional phase present in the spent sample as indicated by the slight misfit in the LCF (Figure 8.20(a)), and see the first derivative XANES spectrum in Figure A.9.1), and the relatively high R-factor of 0.081 (Table 8.3). From the conventional  $\text{H}_2$ -TPR results (Figure 6.9), there was a peak assigned to the possible reduction of Co-Ce oxide species at 400 °C [76–78]. Furthermore, this was also proposed during the magnetometry-based

dry CO-PrOx, together with the possibility of  $\text{CoO}_{1-x}$  encapsulation by partially reduced ceria species (see section 8.2.). Therefore, the misfit in the LCF may be due to the presence of some  $\text{Co}_x\text{Ce}_y\text{O}_z$  species that may have formed under the reducing CO-PrOx environment which, at this stage, cannot be adequately identified using XAS.

The spectrum of the spent  $\text{ZrO}_2$ -supported catalyst resembles the spectrum of the  $\text{Co}_3\text{O}_4$  reference, with the LCF results also indicating the presence of small amounts of CoO (Table 8.3). Since the *in situ* PXRD and magnetometry studies indicated 100% degree of reduction to metallic Co for this catalyst, it can be concluded that the oxides present in the  $\text{Co}_3\text{O}_4/\text{ZrO}_2$  spent catalyst were formed *via* re-oxidation of the metal during the long storage periods before the XAS analysis. Features for any other Co-based phases were not identified.

In the XANES spectrum of the spent  $\text{Co}_3\text{O}_4/\text{SiC}$  sample, there is a pre-edge feature at 7710 eV which indicates the presence of metallic Co. The pronounced main feature after the edge (*i.e.*, the white line) at 7726 eV indicates the presence of CoO. The less intense features between 7726 and 7900 eV correspond to those found in the spectra of the CoO and metallic Co references. Note that SiC has a 1 – 2 nm  $\text{Si}_x\text{O}_y$  or  $\text{Si}_x\text{O}_y\text{C}_z$  around the core SiC particles of the support [70–72] (also see Figure 5.12). This layer is believed to facilitate the wetting of the SiC particles by the aqueous cobalt solution during impregnation and helps anchor the  $\text{Co}_3\text{O}_4$  nanoparticles after calcination. However, the LCF results in Figure 8.20(c) indicate that this thin  $\text{Si}_x\text{O}_y$  or  $\text{Si}_x\text{O}_y\text{C}_z$  layer is stable/inert as it does not react with any cobalt species to form cobalt silicate-like species. The estimated relative metallic Co fraction ( $40.9 \pm 0.5\%$ ) in this spent sample also agrees with the calculated DoR (41.5%) from the magnetometry data at 450 °C (Figure 8.4). This may further suggest that the metallic phase was virtually not re-oxidised during sample storage. Although the XAS analysis may indicate that the thin  $\text{Si}_x\text{O}_y$  or  $\text{Si}_x\text{O}_y\text{C}_z$  layer of the SiC is non-reactive, it remains possible that its interaction with the cobalt oxide species resulted in the relatively low degree of reduction to metallic Co during dry CO-PrOx.

The  $\text{Co}_3\text{O}_4/\text{SiO}_2$  spent sample mostly composes of the CoO phase, but small amounts of  $\text{Co}_3\text{O}_4$ ,  $\text{Co}_2\text{SiO}_4$  and metallic Co were confirmed by the LCF. The formation of  $\text{Co}_2\text{SiO}_4$  ( $7.7 \pm 0.3\%$ ) during dry CO-PrOx possibly indicates that the nature and/or strength of the NPSIs may have caused for some small amounts of  $\text{Co}^{\text{II}}$  species to react with the  $\text{SiO}_2$  [49,50,67,68,73]. The presence of  $3.7 \pm 0.9\%$  of metallic Co also indicates re-oxidation during storage, as this sample had reached a final DoR of 22.1% during the *in situ* magnetometry experiments.

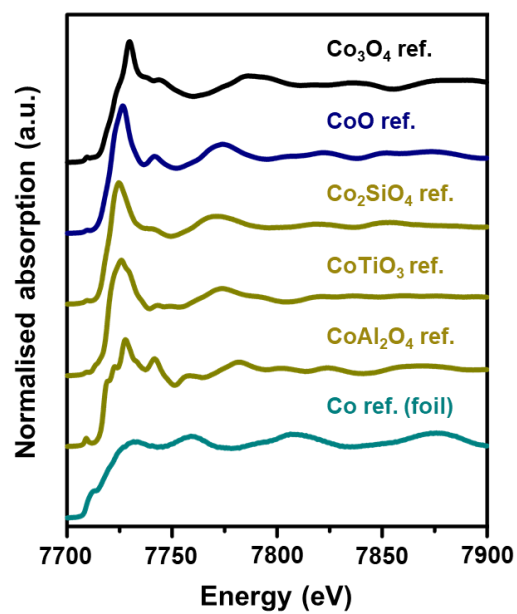


**Figure 8.19:** Normalised XANES spectra of the reference compounds; Co<sub>3</sub>O<sub>4</sub> [66,101], CoO [102], Co<sub>2</sub>SiO<sub>4</sub> [103], CoTiO<sub>3</sub> [100], CoAl<sub>2</sub>O<sub>4</sub> [100,104] and metallic Co [105] (*i.e.*, Co foil) where applicable.

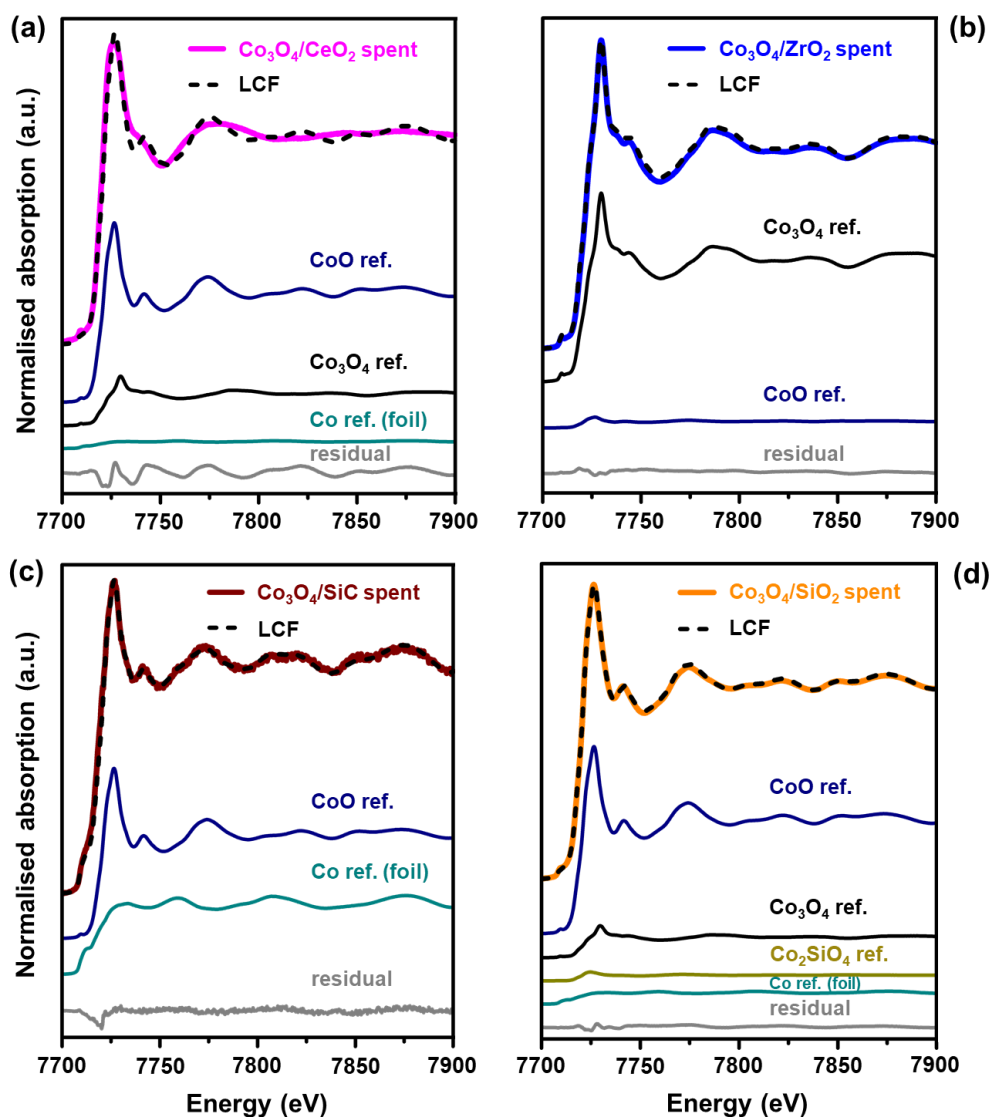


**Figure 8.20:** Normalised XANES spectra of the (a)  $\text{CeO}_2$ -, (b)  $\text{ZrO}_2$ -, (c)  $\text{SiC}$ - and (d)  $\text{SiO}_2$ -supported spent samples obtained after dry CO-PrOx, together with the resulting linear combination fit of the spectral components in each sample.

Figure 8.21 shows the normalised XANES spectra of the spent  $\text{TiO}_2$ - and  $\text{Al}_2\text{O}_3$ -supported catalysts, together with the obtained LCF results for each spent catalysts. Similar to  $\text{Co}_3\text{O}_4/\text{ZrO}_2$ , the spectrum of the  $\text{Co}_3\text{O}_4/\text{TiO}_2$ -P25 spent sample mostly shows the presence of  $\text{Co}_3\text{O}_4$ , with relatively small amounts of the  $\text{CoO}$  phase being confirmed *via* the LCF (also see Table 8.3). The absence of metallic  $\text{Co}$  is due to extensive re-oxidation during sample storage before XAS analysis, since a DoR of 91.9% was achieved by this sample during the magnetometry studies at 450 °C (Figure 8.6(c) and 8.8(d)). Nonetheless, the XANES spectrum of this spent sample showed no evidence for the presence of  $\text{CoTiO}_3$  or any other cobalt titanate-like species.

The pre-edge at 7710 eV in the normalised XANES spectrum of  $\text{Co}_3\text{O}_4/\text{TiO}_2$ -anatase is more pronounced when compared with the pre-edge of the other two  $\text{TiO}_2$ -supported spent samples (see Figure 8.21). This indicates the presence of a relatively high amounts of metallic Co in the anatase-supported spent sample (see Table 8.3). The less pronounced white line feature at 7726 eV is further evidence for the presence of metallic Co but also for the presence of CoO. The LCF also indicated the existence of  $\text{Co}_3\text{O}_4$  and  $\text{CoTiO}_3$  in the same spent catalyst. The  $\text{Co}_3\text{O}_4/\text{TiO}_2$ -rutile sample has the typical white line feature of  $\text{Co}_3\text{O}_4$  at 7729 eV, but the LCF results also indicate the presence of CoO,  $\text{CoTiO}_3$  and metallic Co. Similar to the spent catalysts discussed earlier, the presence of  $\text{Co}_3\text{O}_4$  suggests re-oxidation of the previously formed CoO and metallic Co in the  $\text{TiO}_2$ -anatase- and  $\text{TiO}_2$ -rutile-supported catalysts.

It is worth mentioning that when  $\text{Co}_3\text{O}_4$  is supported on the pure anatase or rutile phase of  $\text{TiO}_2$ , relatively stronger NPSIs are introduced which possibly lead to the formation of  $\text{CoTiO}_3$  under the reducing environment of CO-PrOx [73,84,85]. Furthermore, these two catalysts also reached lower degrees of reduction during the magnetometry studies when compared with the  $\text{Co}_3\text{O}_4/\text{TiO}_2$ -P25 catalyst (Figure 8.8(d)). Note that the amount of  $\text{CoTiO}_3$  in the spent  $\text{Co}_3\text{O}_4/\text{TiO}_2$ -anatase sample ( $13.8 \pm 1.8\%$ ) is higher than that detected in the spent  $\text{Co}_3\text{O}_4/\text{TiO}_2$ -rutile sample ( $8.9 \pm 1.5\%$ ). This can possibly be explained by the higher surface reducibility of the  $\text{TiO}_2$ -anatase support, which leads to the migration and/or reaction of the (partially) reduced  $\text{TiO}_{2-x}$  species with the (partially) reduced  $\text{Co}_{3-x}\text{O}_{4-y}$  species [73,83–89]. The migration of  $\text{TiO}_{2-x}$  can also encapsulate the metallic Co (see Figures 8.14 and A.9.1) and block access to surface active sites, which might explain the absence of  $\text{CH}_4$  in the dry CO-PrOx product stream as shown in Figure 8.5(b). Also, the higher amounts of metallic Co in the spent  $\text{Co}_3\text{O}_4/\text{TiO}_2$ -anatase catalyst, when compared with the spent  $\text{Co}_3\text{O}_4/\text{TiO}_2$ -rutile catalyst, may be a result of the said encapsulation that protects the metal from extensive re-oxidation. The existence of a 4:1 anatase:rutile mixture in the  $\text{TiO}_2$ -P25 support could possibly be stabilising the  $\text{TiO}_2$  phase against partial reduction and/or preventing it from reacting with  $\text{Co}_{3-x}\text{O}_{4-y}$  species during dry CO-PrOx [84,85].

The spectrum of the  $\text{Co}_3\text{O}_4/\text{Al}_2\text{O}_3$  spent sample exhibits features similar to those in the spectrum of the CoO reference. However, the LCF suggests that  $\text{Co}_3\text{O}_4$  and  $\text{CoAl}_2\text{O}_4$  may also be present in the spent sample. The metallic phase was not detected due to re-oxidation, but the magnetometry studies showed that this sample reached the lowest DoR of 16.2% at 450 °C during dry CO-PrOx when compared with the other catalysts. This very low DoR and the formation of relatively high amounts of  $\text{CoAl}_2\text{O}_4$  ( $26.6 \pm 1.6\%$ ) may indicate the existence of very strong NPSIs, which prevented the reduction of some of the cobalt species to  $\text{Co}^0$ , and instead, enabled the reaction of

these cobalt species with the  $\text{Al}_2\text{O}_3$  support [50,53,54,73]. The possible formation of  $\text{CoAl}_2\text{O}_4$  (or similar species) was also confirmed using STEM-EELS as shown in Figure 8.16.

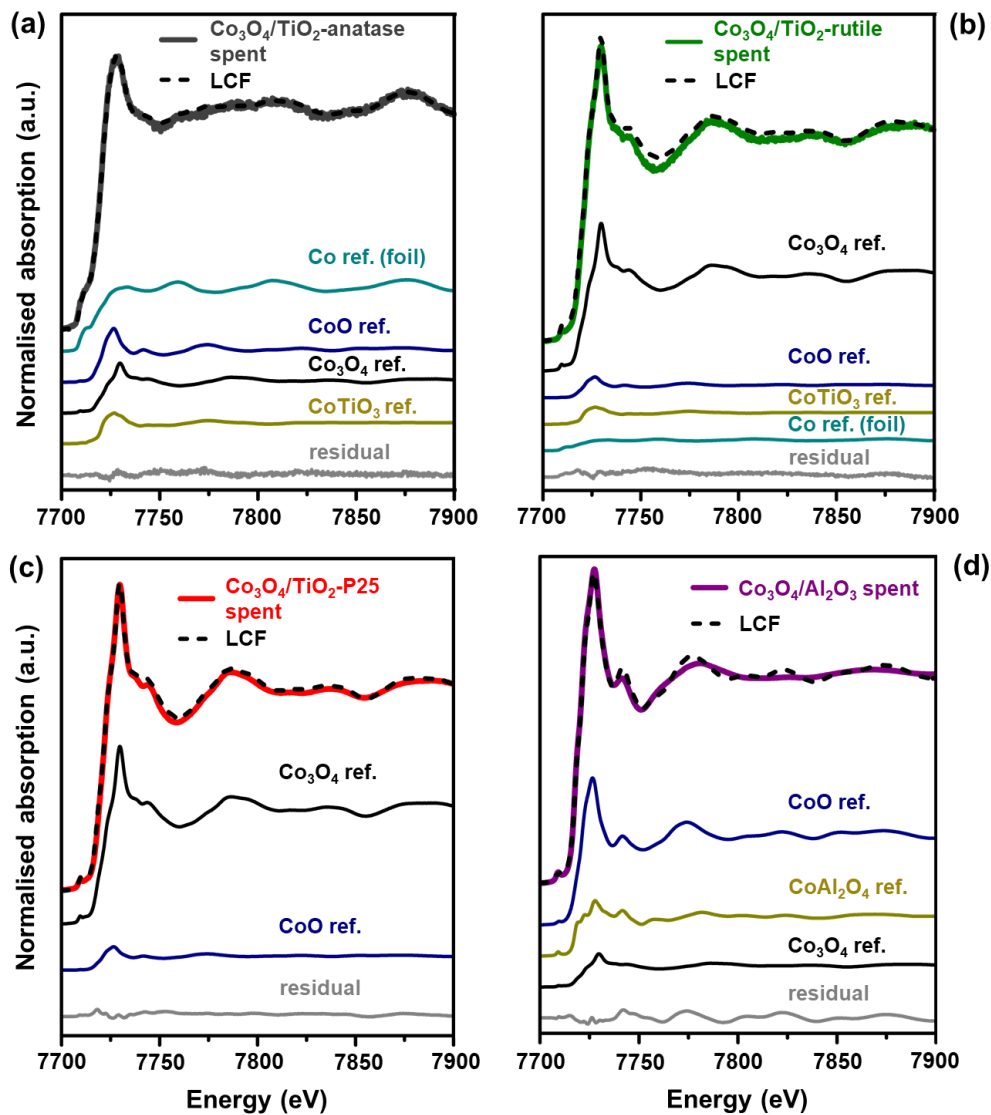


**Figure 8.21:** Normalised XANES spectra of the (a)  $\text{TiO}_2$ -anatase-, (b)  $\text{TiO}_2$ -rutile-, (c)  $\text{TiO}_2$ -P25-, and (d)  $\text{Al}_2\text{O}_3$ -supported spent samples obtained after dry CO-PrOx, together with the resulting linear combination fit of the spectral components in each sample.

**Table 8.3:** Summary of the results obtained after performing a linear combination fit of the normalised XANES spectra.

Sample name	Co <sub>3</sub> O <sub>4</sub> (%)	CoO (%)	Co <sub>a</sub> M <sub>x</sub> O <sub>y+a</sub> (%)*	Co <sup>0</sup> (%)	R-factor (-)
Co <sub>3</sub> O <sub>4</sub> /CeO <sub>2</sub> spent <sup>§, #</sup>	21.4 ± 1.5	73.8 ± 2.3	-	4.7 ± 1.2	0.081
Co <sub>3</sub> O <sub>4</sub> /ZrO <sub>2</sub> spent <sup>§</sup>	94.9 ± 0.6	5.1 ± 0.9	-	-	0.003
Co <sub>3</sub> O <sub>4</sub> /SiC spent	-	59.1 ± 1.1	-	40.9 ± 0.5	0.004
Co <sub>3</sub> O <sub>4</sub> /SiO <sub>2</sub> spent	13.5 ± 2.0	75.1 ± 0.9	7.7 ± 0.3	3.7 ± 0.9	0.001
Co <sub>3</sub> O <sub>4</sub> /TiO <sub>2</sub> -anatase spent	21.3 ± 0.7	21.8 ± 1.5	13.8 ± 1.8	43.2 ± 2.5	0.002
Co <sub>3</sub> O <sub>4</sub> /TiO <sub>2</sub> -rutile spent	73.0 ± 3.1	9.8 ± 1.6	8.9 ± 1.5	8.3 ± 1.2	0.010
Co <sub>3</sub> O <sub>4</sub> /TiO <sub>2</sub> -P25 spent	88.9 ± 0.9	11.1 ± 0.6	-	-	0.003
Co <sub>3</sub> O <sub>4</sub> /Al <sub>2</sub> O <sub>3</sub> spent	14.1 ± 1.9	59.3 ± 1.0	26.6 ± 1.6	-	0.021

\* Co<sub>a</sub>M<sub>x</sub>O<sub>y+a</sub>: a = 1 or 2, x = 1 or 2 and y = 2 or 3 for the MSCs - Co<sub>2</sub>SiO<sub>4</sub>, CoTiO<sub>3</sub> and CoAl<sub>2</sub>O<sub>4</sub>.

§ there are no known or well characterised Co-Ce or Co-Zr oxides reported in the literature.

# there may be some unknown Co-Ce metallic or oxidic phase present that was not included in the LCF.

## 8.6. Summary: Support Effects on CO-PrOx

The kinetic analysis and *in situ* characterisation performed during dry CO-PrOx over unsupported and supported Co<sub>3</sub>O<sub>4</sub> catalysts have provided very valuable insights into the effect of some side reactions on CO oxidation. The presence of H<sub>2</sub> causes H<sub>2</sub> oxidation to take place, which typically dominates above 150 °C by gradually decreasing the O<sub>2</sub> available for CO oxidation. The H<sub>2</sub> also causes the phase change from Co<sub>3</sub>O<sub>4</sub> to the less active CoO phase, further negatively affecting the CO oxidation reaction [2–8]. Above 250 °C, the formation of metallic Co from CoO is observed, which then catalyses the formation of CH<sub>4</sub> through CO hydrogenation.

Co<sub>3</sub>O<sub>4</sub> nanoparticles over the various metal oxide carriers and over SiC, mostly resulted in catalysts that were less active for CO oxidation when compared with the unsupported catalyst, except for the ZrO<sub>2</sub>-supported sample (see Figure 8.8(a)). It is possible that the supported Co<sub>3</sub>O<sub>4</sub> nanoparticles located in the pores of each support may have some of their surface area unavailable to the reacting gas [60,62,63], which negatively affected their catalytic performance. The presence of NPSIs can also negatively affect the adsorption/dissociation capabilities of the nanoparticles through

electronic effects [55,57–59,107]. In the case of the  $\text{Co}_3\text{O}_4/\text{ZrO}_2$  catalyst, these effects may have been less severe or absent, resulting in a more active catalyst for CO oxidation.

In terms of  $\text{Co}_3\text{O}_4$  reduction to metallic Co, most of the less active catalysts exhibit low reducibility. Should CO oxidation be taking place *via* the MvK mechanism, this means that the low activity in some of the supported catalysts may be a consequence of having strongly held  $\text{Co}_3\text{O}_4$  surface oxygen species [2,52,90]. This phenomenon may be more severe for the bulk oxygen species, making the bulk cobalt oxide less reducible. It should be noted that other effects, *e.g.*, crystallite/nanoparticle size, can also influence both catalytic performance [4,31] and phase stability [4,64–68], especially since there exists a distribution of nanoparticle sizes within each fresh supported catalyst. PXRD, magnetometry (based on  $\gamma$  values) and STEM-EELS indicated (slight) sintering in some of the supported nanoparticles, which may have been thermally induced and/or been a result of the changing gas partial pressures (especially  $\text{H}_2$  and  $\text{H}_2\text{O}$ ) under reaction conditions [108–111]. Due to possible granularity effects, the size of the fcc Co crystallites in the unsupported and  $\text{TiO}_2$ -P25-supported catalyst could not be determined, however, sintering may have also taken place in these samples. The formation of both hcp and fcc Co crystallites in the unsupported,  $\text{TiO}_2$ -rutile- and  $\text{TiO}_2$ -P25-supported catalysts may have also been influenced by the starting  $\text{Co}_3\text{O}_4$  size variation in each sample, and/or affected by the nature of the NPSIs (in the case of the supported catalysts).

Although the SiC-supported catalyst does not exhibit better CO oxidation activity than the unsupported and  $\text{ZrO}_2$ -supported catalyst (see Figure 8.8(a)), this catalyst reaches much lower DoRs than the latter two catalysts (see Figure 8.8(d)). This may indicate very suitable NPSIs that enable good catalytic performance (*via* the MvK mechanism) but also limit high degrees of cobalt oxide reduction. However, the low amounts of metallic Co formed over SiC still kinetically favour CO methanation over CO oxidation (similar to the unsupported and  $\text{ZrO}_2$ -supported catalyst – see Figure 8.8(c)).

The studies performed for investigating the reduction mechanism (section 8.3) have shown that the shrinking core model explains the reduction of unsupported  $\text{Co}_3\text{O}_4$  to CoO at 225 °C, and to metallic Co at 275 and 325 °C, respectively. This suggests that during the course of the CO-PrOx reaction, unsupported core-shell  $\text{Co}_3\text{O}_4@\text{CoO}$  and  $\text{CoO}@\text{Co}^0$  particles may have formed at low and high temperatures, respectively. The complete reduction of the outer surface of the oxidic nanoparticles at low DoRs, could explain the rapid changes in the CO oxidation activity and selectivity of the unsupported catalyst that were observed during the *in situ* PXRD and

magnetometry studies (section 8.1.). At 225 °C, the ZrO<sub>2</sub>-supported sample reduced to CoO possibly *via* the nucleation mechanism which indicates a slow start to the reduction. This observation is in-line with the kinetic data in Figure 8.3(c) which showed a relatively slow drop in the CO oxidation activity and selectivity for the Co<sub>3</sub>O<sub>4</sub>/ZrO<sub>2</sub> catalyst upon CoO formation. However, the reduction mechanism changed to a shrinking core mechanism when Co<sub>3</sub>O<sub>4</sub> was reduced to metallic Co, most likely due to the high temperature chosen (*i.e.*, 325 °C).

It is worth mentioning that the slow start to the reduction of Co<sub>3</sub>O<sub>4</sub> to CoO over ZrO<sub>2</sub> at 225 °C, may be a result of the nature/strength of the NPSIs between Co<sub>3</sub>O<sub>4</sub> and ZrO<sub>2</sub> introduced during catalyst synthesis. Furthermore, the low temperature of 225 °C may also affect the rate of Co<sub>3</sub>O<sub>4</sub> reduction over ZrO<sub>2</sub>. Although a similar investigation was not carried out for the other supported catalysts, it may be possible that the low-temperature transformation of Co<sub>3</sub>O<sub>4</sub> to CoO would also be slower over the other supports, since all of these stabilised Co<sub>3</sub>O<sub>4</sub> longer than the unsupported catalyst during dry CO-PrOx (see Figure 8.7(a)). The rate and/or mechanism of the high-temperature CoO transformation to metallic Co may also be affected by the NPSIs between CoO and each support, since the various catalysts reached different DoRs at 450 °C during dry CO-PrOx (see Figure 8.8(d)).

STEM-EELS analysis also gave valuable insight into the chemical changes that took place in some of the supported catalysts, in addition to the earlier mentioned particle size changes. The presence of TiO<sub>2-x</sub>-encapsulated Co<sup>0</sup> or CoO<sub>1-x</sub> nanoparticles in the spent Co<sub>3</sub>O<sub>4</sub>/TiO<sub>2</sub>-anatase sample, could explain the lack of methane formation over this catalyst during dry CO-PrOx. Further supporting evidence was the absence of TiO<sub>2-x</sub> overlayers in the TiO<sub>2</sub>-rutile- and TiO<sub>2</sub>-P25-supported spent samples, as these supports are less reducible than TiO<sub>2</sub>-anatase [73,84,85]. The EELS elemental map of the Co<sub>3</sub>O<sub>4</sub>/Al<sub>2</sub>O<sub>3</sub> spent sample showed regions of Co intricately mixed with Al, Co and O, which possibly indicates the presence of cobalt aluminate-like species. The “wetting” of the CeO<sub>2</sub>, SiC and SiO<sub>2</sub> support, respectively, by Co species, may also indicate some strong interactions between the Co species and each support or indicate the formation of Co-support species. This could explain the drop in CH<sub>4</sub> activity at high temperatures over the CeO<sub>2</sub>-supported catalyst, and also explain the low DoRs reached by the SiC- and SiO<sub>2</sub>-supported catalysts during dry CO-PrOx.

XAS analysis of the spent catalysts showed the presence of MSCs in the SiO<sub>2</sub> (7.7 ± 0.3%), TiO<sub>2</sub>-anatase (13.8 ± 1.8%), TiO<sub>2</sub>-rutile (8.9 ± 1.5%) and Al<sub>2</sub>O<sub>3</sub>-supported (26.6 ± 1.6%) catalysts after dry CO-PrOx. This is possibly due to the existence of relatively strong NPSIs and the reactivity of the supports with Co species, especially the supports TiO<sub>2</sub>-anatase, TiO<sub>2</sub>-rutile and Al<sub>2</sub>O<sub>3</sub>.

Although  $\text{SiO}_2$  is less reactive and forms low amounts of MSCs, a low DoR (22.1%) was confirmed for this sample at 450 °C using magnetometry, which indicates strong interactions between CoO and  $\text{SiO}_2$ . XAS analysis did not show any evidence of  $\text{CoTiO}_3$  in the spent  $\text{TiO}_2$ -P25-supported catalyst, which agreed with the high DoR (91.9%) reached by this catalyst at 450 °C (although the metal re-oxidised during storage). The inertness (or low reactivity) of the  $\text{TiO}_2$ -P25 can be attributed to the presence of a 4:1 anatase:rutile mixture in this support which helps stabilise it under reducing conditions [84,85]. Similarly,  $\text{ZrO}_2$  allowed for 100% DoR of  $\text{Co}_3\text{O}_4$  to metallic fcc Co during CO-PrOx - implying no MSC formation. The SiC-supported spent sample had no MSCs present but only allowed for 41.5% of the initial  $\text{Co}_3\text{O}_4$  to reduce to fcc Co. This implies that the thin  $\text{Si}_x\text{O}_y$  or  $\text{Si}_x\text{O}_y\text{C}_z$  layer around the core SiC particles does not react with the Co species, but may still exert strong interactions that stabilise the cobalt oxide under reaction conditions. The XANES spectrum of the  $\text{CeO}_2$ -supported spent sample may also have a small amount of Co-Ce oxide species (see misfit in LCF in Figure 8.20(a)), which has been proposed in the literature to form under reducing environments [76–78] (also see the results from conventional  $\text{H}_2$ -TPR in subsection 6.2.2.).

## References

- [1] Y. Teng, H. Sakurai, A. Ueda, T. Kobayashi, *Int. J. Hydrog. Energy* 24 (1999) 355–358.
- [2] Z. Zhao, M.M. Yung, U.S. Ozkan, *Catal. Commun.* 9 (2008) 1465–1471.
- [3] L. Lukashuk, K. Föttinger, E. Kolar, C. Rameshan, D. Teschner, M. Hävecker, A. Knop-Gericke, N. Yigit, H. Li, E. McDermott, M. Stöger-Pollach, G. Rupprechter, *J. Catal.* 344 (2016) 1–15.
- [4] T.M. Nyathi, N. Fischer, A.P.E. York, M. Claeys, *Faraday Discuss.* 197 (2017) 269–285.
- [5] M. Khasu, T. Nyathi, D.J. Morgan, G.J. Hutchings, M. Claeys, N. Fischer, *Catal. Sci. Technol.* 7 (2017) 4806–4817.
- [6] T.M. Nyathi, N. Fischer, A.P.E. York, D.J. Morgan, G.J. Hutchings, E.K. Gibson, P.P. Wells, C.R.A. Catlow, M. Claeys, *ACS Catal.* 9 (2019) 7166–7178.
- [7] L. Lukashuk, N. Yigit, R. Rameshan, E. Kolar, D. Teschner, M. Hävecker, A. Knop-Gericke, R. Schlögl, K. Föttinger, G. Rupprechter, *ACS Catal.* 8 (2018) 8630–8641.
- [8] L. Lukashuk, N. Yigit, H. Li, J. Bernardi, K. Föttinger, G. Rupprechter, *Catal. Today* 336 (2019) 139–147.
- [9] M.C.M. Claeys, N.F. Fischer, Sample Presentation Device for Radiation-Based Analytical Equipment, US Patent 8,597,598 B2, 2013.
- [10] N. Fischer, B. Clapham, T. Feltes, E. van Steen, M. Claeys, *Angew. Chemie - Int. Ed.* 53 (2014) 1342–1345.
- [11] N. Fischer, M. Claeys, *Catal. Today* 275 (2016) 149–154.
- [12] N. Fischer, M. Claeys, *J. Phys. D. Appl. Phys.* 53 (2020) 293001.
- [13] M.C.M. Claeys, E.W.J. van Steen, J.L. Visagie, J. van de Loosdrecht, Magnetometer, US Patent 8,773,118 B2, 2014.
- [14] W.L. Roth, *J. Phys.* 25 (1964) 507–515.
- [15] T. Mousavand, T. Naka, K. Sato, S. Ohara, M. Umetsu, S. Takami, T. Nakane, A. Matsushita, T. Adschiri, *Phys. Rev. B Condens. Matter Mater. Phys.* 79 (2009) 144411.
- [16] C.G. Shull, W.A. Strauser, E.O. Wollan, *Phys. Rev.* 83 (1951) 333–345.
- [17] R.E. Newnham, J.H. Fang, R.P. Santoro, *Acta Crystallogr.* 17 (1964) 240–242.
- [18] S. Nomura, R. Santoro, J. Fang, R. Newnham, *J. Phys. Chem. Solids* 25 (1964) 901–905.
- [19] W. Schmidt, C. Brotzeller, P. Schweiss, H. Tietze-Jaensch, R. Geick, W. Treutmann, *J. Magn. Magn. Mater.* 140–144 (1995) 1989–1990.
- [20] I.S. Hagemann, P.G. Khalifah, A.P. Ramirez, R.J. Cava, *Phys. Rev. B Condens. Matter*

- Mater. Phys. 62 (2000) R771–R774.
- [21] T.V. Choudhary, D.W. Goodman, *Catal. Today* 77 (2002) 65–78.
- [22] A.F. Ghenciu, *Curr. Opin. Solid State Mater. Sci.* 6 (2002) 389–399.
- [23] S. Huang, K. Hara, A. Fukuoka, *Energy Environ. Sci.* 2 (2009) 1060–1068.
- [24] E.D. Park, D. Lee, H.C. Lee, *Catal. Today* 139 (2009) 280–290.
- [25] A. Mishra, R. Prasad, *Bull. Chem. React. Eng. Catal.* 6 (2011) 1–14.
- [26] N. Bion, F. Epron, M. Moreno, F. Mariño, D. Duprez, *Top. Catal.* 51 (2008) 76–88.
- [27] P. Mars, D.W. van Krevelen, *Chem. Eng. Sci.* 3 (1954) 41–59.
- [28] D. Perti, R.L. Kabel, G.J. McCarthy, *AIChE J.* 31 (1985) 1435–1440.
- [29] K. Omata, T. Takada, S. Kasahara, M. Yamada, *Appl. Catal. A* 146 (1996) 255–267.
- [30] J. Jansson, A.E.C. Palmqvist, E. Fridell, M. Skoglundh, L. Österlund, P. Thormählen, V. Langer, *J. Catal.* 211 (2002) 387–397.
- [31] V. Iablokov, R. Barbosa, G. Pollefeyt, I. van Driessche, S. Chenakin, N. Kruse, *ACS Catal.* 5 (2015) 5714–5718.
- [32] O. Knacke, O. Kubaschewski, K. Hesselmann, eds., *Thermochemical Properties of Inorganic Substances*, 2nd ed., Springer-Verlag, Berlin, 1991.
- [33] E. Klugmann, H.J. Blythe, F. Walz, *Phys. Status Solidi* 146 (1994) 803–813.
- [34] S. Ram, *Mater. Sci. Eng. A* 304–306 (2001) 923–927.
- [35] L.J. Garces, B. Hincapie, R. Zerger, S.L. Suib, *J. Phys. Chem. C* 119 (2015) 5484–5490.
- [36] O. Ducreux, B. Rebours, J. Lynch, M. Roy-Auberger, D. Bazin, *Oil Gas Sci. Technol.* 64 (2009) 49–62.
- [37] J.-X. Liu, H.-Y. Su, D.-P. Sun, B.-Y. Zhang, W.-X. Li, *J. Am. Chem. Soc.* 135 (2013) 16284–16287.
- [38] S. Lyu, L. Wang, J. Zhang, C. Liu, J. Sun, B. Peng, Y. Wang, K.G. Rappé, Y. Zhang, J. Li, L. Nie, *ACS Catal.* 8 (2018) 7787–7798.
- [39] M.M. Hauman, A. Saib, D.J. Moodley, E. du Plessis, M. Claeys, E. van Steen, *ChemCatChem* 4 (2012) 1411–1419.
- [40] A. Longo, L. Sciortino, F. Giannici, A. Martorana, *J. Appl. Crystallogr.* 47 (2014) 1562–1568.
- [41] K.H. Cats, B.M. Weckhuysen, *ChemCatChem* 8 (2016) 1531–1542.
- [42] H.E. du Plessis, J.P.R. de Villiers, A. Tuling, E.J. Olivier, *Phys. Chem. Chem. Phys.* 18 (2016) 30183–30188.

- [43] S.W.T. Price, D.J. Martin, A.D. Parsons, W.A. Sławiński, A. Vamvakeros, S.J. Keylock, A.M. Beale, J.F.W. Mosselmans, *Sci. Adv.* 3 (2017) e1602838.
- [44] W.A. Sławiński, E. Zacharaki, H. Fjellvåg, A.O. Sjøstad, *Cryst. Growth Des.* 18 (2018) 2316–2325.
- [45] T.W. van Deelen, H. Yoshida, R. Oord, J. Zečević, B.M. Weckhuysen, K.P. de Jong, *Appl. Catal. A* 593 (2020) 117441.
- [46] J.-A. Dalmon, in: B. Imelik, J.C. Vedrine (Eds.), *Catal. Charact. - Phys. Tech. Solid Mater.*, Springer US, Boston, MA, 1994, pp. 585–609.
- [47] A. Barbier, A. Hanif, J.-A. Dalmon, G.A. Martin, *Appl. Catal. A* 168 (1998) 333–343.
- [48] P.A. Chernavskii, J.-A. Dalmon, N.S. Perov, A.Y. Khodakov, *Oil Gas Sci. Technol.* 64 (2009) 25–48.
- [49] E. van Steen, G.S. Sewell, R.A. Makhothe, C. Micklethwaite, H. Manstein, M. de Lange, C.T. O'Connor, *J. Catal.* 162 (1996) 220–229.
- [50] G. Jacobs, T.K. Das, Y. Zhang, J. Li, G. Racoillet, B.H. Davis, *Appl. Catal. A* 233 (2002) 263–281.
- [51] S. Storsæter, Ø. Borg, E.A. Blekkan, A. Holmen, *J. Catal.* 231 (2005) 405–419.
- [52] C.-B. Wang, C.-W. Tang, H.-C. Tsai, S.-H. Chien, *Catal. Lett.* 107 (2006) 223–230.
- [53] N.E. Tsakoumis, R.E. Johnsen, W. van Beek, M. Rønning, E. Rytter, A. Holmen, *Chem. Commun.* 52 (2016) 3239–3242.
- [54] N.E. Tsakoumis, J.C. Walmsley, M. Rønning, W. van Beek, E. Rytter, A. Holmen, *J. Am. Chem. Soc.* 139 (2017) 3706–3715.
- [55] J.M. Herrmann, *J. Catal.* 89 (1984) 404–412.
- [56] B. Delmon, in: G. Ertl, H. Knözinger, J. Weitkamp (Eds.), *Prep. Solid Catal.*, Wiley-VCH Verlag GmbH, Weinheim, Germany, 1999, pp. 541–579.
- [57] W.E. Kaden, T. Wu, W.A. Kunkel, S.L. Anderson, *Science* 326 (2009) 826–829.
- [58] A. Bruix, J.A. Rodriguez, P.J. Ramírez, S.D. Senanayake, J. Evans, J.B. Park, D. Stacchiola, P. Liu, J. Hrbek, F. Illas, *J. Am. Chem. Soc.* 134 (2012) 8968–8974.
- [59] T.W. van Deelen, C. Hernández Mejía, K.P. de Jong, *Nat. Catal.* 2 (2019) 955–970.
- [60] A.A. Adesina, *Appl. Catal. A* 138 (1996) 345–367.
- [61] C. Perego, P. Villa, *Catal. Today* 34 (1997) 281–305.
- [62] E. Marceau, X. Carrier, M. Che, O. Clause, C. Marcilly, in: G. Ertl, H. Knözinger, F. Schüth, J. Weitkamp (Eds.), *Handb. Heterog. Catal.*, Wiley-VCH Verlag GmbH & Co. KGaA, Weinheim, Germany, 2008, pp. 467–484.
- [63] P. Munnik, P.E. de Jongh, K.P. de Jong, *Chem. Rev.* 115 (2015) 6687–6718.

- [64] E. van Steen, M. Claeys, M.E. Dry, J. van de Loosdrecht, E.L. Viljoen, J.L. Visagie, *J. Phys. Chem. B* 109 (2005) 3575–3577.
- [65] E.L. Viljoen, E. van Steen, *Catal. Lett.* 133 (2009) 8–13.
- [66] N. Fischer, E. van Steen, M. Claeys, *Catal. Today* 171 (2011) 174–179.
- [67] M. Wolf, H. Kotzé, N. Fischer, M. Claeys, *Faraday Discuss.* 197 (2017) 243–268.
- [68] M. Wolf, E.K. Gibson, E.J. Olivier, J.H. Neethling, C.R.A. Catlow, N. Fischer, M. Claeys, *Catal. Today* 342 (2020) 71–78.
- [69] C. Weidenthaler, *Nanoscale* 3 (2011) 792–810.
- [70] P. Nguyen, C. Pham, *Appl. Catal. A* 391 (2011) 443–454.
- [71] A.R. de la Osa, A. de Lucas, J. Díaz-Maroto, A. Romero, J.L. Valverde, P. Sánchez., *Catal. Today* 187 (2012) 173–182.
- [72] J. Labuschagne, R. Meyer, Z.H. Chonco, J.M. Botha, D.J. Moodley, *Catal. Today* 275 (2016) 2–10.
- [73] M. Wolf, E.K. Gibson, E.J. Olivier, J.H. Neethling, C.R.A. Catlow, N. Fischer, M. Claeys, *ACS Catal.* 9 (2019) 4902–4918.
- [74] T. Herranz, X. Deng, A. Cabot, J. Guo, M. Salmeron, *J. Phys. Chem. B* 113 (2009) 10721–10727.
- [75] A. Tuxen, S. Carencio, M. Chintapalli, C.-H. Chuang, C. Escudero, E. Pach, P. Jiang, F. Borondics, B. Beberwyck, A.P. Alivisatos, G. Thornton, W.-F. Pong, J. Guo, R. Perez, F. Besenbacher, M. Salmeron, *J. Am. Chem. Soc.* 135 (2013) 2273–2278.
- [76] L. Wang, H. Liu, Y. Chen, S. Yang, *Int. J. Hydrog. Energy* 42 (2017) 3682–3689.
- [77] L. Wang, H. Liu, *Catal. Today* 316 (2018) 155–161.
- [78] Y. Cao, X. Peng, Z. Tan, Y. Liu, X. Wang, W. Zhao, L. Jiang, *Ind. Eng. Chem. Res.* 58 (2019) 17692–17698.
- [79] S. Bernal, J.J. Calvino, M.A. Cauqui, J.M. Gatica, C. Larese, J.A. Pérez Omil, J.M. Pintado, *Catal. Today* 50 (1999) 175–206.
- [80] U. Diebold, *Surf. Sci. Rep.* 48 (2003) 53–229.
- [81] Q. Fu, T. Wagner, S. Olliges, H.D. Carstanjen, *J. Phys. Chem. B* 109 (2005) 944–951.
- [82] Q. Fu, T. Wagner, *Surf. Sci. Rep.* 62 (2007) 431–498.
- [83] V.A. de la Peña O’Shea, M. Consuelo Álvarez Galván, A.E. Platero Prats, J.M. Campos-Martin, J.L.G. Fierro, *Chem. Commun.* 47 (2011) 7131–7133.
- [84] B. Jongsomjit, C. Sakdamnusun, P. Praserttham, *Mater. Chem. Phys.* 89 (2005) 395–401.
- [85] B. Jongsomjit, T. Wongsalee, P. Praserttham, *Mater. Chem. Phys.* 92 (2005) 572–577.

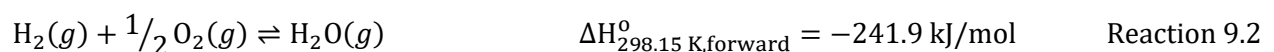
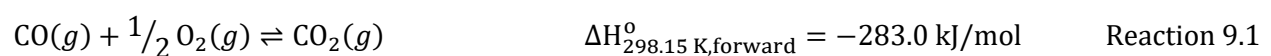
- [86] J. Li, Y. Lin, X. Pan, D. Miao, D. Ding, Y. Cui, J. Dong, X. Bao, *ACS Catal.* 9 (2019) 6342–6348.
- [87] T. Komaya, A.T. Bell, Z. Weng-Sieh, R. Gronsky, F. Engelke, T.S. King, M. Pruski, *J. Catal.* 149 (1994) 142–148.
- [88] T. Komaya, A.T. Bell, Z. Weng-Sieh, R. Gronsky, F. Engelke, T.S. King, M. Pruski, *J. Catal.* 150 (1994) 400–406.
- [89] A.T. Bell, *Science* 299 (2003) 1688–1691.
- [90] W. Li, X. Nie, X. Jiang, A. Zhang, F. Ding, M. Liu, Z. Liu, X. Guo, C. Song, *Appl. Catal. B* 220 (2018) 397–408.
- [91] X. Nie, H. Wang, W. Li, Y. Chen, X. Guo, C. Song, *J. CO<sub>2</sub> Util.* 24 (2018) 99–111.
- [92] Q. Guo, Y. Liu, *React. Kinet. Catal. Lett.* 92 (2007) 19–25.
- [93] P. Gawade, B. Bayram, A.M.C. Alexander, U.S. Ozkan, *Appl. Catal. B* 128 (2012) 21–30.
- [94] T. Cwele, N. Mahadevaiah, S. Singh, H.B. Friedrich, *Appl. Catal. B* 182 (2016) 1–14.
- [95] T. Cwele, N. Mahadevaiah, S. Singh, H.B. Friedrich, A.K. Yadav, S.N. Jha, D. Bhattacharyya, N.K. Sahoo, *Catal. Sci. Technol.* 6 (2016) 8104–8116.
- [96] N.W. Hurst, S.J. Gentry, A. Jones, B.D. McNicol, *Catal. Rev.* 24 (1982) 233–309.
- [97] A. Khawam, D.R. Flanagan, *J. Phys. Chem. B* 110 (2006) 17315–17328.
- [98] J.W. Niemantsverdriet, in: J.W. Niemantsverdriet (Ed.), *Spectrosc. Catal.*, 3rd ed., Wiley-VCH Verlag GmbH & Co. KGaA, Weinheim, Germany, 2007, pp. 11–38.
- [99] A. Gervasini, in: A. Auroux (Ed.), *Calorim. Therm. Methods Catal.*, Springer-Verlag, Berlin, Heidelberg, 2013, pp. 175–195.
- [100] M. Wolf, S.J. Roberts, W. Marquart, E.J. Olivier, N.T.J. Luchters, E.K. Gibson, C.R.A. Catlow, J.H. Neethling, N. Fischer, M. Claeys, *Dalt. Trans.* 48 (2019) 13858–13868.
- [101] N. Fischer, M. Minnermann, M. Baeumer, E. van Steen, M. Claeys, *Catal. Lett.* 142 (2012) 830–837.
- [102] M. Wolf, N. Fischer, M. Claeys, *Mater. Chem. Phys.* 213 (2018) 305–312.
- [103] L.A. Bruce, J.V. Sanders, T.W. Turney, *Clays Clay Miner.* 34 (1986) 25–36.
- [104] M. Karmaoui, N.J.O. Silva, V.S. Amaral, A. Ibarra, Á. Millán, F. Palacio, *Nanoscale* 5 (2013) 4277–4283.
- [105] A.J. Dent, G. Cibir, S. Ramos, A.D. Smith, S.M. Scott, L. Varandas, M.R. Pearson, N.A. Krumpa, C.P. Jones, P.E. Robbins, *J. Phys. Conf. Ser.* 190 (2009) 012039.
- [106] B. Ravel, in: J.A. van Bokhoven, C. Lamberti (Eds.), *X-Ray Absorpt. X-Ray Emiss. Spectrosc.*, John Wiley & Sons, Ltd, Chichester, UK, 2016, pp. 281–302.

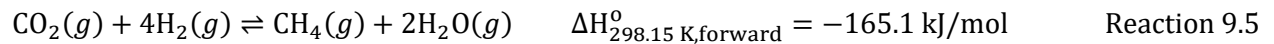
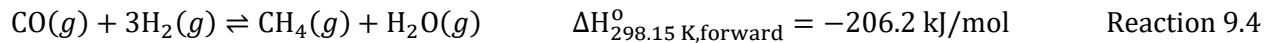
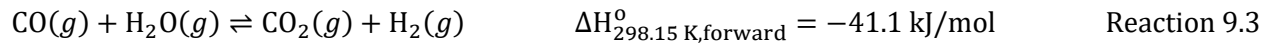
- [107] T. Ishihara, K. Eguchi, H. Arai, *J. Mol. Catal.* 72 (1992) 253–261.
- [108] G.L. Bezemer, T.J. Remans, A.P. van Bavel, A.I. Dugulan, *J. Am. Chem. Soc.* 132 (2010) 8540–8541.
- [109] M. Claeys, M.E. Dry, E. van Steen, P.J. van Berge, S. Booyens, R. Crous, P. van Helden, J. Labuschagne, D.J. Moodley, A.M. Saib, *ACS Catal.* 5 (2015) 841–852.
- [110] N. Fischer, B. Clapham, T. Feltes, M. Claeys, *ACS Catal.* 5 (2015) 113–121.
- [111] M. Wolf, N. Fischer, M. Claeys, *J. Catal.* 374 (2019) 199–207.

# Chapter 9: Gas Environment Effects on the Preferential Oxidation of Carbon Monoxide

## 9.1. Further Thermodynamic Calculations on Gas-Phase Reaction Equilibria

Following from the results of the thermodynamic calculations shown in section 7.1., an investigation into the effect of the CO-PrOx feed gases on the equilibrium conversion ( $X_{eq.}$ ) of certain limiting reactants was performed. Once again, a feed composing of 1% CO, 1% O<sub>2</sub>, 10% CO<sub>2</sub>, 10% H<sub>2</sub>O, 50% H<sub>2</sub> and a balance of N<sub>2</sub>, was assumed for the calculations. The reactions considered were CO oxidation, H<sub>2</sub> oxidation, the forward and reverse water-gas shift, CO methanation and CO<sub>2</sub> methanation (also see Reactions 9.1 to 9.5). Note that all gases (except O<sub>2</sub> and CH<sub>4</sub>) are reactants in one or more reactions and also products in other reactions. Thermodynamically, this implies that the presence of all six gases in the CO-PrOx feed can negatively affect the progress of one or more of the reactions that they form part of [1]. For example, the presence of H<sub>2</sub> and CO<sub>2</sub> in the CO-PrOx feed can affect the equilibrium conversion of CO during the forward water-gas shift reaction as both gases are products of the said reaction. This approach was applied for all reactions to examine the extent of the effect and Equation 9.1 was used to calculate the new  $X_{eq.}$ .





$$\frac{(p_Y)^y \cdot (p_Z)^z}{(p_V)^v \cdot (p_W)^w} = \exp \left\{ -\frac{1}{R} \cdot \left( \frac{\Delta G_{rxn}^{\circ}(T)}{T^{\circ}} - \int_{T^{\circ}}^T \frac{\Delta H_{rxn}^{\circ} + \int_{T^{\circ}}^T \Delta C_{p,rxn}(T) dT}{T^2} dT \right) \right\} \quad \text{Equation 9.1}$$

It is worth mentioning that the presence of 10% CO<sub>2</sub> and 10% H<sub>2</sub>O in the CO-PrOx feed was predicted to not have an appreciable effect on the  $X_{eq.}$  of CO in CO oxidation, and the  $X_{eq.}$  of O<sub>2</sub> in H<sub>2</sub> oxidation, respectively. The very low  $\Delta G$  (Figure 7.1) and resulting high  $K_{eq.}$  of these two reactions make it possible for virtually 100% conversion of CO and O<sub>2</sub>, in the respective reactions, to be achievable even in the presence of CO<sub>2</sub> and H<sub>2</sub>O.

The other reactions considered were the forward and reverse WGS. For the forward reaction, the presence of H<sub>2</sub> and the combined presence of H<sub>2</sub> and CO<sub>2</sub> was considered. These two situations are also in-line with the experiments that will be discussed in sub-sections 9.2.2. and 9.2.4., respectively. For the reverse WGS, the effect of CO as well as the combined effect of CO and H<sub>2</sub>O was considered, which is in-line with the experiments to be discussed in sub-sections 9.2.3. and 9.2.4.

The plots in Figures 9.1(a) and (b) show the  $X_{eq.}$  conversions expected for CO in the forward WGS and of CO<sub>2</sub> in the reverse WGS, respectively. The presence of 50% H<sub>2</sub> in the CO-PrOx feed can cause a decrease in the CO conversion below 100% above 175 °C, ultimately reaching 49.6% at 500 °C. The combined effect of 50% H<sub>2</sub> and 10% CO<sub>2</sub> in the feed causes a decrease of the CO conversion below 100% above 75 °C, reaching 2.7% at 285 °C. Above 285 °C, negative CO conversions are obtained which can be interpreted as the system forming more CO than what is originally in the feed. This would only be possible if the reverse WGS was taking place at these temperatures. As for the CO<sub>2</sub> conversion during the reverse WGS reaction, the presence of 1% CO has a slightly diminishing effect, while the combined presence of 1% CO and 10% H<sub>2</sub>O allows for the reverse WGS to only be feasible from 290 °C. Experimentally, these results point out that in a typical feed composing of all six CO-PrOx gases, the forward WGS will only be possible at

temperatures below 285 °C. From 290 °C, the reverse WGS becomes feasible with a CO<sub>2</sub> conversion of 34.0% being achievable at 500 °C.

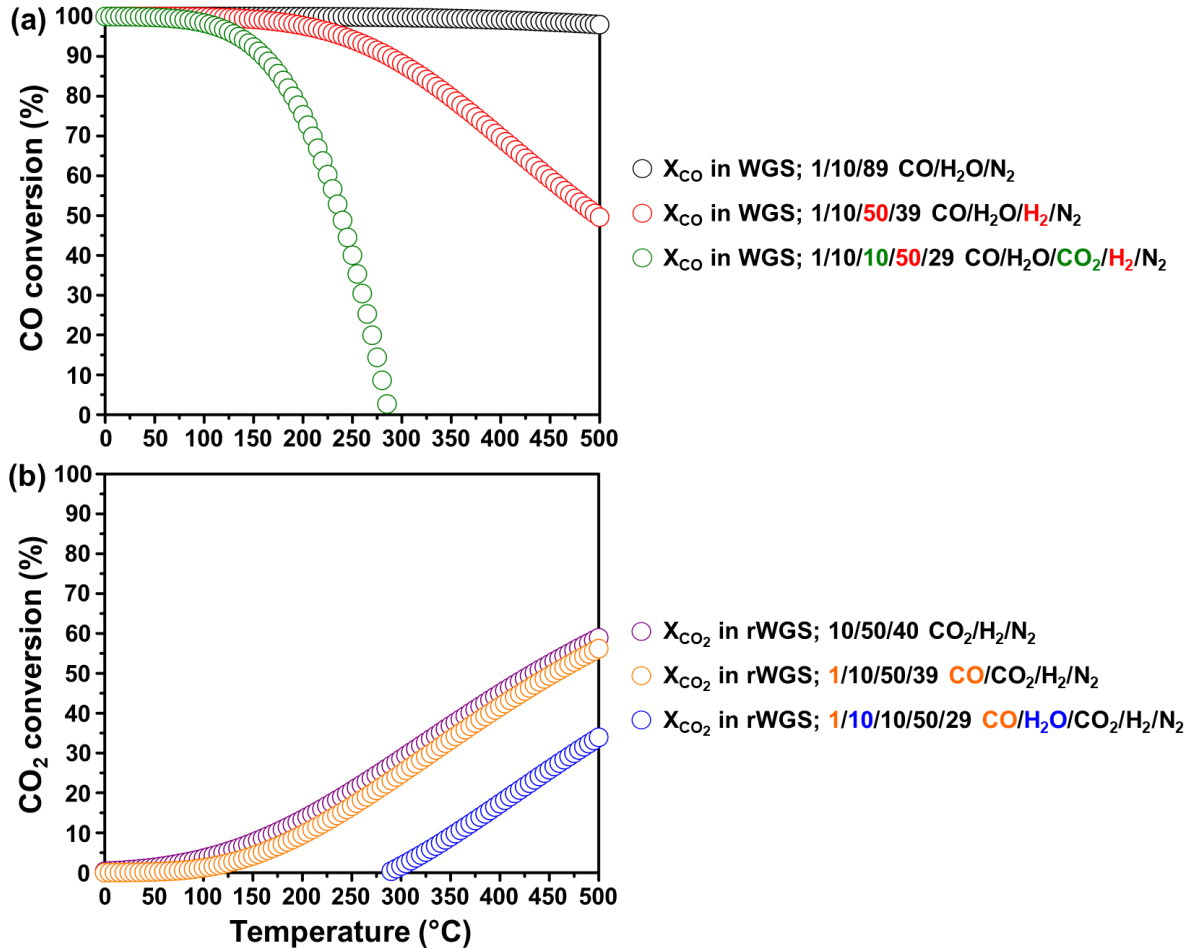


**Figure 9.1:** Changes in the equilibrium conversions of (a) CO, and (b) CO<sub>2</sub> as a function of temperature at 1.013 bar during the forward and reverse WGS reaction, respectively. Note the different feed compositions indicated on the plots.

Lastly, the effect of the 10% H<sub>2</sub>O in the feed was evaluated in the context of CO and CO<sub>2</sub> methanation. This is in-line with the experiments to be discussed in sub-sections 9.2.2. and 9.2.4. Although CH<sub>4</sub> can possibly be formed from CO<sub>2</sub> *via* reverse WGS followed by CO hydrogenation, the effects of this were assumed to be negligible in the performed thermodynamic evaluation. Since CH<sub>4</sub> is not a typical CO-PrOx feed component, its effect on the progress of the methanation reactions was not considered. The results from calculating the  $X_{eq}$  of CO and CO<sub>2</sub> are shown in

Figure 9.2(a) and (b), respectively. The presence of 10% H<sub>2</sub>O does not seem to have a significant effect on the conversion of CO to CH<sub>4</sub> as conversion levels above 99% can still be realised. For CO<sub>2</sub> methanation, an appreciable drop in conversion is only observed above 400 °C, reaching 64.1% at 500 °C compared with the 72.2% achievable in the absence of H<sub>2</sub>O.

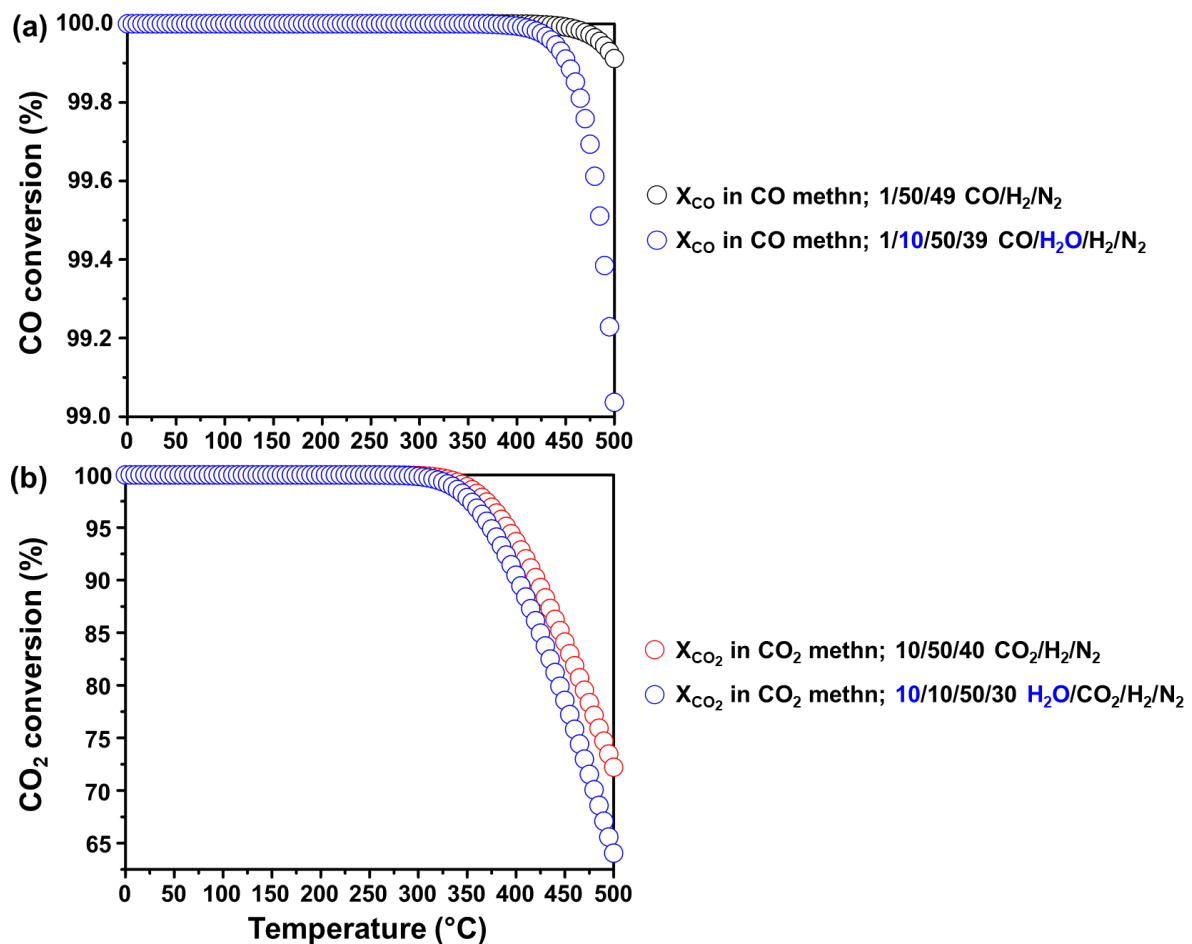


**Figure 9.2:** Changes in the equilibrium conversions of (a) CO, and (b) CO<sub>2</sub>, respectively, as a function of temperature at 1.013 bar during methanation. Note the different feed compositions indicated on the plots.

## 9.2. Effect of CO-PrOx Gas Feed Components on CO Oxidation

### 9.2.1. Total oxidation of CO in the absence of H<sub>2</sub>, H<sub>2</sub>O and CO<sub>2</sub>

To adequately understand the effect of the CO-PrOx gas feed components, *viz.*, H<sub>2</sub>, H<sub>2</sub>O and CO<sub>2</sub>, the dry Total Oxidation of CO (*i.e.*, dry CO-TOx) was performed experimentally in the absence of these gases. This involved flowing a gas composing of a 1:1:98 CO:O<sub>2</sub>:N<sub>2</sub> mixture at a GHSV of 60000 ml(NTP)/g<sub>Co<sub>3</sub>O<sub>4</sub></sub>/hr. Based on the results from after performing the preferential oxidation of CO in the presence of H<sub>2</sub> (but absence of H<sub>2</sub>O and CO<sub>2</sub>) over all prepared catalysts (see Figures 8.8(a) and A.6.2(a)), the unsupported and ZrO<sub>2</sub>-supported Co<sub>3</sub>O<sub>4</sub> catalysts showed the highest CO oxidation activity. Therefore, these two catalysts were chosen for the CO-TOx experiments. Figure 9.3 shows the results from the *in situ* PXRD and gas product analysis obtained during CO-TOx over unsupported and ZrO<sub>2</sub>-supported Co<sub>3</sub>O<sub>4</sub>, respectively.

It can be observed that the catalysts obtain a 100% CO conversion exclusively to CO<sub>2</sub> at 150 °C (unsupported Co<sub>3</sub>O<sub>4</sub>) and 175 °C (Co<sub>3</sub>O<sub>4</sub>/ZrO<sub>2</sub>), and this high conversion is maintained up to 450 °C. In contrast, the thermodynamic predictions in Figure 7.2 show that the conversion of CO to CO<sub>2</sub> can reach a 100% between 0 and 500 °C. Therefore, the delay observed in achieving 100% CO conversion over the two evaluated catalysts can be ascribed to a kinetic hindrance caused by the relatively low starting temperatures and/or low catalytic activity. However, it is important to note that the temperature at which complete oxidation of CO to CO<sub>2</sub> achieved by these catalysts is still much lower than the reported temperature for the non-catalytic combustion of CO in air, which is 605 °C [2]. Since a 1:1 CO:O<sub>2</sub> ratio was used, this means there is an excess of O<sub>2</sub> in the feed according to the stoichiometric reaction, Reaction 9.1. Therefore, at a 100% CO conversion, a corresponding 50% O<sub>2</sub> conversion is expected. For both evaluated catalysts, this was indeed the case as can be seen from Figure 9.3, despite the slight instability of the O<sub>2</sub> conversion/concentration around the 50% mark (see black dashed line in the plots of Figure 9.3(b)), which is elusive at this stage. In contrast, in the presence of H<sub>2</sub> (sections 8.1. and 8.2.), these two catalysts achieved CO<sub>2</sub> yields that were below 100% while achieving O<sub>2</sub> conversions of up to 100% between 50 and 450 °C. This was attributed to the occurrence of H<sub>2</sub> oxidation (Reaction 9.2) which competes with CO oxidation for co-fed O<sub>2</sub>.

The concurrent chemical phase analysis using PXRD shows that the starting  $\text{Co}_3\text{O}_4$  phase in both catalysts remains stable between 50 and 450 °C (see plots in Figure 9.3(a)). Since CO oxidation over  $\text{Co}_3\text{O}_4$  is believed to take place *via* the MvK mechanism, then the presence of excess  $\text{O}_2$  could possibly be the reason for the stabilisation of  $\text{Co}_3\text{O}_4$ , *i.e.*, preventing it from reducing to CoO and metallic Co [3–7]. In the presence of  $\text{H}_2$  (see sections 8.1. and 8.2.),  $\text{O}_2$  is eventually depleted, leaving the  $\text{Co}_3\text{O}_4$  susceptible to reduction as the MvK mechanism can no longer be maintained [8–13]. Furthermore, the *in situ* PXRD results in Figure A.5.3 of Appendix A.6., show that  $\text{Co}_3\text{O}_4$  reduces in a 1:99 CO: $\text{N}_2$  gas mixture, *i.e.*, in the absence  $\text{O}_2$ .

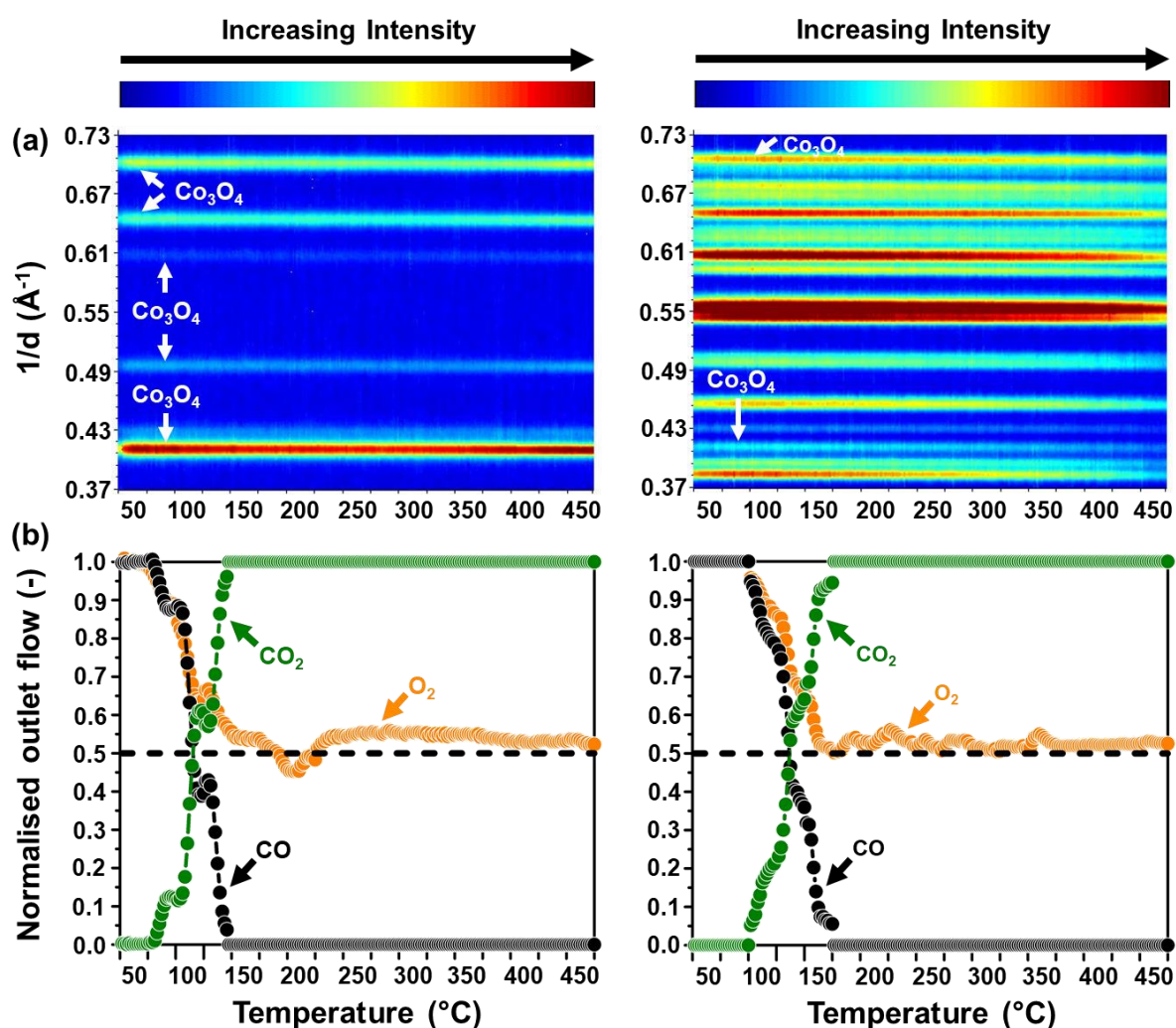


**Figure 9.3:** (a) On-top view of the *in situ* PXRD patterns of (left) unsupported  $\text{Co}_3\text{O}_4$ , and (right)  $\text{Co}_3\text{O}_4/\text{ZrO}_2$  recorded during dry CO-TOX. (b) Changes in the normalised outlet flow rates of CO,  $\text{O}_2$  and  $\text{CO}_2$  calculated from GC-TCD data. (Feed composition: 1% CO, 1%  $\text{O}_2$  and 98%  $\text{N}_2$ ; pressure: atmospheric, GHSV: 60000 mL(NTP)/g $\text{Co}_3\text{O}_4$ /hr).

### 9.2.2. Effect of co-fed H<sub>2</sub>O during CO-PrOx (wet CO-PrOx)

Water vapour forms a significant part (~10%) of a typical CO-PrOx feed since it originates from steam reforming and the subsequent two-step WGS processes [14–18]. The effect of H<sub>2</sub>O has been studied previously but to a lesser extent than H<sub>2</sub>. Regarding metal oxide catalysts, the effect of water addition on the stability of the oxide has also not been reported despite it being a relatively strong oxidising agent [19–25]. A feed gas composing of a 1:1:45:10:43 CO:O<sub>2</sub>:H<sub>2</sub>:H<sub>2</sub>O:N<sub>2</sub> was flowed over unsupported and ZrO<sub>2</sub>-supported Co<sub>3</sub>O<sub>4</sub> (GHSV: 60000 ml(NTP)/g<sub>Co<sub>3</sub>O<sub>4</sub></sub>/hr) to investigate the effect of water on the catalytic performance and phase stability (see Figure 9.4 for the *in situ* characterisation and gas product analysis results).

Note that sub-sections 9.2.2. – 9.2.4. discuss the results obtained during the exposure of unsupported and ZrO<sub>2</sub>-supported Co<sub>3</sub>O<sub>4</sub> to different CO-PrOx conditions (*i.e.*, wet CO-PrOx, dry CO-PrOx with co-fed CO<sub>2</sub>, and wet CO-PrOx with co-fed CO<sub>2</sub> – also see sub-section 4.4.2.3. and Table 4.5 for details) due to their relatively high CO oxidation activity and selectivity during dry CO-PrOx (see Figures 8.8(a), 8.8(b), A.6.2(a) and A.6.2(b)). Wet CO-PrOx with co-fed CO<sub>2</sub> (sub-section 9.2.4.) was also performed over Co<sub>3</sub>O<sub>4</sub>/SiC and Co<sub>3</sub>O<sub>4</sub>/TiO<sub>2</sub>-P25. The choice of SiC was based on it being the only “inert” non-oxidic support material, while TiO<sub>2</sub>-P25 was the best performing “strongly-interacting” oxidic support during dry CO-PrOx when compared with SiO<sub>2</sub>, Al<sub>2</sub>O<sub>3</sub> and the other TiO<sub>2</sub> supports (Figures 8,8(a) and (b)). All wet CO-PrOx experiments were performed between 100 and 450 °C to avoid H<sub>2</sub>O condensation below 100 °C, while dry CO-PrOx with co-fed CO<sub>2</sub> was performed between 50 and 450 °C.

Therefore, Figures 9.11 and 9.12 summarise the range of temperatures in which each cobalt-based phase is observed, the calculated relative fraction and crystallite size of CoO, hcp and fcc Co, respectively, at 450 °C after exposing the above-mentioned catalysts to different CO-PrOx conditions. The CO conversion to CO<sub>2</sub> (*via* oxidation), CO conversion to CH<sub>4</sub> (*via* hydrogenation), CO<sub>2</sub> conversion to CH<sub>4</sub> (*via* hydrogenation), CO<sub>2</sub> conversion to CO (*via* reverse WGS), and the *in situ* magnetometry-derived DoR as a function of temperature are presented in Figures 9.13 and 9.14. The O<sub>2</sub> selectivity to CO<sub>2</sub> achieved by the four catalysts under the different CO-PrOx conditions can be found in Figure A.6.3. The M-H curves derived from the data recorded at 450 °C for each catalyst are presented in Figures 9.5, 9.7 and 9.10, while Table 9.1 shows the calculated  $\gamma$  values (including those obtained after dry CO-PrOx).

Compared with the results obtained during dry CO-PrOx over unsupported (Figure 8.1(d)) and ZrO<sub>2</sub>-supported Co<sub>3</sub>O<sub>4</sub> (Figure 8.3(c)), the presence of co-fed H<sub>2</sub>O decreases the CO conversion to CO<sub>2</sub> achievable between 100 and 450 °C (Figure 9.4(b)). This is also shown in the summary plots of Figure 9.13(a). The observed overall effect on the CO conversion may be attributed to the competitive adsorption of H<sub>2</sub>O which blocks access to surface active sites [20,26–28]. The effect appears to be more severe for the unsupported catalyst which achieves a maximum CO conversion to CO<sub>2</sub> of 50.4% at 225 °C, while the ZrO<sub>2</sub>-supported catalyst achieves a maximum conversion of 84.5% at 200 °C. The adsorption strength of H<sub>2</sub>O over Co<sub>3</sub>O<sub>4</sub>/ZrO<sub>2</sub> might be lowered through the electronic interactions between the Co<sub>3</sub>O<sub>4</sub> nanoparticles and the support, especially at or near the nanoparticle-support interface [29–33]. Furthermore, the competitive surface adsorption of H<sub>2</sub>O on Co<sub>3</sub>O<sub>4</sub> (unsupported or supported) could have a negative impact on the effectiveness of the MvK mechanism for producing CO<sub>2</sub> from CO [34,35]. Therefore, it is possible that due to a weaker adsorption of H<sub>2</sub>O on Co<sub>3</sub>O<sub>4</sub>/ZrO<sub>2</sub>, the MvK mechanism for the oxidation of CO remains highly effective in this catalyst.

According to PXRD, the CoO phase in both catalysts appears at higher temperatures in the presence of water than the temperatures observed for the case with no co-fed water (also see Figure 9.11(a)). This could again be due to the strong surface adsorption, and the oxidising nature of water [19–25] that helps keep the Co<sub>3</sub>O<sub>4</sub> phase stable over a wider temperature range.

Similarly, both the PXRD and magnetometry results show a delay in the formation of metallic Co (Figures 9.11(a) and 9.13(d)), and specifically, magnetometry further shows slightly lower degrees of reduction in the presence of co-fed water than those achieved in the absence of water (Figure 9.13(d)). The PXRD patterns of the unsupported catalyst also faintly show CoO reflections at  $1/d = 0.41$  and  $0.66 \text{ \AA}^{-1}$  between 300 and 425 °C (Figure 9.4((a), *left*)), further suggesting increased stability of CoO in the presence of water. However, PXRD indicates a 100% degree of reduction to metallic Co at 450 °C for both catalysts (Figure 9.11(b)), which could be explained by the intrinsic detection limits of the instrument regarding crystallite size and relative concentration, as well as crystallinity requirements. It is worth noting that the unsupported catalyst experiences a greater depreciation in the DoR than the ZrO<sub>2</sub>-supported catalyst when water is co-fed (Figures 9.4(c) and 9.13(d)). This may be due to a more kinetically hindered adsorption and dissociation of H<sub>2</sub>O over the cobalt species in the supported catalyst, caused by the existence of NPSIs (possibly through electronic effects).

As also observed in the previously discussed reduction (Chapters 6 and 7) and catalyst testing experiments (Chapter 8), unsupported Co<sub>3</sub>O<sub>4</sub> ultimately reduces to (partially) intergrown hcp and

fcc Co, while only fcc Co is formed over the ZrO<sub>2</sub> support during wet CO-PrOx (Figure 9.4(a)). Although the sole formation of fcc Co in the supported catalyst is not clearly understood at this stage, it is possible that this is a result of the NPSIs or an effect caused by the starting size distribution of the nanoparticles in the fresh Co<sub>3</sub>O<sub>4</sub>/ZrO<sub>2</sub> catalyst. The hcp:fcc Co ratio at 450 °C in the unsupported catalyst (Figures 9.11(b) and A.7.2(b), as well as Table A.7.1) decreases from 3.6 (in the absence of co-fed H<sub>2</sub>O) to 1.6 (in the presence of co-fed H<sub>2</sub>O), which may be an effect of changing the reaction gas environment or the changing partial pressures of the reactants and products as a function of temperature [36]. Interestingly, the average crystallite size of fcc Co at 450 °C in the unsupported catalyst is  $26.8 \pm 3.3$  nm, which is higher than the starting Co<sub>3</sub>O<sub>4</sub> size (Table 5.1), but much lower than the fcc Co size obtained under dry CO-PrOx (Figures 9.11(c) and A.7.2(c), as well as Table A.7.1). This result seems to indicate a minimised extent of granularity in the reduced unsupported catalyst, which allowed for a much lower fcc Co size to be calculated from the patterns recorded during wet CO-PrOx (see discussion on granularity effects [37,38] in sub-section 6.2.1.). On the other hand, unsupported hcp Co is present as small crystallites ( $2.7 \pm 0.3$  nm), as was also the case during dry CO-PrOx.

The final average size of fcc Co in the ZrO<sub>2</sub>-supported catalyst is  $40.3 \pm 19.9$  nm (Figure 9.11(c) and Table A.7.1), which indicates extensive sintering in the presence of co-fed water. Water has been reported to facilitate the sintering of metallic Co in other reactions systems (such as FTS) [39–42], which may have also been the case in the present study. However, it should be noted that the main fcc Co reflection overlaps with the ZrO<sub>2</sub> reflection at  $1/d = 0.49 \text{ \AA}^{-1}$ , which could introduce some uncertainty in the calculated crystallite size using Rietveld refinement. This may explain the high error associated with the reported average size.

Noteworthy are the higher yields of CO<sub>2</sub> achieved at temperatures where metallic Co is present in each catalyst when compared with the case with no co-fed water (Figure 9.13(a)). This observation is possibly due to the occurrence of the forward WGS (see Reaction 9.3). In other reaction systems (*i.e.*, those not involving CO-PrOx), the occurrence of the forward WGS has been associated with the metallic Co phase [43–45]. Therefore, it is important to note that the results in Figure 9.4 show the first close association of the forward WGS reaction over metallic Co during CO-PrOx in the presence of water, and using *in situ* characterisation techniques. This further supports the earlier mentioned possibility of an *in situ* WGS reaction during dry CO-PrOx (see section 8.1.), which was also proposed by Khasu *et al.* [12]. From the thermodynamic calculations, the predicted CO conversion/CO<sub>2</sub> yield during the WGS reaction in the presence of co-fed H<sub>2</sub> is 59.2% at 450 °C (Figure 9.1(a)). Below 450 °C, higher conversions/yields are predicted since the WGS reaction is

exothermic. The experimental results in Figures 9.4(b) and 9.13(a), between 275 and 450 °C, show that both catalysts achieve CO<sub>2</sub> yields (maximum for unsupported Co<sub>3</sub>O<sub>4</sub>: 42.1%, and Co<sub>3</sub>O<sub>4</sub>/ZrO<sub>2</sub>: 46.7%) that are below those predicted by the thermodynamic calculations. However, it can be observed that the unsupported catalyst mostly achieves higher CO<sub>2</sub> yields than the supported catalyst, especially in the range from 275 to 400 °C.

Taking place concurrently with the WGS reaction is CO methanation (Reaction 9.4), but to a lesser extent than in the case with no co-fed water (see Figure 9.13(b)). Again, this may be due to the competitive adsorption of the water onto the metallic Co surface which blocks access to active sites for methanation [21,46,47]. The occurrence of the WGS reaction could also be kinetically hindering the progress of the methanation reaction, as both processes consume CO. However, higher methane yields are noted over the reduced ZrO<sub>2</sub>-supported catalyst, which explains the low CO<sub>2</sub> yields reached by this catalyst *via* the WGS. Previously reported DFT [48] and experimental [49] results have shown that the electronic interactions between metallic Co and ZrO<sub>2</sub> allow for high H<sub>2</sub> dissociation rates and strong CO binding on the surface, which would favour high CO conversions to CH<sub>4</sub>. On the other hand, the unsupported catalyst exhibits a gradual loss in both CO methanation and WGS activity above 350 °C, which may be a result of the changing hcp:fcc Co ratio and/or the sintering of fcc Co with temperature (see Figures A.7.2(b) and (c)). The effect of the nanoparticle structure - including (partial) intergrowth of hcp and fcc Co - on the progress of the methanation and WGS reactions, respectively, is also a possibility. The formation of large fcc Co crystallites in the supported catalyst may have also contributed to the slight decrease in methanation activity observed in the presence of water.

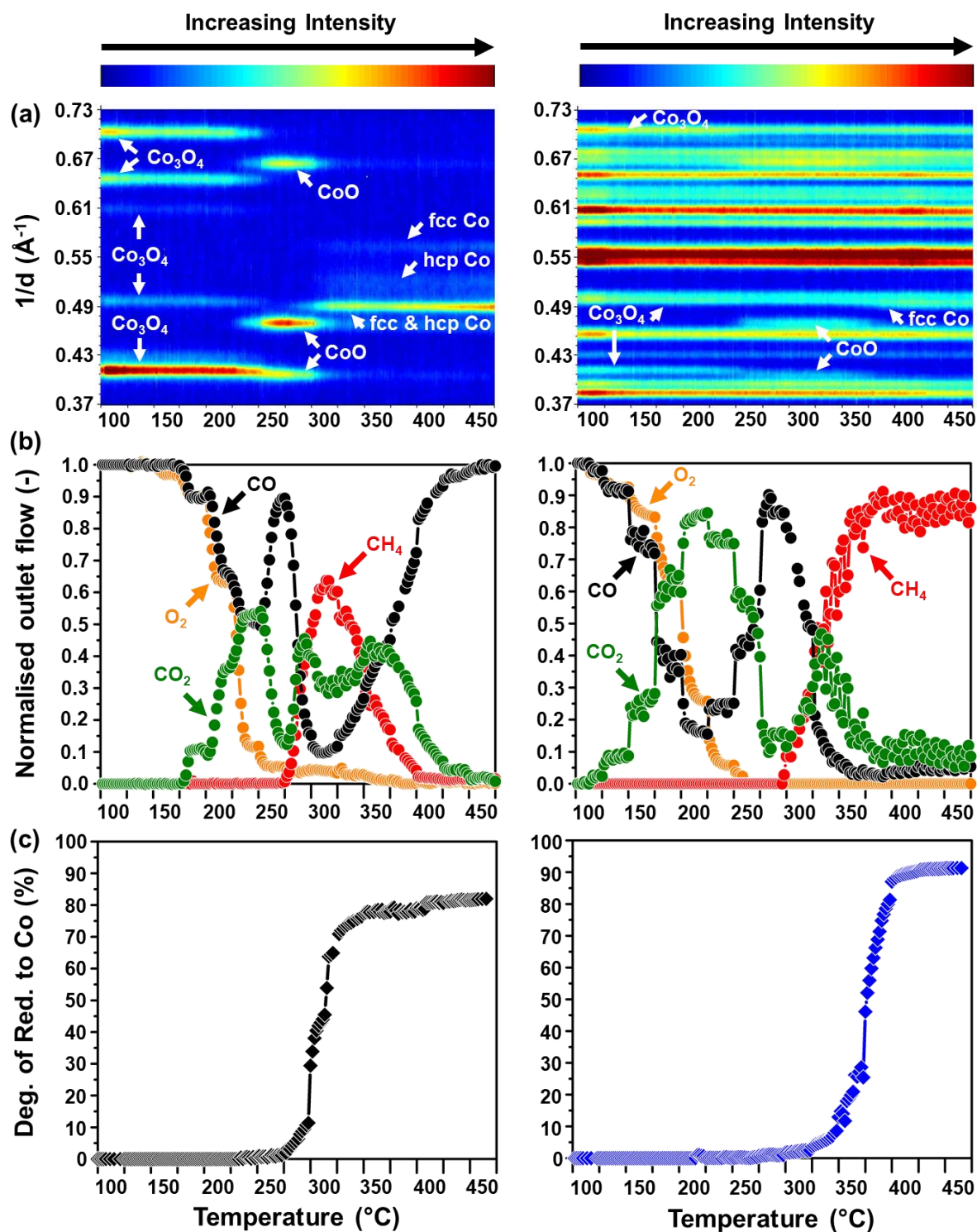


**Figure 9.4:** (a) On-top view of the *in situ* PXRD patterns of (left) unsupported  $\text{Co}_3\text{O}_4$ , and (right)  $\text{Co}_3\text{O}_4/\text{ZrO}_2$  recorded during wet CO-PrOx. (b) Changes in the normalised outlet flow rates of CO,  $\text{O}_2$ ,  $\text{CO}_2$  and  $\text{CH}_4$  calculated from GC-TCD data. (c) Magnetometry-derived degree of reduction of  $\text{Co}_3\text{O}_4$  to metallic Co. (Feed composition: 1% CO, 1%  $\text{O}_2$ , 45%  $\text{H}_2$ , 10%  $\text{H}_2\text{O}$  and 43%  $\text{N}_2$ ; pressure: atmospheric, GHSV: 60000 mL(NTP)/ $g_{\text{Co}_3\text{O}_4}$ /hr).

The M-H curves in Figure 9.5 for the evaluated catalysts show clear hysteresis behaviour at 450 °C, and consequently give higher  $\gamma$  values (40.6 wt.-% - unsupported  $\text{Co}_3\text{O}_4$ , and 52.1 wt.-% -  $\text{Co}_3\text{O}_4/\text{ZrO}_2$ ) than those observed in the absence of co-fed water (33.0 and 33.1 wt.-%, respectively, see Table 9.1). Note that PXRD analysis of the  $\text{ZrO}_2$ -supported catalyst also showed the formation of larger fcc Co crystallites in the presence of co-fed water ( $40.3 \pm 19.9$  nm) than those formed in the absence of water ( $21.2 \pm 0.9$  nm) at 450 °C – see Figure 9.11(c). Due to extensive granularity in the unsupported catalyst, the fcc Co crystallite size could not be reliably determined from the patterns recorded during dry CO-PrOx (see section 8.1), and therefore, cannot be compared with the fcc Co size determined during wet CO-PrOx ( $26.8 \pm 3.3$  nm). However, the unsupported catalyst (unlike  $\text{Co}_3\text{O}_4/\text{ZrO}_2$ ) also reduced to metallic hcp Co under both reaction environments, with crystallite sizes of  $4.6 \pm 0.2$  nm (dry CO-PrOx) and  $2.7 \pm 0.3$  nm (wet CO-PrOx) – see Figure 9.11(c). Since the critical sizes for the superparamagnetism of hcp Co is 11 nm at 450 °C [50], the unsupported metallic hcp Co crystallites formed under both reaction conditions are most likely superparamagnetic. On the other hand, the critical size for the superparamagnetism of metallic fcc Co is 16 – 20(26) nm [50], which could imply that all or most of the fcc Co crystallites are non-superparamagnetic due to these having an average size of  $26 \pm 3.8$  nm. Therefore, the  $\gamma$  of 40.6 wt.-% for the unsupported catalyst is possibly a contribution from the fcc Co crystallites only. Interestingly, this  $\gamma$  value is also close to the PXRD-derived relative concentration of  $38.4 \pm 2.2$  wt.-% for fcc Co at 450 °C (see Figure 9.11(b) and Table A.7.1), further supporting the possibility of fcc Co being non-superparamagnetic. The overall higher  $\gamma$  values and fcc Co crystallite sizes observed in the presence of co-fed water, support the earlier proposed water-induced sintering that may have taken place during wet CO-PrOx [39–42].

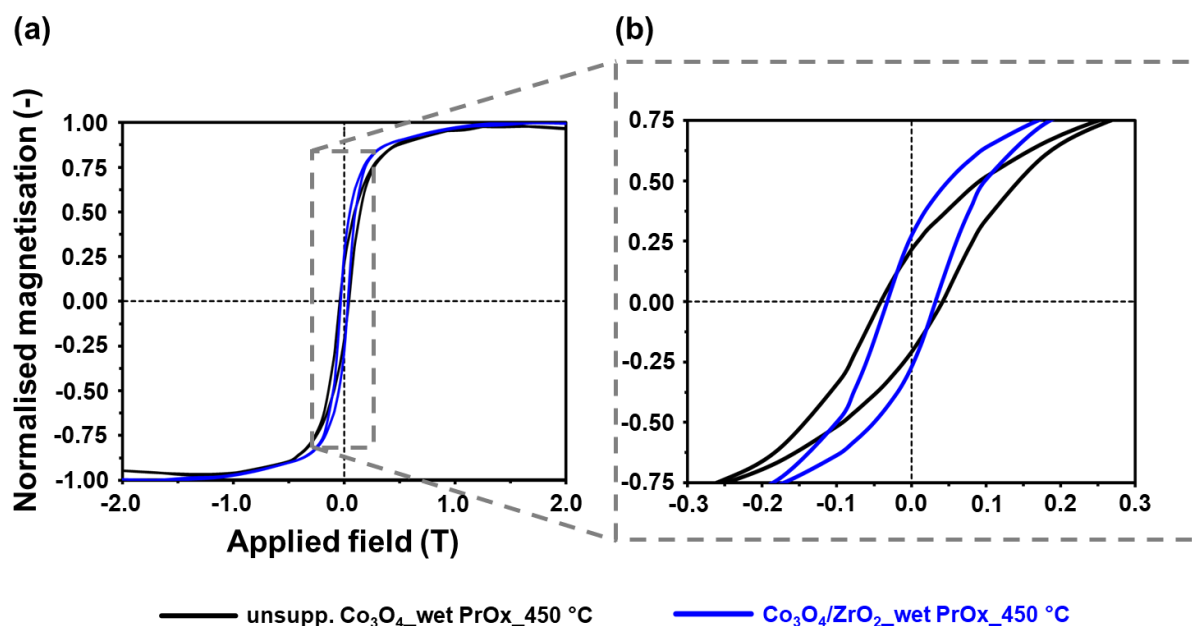


**Figure 9.5:** (a) Magnetometry-derived M-H curves recorded at 450 °C during wet CO-PrOx over unsupported and ZrO<sub>2</sub>-supported Co<sub>3</sub>O<sub>4</sub>. (b) Magnified view of the M-H curves indicating the existence of hysteresis behaviour. (Feed composition: 1% CO, 1% O<sub>2</sub>, 45% H<sub>2</sub>, 10% H<sub>2</sub>O and 43% N<sub>2</sub>; pressure: atmospheric, GHSV: 60000 mL(NTP)/g<sub>Co<sub>3</sub>O<sub>4</sub></sub>/hr).

### 9.2.3. Effect of co-fed CO<sub>2</sub> during CO-PrOx (dry CO-PrOx with co-fed CO<sub>2</sub>)

The effect of CO<sub>2</sub>, similar to H<sub>2</sub>O, has been investigated to a lesser extent than H<sub>2</sub> especially regarding the phase stability of oxide catalysts. Gaseous CO<sub>2</sub> stabilises the oxide phase to a lesser degree than H<sub>2</sub>O and O<sub>2</sub> [20,51–55] (also see results in sub-sections 7.2.2. and 7.2.3.), and therefore, can be expected to have a low (or no) stabilising effect on the Co<sub>3</sub>O<sub>4</sub> (and CoO) phase during CO-PrOx. However, the presence of CO<sub>2</sub> in the feed makes the reverse WGS reaction (reverse of Reaction 9.3) and CO<sub>2</sub> methanation (Reaction 9.5) possible, in addition to CO and H<sub>2</sub> oxidation, as well as CO methanation. This complicates the analysis of the gas effluent as one gas can be a reactant and/or a product of at least two reactions (also see sub-section 4.4.4.).

Therefore, the results from the gas product analysis are first presented as positive and negative net outlet flow rates of CO, O<sub>2</sub>, CO<sub>2</sub> and CH<sub>4</sub> (Figure 9.6(b)), instead of normalised outlet flow rates. These net outlet flow rates were calculated from subtracting, for example, the amount of “Gas A”

entering the reactor from the amount of “Gas A” exiting the reactor. If this difference is positive, then this indicates that “Gas A” was formed over the catalyst, while a negative difference indicates that “Gas A” was consumed. This approach allows for the different possible reactions (*i.e.*, Reactions 9.1 – 9.5, including the reverse of Reaction 9.3) to be identified within the temperature window studied (50 – 450 °C). However, the CO conversion to CO<sub>2</sub> and O<sub>2</sub> selectivity to CO<sub>2</sub> (both *via* oxidation) as a function of temperature, can be found in Figures 9.13(a) and A.6.2, respectively. The CO conversion to CH<sub>4</sub> (*via* hydrogenation), CO<sub>2</sub> conversion to CH<sub>4</sub> (*via* hydrogenation), CO<sub>2</sub> conversion to CO (*via* reverse WGS), and the *in situ* magnetometry-derived DoR as a function of temperature are presented in Figures 9.13(b) – (d). A feed gas composing of a 1:1:50:10:38 CO:O<sub>2</sub>:H<sub>2</sub>:CO<sub>2</sub>:N<sub>2</sub> gas mixture was flowed over the unsupported and ZrO<sub>2</sub>-supported catalyst at a GHSV of 60000 ml(NTP)/g<sub>Co<sub>3</sub>O<sub>4</sub></sub>/hr. The results from the *in situ* PXRD and magnetometry studies have also been included in Figures 9.6(a) and (c), respectively.

At temperatures below 250 °C for both the unsupported and ZrO<sub>2</sub>-supported catalyst, positive net outlet flow rates are observed for CO<sub>2</sub> while, negative net outlet flow rates are observed for CO and O<sub>2</sub>. At this point, no CH<sub>4</sub> is detected, implying that CO is exclusively being converted *via* CO oxidation. Note that the net outlet flow rate of O<sub>2</sub> reaches a steady negative value from 200 °C - corresponding to a full conversion of O<sub>2</sub> - and stays at this value until 450 °C (Figure 9.6(b)). The full consumption of O<sub>2</sub> is a result of the concurrent H<sub>2</sub> oxidation reaction. The unsupported catalyst reaches a maximum CO conversion to CO<sub>2</sub> of 84.2% (and a O<sub>2</sub> selectivity of 44.1%) at 175 °C, while Co<sub>3</sub>O<sub>4</sub>/ZrO<sub>2</sub> reaches a maximum CO conversion of 92.7% (and a O<sub>2</sub> selectivity of 43.3%) at 200 °C (see Figure 9.13(a)). These maximum CO conversions (and corresponding O<sub>2</sub> selectivities) are very close to those achieved by the same catalysts during dry CO-PrOx with no CO<sub>2</sub> co-feeding (unsupported Co<sub>3</sub>O<sub>4</sub>: 84.4% (45.0%), and Co<sub>3</sub>O<sub>4</sub>/ZrO<sub>2</sub>: 91.6% (57.1%)). The presence of CO<sub>2</sub> in the feed seems to have no effect on the CO oxidation activity (and a minor effect on selectivity) of these two catalysts, which possibly suggests a weaker surface adsorption of CO<sub>2</sub> (when compared with H<sub>2</sub>O) on Co<sub>3</sub>O<sub>4</sub> [20,51,53].

The formation of CoO and metallic Co in both catalysts takes place at temperatures similar to those noted in the case with no co-fed CO<sub>2</sub> using PXRD and magnetometry (see summary plots in Figures 9.11(a) and 9.13(d)). The magnetometry-derived DoRs for each catalyst at 450 °C are also very similar under conditions with and without co-fed CO<sub>2</sub> (Figure 9.13(d)). This further confirms that CO<sub>2</sub> is indeed a mild oxidant as it does not provide any stabilisation of the cobalt oxide phases during CO-PrOx, unlike H<sub>2</sub>O [20,51,53]. PXRD analysis again confirmed the formation of fcc and hcp Co in the unsupported state, while only fcc Co was formed in the supported state – with the

latter possibly directed by the nature of the NPSIs. However, the hcp:fcc Co ratio at 450 °C in the unsupported catalyst (Figures 9.11(b) and A.7.2(e), as well as Table A.7.1) decreases from 3.6 (in the absence of co-fed CO<sub>2</sub>) to 2.0 (in the presence of co-fed CO<sub>2</sub>), which could again be attributed to the change in the reaction gas environment or the changing partial pressures of the reactants and products during the reaction [36].

The final average hcp and fcc Co size at 450 °C in the unsupported catalyst is  $2.3 \pm 0.3$  nm and  $25.8 \pm 2.8$  nm, respectively (Figures 9.11(c) and A.7.2(f), as well as Table A.7.1). As observed in the previous sub-section, the minimised extent of granularity in this reduced catalyst allowed for a lower fcc Co size to be calculated using Rietveld refinement. However, sintering may have still taken place as the estimated fcc Co size is larger than the starting Co<sub>3</sub>O<sub>4</sub> size of  $12.3 \pm 0.3$  nm. The average crystallite size of fcc Co in the ZrO<sub>2</sub>-supported catalyst is  $35.9 \pm 13.4$  nm, which also suggests extensive sintering. As will be discussed below, the presence of 10% CO<sub>2</sub> in the feed causes the formation of relatively high amounts of H<sub>2</sub>O *via* CO<sub>2</sub> methanation and the reverse WGS. This is in addition to the water formed during H<sub>2</sub> oxidation and CO methanation. Therefore, the formation of water may have facilitated the sintering process of the reduced nanoparticles, in combination with increasing temperature [39–42]. As mentioned previously, the high reported error linked with the average crystallite size of fcc Co in the ZrO<sub>2</sub>-supported catalyst may be a result of the overlapping fcc Co and ZrO<sub>2</sub> reflections at  $1/d = 0.49 \text{ \AA}^{-1}$ .

Despite CO<sub>2</sub> not having a negative effect on the progress of the CO oxidation reaction, the phase changes in both catalysts do cause a loss in CO oxidation activity and selectivity as CH<sub>4</sub> formation is observed from 250 °C over the unsupported catalyst, and from 300 °C over the ZrO<sub>2</sub>-supported catalyst. Between 250 and 300 °C, the unsupported catalyst forms CH<sub>4</sub> from both CO and CO<sub>2</sub> – as indicated by the positive outlet flow rates of the former gas, and the negative outlet flow rates of the latter gases (Figure 9.6(b)). However, above 300 °C, the net outlet flow of CO becomes positive while the net flow of CH<sub>4</sub> decreases, but still stays positive. This implies that the reverse WGS reaction (reverse of Reaction 9.3) is taking place at these high temperatures, in addition to CO<sub>2</sub> methanation. Over the ZrO<sub>2</sub>-supported catalyst, very low CO methanation activity is observed between 375 and 400 °C (Figure 9.13(b)), as well as very low reverse WGS activity above 400 °C (see Figure 9.13(c)). On the other hand, the ZrO<sub>2</sub>-supported catalyst maintains higher CO<sub>2</sub> methanation activity than the unsupported catalyst between 350 and 450 °C.

According to the thermodynamic calculations, the CO<sub>2</sub> conversion to CH<sub>4</sub> (assuming no effects from the reverse WGS reaction) at 450 °C is 84.1%, and due to the exothermic nature of this

reaction, higher conversions are possible below 450 °C (Figure 9.2(b)). However, the unsupported and ZrO<sub>2</sub>-supported catalyst both achieve much lower CO<sub>2</sub> conversions between 250 and 450 °C (Figure 9.13(c)). In the presence of 1% CO in the feed, the predicted CO<sub>2</sub> conversion to CO *via* the reverse WGS (assuming no effects from CO<sub>2</sub> methanation) is 49.3% at 450 °C (Figure 9.1(b)). The unsupported catalyst reaches a maximum CO<sub>2</sub> conversion to CO of 27.5% at 450 °C, while the ZrO<sub>2</sub>-supported one reaches a maximum conversion of 3.2% at the same temperature (Figure 9.13(c)). The lower experimental CO<sub>2</sub> conversions achieved by the two catalysts, with respect to the individual reactions, possibly suggest a kinetic hindrance over the metallic Co phase. It is worth stating that some researchers have proposed the possibility of CO<sub>2</sub> methanation taking place *via* the reverse WGS reaction [48,56,57]. Although the current experiments were not designed to confirm this reaction pathway, this remains a viable route over the two tested catalysts, which may also explain the lower experimental CO<sub>2</sub> conversions to some extent.

The changing hcp:fcc Co ratio and crystallite sizes of the two allotropes, as well as the structure of the particles (either exhibiting intergrowth or otherwise) in the unsupported catalyst as a function of temperature (see Figures A.7.2(e) and (f)) may be causing the change from CO and CO<sub>2</sub> methanation between 250 and 300 °C, to CO<sub>2</sub> methanation and reverse WGS between 300 and 450 °C (Figure 9.6(b), as well as Figures 9.13(b) and (c)). As previously mentioned, DFT [48] and experimental [49] studies have shown that metallic Co on ZrO<sub>2</sub> exhibits high H<sub>2</sub> dissociation rates and stronger CO<sub>2</sub> adsorption on the surface (due to the nature of the NPSIs), which seem to mostly favour CO<sub>2</sub> hydrogenation (over that of CO) in the present study between 300 and 450 °C.

It is worth pointing out that the results in Figures 9.6 and 9.13, for the first time, show a close association of the metallic Co phase with CO<sub>2</sub> methanation and the reverse WGS reaction. These two reactions have only been mentioned in the literature as being possible under CO-PrOx conditions but there has not yet been a report linking the phase of the catalyst (and temperature) with these two reactions during CO-PrOx.

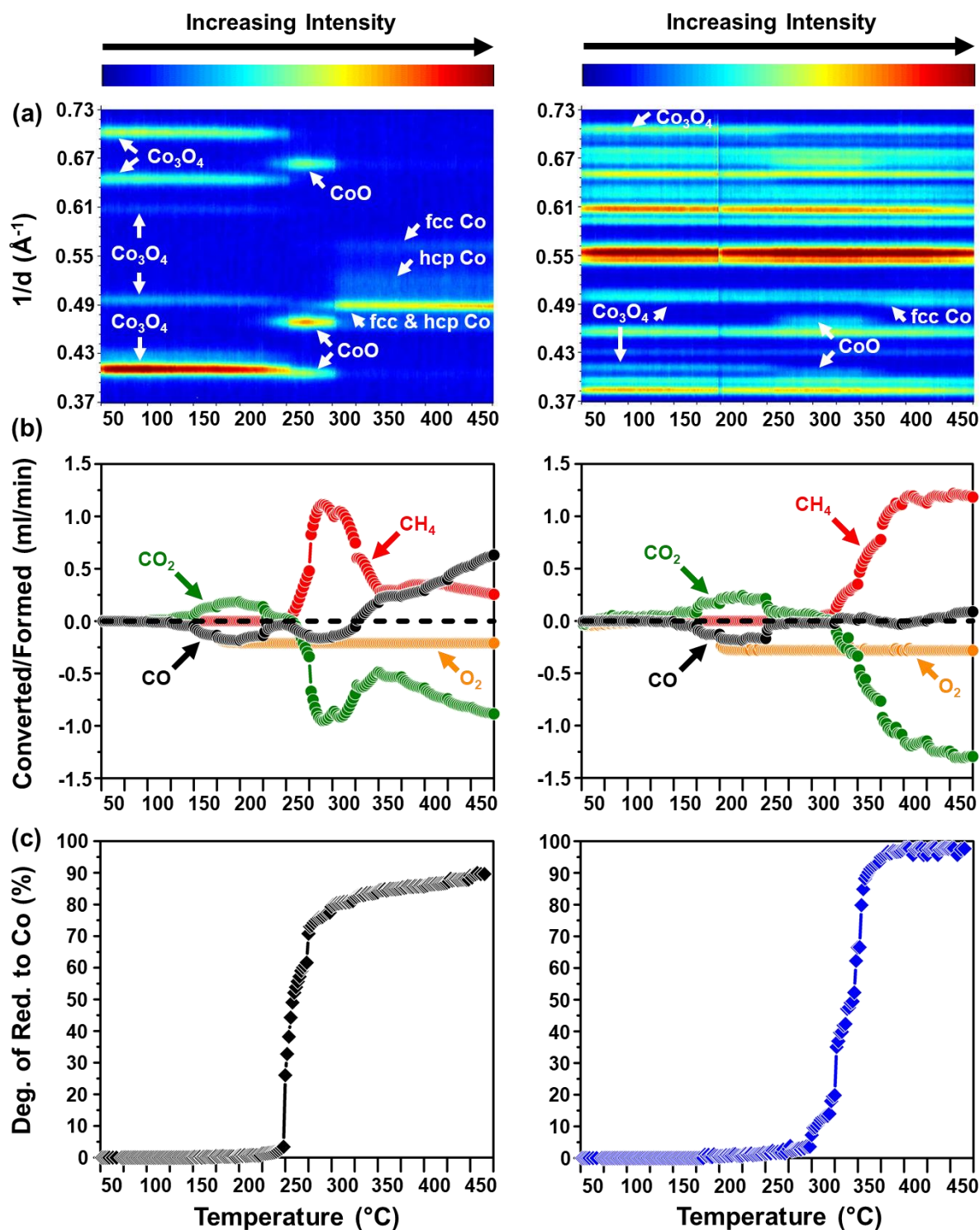


**Figure 9.6:** (a) On-top view of the *in situ* PXRD patterns of (left) unsupported  $\text{Co}_3\text{O}_4$ , and (right)  $\text{Co}_3\text{O}_4/\text{ZrO}_2$  recorded during dry CO-PrOx with co-fed  $\text{CO}_2$ . (b) Changes in the net outlet flow rates of CO,  $\text{O}_2$ ,  $\text{CO}_2$  and  $\text{CH}_4$  calculated from GC-TCD data. (c) Magnetometry-derived degree of reduction of  $\text{Co}_3\text{O}_4$  to metallic Co. (Feed composition: 1% CO, 1%  $\text{O}_2$ , 50%  $\text{H}_2$ , 10%  $\text{CO}_2$  and 38%  $\text{N}_2$ ; pressure: atmospheric, GHSV:  $60000 \text{ mL(NTP)}/\text{g}_{\text{Co}_3\text{O}_4}/\text{hr}$ ).

Figure 9.7 shows the M-H curves for the unsupported and ZrO<sub>2</sub>-supported catalysts recorded at 450 °C during dry CO-PrOx with co-fed CO<sub>2</sub>. Again, these M-H curves display hysteresis behaviour which indicates the presence of crystallites/nanoparticles above the critical size for the superparamagnetism of hcp Co<sup>0</sup> (11 nm at 450 °C [50]) and/or fcc Co<sup>0</sup> (16 – 20(26) nm at 450 °C [50]). The calculated  $\gamma$  value for the unsupported and ZrO<sub>2</sub>-supported sample is 21.1 wt.-% and 23.2 wt.-%, respectively. These values indicate a lower degree of crystallite growth above the critical sizes, when compared with the case where H<sub>2</sub>O was co-fed in the absence of CO<sub>2</sub> (see Table 9.1). Note that the fcc Co sizes determined from PXRD in the presence of co-fed CO<sub>2</sub> (but absence of water) were  $25.8 \pm 2.8$  nm (unsupported Co<sub>3</sub>O<sub>4</sub>) and  $35.9 \pm 13.4$  nm (Co<sub>3</sub>O<sub>4</sub>/ZrO<sub>2</sub>), while the fcc Co sizes determined in the presence of co-fed water (but absence of CO<sub>2</sub>) were  $26.8 \pm 3.3$  nm (unsupported Co<sub>3</sub>O<sub>4</sub>) and  $40.3 \pm 19.9$  nm (Co<sub>3</sub>O<sub>4</sub>/ZrO<sub>2</sub>) at 450 °C – see Figure 9.11(c). These reported PXRD size trends do indicate a slightly lowered sintering degree in the absence of water, but it should be noted that the calculated sizes are within statistical error of each other. Interestingly, the  $\gamma$  values obtained during dry CO-PrOx with co-fed CO<sub>2</sub> are lower than the  $\gamma$  values obtained during dry CO-PrOx with no co-fed CO<sub>2</sub> (see Table 9.1). However, the reasons for this observation are unknown at this stage.

The unsupported metallic hcp Co crystallites formed during dry CO-PrOx with co-fed CO<sub>2</sub> have an average size ( $2.3 \pm 0.2$  nm) that is lower than the critical size of 11 nm, making these crystallites superparamagnetic as they do not contribute to the  $\gamma$  of 21.1 wt.-%. On the other hand, metallic hcp Co was not formed in the ZrO<sub>2</sub>-supported catalyst, implying that the  $\gamma$  of 23.2 wt.-% is due to the presence of large fcc Co crystallites. The relative concentration of fcc Co in the unsupported catalyst was estimated from PXRD to be  $33.8 \pm 2.1$  wt.-%, which is higher than the  $\gamma$  value of 21.1 wt.-%. The overlap between the hcp and fcc Co reflections at  $1/d = 0.49 \text{ \AA}^{-1}$ , can introduce some uncertainty in the calculation of the relative concentration of each allotrope. Therefore, it is possible that the fcc Co concentration was over-estimated using Rietveld refinement, thus causing the observed disagreement with the calculated  $\gamma$  value.

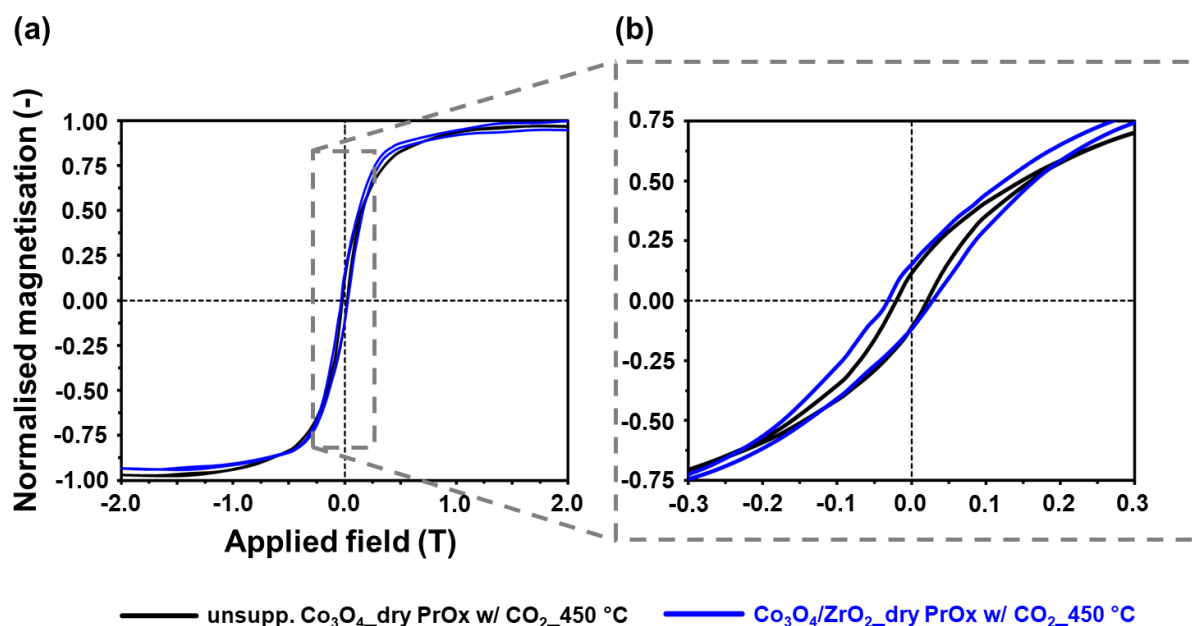


**Figure 9.7:** (a) Magnetometry-derived M-H curves recorded at 450 °C during dry CO-PrOx with co-fed  $\text{CO}_2$  over unsupported and  $\text{ZrO}_2$ -supported  $\text{Co}_3\text{O}_4$ . (b) Magnified view of the M-H curves indicating the existence of hysteresis behaviour. (Feed composition: 1%  $\text{CO}$ , 1%  $\text{O}_2$ , 50%  $\text{H}_2$ , 10%  $\text{CO}_2$  and 38%  $\text{N}_2$ ; pressure: atmospheric, GHSV: 60000 mL(NTP)/g $\text{Co}_3\text{O}_4$ /hr).

#### 9.2.4. Effect of co-fed $\text{H}_2\text{O}$ and $\text{CO}_2$ during CO-PrOx (wet CO-PrOx with co-fed $\text{CO}_2$ )

Finally, co-feeding both  $\text{H}_2\text{O}$  and  $\text{CO}_2$  during CO-PrOx was also considered to investigate their combined effect on catalytic performance and phase stability. A 1:1:46:10:9:33  $\text{CO}:\text{O}_2:\text{H}_2:\text{H}_2\text{O}:\text{CO}_2:\text{N}_2$  gas feed mixture (GHSV: 60000 ml(NTP)/g $\text{Co}_3\text{O}_4$ /hr) was used and four catalysts were tested - unsupported  $\text{Co}_3\text{O}_4$ ,  $\text{Co}_3\text{O}_4/\text{ZrO}_2$ ,  $\text{Co}_3\text{O}_4/\text{SiC}$  and  $\text{Co}_3\text{O}_4/\text{TiO}_2\text{-P25}$  – under this realistic CO-PrOx condition. The results from the gas product analysis are first plotted as positive and negative net outlet flow rates of  $\text{CO}$ ,  $\text{O}_2$ ,  $\text{CO}_2$  and  $\text{CH}_4$  as a function of temperature in Figures 9.8(b) and 9.9(b), as was done in sub-section 9.2.3. The catalysts were also characterised *in situ* using the in-house PXRD and magnetometry set-ups, respectively, the results from which are also shown in Figures 9.8 and 9.9. Furthermore, Figures 9.11 – 9.14, Figure A.6.3, as well as Tables 9.1 and A.7.1, capture all the main *in situ* characterisation and gas product analysis results from the different CO-PrOx reactions performed over all four catalysts.

Below 275 °C, the occurrence of CO oxidation over all catalysts is indicated by the positive net CO<sub>2</sub> outlet flow, as well as the negative net CO and O<sub>2</sub> outlet flow, respectively. Moreover, the net O<sub>2</sub> outlet flow reaches a steady negative value which corresponds to the full consumption of the O<sub>2</sub> in the feed. The results in Figure 9.13(a) and 9.14(a) show that the maximum CO conversion to CO<sub>2</sub> under the current reaction condition follows the order: Co<sub>3</sub>O<sub>4</sub>/ZrO<sub>2</sub> (73.4%, 200 °C) > unsupported Co<sub>3</sub>O<sub>4</sub> (72.1%, 225 °C) > Co<sub>3</sub>O<sub>4</sub>/SiC (67.1%, 200 °C) > Co<sub>3</sub>O<sub>4</sub>/TiO<sub>2</sub>-P25 (61.9%, 225 °C). These maximum CO conversions are lower than those obtained in the absence of H<sub>2</sub>O and CO<sub>2</sub> (see Figure 9.13(a) and 9.14(a)), and even lower than the targeted 99.999% conversion required for fuel cell applications [14–18,58]. The competitive adsorption of mostly H<sub>2</sub>O onto the surface of the catalysts may have caused the decrease in CO oxidation activity [20,26–28]. This H<sub>2</sub>O adsorption may have further affected the effectiveness of the MvK mechanism regarding CO<sub>2</sub> formation from CO [34,35]. It is worth noting that the ZrO<sub>2</sub>-supported catalyst shows better activity than all the other three catalysts under all investigated CO-PrOx conditions. This can possibly be attributed to the electronic interactions between the Co<sub>3</sub>O<sub>4</sub> nanoparticles and the ZrO<sub>2</sub> support - especially near the nanoparticle-support interface - which allow the Co<sub>3</sub>O<sub>4</sub> to maintain relatively high CO oxidation activity under all CO-PrOx conditions.

The further decrease in CO oxidation activity and selectivity above 225 °C is a result of the catalysts reducing to CoO and metallic Co, as confirmed by the two employed *in situ* techniques (see results in Figures 9.8(a) and (c), as well as Figures 9.9(a) and (c)). The onset formation temperature of CoO, according to PXRD, follows the order: unsupported Co<sub>3</sub>O<sub>4</sub> (200 °C) < Co<sub>3</sub>O<sub>4</sub>/ZrO<sub>2</sub> (250 °C) < Co<sub>3</sub>O<sub>4</sub>/TiO<sub>2</sub>-P25 (275 °C) < Co<sub>3</sub>O<sub>4</sub>/SiC (300 °C). These temperatures are higher than those observed during dry CO-PrOx with no co-fed CO<sub>2</sub> (see summary plots in Figure 9.11(a) and 9.12(a)). Interestingly, the trend for the onset CoO formation temperature mentioned above is different from that observed during dry CO-PrOx. The observed increase in the CoO formation temperature is possibly due to the co-adsorption, and the oxidising nature of water [19–25] that helps stabilise the Co<sub>3</sub>O<sub>4</sub> phase. The mentioned dissimilarity in the onset CoO formation temperature trends may also be influenced by the change in the gas environment (*i.e.*, the presence or absence of H<sub>2</sub>O), or the changing partial pressure ratios of H<sub>2</sub>:H<sub>2</sub>O during dry and wet CO-PrOx, respectively.

The presence of H<sub>2</sub>O in the feed also increases the metallic Co formation temperatures over the four catalysts, relative to those observed under dry conditions (compare results in Figures 9.13(d) and 9.14(d)). The trend in the onset metallic Co formation temperature, based on magnetometry, is as follows: unsupported Co<sub>3</sub>O<sub>4</sub> (275 °C) < Co<sub>3</sub>O<sub>4</sub>/ZrO<sub>2</sub>, Co<sub>3</sub>O<sub>4</sub>/TiO<sub>2</sub>-P25 (300 °C) < Co<sub>3</sub>O<sub>4</sub>/SiC

(325 °C). Due to the intrinsic detection limits of PXRD, the metallic Co phase in all catalysts is first noted at higher temperatures than those noted using the magnetometer. For the SiC-supported catalyst, PXRD does not show any metallic Co reflections. This is in-line with the relatively low DoR (13.8%) reached by this catalyst at 450 °C in the magnetometer. The overall trend in the magnetometry-derived DoR at 450 °C (Figures 9.13(d) and 9.14(d)) is as follows:  $\text{Co}_3\text{O}_4/\text{TiO}_2\text{-P25}$  (88.6%) >  $\text{Co}_3\text{O}_4/\text{ZrO}_2$  (81.1%) > unsupported  $\text{Co}_3\text{O}_4$  (80.6%) >  $\text{Co}_3\text{O}_4/\text{SiC}$  (13.8%). As also observed during dry CO-PrOx (sections 8.1. and 8.2.), the SiC-supported catalyst is the least reduced. Also note that the onset formation temperatures of CoO and metallic Co over SiC are at higher temperatures when compared with those of the other three catalysts. Again, this can be attributed to the nature of the  $\text{Co}_3\text{O}_4\text{-SiC}$  and  $\text{CoO-SiC}$  interactions - through the previously shown 1 – 2 nm  $\text{Si}_x\text{O}_y$  or  $\text{Si}_x\text{O}_y\text{C}_z$  layer (Figure 5.12) - that possibly delay and limit oxide reduction.

Metallic Co in the unsupported catalyst exists in both hcp and fcc crystal forms, at a ratio of 2.8, which is lower than the ratio of 3.6 noted during dry CO-PrOx (see Figures 8.1(b), 9.11(b) and A.7.3(b), as well as Table A.7.1). The size of the hcp Co crystallites during wet CO-PrOx with  $\text{CO}_2$  at 450 °C is  $4.2 \pm 0.3$  nm, which is similar to the  $4.6 \pm 0.2$  nm observed under dry conditions in the absence of  $\text{CO}_2$  (see Figures 8.1(c), 9.11(c) and A.7.3(c), as well as Table A.7.1). However, the exact crystallite size of fcc Co during wet CO-PrOx with  $\text{CO}_2$  cannot be reported with certainty due to extensive granularity effects and/or possible intergrowth of hcp and fcc Co. This is again similar to the case with no co-fed  $\text{H}_2\text{O}$  and  $\text{CO}_2$  (section 8.1.), but different from the observation made during wet CO-PrOx without co-fed  $\text{CO}_2$  (sub-section 9.2.2.) and dry CO-PrOx with co-fed  $\text{CO}_2$  (sub-section 9.2.3.), where the fcc Co size at 450 °C is below 30 nm (also see Figures 9.11(c) and A.7.2, as well as Table A.7.1.) – possibly indicating minimised granularity effects. These results also emphasise the possible effect of changing the reaction environment and/or the changing partial pressures of the different gases as a function of temperature on the hcp:fcc ratio, the crystallite sizes of each allotrope and the structure of the nanoparticles (either exhibiting intergrowth or otherwise) [36].

As previously observed during the reduction experiments (sub-section 6.2.2.) and the other CO-PrOx conditions ((sub-)sections 8.2., 9.2.2. and 9.2.3.),  $\text{ZrO}_2$  only stabilises fcc Co, while  $\text{TiO}_2\text{-P25}$  stabilises both hcp and fcc Co at elevated temperatures during wet CO-PrOx with co-fed  $\text{CO}_2$  (Figure 9.8((a), *left*), 9.9((a), *right*), as well as A.7.4(c)). Although reflections from metallic Co are not observed in the PXRD patterns of the SiC-supported catalyst (Figure 9.9((a), *left*)), it is possible that the small amounts of the metallic phase (only confirmed using the magnetometer – Figure 9.9((c), *left*)) are also in the fcc crystal form. The average size of the fcc Co in the  $\text{ZrO}_2$ -supported

catalyst is  $60.8 \pm 24.1$  nm (Figure 9.11(c)) – indicating an even greater extent of sintering than that observed in the previously discussed CO-PrOx conditions. The hcp Co over TiO<sub>2</sub>-P25 is  $15.5 \pm 3.7$  nm, which also indicates sintering as it is larger than the expected metallic Co size of 8.9 nm. The size of the fcc Co crystallites in the TiO<sub>2</sub>-P25-supported catalyst could not be determined due to possible granularity effects. However, the fcc phase may have also undergone some degree of sintering during the reaction. Again, this can be attributed to the relatively high amounts of H<sub>2</sub>O co-fed (10%), and those also formed during H<sub>2</sub> oxidation, CO and CO<sub>2</sub> methanation, as well as in the reverse WGS (see Figures 9.8(b), 9.9(b), 9.13 and 9.14). The size of CoO in the SiC-supported sample is  $9.7 \pm 1.7$  nm, which is lower than the expected size of 12.8 nm, possibly due to the formation of smaller crystallites (or crystalline domains) that make up larger CoO particles [59].

The previously discussed CO-PrOx results have all demonstrated that metallic Co is responsible for the undesired side reactions (Reactions 9.2 – 9.5) that take place at elevated temperatures, most of which consume H<sub>2</sub> (except the forward WGS, which produces H<sub>2</sub>). Thermodynamic calculations were also performed to evaluate the effect of certain gases on the progress of these side reactions (see section 9.1). Under an assumed feed containing CO:O<sub>2</sub>:H<sub>2</sub>:H<sub>2</sub>O:CO<sub>2</sub>:N<sub>2</sub> 1:1:50:10:10:28 (which is similar to the experimental feed for wet CO-PrOx with co-fed CO<sub>2</sub>), the forward and reverse WGS reactions are the most affected (see Figure 9.1). The forward reaction is predicted to only take place below 285 °C (minimum X<sub>CO</sub> = 2.7% at 285 °C), while the reverse reaction is expected to take place between 290 and 450 °C (maximum X<sub>CO<sub>2</sub></sub> = 25.8% at 450 °C). CO methanation is virtually not affected as CO conversions above 99.0% are still possible below 450 °C, while for CO<sub>2</sub> methanation, the predicted CO<sub>2</sub> conversion at 450 °C is 78.6% (but higher conversions are possible below 450 °C – see Figure 9.2)).

During wet CO-PrOx with co-fed CO<sub>2</sub>, the unsupported and TiO<sub>2</sub>-P25-supported reduced catalysts produce significant amounts of CH<sub>4</sub> from CO at relatively low temperatures. However, the unsupported catalyst forms lower amounts of CH<sub>4</sub> under this condition when compared with the conditions with no co-fed H<sub>2</sub>O and/or CO<sub>2</sub> (see Figure 9.13(b)) - an effect believed to be caused by the blockage of active sites by mostly water [21,46,47]. Interestingly, the reduced TiO<sub>2</sub>-P25-supported catalyst forms higher amounts of methane during wet CO-PrOx with co-fed CO<sub>2</sub> between 300 and 350 °C, when compared with the same catalyst under conditions with no H<sub>2</sub>O and CO<sub>2</sub> co-feeding (Figure 9.14(b)). Note that within the above-mentioned temperature range, the TiO<sub>2</sub>-P25-supported catalyst forms relatively high amounts of CO<sub>2</sub> in the absence of co-fed H<sub>2</sub>O and CO<sub>2</sub> (see Figure 9.14(a)), which was earlier attributed to a possible *in situ* WGS reaction, preceded by H<sub>2</sub> oxidation to H<sub>2</sub>O (see section 8.2) [12]. This *in situ* WGS reaction is not observed

when H<sub>2</sub>O and CO<sub>2</sub> are present in the feed, therefore, allowing for higher methane yields to be realised instead. This is also in line with the results from the thermodynamic calculations, which show that the forward WGS is only possible below 285 °C.

On the other hand, the ZrO<sub>2</sub>- and SiC-supported catalysts convert very low amounts of CO to CH<sub>4</sub> over metallic Co, but also show no evidence for the occurrence of the forward WGS reaction as no CO<sub>2</sub> is produced (see Figures 9.13(a) and (b), as well as 9.14(a) and (b)). Instead, the ZrO<sub>2</sub>-supported catalyst mostly carries out CO<sub>2</sub> methanation, reaching a maximum CO<sub>2</sub> conversion of 42.7% between 400 and 450 °C. The same catalyst also converts 3.9% of CO<sub>2</sub> to CO *via* the reverse WGS. Note that these conversions are similar to the condition with co-fed CO<sub>2</sub> but no co-fed H<sub>2</sub>O (see Figure 9.13(c)), which indicates a negligible kinetic effect of H<sub>2</sub>O upon changing the reacting feed. The SiC-supported catalyst carries out both CO<sub>2</sub> methanation (maximum X<sub>CO<sub>2</sub></sub> = 20.7% at 450 °C) and the reverse WGS (maximum X<sub>CO<sub>2</sub></sub> = 13.3% at 450 °C) over metallic Co. The reduced TiO<sub>2</sub>-P25-supported catalyst is also active for CO<sub>2</sub> methanation (maximum X<sub>CO<sub>2</sub></sub> = 16.4% at 450 °C) and the reverse WGS (maximum X<sub>CO<sub>2</sub></sub> = 12.9% at 450 °C). In comparison, the unsupported metallic Co exhibits very different CO<sub>2</sub> methanation and reverse WGS activity – the former reaction is observed between 275 and 400 °C (maximum X<sub>CO<sub>2</sub></sub> = 27.6% at 300 °C), while the latter reaction takes place between 325 and 450 °C (maximum X<sub>CO<sub>2</sub></sub> = 19.8% at 400 °C).

The gradual change from CO<sub>2</sub> methanation to the reverse WGS with temperature, over the unsupported catalyst, may be caused by the changing hcp:fcc Co ratio, crystallite size of each metal phase, or the nanoparticle structure [36]. The relatively high CO<sub>2</sub> methanation activity of the ZrO<sub>2</sub>-supported catalyst may be ascribed to the strong surface adsorption of CO<sub>2</sub> and the high H<sub>2</sub> dissociation rates of the supported metal particles [48,49]. The small amounts of metallic Co supported on SiC may also be binding CO<sub>2</sub> much stronger than CO, since very little CO is converted to methane, while CO<sub>2</sub> is converted *via* methanation and the reverse WGS. On the other hand, reduced TiO<sub>2</sub>-P25-supported Co can adsorb and facilitate the conversion of CO to CH<sub>4</sub> at relatively low temperatures, while high temperatures allow for stronger adsorption and reaction of CO<sub>2</sub> to CH<sub>4</sub> and CO, respectively. An interesting point to note is that the unsupported and TiO<sub>2</sub>-P25-supported catalyst reduce to both hcp and fcc Co, therefore, it is possible that the relatively low-temperature CH<sub>4</sub> formation from CO may be mostly catalysed by hcp Co, which is known to be more active than fcc Co for CO hydrogenation [60–62]. The absence of hcp Co in the ZrO<sub>2</sub>- and SiC-supported samples might be causing the observed low methane formation from CO.

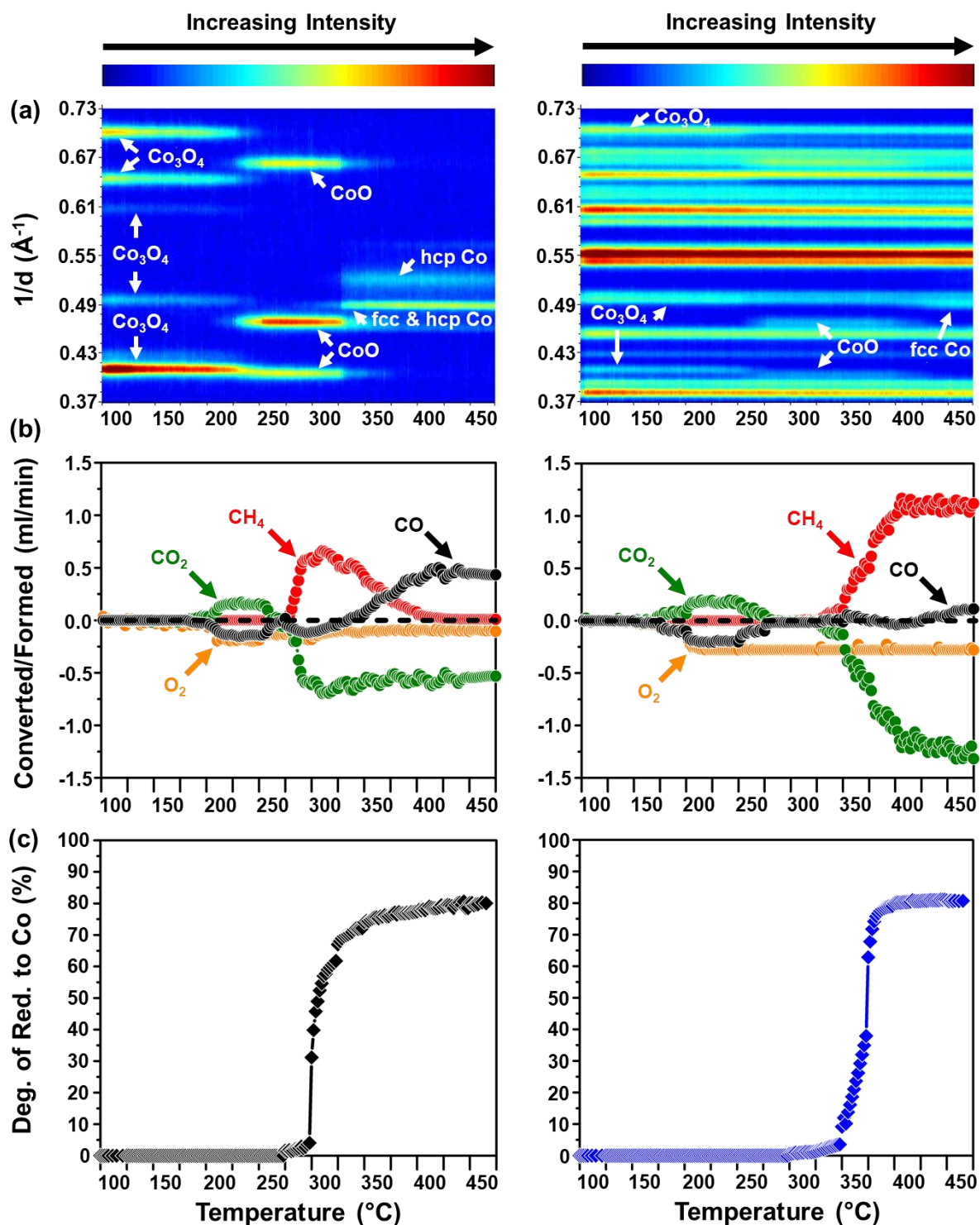


**Figure 9.8:** (a) On-top view of the *in situ* PXR D patterns of (left) unsupported  $\text{Co}_3\text{O}_4$ , and (right)  $\text{Co}_3\text{O}_4/\text{ZrO}_2$  recorded during dry CO-PrOx with co-fed  $\text{CO}_2$ . (b) Changes in the net outlet flow rates of  $\text{CO}$ ,  $\text{O}_2$ ,  $\text{CO}_2$  and  $\text{CH}_4$  calculated from GC-TCD data. (c) Magnetometry-derived degree of reduction of  $\text{Co}_3\text{O}_4$  to metallic Co. (Feed composition: 1%  $\text{CO}$ , 1%  $\text{O}_2$ , 46%  $\text{H}_2$ , 10%  $\text{H}_2\text{O}$ , 9%  $\text{CO}_2$  and 33%  $\text{N}_2$ ; pressure: atmospheric, GHSV: 60000 mL(NTP)/g $\text{Co}_3\text{O}_4$ /hr).

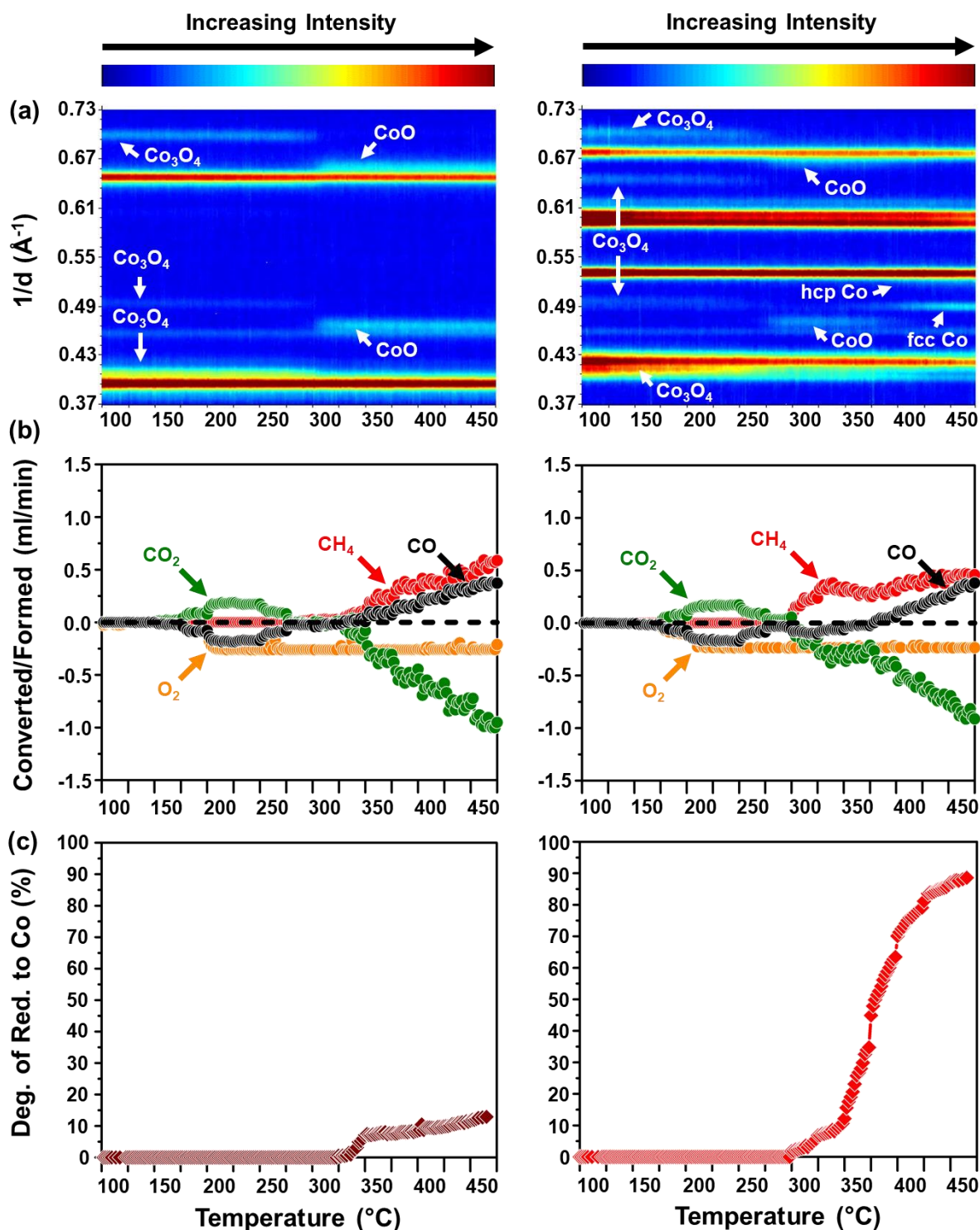


**Figure 9.9:** (a) On-top view of the *in situ* PXRD patterns of (left)  $\text{Co}_3\text{O}_4/\text{SiC}$ , and (right)  $\text{Co}_3\text{O}_4/\text{TiO}_2\text{-P25}$  recorded during dry CO-PrOx with co-fed  $\text{CO}_2$ . (b) Changes in the net outlet flow rates of CO,  $\text{O}_2$ ,  $\text{CO}_2$  and  $\text{CH}_4$  calculated from GC-TCD data. (c) Magnetometry-derived degree of reduction of  $\text{Co}_3\text{O}_4$  to metallic Co. (Feed composition: 1% CO, 1%  $\text{O}_2$ , 46%  $\text{H}_2$ , 10%  $\text{H}_2\text{O}$ , 9%  $\text{CO}_2$  and 33%  $\text{N}_2$ ; pressure: atmospheric, GHSV: 60000 mL(NTP)/g $\text{Co}_3\text{O}_4$ /hr).

As in the previous reaction conditions, M-H data was recorded for the four catalysts evaluated during wet CO-PrOx with co-fed CO<sub>2</sub> and is shown in Figure 9.10. All the plotted curves display hysteresis behaviour, which indicates the presence of metallic Co crystallites/nanoparticles above the critical size for the superparamagnetism of metallic hcp Co (11 nm at 450 °C [50]) and/or fcc Co (16 – 20(26) nm at 450 °C [50]) - also see  $\gamma$  values in Table 9.1. The  $\gamma$  values calculated are higher than those determined for the reactions performed in the absence of H<sub>2</sub>O, but lower than the  $\gamma$  value obtained during the reaction with co-fed H<sub>2</sub>O in the absence of CO<sub>2</sub> (Table 9.1). This observation further supports the explanation provided earlier relating to a water-induced sintering process during CO-PrOx [39–42]. Note that PXRD confirmed the formation of metallic hcp and fcc Co in the unsupported and TiO<sub>2</sub>-P25-supported catalysts at elevated reaction temperatures, with both catalysts exhibiting a higher concentration of hcp Co (unsupported: 73.6 ± 1.2 wt.-%; TiO<sub>2</sub>-P25: 68.0 ± 7.9 wt.-%) than that of fcc Co (unsupported: 26.4 ± 1.2 wt.-%; TiO<sub>2</sub>-P25: 32.0 ± 3.2 wt.-%) – also see Figures 9.11(b) and 9.12(b). On the other hand, the average hcp Co crystallite size was 4.2 ± 0.3 nm (unsupported) and 15.5 ± 3.7 nm (TiO<sub>2</sub>-P25). The hcp Co size for the TiO<sub>2</sub>-P25-supported catalyst indicates slight sintering as it is larger than the starting Co<sub>3</sub>O<sub>4</sub> size of 11.1 ± 1.3 nm. The average fcc Co size could not be determined in both catalysts due to granularity effects, but it is possible that this phase may have also undergone some degree of sintering.

The  $\gamma$  values for the above-mentioned catalysts are 34.8 wt.-% (unsupported) and 34.3 wt.-% (TiO<sub>2</sub>-P25), which are in close agreement with the PXRD-derived fcc Co concentrations also mentioned above. However, with reference to the critical size for the superparamagnetism of hcp Co noted above, there may be some contribution to the  $\gamma$  value from the hcp Co crystallites formed over TiO<sub>2</sub>-P25. The hcp Co crystallites in the unsupported catalyst have an average size that is much smaller than 11 nm, implying that these are possibly superparamagnetic. The  $\gamma$  value for the ZrO<sub>2</sub>-supported catalyst is 41.1 wt.-%, which also indicates severe sintering. This is also in good agreement with the average fcc Co crystallite size determined from PXRD (60.8 ± 24.1 nm). Similarly, the  $\gamma$  obtained for the SiC-supported sample (48.7 wt.-%) also indicates extensive crystallite growth, however, this could not be confirmed using PXRD as metallic Co reflections were not observed in the recorded patterns (see Figure 9.9((a), *left*)). In both the ZrO<sub>2</sub>- and SiC-supported catalysts, only fcc Co contributed to the  $\gamma$  values obtained, as hcp Co was not formed.

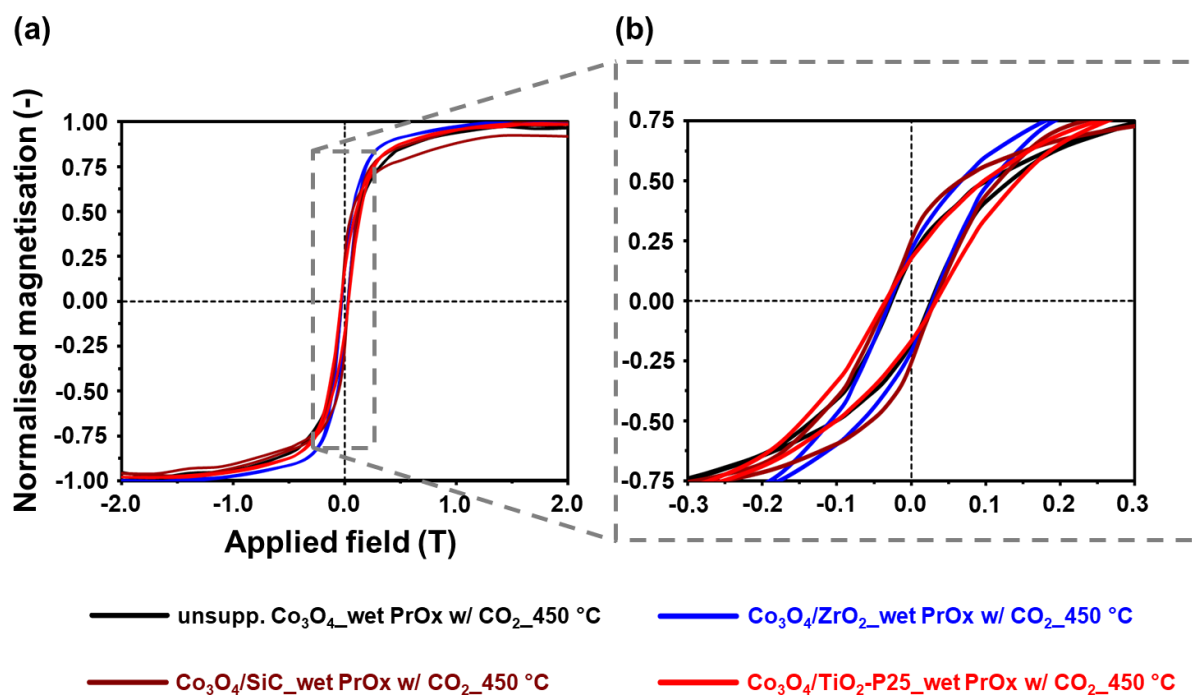


**Figure 9.10:** (a) Magnetometry-derived M-H curves recorded at 450 °C during wet CO-PrOx with co-fed  $\text{CO}_2$  over unsupported,  $\text{ZrO}_2$ -, SiC- and  $\text{TiO}_2\text{-P25}$ -supported  $\text{Co}_3\text{O}_4$ , respectively. (b) Magnified view of the M-H curves indicating the existence of hysteresis behaviour. (Feed composition: 1% CO, 1%  $\text{O}_2$ , 46%  $\text{H}_2$ , 10%  $\text{H}_2\text{O}$ , 9%  $\text{CO}_2$  and 33%  $\text{N}_2$ ; pressure: atmospheric, GHSV: 60000 mL(NTP)/g $\text{Co}_3\text{O}_4$ /hr).

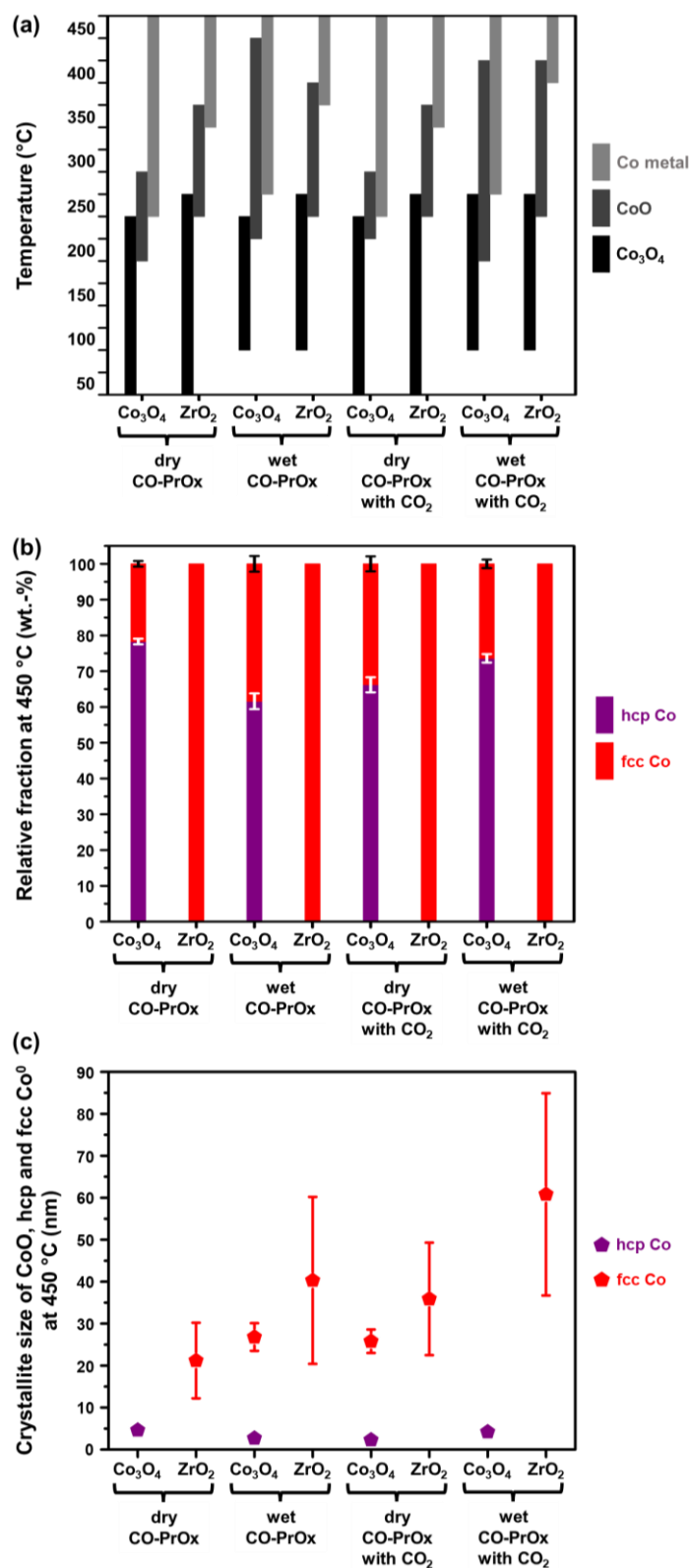


**Figure 9.11:** (a) Temperatures at which the Co-based phases are detected using *in situ* PXRD under different CO-PrOx conditions at atmospheric pressure over unsupported and ZrO<sub>2</sub>-supported Co<sub>3</sub>O<sub>4</sub>. (b) Relative fraction, and (c) crystallite size of CoO, hcp and fcc Co at 450 °C. The white and black error bars in (b) are for hcp and fcc Co, respectively. In some cases, the size of fcc Co in the unsupported catalyst is not reported in (c) due to possible granularity effects and/or intergrowth of hcp and fcc Co.

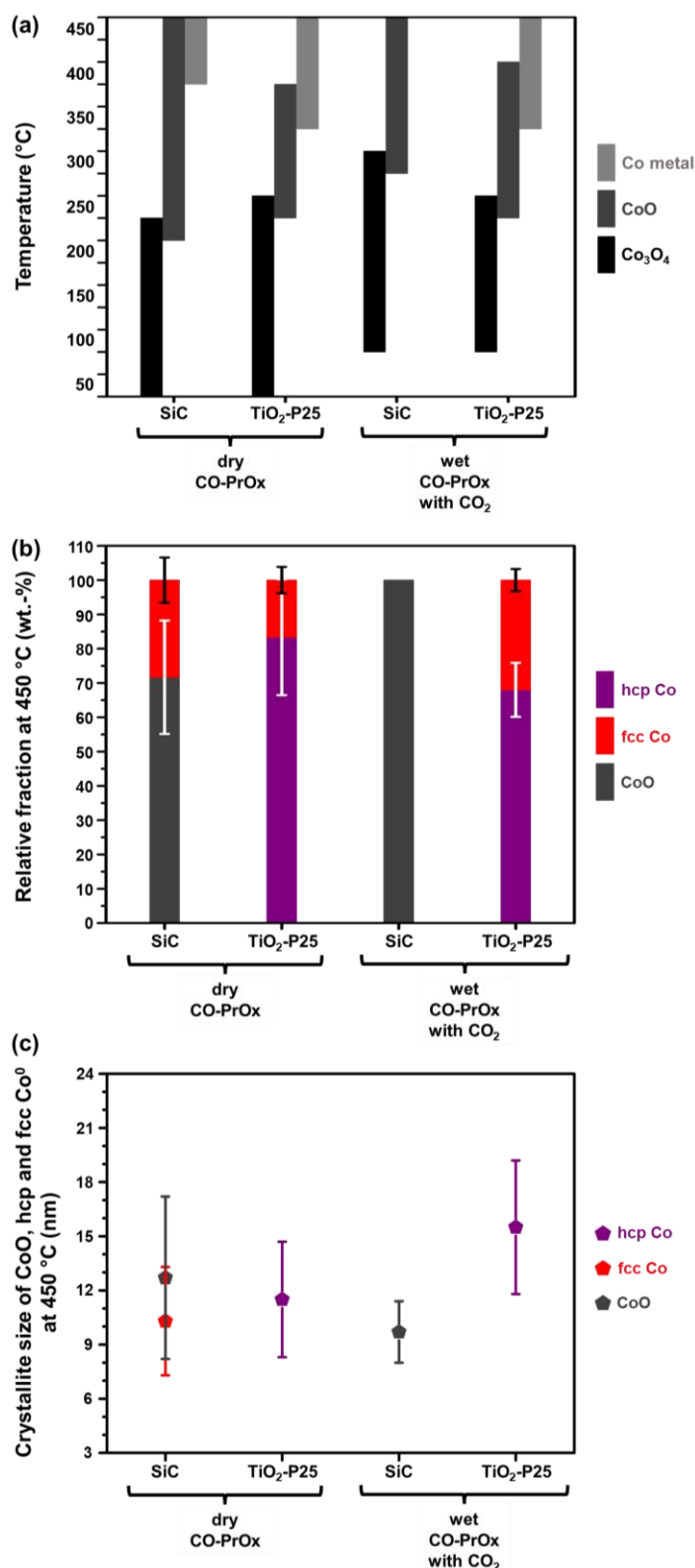


**Figure 9.12:** (a) Temperatures at which the Co-based phases are detected using *in situ* PXRD under different CO-PrOx conditions at atmospheric pressure over Co<sub>3</sub>O<sub>4</sub>/SiC and Co<sub>3</sub>O<sub>4</sub>/TiO<sub>2</sub>-P25. (b) Relative fraction, and (c) crystallite size of CoO and fcc Co at 450 °C. The white error bars in (b) are for CoO and hcp Co, while the black error bars are for fcc Co. The size of fcc Co in the TiO<sub>2</sub>-P25-supported catalyst is not reported in (c) due to possible granularity effects and/or intergrowth of hcp and fcc Co.

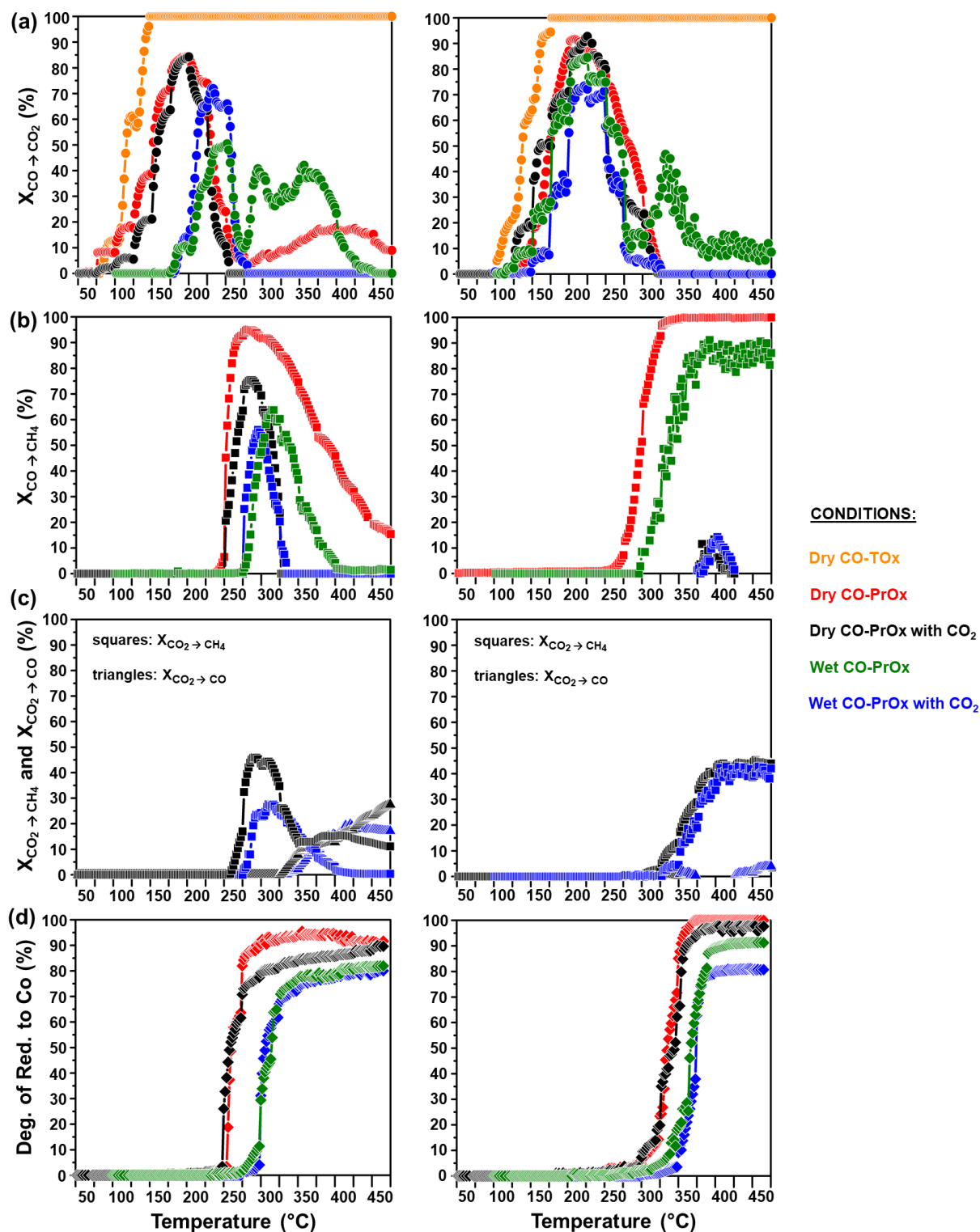


**Figure 9.13:** (a) Changes in the CO conversion to CO<sub>2</sub> ( $X_{\text{CO} \rightarrow \text{CO}_2}$ ) via oxidation, (b) CO conversion to CH<sub>4</sub> ( $X_{\text{CO} \rightarrow \text{CH}_4}$ ) via hydrogenation, (c) CO<sub>2</sub> conversion to CH<sub>4</sub> ( $X_{\text{CO}_2 \rightarrow \text{CH}_4}$ ) via hydrogenation and to CO ( $X_{\text{CO}_2 \rightarrow \text{CO}}$ ) via reverse WGS, respectively, and the (d) magnetometry-derived degree of reduction of Co<sub>3</sub>O<sub>4</sub> to metallic Co under different CO-PrOx conditions at atmospheric pressure performed over (left) unsupported Co<sub>3</sub>O<sub>4</sub>, and (right) Co<sub>3</sub>O<sub>4</sub>/ZrO<sub>2</sub>.

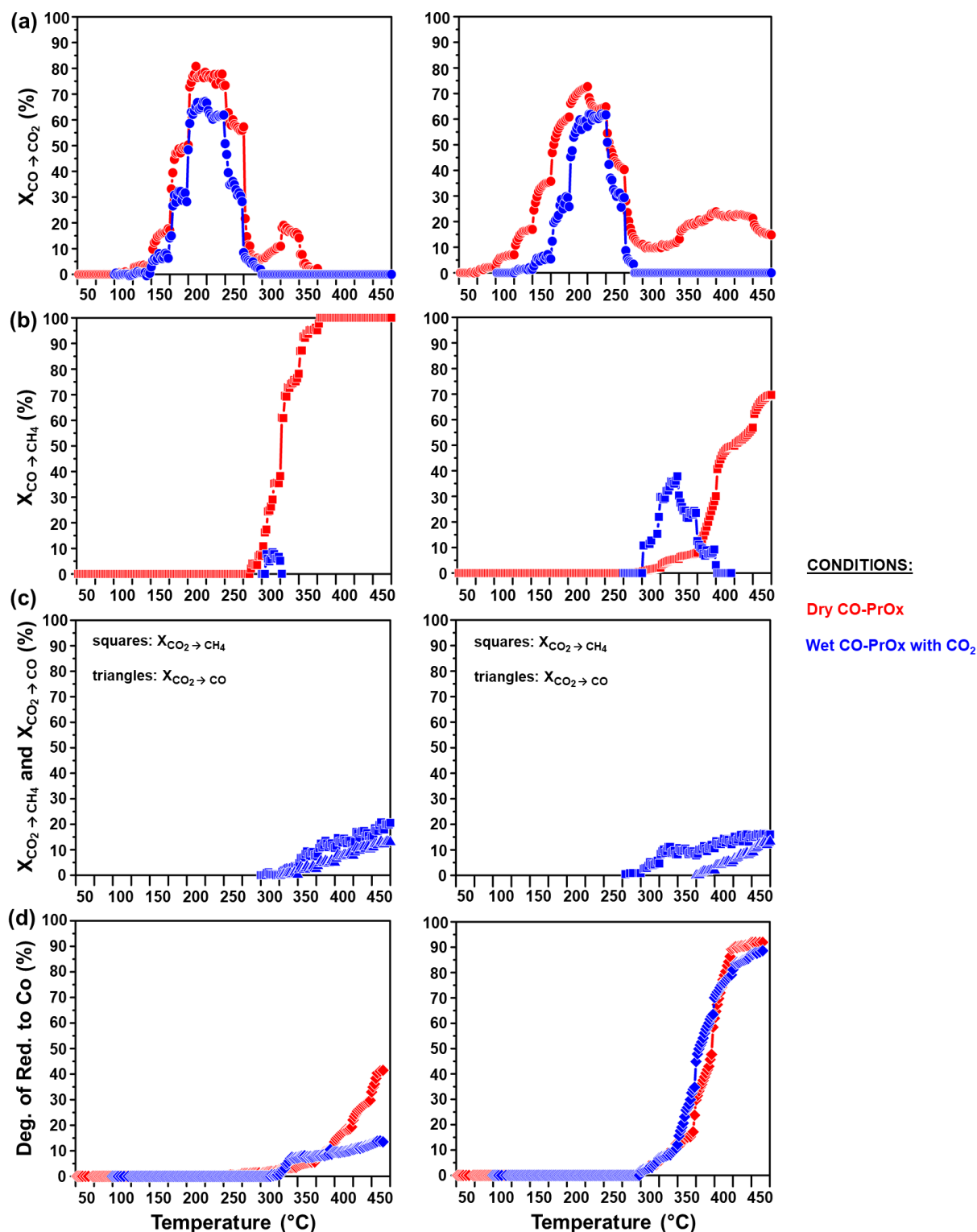


**Figure 9.14:** (a) Changes in the CO conversion to CO<sub>2</sub> ( $X_{\text{CO} \rightarrow \text{CO}_2}$ ) via oxidation, (b) CO conversion to CH<sub>4</sub> ( $X_{\text{CO} \rightarrow \text{CH}_4}$ ) via hydrogenation, (c) CO<sub>2</sub> conversion to CH<sub>4</sub> ( $X_{\text{CO}_2 \rightarrow \text{CH}_4}$ ) via hydrogenation and to CO ( $X_{\text{CO}_2 \rightarrow \text{CO}}$ ) via reverse WGS, respectively, and the (d) magnetometry-derived degree of reduction of Co<sub>3</sub>O<sub>4</sub> to metallic Co under different CO-PrOx conditions at atmospheric pressure performed over (left) Co<sub>3</sub>O<sub>4</sub>/SiC, and (right) Co<sub>3</sub>O<sub>4</sub>/TiO<sub>2</sub>-P25.

**Table 9.1:** Summary of the  $\gamma$  values calculated from magnetometry data recorded at 450 °C under different CO-PrOx conditions at atmospheric pressure.

Condition	Sample name	$\gamma$ at 450 °C (wt.-%)
Dry PrOx	unsupp. Co <sub>3</sub> O <sub>4</sub>	33.0
	Co <sub>3</sub> O <sub>4</sub> /ZrO <sub>2</sub>	33.1
	Co <sub>3</sub> O <sub>4</sub> /SiC	46.2
	Co <sub>3</sub> O <sub>4</sub> /TiO <sub>2</sub> -P25	17.7
Wet PrOx	unsupp. Co <sub>3</sub> O <sub>4</sub>	40.6
	Co <sub>3</sub> O <sub>4</sub> /ZrO <sub>2</sub>	52.8
Dry PrOx with CO <sub>2</sub>	unsupp. Co <sub>3</sub> O <sub>4</sub>	21.1
	Co <sub>3</sub> O <sub>4</sub> /ZrO <sub>2</sub>	23.3
Wet PrOx with CO <sub>2</sub>	unsupp. Co <sub>3</sub> O <sub>4</sub>	34.8
	Co <sub>3</sub> O <sub>4</sub> /ZrO <sub>2</sub>	41.1
	Co <sub>3</sub> O <sub>4</sub> /SiC	48.7
	Co <sub>3</sub> O <sub>4</sub> /TiO <sub>2</sub> -P25	34.3

### 9.2.5. Characterisation of spent catalysts after wet CO-PrOx with co-fed CO<sub>2</sub> using *ex situ* (HR)STEM-EELS

Following the wet CO-PrOx (with co-fed CO<sub>2</sub>) experiments, the spent catalysts recovered from the magnetometer were analysed using STEM-EELS to study the combined effect of H<sub>2</sub>O and CO<sub>2</sub> on the physical (and chemical) properties of the fresh catalysts. Again, EELS elemental mapping was not applied during the analysis of the unsupported spent catalyst. Furthermore, the analysed samples may have partially or fully re-oxidised during the long storage times leading up to their analysis using STEM-EELS, but the re-oxidation is not expected to sinter the particles.

Figure 9.15 shows the bright-field micrograph of the spent unsupported sample, and it can be seen that the material resembles that obtained after dry CO-PrOx (see Figure 8.13). Note that performing CO-PrOx in the presence of H<sub>2</sub>O and CO<sub>2</sub> produced small hcp Co crystallites ( $4.2 \pm 0.3$  nm – from PXRD (see Figure 9.11(c))) and possibly large fcc Co crystallites (the size of which could not be confirmed due to granularity effects). Therefore, it is again possible that the spent material displayed in Figure 9.15 has very small hcp Co particles that make up the large observed clusters. The darker regions may also possess relatively large particles of fcc Co, or particles with

intergrown domains of the hcp and fcc phases. The possible presence of large fcc Co is in line with the  $\gamma$  value of 34.8 wt.-% (Table 9.1), which indicates the presence of metallic particles/crystallites with a size above the critical size for the superparamagnetism of metallic fcc Co (16 – 20(26) nm [50]).

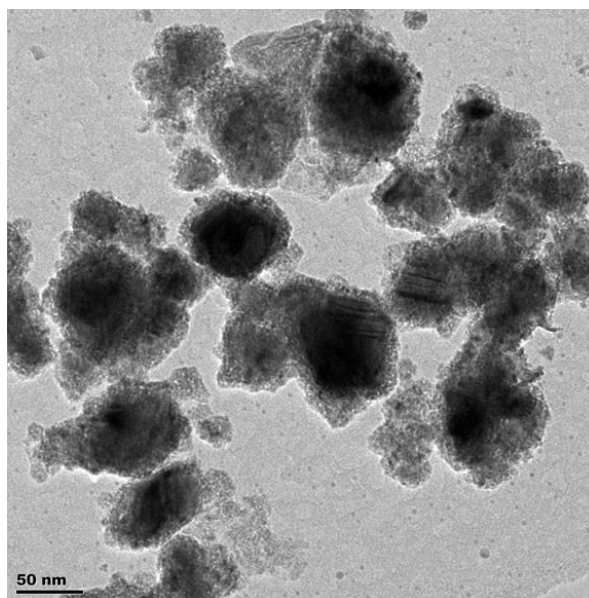


**Figure 9.15:** (a) TEM micrograph of the spent sample after wet CO-PrOx with co-fed CO<sub>2</sub>.

Shown in Figure 9.16 are the high magnification bright-field micrographs of the spent ZrO<sub>2</sub>-, SiC- and TiO<sub>2</sub>-P25-supported catalysts together with the EELS composite maps generated. It can be observed that the cobalt-bearing nanoparticles are mostly located on the edges of the main support particles and the magnified maps show no evidence of any chemical mixing between the Co species and the species of the respective support. More specifically, there were no TiO<sub>2-x</sub> species from the TiO<sub>2</sub>-P25 support extending towards the Co particles, possibly indicating no (or minimal) Co encapsulation in this spent sample. Although not shown in Figure 9.16, most areas studied using STEM-EELS for the spent Co<sub>3</sub>O<sub>4</sub>/SiC catalyst showed extensive wetting of the SiC support (similar to the spent sample obtained after dry CO-PrOx - see Figure A.8.2 in Appendix A.8.), making it difficult to obtain a size distribution. This may have been due to some strong interactions between the Co species and the Si<sub>x</sub>O<sub>y</sub> or Si<sub>x</sub>O<sub>y</sub>C<sub>z</sub> layer around the main SiC particles, which also minimised the degree of reduction of cobalt oxide to metallic Co (see Figure 9.14((d), *left*).

Size distributions for the ZrO<sub>2</sub>- and TiO<sub>2</sub>-P25-supported spent samples were derived and are shown in Figure 9.17. The average number- and volume-based sizes are summarised in Table 9.2. According to PXRD analysis, the fcc Co crystallites in the ZrO<sub>2</sub>-supported catalyst exhibit an average size of  $60.8 \pm 24.1$  nm, while magnetometry indicated a  $\gamma$  value of 41.1 wt.-%. The STEM-derived volume-based particle size was found to be  $18.3 \pm 5.0$  nm, which is much lower than the size estimated by PXRD. Since the PXRD and magnetometry results suggest possible sintering, it is likely that the large crystallites in the spent sample are present in low relative amounts, which makes them difficult to locate during STEM analysis. For the TiO<sub>2</sub>-P25-supported sample, the average fcc Co size could not be confirmed due to possible granularity effects, but hcp Co was found to be  $15.5 \pm 3.7$  nm, which is close to the STEM-derived volume-based size of  $16.7 \pm 5.7$  nm. Magnetometry further confirmed the presence of 34.3 wt.-% of metallic particles/crystallites that are above the critical size for the superparamagnetism of metallic hcp Co (11 nm [50]) and fcc Co (16 – 20(26) nm [50]), The sizes mentioned above are also within error of the volume-based size of the corresponding fresh catalyst ( $14.2 \pm 4.6$  nm) determined using STEM, which suggests a low degree of sintering of the hcp Co crystallites.

Similar to dry CO-PrOx, PXRD, magnetometry and STEM-EELS were able to confirm slight increases in the particle/crystallite size after exposing the catalysts to H<sub>2</sub>O and CO<sub>2</sub> during CO-PrOx, despite some discrepancies in the sizes obtained from each technique. The slight increases in size may be attributed to the high reaction temperatures reached (maximum 450 °C) and the presence of H<sub>2</sub>O, which is known to facilitate sintering [39–42].

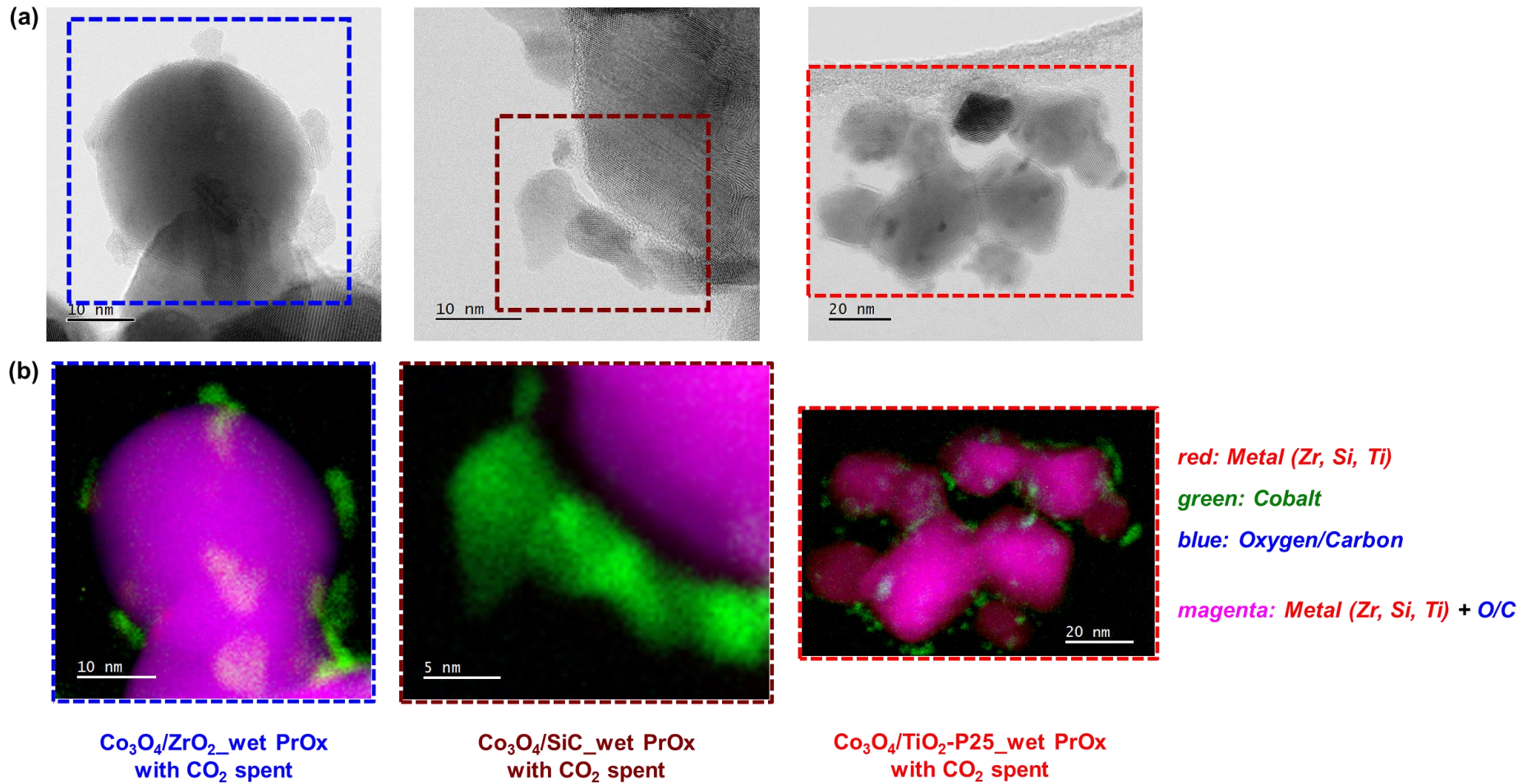


**Figure 9.16:** (a) Bright-field STEM micrographs of the spent  $\text{Co}_3\text{O}_4/\text{ZrO}_2$ ,  $\text{Co}_3\text{O}_4/\text{SiC}$  and  $\text{Co}_3\text{O}_4/\text{TiO}_2\text{-P25}$  catalysts, respectively, obtained after wet CO-PrOx (with co-fed  $\text{CO}_2$ ). (b) Magnified STEM-EELS elemental maps showing the regions with the elements Zr, Si, Ti, O, C and Co where applicable.

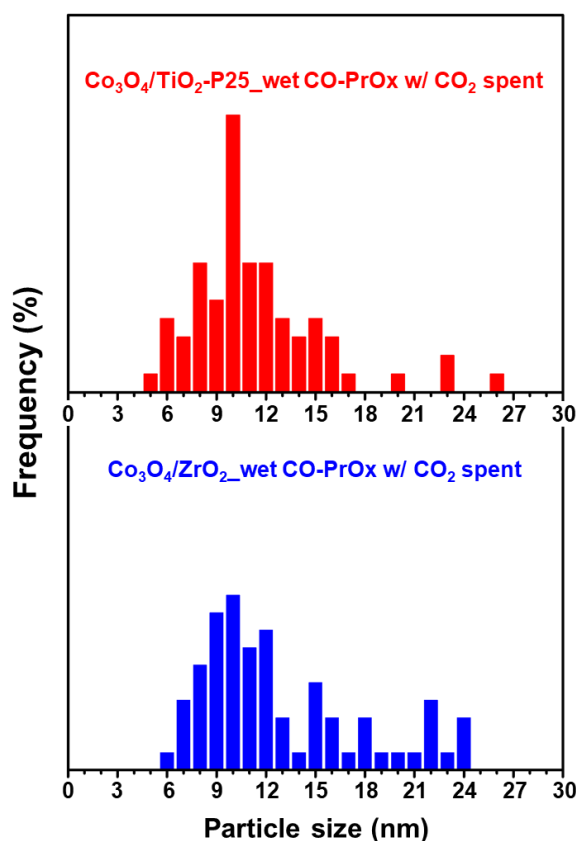


**Figure 9.17:** STEM-derived number-based size distributions for the ZrO<sub>2</sub>- and TiO<sub>2</sub>-P25-supported Co<sub>3</sub>O<sub>4</sub> catalysts.

**Table 9.2:** STEM-derived average number- and volume-based particle sizes for a selected number of spent catalysts.

Sample name	Number-based average size (nm)*	Volume-based average size (nm) <sup>§</sup>
Co <sub>3</sub> O <sub>4</sub> /ZrO <sub>2</sub> _wet CO-PrOx with CO <sub>2</sub> spent	13.2 ± 4.8	18.3 ± 5.0
Co <sub>3</sub> O <sub>4</sub> /TiO <sub>2</sub> -P25_wet CO-PrOx with CO <sub>2</sub> spent	11.9 ± 4.0	16.7 ± 5.7

\* number-based average particle size and standard deviation calculated using Equations 4.9 and 4.11, respectively.

<sup>§</sup> volume-based average particle size and standard deviation calculated using Equations 4.10 and 4.12, respectively.

### 9.2.6. Characterisation of spent catalysts after wet CO-PrOx with co-fed CO<sub>2</sub> using *ex situ* XAS

The three supported catalysts tested under wet CO-PrOx with co-fed CO<sub>2</sub> (sub-section 9.2.4.) were analysed *ex situ* using XAS to determine if there were MSCs present that were not detected under reaction conditions using PXRD or magnetometry. Both *in situ* techniques confirmed the presence of mostly metallic Co and some CoO in the Co<sub>3</sub>O<sub>4</sub>/ZrO<sub>2</sub> and Co<sub>3</sub>O<sub>4</sub>/TiO<sub>2</sub>-P25 catalysts at 450 °C, while the Co<sub>3</sub>O<sub>4</sub>/SiC catalyst had mostly CoO and some metallic Co at the same temperature (see Figures 9.11 - 9.14). It should again be noted that due to the long sample storage times prior to the XAS analysis, some of the metallic Co and CoO could be re-oxidised to Co<sub>3</sub>O<sub>4</sub>. However, as already mentioned, the species of primary interest from the XAS analysis are the MSCs that were not detected during the *in situ* studies. Figure 9.18 shows the normalised XANES spectra of the ZrO<sub>2</sub>-, SiC- and TiO<sub>2</sub>-P25-supported spent samples, respectively, together with the relevant Co-based reference spectra. Also included are the results obtained after performing a linear combination fit of the XANES of each spent catalyst. Table 9.3 summarises the relative fraction of the phases present in each spent sample and the corresponding R-factor of the LCF.

The XANES of the ZrO<sub>2</sub>-supported sample exhibits the typical metallic pre-edge feature at 7710 eV and a less intense white line feature between 7726 and 7729 eV after the edge, possibly indicating the presence of CoO and Co<sub>3</sub>O<sub>4</sub>. The even less intense features from 7729 to 7900 eV may indicate that the sample has mostly metallic character. In contrast, the SiC-supported spent sample exhibits features typical of CoO between 7700 and 7900 eV. The Co<sub>3</sub>O<sub>4</sub>/TiO<sub>2</sub>-P25 sample has mostly Co<sub>3</sub>O<sub>4</sub> features in its spectrum but the shape of the white line between 7726 and 7729 eV is slightly different from that observed for the Co<sub>3</sub>O<sub>4</sub> reference, which may indicate the co-existence of CoO. Furthermore, linear combination fitting also revealed the presence of very small amounts of CoTiO<sub>3</sub> and metallic Co in this spent sample (see Figure 9.18 and Table 9.3). The formation of CoTiO<sub>3</sub> in the Co<sub>3</sub>O<sub>4</sub>/TiO<sub>2</sub>-P25 catalyst during wet CO-PrOx with co-fed CO<sub>2</sub> (in comparison with the dry CO-PrOx experiment – see XAS results in section 8.5.), may have been caused by the co-fed H<sub>2</sub>O, as this has been previously observed in other reaction systems involving TiO<sub>2</sub>-supported cobalt (oxide) catalysts [25]. It is worth noting that in the ZrO<sub>2</sub>- and SiC-supported spent catalysts, MSCs were not detected.

The relatively high concentration of oxidic species in the ZrO<sub>2</sub>- and TiO<sub>2</sub>-P25-supported spent catalysts suggests extensive re-oxidation of the previously formed metallic phase and CoO to

Co<sub>3</sub>O<sub>4</sub> during sample storage. Based on the LCF results for the Co<sub>3</sub>O<sub>4</sub>/SiC spent sample, re-oxidation of the metallic Co and CoO seems to have not taken place, as the DoR at 450 °C calculated from the magnetometry data is 13.8% (Figure 9.14(d)), which is close to the metallic fraction ( $14.6 \pm 0.5\%$ ) estimated from XANES.

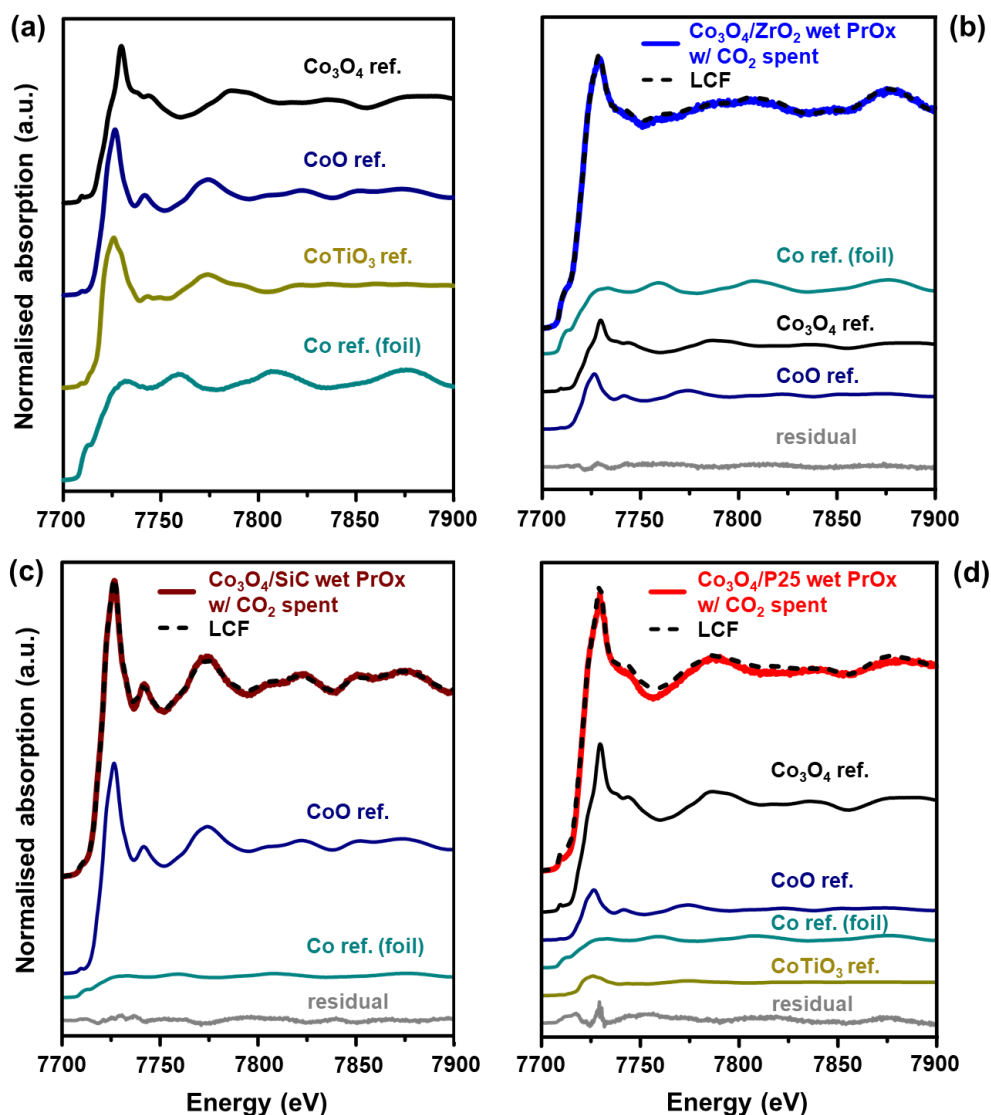


**Figure 9.18:** Normalised XANES spectra of the (a) reference compounds Co<sub>3</sub>O<sub>4</sub> [63,64], CoO [65], Co<sub>2</sub>SiO<sub>4</sub> [66], CoTiO<sub>3</sub> [67] and Co foil [68]; as well as normalised XANES spectra of the (b) ZrO<sub>2</sub>-, (c) SiC- and (d) TiO<sub>2</sub>-P25-supported spent samples obtained after dry CO-PrOx, together with the resulting linear combination fit of the spectral components in each sample.

**Table 9.3:** Summary of the results obtained after performing a linear combination fit of the normalised XANES spectra.

Sample name	Co <sub>3</sub> O <sub>4</sub> (%)	CoO (%)	Co <sub>a</sub> M <sub>x</sub> O <sub>y+a</sub> (%)*	Co <sup>0</sup> (wt.-%)	R-factor (-)
Co <sub>3</sub> O <sub>4</sub> /ZrO <sub>2</sub> _wet CO-PrOx w/ CO <sub>2</sub> spent <sup>§</sup>	31.2 ± 0.7	22.8 ± 0.4	-	46.0 ± 0.4	0.001
Co <sub>3</sub> O <sub>4</sub> /SiC_wet CO-PrOx w/ CO <sub>2</sub> spent	-	85.4 ± 0.4	-	14.6 ± 0.5	0.001
Co <sub>3</sub> O <sub>4</sub> /TiO <sub>2</sub> -P25_wet CO-PrOx w/ CO <sub>2</sub> spent	59.7 ± 1.2	16.9 ± 3.2	7.3 ± 3.5	16.1 ± 5.5	0.007

\* Co<sub>a</sub>M<sub>x</sub>O<sub>y+a</sub>: a = 1 or 2, x = 1 or 2 and y = 2 or 3 for the MSCs - Co<sub>2</sub>SiO<sub>4</sub> and CoTiO<sub>3</sub>.

<sup>§</sup> there are no known or well characterised Co-Zr oxides reported in the literature.

### 9.2.7. Effect of varying the O<sub>2</sub> concentration during dry CO-PrOx

The results in sections 8.1. and 8.2. from the CO-PrOx experiments performed under dry conditions (*i.e.*, in the absence of H<sub>2</sub>O and CO<sub>2</sub>) emphasise the effect of H<sub>2</sub> on the oxidation of CO over unsupported Co<sub>3</sub>O<sub>4</sub> nanoparticles as well as its effect on the phase stability of the nanoparticles. It has been established in this work and in other reported literature [8–13] that H<sub>2</sub> competes with CO for O<sub>2</sub> *via* oxidation to H<sub>2</sub>O. This leads to the depletion of O<sub>2</sub> and negatively affects the CO<sub>2</sub> yield through CO oxidation. Also, the phase change of the Co<sub>3</sub>O<sub>4</sub> nanoparticles forming CoO and metallic Co decreases the activity and selectivity of the catalyst. Therefore, an *in situ* PXRD-based investigation into the effect of varying the feed oxygen concentration was carried out.

Instead of starting with a 1:1 CO:O<sub>2</sub> feed ratio, a 1:0.5 CO:O<sub>2</sub> stoichiometric ratio was chosen and the reaction temperature was varied between 50 and 225 °C at a rate of 1 °C/min, including 60-min holding steps every 25 °C. After reaching 225 °C, the temperature was held for 21 hr while the CO:O<sub>2</sub> feed ratio was changed every 3 hr between 1:0.5 and 1:4 (see further details in subsection 4.4.2.3.). Note that H<sub>2</sub> and N<sub>2</sub> were also co-fed and that their concentrations were adjusted to maintain a GHSV of 60000 ml(NTP)/g<sub>Co<sub>3</sub>O<sub>4</sub></sub>/hr throughout each experiment (see Table 4.5). The catalysts chosen for this investigation were the unsupported and ZrO<sub>2</sub>-supported Co<sub>3</sub>O<sub>4</sub> catalysts, and the temperature of 225 °C was chosen because it is when the phase CoO was first observed and when O<sub>2</sub> was fully depleted during the *in situ* studies discussed in sections 8.1. and 8.2.

Shown in Figure 9.19 and 9.20 are the recorded *in situ* PXRD patterns for the unsupported and ZrO<sub>2</sub>-supported Co<sub>3</sub>O<sub>4</sub> catalysts, respectively, recorded as a function of temperature and time, and the normalised outlet flow rates of CO, O<sub>2</sub>, CO<sub>2</sub> and CH<sub>4</sub>, respectively. Note that CH<sub>4</sub> was not formed throughout these experiments, which may suggest the absence of surface metallic Co species especially at the highest temperature reached of 225 °C. Since a 1:0.5 CO:O<sub>2</sub> ratio was used in the initial stages of the experiment, the CO<sub>2</sub> yields achieved by both catalysts between 50 and 225 °C are lower than those achieved by the same catalysts when a 1:1 ratio was used (see Figures 8.1(d) and 8.3(c)). The co-fed O<sub>2</sub> is fully consumed at 225 °C and at the same temperature, the Co<sub>3</sub>O<sub>4</sub> phase transforms to CoO. These two occurrences are a result of the co-fed H<sub>2</sub> [8–13]. Also note that at 225 °C after 3 hours under the 1:0.5 CO:O<sub>2</sub> ratio, the CO<sub>2</sub> yield reaches 0%.

However, upon increasing the O<sub>2</sub> concentration to attain a 1:1 ratio, the CO<sub>2</sub> yield increases to about 50% over both catalysts. Reverting to a ratio of 1:0.5 decreases the CO<sub>2</sub> yield again to 0%. A ratio of 1:2 increases the CO<sub>2</sub> yield to about 85% over both catalysts and a ratio of 1:4 increases the yield further to almost 100%. Note that despite increasing the O<sub>2</sub> concentration, the O<sub>2</sub> is not detected using the current GC-TCD instrument. Furthermore, the bulk CoO phase does not re-oxidise to Co<sub>3</sub>O<sub>4</sub> during the 21-hr hold at 225 °C. This may suggest that the increased amounts of O<sub>2</sub> are being rapidly consumed *via* CO and H<sub>2</sub> oxidation each time, and are not re-oxidising the (bulk) CoO phase.

At this point, the surface composition of the catalysts is unknown. However, the oxidation of CO may still be taking place *via* the MvK mechanism over CoO. Lukashuk *et al.* [69] proposed that a Co<sup>2+</sup>-Co<sup>3+</sup> redox pair is formed by oxidising the surface Co<sup>2+</sup> to Co<sup>3+</sup> with O<sub>2</sub>, which is then followed by a reduction of the Co<sup>3+</sup> back to Co<sup>2+</sup> by CO. During the reduction step, the CO is oxidised to CO<sub>2</sub> by lattice oxygen. Lukashuk *et al.* also showed, using *in situ* XPS and NEXAFS, that the surface of bulk CoO oxidises to Co<sub>3</sub>O<sub>4</sub> (but in the absence of H<sub>2</sub>) at 200 °C, which explained the high activity of bulk CoO at elevated temperatures. In the present work, it may be possible that a surface Co<sup>2+</sup>-Co<sup>3+</sup> redox pair is also formed at high O<sub>2</sub> concentrations, which improves the activity of the catalyst. A positive kinetic effect brought about by the high O<sub>2</sub> concentrations cannot be ruled out either [7,70,71].

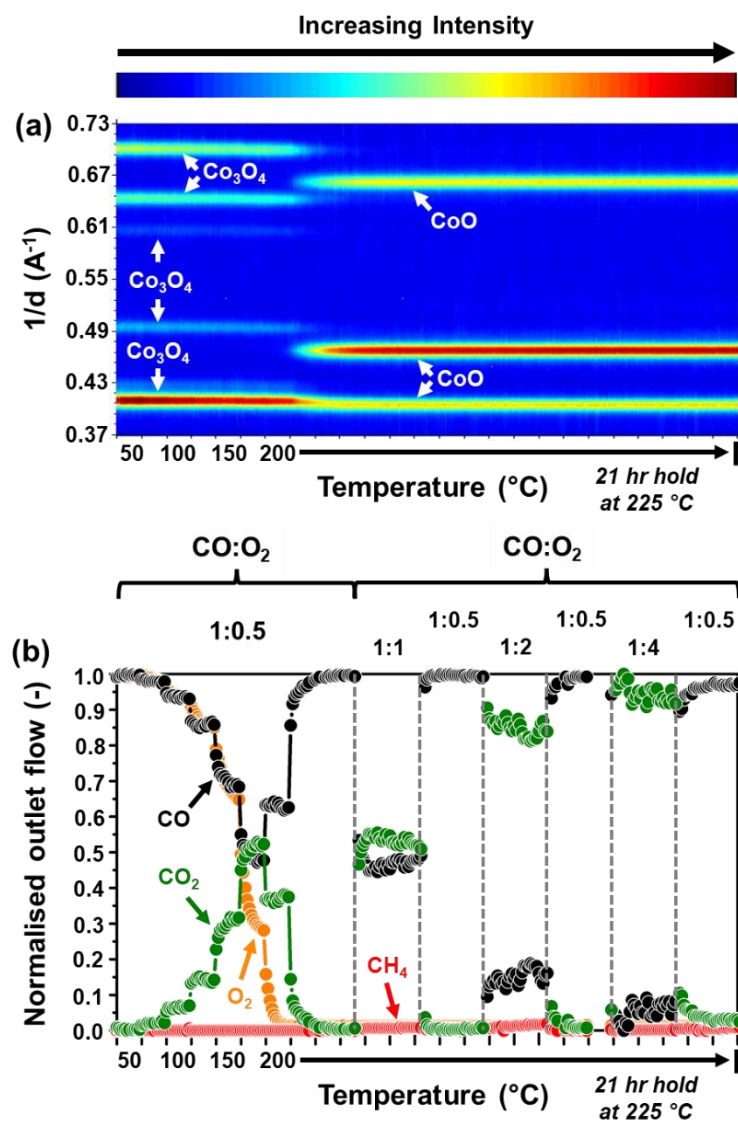


**Figure 9.19:** (a) On-top view of the *in situ* PXRD patterns recorded during dry CO-PrOx at varying CO: $\text{O}_2$  ratios over unsupported  $\text{Co}_3\text{O}_4$ . (b) Changes in the normalised outlet flow rates of CO,  $\text{O}_2$ ,  $\text{CO}_2$  and  $\text{CH}_4$  calculated from GC-TCD data. (Feed composition: 1 – 0.9% CO, 0.5 – 4%  $\text{O}_2$ , 51 – 43%  $\text{H}_2$  and 47.5 – 52.1%  $\text{N}_2$ ; pressure: atmospheric, GHSV: 60000 mL(NTP)/g $\text{Co}_3\text{O}_4$ /hr).

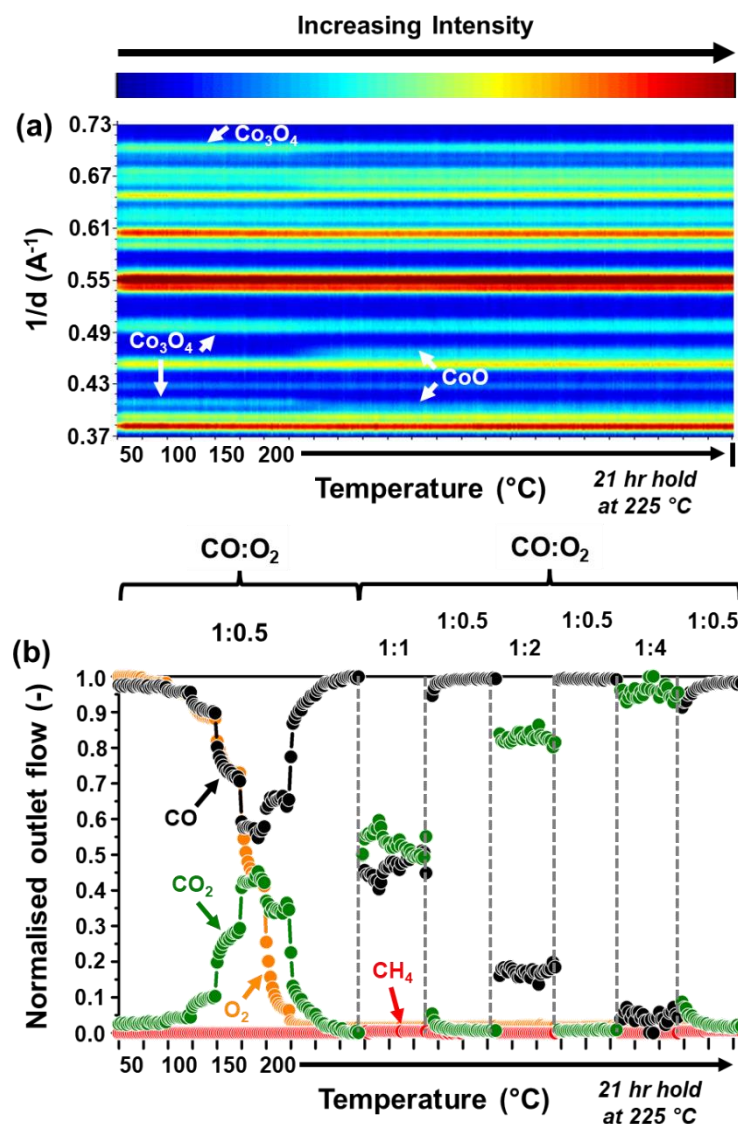


**Figure 9.20:** (a) On-top view of the *in situ* PXRD patterns recorded during dry CO-PrOx at varying CO:O<sub>2</sub> ratios over Co<sub>3</sub>O<sub>4</sub>/ZrO<sub>2</sub>. (b) Changes in the normalised outlet flow rates of CO, O<sub>2</sub>, CO<sub>2</sub> and CH<sub>4</sub> calculated from GC-TCD data. (Feed composition: 1 – 0.9% CO, 0.5 – 4% O<sub>2</sub>, 51 – 43% H<sub>2</sub> and 47.5 – 52.1% N<sub>2</sub>; pressure: atmospheric, GHSV: 60000 mL(NTP)/g<sub>Co<sub>3</sub>O<sub>4</sub></sub>/hr).

### 9.3. Summary: Gas Environment-dependent CO-PrOx

This Chapter has again highlighted the effect of the support material but has also extensively evaluated the effect of the gas feed components of the CO-PrOx reaction on the performance and phase stability of Co<sub>3</sub>O<sub>4</sub>. The presence of H<sub>2</sub>, H<sub>2</sub>O and CO<sub>2</sub> introduce different kinetic and

thermodynamic aspects which affect the targeted CO oxidation reaction and compromise the stability of the  $\text{Co}_3\text{O}_4$  phase (especially in the presence of  $\text{H}_2$ ). During the reaction between CO and  $\text{O}_2$  at a 1:1 feed ratio (in the absence of  $\text{H}_2$  – see sub-section 9.2.1.),  $\text{CO}_2$  yields of up to 100% were realised over both unsupported and  $\text{ZrO}_2$ -supported catalysts. This was also possible because of the stability of the  $\text{Co}_3\text{O}_4$  phase throughout the experiments, *i.e.*, no  $\text{Co}_3\text{O}_4$  reduction took place. Co-feeding high amounts of  $\text{H}_2$  decreased the yield and selectivity to  $\text{CO}_2$  because of the occurrence of  $\text{H}_2$  oxidation. The selectivity is further affected by the phase change of the  $\text{Co}_3\text{O}_4$  to CoO and metallic Co, with the latter phase catalysing the formation of undesired  $\text{CH}_4$  from CO and valuable  $\text{H}_2$  (also see sections 8.1. and 8.2.).

Co-feeding water (but in the absence of  $\text{CO}_2$  – see sub-section 9.2.2.) over the unsupported and  $\text{ZrO}_2$ -supported catalysts possibly resulted in the blockage of surface-active sites [26–28], thus further decreasing the  $\text{CO}_2$  yields over  $\text{Co}_3\text{O}_4$  (Figure 9.13(a)). Although the catalysts ultimately reduced, the reduction takes place at higher temperatures and the final degree of reduction at 450 °C was slightly lower when compared with the case with no co-fed water (Figures 9.11(a) and 9.13(d)). The co-adsorption and oxidising nature of the  $\text{H}_2\text{O}$  may be the reason for this slight phase stability afforded to the catalyst [19–25]. It is worth mentioning that the  $\text{ZrO}_2$ -supported catalyst maintained higher CO activity and selectivity (Figures 9.13(a) and A.6.2, respectively), as well as delayed CoO and metallic Co formation more than the unsupported catalyst (Figures 9.11(a) and 9.13(d)).

For the first time, the forward water-gas shift reaction was observed over the un-/supported metallic Co during wet CO-PrOx - an occurrence that had only been observed in other reaction systems [43–45], but only mentioned in the literature as a possibility during CO-PrOx. Methane formation from CO also took place, but to a lesser extent when compared with the case with no co-fed water. This may have also been a kinetic and thermodynamic effect caused by the co-adsorption of  $\text{H}_2\text{O}$  on the metallic surface, and subsequent reaction with CO to form WGS products (*i.e.*,  $\text{CO}_2$  and  $\text{H}_2$ ). The effect of  $\text{H}_2\text{O}$  adsorption may have been greater for the unsupported catalyst which ultimately lost both CO methanation and WGS activity as the temperature was increased to 450 °C. On the other hand, the  $\text{ZrO}_2$ -supported catalyst maintained relatively high methanation activity up to 450 °C.

On the other hand, the presence of  $\text{CO}_2$  (but in the absence of water – see sub-section 9.2.3.) in the CO-PrOx feed almost had no effect on the catalytic performance and reducibility of unsupported and  $\text{ZrO}_2$ -supported  $\text{Co}_3\text{O}_4$  when compared with the case with no co-fed  $\text{CO}_2$  and  $\text{H}_2\text{O}$  (see Figure

9.11(a), as well as Figures 9.13(a) and (d)). This may be because of the relatively weak binding of CO<sub>2</sub> on the surface, as well as its mild oxidising nature [20,51,53]. Furthermore, the ZrO<sub>2</sub>-supported catalyst exhibited higher CO oxidation activity/selectivity and Co<sub>3</sub>O<sub>4</sub> phase stability in the presence of CO<sub>2</sub> than the unsupported catalyst, as also observed in the presence of water. However, the presence of metallic Co in the unsupported catalyst kinetically favoured CO and CO<sub>2</sub> methanation, as well as the reverse WGS reaction. On the other hand, due to the previously reported high H<sub>2</sub> dissociation activity and stronger CO<sub>2</sub> binding of ZrO<sub>2</sub>-supported metallic Co [48,49], CO<sub>2</sub> hydrogenation to methane was the main reaction observed at high temperatures. It should be noted that these reactions are not desired as they all consume high amounts of valuable H<sub>2</sub> (especially methanation). However, the present study has, for the first time, confirmed the occurrence of CO<sub>2</sub> methanation and the reverse WGS under CO-PrOx conditions, and has linked these two reactions to the presence of metallic Co. This had only been observed in reaction systems that do not involve CO-PrOx [49,72].

Co-feeding both CO<sub>2</sub> and H<sub>2</sub>O (sub-section 9.2.4.) also had a negative effect on the CO conversion to CO<sub>2</sub>, mostly likely due to the strong surface adsorption of water [26–28]. However, the oxide phase was slightly stabilised in the presence of H<sub>2</sub>O in all tested catalysts (*i.e.*, unsupported Co<sub>3</sub>O<sub>4</sub>, Co<sub>3</sub>O<sub>4</sub>/ZrO<sub>2</sub>, Co<sub>3</sub>O<sub>4</sub>/SiC and Co<sub>3</sub>O<sub>4</sub>/TiO<sub>2</sub>-P25). The ZrO<sub>2</sub>-supported catalyst exhibited the highest CO oxidation performance (compare results in Figure 9.13(a) and 9.14(a)), while the SiC-supported catalyst was the least reduced to metallic Co at 450 °C (Figure 9.13(d) and 9.14(d)). The forward WGS reaction did not take place at any temperature over any of the catalysts, which was in line with the thermodynamic calculations showing that this reaction is not feasible above 285 °C in the presence of 50% H<sub>2</sub> and 10% CO<sub>2</sub> in the feed (Figure 9.1(a)). On the other hand, CO<sub>2</sub> methanation and the reverse WGS took place over metallic Co as these reactions were predicted to be thermodynamically feasible (but only above 285 °C for the reverse WGS – see Figure 9.1(b)).

The unsupported and TiO<sub>2</sub>-P25-supported catalysts carried out CO methanation at relatively low temperatures over metallic Co, but at elevated temperatures, CO<sub>2</sub> methanation and the reverse WGS began to dominate. The ZrO<sub>2</sub>- and SiC-supported catalysts converted very low amounts of CO to CH<sub>4</sub>, which may have been caused by the absence of hcp Co (which is more active than fcc Co [60–62]) in these two catalysts, unlike in the unsupported and TiO<sub>2</sub>-P25-supported catalyst (see Figures 9.11(b) and 9.12(b)). However, the SiC-supported catalyst performs CO<sub>2</sub> methanation and the reverse WGS, while the ZrO<sub>2</sub>-supported catalyst mostly carries out CO<sub>2</sub> methanation due to its previously mentioned high H<sub>2</sub> dissociation activity and strong CO<sub>2</sub> binding. The conversions

achieved by all four catalysts during CO and CO<sub>2</sub> methanation, as well as in the reverse WGS, were found to be lower than those predicted by the thermodynamic calculations (compare results in sections 9.1. and 9.2.). This may have been a kinetic and thermodynamic effect caused by the presence of a mixture of gases which form part of the reactants or products of more than one reaction. For example, the presence of co-fed H<sub>2</sub>O may have kinetically and thermodynamically affected the progress of the methanation reactions and the reverse WGS. On the other hand, co-feeding CO<sub>2</sub> and H<sub>2</sub> limits the amounts of CH<sub>4</sub> (*via* methanation) or CO (*via* reverse WGS) that can be obtained.

Note that a size distribution could only be obtained from a two spent catalysts (ZrO<sub>2</sub>- and TiO<sub>2</sub>-P25-supported) using STEM-EELS analysis, and this only showed slight sintering over the TiO<sub>2</sub>-P25 support (compare sizes in Tables 5.2 and 9.2). However, PXRD and magnetometry (*via*  $\gamma$ ) indicated possibilities of severe sintering of fcc Co over ZrO<sub>2</sub>-, especially in the experiments involving co-fed water [39–42] (see Figure 9.11(c) and Table 9.1). The fcc Co crystallites in the unsupported and TiO<sub>2</sub>-P25-supported catalyst could not be determined due to possible granularity effects. However, the fcc crystallites may have also sintered, since the  $\gamma$  values for these catalysts indicate a relatively high amount of particles with a size above 16 – 20(26) nm (see Table 9.1). Due to the wetting of the SiC support by Co species, adequate size analysis could not be performed using STEM-EELS. However, the small amounts of metal (DoR = 13.8%) formed over this support, may have also sintered as the  $\gamma$  value (48.7 wt.-%) obtained indicates the presence of fcc Co particles with a size above 16 – 20(26) nm.

*Ex situ* XAS measurements for the spent catalysts showed no MSCs in the ZrO<sub>2</sub>- and SiC-supported samples, but showed about  $7.3 \pm 3.5\%$  CoTiO<sub>3</sub> in the TiO<sub>2</sub>-P25-supported sample. The formation of this compound may have been induced by the presence of water [25], as it was not observed under the condition with no co-fed water (and CO<sub>2</sub>) discussed in section 8.2.

Finally, it was also shown that the yield of CO<sub>2</sub> *via* CO oxidation can be greatly influenced by the concentration of co-fed oxygen over unsupported and ZrO<sub>2</sub>-supported CoO (sub-section 9.2.7.). At a ratio of 1:0.5 of CO:O<sub>2</sub>, very low yields of CO<sub>2</sub> (< 50%) were realised over the two tested catalysts. Increasing the O<sub>2</sub> concentration to give a 1:4 CO:O<sub>2</sub> ratio also increased the CO<sub>2</sub> yield to almost 100% at 225 °C, without observing any bulk phase changes to the CoO phase. Lukashuk *et al.* [69] have postulated that the improvement in activity could be due to the restoration of the MvK mechanism over the CoO surface, as a possible Co<sup>2+</sup>-Co<sup>3+</sup> redox pair may be formed in the

high O<sub>2</sub> concentrations. However, a kinetic enhancement caused by the availability of high O<sub>2</sub> concentrations (which result in high oxygen surface coverage) cannot be ruled out.

## References

- [1] P. Atkins, J. de Paula, *Atkins' Physical Chemistry 8th Edition*, 8th ed., Oxford University Press, 2009.
- [2] ICSC 0023 - CARBON MONOXIDE.  
<http://www.inchem.org/documents/icsc/icsc/eics0023.htm> (accessed July 2020).
- [3] P. Mars, D.W. van Krevelen, *Chem. Eng. Sci.* 3 (1954) 41–59.
- [4] D. Perti, R.L. Kabel, G.J. McCarthy, *AIChE J.* 31 (1985) 1435–1440.
- [5] J. Jansson, A.E.C. Palmqvist, E. Fridell, M. Skoglundh, L. Österlund, P. Thormählen, V. Langer, *J. Catal.* 211 (2002) 387–397.
- [6] V. Iablokov, R. Barbosa, G. Pollefeyt, I. van Driessche, S. Chenakin, N. Kruse, *ACS Catal.* 5 (2015) 5714–5718.
- [7] L. Lukashuk, N. Yigit, R. Rameshan, E. Kolar, D. Teschner, M. Hävecker, A. Knop-Gericke, R. Schlögl, K. Föttinger, G. Rupprechter, *ACS Catal.* 8 (2018) 8630–8641.
- [8] Y. Teng, H. Sakurai, A. Ueda, T. Kobayashi, *Int. J. Hydrog. Energy* 24 (1999) 355–358.
- [9] Z. Zhao, M.M. Yung, U.S. Ozkan, *Catal. Commun.* 9 (2008) 1465–1471.
- [10] L. Lukashuk, K. Föttinger, E. Kolar, C. Rameshan, D. Teschner, M. Hävecker, A. Knop-Gericke, N. Yigit, H. Li, E. McDermott, M. Stöger-Pollach, G. Rupprechter, *J. Catal.* 344 (2016) 1–15.
- [11] T.M. Nyathi, N. Fischer, A.P.E. York, M. Claeys, *Faraday Discuss.* 197 (2017) 269–285.
- [12] M. Khasu, T. Nyathi, D.J. Morgan, G.J. Hutchings, M. Claeys, N. Fischer, *Catal. Sci. Technol.* 7 (2017) 4806–4817.
- [13] T.M. Nyathi, N. Fischer, A.P.E. York, D.J. Morgan, G.J. Hutchings, E.K. Gibson, P.P. Wells, C.R.A. Catlow, M. Claeys, *ACS Catal.* 9 (2019) 7166–7178.
- [14] T.V. Choudhary, D.W. Goodman, *Catal. Today* 77 (2002) 65–78.
- [15] A.F. Ghenciu, *Curr. Opin. Solid State Mater. Sci.* 6 (2002) 389–399.
- [16] S. Huang, K. Hara, A. Fukuoka, *Energy Environ. Sci.* 2 (2009) 1060–1068.
- [17] E.D. Park, D. Lee, H.C. Lee, *Catal. Today* 139 (2009) 280–290.
- [18] A. Mishra, R. Prasad, *Bull. Chem. React. Eng. Catal.* 6 (2011) 1–14.
- [19] Y. Zhang, D. Wei, S. Hammache, J.G. Goodwin, *J. Catal.* 188 (1999) 281–290.

- [20] D.H. Kim, J.E. Cha, *Catal. Lett.* 86 (2003) 107–112.
- [21] S. Storsæter, Ø. Borg, E.A. Blekkan, A. Holmen, *J. Catal.* 231 (2005) 405–419.
- [22] N. Fischer, B. Clapham, T. Feltes, E. van Steen, M. Claeys, *Angew. Chemie - Int. Ed.* 53 (2014) 1342–1345.
- [23] J. Paterson, M. Peacock, E. Ferguson, M. Ojeda, J. Clarkson, *Appl. Catal. A* 546 (2017) 103–110.
- [24] N.E. Tsakoumis, J.C. Walmsley, M. Rønning, W. van Beek, E. Rytter, A. Holmen, *J. Am. Chem. Soc.* 139 (2017) 3706–3715.
- [25] M. Wolf, E.K. Gibson, E.J. Olivier, J.H. Neethling, C.R.A. Catlow, N. Fischer, M. Claeys, *ACS Catal.* 9 (2019) 4902–4918.
- [26] Q. Guo, Y. Liu, *React. Kinet. Catal. Lett.* 92 (2007) 19–25.
- [27] S. Monyanon, S. Pongstabodee, A. Luengnaruemitchai, *J. Chinese Inst. Chem. Eng.* 38 (2007) 435–441.
- [28] P. Gawade, B. Bayram, A.M.C. Alexander, U.S. Ozkan, *Appl. Catal. B* 128 (2012) 21–30.
- [29] J.M. Herrmann, *J. Catal.* 89 (1984) 404–412.
- [30] B. Delmon, in: G. Ertl, H. Knözinger, J. Weitkamp (Eds.), *Prep. Solid Catal.*, Wiley-VCH Verlag GmbH, Weinheim, Germany, 1999, pp. 541–579.
- [31] W.E. Kaden, T. Wu, W.A. Kunkel, S.L. Anderson, *Science* 326 (2009) 826–829.
- [32] A. Bruix, J.A. Rodriguez, P.J. Ramírez, S.D. Senanayake, J. Evans, J.B. Park, D. Stacchiola, P. Liu, J. Hrbek, F. Illas, *J. Am. Chem. Soc.* 134 (2012) 8968–8974.
- [33] T.W. van Deelen, C. Hernández Mejía, K.P. de Jong, *Nat. Catal.* 2 (2019) 955–970.
- [34] F. Zasada, W. Piskorz, S. Cristol, J.F. Paul, A. Kotarba, Z. Sojka, *J. Phys. Chem. C* 114 (2010) 22245–22253.
- [35] X.L. Xu, J.Q. Li, *Surf. Sci.* 605 (2011) 1962–1967.
- [36] W.A. Sławiński, E. Zacharaki, H. Fjellvåg, A.O. Sjøstad, *Cryst. Growth Des.* 18 (2018) 2316–2325.
- [37] G.W. Brindley, *London, Edinburgh, Dublin Philos. Mag. J. Sci.* 36 (1945) 347–369.
- [38] C.R. Gonzalez, *Acta Crystallogr. Sect. A Found. Crystallogr.* 43 (1987) 769–774.
- [39] G.L. Bezemer, T.J. Remans, A.P. van Bavel, A.I. Dugulan, *J. Am. Chem. Soc.* 132 (2010) 8540–8541.
- [40] M. Claeys, M.E. Dry, E. van Steen, P.J. van Berge, S. Booyens, R. Crous, P. van Helden, J.

- Labuschagne, D.J. Moodley, A.M. Saib, *ACS Catal.* 5 (2015) 841–852.
- [41] N. Fischer, B. Clapham, T. Feltès, M. Claeys, *ACS Catal.* 5 (2015) 113–121.
- [42] M. Wolf, N. Fischer, M. Claeys, *J. Catal.* 374 (2019) 199–207.
- [43] A. Jha, Y.-L. Lee, W.-J. Jang, J.-O. Shim, K.-W. Jeon, H.-S. Na, H.-M. Kim, H.-S. Roh, D.-W. Jeong, S.G. Jeon, J.-G. Na, W.L. Yoon, *Mol. Catal.* 433 (2017) 145–152.
- [44] D. Vovchok, C.J. Guild, S. Dissanayake, J. Llorca, E. Stavitski, Z. Liu, R.M. Palomino, I. Waluyo, Y. Li, A.I. Frenkel, J.A. Rodriguez, S.L. Suib, S.D. Senanayake, *J. Phys. Chem. C* 122 (2018) 8998–9008.
- [45] Y. Cao, X. Peng, Z. Tan, Y. Liu, X. Wang, W. Zhao, L. Jiang, *Ind. Eng. Chem. Res.* 58 (2019) 17692–17698.
- [46] M.E. Dry, in: A.P. Steynberg, M.E. Dry (Eds.), *Fischer-Tropsch Technol.*, Elsevier B.V., Amsterdam, 2004, pp. 533–600.
- [47] A. Tavasoli, A. Nakhaeipour, K. Sadaghiani, *Fuel Process. Technol.* 88 (2007) 461–469.
- [48] X. Nie, H. Wang, W. Li, Y. Chen, X. Guo, C. Song, *J. CO<sub>2</sub> Util.* 24 (2018) 99–111.
- [49] W. Li, X. Nie, X. Jiang, A. Zhang, F. Ding, M. Liu, Z. Liu, X. Guo, C. Song, *Appl. Catal. B* 220 (2018) 397–408.
- [50] N. Fischer, M. Claeys, *J. Phys. D. Appl. Phys.* 53 (2020) 293001.
- [51] E. Colbourn, R.A. Hadden, H.D. Vandervell, K.C. Waugh, G. Webb, *J. Catal.* 130 (1991) 514–527.
- [52] F. Pinna, *Catal. Today* 41 (1998) 129–137.
- [53] A.J. Elliott, M.J. Watson, J. Tabatabaei, F.W. Zemichael, K.C. Waugh, *Catal. Lett.* 79 (2002) 1–6.
- [54] J.M. González-Carballo, S. Sadasivan, P. Landon, R.P. Tooze, *Mater. Charact.* 118 (2016) 519–526.
- [55] M. Wolf, N. Fischer, M. Claeys, *Catal. Today* 275 (2016) 135–140.
- [56] J. Díez-Ramírez, P. Sánchez, V. Kyriakou, S. Zafeiratos, G.E. Marnellos, M. Konsolakis, F. Dorado, *J. CO<sub>2</sub> Util.* 21 (2017) 562–571.
- [57] L. Wang, H. Liu, *Catal. Today* 316 (2018) 155–161.
- [58] N. Bion, F. Epron, M. Moreno, F. Mariño, D. Duprez, *Top. Catal.* 51 (2008) 76–88.
- [59] C. Weidenthaler, *Nanoscale* 3 (2011) 792–810.
- [60] O. Ducreux, B. Rebours, J. Lynch, M. Roy-Auberger, D. Bazin, *Oil Gas Sci. Technol.* 64

- (2009) 49–62.
- [61] J.-X. Liu, H.-Y. Su, D.-P. Sun, B.-Y. Zhang, W.-X. Li, *J. Am. Chem. Soc.* 135 (2013) 16284–16287.
- [62] S. Lyu, L. Wang, J. Zhang, C. Liu, J. Sun, B. Peng, Y. Wang, K.G. Rappé, Y. Zhang, J. Li, L. Nie, *ACS Catal.* 8 (2018) 7787–7798.
- [63] N. Fischer, E. van Steen, M. Claeys, *Catal. Today* 171 (2011) 174–179.
- [64] N. Fischer, M. Minnermann, M. Baeumer, E. van Steen, M. Claeys, *Catal. Lett.* 142 (2012) 830–837.
- [65] M. Wolf, N. Fischer, M. Claeys, *Mater. Chem. Phys.* 213 (2018) 305–312.
- [66] L.A. Bruce, J.V. Sanders, T.W. Turney, *Clays Clay Miner.* 34 (1986) 25–36.
- [67] M. Wolf, S.J. Roberts, W. Marquart, E.J. Olivier, N.T.J. Luchters, E.K. Gibson, C.R.A. Catlow, J.H. Neethling, N. Fischer, M. Claeys, *Dalt. Trans.* 48 (2019) 13858–13868.
- [68] A.J. Dent, G. Cibin, S. Ramos, A.D. Smith, S.M. Scott, L. Varandas, M.R. Pearson, N.A. Krumpa, C.P. Jones, P.E. Robbins, *J. Phys. Conf. Ser.* 190 (2009) 012039.
- [69] L. Lukashuk, N. Yigit, H. Li, J. Bernardi, K. Föttinger, G. Rupprechter, *Catal. Today* 336 (2019) 139–147.
- [70] J. Yan, J. Ma, P. Cao, P. Li, *Catal. Lett.* 93 (2004) 55–60.
- [71] M.P. Woods, P. Gawade, B. Tan, U.S. Ozkan, *Appl. Catal. B* 97 (2010) 28–35.
- [72] L. Wang, H. Liu, Y. Chen, S. Yang, *Int. J. Hydrog. Energy* 42 (2017) 3682–3689.

## Chapter 10: Summary and Conclusions

Proton-exchange or polymer electrolyte membrane fuel cells (PEMFCs) are a rapidly growing technology that provide a cleaner route for producing electrical energy for mobile and stationary applications, with no (or minimal) carbon-based emissions [1]. This type of fuel cell makes use of hydrogen to produce electrical energy, while oxygen is also co-fed to produce the by-product water and heat [2–4]. Currently, hydrogen is derived from carbon-based sources through steam reforming followed by a high- and low-temperature water-gas shift (WGS) process, respectively. The produced gas contains 40 – 75% H<sub>2</sub>, 0.5 – 2% CO, ~10% H<sub>2</sub>O and 10 – 25% CO<sub>2</sub> [5–9]. The CO present in this gas mixture is known to negatively affect the Pt-based anode catalyst of the PEMFC by hindering the adsorption/dissociation of H<sub>2</sub> as well as the subsequent charge transfer processes. Therefore, it is important to remove the CO in the reformat gas after the low-temperature WGS, but prior to feeding the H<sub>2</sub>-rich gas into the fuel cell.

The preferential oxidation of CO (CO-PrOx) has been regarded as the most promising route for removing CO from the reformat gas [5–10]. Ideally, a suitable catalyst is supposed to oxidise CO to CO<sub>2</sub> (which is not (or less) harmful to the PEMFC) but, at the same time, minimise the oxidation of the valuable H<sub>2</sub> to H<sub>2</sub>O. Noble metal-based catalysts are widely used for the CO-PrOx process, but these are very expensive and not readily available. Metal oxides, such as Co<sub>3</sub>O<sub>4</sub>, have shown great promise as cheaper alternatives to noble metal-based catalysts [5,6,8–10]. However, according to recent *in situ* studies [11–14], Co<sub>3</sub>O<sub>4</sub> is susceptible to reduction by H<sub>2</sub>, and transforms into CoO and ultimately metallic Co during CO-PrOx. The formation of metallic Co favours the undesired formation of CH<sub>4</sub> instead of the targeted CO oxidation reaction.

In this study, different support materials were used to understand their influence on CO oxidation and the phase stability of Co<sub>3</sub>O<sub>4</sub> during CO-PrOx. The effect of co-fed H<sub>2</sub>O and CO<sub>2</sub> has been less studied in the context of CO-PrOx, more specifically, their effect on the catalytic performance and

phase stability. Therefore, this study also aimed at understanding the influence of these two CO-PrOx feed gases, in addition to H<sub>2</sub>.

## 10.1. Thermodynamic Calculations

Thermodynamic calculations were performed to predict the thermal decomposition/calcination product from unsupported Co(OH)<sub>2</sub> and supported Co(NO<sub>3</sub>)<sub>2</sub>, respectively. The calculations showed that the likely product during the calcination of Co(OH)<sub>2</sub> in air/oxygen would be Co<sub>3</sub>O<sub>4</sub> rather than CoO or metallic Co, based on the temperature-dependent change in the Gibbs free energy of the considered reaction pathways. This was also not surprising as CoO and metallic Co have a low stability in relatively high concentrations of O<sub>2</sub>, such as in air [15–17]. The products considered for the decomposition of supported Co(NO<sub>3</sub>)<sub>2</sub> were Co<sub>3</sub>O<sub>4</sub>, CoO, metallic Co, Co<sub>2</sub>SiO<sub>4</sub>, CoTiO<sub>3</sub> and CoAl<sub>2</sub>O<sub>4</sub>. The calculations once again showed that Co<sub>3</sub>O<sub>4</sub> would be the likely product of the decomposition (below 400 °C), which has also been supported by experimental findings reported in the literature [18–20].

Another set of thermodynamic calculations were performed to understand the stability of un-/supported cobalt oxides and metallic cobalt in hydrogen-water mixtures. The formation of Co-support compounds in similar gas mixtures was also investigated. It was shown that in the unsupported state, very low H<sub>2</sub> (or high H<sub>2</sub>O) partial pressures stabilise the Co<sub>3</sub>O<sub>4</sub> phase, while high H<sub>2</sub> (or low H<sub>2</sub>O) partial pressures favour the formation of the metallic phase. Intermediate H<sub>2</sub>:H<sub>2</sub>O partial pressure ratios can stabilise the CoO phase. This has been also supported by numerous experimental findings [21–26].

In the supported state, the formation of CoAl<sub>2</sub>O<sub>4</sub>, CoTiO<sub>3</sub> and Co<sub>2</sub>SiO<sub>4</sub> was predicted to be more favourable than the formation of CoO and metallic Co during Co<sub>3</sub>O<sub>4</sub> reduction in H<sub>2</sub>, and also more favourable than the formation of Co<sub>3</sub>O<sub>4</sub> and CoO during the oxidation of metallic Co in high H<sub>2</sub>O partial pressures. Note that in a supported catalyst with pre-formed nanoparticles of Co<sub>3</sub>O<sub>4</sub> or metallic Co for example, there is a relatively small area of the nanoparticle in close contact with the support (depending on particle size). Therefore, the chances of the whole nanoparticle reacting with the support are low. However, very small nanoparticles (< 5 nm) would be more likely to react (almost) completely with the support than large particles (> 10 nm) at suitably high

temperatures [24,26–29]. Furthermore, despite the predicted likelihood of forming metal-support compounds (MSCs) under reducing or oxidising conditions, it should be noted that the formation of these compounds may be kinetically hindered, as shown in previous experimental studies [24,26–29].

All gas-phase reactions that have been mentioned to be possible during CO-PrOx (*viz.*, CO and H<sub>2</sub> oxidation, the forward and reverse WGS, as well as CO and CO<sub>2</sub> methanation) were also evaluated. The thermodynamic effect of having certain gases in the feed on the feasibility and progress of these gas-phase reactions was also evaluated. CO and H<sub>2</sub> oxidation were predicted to be highly feasible even in the presence of CO<sub>2</sub> and H<sub>2</sub>O, respectively. As a result, during these two reactions, very high equilibrium conversions (~100%) are predicted for the limiting substrates. The forward WGS reaction is mostly affected by the presence of H<sub>2</sub> and CO<sub>2</sub> in the feed, in that, the products of this reaction would cease to form above 285 °C. For the reverse WGS, the presence of CO and H<sub>2</sub>O in the feed makes this reaction only possible above 285 °C, which further explains the results of the forward WGS reaction. The methanation of CO is almost not affected by the presence of H<sub>2</sub>O in the feed, while CO<sub>2</sub> methanation can be significantly affected by co-fed H<sub>2</sub>O above 325 °C. Noted that the forward WGS shift can be expected to compete with CO methanation, while the reverse WGS can compete with CO<sub>2</sub> methanation under realistic CO-PrOx conditions, since these reactions have a common reactant(s) – either CO, CO<sub>2</sub> and/or H<sub>2</sub>.

## 10.2. Catalyst Synthesis and *ex situ* Characterisation

Unsupported Co<sub>3</sub>O<sub>4</sub> nanoparticles were prepared using the reverse microemulsion technique, while supported Co<sub>3</sub>O<sub>4</sub> catalysts were prepared using incipient wetness impregnation. The sole presence of Co<sub>3</sub>O<sub>4</sub> in each prepared catalyst was confirmed using *ex situ* PXRD and XAS (in the case of the Co<sub>3</sub>O<sub>4</sub>/CeO<sub>2</sub> only). This was in line with the thermodynamic predictions and previously reported experimental findings [18–20,22,30,31]. The average sizes of the Co<sub>3</sub>O<sub>4</sub> crystallites/particles varied between 11 and 19 nm. The supported catalysts had Co<sub>3</sub>O<sub>4</sub> loadings which were very close to the targeted 10 wt.-% loading. Nitrogen physisorption also confirmed the success of the impregnation method as the BET surface areas, as well as the BJH pore volumes and diameters of the supported catalysts were generally lower than those of the corresponding bare supports.

### 10.3. Effect of the Support on Catalytic Performance and Phase Stability

The *in situ* PXRD- and magnetometry-based CO-PrOx studies under dry CO-PrOx conditions (1% CO, 1% O<sub>2</sub>, 50% H<sub>2</sub> and a balance of N<sub>2</sub>) were used as a basis for comparing all prepared catalysts. These studies also revealed the effect of hydrogen on the progress of the CO oxidation reaction and the reducibility of the Co<sub>3</sub>O<sub>4</sub> phase. In the unsupported state, Co<sub>3</sub>O<sub>4</sub> obtained higher CO conversions to CO<sub>2</sub> at temperatures below 200 °C when compared with the supported catalysts, except for the ZrO<sub>2</sub>-supported catalyst (Figures 8.8(a) and A.6.2(a)). Note that none of the catalysts achieved CO conversions to CO<sub>2</sub> that were above the 99.999% target. This is possibly due to the occurrence of the H<sub>2</sub> oxidation reaction, which is kinetically favoured at elevated temperatures [5–10]. On the other hand, the reduction of unsupported Co<sub>3</sub>O<sub>4</sub> by H<sub>2</sub>, forming CoO and metallic Co, took place at much lower temperatures when compared with the supported catalysts. This may be a result of the nanoparticle-support interactions (NPSI) introduced during the synthesis of the supported catalysts [14,32–34]. There may also exist a relationship between high CO oxidation activity and high Co<sub>3</sub>O<sub>4</sub> reducibility. However, the SiC-supported sample deviated slightly from this observed trend as it performed better than most catalysts (except the unsupported and ZrO<sub>2</sub>-supported samples), while significantly minimising the formation of metallic Co (Figure 8.8).

Assuming the MvK mechanism for CO oxidation, this would require the lattice oxygen atoms to be easily removable (and replenishable) from the surface of Co<sub>3</sub>O<sub>4</sub>. Therefore, a hard-to-reduce Co<sub>3</sub>O<sub>4</sub> nanoparticle (especially on the surface) would most likely be less active for CO oxidation [11,14,32,33]. In addition to this, the interactions between the nanoparticle and the support may also play a role in altering the adsorption/dissociation capabilities of the Co<sub>3</sub>O<sub>4</sub> [35–39]. The nanoparticles located in the pores of the support may have a significant portion of their surface area not exposed to the reacting gas, which may also negatively affect their performance [39–43]. As for the ZrO<sub>2</sub>- and SiC-supported catalysts, the mentioned effects may have been less severe and therefore, resulting in a more active supported catalyst for CO oxidation.

The unsupported, TiO<sub>2</sub>-rutile-, and TiO<sub>2</sub>-P25-supported catalyst reduced to hcp and fcc Co, while only fcc Co was formed over the other support materials during dry CO-PrOx. The size of the fcc Co crystallites in the unsupported and TiO<sub>2</sub>-P25-supported catalyst could not be determined due to possible granularity effects, which resulted from the reduction process. On the other hand, fcc Co over TiO<sub>2</sub>-rutile was  $28.9 \pm 8.8$  nm, which indicated possible sintering as this size was larger

than the size of the corresponding fresh catalyst ( $11.8 \pm 0.8$  nm). The hcp Co in all the three aforementioned catalysts was found to be present as crystallites smaller than 15 nm. Although Rietveld refinement showed no evidence of intergrown hcp and fcc crystallites, this cannot be completely ruled out at this stage. It is important to note that the presence of hcp crystallites smaller than 20 nm is not thermodynamically favoured [34,44,45], however, it has been reported that this may be possible in cases where hcp and fcc crystalline domains are intergrown [46–50]. The sole formation of fcc Co in the other supported catalysts may be a result of the nature of the NPSIs and/or a result of the starting nanoparticle size variations in the corresponding fresh samples. Evidence of possible sintering was also suggested by PXRD and magnetometry (*via*  $\gamma$ ) in these catalysts, which may be thermally induced or caused by the changing gas partial pressures (especially those of  $H_2$  and  $H_2O$  [51–54]).

The presence of metallic Co resulted in methane formation from CO and  $H_2$ , which is an undesirable CO conversion route. Note that the amount of  $CH_4$  formed was not always proportional to the degree of reduction determined using magnetometry. However, methane formation is a surface-catalysed reaction while  $Co_3O_4$  reduction (as studied in the magnetometer) is a bulk phenomenon. Therefore, the formation and access to the required surface active sites for methanation may or may not have been possible in some of the evaluated catalysts, regardless of the degree of reduction of the entire sample [12,55,56]. This could have been the case for the unsupported catalyst which exhibited a change in the hcp:fcc Co ratio and crystallite size of each allotrope as function of temperature. The  $CoO_{1-x}$  species over  $CeO_2$  and  $TiO_2$ -anatase may have been encapsulated by partially reduced support species.

STEM-EELS analysis of the spent supported catalysts also showed (minimal) sintering in some of the cobalt-bearing nanoparticles but also showed wetting of some of the supports by Co species, possibly indicating strong interactions of these species with the support. The STEM-EELS map of the  $Al_2O_3$ -supported spent sample showed regions where Co, Al and O were intricately mixed, which may suggest the presence of a Co-Al oxide phase. XAS analysis of the  $SiO_2$ -,  $TiO_2$ - and  $Al_2O_3$ -supported spent samples showed the presence of  $Co_2SiO_4$  ( $7.7 \pm 0.3\%$ ),  $CoTiO_3$  ( $13.8 \pm 1.8\%$  (from  $TiO_2$ -anatase) and  $8.9 \pm 1.5\%$  (from  $TiO_2$ -rutile)), and  $CoAl_2O_4$  ( $26.6 \pm 1.6\%$ ), respectively. The formation of these MSCs (especially in the currently reported trend) has been observed in other catalytic reactions (*e.g.*, the Fischer-Tropsch synthesis [24,26,29]), but is being shown for the first time during CO-PrOx. The spent samples of SiC and  $ZrO_2$  showed no evidence of MSC formation. The  $CeO_2$ -supported catalyst may have formed metal-support compounds, but

these could not be adequately confirmed using XAS (due to the lack of suitable reference standards) or using reports in the literature.

## 10.4. Effect of the CO-PrOx Gas Feed Components on Catalytic Performance and Phase Stability

Performing CO oxidation in the absence of H<sub>2</sub>, H<sub>2</sub>O and CO<sub>2</sub> (*i.e.*, CO-TOx) showed that yields of up to 100% can be realised for CO<sub>2</sub> over an unsupported and a ZrO<sub>2</sub>-supported Co<sub>3</sub>O<sub>4</sub> catalyst. Concurrently, *in situ* PXRD showed that the Co<sub>3</sub>O<sub>4</sub> phase in both catalysts did not reduce during CO-TOx. This was strong experimental evidence that H<sub>2</sub> is one of the main causes for the relatively low CO<sub>2</sub> yields achieved by each catalyst under dry CO-PrOx conditions, and the main cause of Co<sub>3</sub>O<sub>4</sub> reduction. However, upon reduction of Co<sub>3</sub>O<sub>4</sub> to CoO by co-fed H<sub>2</sub> at very low O<sub>2</sub> partial pressures, increasing the O<sub>2</sub> feed concentration helped restore CO oxidation activity by making more surface O species available despite also enhancing the H<sub>2</sub> oxidation reaction at the same time [57–59] (see sub-section 9.2.7.). The presence of more O<sub>2</sub> in the feed may have also restored the MvK mechanism for CO oxidation by forming a Co<sup>2+</sup>-Co<sup>3+</sup> surface redox pair [59,60].

Co-feeding H<sub>2</sub>O further affected CO oxidation through the blockage of surface active sites (which is a kinetic effect) [61–64], but offered slight stability to the oxide phase against reduction due to its oxidising nature (which is a thermodynamic effect) [23,26,28,61,65–67]. The forward WGS reaction only took place when CO<sub>2</sub> was not present in the feed, which agreed with the thermodynamic predictions (Figure 9.1(a)). Furthermore, this reaction was possible over metallic Co, which is shown in this work for the first time under wet CO-PrOx conditions. Although methane formation also took place, lower yields were realised when compared with the case with no co-fed H<sub>2</sub>O. This could again have been caused by the competitive adsorption of H<sub>2</sub>O on the metallic surface, which could also react with CO to form WGS products – CO<sub>2</sub> and H<sub>2</sub> – instead of CH<sub>4</sub>.

The presence of CO<sub>2</sub> in the feed had no significant effect on the catalytic performance and the phase stability of the catalysts, but resulted in the methanation of CO<sub>2</sub> and in the reverse WGS reaction. These two reactions were still possible even in the presence of H<sub>2</sub>O but lower yields were realised in each case. The methanation of CO<sub>2</sub> and the reverse WGS took place over metallic Co,

which is a correlation also being made in this work for the first time under realistic CO-PrOx conditions. Noted that the forward WGS was not observed in the presence of 9% CO<sub>2</sub> and 46% H<sub>2</sub> in the feed at elevated temperatures where metallic Co was present. This was also in line with the thermodynamic predictions (Figure 9.1(a)) which showed the feasibility of this reaction only below 285 °C in a feed with relatively high amounts of CO<sub>2</sub> and H<sub>2</sub>. Evidence of sintering was observed under all CO-PrOx conditions – mostly using PXRD and magnetometry – but this was more significant in feed mixtures with water vapour, which is known to facilitate sintering [51–54]. The presence of water in the feed also caused the formation of CoTiO<sub>3</sub> (7.3 ± 3.5%) in the TiO<sub>2</sub>-P25-supported catalyst, which was not formed during dry CO-PrOx.

## References

- [1] G. Kolb, in: G. Kolb (Ed.), *Fuel Process. Fuel Cells*, Wiley-VCH Verlag GmbH & Co. KGaA, Weinheim, Germany, 2008, pp. 1–2.
- [2] F. Barbir, S. Yazici, *Int. J. Energy Res.* 32 (2008) 369–378.
- [3] G. Kolb, in: G. Kolb (Ed.), *Fuel Process. Fuel Cells*, Wiley-VCH Verlag GmbH & Co. KGaA, Weinheim, Germany, 2008, pp. 3–16.
- [4] Y.-J. Wang, J. Qiao, R. Baker, J. Zhang, *Chem. Soc. Rev.* 42 (2013) 5768–5787.
- [5] T.V. Choudhary, D.W. Goodman, *Catal. Today* 77 (2002) 65–78.
- [6] A.F. Ghenciu, *Curr. Opin. Solid State Mater. Sci.* 6 (2002) 389–399.
- [7] S. Huang, K. Hara, A. Fukuoka, *Energy Environ. Sci.* 2 (2009) 1060–1068.
- [8] E.D. Park, D. Lee, H.C. Lee, *Catal. Today* 139 (2009) 280–290.
- [9] A. Mishra, R. Prasad, *Bull. Chem. React. Eng. Catal.* 6 (2011) 1–14.
- [10] N. Bion, F. Epron, M. Moreno, F. Mariño, D. Duprez, *Top. Catal.* 51 (2008) 76–88.
- [11] L. Lukashuk, K. Föttinger, E. Kolar, C. Rameshan, D. Teschner, M. Hävecker, A. Knop-Gericke, N. Yigit, H. Li, E. McDermott, M. Stöger-Pollach, G. Rupprechter, *J. Catal.* 344 (2016) 1–15.
- [12] T.M. Nyathi, N. Fischer, A.P.E. York, M. Claeys, *Faraday Discuss.* 197 (2017) 269–285.
- [13] M. Khasu, T. Nyathi, D.J. Morgan, G.J. Hutchings, M. Claeys, N. Fischer, *Catal. Sci. Technol.* 7 (2017) 4806–4817.
- [14] T.M. Nyathi, N. Fischer, A.P.E. York, D.J. Morgan, G.J. Hutchings, E.K. Gibson, P.P. Wells, C.R.A. Catlow, M. Claeys, *ACS Catal.* 9 (2019) 7166–7178.
- [15] F. Pinna, *Catal. Today* 41 (1998) 129–137.
- [16] P.A. Chernavskii, J.-A. Dalmon, N.S. Perov, A.Y. Khodakov, *Oil Gas Sci. Technol.* 64 (2009) 25–48.
- [17] M. Wolf, N. Fischer, M. Claeys, *Catal. Today* 275 (2016) 135–140.
- [18] E. van Steen, G.S. Sewell, R.A. Makhothe, C. Micklethwaite, H. Manstein, M. de Lange, C.T. O'Connor, *J. Catal.* 162 (1996) 220–229.
- [19] J.-S. Girardon, A.S. Lermontov, L. Gengembre, P.A. Chernavskii, A. Griboval-Constant, A.Y. Khodakov, *J. Catal.* 230 (2005) 339–352.

- [20] P.A. Chernavskii, A.Y. Khodakov, G. V. Pankina, J.-S. Girardon, E. Quinet, *Appl. Catal. A* 306 (2006) 108–119.
- [21] E. van Steen, M. Claeys, M.E. Dry, J. van de Loosdrecht, E.L. Viljoen, J.L. Visagie, *J. Phys. Chem. B* 109 (2005) 3575–3577.
- [22] N. Fischer, E. van Steen, M. Claeys, *Catal. Today* 171 (2011) 174–179.
- [23] N. Fischer, B. Clapham, T. Feltes, E. van Steen, M. Claeys, *Angew. Chemie - Int. Ed.* 53 (2014) 1342–1345.
- [24] M. Wolf, H. Kotzé, N. Fischer, M. Claeys, *Faraday Discuss.* 197 (2017) 243–268.
- [25] M. Wolf, B.K. Mutuma, N.J. Coville, N. Fischer, M. Claeys, *ACS Catal.* 8 (2018) 3985–3989.
- [26] M. Wolf, E.K. Gibson, E.J. Olivier, J.H. Neethling, C.R.A. Catlow, N. Fischer, M. Claeys, *ACS Catal.* 9 (2019) 4902–4918.
- [27] N.E. Tsakoumis, R.E. Johnsen, W. van Beek, M. Rønning, E. Rytter, A. Holmen, *Chem. Commun.* 52 (2016) 3239–3242.
- [28] N.E. Tsakoumis, J.C. Walmsley, M. Rønning, W. van Beek, E. Rytter, A. Holmen, *J. Am. Chem. Soc.* 139 (2017) 3706–3715.
- [29] M. Wolf, E.K. Gibson, E.J. Olivier, J.H. Neethling, C.R.A. Catlow, N. Fischer, M. Claeys, *Catal. Today* 342 (2020) 71–78.
- [30] T. Cseri, S. Békássy, G. Kenessey, G. Liptay, F. Figueras, *Thermochim. Acta* 288 (1996) 137–154.
- [31] N. Fischer, M. Minnermann, M. Baeumer, E. van Steen, M. Claeys, *Catal. Lett.* 142 (2012) 830–837.
- [32] C.-B. Wang, C.-W. Tang, H.-C. Tsai, S.-H. Chien, *Catal. Lett.* 107 (2006) 223–230.
- [33] Z. Zhao, M.M. Yung, U.S. Ozkan, *Catal. Commun.* 9 (2008) 1465–1471.
- [34] L.J. Garces, B. Hincapie, R. Zerger, S.L. Suib, *J. Phys. Chem. C* 119 (2015) 5484–5490.
- [35] J.M. Herrmann, *J. Catal.* 89 (1984) 404–412.
- [36] B. Delmon, in: G. Ertl, H. Knözinger, J. Weitkamp (Eds.), *Prep. Solid Catal.*, Wiley-VCH Verlag GmbH, Weinheim, Germany, 1999, pp. 541–579.
- [37] W.E. Kaden, T. Wu, W.A. Kunkel, S.L. Anderson, *Science* 326 (2009) 826–829.
- [38] A. Bruix, J.A. Rodriguez, P.J. Ramírez, S.D. Senanayake, J. Evans, J.B. Park, D. Stacchiola, P. Liu, J. Hrbek, F. Illas, *J. Am. Chem. Soc.* 134 (2012) 8968–8974.
- [39] T.W. van Deelen, C. Hernández Mejía, K.P. de Jong, *Nat. Catal.* 2 (2019) 955–970.

- [40] A.A. Adesina, *Appl. Catal. A* 138 (1996) 345–367.
- [41] C. Perego, P. Villa, *Catal. Today* 34 (1997) 281–305.
- [42] E. Marceau, X. Carrier, M. Che, O. Clause, C. Marcilly, in: G. Ertl, H. Knözinger, F. Schüth, J. Weitkamp (Eds.), *Handb. Heterog. Catal.*, Wiley-VCH Verlag GmbH & Co. KGaA, Weinheim, Germany, 2008, pp. 467–484.
- [43] P. Munnik, P.E. de Jongh, K.P. de Jong, *Chem. Rev.* 115 (2015) 6687–6718.
- [44] E. Klugmann, H.J. Blythe, F. Walz, *Phys. Status Solidi* 146 (1994) 803–813.
- [45] S. Ram, *Mater. Sci. Eng. A* 304–306 (2001) 923–927.
- [46] O. Ducreux, B. Rebours, J. Lynch, M. Roy-Auberger, D. Bazin, *Oil Gas Sci. Technol.* 64 (2009) 49–62.
- [47] A. Longo, L. Sciortino, F. Giannici, A. Martorana, *J. Appl. Crystallogr.* 47 (2014) 1562–1568.
- [48] H.E. du Plessis, J.P.R. de Villiers, A. Tuling, E.J. Olivier, *Phys. Chem. Chem. Phys.* 18 (2016) 30183–30188.
- [49] S.W.T. Price, D.J. Martin, A.D. Parsons, W.A. Sławiński, A. Vamvakeros, S.J. Keylock, A.M. Beale, J.F.W. Mosselmans, *Sci. Adv.* 3 (2017) e1602838.
- [50] W.A. Sławiński, E. Zacharaki, H. Fjellvåg, A.O. Sjøstad, *Cryst. Growth Des.* 18 (2018) 2316–2325.
- [51] G.L. Bezemer, T.J. Remans, A.P. van Bavel, A.I. Dugulan, *J. Am. Chem. Soc.* 132 (2010) 8540–8541.
- [52] M. Claeys, M.E. Dry, E. van Steen, P.J. van Berge, S. Booyens, R. Crous, P. van Helden, J. Labuschagne, D.J. Moodley, A.M. Saib, *ACS Catal.* 5 (2015) 841–852.
- [53] N. Fischer, B. Clapham, T. Feltes, M. Claeys, *ACS Catal.* 5 (2015) 113–121.
- [54] M. Wolf, N. Fischer, M. Claeys, *J. Catal.* 374 (2019) 199–207.
- [55] T. Herranz, X. Deng, A. Cabot, J. Guo, M. Salmeron, *J. Phys. Chem. B* 113 (2009) 10721–10727.
- [56] A. Tuxen, S. Carenco, M. Chintapalli, C.-H. Chuang, C. Escudero, E. Pach, P. Jiang, F. Borondics, B. Beberwyck, A.P. Alivisatos, G. Thornton, W.-F. Pong, J. Guo, R. Perez, F. Besenbacher, M. Salmeron, *J. Am. Chem. Soc.* 135 (2013) 2273–2278.
- [57] J. Yan, J. Ma, P. Cao, P. Li, *Catal. Lett.* 93 (2004) 55–60.
- [58] M.P. Woods, P. Gawade, B. Tan, U.S. Ozkan, *Appl. Catal. B* 97 (2010) 28–35.
- [59] L. Lukashuk, N. Yigit, R. Rameshan, E. Kolar, D. Teschner, M. Hävecker, A. Knop-

- Gericke, R. Schlögl, K. Föttinger, G. Rupprechter, *ACS Catal.* 8 (2018) 8630–8641.
- [60] L. Lukashuk, N. Yigit, H. Li, J. Bernardi, K. Föttinger, G. Rupprechter, *Catal. Today* 336 (2019) 139–147.
- [61] D.H. Kim, J.E. Cha, *Catal. Lett.* 86 (2003) 107–112.
- [62] Q. Guo, Y. Liu, *React. Kinet. Catal. Lett.* 92 (2007) 19–25.
- [63] S. Monyanon, S. Pongstabodee, A. Luengnaruemitchai, *J. Chinese Inst. Chem. Eng.* 38 (2007) 435–441.
- [64] P. Gawade, B. Bayram, A.M.C. Alexander, U.S. Ozkan, *Appl. Catal. B* 128 (2012) 21–30.
- [65] J. Paterson, M. Peacock, E. Ferguson, M. Ojeda, J. Clarkson, *Appl. Catal. A* 546 (2017) 103–110.
- [66] Y. Zhang, D. Wei, S. Hammache, J.G. Goodwin, *J. Catal.* 188 (1999) 281–290.
- [67] S. Storsæter, Ø. Borg, E.A. Blekkan, A. Holmen, *J. Catal.* 231 (2005) 405–419.



# Chapter 11: Recommendations for Future Work

## 11.1. Catalyst Synthesis

One of the main objectives of this study was to investigate the influence of different support materials on the catalytic performance and phase stability of  $\text{Co}_3\text{O}_4$ . The catalysts were prepared using the incipient wetness impregnation method to allow for the support and the  $\text{Co}_3\text{O}_4$  nanoparticles to be in close contact [1–3]. The supporting of the nanoparticles in all cases did improve the phase stability of  $\text{Co}_3\text{O}_4$  and did minimise  $\text{CH}_4$  formation when compared with the case of the unsupported catalyst. However, the CO conversion to  $\text{CO}_2$  in most cases was lower than that of the unsupported catalyst (before any detectable reduction) and lower than the desired minimum CO conversion of 99.999%. Although the ideal minimum CO conversion was not achieved, the  $\text{ZrO}_2$  and SiC supported catalysts seem to show great promise as CO-PrOx catalysts. These supports allowed for decently high  $\text{CO}_2$  yields to be achieved (especially  $\text{ZrO}_2$ ) and delayed both  $\text{Co}_3\text{O}_4$  reduction and  $\text{CH}_4$  formation (especially SiC) relative to the unsupported catalyst.

The introduction of alkaline earth metals and transition metals as promoters in the promising supported catalysts may be of great interest for future studies towards improving their catalytic performance and phase stability. From the literature, metals such as magnesium [4,5], manganese [6–8] and iron [7,9–11], have shown good oxidation promotion for Co-based CO-PrOx catalysts. In addition, these metals have low hydrogen dissociation activity, which would ensure that the oxide phase remains stable over a wide temperature range.

## 11.2. *In situ* Catalyst Characterisation during CO-PrOx

The two *in situ* techniques used in this study proved very useful in following the phase changes of  $\text{Co}_3\text{O}_4$  in all CO-PrOx experiments. Coupling the *in situ* characterisation with the gas product analysis allowed for the establishment of a relationship between the various gas-phase reactions that took place and the different cobalt-based phases that were detected. It should be noted that the *in situ* techniques used were bulk sensitive, implying that the exact surface phase composition could not be ascertained. Knowing the surface phase composition is crucial, especially since most of the catalysts did not fully reduce to the metallic phase and some not being able to convert all the CO (or  $\text{CO}_2$ ) to  $\text{CH}_4$  even at 450 °C. It is possible that the degree of reduction of the nanoparticles within a sample is not the same due to differences in particle size. Furthermore, some particles may have formed a core-shell structure with a CoO core and a metallic Co shell (assuming a shrinking core reduction model, see sub-section 2.3.1.2.) as a result of partial reduction.

The use of *in situ* surface-sensitive techniques, *viz.*, X-ray Photoelectron Spectroscopy (XPS) or Near Edge X-ray Absorption Fine Structure (NEXAFS) [12,13], may help clear this uncertainty. The surface analysis would also further strengthen the relationship established in this current study that is between the cobalt-based (bulk) phases identified and the reactions they seem to catalyse. In addition to surface characterisation, (*quasi*-)*in situ* TEM analysis may also shed light on the structure/phase composition of nanoparticles at certain reaction temperatures [14–16]. This can also be linked back to the changes in activity/selectivity observed at different temperatures.

## 11.3. Catalyst Testing during CO-PrOx

The reaction conditions chosen for performing both dry and wet CO-PrOx mainly allowed for the effect of temperature on the catalytic performance and phase stability to be studied. Parameters such as the holding time at a certain temperature(s) and the gas-hourly space velocity (GHSV) were kept constant in all experiments (except when studying the effect of the  $\text{O}_2$  concentration). Since the holding time at each temperature was limited to 1 hr, it can be said that the kinetic data reported was obtained under *pseudo*-steady state conditions. Therefore, performing time-on-stream studies over periods much longer than 1 hr, can be very useful in understanding catalytic stability

at selected temperatures. This could also be coupled with *in situ* characterisation in cases where a catalyst loses activity because of chemical phase changes (or sintering).

Varying the GHSV at a certain temperature(s) is also important as this parameter can affect CO<sub>2</sub> formation (through CO oxidation) [17–19] and affect Co<sub>3</sub>O<sub>4</sub> reducibility. Generally, low GHSVs favour high CO<sub>2</sub> yields and low oxide reducibility. However, it should be noted that the low GHSV could also favour high H<sub>2</sub> conversions *via* oxidation, which would negatively affect the CO<sub>2</sub> selectivity. Furthermore, should the catalyst still reduce at low GHSVs, other side reactions (*i.e.*, methanation and reverse water-gas shift) could be enhanced as well. Therefore, finding the optimum GHSV that would ensure CO conversions above 99.999% while limiting side reactions and cobalt oxide reduction, is crucial for further development of Co<sub>3</sub>O<sub>4</sub>-based catalysts for CO-PrOx.

## References

- [1] A.A. Adesina, *Appl. Catal. A* 138 (1996) 345–367.
- [2] E. Marceau, X. Carrier, M. Che, O. Clause, C. Marcilly, in: G. Ertl, H. Knözinger, F. Schüth, J. Weitkamp (Eds.), *Handb. Heterog. Catal.*, Wiley-VCH Verlag GmbH & Co. KGaA, Weinheim, Germany, 2008, pp. 467–484.
- [3] P. Munnik, P.E. de Jongh, K.P. de Jong, *Chem. Rev.* 115 (2015) 6687–6718.
- [4] M. Wojciechowska, W. Przystajko, M. Zieliński, *Catal. Today* 119 (2007) 338–341.
- [5] Z. Fattah, M. Rezaei, A. Biabani-Ravandi, A. Irankhah, H.R. Arandiyan, *Chem. Eng. Commun.* 203 (2016) 200–209.
- [6] Z. Zhao, X. Lin, R. Jin, Y. Dai, G. Wang, *Catal. Sci. Technol.* 2 (2012) 554–563.
- [7] Z. Zhao, X. Lin, R. Jin, G. Wang, T. Muhammad, *Appl. Catal. B* 115–116 (2012) 53–62.
- [8] Z. Zhao, Y. Li, T. Bao, G. Wang, T. Muhammad, *Catal. Commun.* 46 (2014) 28–31.
- [9] M. Kotobuki, A. Watanabe, H. Uchida, H. Yamashita, M. Watanabe, *J. Catal.* 236 (2005) 262–269.
- [10] W. Zhang, A. Wang, L. Li, X. Wang, T. Zhang, *Catal. Lett.* 121 (2008) 319–323.
- [11] L.Q. Qwabe, H.B. Friedrich, S. Singh, *J. Mol. Catal. A Chem.* 404–405 (2015) 167–177.
- [12] L. Lukashuk, N. Yigit, H. Li, J. Bernardi, K. Föttinger, G. Rupprechter, *Catal. Today* 336 (2019) 139–147.
- [13] L. Zhong, T. Kropp, W. Baaziz, O. Ersen, D. Teschner, R. Schlögl, M. Mavrikakis, S. Zafeiratos, *ACS Catal.* 9 (2019) 8325–8336.
- [14] R.W. Mitchell, D.C. Lloyd, L.G.A. van de Water, P.R. Ellis, K.A. Metcalfe, C. Sibbald, L.H. Davies, D.I. Enache, G.J. Kelly, E.D. Boyes, P.L. Gai, *ACS Catal.* 8 (2018) 8816–8829.
- [15] J.E. de Vrieze, G.M. Bremmer, M. Aly, V. Navarro, J.W. Thybaut, P.J. Kooyman, M. Saeys, *ACS Catal.* 9 (2019) 7449–7456.
- [16] A. Govender, W. Barnard, E.J. Olivier, R.P. Forbes, E. van Steen, J.H. Neethling, *Mater. Charact.* 121 (2016) 93–102.
- [17] M.M. Yung, Z. Zhao, M.P. Woods, U.S. Ozkan, *J. Mol. Catal. A Chem.* 279 (2008) 1–9.
- [18] M.P. Woods, P. Gawade, B. Tan, U.S. Ozkan, *Appl. Catal. B* 97 (2010) 28–35.
- [19] P. Gawade, B. Bayram, A.M.C. Alexander, U.S. Ozkan, *Appl. Catal. B* 128 (2012) 21–30.

# Appendices

## A.1. Equations and Coefficients for Thermodynamic Calculations

$$\frac{\partial \left( \frac{\Delta G_{rxn}(T)}{T} \right)}{\partial T} = - \frac{\Delta H_{rxn}(T)}{T^2} \quad \text{Equation A. 1.1}$$

$$\frac{\Delta G_{rxn}(T)}{T} - \frac{\Delta G_{rxn}^o(T)}{T^o} = - \int_{T^o}^T \frac{\Delta H_{rxn}(T)}{T^2} dT \quad \text{Equation A. 1.2}$$

$$\Delta H_{rxn}(T) = \Delta H_{rxn}^o + \int_{T^o}^T C_{p,rxn}(T) dT \quad \text{Equation A. 1.3}$$

$$\Delta G_{rxn}(T) = T \cdot \left( \frac{\Delta G_{rxn}^o(T)}{T^o} - \int_{T^o}^T \frac{\Delta H_{rxn}^o + \int_{T^o}^T \Delta C_{p,rxn}(T) dT}{T^2} dT \right) \quad \text{Equation A. 1.4}$$

$$\Delta C_{p,rxn}(T) = \Delta a_{rxn} + \Delta b_{rxn} \cdot \frac{T}{1000} + \Delta c_{rxn} \cdot \left( \frac{1000}{T} \right)^2 + \Delta d_{rxn} \cdot \left( \frac{T}{1000} \right)^2 \quad \text{Equation A. 1.5}$$



$$\Delta G_{rxn}(T) = -RT \ln K_{eq}. \quad \text{Equation A. 1.6}$$

$$K_{eq.} = \frac{(p_Y)^y \cdot (p_Z)^z}{(p_V)^v \cdot (p_W)^w} \quad \text{Equation A. 1.7}$$

$$T \cdot \left( \frac{\Delta G_{rxn}^o(T)}{T^o} - \int_{T^o}^T \frac{\Delta H_{rxn}^o + \int_{T^o}^T \Delta C_{p,rxn}(T) dT}{T^2} dT \right) = -RT \ln \left\{ \frac{(p_Y)^y \cdot (p_Z)^z}{(p_V)^v \cdot (p_W)^w} \right\} \quad \text{Equation A. 1.8}$$

$$\frac{(p_Y)^y \cdot (p_Z)^z}{(p_V)^v \cdot (p_W)^w} = \exp \left\{ -\frac{1}{R} \cdot \left( \frac{\Delta G_{rxn}^o(T)}{T^o} - \int_{T^o}^T \frac{\Delta H_{rxn}^o + \int_{T^o}^T \Delta C_{p,rxn}(T) dT}{T^2} dT \right) \right\} \quad \text{Equation A. 1.9}$$

$$\Delta = \sum \text{products} - \sum \text{reactants} \quad \text{Equation A. 1.10}$$

**Table A.1.1:** Heat capacity coefficients as well as standard formation enthalpy and Gibbs free energy values of each substance considered in the thermodynamic evaluations.

Substances	<i>a</i>	<i>b</i>	<i>c</i>	<i>d</i>	$\Delta H_{f,298.15 K}^{\circ}$	$\Delta G_{f,298.15 K}^{\circ}$
$\alpha$ -Al <sub>2</sub> O <sub>3</sub> (corundum)	117.487	10.376	-3.711	0	-1675.692	-1690.882
C (graphite)*	0.109	38.94	-0.146	-17.385	0	-1.711
Co (hexagonal) <sup>§</sup>	19.125	20.468	0	-4.682	0	-8.964
Co (cubic) <sup>#</sup>	4.469	29.987	2.515	0		
CoAl <sub>2</sub> O <sub>4</sub>	165.686	18.828	-3.473	0	-1947.108	-1976.797
Co(OH) <sub>2</sub>	82.843	47.698	0	0	-541.338	-569.156
Co(NO <sub>3</sub> ) <sub>2</sub>	131.796	83.68	0	0	-421.546	-474.313
CoO	45.258	10.694	0.602	0	-237.944	-253.736
Co <sub>3</sub> O <sub>4</sub>	131.645	66.015	-2.481	0	-918.680	-951.276
Co <sub>2</sub> SiO <sub>4</sub>	157.402	22.05	-2.669	0	-1398.711	-1445.989
CoTiO <sub>3</sub>	123.47	9.707	-1.653	0	-1207.381	-1236.259
SiO <sub>2</sub> ( $\alpha$ -quartz) <sup>‡</sup>	40.497	44.601	-0.833	0	-910.856	-923.219
TiO <sub>2</sub> (anatase)	76.358	0.837	-2.008	0	-941.400	-956.282
TiO <sub>2</sub> (rutile)	73.346	3.054	-1.703	0	-944.747	-959.841
CH <sub>4</sub>	11.933	77.647	0.142	-18.414	-74.872	-130.403
CO	30.962	2.439	-0.28	0	-110.528	-169.457
CO <sub>2</sub>	51.128	4.368	-1.469	0	-393.521	-457.264
H <sub>2</sub>	26.882	3,586	0,105	0	0	-38.961
H <sub>2</sub> O	34.376	7.841	-0.423	0	-241.856	-298.153
NO <sub>2</sub>	34.526	24.665	-0.423	-6.866	33.099	-38.467
O <sub>2</sub>	29.154	6.477	-0.184	-1.017	0	-61.164

\* heat capacity coefficients valid below 1100 K (826.85 °C).

§ stable below 700 K (426.85 °C).

# heat capacity coefficients valid between 700 and 1000 K (426.85 and 726.85 °C).

‡ stable below 847 K (573.85 °C).

## A.2. PXRD Reference Patterns Accessed from the ICDD PDF-2 Database

**Table A.2.1:** ICDD PDF-2 entries of all chemical/crystal phases relevant to the current study.

Chemical formula	Chemical name	Entry
$\gamma$ -Al <sub>2</sub> O <sub>3</sub>	$\gamma$ -Aluminium oxide	00-010-0425
$\gamma$ -AlO(OH)	$\gamma$ -Aluminium oxyhydroxide	01-072-0359
$\delta$ -Al <sub>2</sub> O <sub>3</sub> *	$\delta$ -Aluminium oxide	00-016-0394
$\theta$ -Al <sub>2</sub> O <sub>3</sub>	$\theta$ -Aluminium oxide	00-011-0517
CeO <sub>2</sub>	Cerium(IV) oxide	00-034-0394
$\alpha$ -Co	$\alpha$ -Cobalt (hexagonal)	01-071-4239
$\beta$ -Co	$\beta$ -Cobalt (cubic)	00-015-0806
CoAl <sub>2</sub> O <sub>4</sub>	Cobalt(II) aluminium oxide	00-044-0160
$\alpha$ -Co(OH) <sub>2</sub> *	$\alpha$ -Co(II) hydroxide	00-002-0925
$\beta$ -Co(OH) <sub>2</sub>	$\beta$ -Co(II) hydroxide	00-045-0031
CoO (hcp)	Cobalt(II) oxide (hexagonal)	01-089-2803
CoO (fcc)	Cobalt(II) oxide (cubic)	00-043-1004
Co <sub>3</sub> O <sub>4</sub>	Cobalt(II,III) oxide	01-073-1701
CoSiO <sub>3</sub>	Cobalt(II) silicon oxide	01-072-1508
Co <sub>2</sub> SiO <sub>4</sub> (orthorhombic)	Cobalt(II) silicon oxide (orthorhombic)	00-015-0865
Co <sub>2</sub> SiO <sub>4</sub> (cubic)	Cobalt(II) silicon oxide (cubic)	00-029-0506
CoTiO <sub>3</sub> (rhombohedral)	Cobalt(II) titanium(IV) oxide (rhombohedral)	00-029-0516
CoTiO <sub>3</sub> (cubic)	Cobalt(II) titanium(IV) oxide (cubic)	00-015-0866
Co <sub>2</sub> TiO <sub>4</sub>	Cobalt(II) titanium(IV) oxide	00-018-0428
$\alpha$ -SiC	$\alpha$ -Silicon carbide (hexagonal)	00-031-1232
$\beta$ -SiC	$\beta$ -Silicon carbide (cubic)	03-065-0360
TiO <sub>2</sub> (anatase)	Titanium(IV) oxide (anatase)	01-089-4921
TiO <sub>2</sub> (rutile)	Titanium(IV) oxide (rutile)	01-089-4202
ZrO <sub>2</sub>	Zirconium(IV) oxide	01-081-1314

\* full crystallographic information not available in ICDD PDF-2 database.

### A.3. Magnetometer Calibration

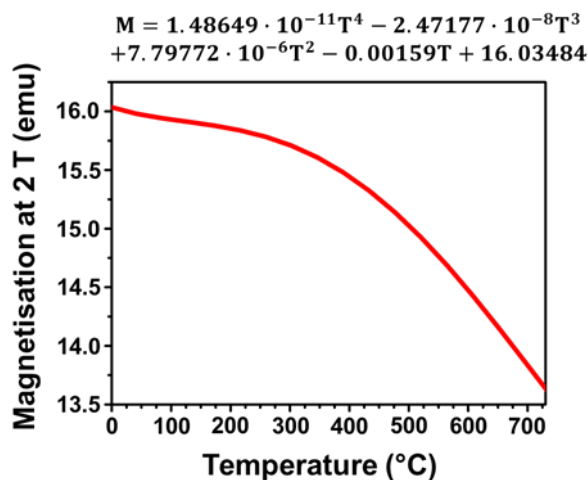


**Figure A.3.1:** Magnetisation (recorded under argon flow) of a 0.1 g pre-reduced unsupported metallic cobalt sample measured as a function of temperature. The sample had been pre-reduced between room temperature and 700 °C under H<sub>2</sub> flow starting from the Co<sub>3</sub>O<sub>4</sub> phase.

$$DoR(\%) = \frac{M_{sample} \cdot 0.1 \text{ g}}{M_{calibration} \cdot X_{loading} \cdot m_{unreduced \ sample}} \times 100 \quad \text{Equation A. 4.1}$$

$M_{sample}$  is the measured magnetisation of the sample (in emu) at a particular temperature and  $M_{calibration}$  is the corresponding magnetisation of Co calculated from the calibration curve (in emu) at the same temperature.  $X_{loading}$  is the metal loading as calculated from ICP-OES (in wt.-%) and  $m_{unreduced \ sample}$  is the mass of unreduced sample (in g) loaded into the reactor.

#### A.4. Example of Results from the Rietveld Refinement of an *ex situ* Pattern

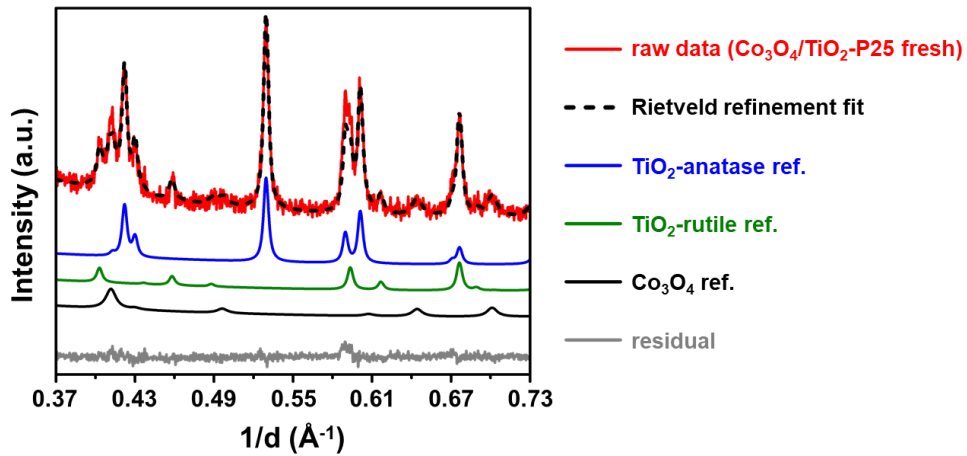


**Figure A.4.1:** Results from after performing Rietveld refinement on the *ex situ* PXRD pattern of the fresh  $\text{Co}_3\text{O}_4/\text{TiO}_2\text{-P25}$  sample.

## A.5. *In situ* PXRD Patterns Recorded during Reduction and Results from Rietveld Refinement

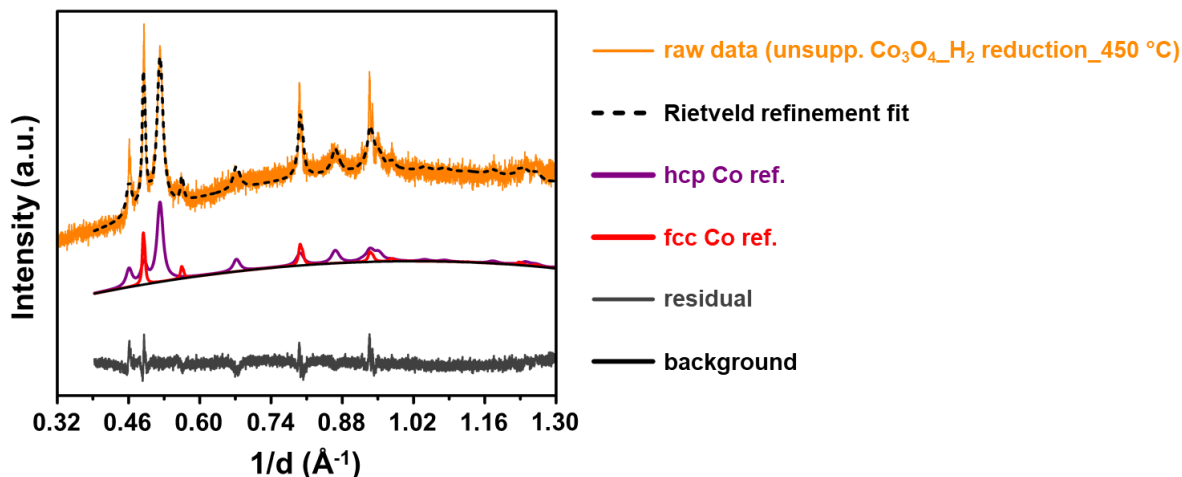


**Figure A.5.1:** Results obtained after performing Rietveld refinement on the last *in situ* PXRD pattern recorded at 450 °C during the reduction of unsupported  $\text{Co}_3\text{O}_4$  at atmospheric pressure in a 50:50  $\text{H}_2$ : $\text{N}_2$  gas mixture.

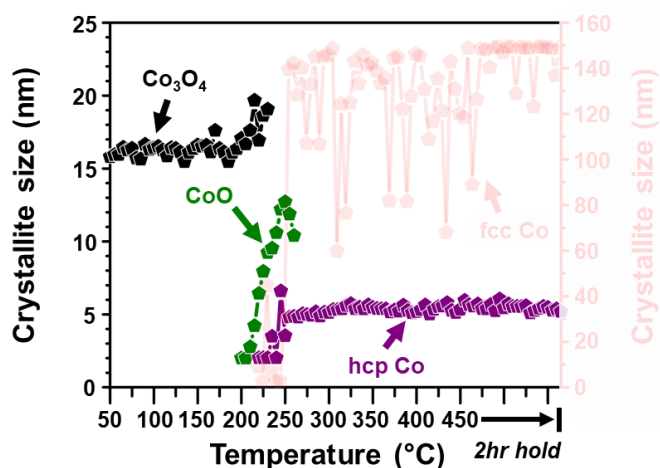


**Figure A.5.2:** Changes in the average crystallite size of the different cobalt phases formed during the reduction of unsupported  $\text{Co}_3\text{O}_4$  at atmospheric pressure in a 1:50:49  $\text{CO}$ : $\text{H}_2$ : $\text{N}_2$  gas mixture. Note that the crystallite sizes for fcc Co (see transparent red plot and y-axis) may not bear significant physical meaning due to granularity effects and/or intergrowth of hcp and fcc Co.

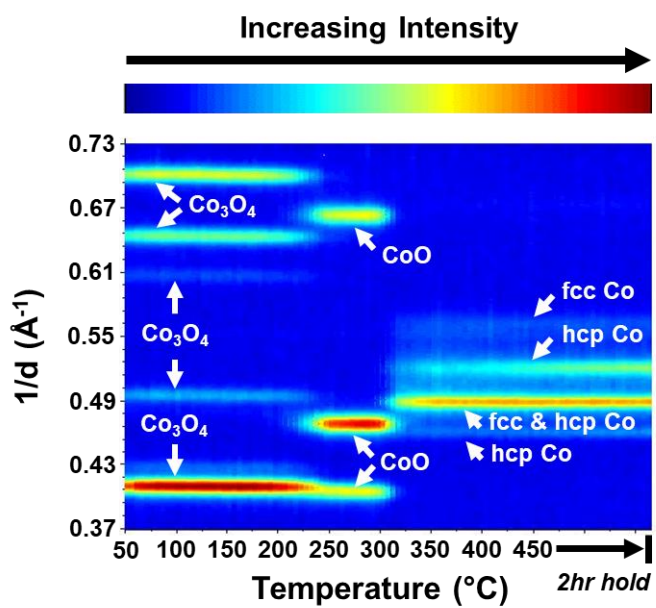


**Figure A.5.3:** On-top view of the *in situ* PXRD patterns recorded during the reduction of unsupported  $\text{Co}_3\text{O}_4$  at atmospheric pressure in a 1:99  $\text{CO}:\text{N}_2$  gas mixture.

**Table A.5.1:** Summary of the Rietveld refinement results performed on the last *in situ* PXRD pattern (*i.e.*, at 450 °C) recorded during reduction at atmospheric pressure in a 50:50 H<sub>2</sub>:N<sub>2</sub> mixture.

Sample name	CoO (wt.-%)	d <sub>CoO</sub> at 450 °C (nm)	hcp Co (wt.-%)	d <sub>hcp Co</sub> at 450 °C (nm)	fcc Co (wt.-%)	d <sub>fcc Co</sub> at 450 °C (nm)
unsupported Co <sub>3</sub> O <sub>4</sub>	-	-	81.9 ± 0.8	10.1 ± 0.4	18.1 ± 0.8	n/a
Co <sub>3</sub> O <sub>4</sub> /ZrO <sub>2</sub>	-	-	-	-	100.0 ± 0.0	7.8 ± 1.0
Co <sub>3</sub> O <sub>4</sub> /SiC	-	-	-	-	100.0 ± 0.0	12.1 ± 1.3
Co <sub>3</sub> O <sub>4</sub> /SiO <sub>2</sub>	-	-	-	-	100.0 ± 0.0	17.4 ± 5.0
Co <sub>3</sub> O <sub>4</sub> /TiO <sub>2</sub> -anatase	-	-	64.1 ± 11.4	5.8 ± 1.6	35.9 ± 4.5	23.0 ± 5.2
Co <sub>3</sub> O <sub>4</sub> /TiO <sub>2</sub> -rutile	-	-	-	-	100.0 ± 0.0	10.6 ± 1.8
Co <sub>3</sub> O <sub>4</sub> /TiO <sub>2</sub> -P25	-	-	71.5 ± 15.1	6.8 ± 1.6	28.5 ± 4.0	20.5 ± 5.2
Co <sub>3</sub> O <sub>4</sub> /Al <sub>2</sub> O <sub>3</sub>	100.0 ± 0.0*	7.4 ± 0.8	-	-	-	-

\* metallic Co might also be present but in very small (undetectable) amounts as the reflections from CoO in Figure 6.6(h) decrease in intensity above 350 °C.

**Table A.5.2:** Summary of the Rietveld refinement results performed on the last *in situ* PXRD pattern (*i.e.*, at 450 °C) recorded under different reduction conditions at atmospheric pressure over unsupported Co<sub>3</sub>O<sub>4</sub>.

<b>Condition</b>	<b>hcp Co (wt.-%)</b>	<b>d<sub>hcp Co</sub> at 450 °C (nm)</b>	<b>fcc Co (wt.-%)</b>
50:50 H <sub>2</sub> :N <sub>2</sub>	81.9 ± 0.8	10.1 ± 0.4	18.1 ± 0.8
1:50:49 CO <sub>2</sub> :H <sub>2</sub> :N <sub>2</sub>	72.2 ± 6.6	7.4 ± 0.3	27.8 ± 6.6
1:50:49 CO:H <sub>2</sub> :N <sub>2</sub>	75.0 ± 0.8	5.9 ± 0.3	25.0 ± 0.8
1:50:49 H <sub>2</sub> O:H <sub>2</sub> :N <sub>2</sub>	71.4 ± 1.2	5.4 ± 0.3	28.6 ± 1.2
1:50:49 O <sub>2</sub> :H <sub>2</sub> :N <sub>2</sub>	72.0 ± 5.4	9.2 ± 0.4	28.0 ± 5.4
10:50:40 CO <sub>2</sub> :H <sub>2</sub> :N <sub>2</sub>	71.0 ± 1.7	5.3 ± 0.2	29.0 ± 1.7
10:50:40 H <sub>2</sub> O:H <sub>2</sub> :N <sub>2</sub>	73.6 ± 1.1	5.1 ± 0.3	26.4 ± 1.1
WGSR	53.1 ± 10.0	5.7 ± 0.3	46.9 ± 10.0

## A.6. Example of *in situ* PXRD-based GC-TCD Data

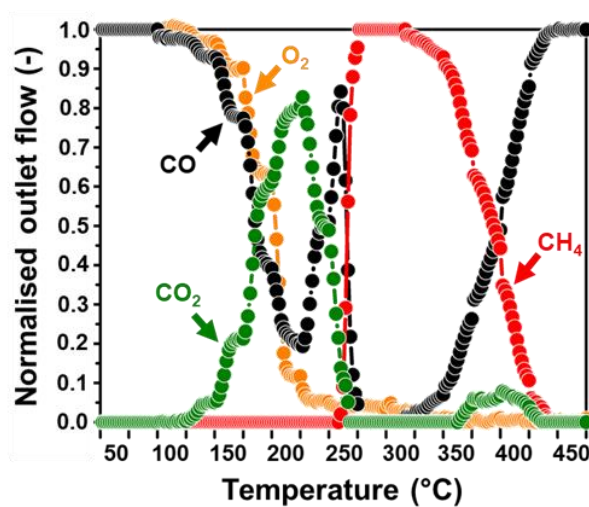


**Figure A.6.1:** Normalised outlet flow rates of CO, O<sub>2</sub>, CO<sub>2</sub> and CH<sub>4</sub> calculated from the GC-TCD data obtained during dry CO-PrOx over unsupported Co<sub>3</sub>O<sub>4</sub> in the *in situ* PXRD cell. (Feed composition: 1% CO, 1% O<sub>2</sub>, 50% H<sub>2</sub> and 48% N<sub>2</sub>; pressure: atmospheric, GHSV: 60000 mL(NTP)/g<sub>Co<sub>3</sub>O<sub>4</sub></sub>/hr).

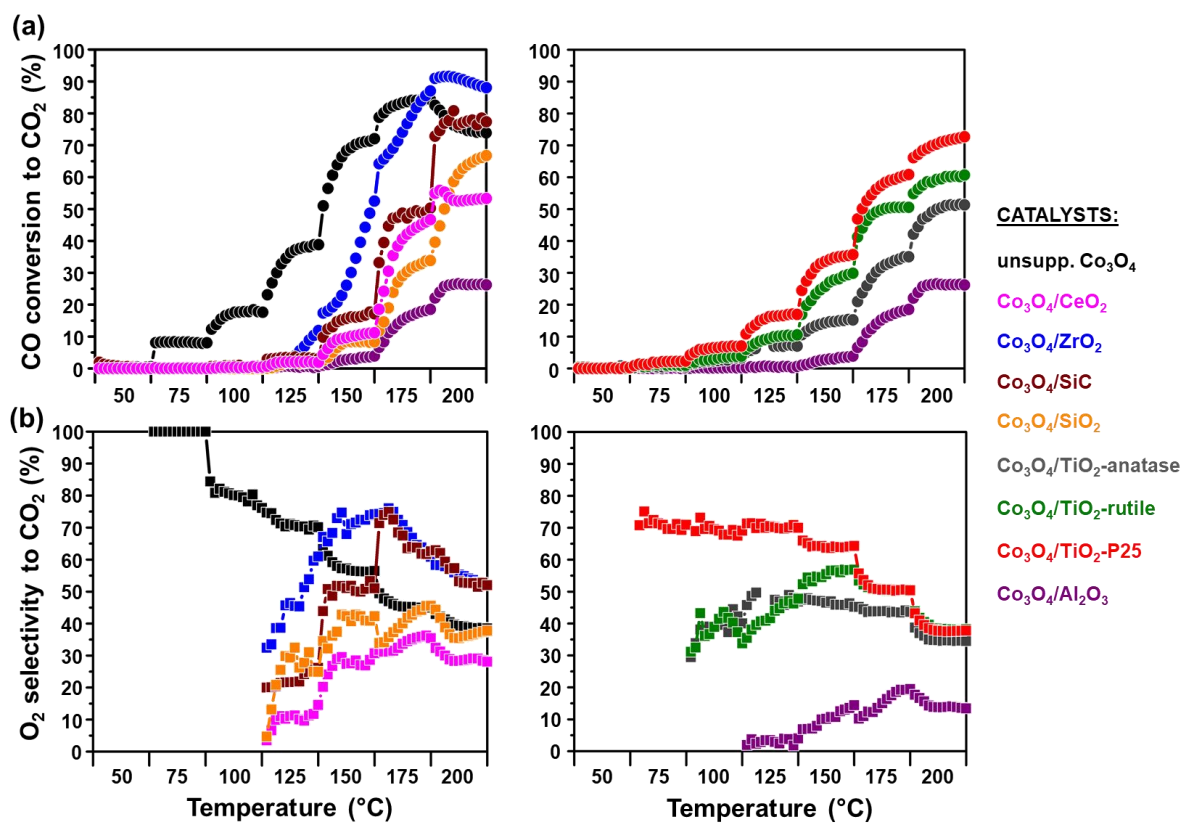


**Figure A.6.2:** Changes in the (a) CO conversion, and (b) O<sub>2</sub> selectivity to CO<sub>2</sub> via oxidation during dry CO-PrOx over all prepared catalysts. Note that the O<sub>2</sub> selectivity to CO<sub>2</sub> was calculated at temperatures where both CO and O<sub>2</sub> were converted (see Figures 8.3 – 8.6). (Feed composition: 1% CO, 1% O<sub>2</sub>, 50% H<sub>2</sub> and 48% N<sub>2</sub>; pressure: atmospheric, GHSV: 60000 mL(NTP)/g<sub>Co<sub>3</sub>O<sub>4</sub></sub>/hr).

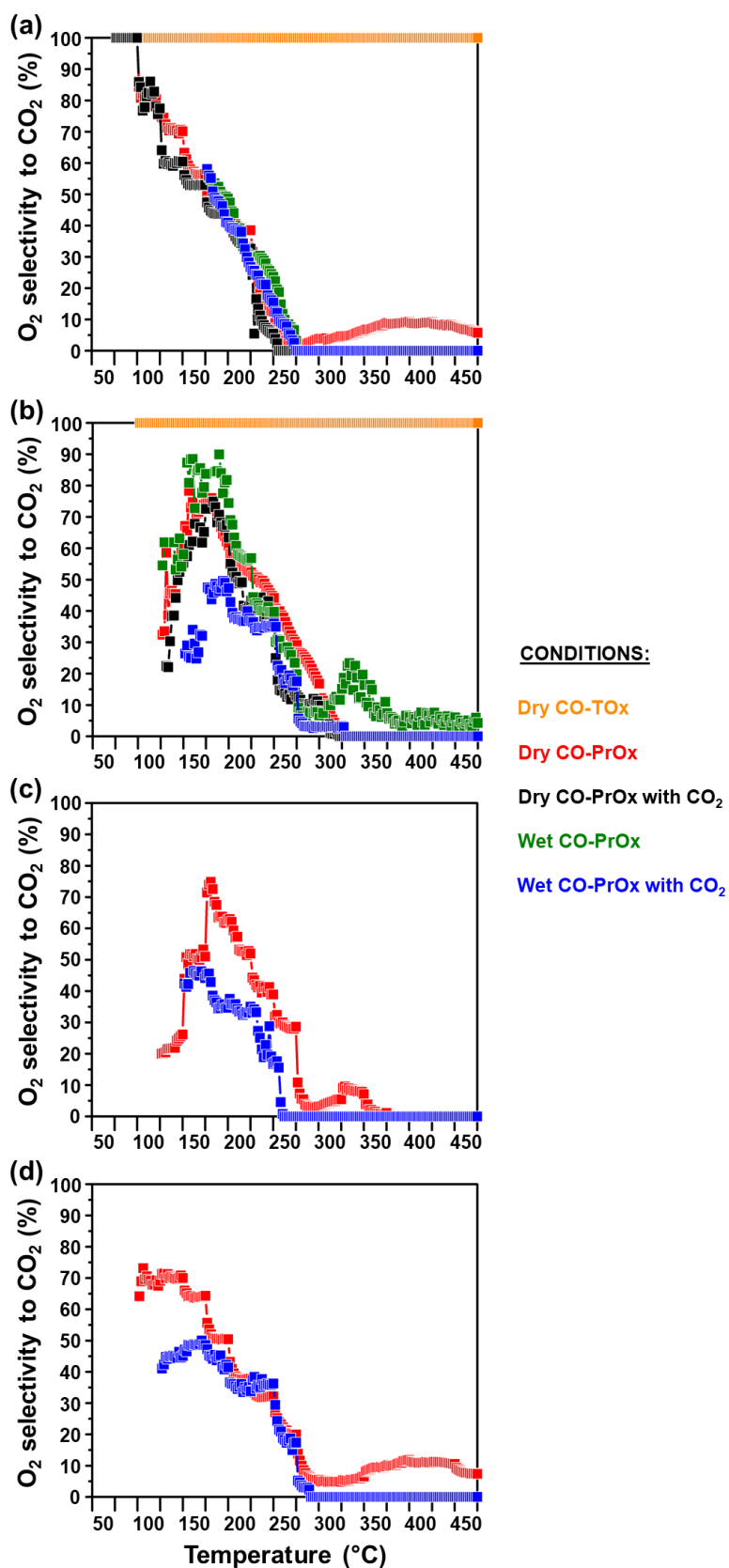


**Figure A.6.3:** Changes in the  $\text{O}_2$  selectivity to  $\text{CO}_2$  under different CO-PrOx conditions at atmospheric pressure and as a function of temperature over (a) unsupported  $\text{Co}_3\text{O}_4$ , (b)  $\text{Co}_3\text{O}_4/\text{ZrO}_2$ , (c)  $\text{Co}_3\text{O}_4/\text{SiC}$ , and (d)  $\text{Co}_3\text{O}_4/\text{TiO}_2\text{-P25}$ .

## A.7. *In situ* PXRD Patterns Recorded under Different CO-PrOx Conditions and Results from Rietveld Refinement

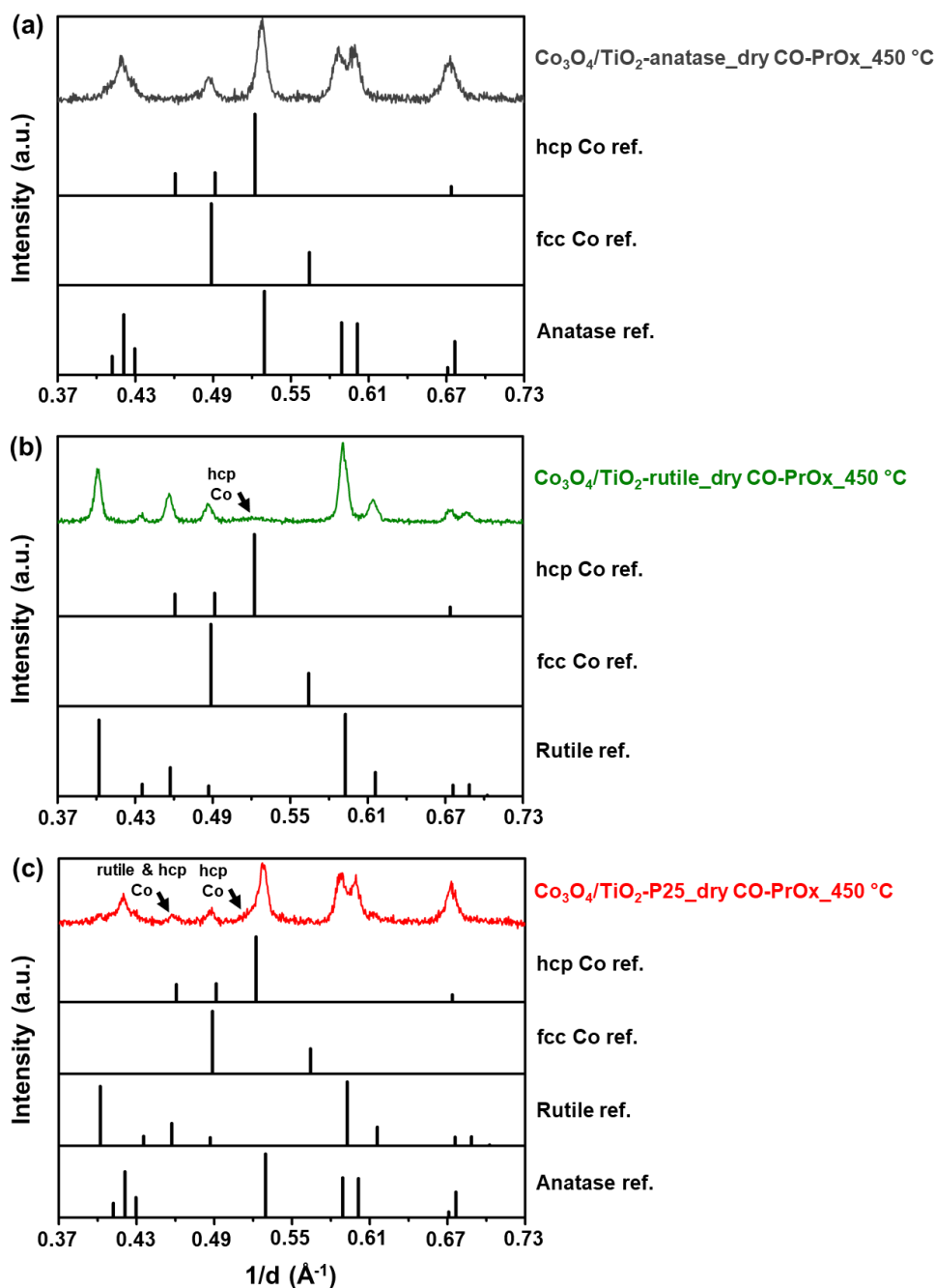


**Figure A.7.1:** *In situ* PXRD patterns of (a)  $\text{Co}_3\text{O}_4/\text{TiO}_2\text{-anatase}$ , (b)  $\text{Co}_3\text{O}_4/\text{TiO}_2\text{-Rutile}$ , and (c)  $\text{Co}_3\text{O}_4/\text{TiO}_2\text{-P25}$  recorded at 450 °C during dry CO-PrOx. The reference reflection lines of hcp and fcc Co, as well as  $\text{TiO}_2\text{-anatase}$  and  $\text{-rutile}$  are also included. See the black arrows in (b) and (c) indicating hcp Co reflections. (Feed composition: 1% CO, 1%  $\text{O}_2$ , 50%  $\text{H}_2$  and 48%  $\text{N}_2$ ; pressure: atmospheric, GHSV: 60000 mL(NTP)/g $\text{Co}_3\text{O}_4$ /hr).

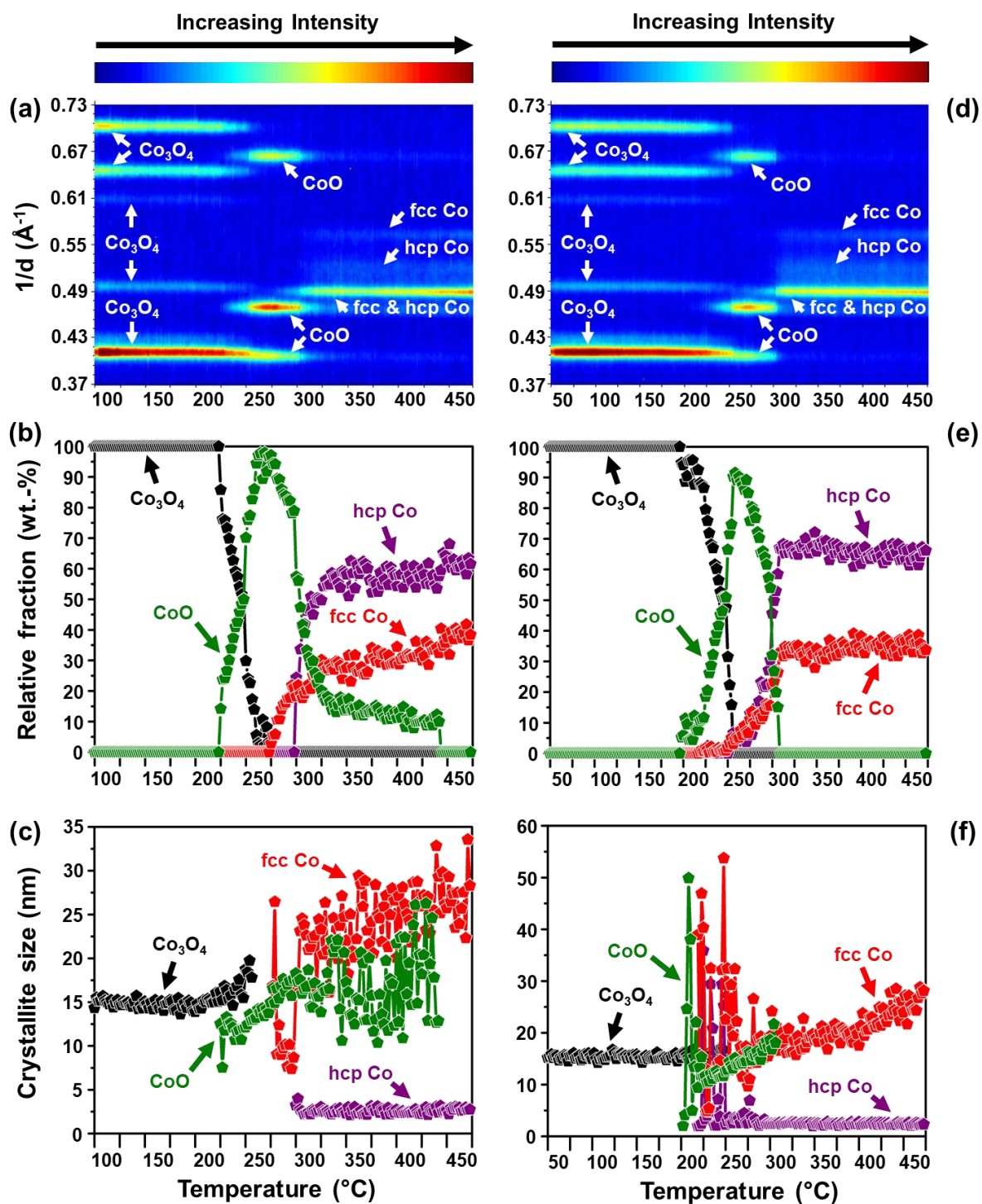


**Figure A.7.2:** ((a) and (d)) On-top view of the PXRD patterns recorded as a function of temperature during (left) wet CO-PrOx, and (right) dry CO-PrOx with co-fed CO<sub>2</sub> at atmospheric pressure. ((b) and (e)) Changes in the relative fraction, and ((c) and (f)) average crystallite size of the different cobalt phases formed during the respective reactions.

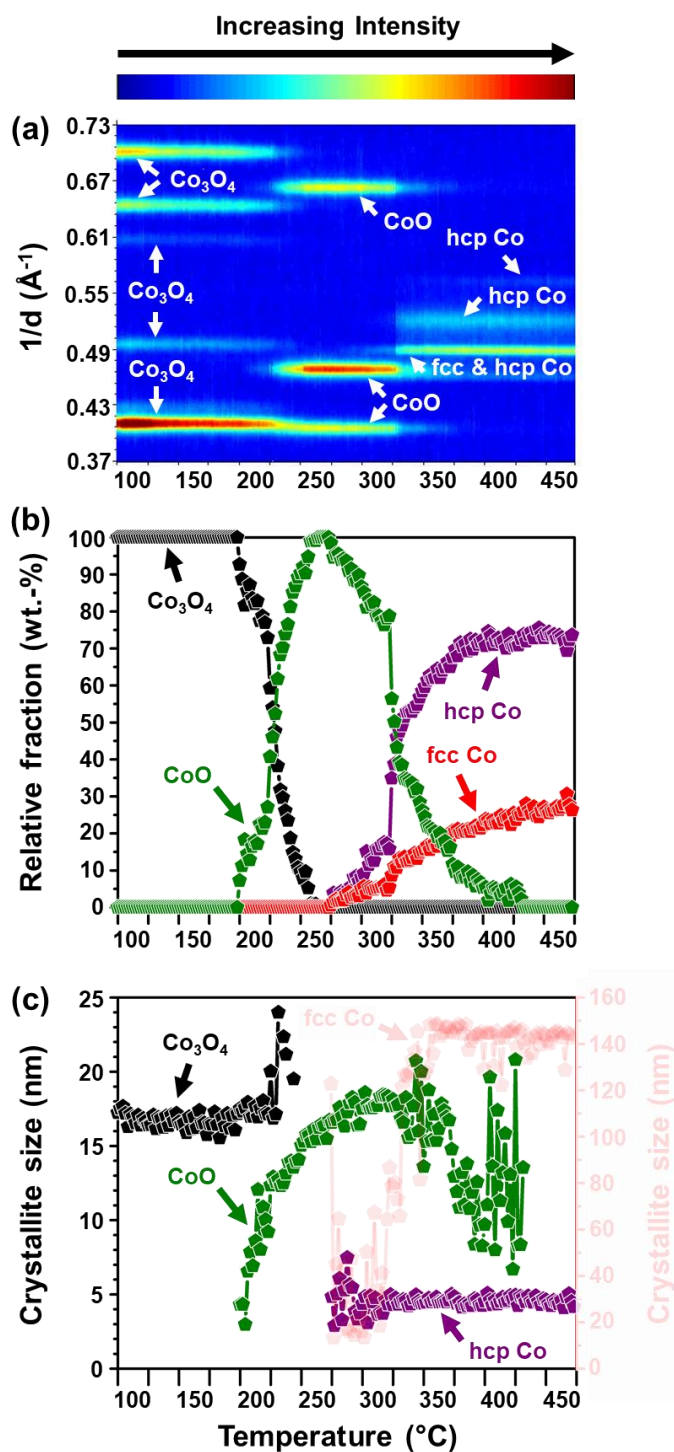


**Figure A.7.3:** (a) On-top view of the PXRD patterns recorded as a function of temperature during wet CO-PrOx with co-fed  $\text{CO}_2$ . (b) Changes in the relative fraction, and (c) average crystallite size of the different cobalt phases formed during the reaction. Note that the crystallite sizes for fcc Co (see transparent red plot and y-axis in (c)) may not bear significant physical meaning due to granularity effects and/or intergrowth of hcp and fcc Co. (Feed composition: 1% CO, 1%  $\text{O}_2$ , 46%  $\text{H}_2$ , 10%  $\text{H}_2\text{O}$ , 9%  $\text{CO}_2$  and 33%  $\text{N}_2$ ; pressure: atmospheric, GHSV: 60000 mL(NTP)/g $\text{Co}_3\text{O}_4$ /hr).

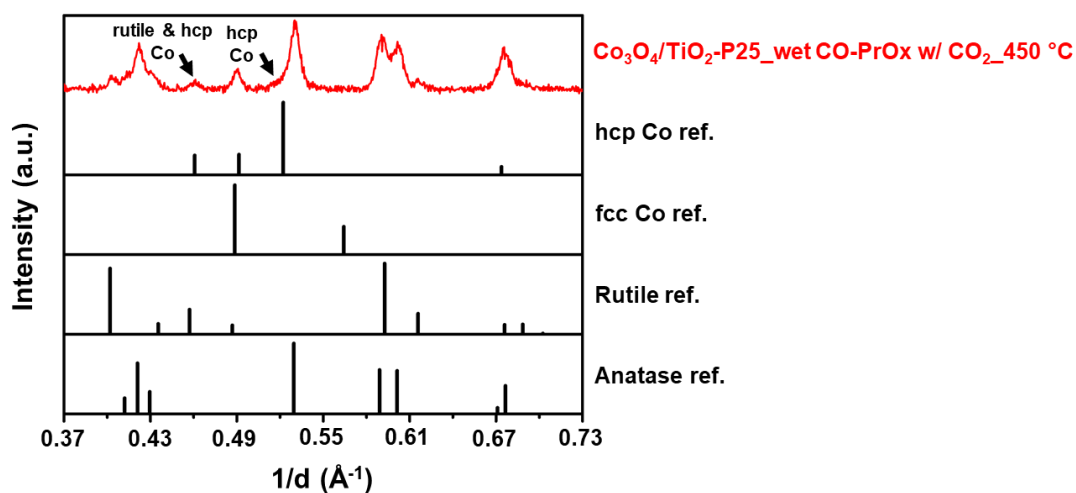


**Figure A.7.4:** *In situ* PXRD pattern of  $\text{Co}_3\text{O}_4/\text{TiO}_2\text{-P25}$  recorded at  $450\text{ }^\circ\text{C}$  during wet CO-PrOx with co-fed  $\text{CO}_2$ . The reference reflection lines of hcp and fcc Co, as well as  $\text{TiO}_2$ -anatase and -rutile are also included. See the black arrows indicating hcp Co reflections. (Feed composition: 1% CO, 1%  $\text{O}_2$ , 46%  $\text{H}_2$ , 10%  $\text{H}_2\text{O}$ , 9%  $\text{CO}_2$  and 33%  $\text{N}_2$ ; pressure: atmospheric, GHSV:  $60000\text{ mL(NTP)/g}_{\text{Co}_3\text{O}_4}/\text{hr}$ ).

**Table A.7.1:** Summary of the Rietveld refinement results performed on the last *in situ* PXRD pattern (*i.e.*, at 450 °C) recorded under different CO-PrOx conditions at atmospheric pressure over selected catalysts.

Sample name	Condition	CoO (wt.-%)	d <sub>CoO</sub> at 450 °C (nm)	hcp Co (wt.-%)	d <sub>hcp Co</sub> at 450 °C (nm)	fcc Co (wt.-%)	d <sub>fcc Co</sub> at 450 °C (nm)
unsupported Co <sub>3</sub> O <sub>4</sub>	dry PrOx	-	-	78.3 ± 0.8	4.6 ± 0.2	21.7 ± 0.8	n/a
	wet PrOx	-	-	61.6 ± 2.2	2.7 ± 0.3	38.4 ± 2.2	26.8 ± 3.3
	dry PrOx+CO <sub>2</sub>	-	-	66.2 ± 2.1	2.3 ± 0.2	33.8 ± 2.1	25.8 ± 2.8
	wet PrOx+CO <sub>2</sub>	-	-	73.6 ± 1.2	4.2 ± 0.3	26.4 ± 1.2	n/a
Co <sub>3</sub> O <sub>4</sub> /ZrO <sub>2</sub>	dry PrOx	-	-	-	-	100.0 ± 0.0	21.2 ± 9.0
	wet PrOx	-	-	-	-	100.0 ± 0.0	40.3 ± 19.9
	dry PrOx+CO <sub>2</sub>	-	-	-	-	100.0 ± 0.0	35.9 ± 13.4
	wet PrOx+CO <sub>2</sub>	-	-	-	-	100.0 ± 0.0	60.8 ± 24.1
Co <sub>3</sub> O <sub>4</sub> /SiC	dry PrOx	71.7 ± 16.5	12.7 ± 4.5	-	-	28.3 ± 6.6	10.3 ± 3.0
	wet PrOx+CO <sub>2</sub>	100.0 ± 0.0*	9.7 ± 1.7	-	-	-	-
Co <sub>3</sub> O <sub>4</sub> /TiO <sub>2</sub> -P25	dry PrOx	-	-	83.4 ± 16.9	11.5 ± 3.2	16.6 ± 3.9	-
	wet PrOx+CO <sub>2</sub>	-	-	68.0 ± 7.9	15.5 ± 3.7	32.0 ± 3.2	-
Co <sub>3</sub> O <sub>4</sub> /SiO <sub>2</sub>	dry PrOx	73.3 ± 6.7	7.2 ± 1.7	-	-	26.7 ± 6.7	11.7 ± 5.5
Co <sub>3</sub> O <sub>4</sub> /TiO <sub>2</sub> -anatase		-	-	-	-	100.0 ± 0.0	20.5 ± 3.4
Co <sub>3</sub> O <sub>4</sub> /TiO <sub>2</sub> -rutile		-	-	72.1 ± 7.6	6.3 ± 0.9	27.9 ± 2.9	28.9 ± 8.8
Co <sub>3</sub> O <sub>4</sub> /Al <sub>2</sub> O <sub>3</sub>		100.0 ± 0.0*	7.8 ± 0.8	-	-	-	-

\* metallic Co might also be present but in very small (undetectable) amounts as the reflections from CoO in Figure 8.6((a), *right*) decrease in intensity at 450 °C.

## A.8. STEM Micrographs and EELS Maps

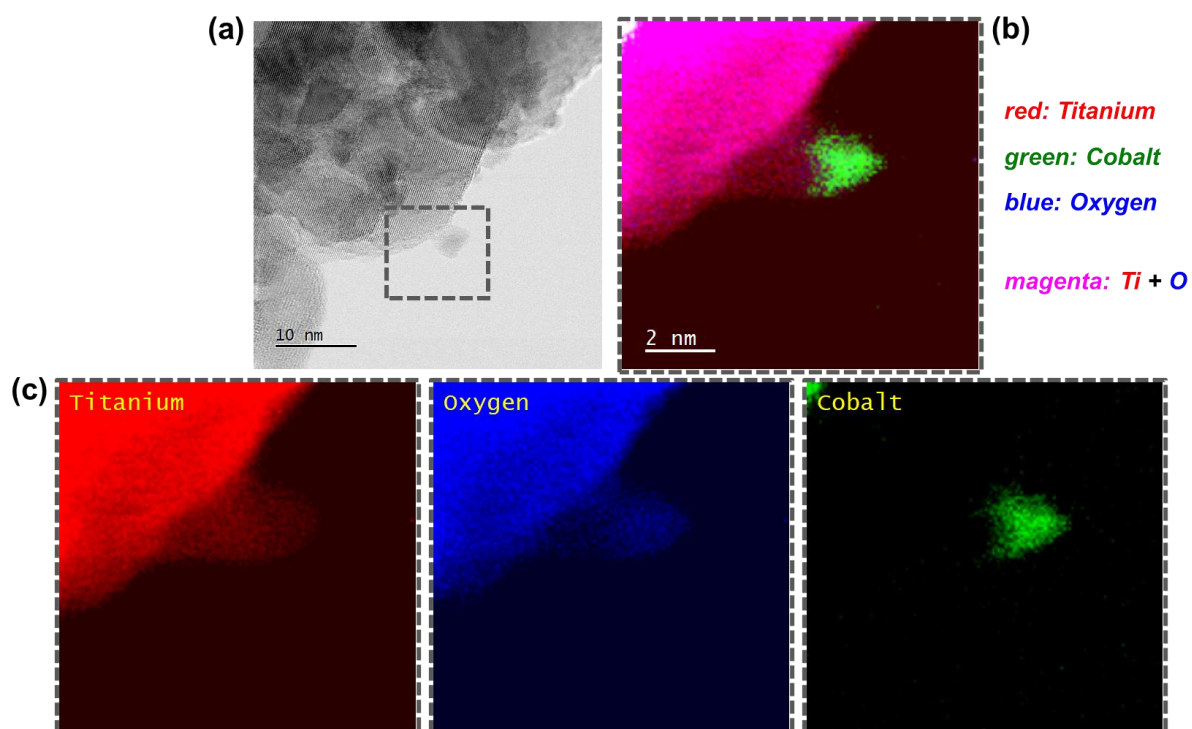


**Figure A.8.1:** (a) Bright-field STEM image of the spent  $\text{Co}_3\text{O}_4/\text{TiO}_2$ -anatase catalyst obtained after dry CO-PrOx. (b) Magnified STEM-EELS elemental map showing the regions with Ti, O and Co. (c) Corresponding magnified STEM-EELS maps of the individual elements.

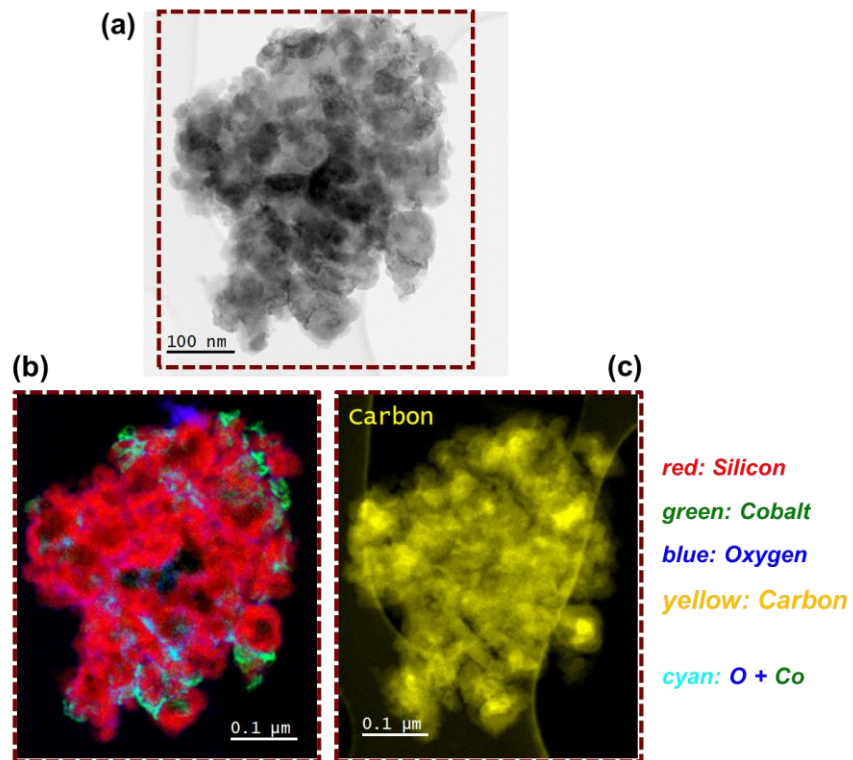


**Figure A.8.2:** (a) Bright-field STEM image of the spent  $\text{Co}_3\text{O}_4/\text{SiC}$  catalyst after dry CO-PrOx. (b) Magnified STEM-EELS elemental map showing the regions with Si, O, Co as well as (c) carbon.

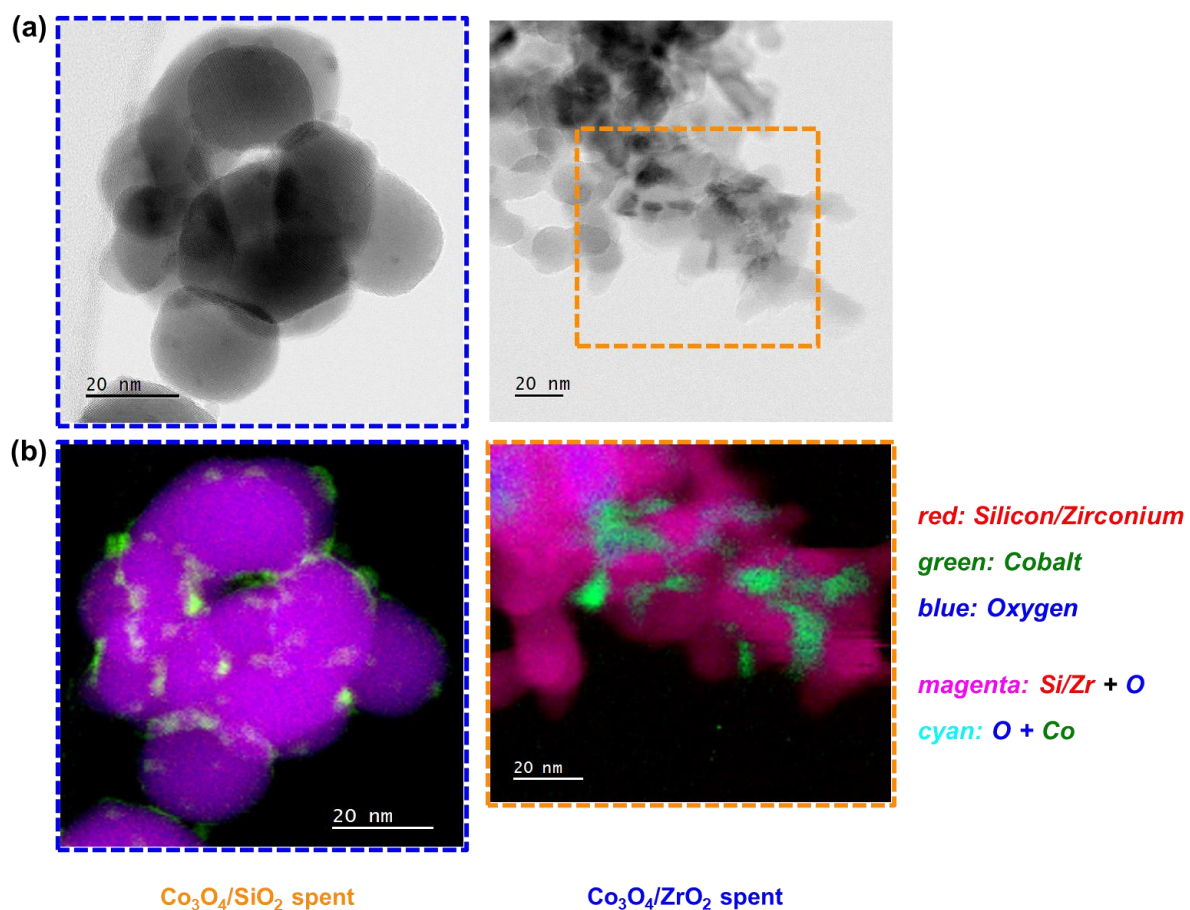


**Figure A.8.3:** (a) Bright-field STEM image of the spent  $\text{Co}_3\text{O}_4/\text{SiO}_2$  and  $\text{Co}_3\text{O}_4/\text{SiO}_2$  catalysts, respectively, obtained after dry CO-PrOx. (b) Magnified STEM-EELS elemental maps showing the regions with the elements Si, Zr, O and Co where applicable.

## A.9. Example of Results from the Linear Combination Fitting of *ex situ* XAS Data

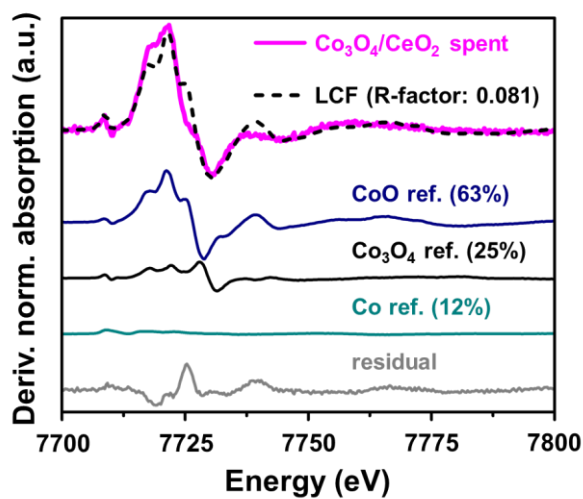


**Figure A.9.1:** Results from after performing a linear combination fitting of the first derivative XANES spectrum of  $\text{Co}_3\text{O}_4/\text{CeO}_2$  obtained after dry CO-PrOx.

## A.10. Curriculum Vitae

### Personal Information

Date and Place of Birth	04 January 1992, Durban, South Africa
Nationality	South African
Languages	IsiZulu, English
Online Profiles	LinkedIn <a href="https://www.linkedin.com/in/thulani-nyathi-ph-d-40977a90/">https://www.linkedin.com/in/thulani-nyathi-ph-d-40977a90/</a> ORCID <a href="https://orcid.org/0000-0002-7684-1258">https://orcid.org/0000-0002-7684-1258</a> ResearchGate <a href="https://www.researchgate.net/profile/Thulani_Nyathi">https://www.researchgate.net/profile/Thulani_Nyathi</a>

### Education

01/2016 – 09/2020	Ph.D. in Chemical Engineering Department of Chemical Engineering, University of Cape Town, South Africa Thesis supervisors: Prof. Michael Claeys and A/Prof. Nico Fischer Thesis title: Supported Cobalt Oxide Catalysts for the Preferential Oxidation of Carbon Monoxide: An <i>in situ</i> Investigation
01/2014 – 12/2015	MSc(Eng) in Chemical Engineering ( <i>awarded with distinction</i> ) Department of Chemical Engineering, University of Cape Town, South Africa Thesis supervisors: Prof. Michael Claeys and A/Prof. Nico Fischer Thesis title: Preferential Oxidation of Carbon Monoxide in Hydrogen-rich Gases over Supported Cobalt Oxide Catalysts
01/2013 – 12/2013	BSc(Hons) in Chemistry Department of Chemistry, University of Cape Town, South Africa Mini-thesis supervisors: Prof. Roger Hunter and A/Prof. David Gammon Mini-thesis title: Exploring a Possible Route Towards the Synthesis of New Carbohydrate-based Organocatalysts
02/2010 – 12/2012	BSc in Chemistry and Biochemistry Faculty of Science, University of Cape Town, South Africa
01/2005 – 12/2009	National Senior Certificate (Matriculation) Brettonwood High School, Durban, South Africa

## Work Experience

09/2020 – present	Postdoctoral Research Fellow Department of Chemical Engineering, University of Cape Town, South Africa
01/2016 – 12/2019	Part-time Research Assistant Department of Chemical Engineering, University of Cape Town, South Africa
02/2013 – 10/2015	First Year Chemistry Demonstrator and Tutor Department of Chemistry, University of Cape Town, South Africa
11/2013 – 12/2013	Vacation Work Student Department of Chemistry, University of Cape Town, South Africa
11/2012 – 01/2013	Vacation Work Student SASOL R&D, Sasolburg, South Africa
11/2011 – 01/2012	Vacation Work Student SASOL R&D, Sasolburg, South Africa

## International Research Travel

04/2018 – 05/2018	Student Visit for Molecular Modelling Department of Chemistry, Cardiff University, Wales, United Kingdom Hosts: Prof. Nora H. de Leeuw and Dr. David Santos-Carballal
07/2017 – 09/2017	Student Visit for Molecular Modelling Department of Chemistry, Cardiff University, Wales, United Kingdom Hosts: Prof. Nora H. de Leeuw and Dr. David Santos-Carballal
06/2017	Standard Synchrotron Beamtime Access for Combined <i>in situ</i> XAS- DRIFTS Diamond Light Source, Harwell, England, United Kingdom Hosts: Prof. C. Richard A. Catlow and Dr. Emma K. Gibson
11/2016	Student Visit for X-Ray Photoelectron Spectroscopy Department of Chemistry, Cardiff University, Wales, United Kingdom Hosts: Prof. Graham J. Hutchings and Dr. David J. Morgan
10/2015	Student Visit for X-Ray Photoelectron Spectroscopy Department of Chemistry, Cardiff University, Wales, United Kingdom Hosts: Prof. Graham J. Hutchings and Dr. David J. Morgan

## Awards, Scholarships and Grants

09/2020 – present	GCRF-START Postdoctoral Research Fellowship University of Cape Town, South Africa, and the Science & Technology Facilities Council, United Kingdom
04/2018	Student Oral Presentation Runner-up Johnson Matthey Academic Conference, Loughborough, England, United Kingdom
01/2017 – 12/2019	Innovation Doctoral Scholarship National Research Foundation (NRF), South Africa
01/2017	International Conference Travel Grant Catalysis Society of South Africa (CATSA)
11/2015	Clariant Best Student Oral Presentation Award 26 <sup>th</sup> Annual Conference of the Catalysis Society of South Africa Arabella Hotel & Spa, Hermanus, South Africa
01/2014 – 08/2020	Postgraduate Bursary DSI-NRF Centre of Excellence in Catalysis (c*change)
01/2014 – 12/2019	Postgraduate Studentship Johnson Matthey p.l.c., United Kingdom
01/2014 – 12/2015	Scarce Skills Masters Scholarship National Research Foundation (NRF), South Africa
02/2010 – 12/2013	Undergraduate Bursary SASOL LTD, South Africa
12/2009	Dux Award Brettonwood High School, Durban, South Africa

## A.11. List of Publications

### Publications from the Ph.D. Thesis

- 1) Environment-dependent catalytic performance and phase stability of  $\text{Co}_3\text{O}_4$  in the preferential oxidation of carbon monoxide studied *in situ*.  
T.M. Nyathi, N. Fischer, A.P.E. York, M. Claeys, ACS Catal. 10 (2020) 11892–11911. DOI: [10.1021/acscatal.0c02653](https://doi.org/10.1021/acscatal.0c02653).
- 2) Support and gas environment effects on the preferential oxidation of carbon monoxide over  $\text{Co}_3\text{O}_4$  catalysts studied *in situ*. [in submission].
- 3)  $\text{Co}_3\text{O}_4/\text{TiO}_2$  catalysts for the preferential oxidation of carbon monoxide: Effect of the crystalline phase of  $\text{TiO}_2$  studied *in situ*. [in preparation].
- 4) Preferential oxidation of carbon monoxide over unsupported and  $\text{ZrO}_2$ -supported  $\text{Co}_3\text{O}_4$  nanoparticles: An *in situ* investigation into the reduction mechanism of  $\text{Co}_3\text{O}_4$ . [in preparation].

### Other Publications (including collaborations)

- 1) Enhanced oxygenates formation in the Fischer-Tropsch synthesis over Co- and/or Ni-Containing Fe alloys: Characterization and 2D gas chromatographic product analysis.  
M.I. Fadlalla, S. Ganesh Babu, T.M. Nyathi, C.J. Kees-Jan Weststrate, N. Fischer, J.W. Hans Niemantsverdriet, M. Claeys, ACS Catal. 10 (2020) 14661–14677. DOI: [10.1021/acscatal.0c03346](https://doi.org/10.1021/acscatal.0c03346).
- 2) Impact of nanoparticle–support interactions in  $\text{Co}_3\text{O}_4/\text{Al}_2\text{O}_3$  catalysts for the preferential oxidation of carbon monoxide.  
T.M. Nyathi, N. Fischer, A.P.E. York, D.J. Morgan, G.J. Hutchings, E.K. Gibson, P.P. Wells, C.R.A. Catlow, M. Claeys, ACS Catal. 9 (2019) 7166–7178. DOI: [10.1021/acscatal.9b00685](https://doi.org/10.1021/acscatal.9b00685).
- 3)  $\text{Co}_3\text{O}_4$  morphology in the preferential oxidation of CO.  
M. Khasu, T. Nyathi, D.J. Morgan, G.J. Hutchings, M. Claeys, N. Fischer, Catal. Sci. Technol. 7 (2017) 4806–4817. DOI: [10.1039/C7CY01194F](https://doi.org/10.1039/C7CY01194F).
- 4) Effect of crystallite size on the performance and phase transformation of  $\text{Co}_3\text{O}_4/\text{Al}_2\text{O}_3$  catalysts during CO-PrOx - An *in situ* study.  
T.M. Nyathi, N. Fischer, A.P.E. York, M. Claeys, Faraday Discuss. 197 (2017) 269–285. DOI: [10.1039/c6fd00217j](https://doi.org/10.1039/c6fd00217j).

## A.12. List of Conference Contributions

### Orals

#### 2019

- 1) Gas environment & support effects on the  $\text{Co}_3\text{O}_4$ -catalysed CO-PrOx reaction: An *in situ* PXRD & magnetometry study.  
T.M. Nyathi, N. Fischer, A.P.E. York, M. Claeys  
*Johnson Matthey Academic Meeting*  
*Farm-inn Hotel, Pretoria, South Africa*
- 2) An *in situ* study on the preferential oxidation of CO over unsupported  $\text{Co}_3\text{O}_4$ : Effect of co-fed  $\text{H}_2$ ,  $\text{H}_2\text{O}$  and  $\text{CO}_2$ .  
T.M. Nyathi, N. Fischer, A.P.E. York, M. Claeys  
*30<sup>th</sup> Annual Conference of the Catalysis Society of South Africa (CATSA)*  
*Club Mykonos Resort, Langebaan, South Africa*
- 3) An *in situ* study on the preferential oxidation of CO over unsupported  $\text{Co}_3\text{O}_4$ : Effect of co-fed  $\text{H}_2$ ,  $\text{H}_2\text{O}$  and  $\text{CO}_2$ .  
T.M. Nyathi, N. Fischer, A.P.E. York, M. Claeys  
*DST-NRF Centre of Excellence in Catalysis (c\*change) Symposium*  
*Krystal Beach Hotel, Gordon's Bay, South Africa*
- 4) Environment-dependent phase stability of  $\text{Co}_3\text{O}_4$ : An experimental and computational approach.  
T.M. Nyathi, N. Fischer, A.P.E. York, E.K. Gibson, P.P. Wells, C.R.A. Catlow, A. Cadi-Essadek, D. Santos-Carballal, N.H. de Leeuw, M. Claeys  
*Closing Conference for ESRC/NRF-funded Newton Project for UK-RSA Ph.D. Exchanges*  
*North-West University, Potchefstroom, South Africa*

#### 2018

- 1) Effect of nanoparticle-support interactions during CO-PrOx over  $\text{Co}_3\text{O}_4/\text{Al}_2\text{O}_3$ : An *in situ* study.  
T.M. Nyathi, N. Fischer, A.P.E. York, E.K. Gibson, P.P. Wells, C.R.A. Catlow, M. Claeys  
*Johnson Matthey Academic Meeting*  
*Council for Scientific and Industrial Research (CSIR), Pretoria, South Africa*

- 2) Effect of nanoparticle-support interactions during CO-PrOx over  $\text{Co}_3\text{O}_4/\text{Al}_2\text{O}_3$ : An *in situ* XAS study.  
T.M. Nyathi, N. Fischer, A.P.E. York, E.K. Gibson, P.P. Wells, C.R.A. Catlow, M. Claeys  
*DST-NRF Centre of Excellence in Catalysis (c\*change) Symposium*  
*Shangri-La Country Hotel & Spa, Modimolle, South Africa*
- 3) Support effects on the  $\text{Co}_3\text{O}_4$ -catalysed dry CO-PrOx: An *in situ* PXRD & magnetometry study.  
T.M. Nyathi, N. Fischer, A.P.E. York, M. Claeys  
*Johnson Matthey Academic Conference*  
*Loughborough University, Loughborough, United Kingdom*
- 4) Support effects on the  $\text{Co}_3\text{O}_4$ -catalysed dry CO-PrOx: An *in situ* PXRD & magnetometry study.  
T.M. Nyathi, N. Fischer, A.P.E. York, M. Claeys  
*Syngas Convention - Fuels and Chemicals from Synthesis Gas: State of the Art 3*  
*Vineyard Hotel, Cape Town, South Africa*

## 2017

- 1) Effect of the support and different gas environments on  $\text{Co}_3\text{O}_4$  reduction: An *in situ* PXRD study.  
T.M. Nyathi, N. Fischer, A.P.E. York, M. Claeys  
*Johnson Matthey Academic Meeting*  
*Farm-inn Hotel, Pretoria, South Africa*
- 2) Effect of the support and different gas environments on  $\text{Co}_3\text{O}_4$  reduction: An *in situ* PXRD study.  
T.M. Nyathi, N. Fischer, A.P.E. York, M. Claeys  
*DST-NRF Centre of Excellence in Catalysis (c\*change) Symposium*  
*Shumba Valley Lodge, Lanseria, South Africa*
- 3) Effect of crystallite size on the performance and phase transformation of  $\text{Co}_3\text{O}_4/\text{Al}_2\text{O}_3$  catalysts during CO-PrOx: An *in situ* study  
T.M. Nyathi, N. Fischer, A.P.E. York, M. Claeys  
*Faraday Discussions: Catalysis for Fuels*  
*Lagoon Beach Hotel & Spa, Cape Town, South Africa*

**2016**

- 1) Effect of metal-support interactions on the preferential oxidation of CO over  $\text{Co}_3\text{O}_4/\text{Al}_2\text{O}_3$  catalysts.  
T.M. Nyathi, N. Fischer, A.P.E. York, M. Claeys  
*27<sup>th</sup> Annual Conference of the Catalysis Society of South Africa (CATSA)*  
*Champagne Sports Resort, Drakensberg, South Africa*
- 2) An *in situ* study on the preferential oxidation of CO in  $\text{H}_2$ -rich gases over supported  $\text{Co}_3\text{O}_4$  catalysts.  
T.M. Nyathi, N. Fischer, A.P.E. York, M. Claeys  
*DST-NRF Centre of Excellence in Catalysis (c\*change) Symposium*  
*Champagne Sports Resort, Drakensberg, South Africa*
- 3) An *in situ* study on the preferential oxidation of CO in  $\text{H}_2$ -rich gases over supported  $\text{Co}_3\text{O}_4$  catalysts.  
T.M. Nyathi, N. Fischer, A.P.E. York, M. Claeys  
*Johnson Matthey Academic Meeting*  
*Council for Scientific and Industrial Research (CSIR), Pretoria, South Africa*

**Posters****2019**

- 1) Environment-dependent redox behaviour of the low Miller index facets of  $\text{Co}_3\text{O}_4$ : A DFT investigation.  
T.M. Nyathi, D. Santos-Carballal, A. Cadi-Essadek, M. Claeys, N.H. de Leeuw  
*Closing Conference for ESRC/NRF-funded Newton Project for UK-RSA Ph.D. Exchanges*  
*North-West University, Potchefstroom, South Africa*

**2018**

- 1) Effect of nanoparticle-support interactions (NPSI) on CO-PrOx over  $\text{Co}_3\text{O}_4/\text{Al}_2\text{O}_3$  catalysts: An *in situ* study  
T.M. Nyathi, N. Fischer, A.P.E. York, E.K. Gibson, P.P. Wells, C.R.A. Catlow, M. Claeys  
*29<sup>th</sup> Annual Conference of the Catalysis Society of South Africa (CATSA)*  
*Legend Golf & Safari Resort, Sterkrivier, South Africa*
- 2) Effect of nanoparticle-support interactions (NPSI) on CO-PrOx over  $\text{Co}_3\text{O}_4/\text{Al}_2\text{O}_3$  catalysts: An *in situ* study.  
T.M. Nyathi, N. Fischer, A.P.E. York, D.J. Morgan, G.J. Hutchings, M. Claeys  
*Syngas Convention - Fuels and Chemicals from Synthesis Gas: State of the Art 3*  
*Vineyard Hotel, Cape Town, South Africa*

**2017**

- 1) Effect of the support and gas environment on the reduction of  $\text{Co}_3\text{O}_4$ : An *in situ* PXRD study.

T.M. Nyathi, N. Fischer, A.P.E. York, M. Claeys

*28<sup>th</sup> Annual Conference of the Catalysis Society of South Africa (CATSA)*

*Kwa Maritane Bush Lodge, Pilanesberg, South Africa*

- 2) Effect of metal-support interactions during CO-PrOx over  $\text{Co}_3\text{O}_4/\text{Al}_2\text{O}_3$  catalysts: An *in situ* study.

T.M. Nyathi, N. Fischer, A.P.E. York, M. Claeys

*Faraday Discussions: Catalysis for Fuels*

*Lagoon Beach Hotel & Spa, Cape Town, South Africa*

*“Be grateful for the rocks life rolls in your path, for one day, you will see them as stepping-stones.”*

*Edward Leonard O’Neill*